



**Universidade do Minho**

I3Bs - Instituto de Investigação em Biomateriais, Biodegradáveis e Biomiméticos

Novel cork-based compounds for biomedical applications:  
from antibacterials to themodulation of neurodegeneration

Ana Rita Rodrigues Araújo

**Novel cork-based compounds for biomedical  
applications: from antibacterials to the  
modulation of neurodegeneration**



UMinho | 2020

Ana Rita Rodrigues Araújo

Junho de 2020





**Universidade do Minho**

I3Bs - Instituto de Investigação em Biomateriais, Biodegradáveis e Biomiméticos

Ana Rita Rodrigues Araújo

**Novel cork-based compounds for biomedical applications: from antibacterials to the modulation of neurodegeneration**

Tese de Doutoramento

Doutoramento em Engenharia de Tecidos, Medicina Regenerativa e Células Estaminais

Trabalho efetuado sob a orientação de

**Doutor Ricardo Alexandre Rodrigues Pires**

**Professor Doutor Rui Luís Gonçalves dos Reis**

Junho 2020

## DIREITOS DE AUTOR E CONDIÇÕES DE UTILIZAÇÃO DO TRABALHO POR TERCEIROS

Este é um trabalho académico que pode ser utilizado por terceiros desde que respeitadas as regras e boas práticas internacionalmente aceites, no que concerne aos direitos de autor e direitos conexos.

Assim, o presente trabalho pode ser utilizado nos termos previstos na licença abaixo indicada.

Caso o utilizador necessite de permissão para poder fazer um uso do trabalho em condições não previstas no licenciamento indicado, deverá contactar o autor, através do RepositóriUM da Universidade do Minho.

*Licença concedida aos utilizadores deste trabalho*



**Atribuição-NãoComercial-SemDerivações**

**CC BY-NC-ND**

<https://creativecommons.org/licenses/by-nc-nd/4.0/>

## ACKNOWLEDGMENTS

I want to start by acknowledging Professor Rui Reis and all the opportunities given to me during all these years. I was able to work in a field that I found to suit me so well; develop my soft skills, learn and have access to everything that my work required. I was also given the chance to participate in several worldwide scientific opportunities, with everything being supported by Professor Rui and his impressive leadership capacities at 3B's.

I would like to acknowledge the funding, specifically the Programa Operacional Regional do Norte (Norte 2020): NORTE-08-5369-FSE-000037 (PhD scholarship) and NORTE-01-0246-FEDER-000022 (Northern Discoveries: The Discoveries CTR – Setting Sails). This work was also supported by the European Commission: FP7-REGPOT-CT2012-316331-POLARIS, H2020-TWINN-2015-692333-CHEM2NATURE, 739572-THE DISCOVERIES CTR and the Portuguese Foundation for Science and Technology (FCT): AL ICVS/3Bs #50026.

Obviously, as all the PhD students in the world, I had to stand against various obstacles that I overcame with persistence, hard work, but more importantly, with the help of people, some of which were determinant for this achievement.

I want to stress the luck that I had to have Doctor Ricardo A. Pires as my super-supervisor. He believed in my capacities more than myself. He literally taught me how to run, especially for the will to be a greater student and scientist, how to be critical with my work and how to be a little more patient (he tried, at least). He became my friend, my mentor, a “pires”, holding all the problems like nobody else. Thank you, I'm grateful.

To Professor Eduardo Fernández-Megía, for receiving me at his lab in CIQUS (Santiago de Compostela), helping me with the synthesis of the Dendrimers (a big challenge for me) and for being always available for scientific discussions. To Juan Correa and all my colleagues in CIQUS lab that make my life easier, they taught a lot about organic chemistry and how to get along with a PhD, in a very Spanish/Galician way. Thank you!

A special acknowledgement to Iva Pashkuleva for the scientific discussions and support, she always shared her knowledge and was available to help me.

To all my co-workers, colleagues and friends in 3B's that taught me something, a technique, a perspective (that is so important in this field), particularly to Ivo Aroso, my first lab trainer at 3B's, thank you. To all the others (there are so many), thanks for sharing your knowledge with me.

I would also like to thank all my 3B's colleagues that heard me complain (I do that a lot) but stayed reliable and by my side regardless all these years, especially to Liliana Gomes and Ana Cristina Araújo – they heard me a lot.

To my lunch crew (Babo, Canadas and Gonçalves), thanks for all the laughing and all the stress-relieving in insane theories, conversations and brainstorming.

My special acknowledgement to my dearest Vivana Ribeiro, for all the given positive viewpoints, practical decisions, support, and motivation. I'm so grateful for our friendship. To my favourite half-desk partner, Sara Amorim, you are the Rock, and I'm the "Amiga". Thanks for all the "total eclipse of the heart" and laughs. For all the support every single day, always with hope and dreams. I know that both of you were always there for me, holding my hand (even when my dramatic diva personality possessed me).

To my Yolo friends, Pedro Silva and Juliana Ramalho, that have always been there, listening to my complaining and fears as well as celebrating with me daily victories, always with smiles, hugs and beer. Thank you, for all the genuine love.

Lastly, my deepest gratitude goes to my family: my lovely mother, father, brothers, nephews and my "half-sisters" and cousins (Marta and Luísa Silva). You are all that I have, and what I am! I know that I have everything that I could wish for: love, care and infinite support. And I know that this thesis is part of each of you too. Thank you for your unconditional love!

I am truly grateful to have my mother in my life. She is my superpower. Everything in life is much easier thanks to her - we did it *Mami*, both of us!

I know that this thesis makes all my friends and family proud (also me, by the way), but especially to my father (I know him), he will tell all his friends about it. So, I dedicate this thesis to him, because he always saw me as more, and he never stopped believing in me, even when he couldn't reach me (because of my occasional bad temper). You are my guardian, I admire you so much, *Papi!*.

Thank you!

*"You can't start a fire  
You can't start a fire without a spark". BS*

## STATEMENT OF INTEGRITY

I hereby declare having conducted this academic work with integrity. I confirm that I have not used plagiarism or any form of undue use of information or falsification of results along the process leading to its elaboration.

I further declare that I have fully acknowledged the Code of Ethical Conduct of the University of Minho.

# Novel Cork-Based Compounds for Biomedical Applications: from Antibacterials to the Modulation of Neurodegeneration

## ABSTRACT

Polyphenols are extensively studied due to their wide range of bioactivities. In this thesis we used this knowledge to evaluate a series of cork-based polyphenols/extracts to act: as anti-bacterial agents (Chapter 3); in the reduction of UV-mediated toxicity (Chapter 4); and as modulators of amyloid- $\beta$  ( $A\beta$ ) aggregation/cytotoxicity (hallmark of Alzheimer's disease, AD, Chapter 5). We found that vescalagin/castalagin (extracted/purified from cork powder) are the main responsables for the bioactivities of cork extracts due to their galloyl (Ga) units. Cork extracts rich in vescalagin/castalagin protected cells from UV-mediated cell death (Chapter 4). They also inhibited the folding of amyloid-like peptides/proteins from the extracellular matrix of bacteria, blocking the formation of biofilms (Chapter 3); as well as to remodel the  $A\beta$  aggregation into non-toxic forms (Chapter 5). We then synthesized (Chapter 6) three Ga-presenting dendrimers that recapitulate the vescalagin/castalagin bioactivities, and showed that dendrimers with 6 Ga units present a compromise between bioactivity and hydrophilicity enabling their use in the cellular environment while drastically reducing the presence of toxic  $A\beta$  oligomers. We also showed (Chapter 7) that glycosaminoglycans' (GAGs) building blocks and their analogues, *e.g.* glucosamine-6-sulfate (GlcN6S) and glucosamine-6-phosphate (GlcN6P), complement the bioactivities of vescalagin/castalagin in the context of AD by: modulating the  $A\beta$ -mediated toxicity; reducing membrane dysfunction; re-establishing healthy insulin signaling; lowering the acetylcholinesterase activity to basal levels; and reducing inflammation markers. We further developed a self-assemble monolayer (SAM) platform (Chapter 8) able to recapitulate the influence of the GAGs sulfation degree on the presentation of fibronectin (Fn) and its impact in the adhesion/morphology of stem cells. Overall, we show that cork-based compounds, *e.g.* vescalagin/castalagin, present a wide range of bioactivities (*e.g.* anti-UV, anti-bacterial, anti-amyloidogenic) that are recapitulated by Ga-presenting dendrimers. Vescalagin/castalagin/Ga-terminated dendrimers can be used alone or in combination with GlcN6S or GlcN6P to reduce AD hallmarks. We also show that the sulfation degree presented on SAM-coated surfaces is critical for their bioactive character.

**Keywords:** Alzheimer Disease; Amyloid- $\beta$  peptide; Cork; Dendrimers; Vescalagin



# Novos Compostos Baseados Em Cortiça Para Aplicações Biomédicas: De Antibacterianos A Modeladores De Neurodegeneração

## RESUMO

Os polifenóis são muito estudados dado a sua ampla bioatividade. Nesta tese, usámos este conhecimento para avaliar vários compostos/extratos da cortiça para atuarem como: anti-bacterianos (Capítulo 3); anti-UV (Capítulo 4); e moduladores da agregação/toxicidade da  $\beta$ -amilóide (A $\beta$ ) (associado à doença de Alzheimer, AD, Capítulo 5). Demonstrámos que a vescalagina/castalagina presentes nos extratos de cortiça são essenciais para a sua bioatividade, dada a presença do grupo galoil (Ga). Extratos ricos em vescalagina/castalagina reduziram a morte celular mediada pela radiação UV (Capítulo 4) e inibiram a organização dos péptidos/proteínas da matriz extracelular de bactérias, bloqueando a formação de biofilme (Capítulo 3). A vescalagina/castalagina foram ainda capazes de remodelar o A $\beta$  em formas não tóxicas (Capítulo 5). Também sintetizámos dendrímeros apresentando a unidade Ga (Capítulo 6) mimetizando a bioatividade da vescalagina/castalagina. O dendrímero com 6 Gas apresentou um compromisso entre bioatividade/hidrofilicidade, permitindo a sua utilização no ambiente celular e reduzindo a toxicidade dos oligómeros de A $\beta$ . Provámos ainda (Capítulo 7) que a glucosamina-6-sulfato (GlcN6S) e a glucosamina-6-fosfato (GlcN6P) apresentam bioatividade complementar à da vescalagina/castalagina no contexto da AD, reduzindo a toxicidade do A $\beta$ , protegendo a membrana celular, normalizando a sinalização da insulina, reduzindo a atividade da acetilcolinesterase e a expressão dos marcadores de inflamação. Também desenvolvemos uma plataforma de “self-assemble monolayers” (SAMs, Capítulo 8) capaz de mimetizar a influência do grau de sulfatação dos glicosaminoglicanos (GAGs) na apresentação de fibronectina e o seu impacto na adesão/morfologia de células estaminais. Em resumo, identificámos uma vasta bioatividade da vescalagina/castalagina (ex. anti-UV, anti-bacteriana, anti-amiloidogénica) que pode ser mimetizada por dendrímeros apresentando unidades de Ga. A vescalagina/castalagina/dendrímeros de Ga são capazes de reduzir as várias características da AD, de uma forma individual ou em combinação com GlcN6S/GlcN6P. Também demonstrámos que o grau de sulfatação apresentado em superfícies cobertas por SAMs é crítico para o seu carácter bioativo.

**Palavras-chave:**  $\beta$ -Amilóide; Cortiça; Dendrímeros; Doença de Alzheimer; Vescalagina

## TABLE OF CONTENTS

ACKNOWLEDGMENTS.....	iii
STATEMENT OF INTEGRITY.....	v
ABSTRACT .....	vi
RESUMO.....	vii
TABLE OF CONTENTS.....	viii
LIST OF ABBREVIATIONS .....	xiii
LIST OF EQUATIONS.....	xxiv
LIST OF FIGURES.....	xxv
LIST OF SUPPLEMENTARY FIGURES.....	xxvii
LIST OF TABLES .....	xxxiv
LIST OF SUPPLEMENTARY TABLES.....	xxxv
SHORT CURRICULUM VITAE .....	xxxvi
LIST OF PUBLICATIONS.....	xxxvii
INTRODUCTION TO THE THESIS FORMAT.....	xli
SECTION I.....	44
1 Natural polyphenols and nanosystems for Alzheimer’s Disease .....	46
Abstract .....	46
1.1 Alzheimer’s Disease and it hallmarks.....	47
1.1.1 The amyloid aggregation pathway.....	48
1.1.2 The A $\beta$ FOLDING process.....	49
1.1.3 The mechanism of A $\beta$ cytotoxicity.....	50
1.2 Natural compounds as drug leads for AD.....	56
1.3 Nanosystems for AD.....	61
1.3.1 Drug-delivery systems for AD – crossing the BBB .....	62
1.3.2 Dendrimers as CNS delivery systems and therapeutic nanosystems .....	65

1.4	Conclusions and Future directions .....	67
1.5	References.....	68
SECTION II.....		84
2	Materials and Methods.....	86
2.1	Materials.....	86
2.1.1	Cork-based materials.....	86
2.1.2	Dendrimers .....	87
2.1.3	Glucosamine and its analogues.....	88
2.1.4	Amyloid- $\beta$ (1-42) peptide .....	88
2.1.5	self-assembled monolayers (SAMs) .....	90
2.2	Methods.....	90
2.2.1	Preparation of cork-based extracts .....	90
2.2.2	Synthesis of Ga-terminated dendrimers.....	92
2.2.3	Peptide preparation .....	95
2.2.4	PREPARATION OF SINGLE AND MIXED SAMs.....	95
2.2.5	High Performance Liquid Chromatography (HPLC) analysis.....	96
2.2.6	Mass spectrometry analysis.....	97
2.2.7	Column chromatography .....	97
2.2.8	Gel permeation chromatography (GPC).....	97
2.2.9	Nuclear Magnetic Resonance (NMR) .....	98
2.2.10	Infrared Spectroscopy (FTIR) assessment.....	98
2.2.11	Isothermal Titration Calorimetry (ITC) studies.....	98
2.2.12	Circular Dichroism (CD).....	99
2.2.13	Scanning Transmission Electron Microscopy (STEM) analysis .....	99
2.2.14	SURFACE PLASMON RESONANCE (MP-SPR) .....	100
2.2.15	Antioxidant (AO) activity by DPPH.....	100
2.2.16	Oxygen radical absorbance capacity (ORAC).....	100
2.2.17	Total phenolic content (TPC) measurements .....	101
2.2.18	Microbiological culture conditions .....	101
2.2.19	Disk diffusion assay.....	102
2.2.20	Minimal inhibitory concentrations (MICs) and minimal bactericidal concentration (MBCs) .....	102
2.2.21	Congo red Agar (CRA) assay .....	103
2.2.22	Scanning Electron Microscope (SEM).....	103
2.2.23	Cell culture conditions .....	103
2.2.24	Cellular metabolic activity .....	105
2.2.25	Cell viability by DNA quantification .....	106

2.2.26	Cell viability by Live/Dead assay .....	106
2.2.27	Intracellular Reactive Oxygen Species (ROS).....	107
2.2.28	TUNEL assay.....	107
2.2.29	Protein expression by immunocytochemistry.....	107
2.2.30	Thioflavin-T (ThT) studies.....	108
2.2.31	Protein expression by Western-blotting (WB).....	109
2.2.32	Atomic Force Microscope (AFM) studies.....	110
2.2.33	Measurements of cytosolic Ca <sup>2+</sup> levels .....	111
2.2.34	Acetylcholinesterase (AChE) activity .....	111
2.2.35	Quartz crystal microbalance with dissipation (QCM-d).....	112
2.2.36	Characterization of cells spreading by live imaging.....	112
SECTION III.....		118
3	Vescalagin and castalagin present bactericidal activity towards Methicillin-resistant bacteria ....	120
Abstract .....		120
3.1	Main text.....	121
3.2	Results and Discussion.....	123
3.3	Conclusions .....	128
3.4	References.....	129
Supplementary Information .....		132
4	Cork extracts reduce UV-mediated DNA fragmentation and cell death.....	143
Abstract .....		143
4.1	Introduction.....	144
4.2	Materials and methods.....	145
4.2.1	Materials .....	145
4.2.2	Chemical characterization of cork extracts .....	145
4.3	Results and Discussion.....	148
4.4	Conclusions .....	154
4.5	References.....	154
Supplementary Information .....		157

5	Vescalagin and castalagin reduce the toxicity of amyloid-beta 42 oligomers through the remodelling of its secondary structure.....	161
	Abstract .....	161
5.1	Main text.....	162
5.2	References.....	169
	Supplementary information .....	171
6	Functional gallic acid-based dendrimers as synthetic nanotools to remodel amyloid-beta 42 into non-cytotoxic forms .....	193
	Abstract .....	193
6.1	Main Text.....	194
6.2	References.....	199
	Supplementary Information .....	202
	Chapter 7 .....	253
7	Glucosamine analogues as modulators of amyloid- $\beta$ toxicity .....	253
	Abstract .....	253
7.1	Main text.....	254
7.2	References.....	263
	SUPPLEMENTARY INFORMATION .....	266
	Chapter 8 .....	279
8	Surfaces mimicking glycosaminoglycans trigger different response of stem cells via distinct fibronectin adsorption and reorganization.....	279
	Abstract .....	279
8.1	Introduction.....	280
8.2	Experimental section .....	281
8.3	Results and Discussion.....	283
8.4	Conclusions .....	293
8.5	References.....	293

SUPPLEMENTARY INFORMATION .....	297
SECTION IV.....	304
9 GENERAL CONCLUSIONS AND FINAL REMARKS .....	306

## LIST OF ABBREVIATIONS

### A

$\alpha$ -MEM –  $\alpha$ -modified Eagle's medium

AAPH – 2,2'-azobis(2-methylpropionamide) dihydrochloride

A $\beta$  – Amyloid- $\beta$

A $\beta$ 42/A $\beta$ 40 - Amyloid- $\beta$  with 40/42 amino acids

ABCA7 – ATP-binding cassette transporter A7

ACh – Acetylcholine

AChE – Acetylcholinesterase

AD – Alzheimer's Disease

AFM – Atomic Force Microscopy

AICD – APP intra cellular domain

AKT – Protein kinase B

APCI – Atmospheric-pressure chemical ionization

APP – Amyloid precursor protein

ASCs – Adipose derived stem cells

ATB – Antibiotics mixture

ATP – Adenosine triphosphate

Au – Gold

ApoE – Apolipoprotein E

$\approx$  – Approximately

### B

BACE1 –  $\beta$ -site amyloid precursor protein cleaving enzyme 1

BBB – Blood Brain Barrier

BCSFB – Blood-CSF barrier

Bn – Benzyl group

BSA – Bovine serum albumin

## **C**

C – Carbon

C-terminal – Carboxyl group terminal

Ca<sup>2+</sup> – Calcium ion

Calcein-AM – Calcein-Acetoxyethyl

CD – Circular Dichroism

CDCl<sub>3</sub> – Deuterated Chloroform

CD<sub>3</sub>OD – Deuterated methanol

CFU – Colony-forming unit

CH<sub>3</sub> – Methyl radical

CH<sub>2</sub>Cl<sub>2</sub> – Dichloromethane

CLU – Clusterin

cm – Centimetre

CRA – Congo Red Agar

CNS – Central Nervous System

CO<sub>2</sub> – Carbon dioxide

CS – Chondroitin sulphate

CSF – Cerebrospinal fluid

CWE – Cork Water Extract

CWE-E – Cork Water Enriched Extract

CWEE – Cork Water Ethanol Extract

## **D**

Da – Dalton



DAPI – 4',6'-diamino-2-phenyl-indol

DCF – 2',7'-dichlorofluorescein

DCDHF-DA – 2',7'-dichlorodihydrofluorescein diacetate

D<sub>2</sub>O – Deuterium oxide

DMEM – Dulbecco's Modified Eagle Medium

DMEM/F12 – Dulbecco's Modified Eagle Medium/Nutrient Mixture F-12

DMF – N,N-Dimethylmethanamide

DMSO – Dimethyl sulfoxide

DMSO-d<sub>6</sub> – Deuterated DMSO

DNA – Deoxyribonucleic Acid

DPBS – Dulbecco's phosphate-buffered saline

DPPH – 2,2-diphenyl-1-picrylhydrazyl

°C – Degree Celsius

δ – chemical shifts

ΔD – Energy dissipation

Δf – Resonance frequency

ΔG – Gibbs free energy

ΔH – Enthalpy

ΔS – Entropy

## **E**

EC50 – Half maximal effective concentration

EC – (-)-epicatechin

ECG – (-)-epicatechin-3-gallate

EGC – (-)-epigallocatechin

EGCG – (-)-epigallocatechin-3-gallate

ECM – Extracellular matrix

EDC – N-(3-dimethylaminopropyl)-N'-ethylcarbodiimide hydrochloride

*e.g.* – “for example”, form Latin *exempli gratia*

ER – Endoplasmic Reticulum

ERK – Extracellular signal-regulated kinase

ESI – electrospray ionization

Et<sub>3</sub>N – Triethylamine

EtOAc – Ethyl acetate

## **F**

FA – Focal adhesions

FBS - Fetal bovine serum

fCWE– Fraction Of Cork Water Ethanol Extract

FIA – Flow injection analysis

Fig. – Figure

Fn – Fibronectin

FTIR – Infrared Spectroscopy

## **G**

Ga – Galloyl units

GAGs – Glycosaminoglycans

GATG – Gallic acid-triethylene glycol dendrimers

GC – (-)-gallocatechin

GlcN – Glucosamine

GlcNAc – N-Acetyl-Glucosamine

GlcN6P – Glucosamine-6-Phosphate

GlcN6S – Glucosamine-6-Sulphate

GLUT3/4 – Glucose transporter 3/4

GPC – Gel Permeation Chromatography

## **H**

h – hour

H – Hydrogen

HABS – Harvard Aging Brain Study

HBOt – Hydroxybenzotriazole

HCl – Hydrogen Chloride

HFIP – Hexofluoro-2-propanol

HPLC – High Performance Liquid Chromatography

H<sub>2</sub>O – Water

Hz – Hertz

## **I**

*i.e.* – “in other words”, form Latin *id est*

IRS1 – insulin receptor substrate 1

IDE – insulin-degrading enzyme

ICC – Immunocytochemistry

ISF – Interstitial fluid

## **J**

J – Joule

## **K**

K – Equilibrium association constant

K<sup>+</sup> – Potassium ion

KBr – Potassium Bromide

K<sub>2</sub>CO<sub>3</sub> – Potassium carbonate

kDa – Kilodalton

kg – Kilogram

KOH – Potassium hydroxide

kV– Kilovolt

## **L**

L – Litre

Leu – Leucine (L)

LPR1/2 – Lipoprotein receptor 1/2

Lys – Lysine (K)

## **M**

m - meter

M – Molar

mAChR – Muscarinic acetylcholine receptor

MAPK – Mitogen-activated protein kinase

MBC – Minimum bactericidal concentration

mdeg – Milidegree

MES – 2-(N-morpholino)ethanesulfonic acid

MeOH – Methanol

mg – Milligram

MHA - Muller-Hinton Agar plate

MHB – Meller-Hinton Broth medium

MHz – Megahertz

MIC – Minimum inhibitory concentration

min – minute

mL – Mililiter

mm – Millimeter

mM - Millimolar

mmol – Milimol

MP – Multi-parametric

MPLC – Medium-pressure Liquid Chromatography

MRSA – Methicillin-resistant *Staphylococcus aureus*

MRSE – Methicillin-resistant *Staphylococcus epidermidis*

MS – Mass spectrometer

$M_w$  – Molecular weight

m/z – mass-to-charge ratio of ions

$\mu\text{L}$  – Microliter

$\mu\text{g}$  – Microgram

$\mu\text{m}$  – Micrometre

$\mu\text{M}$  – Micromolar

## **N**

N – Newton

$\text{N}_2$  – Nitrogen

NaCl – Sodium chloride

NaOH – Sodium hydroxide

nAChR – Nicotinic acetylcholine receptor

NaI – Sodium iodide

NBT – Nitroblue tetrazolium

$\text{NH}_2$  – Amino radical

NMR – Nuclear magnetic resonance

NP – Nanoparticle

NTS – neurofibrillary tangles

nm – Nanometers

## O

O – Oxygen

OH – Hydroxyl group

ORAC –Oxygen radical absorbance capacity

OS – Oxidative stress

$\Omega$  – Ohms

## P

$p$  – Statistical level of significance

p38 – p38 mitogen-activated protein kinases/Cytokinin Specific Binding Protein

Pa – Pascal

PA – *Pseudomonas aeruginosa*

Pd – Palladium

PDA – Photodiode Array Detector

PAMAM – poly(aminoamine) dendrimer

PBS – Phosphate-buffered saline

P-dendrimers – Phosphorus dendrimers

PEHAM – poly-(etherhydroxylamine) dendrimer

pH – Potential hydrogenionic

Phe – Phenylalanine (F)

p-JNK/p-c-Jun – Phosphorylated Protein kinase B

PPI – poly(propyleneimine) dendrimer

p(Ser) – Phosphorylated serine residues

PI – Propidium iodide

PLGA – Poly [(lactic acid) -co- (glycolic acid)]

Ptd-L-Ser – Phosphatidylserine

PTFE – Polytetrafluoroethylene

PS1/PS2 – Presenilin-1/Presenilin-2

% – Percentage

## **Q**

QCM-D – Quartz crystal microbalance with dissipation

## **R**

R – gas constant

Ref. – Reference

ROS – Reactive oxygen species

rpm – Rotations per minute

RT – Room temperature

## **S**

s – Seconds

S. – Supplementary

SA – *Staphylococcus aureus*

SAMs – Self-assembled monolayers

SDS-PAGE – Sodium dodecyl sulphate-polyacrylamide gel electrophoresis

SEM – Scanning Electron Microscopy

SO<sub>3</sub>H – Sulfonic group

SPR – Surface plasmon resonance

STEM – Scanning Transmission Electron Microscopy

SUVR – standardized uptake value ratios of amyloid accumulation

## T

T – Temperature

TAT-peptide – Trans-acting activator of transcription

TBS – Tris-buffered saline

TBS-T – Tris-buffered saline with tween 20

TE – Trolox equivalents

TEER – Transendothelial electrical resistance

TEM – Transmission electron microscopy

THF – Tetrahydrofuran

ThT – Thioflavin-T

Tet1-peptide – Ten-eleven translocation methylcytosine dioxygenase 1

TiO<sub>x</sub> – titanium oxide

TPC – Total phenolic content

TREM2 – Triggering Receptor Expressed On Myeloid Cells 2

TSB – Tryptic Soy Broth

TSA – Tryptic Soy Agar

TUNEL – Terminal deoxynucleotidyl transferase dUTP nick end labelling

3D – Three-dimensional

$\theta$  – Molar ellipticity

## U

UK – United Kingdom

USA – United States of America

UV – Ultraviolet

UVA/UVB/UVC – Ultraviolet radiation A/B/C



## **V**

v – Volume

V – Volt (AFM studies) and Vehicle (Cell studies)

Val – Valine (V)

## **W**

$\lambda$  – Wavelength

WB – Western blot or Western blotting

## **X**

X-ray – Electromagnetic waves

## LIST OF EQUATIONS

Equation 1-1 Gibbs energy equation (calculated from the equilibrium association constant K) .....	99
Equation 1-2 Gibbs energy equation (calculated from the enthalpic and entropic contributions).....	99

## LIST OF FIGURES

Figure 1-1 Schematic overview of the A $\beta$ cleavage and folding showing the formation of A $\beta$ through the cleavage of APP (amyloid precursor protein), and its interactions with the lipid bilayer surface promoted by the different A $\beta$ supramolecular forms.....	52
Figure 1-2 EGCG induces the formation of off-pathway A $\beta$ 42 aggregates. ....	58
Figure 1-3 3D representation of the most studied natural-occurring Ga-based polyphenols that are able to inhibit or remodel the A $\beta$ supramolecular organization, and protect neuronal cells from their cytotoxicity. ....	60
Figure 2-1. Synthetic route for the multigram preparation of the core of the Ga-dendrimers.....	93
Figure 2-2. Chemical structure of Ga-terminated dendrimers: (1) 2G0-GaOH, (2) 2G1-GaOH and (3) 3G1-GaOH.....	94
Figure 3-1. (A) Chemical structure of the polyphenols vescalagin and castalagin purified from CWE. (B) Schematic presentation of the mechanism of action of vescalagin/castalagin againsts Gram-negative and Gram-positive bacteria strains.....	122
Figure 3-2. Representative Live/Dead images showing the antibacterial activity of vescalagin and castalagin (at their MIC concentration) towards Methicillin-resistant Staphylococcus epidermidis, Staphylococcus aureus, Methicillin-resistant Staphylococcus aureus and Pseudomonas aeruginosa. ....	125
Figure 3-3. Representative SEM images showing a deterioration of cell wall of each strain of bacteria, namely, Methicillin-resistant Staphylococcus epidermidis; Staphylococcus aureus, Methicillin-resistant Staphylococcus aureus and Pseudomonas aeruginosa.....	126
Figure 3-4. Representative Congo red assay images showing a decrease in the dark pigmentation consistent with a decrease of amyloid-like protein presentations for the tested strains of bacteria. ....	127
Figure 4-1. Metabolic activity of L929 cells measured 27h after exposure to UV radiation for different timeframes/UV doses (upon UV exposure, cells were pre-incubated for 24h in the absence of cork extracts, and an additional 3h for MTS incubation).....	150
Figure 4-2. Metabolic activity of L929 cells pre-incubated with 75 $\mu$ g/ml of each cork extract for 24h, followed by a UVA dose of 17.1J/cm <sup>2</sup> in combination with a UVB dose of 4.1J/cm <sup>2</sup> .....	151
Figure 4-3. Intracellular ROS levels assessed with the DCDHF-DA probe. Results are expressed in relation to the positive control C+ (100% of ROS), i.e. UV-exposed cells in the absence of cork extracts. ....	152
Figure 4-4. Assessment of the morphology (Giemsa staining), viability (Live/Dead) and apoptosis level (Tunel assay, nuclei and DNA fragmentation) upon UV irradiation, in the absence (C+) and presence of cork extract (at a concentration of 75 $\mu$ g/ml).....	153
Figure 5-1. Chemical structure of the polyphenols vescalagin and castalagin extracted and purified from cork powder.....	163
Figure 5-2. Aggregation of A $\beta$ 42 (25 $\mu$ M) followed by ThT fluorescence upon incubation over 140h under different A $\beta$ 42:polyphenol molar ratios, i.e. 1:0.5, 1:1 and 1:2; Relative densitometric bar graphs A $\beta$ 42 (25 $\mu$ M) assembly and disassembly quantified by WB.....	165

Figure 5-3. Loss of parallel $\beta$ -sheets by A $\beta$ 42 (25 $\mu$ M) monitored by CD upon incubation with 1 and 2 under constant agitation at 37°C, during 24h; B-C. A $\beta$ 42 (25 $\mu$ M) refolding into spherical assemblies detected by AFM and STEM, respectively..	166
Figure 5-4. Live/Dead assay using SH-SY5Y cells incubated with different A $\beta$ 42:polyphenol ratios during 24h; Immunofluorescence analysis of A $\beta$ 42 aggregates in the SH-SY5Y cell culture visualized by confocal microscopy...	168
Figure 6-1. Chemical structure of Ga-terminated dendrimers: A. 2G0-GaOH, B. 2G1-GaOH and C. 3G1-GaOH.....	195
Figure 6-2. Relative densitometric bar graphs of A $\beta$ o and A $\beta$ f quantified by WB.....	197
Figure 6-3. Immunofluorescence analysis of A $\beta$ o (assembly) and A $\beta$ f (disassembly) species in the SH-SY5Y cell culture (mAb 6E10) after incubation with 2G1-GaOH for 1 and 5 days. ....	198
Figure 6-4. Representative Bio-AFM topographic images of SH-SY5Y cells cultured in the presence of A $\beta$ and a 1:1 molar ratio of 2G1-GaOH; Cell height profile; and, Young's modulus of SH-SY5Y cells as a function of the presence of A $\beta$ and dendrimers (molar ratio 1:1).....	199
Figure 7-1. Relative densitometric bar graphs of A $\beta$ assembly quantified by WB after 1 day or 5 days of incubation, using the antibody 6E10. Loss of antiparallel $\beta$ -sheets in the supramolecular organization of A $\beta$ followed by CD during 1 and 5 days.....	257
Figure 7-2. Representative AFM images of A $\beta$ aggregates formed in the presence and absence of 1mM of GlcN6S and GlcN6P. All the samples were incubated for 1 or 5 days under constant agitation.....	258
Figure 7-3. Representative fluorescence images of SH-SY5Y cells cultured for 24h in the presence of A $\beta$ and each monosaccharide showing the levels of intracellular free Ca <sup>2+</sup> in the cytosol of the cells measured using fluorescence probes; and Graphical representation showing the Ca <sup>2+</sup> imbalance caused by the supramolecular A $\beta$ forms through their interaction with the lipid raft.....	259
Figure 7-4. Ability of each monosaccharide to modulate the expression of pIRS1; pAKT1 and Annexin 1 by SH-SY5Y cells cultured for 1h in the absence/presence of A $\beta$ (by WB); and, schematic representation of the insulin signalling pathway affected by the A $\beta$ supramolecular forms.....	260
Figure 8-1. Adsorption profiles of Fn on different surfaces characterized by QCM-D, SPR and AFM and the respective cellular response.....	285
Figure 8-2. Representative $\Delta D/\Delta f$ plots showing changes during adhesion of ASCs onto SAMs' surfaces with different concentration of -SO <sub>3</sub> H groups in the presence and in the absence of Fn on the sensor surface. ....	289
Figure 8-3. Live imaging of adipose-derived stem cells adhering and spreading on the studied substrates without Fn adsorption. ....	290
Figure 8-4. Live imaging of adipose-derived stem cells seeded on the studied substrates after Fn adsorption.....	291
Figure 8-5. Representative fluorescence microscopy images of adipose-derived stem cells cultured on single and mixed SAMs at two different time points: 1 and 3 h without and with Fn.....	292

## LIST OF SUPPLEMENTARY FIGURES

Supplementary Fig. 3-1. Preparative HPLC chromatograms of cork water extract (CWE) and cork water extract ethanol (CWE-E) with the identification of the peaks that correspond to vescalagin and castalagin. ....	132
Supplementary Fig. 3-2. Quantification of vescalagin and castalagin present in CWE and CWE-E.....	132
Supplementary Fig. 3-3. HPLC chromatograms showing the purified compounds: vescalagin and castalagin.....	133
Supplementary Fig. 3-4. Positive ESI-MS spectrum of vescalagin. ....	133
Supplementary Fig. 3-5. Positive ESI-MS spectrum of castalagin.....	134
Supplementary Fig. 3-6. DPPH assay. Free radical scavenging activity of the cork-based compounds. ....	134
Supplementary Fig. 3-7. Disc diffusion assay in agar media showing the zone of inhibition for each extract/polyphenol against the tested bacteria.....	135
Supplementary Fig. 3-8. Disc diffusion assay in agar media showing the zone of inhibition for each extract/polyphenol against <i>Pseudomonas Aeruginosa</i> . ....	135
Supplementary Fig. 3-9. Live/Dead assay using BacLight Viability Kit showing the ability of the extracts/polyphenols to drastically reduce the viability of Methicillin-resistant <i>Staphylococcus epidermidis</i> , <i>Staphylococcus Aureus</i> and Methicillin-resistant <i>Staphylococcus aureus</i> .....	137
Supplementary Fig. 3-10. Representative SEM images showing a deterioration of the cell wall caused by CWE and CWE-E on each strain of bacteria. ....	137
Supplementary Fig. 3-11. Congo red agar assay for vescalagin/castalagin on Methicillin-resistant <i>Staphylococcus epidermidis</i> . ....	138
Supplementary Fig. 3-12. Congo red agar assay for vescalagin/castalagin on <i>Staphylococcus aureus</i> .....	138
Supplementary Fig. 3-13. Congo red agar assay for vescalagin/castalagin on Methicillin-resistant <i>Staphylococcus aureus</i> . ....	139
Supplementary Fig. 3-14. Congo red agar assay for vescalagin/castalagin on <i>Pseudomonas aeruginosa</i> .....	139
Supplementary Fig. 3-15. Cytocompatibility of CWE towards the L929 cell line, measured by their metabolic activity using AlamarBlue®.....	140
Supplementary Fig. 3-16. Cytocompatibility of CWE-E towards the L929 cell line, measured by their metabolic activity using AlamarBlue®.....	140
Supplementary Fig. 3-17. Cytocompatibility of vescalagin towards the L929 cell line, measured by their metabolic activity using AlamarBlue®.....	141
Supplementary Fig. 3-18. Cytocompatibility of castalagin towards the L929 cell line, measured by their metabolic activity using AlamarBlue®.....	141

Supplementary Fig. 4-1. HPLC chromatographic profiles of samples CWE, CWEE and fCWEE obtained using UV detection at $\lambda=280\text{nm}$ .....	157
Supplementary Fig. 4-2. Metabolic activity of L929 cells cultured with 300, 150, 100, 75, 50 and 25 $\mu\text{g/ml}$ of each cork extract for 24h.....	158
Supplementary Fig. 4-3. Assessment of viability of the cells cultured in the absence and presence of cork extracts as well as in the presence or absence of UV-exposure.....	159
Supplementary Fig. 5-1. A. Preparative HLPC chromatogram of cork water extract with the identification of the peaks that correspond to vescalagin and castalagin.....	175
Supplementary Fig. 5-2. HPLC run showing the purified compound 1 - vescalagin.....	175
Supplementary Fig. 5-3. HPLC run showing the purified compound 2 - castalagin.....	176
Supplementary Fig. 5-4. Positive ESI-MS spectrum of vescalagin.....	176
Supplementary Fig. 5-5. Positive ESI-MS spectrum of castalagin.....	177
Supplementary Fig. 5-6. $^1\text{H}$ NMR spectra of vescalagin.....	177
Supplementary Fig. 5-7. $^1\text{H}$ NMR spectra of castalagin.....	178
Supplementary Fig. 5-8. Fluorescence spectrum of vescalagin acquired using a $\lambda_{\text{ex}} = 435 \text{ nm}$ and a $\lambda_{\text{em}} = 445\text{-}600 \text{ nm}$ ....	179
Supplementary Fig. 5-9. Fluorescence spectrum of castalagin acquired using a $\lambda_{\text{ex}} = 435 \text{ nm}$ and a $\lambda_{\text{em}} = 445\text{-}600 \text{ nm}$ ....	179
Supplementary Fig. 5-10. HPLC run of the A $\beta$ 42 peptide used throughout the present work.....	180
Supplementary Fig. 5-11. Positive ESI-MS spectrum of A $\beta$ 42 sample used throughout the present work.....	180
Supplementary Fig. 5-12. A $\beta$ 42 aggregation kinetics monitored by the ThT binding assay.....	181
Supplementary Fig. 5-13. A $\beta$ 42 assembly kinetics (Method 2) using the ThT assay.....	181
Supplementary Fig. 5-14. A $\beta$ 42 disassembly kinetics (Method 2) using the ThT assay.....	182
Supplementary Fig. 5-15. Representative WB image and B. relative densitometric bar graphs of the A $\beta$ 42 assembly in the presence of vescalagin and castalagin (24h).....	182
Supplementary Fig. 5-16. Representative WB image and relative densitometric bar graphs of the A $\beta$ 42 assembly in the presence of vescalagin and castalagin (7 days).....	183
Supplementary Fig. 5-17. Representative WB image and B. relative densitometric bar graphs of the A $\beta$ 42 disassembly in the presence of vescalagin and castalagin (24h).....	183
Supplementary Fig. 5-18. Representative WB image and relative densitometric bar graphs of the A $\beta$ 42 disassembly in the presence of vescalagin and castalagin (7 days).....	184
Supplementary Fig. 5-19. Relative densitometric bar graphs of A $\beta$ 42 assembly and disassembly for 24h and 7 days, respectively.....	184

Supplementary Fig. 5-20. CD spectra of A $\beta$ 42 peptide (25 $\mu$ M) in the presence and absence of vescalagin or castalagin during 7 days.....	185
Supplementary Fig. 5-21. CD spectra of A $\beta$ 42 pre-formed fibrils in the absence and presence of vescalagin or castalagin during 1 day. ....	186
Supplementary Fig. 5-22. AFM images of A $\beta$ 42 fibrils formed for 10 days. Vescalagin and castalagin were added into an A $\beta$ 42 solution (ratios A $\beta$ 42:polyphenol of 1:1 and 1:2) and left to incubate for 24h under constant agitation.....	186
Supplementary Fig. 5-23. AFM representative images of A $\beta$ 42 (25 $\mu$ M): Assembly and disassembly of A $\beta$ 42: vescalagin and castalagi were added into an A $\beta$ 42 monomeric solution (ratio of A $\beta$ 42:polyphenol of: 1:1) and left to incubate for 7 days.....	187
Supplementary Fig. 5-24. Isothermal titration calorimetry (ITC) curves for the binding of vescalagin and castalagin to A $\beta$ 42 peptide.....	187
Supplementary Fig. 5-25. SH-SY5Y cell viability in the presence of A $\beta$ 42 fibrils during 24h. ....	188
Supplementary Fig. 5-26. MTS assay: SH-SY5Y metabolic activity in the presence of a solution of A $\beta$ 42 pre-formed fibrils (25 $\mu$ M) and filtered A $\beta$ 42 (25 $\mu$ M) during 24h.....	189
Supplementary Fig. 5-27. Fluorescence quantification of live cells stained in green in the presence of a solution of A $\beta$ 42 pre-formed fibrils (25 $\mu$ M) and filtered fibrillar A $\beta$ 42 (25 $\mu$ M), during 24h.....	189
Supplementary Fig. 5-28. Live/Dead assay of SH-SY5Y: A. fluorescence quantification of live cells stained in green in the presence of a solution of A $\beta$ 42 pre-formed fibrils (25 $\mu$ M) and vescalagin or castalagin at different molar ratios (A $\beta$ 42:polyphenol 1:0.5; 1:1; 1:2) during 24h.....	189
Supplementary Fig. 5-29. MTS assay: SH-SY5Y cell viability in the presence of A $\beta$ 42 (25 $\mu$ M) and vescalagin or castalagin at different molar ratios (A $\beta$ 42:polyphenol 1:0.5; 1:1; 1:2) during 24h.....	190
Supplementary Fig. 5-30. Representative fluorescence microscopy images of SH-SY5Y cells treated with different molar ratios of A $\beta$ 42:polyphenol, i.e. 1:0.5, 1:1 and 1:2, of vescalagin and castalagin, as well as A $\beta$ 42 (25 $\mu$ M) during 24h.....	190
Supplementary Fig. 6-1. $^1\text{H}$ NMR spectrum (DMSO- $d_6$ ) of benzyl 3,4,5-tris(benzyloxy)benzoate. ....	207
Supplementary Fig. 6-2. $^{13}\text{C}$ NMR spectrum (DMSO- $d_6$ ) of benzyl 3,4,5-tris(benzyloxy)benzoate.....	207
Supplementary Fig. 6-3. IR spectrum of benzyl 3,4,5-tris(benzyloxy)benzoate. ....	208
Supplementary Fig. 6-4. HR-MS of benzyl 3,4,5-tris(benzyloxy)benzoate.....	209
Supplementary Fig. 6-5. $^1\text{H}$ NMR spectrum (DMSO- $d_6$ ) of 3,4,5-tris(benzyloxy)benzoic acid. ....	210
Supplementary Fig. 6-6. $^{13}\text{C}$ NMR spectrum (DMSO- $d_6$ ) of 3,4,5-tris(benzyloxy)benzoic acid. ....	211
Supplementary Fig. 6-7. IR spectrum of 3,4,5-tris(benzyloxy)benzoic acid.....	211
Supplementary Fig. 6-8. HR-MS of 3,4,5-tris(benzyloxy)benzoic acid. ....	212
Supplementary Fig. 6-9. $^1\text{H}$ NMR spectrum ( $\text{CDCl}_3$ ) of 2G0-GaOBn.....	213

Supplementary Fig. 6-10. <sup>13</sup> C NMR spectrum (CDCl <sub>3</sub> ) of 2G0-GaOBn.....	214
Supplementary Fig. 6-11. IR spectrum of 2G0-GaOBn.....	214
Supplementary Fig. 6-12. <sup>1</sup> H NMR spectrum (CD <sub>3</sub> OD) of 2G0-GaOH.....	215
Supplementary Fig. 6-13. IR spectrum of 2G0-GaOH.....	216
Supplementary Fig. 6-14. <sup>1</sup> H NMR spectrum (CDCl <sub>3</sub> ) of 2G1-GaOBn.....	217
Supplementary Fig. 6-15. <sup>13</sup> C NMR spectrum (CDCl <sub>3</sub> ) of 2G1-GaOBn.....	218
Supplementary Fig. 6-16. IR spectrum of 2G1-GaOBn.....	218
Supplementary Fig. 6-17. <sup>1</sup> H NMR spectrum (CD <sub>3</sub> OD) of 2G1-GaOH.....	219
Supplementary Fig. 6-18. IR spectrum of 2G1-GaOH.....	220
Supplementary Fig. 6-19. <sup>1</sup> H NMR spectrum (CDCl <sub>3</sub> ) of 3G1-GaOBn.....	222
Supplementary Fig. 6-20. <sup>13</sup> C NMR spectrum (CDCl <sub>3</sub> ) of 3G1-GaOBn.....	222
Supplementary Fig. 6-21. IR spectrum of 3G1-GaOBn.....	223
Supplementary Fig. 6-22. <sup>1</sup> H NMR spectrum (DMSO-d <sub>6</sub> ) of 3G1-GaOH.....	224
Supplementary Fig. 6-23. IR spectrum of 3G1-GaOH.....	225
Supplementary Fig. 6-24. GPC elugrams of x[Gn]-GaOBn (THF).....	225
Supplementary Fig. 6-25. Optimized geometry for Ga, 2G0-GaOH, 2G1-GaOH and, 3G1-GaOH dendrimers interacting with the Aβ <sub>i</sub> at its Glu, Val and Ala residues.....	226
Supplementary Fig. 6-26. Dynamic interaction energy between Aβ <sub>i</sub> (2MXU pdb file <sup>4</sup> ) and Ga (1:1 ratio).....	227
Supplementary Fig. 6-27. Dynamic interaction energy between Aβ <sub>i</sub> (2MXU pdb file <sup>4</sup> ) and 2G0-GaOH (1:1 ratio).....	228
Supplementary Fig. 6-28. Dynamic interaction energy between Aβ <sub>i</sub> (2MXU pdb file <sup>4</sup> ) and 2G1-GaOH (1:1 ratio).....	228
Supplementary Fig. 6-29. Dynamic interaction energy between Aβ <sub>i</sub> (2MXU pdb file <sup>4</sup> ) and 3G1-GaOH (1:1 ratio).....	229
Supplementary Fig. 6-30. A. 3D fluorescence spectra of Gallic acid (Ga, 50μM) using the following acquisition parameters: λ <sub>ex</sub> = 400-580 nm; λ <sub>em</sub> = 415-600 nm.....	230
Supplementary Fig. 6-31. A. 3D fluorescence spectra of 2G0-GaOH (50μM) using the following acquisition parameters: λ <sub>ex</sub> = 400-580 nm; λ <sub>em</sub> = 415-600 nm.....	230
Supplementary Fig. 6-32. A. 3D fluorescence spectra of 2G1-GaOH (50μM) using the following acquisition parameters: λ <sub>ex</sub> = 400-580 nm; λ <sub>em</sub> = 415-600 nm.....	231
Supplementary Fig. 6-33. A. 3D fluorescence spectra of 3G1-GaOH (50μM) using the following acquisition parameters: λ <sub>ex</sub> = 400-580 nm; λ <sub>em</sub> = 415-600 nm.....	231



Supplementary Fig. 6-34. Inhibition of the A $\beta$ <sub>42</sub> aggregation kinetics evaluated using the ThT assay. Ga, 2G0-GaOH, 2G1-GaOH and 3G1-GaOH inhibited the A $\beta$ fibril elongation at different molar ratios: 1:0.5, 1:1, and 1:2.....	232
Supplementary Fig. 6-35. Disassembling of A $\beta$ <sub>42</sub> fibrils evaluated using the ThT assay. Ga, 2G0-GaOH, 2G1-GaOH and 3G1-GaOH promoted the rupture of A $\beta$ fibrils at different A $\beta$ :dendrimer molar ratios: 1:0.5; 1:1, and 1:2. ....	232
Supplementary Fig. 6-36. CD spectra of A $\beta$ <sub>42</sub> recorded for 5 days in the presence of different molar ratios of Ga. ....	233
Supplementary Fig. 6-37. CD spectra of A $\beta$ <sub>42</sub> recorded for 5 days in the presence of different molar ratios of 2G0-GaOH. ...	234
Supplementary Fig. 6-38. CD spectra of A $\beta$ <sub>42</sub> recorded for 5 days in the presence of different molar ratios of 2G1-GaOH. ...	235
Supplementary Fig. 6-39. CD spectra of A $\beta$ <sub>40</sub> recorded for 5 days in the presence of different molar ratios of 3G1-GaOH. ...	236
Supplementary Fig. 6-40. CD spectra of A $\beta$ <sub>42</sub> recorded for 5 days in the presence of different molar ratios of Ga.....	237
Supplementary Fig. 6-41. CD spectra of A $\beta$ <sub>42</sub> recorded for 5 days in the presence of different molar ratios of 2G0-GaOH. ...	238
Supplementary Fig. 6-42. CD spectra of A $\beta$ <sub>42</sub> recorded for 5 days in the presence of different molar ratios of 2G1-GaOH. ...	239
Supplementary Fig. 6-43. CD spectra of A $\beta$ <sub>42</sub> recorded for 5 days in the presence of different molar ratios of 3G1-GaOH. ...	240
Supplementary Fig. 6-44. Loss of antiparallel $\beta$ -sheets for the A. aggregation pathway (A $\beta$ <sub>42</sub> ) and B. disaggregation of (A $\beta$ <sub>42</sub> ) followed CD during 1 and 5 days. ....	241
Supplementary Fig. 6-45. Representative AFM images of A $\beta$ <sub>42</sub> . Each dendrimer was added into an A $\beta$ <sub>42</sub> solution (at A $\beta$ :dendrimer concentration ratios of 1:0.5, 1:1 and 1:2) and left to incubate for 24h under constant agitation.....	242
Supplementary Fig. 6-46. Representative STEM images of A $\beta$ <sub>42</sub> samples. Each dendrimer was added into an A $\beta$ <sub>42</sub> solution (under A $\beta$ :dendrimer concentration ratios of 1:0.5, 1:1 and 1:2) and left to incubate for 24h under constant agitation.....	243
Supplementary Fig. 6-47. A $\beta$ peptide assembly and disassembly pathways. ....	244
Supplementary Fig. 6-48. Relative densitometric bar graphs of A $\beta$ <sub>42</sub> (25 $\mu$ M) assembly quantified by WB. ....	244
Supplementary Fig. 6-49. Relative densitometric bar graphs of A $\beta$ <sub>42</sub> (25 $\mu$ M) disassembly quantified by WB. ....	245
Supplementary Fig. 6-50. SH-SY5Y cell viability in the presence of A $\beta$ oligomers (A $\beta$ <sub>42</sub> ) and A $\beta$ fibrils (A $\beta$ <sub>42</sub> ) during 24h (using AlmarBlue® assay).....	246
Supplementary Fig. 6-51. A. Metabolic activity measured by AlamarBlue® assay of SH-SY5Y in the presence of a solution of A $\beta$ <sub>42</sub> oligomeric species (25 $\mu$ M) during 24h, for a A $\beta$ :dendrimers concentration ratio of 1:1. ....	246
Supplementary Fig. 6-52. A. Metabolic activity measured by AlamarBlue® assay of SH-SY5Y in the presence of a solution of A $\beta$ <sub>42</sub> pre-formed fibrils (25 $\mu$ M) during 24h, for a A $\beta$ :dendrimers concentration ratio of 1:1. ....	247
Supplementary Fig. 6-53. ThT fluorescence measurements in SH-SY5Y cell culture, after incubation with A $\beta$ <sub>42</sub> (A) and A $\beta$ <sub>42</sub> (B) species and dendrimers for a A $\beta$ :dendrimers concentration ratio of 1:1 ratio, during 1 day of culture. ....	247
Supplementary Fig. 6-54. Immunofluorescence analysis of A $\beta$ <sub>42</sub> species in the SH-SY5Y cell culture visualized by confocal microscopy (mAb 6E10, green) after incubation with dendrimers for a A $\beta$ :dendrimer concentration ratio of 1:1, during 1 and 5 days.....	248

Supplementary Fig. 6-55. Immunofluorescence analysis of A $\beta$ species in the SH-SY5Y cell culture visualized by confocal microscopy (mAb 6E10, green) after incubation of dendrimers for a A $\beta$ :dendrimers concentration ratio of 1:1, during 1 and 5 days.....	248
Supplementary Fig. 6-56. Immunofluorescence analysis of A $\beta$ species in the SH-SY5Y cell culture visualized by confocal microscopy (A11 antibody, green) after incubation of dendrimers for a A $\beta$ :dendrimers concentration ratio of 1:1, during 1 and 5 days.....	249
Supplementary Fig. 6-57. Immunofluorescence analysis of A $\beta$ species in the SH-SY5Y cell culture visualized by confocal microscopy (A11 antibody, green) after incubation of dendrimers to a 1:1 ratio, for 1 and 5 days .....	249
Supplementary Fig. 6-58. Representative AFM topographic images of SH-SY5Y cells cultured during 24h in the presence of A $\beta$ . (A, assembly) and A $\beta$ . (B, disassembly) and Ga, 2G0-GaOH, 2G1-GaOH and 3G1-GaOH.....	250
Supplementary Fig. 6-59. Statistical comparison of the cells height profile from the nanomechanical properties obtained by AFM topographic images of normal SH-SY5Y cells with 1:1 ratio of A $\beta$ :dendrimers .....	250
Supplementary Fig. 7-1. Chemical structure of the glucosamine and its analogues. ....	270
Supplementary Fig. 7-2. A $\beta$ aggregation kinetics evaluated using the ThT assay in the presence of the tested monosaccharides GlcN, GlcNAc, GlcN6S, and GlcN6P.....	270
Supplementary Fig. 7-3. CD spectra of A $\beta$ measured during 5 days, in the presence of different concentrations of GlcN. .	271
Supplementary Fig. 7-4. CD spectra of A $\beta$ measured during 5 days, in the presence of different concentrations of GlcNAc.. .....	271
Supplementary Fig. 7-5. CD spectra of A $\beta$ measured during 5 days, in the presence of different concentrations of GlcN6S.. .....	272
Supplementary Fig. 7-6. CD spectra of A $\beta$ measured during 5 days, in the presence of different concentrations of GlcN6P.. .....	272
Supplementary Fig. 7-7. Representative WB membranes revealed using the 6E10 antibody for A $\beta$ in the absence and presence of 1mM of each monosaccharide.....	273
Supplementary Fig. 7-8. Representative AFM images of A $\beta$ (at a concentration of 25 $\mu$ M) incubated in the absence and presence of 1mM of GlcN, GlcNAc, GlcN6S and GlcN6P during 1 day and 5 days.....	273
Supplementary Fig. 7-9. Metabolic activity of SH-SY5Y cells (using AlmarBlue® assay) in the presence of each monosaccharide in the absence and in the presence of 25 $\mu$ M of A $\beta$ . Proliferation of SH-SY5Y cells, measured by quantification of the DNA content.....	274
Supplementary Fig. 7-10. Representative images of SH-SY5Y cells treated for 24h with A $\beta$ and each monosaccharide showing the levels of intracellular free Ca <sup>2+</sup> in the cytosol of the cells using the Fluo3-AM probe. ....	274
Supplementary Fig. 7-11. Representative images of SH-SY5Y cells treated for 1 day with A $\beta$ and each monosaccharide showing degree of membrane permeability using the probe Calcein-AM.....	275

Supplementary Fig. 7-12. Quantification of the AChE enzymatic activity in the SH-SY5Y cells cultured for 1 day in the presence of A $\beta$ and of each monosaccharide.....	275
Supplementary Fig. 7-13. Relative densitometric bar graphs of pIRS1 (measured using the WB membrane) expressed by SH-SY5Y cells treated for 1h with A $\beta$ and different concentrations of insulin. In all the cases the results were normalized considering the $\beta$ -actin expression.....	276
Supplementary Fig. 7-14. Relative densitometric bar graphs of pIRS1 and pAKT1/AKT1 (measured using the WB membranes) expressed by SH-SY5Y cells treated for 1h with A $\beta$ , insulin, and each monosaccharide.....	276
Supplementary Fig. 7-15. Relative densitometric bar graphs of Annexin 1 (measured using the WB membranes) expressed by SH-SY5Y cells treated for 1h with A $\beta$ , insulin, and each monosaccharide.....	277
Supplementary Fig. 8-1. Schematic presentation of the used single component and mixed self-assembled monolayers (SAMs)..	297
Supplementary Fig. 8-2. Schematic presentation of Fn structure and its domains to which ECM molecules and cell surface receptors bind.....	298
Supplementary Fig. 8-3 The QCM-D derivative plot with the initial adsorption profiles of Fn onto the SAM surfaces containing both -SO <sub>3</sub> H and -OH functional groups.....	299
Supplementary Fig. 8-4 Reflectivity curves (SPR curves) of the fibronectin adsorption onto different substrates at two wavelengths (670 and 785 nm).....	299
Supplementary Fig. 8-5. Representative AFM images of fibronectin adsorbed on different self-assembled monolayers. ....	300
Supplementary Fig. 8-6. Raw data QCM-D data showing frequency and dissipation shifts measured during adipose-derived stem cells adhesion on different substrates without (up) and with (down) pre-adsorbed fibronectin.....	300
Supplementary Fig. 8-7. Immunostaining of adipose-derived stem cells (ASCs) after QCM-D characterization (1h in the QCM-D cell) in the absence of Fn.....	301
Supplementary Fig. 8-8. Morphometric analysis of ASCs on QCM-D crystals (1h) with different surface concentration of -SO <sub>3</sub> H groups in the absence and presence of pre-adsorbed Fn.....	301
Supplementary Fig. 8-9 Morphometric analysis of ASCs cultured under standard conditions on single and mixed SAMs (in the presence and absence of Fn).....	302

## LIST OF TABLES

Table 3-1. Minimum inhibitory concentration (MIC, mg/mL) of each extract/polyphenol, i.e. CWE, CWE-E, vescalagin and castalagin, towards the four tested strains of bacteria.....	124
Table 4-1. Yield of extraction, TPC and AO activity of the cork extracts (CWE and CWEE) and chromatographically fractionated sample (fCWEE).....	148
Table 4-2. Quantitative analysis of the cork extracts (CWE and CWEE) and the fractioned sample (fCWEE), expressed as mg of compound/g of extract.....	149
Table 5-1. ITC analysis of the interaction between A $\beta$ 42 and 1 or 2 under a A $\beta$ 42:polyphenol ratio of 1:1.....	167

## LIST OF SUPPLEMENTARY TABLES

Supplementary Table 3-1. Quantification of disc diffusion assay for vescalagin and castalagin, towards Gram-positive bacteria .....	136
Supplementary Table 3-2. Minimum bactericidal concentration (MBC, mg/mL) of each extract/polyphenol (i.e. CWE, CWE-E, vescalagin and castalagin), towards the four tested strains of bacteria. ....	136
Supplementary Table 4-1. HPLC-ESI/MS analysis and identification of main cork extract compounds .....	158
Supplementary Table 5-1. Secondary structure of A $\beta$ 42 during assembly (aggregation from the monomeric form) and disassembly (disaggregation of the pre-formed fibrils) in the presence of vescalagin and castalagin.....	185
Supplementary Table 6-1 MD simulation analysis of the interaction between A $\beta$ <sub>i</sub> and dendrimers under a A $\beta$ :dendrimers ratio of 1:1.....	227
Supplementary Table 8-1 Characteristics of the SAM coated surfaces used in this work.....	297

## **SHORT CURRICULUM VITAE**

**Ana Rita Araújo** was born in 1986 in Sande São Martinho. Her academic journey started on 2006 at the Institute of Engineering of Porto (ISEP), with a graduation in Chemical Engineering, which was concluded in 2009 with a final grade of 13/20. In 2009 she enrolled in a Master degree course in Chemical Engineering - Environmental Protection Technologies (at ISEP), which she finished by 2011 with a final grade of 15/20. During her masters she participated in the Erasmus Program, where she had the opportunity to visit the Kaho Sint-Lieven University, Gent. During 6 months she developed her final research Project with a final degree grade of 18/20.

Nowadays, Ana Rita is a PhD student at the 3B's Research Group enrolled in the Tissue Engineering, Regenerative Medicine and Stem Cells Doctoral Program. She arrived at the 3B's Research Group in 2011, to work in the "WaterCork" project. Since then, she has been working in the exploitation of cork-based compounds using different methodologies to assess their biological activity and potential applicability, under the scope of different projects, namely, "GlueCork" and "BioactiveCork" and "LA ICVS/3Bs" projects. Additionally, she participated in the functionalization of 2D surfaces using self-assembled monolayers (SAMs) for biosensing applications, under the scope of the project "Find & Bind" financed under the 7<sup>th</sup> Framework Program of the European Commission. In September 2014 she enrolled in her PhD at the 3B's Research Group from the University of Minho and in September 2016 she was awarded a PhD scholarship by the "Programa Operacional Regional do Norte" (Norte 2020). Under the supervision of Dr. Ricardo Pires and Prof. Dr. Rui L. Reis, she dedicated her PhD work to the development of cork-based compounds/extracts and the exploitation of their bioactivities as anti-bacterial and anti-UV agents, as well as in the field of Alzheimer's disease (AD), evaluating their ability to modulate the supramolecular assembly of amyloidogenic peptides/proteins. Based on her initial results she also developed dendrimers presenting the bioactive chemical features of the cork compounds and tested them (as well as different glucosamine analogues) in their ability to ameliorate several AD hallmarks.

Ana Rita Araújo was board member of the Portuguese Young Chemists group (GQJ) from the Portuguese Chemical Society (SPQ), from 2016 to 2018; and a Portuguese Delegate member in the 13<sup>th</sup> EYCN Delegates Assembly of the European Young Chemists Network (EYCN) from the Young Chemists of the European Chemical Society (EuChemS), contributing to the organization of the 1<sup>st</sup> European Young Chemists Meeting (EYCheM), held together with 5<sup>th</sup> Portuguese Young Chemists Meeting (2016) in Guimarães, Portugal. More recently, she was founding member of the PhDynamics Group from 3B's Research Group (2018).

She was also involved in the execution of the Twinning project "Chem2Nature" and in the project "NORTHERN DISCOVERIES CTR" of the H2020 Program of the European Commission and Norte2020 regional programme, respectively.

As result of her research work, she is author or co-author of 9 full length papers published in international scientific journals, 1 book chapter, 1 published conference abstract, 7 oral communications, 9 poster presentations.

## LIST OF PUBLICATIONS

The work performed during the PhD period resulted in the publications listed below.

### *Papers in international scientific journals with referees (as first author)*

1. **Araújo A. R.**, Reis, R. L. & Pires, R. A, (2020), From natural compounds to polyphenol-terminated nanosystems in Alzheimer disease. (submitted)
2. **Araújo A. R.**, Araújo, C. A., Reis, R. L. & Pires, R. A, (2020), Vescalagin and castalagin present bactericidal activity towards Methicillin-resistant bacteria. (submitted)
3. **Araújo A. R.**, Reis, R. L. & Pires, R. A, (2020), Glucosamine analogues as modulators of amyloid- $\beta$  toxicity. (submitted)
4. **Araújo A. R.**, Correa J., Dominguez-Arca V., Reis, R. L., Fernandez-Megia E. & Pires, R. A, (2020), Functional gallic acid-based dendrimers as synthetic nanotools to remodel amyloid-beta 42 into non-cytotoxic forms. (submitted)
5. **Araújo A. R.**, Gigante S. C., Taboada P., Reis R. L., and Pires R. A., "Vescalagin and castalagin reduce the toxicity of amyloid-beta42 oligomers through the remodelling of its secondary structure", Chemical Communications (RSC), doi:10.1039/DOCC00192A, 2020).
6. **Araújo A. R.**, Soares da Costa D., Amorim S., Reis R. L., Pires R. A., and Pashkuleva I., "Surfaces mimicking glycosaminoglycans trigger different response of stem cells via distinct fibronectin adsorption and reorganization", ACS Applied Materials & Interfaces, vol. 8, issue 42, pp. 28428 - 28436, doi:10.1021/acsami.6b04472, 2016.
7. **Araújo A. R.**, Pereira D. M., Aroso I. M., Santos T., Batista M. T., Cerqueira M. T., Marques A. P., Reis R. L., and Pires R. A., "Cork extracts reduce UV-mediated DNA fragmentation and cell death", RSC Advances , issue 5, pp. 96151 - 96157, doi:0.1039/C5RA15712A, 2015

*Papers in international scientific journals with referees (as co-author)*

1. Aroso, I.M., **Araújo A. R.**, Pires R. A., and Reis R. L., "Cork: Current Technological Developments and Future Perspectives for this Natural, Renewable, and Sustainable Material", ACS Sustainable Chemistry & Engineering, vol. 5, issue 12, pp. 11130–11146, doi:10.1021/acssuschemeng.7b00751, 2017
2. Aroso I. M., **Araújo A. R.**, Fernandes J. S., Santos T., Batista M. T., Pires R. A., Mano J. F., and Reis R. L., "Hydroalcoholic extracts from the bark of Quercus suber L. (Cork): optimization of extraction conditions, chemical composition and antioxidant potential", Wood Science and Technology, vol. 51, issue 4, pp. 855-872, doi:10.1007/s00226-017-0904-y, 2017

*Book Chapter*

1. **Araújo A. R.**, Reis R. L., Pires R. A. "Natural Polyphenols as Modulators of the Fibrillization of Islet Amyloid Polypeptide" (*In Press*)

*Conference oral presentations (as first author and as speaker)*

1. **Araújo A. R.**, Alexandra Brito, Reis R. L., and Pires R. A., " Supramolecular inhibition of A $\beta$ 42 intermediates by GlcN analogues", 13th International Meeting of the Portuguese Carbohydrate Group – GLUPOR 13, Porto, 2019.
2. **Araújo A. R.**, Gigante S. C., Moura L., Reis R. L., and Pires R. A., "Natural aromatic small molecules redesign toxic soluble A $\beta$ 42 oligomers", TERMIS EU-Rhodes 2019 , 2019. Supramolecular inhibition of A $\beta$ 42 intermediates by GlcN analogues
3. **Araújo A. R.**, Correa J., Fernandez-Megia E., Reis R. L., and Pires R. A., "GaOH-dendrimers remodel the conformation of A $\beta$  oligomers and reduce their toxicity towards SH-SY5Y cells", GENE2SKIN AND CHEM2NATURE FINAL CONFERENCES, 2018.
4. **Araújo A. R.**, Correa J., Fernandez-Megia E., Reis R. L., and Pires R. A., "Polygalloyl-dendrimers rescue cell viability through the modulation of amyloid-beta fibrillization", CHEM2NATURE and GENE2SKIN Summer Schools, 2018.
5. **Araújo A. R.**, Correa J., Fernandez-Megia E., Reis R. L., and Pires R. A., "Galloyl-terminated dendrimers modulate A $\beta$ 42 fibrillization and reduces cellular toxicity", 13th EYCN Delegates Assembly , 2018.



6. **Araújo A. R.**, Soares da Costa D., Amorim S., Reis R. L., Pires R. A., and Pashkuleva I., "Glycosaminoglycan mimicking surfaces trigger distinct response of stem cells via fibronectin adsorption", 27th European Conference on Biomaterials 2015, 2015.
7. **Araújo A. R.**, Jalles A., Aroso I. M., Teixeira-Castro A., Maciel P., Reis R. L., and Pires R. A., "Bioactive phenolic compounds as an unconventional approach against Machado-Joseph Disease", The POLARIS Conference, 2015.

*Conference posters (as first author)*

1. **Araújo A. R.**, Correa J., Fernandez-Megia E., Reis R. L., and Pires R. A., "Galloyl-terminated dendrimers block the formation of amyloid fibrils and rescue cell viability", 29th Annual Meeting of the European Society for Biomaterials , 2018.
2. **Araújo A. R.**, Correa J., Fernandez-Megia E., Reis R. L., and Pires R. A., "Gallic acid-based dendrimers modulate A $\beta$ 42 fibrillization and reduces cellular toxicity", 2018 TERMIS World Congress, 2018.
3. **Araújo A. R.**, Correa J., Fernandez-Megia E., Reis R. L., and Pires R. A., "GA-Dendrimer remodels A $\beta$ 42 peptide fibrils and reduces cellular toxicity", Ciência 2018, 2018.
4. **Araújo A. R.**, Gigante S. C., Reis R. L., and Pires R. A., "Vescalagin and castalagin inhibit the fibrillization of amyloid-beta and rescue cell viability", TERM STEM / FORECAST 2017, 2017.
5. **Araújo A. R.**, Gigante S. C., Reis R. L., and Pires R. A., "Vescalagin and castalagin rescue cell viability through the inhibition of amyloid-beta fibrillization", INTERNATIONAL SYMPOSIUM ON BIOINSPIRED MACROMOLECULAR SYSTEMS , 2017.
6. **Araújo A. R.**, Gigante S. C., Reis R. L., and Pires R. A., "Cork polyphenols, an alternative strategy against amyloid-beta fibrillization", CHEM2NATURE second school, 2017.
7. **Araújo A. R.**, Gigante S. C., Reis R. L., and Pires R. A., "Natural polyphenols from cork as an alternative strategy against amyloid-beta fibrillization", CHEM2NATURE, 2016.
8. **Araújo A. R.**, Pereira D. M., Aroso I. M., Santos T., Batista M. T., Cerqueira M. T., Marques A. P., Reis R. L., and Pires R. A., "Cork extracts as bioactive compounds against UV-mediated DNA fragmentation ", Gen2Skin and Term Stem Conference, 2016.
9. **Araújo A. R.**, Fernandes J. S., Aroso I. M., Pires R. A., and Reis R. L., "CORK EXTRACTS AS UV PROTECTIVE AGENTS", 3rd ICVS-3B's Associated Laboratory Meeting, Braga, Portugal, June 2013, 2013.

***Awarded grants***

Programa Operacional Regional do Norte (Norte 2020) - *Programa Doutoramento em Terapias Avançadas para a Saúde* for the PhD scholarship (NORTE-08-5369-FSE-000037)

## INTRODUCTION TO THE THESIS FORMAT

This thesis contains four general **Section (I to IV)** comprising eight **Chapters (1 to 8)**. The **Section I** provides a broad introduction to the main materials used in this thesis and their capacities, based on their anti-amyloidogenic properties (**Chapter 1**). The **Section II** details the materials and methods (**Chapter 2**) used on the development of the experimental work. In **Section III**, the experimental work and results are described and discussed, divided in five **Chapters (3 to 7)**. Finally, the **Section IV** relies on the final conclusions of the thesis (**Chapter 8**). The thesis format is based on published or submitted papers, containing the following structure: abstract, introduction, experimental section, results and discussion and conclusion. The content of each chapter is summarized below.

### *Section I – General introduction*

*Chapter 1 – Natural polyphenols and nanosystems for Alzheimer’s disease:* provides an overview on the developed polyphenolic-based methodologies, for the remodelling/inhibiting of Amyloid- $\beta$  peptide in Alzheimer disease.

### *Section II – Detailed description of experimental materials and methodologies*

*Chapter 2 – Materials and Methods:* presents the developed materials, experimental studies and characterization techniques used within the experimental work developed on Chapters 3 to 7.

### *Section III – Experimental studies*

*Chapter 3 – Vescalagin and castalagin present bactericidal activity towards Methicillin-resistant bacteria:* presents the anti-bactericidal capacity of vescalagin and castalagin against four bacterial strain, in particular towards the Methicillin-resistant ones (MRSA and MRSE), and the ability to inhibit the formation of biofilms.

*Chapter 4 – Cork extracts reduce UV-mediated DNA fragmentation and cell death:* shows the ability of polyphenolic cork-based compounds as relevant source of antioxidant compounds able to act in the cellular environment, protecting cells against oxidation, reducing the number of ROS species and limiting the negative impact of UV radiation.

*Chapter 5 – Vescalagin and castalagin reduce the toxicity of amyloid-beta42 oligomers through the remodelling of its secondary structure:* reports the anti-amyloidogenic capacity of the two isomers, vescalagin and castalagin extracted from cork-based compounds, as well their protecting effect in SH-SY5Y cells from A $\beta$ 42-mediated death.

Chapter 6 – Functional gallic acid-based dendrimers as synthetic nanotools to remodel amyloid-beta 42 into non-cytotoxic forms: demonstrates the interaction with the monomeric/oligomeric A $\beta$  species at their Glu, Ala and Val residues by H-bonding, promoting the peptide remodelling into non-cytotoxic aggregates in a process controlled by the Ga units.

Chapter 7 – Glucosamine analogues as modulators of amyloid amyloid- $\beta$  toxicity: shows the effect of the monosaccharides, in particular, GlcN6S and GlcN6P, in interact with the oligomeric A $\beta$  species, reducing: neuronal cell death, A $\beta$ -mediated damage to the cellular membrane; acetylcholinesterase activity; insulin resistance and pro-inflammation levels.

Chapter 8 – Surfaces mimicking glycosaminoglycans trigger different response of stem cells via distinct fibronectin adsorption and reorganization: reports the influence of the degree of sulfation of glycosaminoglycans on their interactions with fibronectin and the impact of these interactions on the adhesion and morphology of human adipose derived stem cells.

#### ***Section IV – Final conclusions and perspectives***

Chapter 9 – General Conclusions and Final remarks: contains a concluding summary of each Chapter presented on the thesis. General conclusions comprising the limitations and innovative features of the developed work is described. Finally, future perspectives and applications of the knowledge acquired on the thesis is also provided.

*“Saber? Que sei eu?  
Pensar é descrever.  
– Leve e azul é o céu –  
Tudo é tão difícil  
De compreender!...”*

*A ciência, uma fada  
Num conto de louco...  
– A luz é lavada –  
Como o que nós vemos  
É nítido e pouco!*

*Que sei eu que abrande  
Meu anseio fundo?  
Ó céu real e grande,  
Não saber o modo  
De pensar o mundo!”*

*Fernando Pessoa*

## SECTION I

# Chapter 1

## Natural polyphenols and nanosystems for Alzheimer's disease

## CHAPTER 1

### Natural polyphenols and nanosystems for Alzheimer's Disease <sup>1</sup>

#### ABSTRACT

Natural polyphenols present a wide range of bioactive properties. In the context of Alzheimer's disease (AD) they are usually able to ameliorate several of its pathological hallmarks. Their activity is usually associated with the number of galloyl units (Ga) in their structure. As examples, epigallocatechin-3-gallate (EGCG) and vescalagin are reported to present anti-amyloidogenic activity and ability to drastically reduce the amyloid-mediated cytotoxicity. In general, they are able to remodel the toxic amyloid- $\beta$  (A $\beta$ ) oligomeric species (an important hallmark of AD) into non-cytotoxic forms. However, they have not been effective when evaluated under the *in vivo* and clinical trials scenarios, mainly due to their poor stability and difficulties to cross the blood-brain barrier (BBB). In this context, different nanosystems have been designed to cross the BBB and deliver different types of drugs into the brain, however, by themselves, they lack the bioactivity necessary to be considered as a valid therapeutic strategy for AD and other central nervous system (CNS) disorders. Nanosystems have been functionalized/loaded with (poly)phenols improving their delivery rates into the CNS with a comparative reduction on the A $\beta$  cytotoxicity. Among these nanomaterials, dendrimers have obtained enormous attention because of their nanoscale uniform size, ability to modulate their surface multifunctionality and to tune their ability to cross the BBB. With a hyper-branched 3D structure, they have the potential to be designed to transport diverse Ga-based polyphenolic compounds and improving their delivery to the CNS.

Herein we provide an overview of the main natural polyphenols tested as modulators of A $\beta$  cytotoxicity (and its pathological outcomes in AD), as well as their combination with nanosystems (both by surface conjugation or encapsulation strategies) to improve their crossing through the BBB so that they can exert their therapeutic activity in the brain.

**Keywords:** Alzheimer Disease, Dendrimers, Galloyl group, amyloid- $\beta$  peptide, Nanoparticles.

---

<sup>1</sup> This Chapter is based on the publication: "Araújo A. R., Reis, R. L. & Pires, R. A, (2020), Natural polyphenols and nanosystems for Alzheimer's disease (submitted)"



## 1.1 ALZHEIMER'S DISEASE AND IT HALLMARKS

Alzheimer's disease (AD) is the most common neurodegenerative disease and the main cause of dementia.[1] The current therapeutic strategies is not able to stop the onset and progression of AD and the subsequent damage to neurons of the affected regions of the brain, *i.e.* hippocampus, entorhinal cortex or cingulate gyrus. The available AD drugs can only help to reduce or stabilize the symptoms for a limited time frame, as for example by inhibiting the acetylcholinesterase activity, one of the main responsables for the reduced concentration of acetylcholine neurotransmitter (vital for synaptic transmission) detected in AD patients.[2] These drugs are designed to ameliorate the AD-related confusion, memory loss, problems with thinking, reasoning and learning.[3] The exact trigger of AD is still unknown, however it has been reported that the onset of the disease begins several years before symptoms to appear.[4] Ageing is the most significant risk factor, while genetic factors and chronic disorders (*e.g.* Down's syndrome[5], cardiovascular diseases[6] or diabetes[7]) are related with more severe cases of AD.[8, 9]

AD is a complex disease that triggers a neurodegeneration scenario that leads to severe dementia and death.[10] The concept of AD-mediated neurodegeneration has been expanded from the idea of general neuronal loss and astrogliosis, to include earlier alterations. These events start with synaptic and dendritic injuries, followed by disturbances in the process of adult neurogenesis, circuitry dysfunction (disrupting the balance of synaptic excitation and inhibition), aberrant innervation and inflammation.[11-13] The evolution of the disease throughout the brain (from the hippocampus and entorhinal cortex to the cerebral cortex) is related to important biochemical events, such as the deposition of extracellular amyloid plaques and generation of intracellular neurofibrillary tangles (NTs).[14]

NTs are composed by twisted ribbon-like assemblies of the microtubule-associated tau protein, which is hyperphosphorylated and aberrantly misfolded resulting in the breakdown of the dendrites and axons of the neurons.[15] While AD-mediated dementia only occurs in patients that present NTs in the affected regions of the brain (*i.e.* outside the medial temporal lobe)[16], recent imaging studies have shown that the spread of amyloid through the cortex triggers NT to occur out of the medial temporal region.[17] In addition, it has been reported that NT-mediated neuronal loss and dementia requires the accumulation of amyloid plaques in the brain above a certain threshold.[18] This data (from the participants in the Harvard Aging Brain Study, HABS) indicates that a standardized uptake value ratios of amyloid accumulation (SUVR) of, approximately, 1.2 is needed to initiate the deposition of

hyperphosphorylated tau.[18, 19] These observations are at the basis of the present notion that the increased amyloid deposition in the brain is at the onset of AD.[20]

Amyloid plaques are formed from the abnormal extracellular generation, aggregation and deposition of the amyloid- $\beta$  peptide ( $A\beta$ ).[1]  $A\beta$  is produced at the cell membrane, upon the sequential cleavage of the transmembrane amyloid precursor protein (APP) by  $\beta$ -site amyloid precursor protein cleaving enzyme 1 (BACE1) and  $\gamma$ -secretase complex. Its accumulation leads to the triggering of several elimination mechanisms in the brain, *e.g.* phagocytosis/endocytosis, or the transportation of  $A\beta$  to the brain's periphery. When these mechanisms are not able to completely eliminate the misfolded  $A\beta$ , it starts to accumulate in the brain under different amyloid supramolecular forms. Importantly, specific  $A\beta$  intermediated species, *i.e.* oligomers, are associated with: deficiencies in lipid metabolism; membrane disruption (*i.e.*  $Ca^{2+}$  imbalance); oxidative stress causing mitochondria and endoplasmic reticulum dysfunction; insulin resistance signalling; and synaptic impairments.[21, 22]

### 1.1.1 THE AMYLOID AGGREGATION PATHWAY

$A\beta$  is generated from the processing of the amyloid precursor protein (APP) during its sequential cleavage by two membrane-bound endoproteases, the enzymes  $\beta$  (BACE1) and  $\gamma$ -secretase (a protein complex formed by several subunits, including Presenilin-1/Presenilin-2) in neurons (Figure 1-1a). After cleavage, the  $A\beta$  monomers are secreted as a soluble form during normal cellular metabolism, and can be found in the plasma and cerebrospinal fluid (CSF).[23] The cleavage by  $\gamma$ -secretase is not always at the same position, resulting in an  $A\beta$  population (of  $\sim 4$ kDa) with an important C-terminal heterogeneity and peptide length, where the most common ones present 38, 40 or 42 amino acids.

There are genetic factors that increase the risk of developing AD, these include mutations in the genes associated with Presenilin-1 and Presenilin-2, which enhance the probability to generate  $A\beta_{42}/A\beta_{40}$  and the deposition of extracellular senile plaques. However, the vast majority of AD patients do not present these genetic mutations and are still able to accumulate  $A\beta$ , but typically at older ages.[24]

$A\beta_{42}$  is mainly found in the extracellular senile plaques, whereas  $A\beta_{40}$  is more prominent in the vascular amyloid deposits.[25, 26] In fact,  $A\beta_{40}$  represents 80-90% of the total  $A\beta$  population in the CSF.[27] However, and despite being present at lower concentration,  $A\beta_{42}$  has been reported to be more pathological due to its insolubility and higher propensity to aggregate.[28, 29] In fact, recent studies have shown that  $A\beta_{42}$  and its oligomers are the most toxic species from the ones found in the senile plaques.[30]

In 1991 it was proposed the A $\beta$  hypothesis, that considers A $\beta$  as the trigger of AD and the main responsible for the spreading of the disease from the isocortex (stage I) to the isocortical areas (stage II) and then all across all the cortex areas (*e.g.* sensory and motor cortex – stage III), leading to its accumulation in the whole brain.[31] This hypothesis has been both confirmed and questioned over time. Importantly, the plaque-associated neuritic impairments are the most notorious evidence of the A $\beta$  neurotoxic capacity (*i.e.* triggering the tau hyperphosphorylation and the microtubule dysfunction).[18]

The abnormal aggregation of A $\beta$  is at the basis of its toxicity. In 1995, A $\beta$  oligomers were first reported as intermediate species present during the amyloid aggregation pathway.[32] Nowadays, it's well established that these oligomeric species are part of the complex dynamic equilibrium between soluble monomeric or oligomeric states and various insoluble states of higher-order aggregates (Figure 1-1b).[3] Since 2008, some studies started to be published proposing that A $\beta$  oligomers are the key-players in cellular toxicity.[33, 34] The idea that the newly generated A $\beta$  are either free in the extracellular space or remains linked to the plasma membrane and lipid raft constituents, became clear. The capacity of the A $\beta$  oligomers to diffuse in the cellular space is an important factor that contributes to their toxic character. Of note, endocytosed A $\beta$  monomers/oligomers are able to access different subcellular compartments through the vesicular transport system.[35] In addition, the intermediated A $\beta$  species that start to assemble near the plasma membrane, can spread or interact with its lipid rafts, and trigger several downstream cascades in AD.[36]

More recently, these theories have been confirmed through a series of increasingly sophisticated characterization methods, including selective radiolabelling, size-exclusion chromatography, mass spectrometry, X-ray crystallography and also NMR spectroscopy and electron microscopy.[37] These studies paved the way to an extensive evaluation of the ability of A $\beta$  to promote different biochemical pathological cascades in the cellular environment.[38]

### 1.1.2 THE A $\beta$ FOLDING PROCESS

The A $\beta$  folding process starts with the primary nucleation stage, where oligomers are generated from a pool of monomers.[38] These oligomers are described as "intrinsically disordered" or "natively unfolded", capable of interacting with other proteins/receptors, in a free soluble state (thermodynamically stable).[39] At higher concentrations, the thermodynamic stability of the native state is lost, generating a metastable state which is sensitive to supramolecular interactions, that lead to their aggregation (Figure 1-1d).[40] The nuclei/seeds of A $\beta$  are polymorphic with distinct arrangement of its units, namely through antiparallel  $\beta$ -sheet secondary structures (also called on-pathway oligomers), acting as a template for the

generation of the nanofiber backbone. It is still controversial how the oligomers are transformed into fibrils, however, it has been proposed that they interact between each other stacking them into a fibre through a combination of non-covalent and steric interactions.[41] This transformation promotes the dynamic re-arrangement of their supramolecular organization, forming parallel  $\beta$ -sheets (thermodynamically stable) and nanofibers that are the main constituents of the extracellular senile plaques detected in the brain AD patients (Figure 1-1b).

The kinetics of these steps can be followed using the Thioflavin-T (ThT) dye. ThT binds to species maintained by  $\beta$ -sheets, upon binding it shifts its excitation/emission wavelengths and increases its fluorescence.[42] Under these conditions, a sigmoidal curve of ThT fluorescence is generated which can be translated into the different phases of the aggregation process, namely: i) lag phase – generation of monomeric and oligomeric species until a critical concentration is reached; ii) exponential growth – where the formation of  $\beta$ -sheets and fibril formation increases exponentially; and iii) plateau phase – where the aggregation rate declines as a result of the reduction of the soluble species (oligomers that were converted into fibrils).[43] However, under physiological conditions there is no decline in the soluble species because the cleavage of APP continues to produce  $A\beta$ , and the conversion of the oligomers from its soluble state into the amyloid fibrils occur through a secondary nucleation mechanism.[44] Under secondary nucleation, new aggregates are generated at a rate dependent on the concentration of existing fibrils, because they catalyse their nucleation from the monomeric/oligomeric state at the fibre surface.[45]

As mentioned before, these events occur in the extracellular space, close to the lipid bilayer. Thus, the close proximity of the  $A\beta$  oligomers and the cell membrane, as well as their chemical affinity, promote their direct binding leading to: i) deficiencies in the lipid metabolism (*i.e.* impaired cholesterol transport); ii) aberrant cellular signalling (*e.g.* acetylcholine, glucose metabolism and insulin resistance, oxidative stress causing mitochondria and endoplasmic reticulum dysfunction, among others; and iii) membrane disruption through the insertion of  $A\beta$  structures into the membrane leading to the creation of ion-permeable pores and their unregulated efflux/influx (*i.e.* promoting  $Ca^{2+}$  imbalance, Figure 1-1c). All these features occur simultaneously leading to a knock-on effect and triggering neuronal cell death.

### 1.1.3 THE MECHANISM OF $A\beta$ CYTOTOXICITY

#### 1.1.3.1 LIPID METABOLISM

The clearance of  $A\beta$  from the brain is dependent on a series of synergistic pathways that includes their transportation to its periphery (*e.g.*  $\approx 60\%$  of  $A\beta$  is removed from the brain via this type of clearance).[46] Cellular mechanisms that are able to remove  $A\beta$  from the brain includes: uptake and

phagocytosis/endocytosis (*i.e.* by monocytes or neutrophils); proteolytic degradation by A $\beta$ -degrading enzymes; blood clearance-mediated by A $\beta$ -binding proteins, such as, albumin, antithrombin III and lipoproteins (*i.e.* apolipoprotein E, ApoE).[9, 47]

The expression of ApoE isoforms (ApoE 2-4) are a strong genetic factor of familial AD, being also essential regulators of the cholesterol metabolism, bridging the lipoprotein receptor (LPR1) expression, the clusterin (CLU or apolipoprotein J) and the ATP-binding cassette transporter A7 (ABCA7). They trigger the receptor expressed on myeloid cells 2 (TREM2) also linked to lipid homeostasis and an AD genetic risk factor.[48] The APP insertion onto the membrane depends on its cholesterol content, which increases with aging. Hence, the cholesterol compartmentalization and the equilibrium between free cholesterol and cholesteryl esters are determinant for A $\beta$  accumulation at the membrane and the promotion of cellular dysfunction.[49]

In addition, ABCA7 is a phospholipid transporter linked to TREM2 that, in turn, is a phospholipid receptor associated with ApoE (with important role in the transportation of phospholipids).[50] The lipoproteins codified by these genes are implicated in the recovery of membrane damage triggered by the amyloid deposits.[51] Failure in these recovery mechanisms triggers A $\beta$  cytotoxicity.[47, 52] In fact, some reports show that ApoE acts as a chaperone for A $\beta$ , and the knockout of ApoE or CLU results in the inhibition of amyloid plaque deposition, which have been reported to occur via a decrease in the number of A $\beta$  seeds/nuclei.[51]

Moreover, TREM2 can alter the inflammatory cascade both through the promotion of macrophage-mediated response, as well as by modulation of astrocyte activation. These alterations can lead to aberrant microglia activation, and upregulation of a number of pro- and anti-inflammatory cytokines associated with the immune response.[48]

Accordingly, A $\beta$  oligomers are able to bind to lipoproteins, such as ApoE and CLU[51], forming A $\beta$ -lipoprotein complexes that limit their activity and function in maintaining the lipid homeostasis. Importantly, these structures can be seen as possible targets for drug development, in an attempt to modulate their formation.

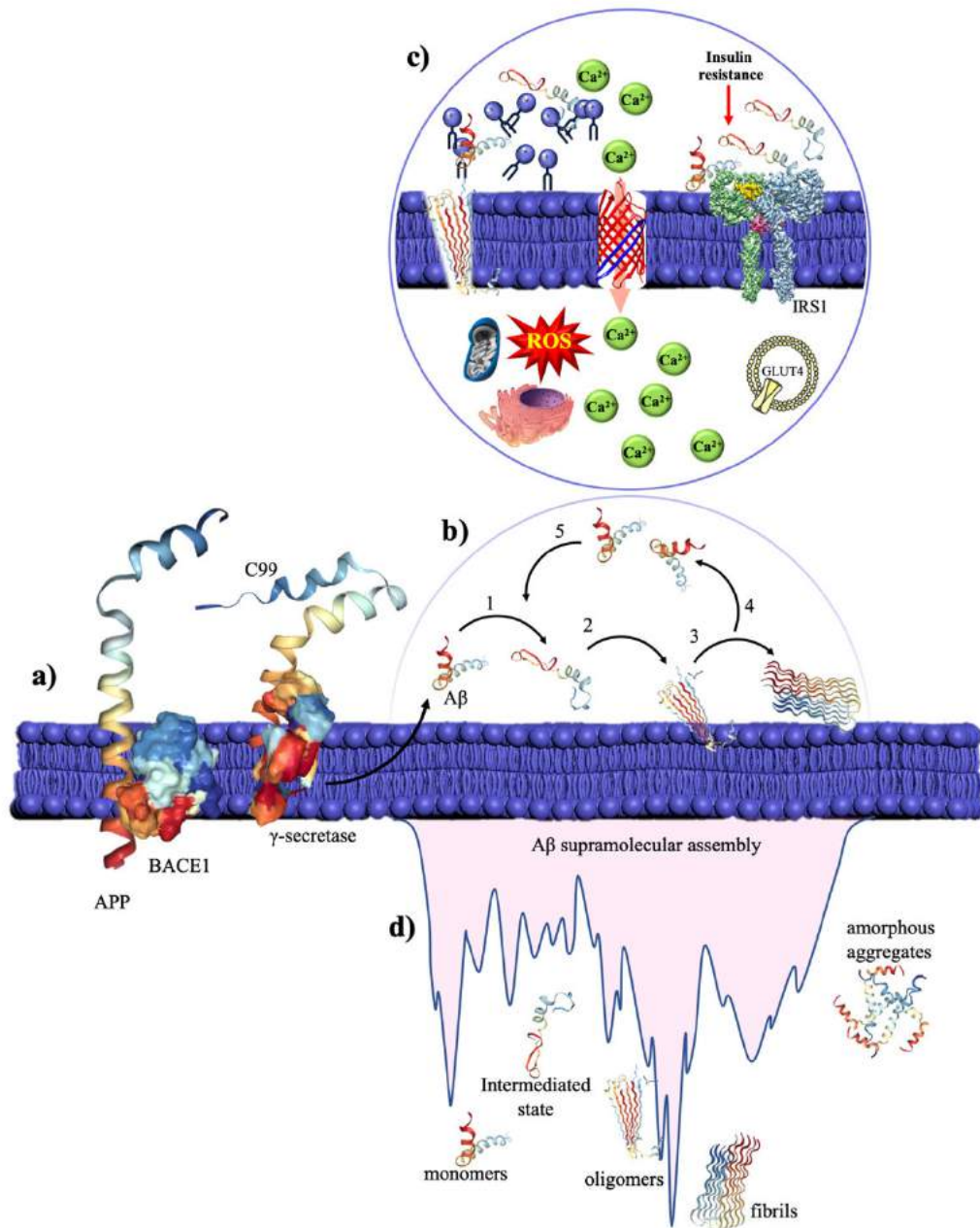


Figure 1-1 Schematic overview of the Aβ cleavage and folding showing a) the formation of Aβ through the cleavage of APP (amyloid precursor protein), and b) its interactions with the lipid bilayer surface promoted by the different Aβ supramolecular forms, namely: 1. Conversion (formation of pre-fold structures); 2. Aβ-mediated formation of pores; 3. Elongation and stabilization of the fibrils; 4. Oligomers formation (fragmentation of the fibres); 5. Additional fibrillization through secondary nucleation. c) The cytotoxicity pathway associated with the lipid rafts and d) the thermodynamic energy landscape of the Aβ species during its supramolecular assembly.

### 1.1.3.2 CELLULAR SIGNALLING CASCADE

It has been suggested that the cholesterol metabolism (through ApoE and lipid peroxidation), in association with the interactions of Aβ with the cell membrane, leads different pathological alterations in the neurons, namely: disruption of the cholinergic pathways, specifically in the cerebral cortex and the

basal forebrain; impairment in the glucose metabolism through the modulation of the insulin signalling; as well as mitochondrial and ER dysfunction due to increased levels of intracellular oxidative stress.[53]

The cholinergic hypothesis has been first reported in 1978 by Perry *et al*[54]. They initially found a correlation between the activity of acetylcholinesterase (AChE) and the amount of amyloid plaques in the post-mortem brains of AD patients. The acetylcholine neurotransmitter (ACh) present a vital role in memory, motivation and movement, as it participates in the signal transmission. After crossing the synaptic cleft, it binds to the nicotinic acetylcholine receptor (nAChR ionotropic) or the muscarinic acetylcholine receptor (mAChR metabotropic) for subsequent signal transduction, which is essential in the cerebral cortex, basal ganglia, basal forebrain, and neocortical cholinergic innervation.[55-57] The main role of AChE is to cleave ACh into acetate and choline after its binding to the receptors at the post-synaptic membrane, an essential activity necessary to terminate signal transmission.

AChE is usually overexpressed in AD leading to the use of inhibitors as part of the available clinical treatments. These are used in an attempt to promote signal transmission by increasing the amount of ACh available at the synapse cleft, which leads to the amelioration of the clinical symptoms of AD. However, the use of AChE inhibitors *per se* are not enough to stop the progression of the disease.[58]

Several reports state that the soluble forms of A $\beta$  are able to interact with AChE and  $\alpha$ 7-nAChR with enough affinity to regulate its functions[59]. However, there are others reports that indicate that A $\beta$  might not bind directly to these ACh receptors, but rather to the lipid rafts, perturbing membrane fluidity and altering the lipid microenvironment. In either scenarios it is known that A $\beta$  toxicity is triggered by hampering the function of the ACh receptors.[60]

A $\beta$  also presents an impact in the regulation of insulin signalling and glucose metabolism in the brain. In general, insulin is essential in the modulation of different cascades that integrate biochemical, hormonal, and neurogenic signals in peripheral tissues and organs such as the liver, skeletal muscle or adipose tissue.[3, 61] Most of the impairment of insulin signalling has been linked to diabetes mellitus, in fact it is known that diabetic patients present a higher probability to develop AD than healthy individuals.[7, 62] Importantly, the brain uses, approximately, 20% of the whole glucose consumed by the body in a process that is largely insulin independent (glucose uptake in neurons occurs mainly via GLUT3, an insulin-independent glucose transporter).[63] However, several studies reported that hyperglycemia and hyperinsulinemia foster the abnormal accumulation of toxic A $\beta$ . This increase of A $\beta$  cytotoxic forms is a result of the stimulation of APP processing, which is mediated by the insulin-dependent activation of the mitogen-activated protein kinase (MAPK) pathway.[64, 65] Cellular stress and inflammation, can also activate signalling molecules like p-JNK (c-Jun N-terminal kinase pathway is one

of the major signalling cassettes of MAPK) leading to an increase in the phosphorylation of the insulin receptor substrate (IRS1) at its serine residues, *i.e.* p(Ser)-IRS1, causing the inhibition of the translocation of GLUT4 onto the cell surface. In turn, the lower availability of GLUT4 at the plasma membrane lead to a lower glucose transport, while triggering hyperinsulinemia as a compensatory mechanism.[66, 67] In addition, the excess of insulin can competitively inhibit IDE-mediated A $\beta$  degradation (IDE is a metalloproteinase that degrades insulin and other small peptides).[68, 69] Importantly, amylin (an amyloidogenic peptide usually deposited in the pancreas of patients with type 2 diabetes mellitus) can enter the brain, where it accelerates and exacerbates the misfolding and aggregation of A $\beta$ .[61] Finally, other pathological features of diabetes mellitus, such as oxidative stress (OS), BBB disruption and reduced cell energy supply, has been also described to affect the formation of A $\beta$  and its clearance from the cellular environment.[70]

Neuronal cells are particularly susceptible to OS-mediated cellular damage, due to fact that the brain presents a very high oxygen consumption, *i.e.* approximately 20% of the total oxygen consumed by the body. In this context, OS has been considered one of the main triggers of the pathological hallmarks of AD.[71, 72] In fact, it is known that OS can influence the amyloid cascade (*i.e.* APP cleavage), as well as the excretion of copper and zinc within the synaptic cleft of some neurons. Since both copper and zinc are able to form complexes with A $\beta$ , they are considered as modulators of its bioactivity/cytotoxicity.[73] In general, different metal-ions have been found in the amyloid plaques, forming redox-active A $\beta$  complexes that are recognised to be highly toxic. They can generate reactive oxygen species (ROS) that, in turn promote the degradation of its surrounding biological environment.[74] Recently, it has been confirmed that protein and lipid oxidation mediated by OS occurs in the A $\beta$ -rich brain regions, where oxidized proteins were detected in the early stages of the disease.[75] The oxidation of the membrane lipids (*e.g.* cholesterol), proteins and nucleic acids, and the impairment of A $\beta$  clearance by the oxidized LRP1 leads to the disruption of the lipid rafts integrity.[76, 77] In addition, it has been shown that OS can be directly responsible for the disruption of membrane integrity, by promoting the loss of phospholipid asymmetry.[78, 79] This mechanism can also lead to decreased ATP levels that generate electron leakage and increased production of mitochondrial ROS, *i.e.* another source of OS in AD.[80]

Of note, the oxidation-induced impairment of the enzymatic activity involved in ATP production can also induce transportation abnormalities, as well as dysfunction of intracellular glucose catabolism.[81] Thus, it has been suggested that, increased OS mediated by A $\beta$  (as well as tau[71]) is an important contributor to the impairment of insulin signalling in the brains of AD patients.[82]



### 1.1.3.3 MEMBRANE DISRUPTION AND CALCIUM IMBALANCE

The increased OS and reduced metabolism faced by neurons during aging compromise the normal functioning of proteins that control membrane excitability (that allows a cell to generate an electrical signal in response to a stimuli) and the subcellular  $\text{Ca}^{2+}$  dynamics.[79, 83] In addition to OS, it is known that supramolecular  $\text{A}\beta$  oligomers are also able to perturb neuronal  $\text{Ca}^{2+}$  homeostasis, through their insertion into the plasma membrane and the subsequent generation of pores that act as entry points of  $\text{Ca}^{2+}$  into the cytosol.[84, 85] The increase in the number of these ion-permeable pores results in elevated intracellular (cytoplasmic)  $\text{Ca}^{2+}$  concentrations and increased vulnerability that, in turn, facilitates the binding of  $\text{A}\beta$  to phospholipids, such as phosphatidylserine (Ptd-L-Ser).[86] As a consequence Ptd-L-Ser is transferred from the inner portion of the plasma membrane onto the cell surface, which acts as a signal for processing by macrophages. Of note, the increased  $\text{Ca}^{2+}$  influx also triggers the apoptotic pathway, contributing to the overall cytotoxicity associated with the oligomeric  $\text{A}\beta$ . [20]

As mentioned before,  $\text{A}\beta$  can also interact with metal-ions generating hydrogen peroxide and hydroxyl radicals ( $\text{OH}\bullet$ ), resulting in membrane lipid peroxidation which generates toxic aldehydes that impair the function of membrane ion-motive ATPases.[87] Consequently, the membrane becomes depolarized, promoting the opening of glutamate receptor and voltage-dependent  $\text{Ca}^{2+}$  channels, promoting a similar outcome as the direct interaction of  $\text{A}\beta$  with the membrane, *i.e.* the influx of toxic amounts of  $\text{Ca}^{2+}$  into the cytoplasm. Furthermore,  $\text{A}\beta$  is also able to interact with the mitochondria causing an increment of the concentration of free-radicals that, in turn, instigates the elevation of the concentration of cytoplasmic  $\text{Ca}^{2+}$  and the level of OS.[88] Additionally, the release of the APP intracellular domain (*i.e.* AICD) upon processing of APP by BACE1, leads to its translocation into the nucleus, which has been reported to alter gene transcription in a way that perturb the  $\text{Ca}^{2+}$  homeostasis.[89] Genetic mutations on presenilins are also known to impair the function of  $\text{Ca}^{2+}$  leak-channels, resulting in excessive accumulation of  $\text{Ca}^{2+}$  in the ER.[90]

There are also evidences that  $\text{A}\beta$  is able to induce the interaction of presenilins with proteins associated with the ApoE receptor, contributing to an enhancement of  $\text{Ca}^{2+}$  influx and the pathological hallmarks of AD. In this case, the activation of the  $\text{K}^+$  channels is compromised contributing to the hyperpolarization of the cell membrane, promoting a dysregulation of the mechanism responsible for the  $\text{Ca}^{2+}$  homeostasis.[91]

All these  $\text{A}\beta$ -mediated mechanisms contribute to abnormal cellular functions, which ultimately leads to neuronal cell death

## 1.2 NATURAL COMPOUNDS AS DRUG LEADS FOR AD

Natural molecules derived from animals, plants, fungi, bacteria and other organisms show a wide structural diversity, as well as a broad range of biological activities, namely: anti-cancer, anti-oxidant, anti-microbial, anti-amyloidogenic, among others.[92, 93] There are multiple ways to identify possible disease-modifying molecules against amyloid-based pathologies.[94] In the case of natural compounds, there are a series of epidemiological studies that suggest that specific diets containing high intake of flavonoids and polyphenolic compounds have a preventive effect against dementia (*e.g.* including the AD-triggered one).[95] These studies suggest a reduced risk of AD and mild cognitive impairment in persons that have diets rich in grains, vegetables, fruit, fish, and nuts, specifically in  $\omega$ -3 fatty acids, vitamins, and diverse groups of polyphenolic compounds from the vast range of secondary metabolites from plants.[96, 97]

It has been shown that this type of molecules are effective against several AD pathological hallmarks, including abnormal A $\beta$  processing, synaptic degeneration, OS, and inflammation. It has been proven that some of them are able to reduce the rate of the progression of cognitive decline. Nevertheless, the positive effect of these compounds (administered through the diet) in the disease progression is not enough to reverse the disease and achieve a cure. However, these outcomes led researchers to evaluate their activity towards the different AD pathological hallmarks and to the successful identification of several natural compounds as inhibitors of amyloid aggregation.[98]

Several polyphenols[99, 100] are able to remodel the A $\beta$  secondary structure generating non-toxic species, as well as to modulate several AD hallmarks.[101, 102] The most common naturally-occurring polyphenols tested for AD are extracted from: green tea (*e.g.* EGCG and myricetin); red wine (*e.g.* resveratrol and ellagitannins); or curry/turmeric (*e.g.* curcumin).[103]

*In vitro* studies with EGCG, resveratrol, or other polyphenols show that they can inhibit the formation of toxic pre-fibrillar oligomers and amyloid fibrils, while converting previously existing fibres into insoluble aggregates of lower toxicity.[104, 105] However, despite the known outcome of the interaction between the polyphenols and different amyloidogenic peptides/proteins (*e.g.* A $\beta$ ), their mechanism of action is still not completely understood.[106] Importantly, it is known that these polyphenols affect the amyloid aggregation pathway contributing to: the reduction of the concentration of toxic oligomers; inhibiting fibril elongation; the disassembling of preformed fibrils into off-pathway species; inhibiting amyloid-membrane interactions; scavenging of ROS; among others.[107-111]

As mentioned before, the supramolecular assembly of A $\beta$  can be monitored using the ThT, as it increases its fluorescence when bound to the cross- $\beta$ -sheets of amyloid aggregates.[112] In addition, the intensity of the ThT fluorescence is considered to be proportional to the concentration of the  $\beta$ -sheet-rich

amyloid fibres.[42] Therefore, the characteristic sigmoidal curve observed during the amyloid aggregation pathway is usually altered by the presence of polyphenols, making the ThT assay as one of the most widely used techniques to assess their ability to modulate supramolecular assembly of different amyloids (*e.g.* A $\beta$ ).[113, 114] As an example, when EGCG is added to a solution of monomeric A $\beta$  (Figure 1-2a) it is observed a reduction of ThT fluorescence extending the lag phase of the A $\beta$  aggregation profile, due to the remodelling its supramolecular structure.[115] This observation is reported to be related with formation of small off-pathway amyloid aggregates, mediated by the interaction between EGCG and A $\beta$  through non-covalent interactions, such as H-bonds and  $\pi$ - $\pi$  stacking. This remodelling is also reflected in the morphological presentation and size of the A $\beta$  aggregates that can also be followed by TEM/AFM or SDS-PAGE and NBT assays (*e.g.* Figure 1-2b-d). Circular dichroism can also be used to assess these changes because they are usually associated with alterations in the A $\beta$  secondary structure.[116, 117] The aromatic moieties, *e.g.* galloyl (Ga) units, of the natural polyphenols have been reported to be the main responsables of their ability to interfere with the formation of the peptide  $\beta$ -sheets. In addition to the above mentioned H-bonds and  $\pi$ - $\pi$  stacking between the Ga moieties and A $\beta$ , it has been also reported the presence of electrostatic and van der Waals forces that also contribute to the interaction between the polyphenols and the A $\beta$  hydrophobic sections (from the peptide backbone or its side chains).[108] All these interactions interfere with the stability of the A $\beta$  supramolecular aggregates disrupting its secondary structure. In addition, the existing hydroxyl groups in *ortho* or *para* positions of several polyphenols are essential for their anti-oxidant capacity, which contribute to a synergetic effect on the activity of these compounds towards AD.[99]

The alterations that natural polyphenols are producing in the A $\beta$  secondary structure have been studied by computational modelling, including their capacity to bind to A $\beta$ 42 monomers, oligomeric or  $\beta$ -sheet structures.[118] As an example, Das *et al* [109] recently compared four different polyphenols (*i.e.* honokiol, myricetin, luteolin and punicalagin) and concluded that they were able to bind to A $\beta$ 42 oligomers mainly through steric and H-bonding interactions. Important targets in the peptide backbone were identified from the A $\beta$ 42 hydrophobic section (*i.e.* Lys16, Leu17, Val18 and Phe19).[109] It has been also shown that polyphenols may also exert their anti-aggregation capacity by targeting the lysine

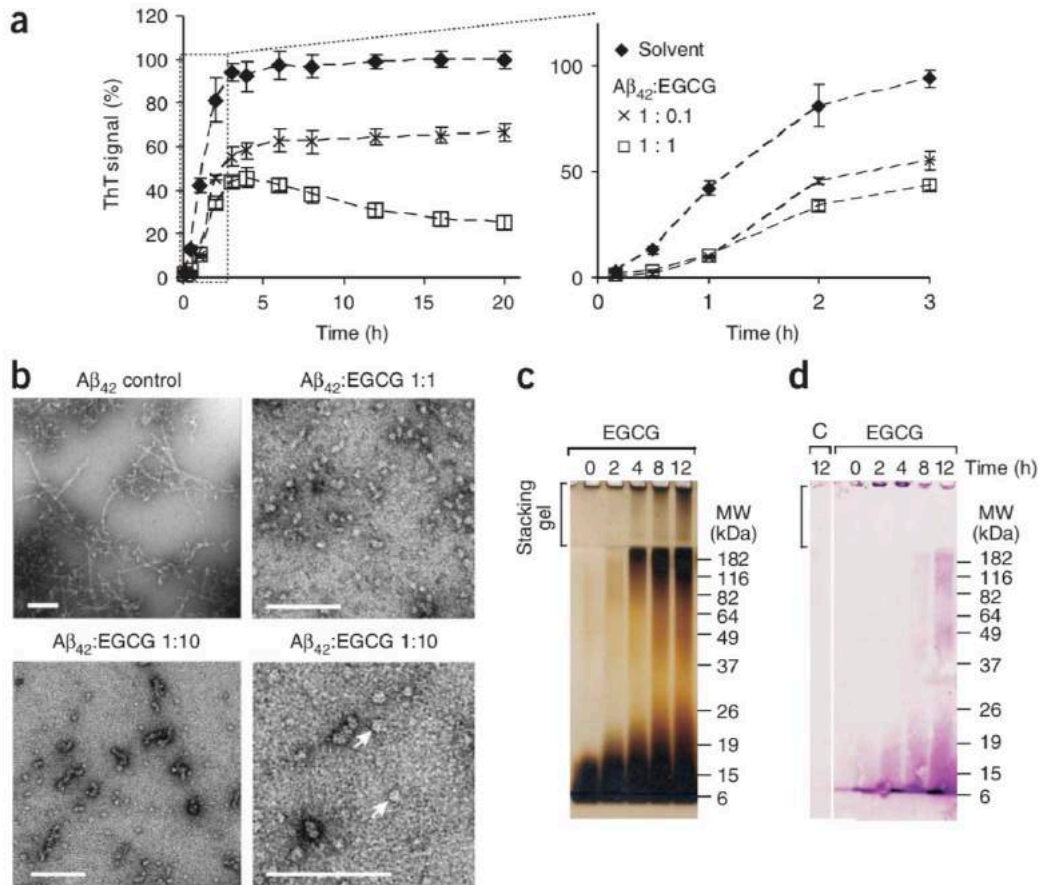


**Figure 1-2 EGCG induces the formation of off-pathway Aβ<sub>42</sub> aggregates. (a) Impact of EGCG on the Aβ<sub>42</sub> aggregation profile monitored by ThT fluorescence. (b) Morphological presentation of Aβ in the presence and absence of EGCG evaluated by electron microscopy after 72h of incubation; Scale bars = 100 nm. (c, d) Evaluation of the ability of EGCG to change the size of Aβ<sub>42</sub> aggregates followed by (c) SDS-PAGE and (d) NBT assays.[115]**

residues of the Aβ sequence.[119] In most of the cases, a destabilization of the Aβ supramolecular conformation occurs through the formation of H-bonds between the polyphenols and the Aβ residues responsible for the formation of the β-sheets (*i.e.* residues with exposed side chains in the fibril structure).[120]

Different studies also compared the activity of several tea catechins, namely: (-)-epicatechin (EC); (-)-gallocatechin (GC); (-)-epicatechin-3-gallate (ECG); (-)-epigallocatechin (EGC), and EGCG. Overall, only ECG and EGCG (due to the presence of the Ga units) contributed to a neuroprotective effect on hippocampal cell cultures, through their ability to inhibit the formation of Aβ oligomers/fibrils.[121, 122] Therefore, it has been concluded that the polyphenol-induced Aβ remodelling, via a combination of hydrophobic and H-bonding interactions, is mediated by the Ga moieties, contributing to the reduction of Aβ cytotoxic species. All the reported data supports the use of Ga-based molecules as a promising strategy to minimize neuronal damage.

The high structural diversity of polyphenols is what gives them a wide range of biological activities.[94, 123, 124] The number and positioning of the hydroxy groups is a critical factor that affects their bioactivity, as they are reported to be essential in their ability to interact with the exposed amino acid side chains from the A $\beta$  sequence.[107, 125] They are also important modulators of the aggregation energy barrier, mitigating the spreading of A $\beta$  oligomers and associated toxicity by reducing its lifetime and concentration.[99, 111] Another important feature of the Ga-based compounds is the coplanarity of the aromatic moieties, that has been recognised to favour hydrophobic and  $\pi$ - $\pi$  stacking interactions.[126] In addition, rigid planar molecules, as some of the polyphenols, may also embed within the cross- $\beta$  sheets structure of A $\beta$ , blocking the stacking of additional A $\beta$  molecules, hampering fibril elongation, while also impeding the secondary nucleation (dependent on the fibril's concentration).[124, 127, 128]

As mentioned before, in general Ga-based molecules (Figure 1-3) can also protect cells against oxidative damage due to their known ability to scavenge ROS.[129] Of note, this protection can be extended to membrane lipids and transmembrane proteins, due to their ability to penetrate into the lipid bilayer.[130]

In general, the ability to remodel the A $\beta$  supramolecular structure is imperative to be able to rescue cell viability. In addition to their A $\beta$  remodelling capacity, Ga-based compounds have been associated with the ability to decrease mitochondria and ER dysfunctions (driving them into an equilibrium in the intracellular redox state), as well as to decrease membrane permeability (re-establishing the homeostasis of intracellular Ca<sup>2+</sup> concentration).[131] As an example, EGCG and tannic acid affect the processing of APP through their ability to modulate the activity of different secretases, such as BACE-1,[132, 133] leading to a reduction of the A $\beta$ -mediated formation of non-specific pores and a stabilization of the lipid membrane, impeding its dysruption.[134] [135] In another perspective, the A $\beta$ -mediated Ca<sup>2+</sup> imbalance increments ATP production causing an additional boost in the intracellular concentration of ROS.[136] However, Ga-based compounds, due to their anti-oxidant activity, are able to reduce the intracellular ROS concentration contributing to the repair of mitochondrial damage, and reducing the cellular oxidative state that modifies proteins, while preventing changes in the superoxide dismutase expression (caused by neuronal OS).[137] Finally, since they usually act in the glutamate cysteine ligase expression, they can also promote an increase in the protein levels of the beta subunit of ATP synthase that is able to regulate acetylcholinesterase activity.[138] Of note, EGCG has been shown to induce neuroprotective activity acting on ERK (extracellular-signal-regulated kinase), JNK, and p38 through the MAPK pathway.[139, 140]

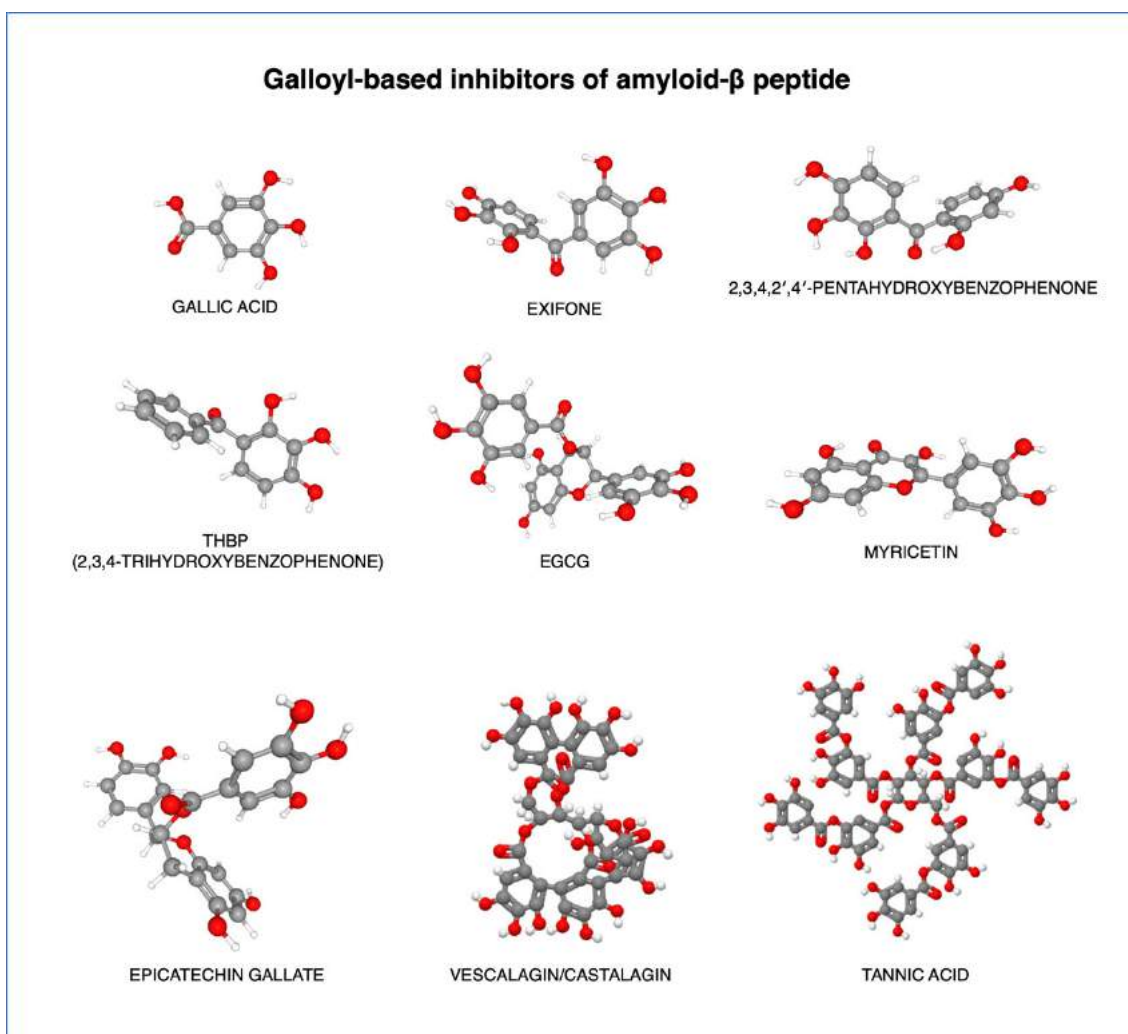


**Figure 1-3** 3D representation of the most studied natural-occurring Ga-based polyphenols that are able to inhibit or remodel the A $\beta$  supramolecular organization, and protect neuronal cells from their cytotoxicity.

A small number of reports discuss the molecular mechanisms that lead to amyloid inhibition in the cellular or *in vivo* environments. This is probably due to the complexity of the biological environment, where molecular discrimination is difficult to achieve.[141] The majority of the studies describes the effect of the Ga-based compounds on animals, evaluating their neurobehavioral functions or examining relevant amyloid plaques by immunohistochemistry staining.[133] In these cases, it has been shown that EGCG can reduce the burden of A $\beta$  plaque and lower the toxicity of oligomers in the brain of an AD-transgenic mouse model. It is also able to re-establish healthy mitochondrial activity, ROS production and ATP levels (in mitochondria isolated from the hippocampus, cortex, and striatum).[134] Cognitive decline is also a pathological hallmark of AD that has been reported to be reduced by EGCG. Additional beneficial effects include a reduction of microglia activation, an increased autophagic response, reduced inflammation levels, and recovery of redox homeostasis.[142, 143]

There are few human trials using Ga-based compounds in the context of AD. Most of them use EGCG and curcumin to target A $\beta$  and reduce its accumulation, however, no significant benefits have been observed (ClinicalTrials.gov - NCT00951834)[144]. Importantly, the levels of these molecules were untraceable in the brain (and undetectable in the CSF), suggesting that one of the main problems with their use is the limited bioavailability in the brain.[145]

Therefore, brain bioavailability studies are critical to assess the suitability of AD drugs. Of note, polyphenols are easily oxidizable by the heat and light.[146] This characteristic in combination with their typical low water solubility and the fact that they are metabolized at a high rate, leads to their fast removal from the body.[147] These aspects are at the basis of the poor stability and bioavailability, drastically reducing their effectiveness in the *in vivo* setting.

Importantly, due to their physicochemical characteristics, some polyphenols may not be able to cross the BBB and reach the brain cells, where they could modulate microglia-mediated inflammation or exert their neuroprotective activity, leading to contradictory results when compared to the *in vitro* assays.[148] Therefore, it might be necessary to optimize their chemical structure and/or exploit them in combination with drug delivery vehicles.

### 1.3 NANOSYSTEMS FOR AD

Different types of nanosystems have been tested in the context of AD, namely, polymeric nanoparticles (NP), solid lipid NPs, nanostructured lipid carriers, nanoemulsions, and liquid crystals. They are usually used for the successful delivery of AD drugs, including polyphenols and other natural compounds.[149]

The main concept based on the exploitation of these systems is to efficiently enable the crossing of the BBB, which implies a high lipid solubility and a low  $M_w$  (*i.e.* < 400–500Da) to cross the BBB through the tight junctions or by lipid diffusion. However, only 2% of CNS drugs are able to cross the BBB and reach their therapeutic targets in the brain. As mentioned before, hydrophobicity, unfavourable absorption by biological membranes, weak pharmacokinetic parameters, instability of the drugs (susceptible to oxidation, hydrolysis or photolysis), and toxicity to tissues (*e.g.* hepato-toxicity, neuro-toxicity, or kidney toxicity) are all characteristics that hamper their use to target the CNS. In this case, suitable nanosystems (conjugated or loaded with the drug) are necessary to reach their final destination in the brain.[150] [141]

In the following subsections we review the different nanosystems that have been proposed to be used to reach the brain of AD patients (giving particular attention to the ones that are tested for the delivery of polyphenols) and the nanosystems (*e.g.* dendrimers) that have been tested as therapeutic agents by themselves.

### 1.3.1 DRUG-DELIVERY SYSTEMS FOR AD – CROSSING THE BBB

The brain and the whole CNS are one of the most protected regions of the body. Its extracellular fluids are protected by three main borders: 1) the BBB, where the brain capillary blood is separated from the interstitial fluid (ISF) by endothelium cells, pericytes and astrocytes, which are followed by a layer of neuronal cells; 2) the ependymal layer that separates neurons from the cerebrospinal fluid (CSF); and 3) the choroid plexus that separates the CSF from the choroidal capillary blood (*i.e.* the Blood-CSF barrier – BCSFB).[151] The BBB and the BCSFB prevent the free paracellular diffusion of polar molecules by a series of complex features (*i.e.* tight junctions and transendothelial electrical resistance, TEER), limiting their passage through a minimal pinocytosis.[152] In the tight junctions, the TEER (responsible for the permeability to small ions) is mainly dependent on the profusion and complexity of several transmembrane proteins (*i.e.* occludins, claudins, and junctional adhesion proteins) that contribute to reaching a TEER of 8000  $\Omega\text{cm}^2$ , which, in turn, leads to high paracellular diffusion constraints.

Usually, in the case of paracellular/transcellular diffusion it is only possible for small molecules (< 500 Da), such as lipophilic compounds, ethyl alcohol, oxygen or carbon dioxide, as they can diffuse through the cell membrane. However, in general, approximately 98% of low molecular weight drugs cannot cross the BBB through these mechanisms.[153] Small molecules/drugs can also enter the brain through a receptor-mediated mechanism or metabolic pathways (altering the drug during the process of crossing from the blood into the brain).[154]

Another constraint in the crossing of the BBB is related with the ATP-binding cassette and P-glycoproteins, present at the BBB, and acting as efflux transporters responsible for clearing the waste products from the brain into the blood and prevent the entry of potentially neurotoxic compounds. In this case, there are several enzymes, such as  $\gamma$ -glutamyl transpeptidase or alkaline phosphatase, that are able to metabolize drugs and nutrients promoting their fast removal, hampering their bioavailability in the brain.

To overcome these hurdles, it has been proposed a series of nanosystems to act as biocompatible drug carriers to cross the BBB and deliver the cargo in the regions of the brain affected by cancer, CNS disorders or that require tissue regeneration.[141, 155] As mentioned before, it is well established that an intact BBB restricts the majority of molecules based on their molecular weight and lipid solubility, *i.e.* lipid soluble molecules can cross the BBB easier than the water-soluble ones. While results in patients with early AD showed global BBB leakage[156], the developing of nanosystems for AD should not be considering this BBB disturbance, as A $\beta$  toxicity and its spreading throughout the brain starts 20 years before the patients get the first symptoms.[157] In fact, clinical trials suggest a better outcome when A $\beta$ -



targeting drugs are administered during this pre-AD condition.[158] Consequently, new drugs are currently being administered in asymptomatic stages of AD, where the BBB is still not compromised.[159] Therefore, a successful therapeutic strategy has to be effective at reducing the presence of cytotoxic A $\beta$  oligomers and inhibiting their secondary nucleation pathway, but also designed to cross the BBB and reach the affected regions of the brain.

Most drugs/nanosystems cross the BBB through one of the following pathways: paracellular crossing; transcellular lipophilic crossing; receptor-mediated transcytosis; or adsorption-mediated transcytosis.[160] To date, the latter two are the major routes for the delivery of NPs across the BBB. However, alternatives, such as nose-to-brain delivery has been proven to be a relevant, non-invasive and a cost-efficient choice that leads to a more direct transport of drugs into the brain.[161]

Receptor-mediated transcytosis occurs through a series of unique receptors expressed by endothelial cells present at the BBB, including: i) the transferrin receptor, that has an important role in the uptake and translocation of transferrin-bound iron;[162] ii) the insulin receptor, since insulin is transported into the brain through this receptor that is expressed on the surface of endothelial and neuronal cells; iii) the low density lipoprotein (*i.e.* LPR1 and LPR2), as there are several ligands can bind to these receptors (*e.g.* Angiopep-2);[163] among many others.[164] Of note, A $\beta$  has been described to inhibit the binding of insulin to its receptor, impairing the healthy insulin signalling cascade.[165] Therefore, a drug able to bind to the insulin receptor is a valid mechanism to enter the brain and exert its therapeutic action towards A $\beta$  oligomerization and fibrillization, as well as to disaggregate amyloid plaques.

Finally, in the adsorptive-mediated transcytosis, positively charged molecules interact with the negatively charged plasma membrane. Usually this type of transport involves cationic proteins or cell penetrating peptides (*e.g.* Tat-derived peptides, Syn-B vectors, among others), however, current use is limited by a lack of cell specificity during the delivery.[166]

In the development of therapeutic strategies to target the brain a wide range of carriers have been tested conjugated with different drugs, where the carrier promotes the crossing of the BBB (through one of the above mentioned mechanisms) and the drug targets the pathological features of AD and other CNS diseases.[150, 160] In this context, several nanosystems have been reported to deliver macromolecules, *e.g.* PLGA nanoparticles or liposomes, into the brain, and to do it at pharmacologically relevant rates (since they present a very low bioavailability in the CNS on their own).[167-169]

The most commonly used NPs for crossing the BBB, while presenting therapeutic potential in the AD context, can be classified by their structure (inorganic and organic), size, and phase composition, *e.g.*



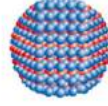


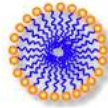

polymeric NPs, micelles, dendrimers, drug conjugates, metallic NPs, and quantum dots.[170-173] Inorganic NPs are reported to induce a retardation of amyloid fibrillation when presented as: quantum dots bioconjugates; iron, gold, carbon or selenium NPs; coated graphene oxide and protein microspheres.[174] However, their bioactivity, in most of the cases, need to be enhanced via their surface conjugation with different chemical moieties.[175] Polyphenols (*e.g.* gallic acid, curcumin, EGCG) due to their proven bioactivity against AD hallmarks have been successfully tested in combination with quantum dots, gold NPs and selenium NPs.[175-178] They are able to inhibit amyloid fibrillation and improve the disruption of amyloid fibril, as proven for curcumin-functionalized gold nanoparticles, as well as (EGCG)-stabilized selenium nanoparticles coated with Tet-1 peptide.[175, 177] Moreover, their conjugation with Tet-1 peptides enhanced the cellular uptake of the NPs, allowing EGCG to effectively inhibit A $\beta$  fibrillation and to disaggregate preformed A $\beta$  fibrils (into non-cytotoxic aggregates) in PC12 cells.[177]

Organic NPs are the most extensively studied to target the CNS, exploiting their ability to cross the BBB acting as drug delivery vehicles. [179-181] As an example, PLGA micro/nanoparticles have been shown to be a modulator of A $\beta$  peptide aggregation after conjugation with curcumin, gallic acid or quercetin.[182-186] Liposomes, spherical vesicles with one or more phospholipid bilayers[179, 187-189] can also cross the BBB through receptor-mediated transcytosis, and deliver different drugs (*e.g.* quercetin) and significantly diminish A $\beta$ -induced neurotoxicity, with an impact on downstream MAPK signaling cascades, significantly retarding the expressions of apoptotic markers, such as JNK and p38.[190, 191] Nanoemulsions are also an alternative to encapsulate these polyphenolic molecules.[192] Nanosized oil droplets dispersed in an aqueous phase can be used to encapsulate lipophilic molecules, such as curcumin. These systems have been tested for intranasal delivery of curcumin exploiting their ability to inhibit amyloid accumulation in the brain.[193] Micelles, are also a commonly exploited tool. In this case amphiphilic block copolymer-based micelles can self-assemble into NPs capturing hydrophobic drugs (*e.g.* curcumin) in their cores and their amphiphilic character allows them to easily disperse in aqueous medium.[194, 195] Xiaowei *et al.*, also demonstrated that it is possible to load resveratrol into micelles that are able to protect cells against A $\beta$ -induced damage, attenuating OS and halting apoptosis without any long-term cytotoxicity.[196] Among the many achievements of NPs (Table 1-1) and other nanosystems, dendrimers are an additional class that shows a high potential to reach the brain presenting therapeutic potential towards AD and other neurodegenerative disorders.

### 1.3.2 DENDRIMERS AS CNS DELIVERY SYSTEMS AND THERAPEUTIC NANOSYSTEMS

Dendrimers are described as one of the most tuneable nanomaterials for therapeutic and diagnostic applications.[197] They have a well-defined 3D structure (size and shape that can be precisely controlled) containing an initiator core with several inner layers, composed of repeating units, and different active surface end-groups.[198] They possess high functionality, which increases with the generations, by increasing the number of repeating units. Moreover, they present an hydrophobic core that promote a high loading capacity, especially for lipophilic drugs.[199] They are able to cross the cell membrane or biological barriers (such as the BBB) via endocytosis-mediated mechanisms and through the modulation of proteins from the tight junctions (*e.g.* occludin and actin).

Table 1-1 Representative examples of NPs designed to target the CNS and deliver polyphenolic drugs.

TYPE OF SYSTEM	EXAMPLE	ACTIVE MOLECULE	Therapeutic effect	SCHEMATIC REPRESENTATION	BBB permeability	REFS
Inorganic nanoparticles	Gold NPs		Inhibition of amyloid fibrillization and disruption of amyloid fibrils.			
	Selenium NPs	Gallic acid EGCG Quercetin Curcumin	Inhibit A $\beta$ fibrillization and disaggregate preformed A $\beta$ fibrils into nontoxic aggregates; Label A $\beta$ fibrils with a high affinity; Enhanced cellular uptake.		<i>In vitro</i> studies but no BBB model; enhanced cellular uptake.	187-190
	Quantum dots		Sensitive dual electrochemical and fluorescence detection of APOE4 DNA.			
Organic nanoparticles	Polymeric NPs	Gallic acid EGCG Quercetin Resveratrol Curcumin	Enhancement of paracellular drug delivery; Protection against neurodegeneration caused by A $\beta$ -induced neurotoxicity.		Penetration into the BBB through destabilization of the tight junctions.	35,39, 192-195
	Liposomes/nanoemulsions	EGCG Quercetin Resveratrol Curcumin	Improves enzymatic antioxidant defences; Inhibit brain A $\beta$ plaque formation; Enhance oral bioavailability; Improves the neuronal $\alpha$ -secretase activity.		Enhance cerebral biodistribution; Doubles the oral bioavailability.	38, 196-201
	Micelles	Curcumin Resveratrol	Positive effects on mitochondrial membrane potential and respiratory control ratio; Decreased levels of soluble A $\beta$ in brains of transgenic mice.		Significantly improves oral bioavailability.	203-205
	Dendrimers	Gallic acid EGCG Curcumin Quercetin Resveratrol	Antioxidant activity relevant for diseases associated with oxidative stress.		Improves drug concentration; Extension of the biological half-life of the polyphenols.	224-228

In addition, the ability of the dendrimers to cross the BBB is affected by the generation of the dendrimer, and its surface charge.[200] via receptor-mediated endocytosis through clathrin and caveolae-coated

vesicles.[201, 202]. The mechanism can generally be explained as: i) the positively-charged drug-loaded dendrimers are attracted to the negatively-charged cell membrane; and ii) their internalization. Amines present in the surface of dendrimers can facilitate the drug release due to their ability to induce osmotic swelling (through the activity of ATPases) and rupture of the endosome membrane to release the dendrimers into the cytoplasm.[203] In addition, dendrimers can cross the BBB, avoiding more invasive approaches to target the brain (*e.g.* intracranial or carotid injections used for several other nanosystems).[204] Several dendrimers have been tested to reach the CNS, namely: poly(aminoamine) – PAMAM; poly-(etherhydroxylamine) – PEHAM; poly(propyleneimine) – PPI; phosphorus dendrimers – P-dendrimers; and gallic acid-triethylene glycol dendrimers – GATG.[171, 199, 205, 206] Specific carboxylic-terminated PAMAM dendrimers are one of the most explored, due to their polyanionic character. They present lower toxicity, and a promising drug pharmacokinetics.[207, 208]

In the case of their anti-amyloidogenic properties, PAMAM dendrimers surface functionalized with monosaccharides, such as sialic acid (presenting 32 or 64 terminal groups, generation 3 and 4, respectively) are able to attenuate A $\beta$  toxicity under cell culture conditions.[209] Others dendrimers, such as PPI (generation 3), P-dendrimers (generation 4), or GATG (generation 3) were also tested.[113] In general, PPI and PAMAM dendrimers were effective in perturbing the A $\beta$  aggregation and its self-assembly process.[210] In addition, GATG dendrimers are also able to stabilize the fibril formation process, reducing the concentration of cytotoxic oligomeric forms.[113] However, in the case of cationic PAMAM and PPI dendrimers, they have been associated with toxicity in several *in vitro* studies, since they establish excessive electrostatic interactions with the negatively charged components at the surface of the cell membrane.[211] Therefore, their surface end-groups and the molecular mass is determinant for the dynamics of cellular entry and cytotoxicity.[212] Klementieva *et al*[213] reported the surface functionalization of PPI dendrimers with oligosaccharide units (*e.g.* maltose). The generated PPI-Maltose dendrimers (generation 4 and 5) were non-cytotoxic to neuronal cell lines, able to reduced amyloid toxicity through the bundling of amyloid species, and stabilizing the A $\beta$  aggregates. In addition, Chafekar *et al*[214] also tested the functionalization of dendrimers with the KLVFF peptide sequence, leading to the stabilization of the larger A $\beta$  supramolecular aggregates while promoting the formation of non-cytotoxic low molecular weight A $\beta$  forms.

Finally, PAMAM dendrimers have been loaded with gallic acid, EGCG, quercetin and curcumin.[215-219] They have been tested to target cancers, however, these polyphenolic-containing dendrimers have a high potential as modulators of the cytotoxicity of amyloidogenic peptides/proteins, such as A $\beta$  in the case of AD.

## 1.4 CONCLUSIONS AND FUTURE DIRECTIONS

AD is a multifactorial disease that is still not completely understood. Despite the existence of large body of evidence that the aggregation of A $\beta$  is at the centre of disease onset and progression, this view is still not unanimous in the scientific community. However, there are a vast number of A $\beta$ -mediated pathophysiological changes that have been reported to be associated with the disease. These include the interaction of A $\beta$  oligomers with the cell membrane promoting the formation of pores and disruption of the lipid rafts, leading to increased influx of Ca<sup>2+</sup>; their ability to interact with the insulin receptor hampering its signalling and reducing the expression of glucose transporters on the cell surface; impact in the expression of different enzymes, such as acetylcholinesterase; increased inflammation levels; among many others.

It has been reported that a series of natural compounds can abolish or ameliorate these AD pathological hallmarks; however, their use in the clinical practice has been facing a series of hurdles, namely: reduced biostability, inadequate pharmacokinetics, low bioavailability, among others. In fact, one of the main reasons for the low bioavailability of the tested natural compounds as AD therapeutic strategies is their low capacity to cross the BBB and reach the affected regions of the brain.

There are a series of nanosystems (*e.g.* inorganic nanoparticles, liposomes, dendrimers, etc.) that can be used in conjunction with the natural compounds, both by chemical conjugation or encapsulation strategies that can improve significantly the reported hurdles. While there are different systems that have been reported to improve the biostability and bioavailability, their use in the context of AD is still not completely exploited.

Further experimental assessments should be considered in the use of these nanosystems-polyphenols for AD before they can be exploited in the clinical setting, namely:

1. Fundamental toxicological and cytocompatibility studies of the brain-targeting nanotools with and without the loading/conjugation of polyphenols are essential. CNS disorders, and in particular AD, require a continued treatment over long periods of time, therefore, acute toxicity response and cumulative effects in the brain tissue needs to be assessed. Some studies evaluating the cytotoxicity of dendrimers have been performed *in vivo* but these usually are not reported in the context for the drug delivery to the CNS.[220, 221] Recently, *in vivo* imaging studies, demonstrate that a BBB-permeable PAMAM dendrimers (decorated with Angiopep-2) is able to efficiently cross an intact BBB and reach the desired target.[222]
2. Specific and efficient transport over the BBB are usually based on the adsorptive- and receptor-mediated transcytoses. However, other routes might be explored to facilitate the

development of safer and more efficient delivery systems to the CNS, since the current targets (*e.g.* insulin receptor, LPR1 and transferrin receptor) are also found in other tissues, compromising the specificity of the targeting. Nevertheless, new drug-administration methods, such as oral, transbuccal mucosal, sublingual, or nasal delivery can be further exploited without compromising the efficacy of the treatment.

3. Unmodified nanosystems (*e.g.* dendrimers presenting free surface amine groups) are widely described to present a concentration- and generation-dependent cytotoxicity. Therefore, the surface conjugation of (poly)phenolic moieties can be beneficial. (Poly)phenolic-terminated dendrimers are expected to be more effective in the cellular and subcellular targeting, increasing their bioactivity taking advantage of their anti-amyloidogenic properties, highly relevant in the AD case. In addition, the reduction of the population of cytotoxic A $\beta$  oligomers induced by the presence of (poly)phenolic moieties at the surface of the dendrimers is a promising approach that need to be further assessed using *in vitro* and *in vivo* models. These nanosystems are expected to have the capacity to: inhibit peptide/protein aggregation; ameliorate inflammatory/oxidative pathways as successfully demonstrated using NPs decorated or encapsulated with EGCG or curcumin (with proven biostability and bioactivity); among many other benefits in the context of AD and other neurodegenerative disorders.[141, 192]

In general, dendrimers represent promising nanosystem for a plethora of biomedical applications, with a high tunability and versatility. Several studies have reported their capacity to improve the solubility, biodistribution, and efficacy of a number of drugs. BBB-crossing can be achieved by tuning their surface chemistry, adapting the delivery rate and concentration of drugs in the CNS. However, further developments should be performed to improve their bioactivity, as well as to evaluate these nanosystems in terms of safety to enable their long-term use without relevant adverse effects.

Finally, the ability to modulate the A $\beta$  supramolecular assembly and to ameliorate AD pathological hallmarks by different nanosystems is expected to be further exploited in the future. However, parameters such as, biodegradability, immunogenicity, or bioaccumulation, among others, will have to be carefully evaluated to validate their clinical potential.

## 1.5 REFERENCES

1. A., A., Über eine eigenartige Erkrankung der Hirnrinde. Allgemeine Zeitschrift für Psychiatrie und Psychisch-gerichtliche Medizin, 1907(64).

2. Huang, Y. and L. Mucke, Alzheimer mechanisms and therapeutic strategies. *Cell*, 2012. 148(6): p. 1204-1222.
3. Aguzzi, A. and T. O'Connor, Protein aggregation diseases: pathogenicity and therapeutic perspectives. *Nat Rev Drug Discov*, 2010. 9(3): p. 237-48.
4. Mattsson, N., et al., The Alzheimer's Association external quality control program for cerebrospinal fluid biomarkers. *Alzheimer's & Dementia*, 2011. 7(4): p. 386-395. e6.
5. Wiseman, F.K., et al., A genetic cause of Alzheimer disease: mechanistic insights from Down syndrome. *Nature Reviews Neuroscience*, 2015. 16(9): p. 564-574.
6. Iadecola, C., Neurovascular regulation in the normal brain and in Alzheimer's disease. *Nature Reviews Neuroscience*, 2004. 5(5): p. 347-360.
7. Arnold, S.E., et al., Brain insulin resistance in type 2 diabetes and Alzheimer disease: concepts and conundrums. *Nat Rev Neurol*, 2018. 14(3): p. 168-181.
8. Chen, G.-F., et al., Amyloid beta: structure, biology and structure-based therapeutic development. *Acta pharmacologica Sinica*, 2017. 38(9): p. 1205-1235.
9. Wang, J., et al., A systemic view of Alzheimer disease—insights from amyloid- $\beta$  metabolism beyond the brain. *Nature reviews neurology*, 2017. 13(10): p. 612.
10. De Strooper, B. and E. Karran, The Cellular Phase of Alzheimer's Disease. *Cell*, 2016. 164(4): p. 603-15.
11. Heneka, M.T., et al., Neuroinflammation in Alzheimer's disease. *The Lancet Neurology*, 2015. 14(4): p. 388-405.
12. Kapogiannis, D. and M.P. Mattson, Disrupted energy metabolism and neuronal circuit dysfunction in cognitive impairment and Alzheimer's disease. *The Lancet Neurology*, 2011. 10(2): p. 187-198.
13. Zhao, C., W. Deng, and F.H. Gage, Mechanisms and Functional Implications of Adult Neurogenesis. *Cell*, 2008. 132(4): p. 645-660.
14. Serrano-Pozo, A., et al., Neuropathological alterations in Alzheimer disease. *Cold Spring Harbor perspectives in medicine*, 2011. 1(1): p. a006189.
15. Kuret, J., et al., Pathways of tau fibrillization. *Biochimica et Biophysica Acta (BBA) - Molecular Basis of Disease*, 2005. 1739(2-3): p. 167-178.
16. Zhang, F., et al., beta-amyloid redirects norepinephrine signaling to activate the pathogenic GSK3beta/tau cascade. *Sci Transl Med*, 2020. 12(526).
17. Maass, A., et al., Comparison of multiple tau-PET measures as biomarkers in aging and Alzheimer's disease. *NeuroImage*, 2017. 157: p. 448-463.
18. Reimand, J., et al., Amyloid-beta CSF/PET discordance vs tau load 5 years later: It takes two to tangle. *medRxiv*, 2020.
19. Pontecorvo, M.J., et al., Relationships between flortaucipir PET tau binding and amyloid burden, clinical diagnosis, age and cognition. *Brain*, 2017. 140(3): p. 748-763.

20. Hanseeuw, B.J., et al., Association of Amyloid and Tau With Cognition in Preclinical Alzheimer Disease: A Longitudinal Study. *JAMA Neurol*, 2019.
21. Hook, V.Y., Protease pathways in peptide neurotransmission and neurodegenerative diseases. *Cellular and molecular neurobiology*, 2006. 26(4-6): p. 447-467.
22. Liu, Y.-H., et al., Clearance of Amyloid-Beta in Alzheimer's Disease: Shifting the Action Site from Center to Periphery. *Molecular Neurobiology*, 2015. 51(1): p. 1-7.
23. Selkoe, D.J., Normal and abnormal biology of the beta-amyloid precursor protein. *Annual review of neuroscience*, 1994. 17(1): p. 489-517.
24. J. Baranello, R., et al., Amyloid-Beta Protein Clearance and Degradation (ABCD) Pathways and their Role in Alzheimer's Disease. *Current Alzheimer Research*, 2015. 12(1): p. 32-46.
25. Scheuner, D., et al., Secreted amyloid  $\beta$ -protein similar to that in the senile plaques of Alzheimer's disease is increased in vivo by the presenilin 1 and 2 and APP mutations linked to familial Alzheimer's disease. *Nature medicine*, 1996. 2(8): p. 864-870.
26. Gravina, S.A., et al., Amyloid  $\beta$  Protein (A $\beta$ ) in Alzheimer's Disease Brain Biochemical and immunocytochemical analysis with antibodies specific for forms ending at A $\beta$  40 or A $\beta$  42 (43). *Journal of Biological Chemistry*, 1995. 270(13): p. 7013-7016.
27. Lewczuk, P., et al., Cerebrospinal Fluid A $\beta$ 42/40 Corresponds Better than A $\beta$ 42 to Amyloid PET in Alzheimer's Disease. *J Alzheimers Dis*, 2017. 55(2): p. 813-822.
28. Hamley, I.W., The Amyloid Beta Peptide: A Chemist's Perspective. Role in Alzheimer's and Fibrillization. *Chemical Reviews*, 2012. 112(10): p. 5147-5192.
29. Lührs, T., et al., 3D structure of Alzheimer's amyloid- $\beta$  (1-42) fibrils. *Proceedings of the National Academy of Sciences of the United States of America*, 2005. 102(48): p. 17342-17347.
30. Yu, L., et al., Structural characterization of a soluble amyloid beta-peptide oligomer. *Biochemistry*, 2009. 48(9): p. 1870-7.
31. Hardy, J. and D. Allsop, Amyloid deposition as the central event in the aetiology of Alzheimer's disease. *Trends Pharmacol Sci*, 1991. 12(10): p. 383-8.
32. Podlisny, M.B., et al., Aggregation of secreted amyloid-protein into sodium dodecyl sulfate-stable oligomers in cell culture. *Journal of Biological Chemistry*, 1995. 270(16): p. 9564-9570.
33. Shankar, G.M., et al., Amyloid-beta protein dimers isolated directly from Alzheimer's brains impair synaptic plasticity and memory. *Nat Med*, 2008. 14(8): p. 837-42.
34. Li, S., et al., Soluble oligomers of amyloid Beta protein facilitate hippocampal long-term depression by disrupting neuronal glutamate uptake. *Neuron*, 2009. 62(6): p. 788-801.
35. Ruzali, W.A.W., P.G. Kehoe, and S. Love, Influence of LRP-1 and apolipoprotein E on amyloid- $\beta$  uptake and toxicity to cerebrovascular smooth muscle cells. *Journal of Alzheimer's Disease*, 2013. 33(1): p. 95-110.



36. Sandberg, A., et al., Stabilization of neurotoxic Alzheimer amyloid-beta oligomers by protein engineering. *Proceedings of the National Academy of Sciences of the United States of America*, 2010. 107(35): p. 15595-15600.
37. Drolle, E., et al., Atomic force microscopy to study molecular mechanisms of amyloid fibril formation and toxicity in Alzheimer's disease. *Drug metabolism reviews*, 2014. 46(2): p. 207-223.
38. Knowles, T.P., M. Vendruscolo, and C.M. Dobson, The amyloid state and its association with protein misfolding diseases. *Nat Rev Mol Cell Biol*, 2014. 15(6): p. 384-96.
39. L Almeida, Z. and R. MM Brito, Structure and Aggregation Mechanisms in Amyloids. *Molecules*, 2020. 25(5): p. 1195.
40. Gazit, E., The "Correctly Folded" State of Proteins: Is It a Metastable State? *Angewandte Chemie International Edition*, 2002. 41(2): p. 257-259.
41. Gallardo, R., N.A. Ranson, and S.E. Radford, Amyloid structures: much more than just a cross- $\beta$  fold. *Current Opinion in Structural Biology*, 2020. 60: p. 7-16.
42. Biancalana, M. and S. Koide, Molecular mechanism of Thioflavin-T binding to amyloid fibrils. *Biochim Biophys Acta*, 2010. 1804(7): p. 1405-12.
43. Lee, S.J.C., et al., Towards an understanding of amyloid- $\beta$  oligomers: characterization, toxicity mechanisms, and inhibitors. *Chemical Society Reviews*, 2017. 46(2): p. 310-323.
44. Cohen, S.I., et al., Proliferation of amyloid-beta42 aggregates occurs through a secondary nucleation mechanism. *Proc Natl Acad Sci U S A*, 2013. 110(24): p. 9758-63.
45. Arosio, P., T.P. Knowles, and S. Linse, On the lag phase in amyloid fibril formation. *Phys. Chem. Chem. Phys*, 2015. 17: p. 7606-7618.
46. Qosa, H., et al., Differences in amyloid- $\beta$  clearance across mouse and human blood-brain barrier models: kinetic analysis and mechanistic modeling. *Neuropharmacology*, 2014. 79: p. 668-678.
47. Hardy, J., Membrane damage is at the core of Alzheimer's disease. *The Lancet Neurology*, 2017. 16(5): p. 342.
48. Wolfe, C.M., et al., The role of APOE and TREM2 in Alzheimer's disease—current understanding and perspectives. *International journal of molecular sciences*, 2019. 20(1): p. 81.
49. Lahdo, R. and L. de LA FOURNIÈRE-BESSUEILLE, Insertion of the amyloid precursor protein into lipid monolayers: effects of cholesterol and apolipoprotein E. *Biochemical Journal*, 2004. 382(3): p. 987-994.
50. Quazi, F. and R.S. Molday, Differential phospholipid substrates and directional transport by ATP-binding cassette proteins ABCA1, ABCA7, and ABCA4 and disease-causing mutants. *Journal of Biological Chemistry*, 2013. 288(48): p. 34414-34426.
51. Yeh, F.L., et al., TREM2 binds to apolipoproteins, including APOE and CLU/APOJ, and thereby facilitates uptake of amyloid-beta by microglia. *Neuron*, 2016. 91(2): p. 328-340.
52. Foster, E.M., et al., Clusterin in Alzheimer's Disease: Mechanisms, Genetics, and Lessons From Other Pathologies. *Frontiers in Neuroscience*, 2019. 13(164).

53. Rushworth, J.V. and N.M. Hooper, Lipid Rafts: Linking Alzheimer's Amyloid- $\beta$  Production, Aggregation, and Toxicity at Neuronal Membranes. *International journal of Alzheimer's disease*, 2010. 2011: p. 603052-603052.
54. Perry, E.K., et al., Correlation of cholinergic abnormalities with senile plaques and mental test scores in senile dementia. *Br Med J*, 1978. 2(6150): p. 1457-1459.
55. Liu, Q. and J. Wu, Neuronal nicotinic acetylcholine receptors serve as sensitive targets that mediate  $\beta$  - amyloid neurotoxicity 1. *Acta Pharmacologica Sinica*, 2006. 27(10): p. 1277-1286.
56. Hampel, H., et al., The cholinergic system in the pathophysiology and treatment of Alzheimer's disease. *Brain*, 2018. 141(7): p. 1917-1933.
57. Coyle, J., D. Price, and M. DeLong, Alzheimer's disease: a disorder of cortical cholinergic innervation. *Science*, 1983. 219(4589): p. 1184-1190.
58. Fabiani, C. and S.S. Antollini, Alzheimer's Disease as a Membrane Disorder: Spatial Cross-Talk Among Beta-Amyloid Peptides, Nicotinic Acetylcholine Receptors and Lipid Rafts. *Frontiers in Cellular Neuroscience*, 2019. 13(309).
59. Wang, H.-Y., et al.,  $\beta$ -Amyloid1-42 Binds to  $\alpha$ 7 Nicotinic Acetylcholine Receptor with High Affinity implications for alzheimer's disease pathology. *Journal of Biological Chemistry*, 2000. 275(8): p. 5626-5632.
60. Small, D.H., et al., The  $\beta$  - amyloid protein of Alzheimer's disease binds to membrane lipids but does not bind to the  $\alpha$ 7 nicotinic acetylcholine receptor. *Journal of neurochemistry*, 2007. 101(6): p. 1527-1538.
61. DeToma, A.S., et al., Misfolded proteins in Alzheimer's disease and type II diabetes. *Chemical Society Reviews*, 2012. 41(2): p. 608-621.
62. de la Monte, S.M., Insulin Resistance and Neurodegeneration: Progress Towards the Development of New Therapeutics for Alzheimer's Disease. *Drugs*, 2017. 77(1): p. 47-65.
63. Fernandez, A.M. and I. Torres-Alemán, The many faces of insulin-like peptide signalling in the brain. *Nature Reviews Neuroscience*, 2012. 13(4): p. 225-239.
64. Gasparini, L., et al., Stimulation of  $\beta$ -amyloid precursor protein trafficking by insulin reduces intraneuronal  $\beta$ -amyloid and requires mitogen-activated protein kinase signaling. *Journal of Neuroscience*, 2001. 21(8): p. 2561-2570.
65. Najem, D., et al., Insulin resistance, neuroinflammation, and Alzheimer's disease. *Reviews in the Neurosciences*, 2014. 25(4): p. 509-525.
66. Copps, K.D. and M.F. White, Regulation of insulin sensitivity by serine/threonine phosphorylation of insulin receptor substrate proteins IRS1 and IRS2. *Diabetologia*, 2012. 55(10): p. 2565-2582.
67. Ruffels, J., M. Griffin, and J.M. Dickenson, Activation of ERK1/2, JNK and PKB by hydrogen peroxide in human SH-SY5Y neuroblastoma cells: role of ERK1/2 in H<sub>2</sub>O<sub>2</sub>-induced cell death. *Eur J Pharmacol*, 2004. 483(2-3): p. 163-73.

68. Świdarska, E., et al., Role of PI3K/AKT pathway in insulin-mediated glucose uptake, in *Blood Glucose Levels*. 2018, IntechOpen.
69. Arrieta-Cruz, I. and R. Gutiérrez-Juárez, The role of insulin resistance and glucose metabolism dysregulation in the development of Alzheimer's disease. *Revista de Investigacion Clinica*, 2016. 68(2): p. 53-58.
70. Stanley, M., S.L. Macauley, and D.M. Holtzman, Changes in insulin and insulin signaling in Alzheimer's disease: cause or consequence? *Journal of Experimental Medicine*, 2016. 213(8): p. 1375-1385.
71. Behl, C., Alzheimer's disease and oxidative stress: implications for novel therapeutic approaches. *Prog Neurobiol*, 1999. 57(3): p. 301-23.
72. Cheignon, C., et al., Oxidative stress and the amyloid beta peptide in Alzheimer's disease. *Redox Biol*, 2018. 14: p. 450-464.
73. Faller, P., C. Hureau, and O. Berthoumieu, Role of metal ions in the self-assembly of the Alzheimer's amyloid- $\beta$  peptide. *Inorganic chemistry*, 2013. 52(21): p. 12193-12206.
74. Tiiman, A., P. Palumaa, and V. Tougu, The missing link in the amyloid cascade of Alzheimer's disease—metal ions. *Neurochemistry international*, 2013. 62(4): p. 367-378.
75. Granold, M., et al., High membrane protein oxidation in the human cerebral cortex. *Redox biology*, 2015. 4: p. 200-207.
76. Butterfield, D.A. and C.M. Lauderback, Lipid peroxidation and protein oxidation in Alzheimer's disease brain: potential causes and consequences involving amyloid  $\beta$ -peptide-associated free radical oxidative stress. *Free Radical Biology and Medicine*, 2002. 32(11): p. 1050-1060.
77. Mecocci, P., U. MacGarvey, and M.F. Beal, Oxidative damage to mitochondrial DNA is increased in Alzheimer's disease. *Annals of Neurology: Official Journal of the American Neurological Association and the Child Neurology Society*, 1994. 36(5): p. 747-751.
78. Selfridge, J.E., et al., Role of mitochondrial homeostasis and dynamics in Alzheimer's disease. *Neurobiology of disease*, 2013. 51: p. 3-12.
79. Butterfield, S.M. and H.A. Lashuel, Amyloidogenic protein–membrane interactions: mechanistic insight from model systems. *Angewandte Chemie International Edition*, 2010. 49(33): p. 5628-5654.
80. Aluise, C.D., et al., Redox proteomics analysis of brains from subjects with amnesic mild cognitive impairment compared to brains from subjects with preclinical Alzheimer's disease: insights into memory loss in MCI. *Journal of Alzheimer's Disease*, 2011. 23(2): p. 257-269.
81. Chen, Z. and C. Zhong, Decoding Alzheimer's disease from perturbed cerebral glucose metabolism: implications for diagnostic and therapeutic strategies. *Progress in neurobiology*, 2013. 108: p. 21-43.
82. Barone, E., et al., Impairment of biliverdin reductase-A promotes brain insulin resistance in Alzheimer disease: a new paradigm. *Free Radical Biology and Medicine*, 2016. 91: p. 127-142.

83. Supnet, C. and I. Bezprozvanny, The dysregulation of intracellular calcium in Alzheimer disease. *Cell calcium*, 2010. 47(2): p. 183-189.
84. Mattson, M.P., et al., beta-Amyloid peptides destabilize calcium homeostasis and render human cortical neurons vulnerable to excitotoxicity. *Journal of Neuroscience*, 1992. 12(2): p. 376-389.
85. Demuro, A., et al., Calcium dysregulation and membrane disruption as a ubiquitous neurotoxic mechanism of soluble amyloid oligomers. *Journal of Biological Chemistry*, 2005. 280(17): p. 17294-17300.
86. Simakova, O. and N.J. Arispe, The Cell-Selective Neurotoxicity of the Alzheimer's A $\beta$  Peptide Is Determined by Surface Phosphatidylserine and Cytosolic ATP Levels. Membrane Binding Is Required for A $\beta$  Toxicity. *The Journal of Neuroscience*, 2007. 27(50): p. 13719-13729.
87. Lau, T.-L., et al., Amyloid- $\beta$  peptide disruption of lipid membranes and the effect of metal ions. *Journal of molecular biology*, 2006. 356(3): p. 759-770.
88. Lynch, T., Oxidative processes in Alzheimer's disease: the role of A $\beta$ -metal interactions. *Experimental Gerontology*, 2000. 35(4): p. 445-451.
89. Barucker, C., et al., Nuclear translocation uncovers the amyloid peptide Abeta42 as a regulator of gene transcription. *J Biol Chem*, 2014. 289(29): p. 20182-91.
90. Stutzmann, G.E., et al., Dysregulated IP3 signaling in cortical neurons of knock-in mice expressing an Alzheimer's-linked mutation in presenilin1 results in exaggerated Ca<sup>2+</sup> signals and altered membrane excitability. *Journal of Neuroscience*, 2004. 24(2): p. 508-513.
91. Furukawa, K., et al., Activation of K<sup>+</sup> channels and suppression of neuronal activity by secreted  $\beta$ -amyloid-precursor protein. *Nature*, 1996. 379(6560): p. 74-78.
92. Balandrin, M.F., A.D. Kinghorn, and N.R. Farnsworth, Plant-Derived Natural Products in Drug Discovery and Development, in *Human Medicinal Agents from Plants*. 1993, American Chemical Society. p. 2-12.
93. Crozier, A., I.B. Jaganath, and M.N. Clifford, Dietary phenolics: chemistry, bioavailability and effects on health. *Nat Prod Rep*, 2009. 26(8): p. 1001-43.
94. Kennedy, D.O. and E.L. Wightman, Herbal extracts and phytochemicals: plant secondary metabolites and the enhancement of human brain function. *Advances in Nutrition*, 2011. 2(1): p. 32-50.
95. Gu, Y., et al., Food combination and Alzheimer disease risk: a protective diet. *Archives of neurology*, 2010. 67(6): p. 699-706.
96. Gustaw-Rothenberg, K., Dietary patterns associated with Alzheimer's disease: population based study. *International journal of environmental research and public health*, 2009. 6(4): p. 1335-1340.
97. Weih, M., J. Wiltfang, and J. Kornhuber, Non-pharmacologic prevention of Alzheimer's disease: nutritional and life-style risk factors. *Journal of Neural Transmission*, 2007. 114(9): p. 1187.

98. Fang, L., et al., Current progresses of novel natural products and their derivatives/analogs as anti-Alzheimer candidates: an update. *Mini reviews in medicinal chemistry*, 2013. 13(6): p. 870-887.
99. Velander, P., et al., Natural product-based amyloid inhibitors. *Biochem Pharmacol*, 2017. 139: p. 40-55.
100. Zhang, H. and R. Tsao, Dietary polyphenols, oxidative stress and antioxidant and anti-inflammatory effects. *Current Opinion in Food Science*, 2016. 8: p. 33-42.
101. Gauci, A.J., et al., Identification of polyphenolic compounds and black tea extract as potent inhibitors of lipid membrane destabilization by A $\beta$  42 aggregates. *Journal of Alzheimer's Disease*, 2011. 27(4): p. 767-779.
102. Schaffer, S., et al., Effects of polyphenols on brain ageing and Alzheimer's disease: focus on mitochondria. *Molecular neurobiology*, 2012. 46(1): p. 161-178.
103. Marambaud, P., H. Zhao, and P. Davies, Resveratrol promotes clearance of Alzheimer's disease amyloid-beta peptides. *The Journal of Biological Chemistry*, 2005. 280(45): p. 37377-82.
104. Lopez del Amo, J.M., et al., Structural properties of EGCG-induced, nontoxic Alzheimer's disease Abeta oligomers. *J Mol Biol*, 2012. 421(4-5): p. 517-24.
105. Bieschke, J., et al., EGCG remodels mature  $\alpha$ -synuclein and amyloid- $\beta$  fibrils and reduces cellular toxicity. *Proceedings of the National Academy of Sciences*, 2010. 107(17): p. 7710-7715.
106. Andrich, K. and J. Bieschke, The Effect of (-)-Epigallo-catechin-(3)-gallate on Amyloidogenic Proteins Suggests a Common Mechanism. *Advances in experimental medicine and biology*, 2015. 863: p. 139-161.
107. Porat, Y., A. Abramowitz, and E. Gazit, Inhibition of amyloid fibril formation by polyphenols: structural similarity and aromatic interactions as a common inhibition mechanism. *Chem Biol Drug Des*, 2006. 67(1): p. 27-37.
108. Sgarbossa, A., Natural biomolecules and protein aggregation: emerging strategies against amyloidogenesis. *Int J Mol Sci*, 2012. 13(12): p. 17121-37.
109. Das, S., et al., Bioactive polyphenol interactions with beta amyloid: a comparison of binding modelling, effects on fibril and aggregate formation and neuroprotective capacity. *Food Funct*, 2016. 7(2): p. 1138-46.
110. Molino, S., et al., Polyphenols in dementia: From molecular basis to clinical trials. *Life Sci*, 2016. 161: p. 69-77.
111. Gazit, E., A possible role for pi-stacking in the self-assembly of amyloid fibrils. *FASEB J*, 2002. 16(1): p. 77-83.
112. Khurana, R., et al., Mechanism of thioflavin T binding to amyloid fibrils. *J Struct Biol*, 2005. 151(3): p. 229-38.
113. Klajnert, B., et al., Dendrimers reduce toxicity of Abeta 1-28 peptide during aggregation and accelerate fibril formation. *Nanomedicine*, 2012. 8(8): p. 1372-8.

114. Ehrnhoefer, D.E., et al., EGCG redirects amyloidogenic polypeptides into unstructured, off-pathway oligomers. *Nat Struct Mol Biol*, 2008. 15(6): p. 558-566.
115. Ehrnhoefer, D.E., et al., EGCG redirects amyloidogenic polypeptides into unstructured, off-pathway oligomers. *Nature Structural & Molecular Biology*, 2008. 15(6): p. 558-566.
116. Micsonai, A., et al., Accurate secondary structure prediction and fold recognition for circular dichroism spectroscopy. *Proc Natl Acad Sci U S A*, 2015. 112(24): p. E3095-103.
117. Bieschke, J., et al., EGCG remodels mature alpha-synuclein and amyloid-beta fibrils and reduces cellular toxicity. *Proc Natl Acad Sci U S A*, 2010. 107(17): p. 7710-5.
118. Rose, P.W., et al., The RCSB protein data bank: integrative view of protein, gene and 3D structural information. *Nucleic acids research*, 2016: p. gkw1000.
119. Sato, M., et al., Site-specific inhibitory mechanism for amyloid beta42 aggregation by catechol-type flavonoids targeting the Lys residues. *J Biol Chem*, 2013. 288(32): p. 23212-24.
120. Naldi, M., et al., Amyloid  $\beta$ -peptide 25-35 self-assembly and its inhibition: a model undecapeptide system to gain atomistic and secondary structure details of the Alzheimer's disease process and treatment. *ACS chemical neuroscience*, 2012. 3(11): p. 952-962.
121. Bastianetto, S., et al., Neuroprotective effects of green and black teas and their catechin gallate esters against  $\beta$ -amyloid-induced toxicity. *European Journal of Neuroscience*, 2006. 23(1): p. 55-64.
122. Lin, C.-L., et al., Epigallocatechin gallate (EGCG) suppresses  $\beta$ -amyloid-induced neurotoxicity through inhibiting c-Abl/FE65 nuclear translocation and GSK3 $\beta$  activation. *Neurobiology of Aging*, 2009. 30(1): p. 81-92.
123. Berhanu, W.M. and A.E. Masunov, Atomistic mechanism of polyphenol amyloid aggregation inhibitors: molecular dynamics study of Curcumin, Exifone, and Myricetin interaction with the segment of tau peptide oligomer. *J Biomol Struct Dyn*, 2015. 33(7): p. 1399-411.
124. Araújo, A.R., et al., Vescalagin and castalagin reduce the toxicity of amyloid-beta42 oligomers through the remodelling of its secondary structure. *Chemical Communications*, 2020.
125. Porat, Y., et al., Inhibition of islet amyloid polypeptide fibril formation: A potential role for heteroaromatic interactions. *Biochemistry*, 2004. 43(45): p. 14454-14462.
126. Phan, H.T.T., et al., Polyphenols Modulate Alzheimer's Amyloid Beta Aggregation in a Structure-Dependent Manner. *Nutrients*, 2019. 11(4): p. 756.
127. Velander, P., et al., Natural product-based amyloid inhibitors. *Biochemical pharmacology*, 2017. 139: p. 40-55.
128. Ono, K., et al., Anti-amyloidogenic activity of tannic acid and its activity to destabilize Alzheimer's  $\beta$ -amyloid fibrils in vitro. *Biochimica et Biophysica Acta (BBA) - Molecular Basis of Disease*, 2004. 1690(3): p. 193-202.
129. Colon, M. and C. Nerín, Synergistic, antagonistic and additive interactions of green tea polyphenols. *European Food Research and Technology*, 2016. 242(2): p. 211-220.

130. Saffari, Y. and S.H. Sadrzadeh, Green tea metabolite EGCG protects membranes against oxidative damage in vitro. *Life sciences*, 2004. 74(12): p. 1513-1518.
131. Apetz, N., et al., Natural compounds and plant extracts as therapeutics against chronic inflammation in Alzheimer's disease—a translational perspective. *CNS & Neurological Disorders-Drug Targets (Formerly Current Drug Targets-CNS & Neurological Disorders)*, 2014. 13(7): p. 1175-1191.
132. Jeon, S.-Y., et al., Green tea catechins as a BACE1 ( $\beta$ -secretase) inhibitor. *Bioorganic & medicinal chemistry letters*, 2003. 13(22): p. 3905-3908.
133. Mori, T., et al., Tannic acid is a natural beta-secretase inhibitor that prevents cognitive impairment and mitigates Alzheimer-like pathology in transgenic mice. *J Biol Chem*, 2012. 287(9): p. 6912-27.
134. Dragicevic, N., et al., Green tea epigallocatechin-3-gallate (EGCG) and other flavonoids reduce Alzheimer's amyloid-induced mitochondrial dysfunction. *Journal of Alzheimer's Disease*, 2011. 26(3): p. 507-521.
135. Lopez del Amo, J.M., et al., Structural Properties of EGCG-Induced, Nontoxic Alzheimer's Disease A $\beta$  Oligomers. *Journal of Molecular Biology*, 2012. 421(4): p. 517-524.
136. Sciacca, M.F.M., et al., The active role of Ca(2+) ions in Abeta-mediated membrane damage. *Chem Commun (Camb)*, 2018. 54(29): p. 3629-3631.
137. Srividhya, R., et al., Mitochondrial alterations in aging rat brain: effective role of (–)-epigallo catechin gallate. *International journal of developmental neuroscience*, 2009. 27(3): p. 223-231.
138. Gerzson, M.F.B., et al., Effects of tannic acid in streptozotocin-induced sporadic Alzheimer's Disease: insights into memory, redox status, Na<sup>+</sup>, K<sup>+</sup>-ATPase and acetylcholinesterase activity. *Archives of Physiology and Biochemistry*, 2019: p. 1-8.
139. Levites, Y., et al., Neuroprotection and neurorescue against A $\beta$  toxicity and PKC-dependent release of nonamyloidogenic soluble precursor protein by green tea polyphenol (–)-epigallocatechin-3-gallate. *The FASEB Journal*, 2003. 17(8): p. 952-954.
140. Noor, H., P. Cao, and D.P. Raleigh, Morin hydrate inhibits amyloid formation by islet amyloid polypeptide and disaggregates amyloid fibers. *Protein Sci*, 2012. 21(3): p. 373-82.
141. Ke, P.C., et al., Mitigation of amyloidosis with nanomaterials. *Advanced Materials*, 2019: p. 1901690.
142. Hamaguchi, T., et al., Phenolic compounds prevent Alzheimer's pathology through different effects on the amyloid- $\beta$  aggregation pathway. *The American journal of pathology*, 2009. 175(6): p. 2557-2565.
143. Mandel, S., et al., Cell signaling pathways in the neuroprotective actions of the green tea polyphenol (–)-epigallocatechin-3-gallate: implications for neurodegenerative diseases. *Journal of neurochemistry*, 2004. 88(6): p. 1555-1569.
144. Paul, F., Sunphenon EGCG (Epigallocatechin-Gallate) in the Early Stage of Alzheimer's Disease (SUN-AK). *ClinicalTrials.gov*, 2020.

145. Ringman, J.M., et al., Oral curcumin for Alzheimer's disease: tolerability and efficacy in a 24-week randomized, double blind, placebo-controlled study. *Alzheimer's research & therapy*, 2012. 4(5): p. 43.
146. Munin, A. and F. Edwards-Lévy, Encapsulation of natural polyphenolic compounds; a review. *Pharmaceutics*, 2011. 3(4): p. 793-829.
147. Parisi, O.I., et al., Chapter 4 - Polyphenols and Their Formulations: Different Strategies to Overcome the Drawbacks Associated with Their Poor Stability and Bioavailability, in *Polyphenols in Human Health and Disease*, R.R. Watson, V.R. Preedy, and S. Zibadi, Editors. 2014, Academic Press: San Diego. p. 29-45.
148. Figueira, I., et al., Polyphenols journey through blood-brain barrier towards neuronal protection. *Scientific reports*, 2017. 7(1): p. 11456-11456.
149. Singh, A.P., et al., Targeted therapy in chronic diseases using nanomaterial-based drug delivery vehicles. *Signal Transduction and Targeted Therapy*, 2019. 4(1): p. 33.
150. Fonseca-Santos, B., M.P.D. Gremião, and M. Chorilli, Nanotechnology-based drug delivery systems for the treatment of Alzheimer's disease. *International journal of nanomedicine*, 2015. 10: p. 4981-5003.
151. Kushihara, H. and Y. Sugiyama, Efflux transport systems for drugs at the blood-brain barrier and blood-cerebrospinal fluid barrier (Part 1). *Drug discovery today*, 2001. 6(3): p. 150-156.
152. Abbott, N.J., et al., Structure and function of the blood-brain barrier. *Neurobiology of disease*, 2010. 37(1): p. 13-25.
153. Fong, C.W., Permeability of the blood-brain barrier: molecular mechanism of transport of drugs and physiologically important compounds. *The Journal of membrane biology*, 2015. 248(4): p. 651-669.
154. Di, L., E.H. Kerns, and G.T. Carter, Strategies to assess blood-brain barrier penetration. *Expert opinion on drug discovery*, 2008. 3(6): p. 677-687.
155. Mignani, S., et al., Can dendrimer based nanoparticles fight neurodegenerative diseases? Current situation versus other established approaches. *Progress in Polymer Science*, 2017. 64: p. 23-51.
156. van de Haar, H.J., et al., Blood-Brain Barrier Leakage in Patients with Early Alzheimer Disease. *Radiology*, 2016. 281(2): p. 527-535.
157. Masters, C.L., et al., Alzheimer's disease. *Nat Rev Dis Primers*, 2015. 1: p. 15056.
158. Budd, S.H., et al., Clinical Development of Aducanumab, an Anti-A $\beta$  Human Monoclonal Antibody Being Investigated for the Treatment of Early Alzheimer's Disease. *The journal of prevention of Alzheimer's disease*, 2017. 4(4): p. 255-263.
159. Panza, F., et al., A critical appraisal of amyloid- $\beta$ -targeting therapies for Alzheimer disease. *Nature Reviews Neurology*, 2019. 15(2): p. 73-88.



160. Mir, M., et al., Nanotechnology: from in vivo imaging system to controlled drug delivery. *Nanoscale research letters*, 2017. 12(1): p. 500.
161. Patel, A., N. Surti, and A. Mahajan, Intranasal drug delivery: Novel delivery route for effective management of neurological disorders. *Journal of Drug Delivery Science and Technology*, 2019.
162. Saito, Y., et al., Vector-mediated delivery of 125I-labeled beta-amyloid peptide A beta 1-40 through the blood-brain barrier and binding to Alzheimer disease amyloid of the A beta 1-40/vector complex. *Proc Natl Acad Sci U S A*, 1995. 92(22): p. 10227-31.
163. Harris-White, M.E. and S.A. Frautschy, Low density lipoprotein receptor-related proteins (LRPs), Alzheimer's and cognition. *Curr Drug Targets CNS Neurol Disord*, 2005. 4(5): p. 469-80.
164. Coloma, M.J., et al., Transport across the primate blood-brain barrier of a genetically engineered chimeric monoclonal antibody to the human insulin receptor. *Pharm Res*, 2000. 17(3): p. 266-74.
165. Xie, L., et al., Alzheimer's beta-amyloid peptides compete for insulin binding to the insulin receptor. *J Neurosci*, 2002. 22(10): p. Rc221.
166. Saraiva, C., et al., Nanoparticle-mediated brain drug delivery: Overcoming blood-brain barrier to treat neurodegenerative diseases. *Journal of Controlled Release*, 2016. 235: p. 34-47.
167. A. C. R. G., et al., A BioMEMS review: MEMS technology for physiologically integrated devices. *Proceedings of the IEEE*, 2004. 92(1): p. 6-21.
168. Chandrasekhar, S., et al., Microarrays and microneedle arrays for delivery of peptides, proteins, vaccines and other applications. *Expert Opinion on Drug Delivery*, 2013. 10(8): p. 1155-1170.
169. Li, J., et al., Micro/nanorobots for biomedicine: Delivery, surgery, sensing, and detoxification. *Science Robotics*, 2017. 2(4).
170. Bard, F., et al., Peripherally administered antibodies against amyloid beta-peptide enter the central nervous system and reduce pathology in a mouse model of Alzheimer disease. *Nat Med*, 2000. 6(8): p. 916-9.
171. Zhu, Y., C. Liu, and Z. Pang, Dendrimer-Based Drug Delivery Systems for Brain Targeting. *Biomolecules*, 2019. 9(12): p. 790.
172. Huang, F., et al., Maintenance of Amyloid  $\beta$  Peptide Homeostasis by Artificial Chaperones Based on Mixed-Shell Polymeric Micelles. *Angewandte Chemie International Edition*, 2014. 53(34): p. 8985-8990.
173. Xiao, L., et al., Inhibition of beta 1-40 amyloid fibrillation with N-acetyl-L-cysteine capped quantum dots. *Biomaterials*, 2010. 31(1): p. 91-98.
174. Yoo, S.I., et al., Inhibition of amyloid peptide fibrillation by inorganic nanoparticles: functional similarities with proteins. *Angewandte Chemie International Edition*, 2011. 50(22): p. 5110-5115.
175. Palmal, S., et al., Inhibition of amyloid fibril growth and dissolution of amyloid fibrils by curcumin-gold nanoparticles. *Chemistry*, 2014. 20(20): p. 6184-91.

176. Mars, A., et al., Curcumin-graphene quantum dots for dual mode sensing platform: Electrochemical and fluorescence detection of APOe4, responsible of Alzheimer's disease. *Analytica chimica acta*, 2018. 1036: p. 141-146.
177. Zhang, J., et al., Epigallocatechin-3-gallate (EGCG)-stabilized selenium nanoparticles coated with Tet-1 peptide to reduce amyloid- $\beta$  aggregation and cytotoxicity. *ACS applied materials & interfaces*, 2014. 6(11): p. 8475-8487.
178. Ganesh, H.V.S., et al., Electrochemical Detection of Gallic Acid-Capped Gold Nanoparticles Using a Multiwalled Carbon Nanotube-Reduced Graphene Oxide Nanocomposite Electrode. *Analytical Chemistry*, 2019. 91(15): p. 10116-10124.
179. Smith, A., et al., Nanolipidic particles improve the bioavailability and  $\alpha$ -secretase inducing ability of epigallocatechin-3-gallate (EGCG) for the treatment of Alzheimer's disease. *International Journal of Pharmaceutics*, 2010. 389(1): p. 207-212.
180. Safer, A.-M., et al., Conjugation Of EGCG And Chitosan NPs As A Novel Nano-Drug Delivery System. *International journal of nanomedicine*, 2019. 14: p. 8033-8046.
181. Faridi Esfanjani, A. and S.M. Jafari, Biopolymer nano-particles and natural nano-carriers for nano-encapsulation of phenolic compounds. *Colloids and Surfaces B: Biointerfaces*, 2016. 146: p. 532-543.
182. Mathew, A., et al., Curcumin loaded-PLGA nanoparticles conjugated with Tet-1 peptide for potential use in Alzheimer's disease. *PLoS one*, 2012. 7(3).
183. de Cristo Soares Alves, A., R.M. Mainardes, and N.M. Khalil, Nanoencapsulation of gallic acid and evaluation of its cytotoxicity and antioxidant activity. *Materials Science and Engineering: C*, 2016. 60: p. 126-134.
184. Sun, D., et al., Design of PLGA-functionalized quercetin nanoparticles for potential use in Alzheimer's disease. *Colloids and Surfaces B: Biointerfaces*, 2016. 148: p. 116-129.
185. Cano, A., et al., Dual-drug loaded nanoparticles of Epigallocatechin-3-gallate (EGCG)/Ascorbic acid enhance therapeutic efficacy of EGCG in a APP<sup>swe</sup>/PS1<sup>dE9</sup> Alzheimer's disease mice model. *Journal of Controlled Release*, 2019. 301: p. 62-75.
186. da Rocha Lindner, G., N.M. Khalil, and R.M. Mainardes, Resveratrol-loaded polymeric nanoparticles: validation of an HPLC-PDA method to determine the drug entrapment and evaluation of its antioxidant activity. *The Scientific World Journal*, 2013. 2013.
187. Ethemoglu, M.S., et al., Anticonvulsant activity of resveratrol-loaded liposomes in vivo. *Neuroscience*, 2017. 357: p. 12-19.
188. Taylor, M., et al., Effect of curcumin-associated and lipid ligand-functionalized nanoliposomes on aggregation of the Alzheimer's A $\beta$  peptide. *Nanomedicine: Nanotechnology, Biology and Medicine*, 2011. 7(5): p. 541-550.
189. Mourtas, S., et al., Multifunctional nanoliposomes with curcumin-lipid derivative and brain targeting functionality with potential applications for Alzheimer disease. *European Journal of Medicinal Chemistry*, 2014. 80: p. 175-183.

190. Kuo, Y.-c. and C.-W. Tsao, Neuroprotection against apoptosis of SK-N-MC cells using RMP-7-and lactoferrin-grafted liposomes carrying quercetin. *International journal of nanomedicine*, 2017. 12: p. 2857.
191. Frozza, R.L., et al., Neuroprotective Effects of Resveratrol Against A $\beta$  Administration in Rats are Improved by Lipid-Core Nanocapsules. *Molecular Neurobiology*, 2013. 47(3): p. 1066-1080.
192. Sood, S., K. Jain, and K. Gowthamarajan, Delivery of neuroprotective polyphenol to the brain via an intranasal route for management of Alzheimer's disease. *Alzheimer's & Dementia: The Journal of the Alzheimer's Association*, 2013. 9(4): p. P299.
193. Sood, S., K. Jain, and K. Gowthamarajan, Intranasal delivery of curcumin-/INS; donepezil nanoemulsion for brain targeting in Alzheimer's disease. *Journal of the Neurological Sciences*, 2013. 333: p. e316-e317.
194. Hagl, S., et al., Curcumin micelles improve mitochondrial function in a mouse model of Alzheimer's disease. *J Prev Alzheimers Dis*, 2014. 1: p. 80-83.
195. Schiborr, C., et al., The oral bioavailability of curcumin from micronized powder and liquid micelles is significantly increased in healthy humans and differs between sexes. *Mol Nutr Food Res*, 2014. 58(3): p. 516-27.
196. Lu, X., et al., Resveratrol-loaded polymeric micelles protect cells from A $\beta$  -induced oxidative stress. *International Journal of Pharmaceutics*, 2009. 375(1): p. 89-96.
197. Bosman, d.A., H. Janssen, and E. Meijer, About dendrimers: structure, physical properties, and applications. *Chemical reviews*, 1999. 99(7): p. 1665-1688.
198. Tomalia, D.A. Starburst dendrimers—Nanoscopic supermolecules according to dendritic rules and principles. in *Macromolecular Symposia*. 1996. Wiley Online Library.
199. Sousa-Herves, A., et al., GATG Dendrimers and PEGylated Block Copolymers: from Synthesis to Bioapplications. *Aaps Journal*, 2014. 16(5): p. 948-961.
200. Imae, T., Physicochemical properties of dendrimers and dendrimer complexes. *Dendrimer-Based Drug Delivery Systems*, 2012: p. 55-92.
201. Ke, W., et al., Gene delivery targeted to the brain using an Angiopep-conjugated polyethyleneglycol-modified polyamidoamine dendrimer. *Biomaterials*, 2009. 30(36): p. 6976-6985.
202. Moscariello, P., et al., Brain delivery of multifunctional dendrimer protein bioconjugates. *Advanced Science*, 2018. 5(5): p. 1700897.
203. Xu, L., H. Zhang, and Y. Wu, Dendrimer advances for the central nervous system delivery of therapeutics. *ACS chemical neuroscience*, 2014. 5(1): p. 2-13.
204. Srinageshwar, B., et al., PAMAM dendrimers cross the blood-brain barrier when administered through the carotid artery in C57BL/6J mice. *International journal of molecular sciences*, 2017. 18(3): p. 628.
205. Wasiak, T., et al., Phosphorus dendrimers affect Alzheimer's (A $\beta$  1-28) peptide and MAP-Tau protein aggregation. *Molecular pharmaceutics*, 2012. 9(3): p. 458-469.

206. Amaral, S.P., et al., Tuning the Size of Nanoassemblies: A Hierarchical Transfer of Information from Dendrimers to Polyion Complexes. *Angewandte Chemie-International Edition*, 2018. 57(19): p. 5273-5277.
207. Duncan, R. and L. Izzo, Dendrimer biocompatibility and toxicity. *Advanced drug delivery reviews*, 2005. 57(15): p. 2215-2237.
208. He, H., et al., PEGylated Poly (amidoamine) dendrimer-based dual-targeting carrier for treating brain tumors. *Biomaterials*, 2011. 32(2): p. 478-487.
209. Patel, D., J. Henry, and T. Good, Attenuation of  $\beta$ -amyloid induced toxicity by sialic acid-conjugated dendrimeric polymers. *Biochimica et Biophysica Acta (BBA)-General Subjects*, 2006. 1760(12): p. 1802-1809.
210. Klajnert, B., et al., EPR Study of the Interactions between Dendrimers and Peptides Involved in Alzheimer's and Prion Diseases. *Macromolecular Bioscience*, 2007. 7(8): p. 1065-1074.
211. Jain, K., et al., Dendrimer toxicity: Let's meet the challenge. *Int J Pharm*, 2010. 394(1-2): p. 122-42.
212. Benseny-Cases, N., O. Klementieva, and J. Cladera, Dendrimers antiamyloidogenic potential in neurodegenerative diseases. *New Journal of Chemistry*, 2012. 36(2): p. 211-216.
213. Klementieva, O., et al., Dense Shell Glycodendrimers as Potential Nontoxic Anti-amyloidogenic Agents in Alzheimer's Disease. *Amyloid-Dendrimer Aggregates Morphology and Cell Toxicity. Biomacromolecules*, 2011. 12(11): p. 3903-3909.
214. Chafekar, S.M., et al., Branched KLVFF tetramers strongly potentiate inhibition of  $\beta$  - Amyloid aggregation. *ChemBioChem*, 2007. 8(15): p. 1857-1864.
215. Shetty, P.K., et al., Skin Delivery of EGCG and Silibinin: Potential of Peptide Dendrimers for Enhanced Skin Permeation and Deposition. *AAPS PharmSciTech*, 2017. 18(6): p. 2346-2357.
216. Shi, W., et al., Synthesis of Monofunctional Curcumin Derivatives, Clicked Curcumin Dimer, and a PAMAM Dendrimer Curcumin Conjugate for Therapeutic Applications. *Organic Letters*, 2007. 9(26): p. 5461-5464.
217. Madaan, K., V. Lather, and D. Pandita, Evaluation of polyamidoamine dendrimers as potential carriers for quercetin, a versatile flavonoid. *Drug delivery*, 2016. 23(1): p. 254-262.
218. Chauhan, A.S., Dendrimer nanotechnology for enhanced formulation and controlled delivery of resveratrol. *Annals of the New York Academy of Sciences*, 2015. 1348(1): p. 134-140.
219. Sharma, A., S.P. Gautam, and A.K. Gupta, Surface modified dendrimers: Synthesis and characterization for cancer targeted drug delivery. *Bioorganic & Medicinal Chemistry*, 2011. 19(11): p. 3341-3346.
220. Chen, H.-T., et al., Cytotoxicity, hemolysis, and acute in vivo toxicity of dendrimers based on melamine, candidate vehicles for drug delivery. *Journal of the American Chemical Society*, 2004. 126(32): p. 10044-10048.

- 
221. Nakanishi, H., et al., Nonviral genetic transfer of Fas ligand induced significant growth suppression and apoptotic tumor cell death in prostate cancer in vivo. *Gene Therapy*, 2003. 10(5): p. 434-442.
222. Yan, H., et al., Two-Order Targeted Brain Tumor Imaging by Using an Optical/Paramagnetic Nanoprobe across the Blood Brain Barrier. *ACS Nano*, 2012. 6(1): p. 410-420.

## SECTION II

## Chapter 2

### Materials and Methods

## CHAPTER 2

### Materials and Methods

This Chapter comprises the detailed information on the experimental procedures used throughout this thesis. Overall, here we specify the materials and methods used for the extraction of the natural polyphenols used in Chapters 3-5, details on the synthesis of the Ga-terminated dendrimers performed in Chapter 6; the preparation of single and mixed self-assembled monolayers in Chapter 8; as well as the experimental conditions used for the preparation of amyloid- $\beta$  (A $\beta$ ) and the chemical and biological characterization techniques used during the studies presented in the experimental chapters.

#### 2.1 MATERIALS

The following section describes in more detail the main materials used in this thesis.

##### 2.1.1 CORK-BASED MATERIALS

Cork is the outer bark of *Quercus suber L.*, the cork oak tree. Its main industrial application is to produce stoppers for wine bottles, however, during its processing there are a series of by-products that are generated and are further used to generate a wide range of cork-based products, namely: cork-polymer composites, agglomerated materials for a wide range of applications (*e.g.* construction, automobile, aerospace, etc.), among many others.[1-3] The chemical structure of cork includes 30–50% suberin, 15–30% lignin, 6–25% polysaccharides, and 8–20% of extractives, where the indicated ranges are derived from the known variability of natural materials.[4] The cork extractives fraction is composed by low molecular weight molecules that have weak interaction with the cell wall composition (*i.e.* suberin, lignin and cellulose).[5] They are usually referred to as secondary metabolites, as their function is associated with signalling pathways, as well as with defence mechanisms against different pathogens, ultraviolet (UV)



radiation, oxidative stress, among others.[6, 7] These extractives fraction comprises phenols and polyphenols, triterpenes, sterols, fatty acids, among other compounds. The (poly)phenolic compounds present in cork (and usually extracted using polar solvents) are tannins (condensed tannins or proanthocyanidins) and hydrolysable tannins. The hydrolysable tannins comprise the ellagitannins and gallotannins (composed by a glucose central unit and a series of galloyl esters).[8] Therefore, compounds such as ellagic acid,  $\beta$ -O-ethylvescalagin or the isomers vescalagin/castalagin can be obtain from cork powder.[9]

The cork powder used between Chapters 3 to 5 was supplied by Amorim Cork Composites S.A. (Santa Maria da Feira, Portugal). It was collected at their facilities directly from the industrial processing of cork and was used as received. The extraction procedures used to obtain the hydrolysable ellagitannins fractions and isolated compounds (*i.e.* CWE, CWEE, fCWEE, vescalagin and castalagin) are described in section 2-2.1.

### 2.1.2 DENDRIMERS

Dendrimers are 3D highly branched nanosystems that present a multivalent character due to the presentation of a number of repeating units at their surface.[10] They are monodisperse molecular nanostructures with a regular architecture, with well-defined particle size and shape.[11] They can be synthesised by a “divergent method” in which the synthesis start with a multifunctional core molecule that is extended to the periphery, or by a “convergent growth process”, where the synthesis starts at the periphery and it develops into the core.[12] Their structure is divided into three distinct regions: (i) a core or focal moiety; (ii) layers of branched repeating units originating from the core, and (iii) end groups on the outer layer composed by the repeating units.[13] Of note, the number of repeating units increases exponentially with the dendrimer generation (repeating units layered around the core of the molecule, building up a stratified structure, where each layer is called a generation), while the volume of the dendrimer grows only proportionally to  $r^n$ , and they present, in general, a globular conformation as their generation increases.[14]

Their main disadvantage relies in their synthesis. For each additional generation it is required a high-yield coupling chemistry to be able to obtain a relevant amount of pure dendrimer. In addition, as their generation and molecular weight increases, the properties of dendrimers (*i.e.* solubility or chemical reactivity) are dominated by the nature of the end groups, which, in some cases, becomes a drawback.[11]

In Chapter 6, three different generations of galloyl (Ga)-terminated dendrimers (2G0-GaOH, 2G1-GaOH and 3G1-GaOH) were synthesised using the divergent method as described in section 2-2.2.

### 2.1.3 GLUCOSAMINE AND ITS ANALOGUES

Glucosamine (GlcN) is a monosaccharide synthesized naturally by the body.[15] GlcN is used in the biosynthesis of glycosaminoglycans (GAGs) and proteoglycans, which are the building blocks of the extracellular matrix.[16] It is also an important component of the chemical structure of polysaccharides, such as chitosan. GlcN is converted into glucosamine-6-phosphate (GlcN6P), glucosamine-6-sulphate (GlcN6S) and N-acetylglucosamine (GlcNAc) by the body through the action of different enzymes.[17] GlcN has been evaluated for its efficacy in relieving the symptoms of osteoarthritis (it is a widely used dietary supplement for arthritic conditions) with a disease-modifying potential.[18] It is usually produced commercially by the hydrolysis of shellfish exoskeletons and by fermentation of grains (corn or wheat).[19]

GlcNAc is a monosaccharide, which is a chemical analogue of GlcN. It is the monomeric unit of the chitin, the second most abundant carbohydrate in nature, after cellulose.[20] Importantly, proteins in the cellular environment can be modified through the reversible addition of a GlcNAc residues (*i.e.* O-GlcNAc glycosylation at serine and threonine residues).[21] GlcNAc is involved in the regulation of phosphorylation-based signalling, and it is also a component of hyaluronic acid and keratan sulphate on the cell surface.[22, 23]. Its industrial production is usually based in the hydrolysis of chitin.[19, 24]

GlcN6P is another monosaccharide, which takes part of the glucose metabolism, namely in the hexosamine biosynthetic pathway (HBP), as well as in the O-GlcNAcylation. GlcN and GlcNAc join at the HBP in the conversion of fructose-6-phosphate into GlcN6P (a key step in both anabolic and catabolic processes).[15]

GlcN6S is a naturally occurring monosaccharide, normally present with most of the GAGs, with the exception of hyaluronic acid.[25] In pharmaceutical formulations, GlcN6S is often combined with chondroitin sulphate. GlcN6S is reported to have as high biological relevance due to the presence of the sulphate group.[26]

The monosaccharides were used in Chapter 7, obtained from: GlcN – Sigma-Aldrich; GlcNAc – Laborspirit; GlcN6S and GlcN6P – Carbosynth.

### 2.1.4 AMYLOID- $\beta$ (1-42) PEPTIDE

Amyloid- $\beta$  (A $\beta$ ) peptides of varying lengths (from 38-42 amino acids) are generated during the sequential proteolytic cleavage of the transmembrane amyloid precursor protein (APP) by  $\beta$ - and  $\gamma$ -secretases.[27]

Its most common form is A $\beta$ 40, however, the A $\beta$ 42 version (presenting two extra hydrophobic residues) is the one with a higher propensity to aggregate into soluble oligomers, as well as insoluble deposits. During the supramolecular assembly of A $\beta$  species, it is observed the co-existence of multiple aggregated forms, from dimers to oligomers and  $\beta$ -sheet rich fibrils that, over time, contributes to the build-up of compact extracellular senile plaques, a characteristic hallmark of Alzheimer disease (AD).[28] The oligomeric forms (presenting anti-parallel  $\beta$ -sheet conformations) are reported to be more toxic than the A $\beta$  nanofibres (that present parallel  $\beta$ -sheet conformations). These oligomers present a dynamic thermodynamic state (metastable), small size and high ability to diffuse through the cellular environment, which privileges their ability to spread its toxicity throughout the brain.[29] Thus, they can interact with the cell membrane, and compete with several membrane receptors and proteins, triggering downstream pathological cascades, namely: membrane disruption and formation of Ca<sup>2+</sup> permeable pores; oxidative stress in the endoplasmic reticulum and mitochondrial dysfunction; imbalance in the activity of neurotransmitters; insulin resistance; among others.[30]

Two major hallmarks are associated with AD, the presence of extracellular senile plaques composed by A $\beta$  and neurofibrillary tangles of hyperphosphorylated tau. The importance of the A $\beta$ -mediated pathological pathways and its involvement in the onset of AD is still under debate. However, in all the AD cases, A $\beta$  is present above a certain threshold in the biological environment before the deposition of hyperphosphorylated tau and the beginning of dementia.[31, 32] It has been also reported that AD-mediated dementia only occurs in patients that present neurofibrillary tangles in the affected regions of the brain (*i.e.* medial temporal lobe and peripheral cortex).[33] Therefore, the pathological hallmarks of AD are dependent on two variables: the transcellular spread and templated seeding of A $\beta$  and the resulting deposition of neurofibrillary tangles; and the presence of dystrophic neurites associated within the formation of amyloid plaques.[34]

Despite the controversies about which event is at the onset of AD, if the A $\beta$  accumulation or the hyperphosphorylation of tau, it is clear that mutations associated to the familial AD (*i.e.* APP, ApoE4, Presenilin 1 or 2 genes) generally contribute to faster pathological consequences by an overall increase of the A $\beta$  levels and/or the A $\beta$ 42:A $\beta$ 40 ratio. However, the familial patients only accounts to, approximately, 7% of the total AD cases.[35] Anyway, it is known that the clearance of A $\beta$  through the recruitment of enzymes, transport through the brain's vasculature, or microglial phagocytosis, is known to decrease with aging or as a result of interaction with other risk factors for AD (*i.e.* cardiovascular disease, type 2 diabetes mellitus, depression, etc.) contributing to its accumulation in the brain and the onset of AD.[36] Therefore, there is a vast body of evidence that the accumulation and spreading of A $\beta$

can induce a variety of pathological processes, such as glial dysfunction, synaptic deficits, impairment of neurotransmitters concentration and function, and cognition deficits, as well as the abnormal aggregation of hyperphosphorylated tau.[37]

Based on the previously presented evidences, it is important to develop effective drugs that are able to eliminate the A $\beta$  cytotoxic forms through: 1) the remodelling of their oligomeric structures into thermodynamically stable off-pathway non-cytotoxic forms; or 2) the development of strategies that stabilize fibrils by blocking their disassembly into the cytotoxic A $\beta$  oligomers.

In Chapter 5, 6 and 7, we used the A $\beta$  peptide presenting 42 amino acids to evaluate the capacity of different compounds (*i.e.* vescalagin/castalagin extracted and purified from cork powder, Ga-terminated dendrimers, as well as GlcN and its analogues) to reduce the A $\beta$ -mediated cellular dysfunctions. Its preparation methodology is described in section 2-2.3.

#### 2.1.5 SELF-ASSEMBLED MONOLAYERS (SAMs)

Single component or mixed self-assembled monolayers (SAMs) have been widely used to elucidate the effect of surface chemistry, hydrophobicity and/or charge on protein adsorption and the following cellular behavior.[38-45]

In Chapter 8, we used SAMs to mimic GAGs with different sulfation degree (simulated by mixing alkanethiol with –SO<sub>3</sub>H and –OH end groups at different ratios) and to characterize *in situ* their interactions with another ECM component – fibronectin (Fn). Because Fn plays a main role in cell adhesion and growth, we have further investigated the impact of the substrate-protein interactions on the cellular behaviour using adipose derived stem cells (ASCs).

## 2.2 METHODS

The methodologies used during the experimental sections of this thesis (*i.e.* Chapters 3-7) are described in the present section, including all the experimental/characterization techniques.

### 2.2.1 PREPARATION OF CORK-BASED EXTRACTS

**Cork Water Extract (CWE).** CWE was extracted using the experimental conditions previously reported.[9] Briefly, CWE was obtained by maintaining cork powder in contact with water (1 g of powder per 50 mL of water) under reflux for a period of 6h. After cooling, the liquid fraction was recovered by filtration, the solvent was partially removed by vacuum evaporation, and the final solid extracts were recovered upon freeze-drying.

**Cork Water Enriched Extract (CWE-E).** CWE-E described and used in Chapter 3 was obtained from CWE, by an additional step using ethanol. In this case, a solution of CWE (5mg/mL in water) was added to 20mL of ethanol. The supernatant was collected, the solvent was partially removed by vacuum evaporation and the final solid extract was recovered by freeze-drying.

**Cork Water Ethanol Extract (CWEE).** CWEE described and used in Chapter 4 was obtained using the experimental conditions previously reported.[9] Briefly, CWEE was obtained by maintaining cork powder in contact with a mixture of water and ethanol (50:50 v/v) and a ratio of 1g of powder to 50mL of solution under reflux conditions for a period of 6h. Upon cooling, the liquid fraction was recovered by filtration, the solvent was partially removed by vacuum evaporation, and the final solid extract were recovered upon freeze-drying.

**Fraction of Cork Water Ethanol Extract (fCWEE).** fCWEE described and used in Chapter 4 was obtained from CWEE. In this case, CWEE was loaded into a chromatographic column, packed with Sephadex LH-20 as stationary phase and stabilized in water. CWEE was eluted with water, followed by mixtures of water and increasing percentages of ethanol, yielding fCWEE. Afterwards, the solvent was partially removed by vacuum evaporation, and the final solid extract was recovered upon freeze-drying.

**Vescalagin/castalagin.** The extraction, purification and identification of vescalagin and castalagin (used in Chapters 3, 4 and 5) was optimized and performed as follow: CWE was loaded into a semi-preparative chromatographic column (Waters Atlantis OBD Prep T3, 5 $\mu$ m 19 x 250mm) and vescalagin/castalagin were collected at their respective retention times using the mobile phases A - water:acetic acid 98:2 (v/v) and B - water:acetonitrile:acetic acid 78:20:2 (v/v/v), under the following gradient: 100% A (t=0min) – 100% A (t=15min) – 70% A : 30% B (t=30min) – 100% B (t=35min) – 100% B (t=50min) – 100% A (t=52min) – 100% A (t=57min). The flow rate was maintained at 5mL.min<sup>-1</sup> and the injection volume was 5mL. The purity of vescalagin and castalagin was determined by quantitative HPLC (KANUER, Germany) using a reverse-phase C18 column (4.6 x 250mm, Atlantis, Waters, UK) at flow rate of 1mL/min, using the same mobile phases and gradients as the ones used for the chromatographic separation. Mass spectra were acquired on an electrospray ionization (ESI) mass spectrometer (MS, Micromass Quattro, Waters, USA) under positive-ion mode. <sup>1</sup>H NMR spectra of both vescalagin and castalagin were recorded using a Bruker Avance III spectrometer (Bruker, Germany) at 25°C in D<sub>2</sub>O. The solvent signal was used as a reference and the chemical shifts ( $\delta$ ) were reported in ppm.

## 2.2.2 SYNTHESIS OF GA-TERMINATED DENDRIMERS

The dendrimers used in Chapter 6 were synthesized gallic acid using the divergent method. Their chemical structure is composed by a hydrophilic triethylene glycol molecule to which terminal Ga moieties were conjugated.

To perform the synthesis of the dendrimers the OH moieties of gallic acid were protected with benzyl groups, yielding benzyl 3,4,5-tris(benzyloxy)benzoate. Briefly, to a gallic acid solution (3.0 g, 17.43 mmol) in MeOH (180 mL) were added  $K_2CO_3$  (12.04 g, 87.15 mmol), benzyl bromide (14.91 g, 87.15 mmol) and NaI (2.61 g, 17.43 mmol) under constant stirring at RT. After 16h of reaction time (under reflux) 30mL of  $H_2O$  was added. After solvent evaporation, the resulting mixture was suspended in  $H_2O$  (50mL) and extracted with EtOAc (3 x 20mL). The combined organic layers were dried and concentrated to give a crude product that was recrystallized from ethanol to give benzyl 3,4,5-tris(benzyloxy)benzoate as a white solid (8.19 g, 88%). Afterwards, the carboxylic acid group of the benzyl 3,4,5-tris(benzyloxy)benzoate was deprotected by stirring 5.69g of benzyl 3,4,5-tris(benzyloxy)benzoate (10.7mmol) in a 3M KOH solution (285mL of MeOH) under reflux overnight. Afterwards, the mixture was cooled down to RT, acidified (pH= 3-4) with HCl (3M) and filtered. The resulting precipitate was dissolved in EtOAc (80mL) and washed with  $H_2O$  (40mL).  $CH_2Cl_2$  (3 x 30mL) was used to extract the product from the aqueous phase. The combined organic phases were concentrated and finally dried. The crude product was purified by automated medium pressure liquid chromatography (MPLC, gradient from hexane to EtOAc, silica, 40min – as detailed under section 2-2.7) to afford 3,4,5-tris(benzyloxy)benzoic acid as a white solid (4.20g, 89%).

With the free carboxylic acid, the 3,4,5-tris(benzyloxy)benzoic acid (334mg, 0.76mmol), HOBt (103mg, 0.76mmol) and EDC (145mg, 0.76mmol) were added to a solution of 2,2'-(ethylenedioxy)bis(ethylamine) (45mg, 0.30mmol) in DMSO (6mL) and stirred for 20h at RT, for the synthesis of the 2G0-GaBn compound. Afterwards, the reaction mixture was added into EtOAc (30mL) and brine (30mL). Several EtOAc portions (3 x 30 mL) were mixed with the aqueous phase for extraction. The combined organic phase was washed with  $H_2O$  (30mL), dried and evaporated under vacuum. The crude product was purified by automated MPLC (gradient from hexane to 100% EtOAc and then to 100%  $CH_2Cl_2$ , using neutral alumina, 25min – more details in section 2-2.7) to afford 2[G0]-GaOBn (255mg, 85%) as a white solid, (Figure 2-1).

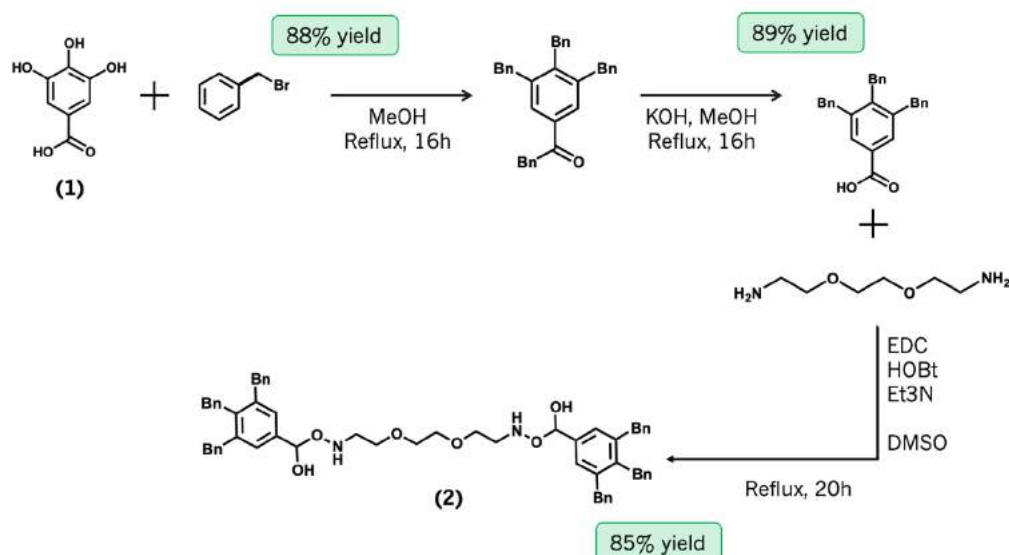


Figure 2-1. Synthetic route for the multigram preparation of the core of the Ga-dendrimers. (1) repeating unit (Ga); (2) 2G0-GaBn (before the deprotection step).

Afterwards, for the deprotection step of the hydroxyl groups of the Ga moieties, Pd/C (16mg, 10%) was added to a solution of 2[G0]-GaOBn (160mg, 0.16mmol) in a mixture of DMF-MeOH 3:1 (4mL). The resulting mixture was stirred under H<sub>2</sub> (1atm) for 20h. The catalyst was removed by filtration through Celite. The filtrate was concentrated and purified by short column chromatography (MeOH-CH<sub>2</sub>Cl<sub>2</sub>-H<sub>2</sub>O 3:3:0.2, silica) to yield 2[G0]-GaOH as a green solid (71mg, 98%) – Ga-dendrimer with two Ga units (*i.e.* 2[G0]-GaOH).

For the synthesis of the 2[G1]-GaOH, 3,4,5-Tris(benzyloxy)benzoic acid (466mg, 1.06mmol), Et<sub>3</sub>N (0.224mL, 1.06mmol), HOBT (143mg, 1.06mmol) and EDC (210mg, 1.06mmol) were added to a solution of 2[G1]-NH<sub>2</sub>·HCl (205mg, 0.14 mmol) in DMSO (8mL). After 24h of stirring at RT, the reaction mixture was distributed between EtOAc (50mL) and brine (50mL). The aqueous phase was extracted with EtOAc (3 x 50mL) and the combined organic phase was washed with 0.1M HCl (30mL) and H<sub>2</sub>O (50mL), dried and evaporated under vacuum. The crude product was purified by automated MPLC (gradient from EtOAc to 25% MeOH, using neutral alumina, 25min – more details in section 2-2.7) to afford 2[G1]-GaOBn (428mg, 75%) as a pale yellow solid. The deprotection step was once again executed by adding Pd/C (60mg, 20%) into a solution of 2[G1]-GaOBn (300mg, 0.075mmol) in a mixture of EtOAc-MeOH 1:1 (8mL). The resulting mixture was stirred under H<sub>2</sub> (1atm) for 14h. The catalyst was removed by filtration through Celite. The filtrate was concentrated and purified by column chromatography (MeOH-CH<sub>2</sub>Cl<sub>2</sub>-H<sub>2</sub>O 3:3:0.2, using silica) to yield 2[G1]-GaOH as a green solid (133mg, 82%) – Ga-dendrimer with six Ga units.

For the synthesis of the dendrimer 3[G1]-GaOH, a gallic acid-triethylene glycol (GATG) dendrimers of the 2G family was decorated with peripheral Ga units.[38] Therefore, 3,4,5-Tris(benzyloxy)benzoic acid (268mg, 0.61mmol), Et<sub>3</sub>N (0.128mL, 0.6mmol), HOBT (82mg, 0.61mmol) and EDC (120mg, 0.61mmol) were added to a solution of 3[G1]-NH<sub>2</sub>·HCl (134mg, 0.05mmol) in DMSO (4.9mL). After 36h of stirring at RT, the reaction mixture was added to EtOAc (50mL) and brine (50mL). The aqueous phase was extracted with EtOAc (3 x 50mL). The combined organic phase was washed with 0.1M HCl (30mL) and H<sub>2</sub>O (50mL), dried and evaporated under vacuum.

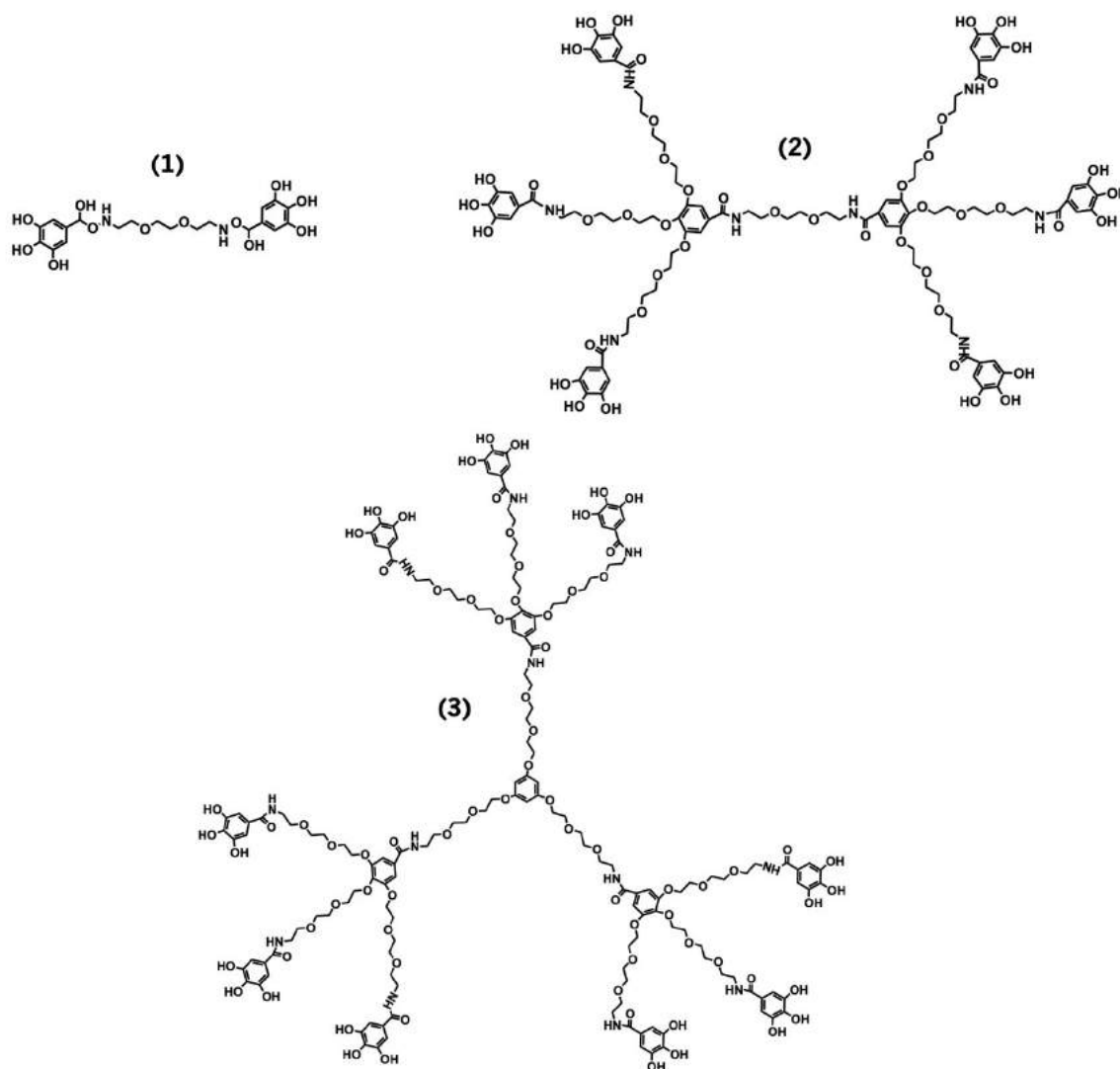


Figure 2-2. Chemical structure of Ga-terminated dendrimers: (1) 2G0-GaOH, (2) 2G1-GaOH and (3) 3G1-GaOH.

The crude product was purified by automated MPLC (gradient from EtOAc to 25% MeOH, using neutral alumina, 25 min – more details in section 2-2.7) to yield 3[G1]-GaOBn (413mg, 84%) as a pale yellow solid. Pd/C (10 mg, 20%) was added to a solution of 3[G1]-GaOBn (49mg, 0.008 mmol) in a mixture of DMF-MeOH 4:1 (3mL). The resulting mixture was stirred under H<sub>2</sub> (1atm) for 24h. The catalyst



was removed by filtration through Celite. The filtrate was concentrated and then purified by column chromatography (MeOH-CH<sub>2</sub>Cl<sub>2</sub>-H<sub>2</sub>O 3:3:0.2, using silica) to yield 3[G1]-GaOH as a green solid (26mg, 90%) – Ga-presenting dendrimer with nine Ga units.

All dendrimers, 2G0-GaOH, 2G1-GaOH and 3G1-GaOH (Figure 2-2) were dissolved in DMSO, as a stock solution before use.

### 2.2.3 PEPTIDE PREPARATION

In Chapters 5 to 7 human A $\beta$  peptide (1-42) was obtained by custom synthesis from GeneCust Europe (Luxembourg). Stock A $\beta$  aliquots (*i.e.* 0.45mg of peptide) were prepared according to the protocol described by Stine *et al.* [39] In brief, A $\beta$  was dissolved in HFIP (approximately 5mg/mL) during 30min at RT. The solution was separated into different eppendorfs (100 $\mu$ L each), HFIP was allowed to evaporate in open eppendorfs overnight in the fume hood, and afterwards during an additional 1h under vacuum. The A $\beta$  aliquots were then stored at -20°C and reconstituted immediately before use.

In Chapter 6, for the monomeric A $\beta$  (A $\beta$ <sub>s</sub>) studies, it was added 20 $\mu$ L of DMSO (sonicated for 10min in an ultra-sound bath) and immediately maintained in ice-cold water (followed by 15s of vortex) to a final concentration of 100 $\mu$ M. In the case of the fibrillar A $\beta$  (A $\beta$ <sub>f</sub>) experiments it was added 20 $\mu$ L of DMSO (sonicated for 10min in an ultra-sound bath) and immediately added 10mM HCl at RT, diluting to a final concentration of 100 $\mu$ M of A $\beta$ , followed by vortex for 15s, and then incubated for 24h at 37°C.

### 2.2.4 PREPARATION OF SINGLE AND MIXED SAMS

In Chapters 8, the single component and mixed SAMs were formed on the substrates as previously described.[48] Briefly, the cleaned substrates (QCM crystals, SPR sensors and gold-coated glass) were immersed in 20 mM ethanol solution of HS(CH<sub>2</sub>)<sub>11</sub>OH (samples designated as SO<sub>3</sub>H 0), HS(CH<sub>2</sub>)<sub>11</sub>SO<sub>3</sub>H (synthesised in our lab[48], designated as SO<sub>3</sub>H 100) or mixture of these at –SO<sub>3</sub>H : –OH ratios of 1 : 3 and 3 : 1 in order to obtain 25% and 75% of –SO<sub>3</sub>H groups on the surface (samples referred to as SO<sub>3</sub>H 25 and SO<sub>3</sub>H 75, respectively). After 48 hrs, the coated substrates were washed several times with ethanol, dried under N<sub>2</sub> and immediately used in the following studies.

Of note, gold-coated quartz crystals (QSX301, Q-Sense, Sweden) were used for the QCM-D measurements (section 2-2.36). Gold-coated sensors (BioNavis, Finland) were used for the SPR characterization (section 2-2.14). The substrates used for the live imaging (section 2-2.37) were glass slides uniformly coated with gold (20 nm) by the e-beam physical vapour deposition (ATC Orion series UHV Evaporation system, AJA International Inc.). Titanium (3–5 nm film) was used as a primer improving

the adhesion between the gold and the glass. All the substrates were cleaned (piranha solution, 10 min) prior use.

## 2.2.5 HIGH PERFORMANCE LIQUID CHROMATOGRAPHY (HPLC) ANALYSIS

HPLC is used to detect, separate and identify/quantify compounds in a solution. It is constituted by a pump that pressurize a liquid solvent (pressure ranges from 50–350bar) containing the sample that flows through a column filled with a solid adsorbent material (*e.g.* modified silica). Each molecule in the sample interacts differently with the adsorbent material, producing different retention times for each molecule, promoting their separation. Different detectors can be used (*e.g.* UV, refractive index, etc.) to record the chromatographic profiles of mixtures of molecules.

In Chapters 3 and 5, it was used an analytical HPLC (KANUER, Germany) to quantify the concentration of vescalagin and castalagin present in CWE and CWE-E. Experiments were performed using a reverse-phase C18 column (4.6 x 250mm, Atlantis, Waters, UK) at a flow rate of 1mL/min, and the following mobile phases: A - water:acetic acid 98:2 (v/v) and B - water:acetonitrile:acetic acid 78:20:2 (v/v/v); under the following gradient: 100% A (t=0min) – 100% A (t=15min) – 70% A : 30% B (t=30min) – 100% B (t=35min) – 100% B (t=50min) – 100% A (t=52min) – 100% A (t=57min).

In Chapter 4, HPLC was used to identify vescalagin, castalagin, gallic acid and ellagic acid in the CWE, CWEE and fCWEE extracts. The analysis was performed using a Knauer equipment equipped with a photodiode array detector (PDA, Smartline UV detector 2600) and using C18 column (4.6 x 250mm, 5 $\mu$ m particle size, Atlantis T3, Waters, UK) protected by an C18 guard column (4.6 x 20mm, 5 $\mu$ m particle size, Atlantis T3, Waters, UK). The mobile phase was a mixture between buffer A (water:methanol:acetic acid 88:10:2 (v/v/v)) and buffer B (methanol:acetic acid 98:2 (v/v)) and the following gradient: 0% B (0-2min), 0-100% B (2-50min), 100% B (50-60min), 100-0% B (60-70min) and 0% B (70-80min). The flow rate was 1mL.min<sup>-1</sup> and the injection volume was 100 $\mu$ L. The identification of each compound was performed by MS and PDA and the quantification was performed using calibration curves of standard solutions, *i.e.* vescalagin and castalagin purified in our lab by semi-preparative HPLC (Atlantis T3 column, 25 x 250mm and injection volume of 2mL) using the same buffers and gradient as in the analytical program; additional standards, *i.e.* gallic acid and ellagic acid, to quantify their concentration in the cork extracts were acquired from Sigma-Aldrich.

## 2.2.6 MASS SPECTROMETRY ANALYSIS

MS measures the mass-to-charge ratio ( $m/z$ ) of ions of a pure samples. The analyte is ionized (the vaporised sample passes into the ionisation chamber) and is deflected by a magnetic field according to their masses (weight) of the charged particles.

In Chapters 3, 4 and 5, we used MS to identify vescalagin and castalagin (Chapters 3 and 5), but also gallic acid and ellagic acid (Chapter 4), as well as to act as a support of the HPLC analysis. MS spectra were acquired after chromatographic separation using an electrospray ionization (ESI) mass spectrometer (MS) Water Micromass Quattro (Waters, USA) under positive-ion mode.

In Chapter 6, MS spectra were recorder on a Bruker Microtof spectrometer coupled to a HPLC Agilent 1100 using atmospheric-pressure chemical ionization (APCI). Samples were injected via flow injection analysis (FIA) using a MeOH/aqueous solution of formic acid 0.1% 1:1, flow 0.2mL/min.

## 2.2.7 COLUMN CHROMATOGRAPHY

Column chromatography was used to separate the chemical compounds necessary for the synthesis of the different dendrimers. In a similar fashion as for HPLC (without higher pressures, section 2-2.4) it is based on differential retention of compounds when passing through an adsorbent, allowing the separation of a mixture of compounds. In this case automated column chromatography was performed using a MPLC (Teledyne ISCO CombiFlash RF) using a pressure of 200 psi with silica columns (40mm, RediSep Rf, VWR Chemicals) or neutral aluminium oxide 60 mesh (from Alfa Aesar). Samples were adsorbed onto silica or neutral aluminium oxide 60 mesh into solid cartridges.

## 2.2.8 GEL PERMEATION CHROMATOGRAPHY (GPC)

GPC is a well-established technique to separate compounds by their molecular weight, as well as to evaluate the distribution of molecular weights in a sample.[40] The principle is also similar to other liquid chromatography (*e.g.* HPLC in section 2-2.4). The separation is based on the interaction of the analyte and its molecular sizes with a gel (stationary phase). The flow of the mobile phase forces larger molecules to flow through the column (without penetrating into the gel matrix) whereas smaller molecules are delayed according to their penetration into the gel.

GPC elugrams were used to evaluate the monodispersed character of the Ga-terminated dendrimers, used in Chapter 6. Experiments were performed on an Agilent 1100 series separation module using a PSS SDV pre-column (8 x 50 mm), a PSS SDV Linear S column (8 x 300 mm) and a PSS SDV Lux Linear M column (8 x 300 mm) equipped with an Agilent 1100 series refractive index and UV

detectors. THF was used as eluent at a flow rate of 1mL/min. The samples were filtered through a 0.45 $\mu$ m PTFE filter before injection.

### 2.2.9 NUCLEAR MAGNETIC RESONANCE (NMR)

NMR spectra of the compounds were acquired by dissolving them in deuterated solvents (so that the hydrogens from the water are not overlaying the ones from the sample) and the chemical shifts characteristics of the surroundings of the each  $^1\text{H}$  or  $^{13}\text{C}$  nuclei present in the molecule are recorded in the NMR spectra. NMR spectra acquisitions were used to determine the content, purity, and molecular structure of vescalagin, castalagin (in Chapter 5) and Ga-terminated dendrimers (in Chapter 6).

In Chapter 5,  $^1\text{H}$  NMR spectra of vescalagin/castalagin were recorded using a Bruker Avance III spectrometer (Bruker, Germany) at 25 $^\circ\text{C}$  in  $\text{D}_2\text{O}$ . The chemical shifts ( $\delta$ ) are reported in ppm using the solvent signal as a reference.

In Chapter 6,  $^1\text{H}$  and  $^{13}\text{C}$  NMR spectra were recorded using a Varian Mercury 300 MHz spectrometer (Varian, USA). Chemical shifts ( $\delta$ ) were reported in ppm using as reference the HOD peak (or  $\text{CD}_3\text{OD}$ ), internal tetramethylsilane (in  $\text{CDCl}_3$ ), or residual solvent peak ( $\text{DMSO-d}_6$ ). For all acquisitions, Mestre Nova 9.0 software (Mestrelab Research) was used for spectral processing.

### 2.2.10 INFRARED SPECTROSCOPY (FTIR) ASSESSMENT

FTIR spectroscopy was used to identify the functional groups on the Ga-terminated dendrimer structure (Chapter 6). FTIR spectra were recorded on a Perkin-Elmer Spectrum Two spectrophotometer equipped with a UATR accessory or a Bruker Vertex 70V spectrometer using KBr pellets.

### 2.2.11 ISOTHERMAL TITRATION CALORIMETRY (ITC) STUDIES

ITC was used to evaluate the chemical interactions between vescalagin/castalagin and  $\text{A}\beta$  in Chapter 5. ITC measurements were performed using a MicroCal VP-ITC (MicroCal Inc., Northampton, MA, USA). Samples were degassed in a ThermoVac system (MicroCal) prior to use. Vescalagin/castalagin were titrated into an  $\text{A}\beta$  solution (10 $\mu\text{M}$ ) in PBS. A first injection of 2 $\mu\text{L}$  (neglected in the analysis) followed by other 27 injections of 10 $\mu\text{L}$  each were performed under continuous stirring at 286rpm. All the measurements were done at 25 $^\circ\text{C}$ . PBS buffer was titrated to peptide solution to establish the baseline analysis.

ITC experiment offers the basic thermodynamic profile for the established interactions, including three key binding parameters: Gibbs energy (that can be calculated from the equilibrium association constant  $K$ ), enthalpy and entropy of interaction:

*Equation 2-1*

$$\Delta G = -RT \ln K = RT \ln k_d$$

where  $K$  is the equilibrium association constant,  $k_d$  is the equilibrium dissociation constant,  $T$  is the thermodynamic or absolute temperature and  $R$  is the gas constant.

The binding Gibbs energy change can be calculated from the enthalpic and entropic contributions by means of:

*Equation 2-2*

$$\Delta G = \Delta H - T\Delta S$$

to obtain such thermodynamic parameters, the raw data of ligand interaction were analysed by fitting the heat isotherms using a nonlinear least-squares analysis to a one-binding-site model.

### 2.2.12 CIRCULAR DICHROISM (CD)

CD was used in Chapters 5 through 7 to evaluate the A $\beta$  secondary structure. The CD technique is able to probe the secondary structure of peptides/proteins, such as  $\alpha$ -helices,  $\beta$ -sheets, etc.[41] As an example, the CD spectra of a peptide/protein can show an antiparallel  $\beta$ -sheets when a negative peak at 218 nm is accompanied by a positive peak at 195 nm, while disordered peptide/proteins have negative bands at 195 and low ellipticity above 210 nm.[42]

Therefore, CD spectra were recorded in the range between 190–260nm with a scan rate of 10nm/min, a response time of 1s, using 1mm path length cells at 37°C using a CD spectrometer (Jasco J1500, Japan). Three scans were accumulated for each spectrum. For all the CD experiments, the A $\beta$  concentration was 25 $\mu$ M. The A $\beta$ /compound ratios were defined taking into account the experimental conditions adopted in each Chapter (between 5 and 7). Results are expressed as  $\theta$  [mdeg].

### 2.2.13 SCANNING TRANSMISSION ELECTRON MICROSCOPY (STEM) ANALYSIS

STEM was used in Chapter 5 and 6, to analyse the morphological presentation of A $\beta$  supramolecular assemblies, in the presence and absence of each tested compound.

STEM is a type of transmission electron microscopy, where the beam of electrons is transmitted through an ultrathin section of a grid. The images are produced as a result of the transmission through the specimen when the beam of electrons interacts with the sample.

For the acquisitions of the STEM images, fibrillar A $\beta$  peptide (30 $\mu$ M) in the presence and absence of polyphenols (Chapter 5) and dendrimers (Chapter 6) were spotted onto the TEM grids (Carbon Type-B

400M Cu, IESMAT, Spain) during 3min, followed by the classic staining with UranylLess (10 $\mu$ L each sample, for 2 minutes) (EMS, UK). All the samples were washed with water and dried under a gentle nitrogen flux. STEM images were obtained using a High-Resolution Field Emission Scanning Electron Microscope (SEM - Auriga Compact, Zeiss, Germany). The scans were acquired at a resolution of 2048  $\times$  1536 pixels, EHT = 3000kV, WD = 2.9mm and a magnification = 30000.

#### 2.2.14 SURFACE PLASMON RESONANCE (MP-SPR)

In Chapter 8, Fn adsorption was followed in real time with a multi-parametric instrument SPR Navi 200 (BioNavis, Finland), equipped with two lasers (670 and 785 nm) in both measurement channels. All measurements were performed using a full angular scans. The protein adsorption was performed *in situ* by injecting Fn (10  $\mu$ g/mL in a serum free  $\alpha$ -MEM) at a rate of 50  $\mu$ L/min. Upon signal stabilization, a washing step with a serum free  $\alpha$ -MEM was carried out and the liquid flow was replaced by air. The measurements in air were performed immediately after changing the media (detected by a pronounced shift in the resonance curves to lower angles) to guarantee the preservation of the protein organization. The spectra in  $\alpha$ -MEM and in air, both at 670 and 785 nm, were fitted using the Winspall software (version 3.02, Max Planck Institute for Polymer Research, Mainz, Germany). SPR angular scans of bare sensor surfaces were simulated first, and the parameters obtained in the fitting of the first layers (glass-chromium-gold) were used in further simulations with the films. The simultaneous determination of both thickness and refractive index (RI) was performed following previously described procedure.[52, 53]

#### 2.2.15 ANTIOXIDANT (AO) ACTIVITY BY DPPH

The radical scavenging activity was measured using 2,2-diphenyl-1-picrylhydrazyl (DPPH, Chapters 3 and 4), following the methodology reported by Santos *et al.*[43] DPPH is a stable free radical with violet colour (absorbing at 517nm) that, in the presence of an antioxidant molecule is reduced, giving rise to light yellow colour.

Briefly, 50 $\mu$ M of suitable sample dilutions was added to 900 $\mu$ M of DPPH (6.2mg in 100 mL of methanol, initial absorbance of 1.02 $\pm$ 0.03) and the absorbance was measured at 517nm using a microplate reader. The EC50 was calculated as the concentration of compounds necessary to reduce the initial absorbance by 50%.

#### 2.2.16 OXYGEN RADICAL ABSORBANCE CAPACITY (ORAC)

The ORAC assay is based on *in situ* production of reactive oxygen species (ROS) generated via the 2,2'-azobis(2-methylpropionamidine) dihydrochloride (AAPH) compound. AAPH generates free radicals which,

in the presence of oxygen generates ROS, which interact with a fluorescent probe that, in turn, reacts with an oxidizable fluorescent probe (*i.e.* fluorescein), enhancing its fluorescence intensity. A fluorescence decay is observed in the presence of an antioxidant compound.[44]

The ORAC assay (in Chapter 4) was adapted from the methodology described by Huang *et al.*[45] The reaction mixture consisted of 25 $\mu$ M of sample or trolox (as standard), 25 $\mu$ M of 250mM AAPH and 150 $\mu$ M of fluorescein at a concentration of 0.025 $\mu$ M. Fluorescence measurements (excitation wavelength at 485nm and emission wavelength at 520nm) were performed in the microplate reader at 37°C, with readings taken at 2min intervals and with agitation in between each measurement. The results are expressed as mg of trolox equivalents (TE) per g of cork-based compounds.

#### 2.2.17 TOTAL PHENOLIC CONTENT (TPC) MEASUREMENTS

The total phenolic content (TPC) in a sample can be evaluated by the reaction of phenolic compounds in the presence of a redox reagents (Folin-Ciocalteu reagent).[46] The reaction forms a blue chromophore constituted by a phosphotungstic/phosphomolybdenum complex, where the maximum absorption of the chromophores depends on the concentration of phenolic compound.

Thus, the TPC (in Chapter 4) was determined according to the Folin-Ciocalteu method[46] and adapted from Santos *et al.*[43] Briefly, 50 $\mu$ M of sample solution (1mg/mL) was added to 500 $\mu$ M of Folin reagent (diluted 1:10) and 450 $\mu$ M of sodium carbonate solution (75g/L). After heating to 50°C for 5min, the absorbance at 756nm was read in a microplate reader (Synergy HT, BioTek, USA). The TPC was calculated from a calibration curve obtained with gallic acid standards and expressed as mg of gallic acid equivalents per g of cork-based compounds.

#### 2.2.18 MICROBIOLOGICAL CULTURE CONDITIONS

In Chapter 3 it was used four bacteria strains to conduct the anti-bacterial studies. Therefore, *Staphylococcus aureus* (SA, ATCC 25923), Methicillin-resistant *Staphylococcus aureus* (MRSA, ATCC 700698), Methicillin-resistant *Staphylococcus epidermidis* (MRSE, ATCC 35984) and *Pseudomonas aeruginosa* (PA, ATCC 27853) were obtained from the American Type Culture Collection and subcultures were incubated at 37°C for 18-24h on Tryptic Soy Agar (TSA, ref 610053 and 611001, Liofilchem). Suspension cultures were prepared by inoculation of single colonies in 10mL of Tryptic Soy Broth (TSB). Afterwards, for the preparation of anti-bacterial assays, bacteria cells were re-suspended in culture media and the absorbance was adjusted to a turbidity of 0.5 McFarland scale (measured at 640nm), to an

equivalent concentration of  $1-2 \times 10^8$  colony forming units (CFUs)/mL. The anti-bacterial tests performed with these strains can be found in sections from 2-2.17 to 2-2.20 and 2-2.24.

### 2.2.19 DISK DIFFUSION ASSAY

Disk diffusion assay (or agar diffusion test) allows the visualization of the ability of an anti-bacterial agent to reduce or abolish bacterial growth. These tests are performed in an agar plate (inoculated with bacteria) to which a disc soaked with an anti-bacterial compound is placed, followed by incubation over a determined time period. If the anti-bacterial compound inhibits the bacterial growth it is expected the appearance of an halo around the disk, that the bacteria is not able to colonize – the zone of inhibition.[47]

In Chapter 3, the anti-bacterial activity was first evaluated using the disc diffusion method. Briefly, bacterial suspensions were prepared on TSB for 24h at 37°C under constant agitation at 120rpm. Afterwards, the equivalent bacterial concentration was adjusted to  $1-2 \times 10^8$  CFUs/mL, followed by a homogeneous spreading onto a Muller-Hinton Agar plate (MHA, 70192, Sigma-Aldrich and 611001, Liofilchem) with a sterile swab. Sterile water was used as negative control and gentamicin sulfate (G1914, Sigma-Aldrich) at 50mg/mL were used as positive control. Disks (9999, Liofilchem) were impregnated with 10µL of each the cork-based compounds/extracts and, together with the controls, were placed on the inoculated plates and incubated at 37°C, during 18-24h. After the incubation period, the diameter of the halo (*i.e.* inhibition zone) was determined to assess the anti-bacterial activity of each tested compound/extract.

### 2.2.20 MINIMAL INHIBITORY CONCENTRATIONS (MICS) AND MINIMAL BACTERICIDAL CONCENTRATION (MBCS)

The lowest concentration of an anti-bacterial compound, which is able to prevent the growth of a bacteria, is called minimum inhibitory concentration (MIC). Another parameter is the minimum bactericidal concentration (MBC), which is the lowest concentration of the anti-bacterial compound to kill a specific type of bacterium. In general, MICs and MBCs are used during *in vitro* studies to confirm if a specific compound is able to act against bacteria.[48]

Both MIC and MBC values were quantified by the Broth microdilution method, in Chapter 3. Cork-based compounds/extracts were serially diluted and dispensed into culture wells (50µL/well) which were previously inoculated with 50µL of the bacterial suspension at a concentration of  $1-2 \times 10^6$  CFUs/mL in Mueller-Hinton Broth medium (MHB, 70192, Sigma-Aldrich). The well plates were incubated at 37°C for 24h under constant shaking. The MICs of each compound/extract were considered to be the concentrations at which no turbidity was observed. Nevertheless, to confirm these results, subcultures of



each concentration were dispensed (10 $\mu$ L) onto TSA for 24h. The experiments were performed using three independent experiments, each one in triplicate.

#### 2.2.21 CONGO RED AGAR (CRA) ASSAY

CRA assay is usually a sensitive method to detect the presence of amyloid-like protein structures in biofilms. Congo red can bind to the components of the extracellular matrix of bacteria, *i.e.* polysaccharides and amyloid-based peptides/proteins.[49]

In Chapter 3, CRA was used to assess the ability of vescalagin/castalagin to inhibit the formation of bacterial biofilm. Each compound was dispensed into the wells (50 $\mu$ L/well) of a 96-well plate previously inoculated with 50 $\mu$ L of the bacterial suspension at 1–2 $\times$ 10<sup>6</sup> CFUs/mL in MHB. The well plates were incubated at 37 $^{\circ}$ C for 24h under constant shaking. Afterwards, each suspension was dispensed (10 $\mu$ L) onto TSA plates with 0.08% (w/v) of Congo red (C6767, Sigma-Aldrich) and supplemented with 5% (w/v) sucrose (S0389, Sigma-Aldrich). The plates were incubated at 37 $^{\circ}$ C for 24h. The colony morphology and colour were further analysed, where black colonies were assigned to biofilm forming conditions, while the non-biofilm forming conditions generated red colonies.

#### 2.2.22 SCANNING ELECTRON MICROSCOPE (SEM)

In general, SEM generates images by scanning a sample with an electron beam, using different types of detectors it is possible to collect information about surface topography and composition of the sample. SEM was used in Chapter 3 to evaluate the alterations of the morphology of the bacteria incubated in the presence of the cork-based compounds/extracts, more specifically, how they induced changes in the bacterial cell wall. Briefly, coverslips were placed into the wells with a suspension of 50 $\mu$ L of the bacterial suspension at 1–2 $\times$ 10<sup>6</sup> CFUs/mL and 50 $\mu$ L of cork-based compound/extract at their respective MIC concentrations. After 24h of incubation, the culture medium was removed and the samples were fixed with 2.5% (v/v) glutaraldehyde solution in PBS for 1h, at 4 $^{\circ}$ C under dark conditions. Afterwards, the glutaraldehyde solution was removed, and the samples were washed with PBS, followed by dehydration of the samples in a series of ethanol concentrations (from 10-100% of ethanol). After drying, the samples were platinum sputtered and visualized by high-resolution SEM (FIB-SEM, Auriga Compact, Zeiss, Germany).

#### 2.2.23 CELL CULTURE CONDITIONS

The cells studies described under Chapters 3 to 7 were executed using the L929 and SH-SY5Y cell lines, under the following cell culture conditions:

- Chapter 3: L929 cells (passages 15 to 18) were maintained in DMEM, supplemented with 10% FBS (Alfagene) and 1% penicillin/streptomycin (Alfagene). Cells were plated at a concentration of 1 000 cells/mL, in 96-well plates, incubated at 37°C under 5% CO<sub>2</sub> with the cork-based compounds/extracts from 2 to 0.125mg/mL, during 24h. Cells were then assessed for their cytocompatibility (as described in section 2-2.22).
- Chapter 4: L929 cells (passages 10 to 12) were maintained in DMEM, supplemented with 10% FBS (Alfagene) and 1% penicillin/streptomycin (Alfagene). Cells were plated at a concentration of 45 000 cells/mL, in 24-well plates; incubated at 37°C under 5% CO<sub>2</sub> with the sample extracts at a concentration of 75µg/mL (for each cork-based compound/extract) during 24h. Afterwards, the cell culture plates were positioned over an ice dish and irradiated with a 400 W HPA lamp (Hapro Summer Glow HB 404, Germany) during 15min. The UV dose during exposure was measured using a radiometer (UVP UVX, USA) at different wavelengths: 365nm (UVA), 302nm (UVB) and 254nm (UVC). Only UVA and UVB were detected at an exposure dose of 17.1J/cm<sup>2</sup> and 4.1J/cm<sup>2</sup>, respectively. Following an additional 24h of cell culture under standard conditions, cells were evaluated for several parameters as described afterwards in section 2-2.22, and sections from 2-2.24 to 2-2.27.
- Chapters 5-7: SH-SY5Y cells (passages 11 to 15) were cultured at 37°C in a humidified 95/5% air/CO<sub>2</sub> atmosphere using DMEM/F-12 (Gibco, UK) supplemented with 10% FBS (Gibco, UK) and 1% ATB (Gibco, UK) solution. Cell medium were replaced each 2 days and cells were sub-cultured once they reached 90% confluence. Cells were plated at a density of 25 000 cells per well on 96-well plates containing DMEM/F-12 media (for MTS assay) and plated at a density of 50 000 cells per well on 24-well plates containing DMEM/F-12 media (for the live/dead assay – as described under section 2-2.24).
- The typical experiment included the culture of the SH-SY5Y cells during 24h in the absence or presence, of different concentrations of: i) vescalagin/castalagin (in Chapter 5); ii) Ga-terminated dendrimers (in Chapter 6); and iii) GlcN analogues (in Chapter 7). Afterwards, Aβ were added to the culture medium and, after an additional 24h, cells were assessed for their metabolic activity (as detailed in section 2-2.22). All compounds were sterilized by autoclaving before use. Aβ peptide was sterilized by UV and immediately added to the cells after being reconstituted in DMSO (0.02%) and diluted into DMEM/F-12 media.
- In Chapter 6, it was used an additional time point of 5 days of cell culture in the absence or presence of the Ga-terminated dendrimers at different concentrations.

- Chapters 8: ASCs were isolated from human subcutaneous adipose tissue (age range between 20-36 years) obtained from lipoaspiration procedures under the scope of a cooperation agreement with Hospital da Prelada (Porto, Portugal). Aspirates were washed with PBS containing 10% Antibiotic/Antimycotic and then the adipose tissue was digested with a phosphate buffer saline (PBS) solution containing 0.1% collagenase from *Clostridium histolyticum* (Sigma-Aldrich) during 45min at 37°C, under stirring. The digested tissue was gently pressed through a strainer and centrifuged at 1000 *g* for 10min. The cell pellet was incubated in lysis buffer (155mM NH<sub>4</sub>Cl, 5.7mM K<sub>2</sub>HPO<sub>4</sub>, 0.1mM EDTA) for 10 min to remove erythrocytes and then centrifuged at 800 *g* for 10 min. Cells were expanded in  $\alpha$ -modified Eagle's medium (Sigma-Aldrich) supplemented with 1% Antibiotic/Antimycotic (Gibco) and 10% Fetal Bovine Serum (FBS, Gibco)

Finally, cells were evaluated for several parameters as described in the following subsections from 2-2.27 to 2-2.36.

#### 2.2.24 CELLULAR METABOLIC ACTIVITY

The cytocompatibility of the cork-based compounds/extracts (in Chapter 3), Ga-terminated dendrimers (in Chapter 6) and GlcN analogues (in Chapter 7) were evaluated over time using AlamarBlue® (indicator dye BUF012B, Bio-Rad) according to the manufacturer's instructions. In the case of Chapters 4 and 5, instead of AlamarBlue it was used a commercial MTS assay kit (CellTiter 96® Aqueous One Solution Cell Proliferation Assay, Promega) according to the supplier's instructions.

The fluorescence intensity of AlamarBlue® for each experimental condition was measured using an excitation wavelength of 530nm and an emission wavelength of 590nm. AlamarBlue® active ingredient resazurin (with blue colour), is a cell-permeable molecule, that upon entering the cytoplasm of the cell is reduced to resorufin, a red fluorescence colour end-product. The continuous generation/inhibition of resorufin allows a quantitative measurement of the viability and cytotoxicity of the cells. In the case of MTS, a tetrazolium derivative is subsequently reduced, by viable cells, to a water-soluble brown formazan product (absorbed at 490 nm, incubation period of 3h). Both types of assays were analysed using a Synergy HT microplate reader (Bio-Tek Instruments).

Cytotoxicity assays, were also executed using both types of assays, *i.e.* AlamarBlue® and MTS. Briefly, in Chapter 4, the effect of oxidative stress and UV radiation, as well the ability of the cork-based compounds/extracts to reduce their cytotoxicity, was evaluated by the cellular metabolic activity measured using the MTS assay. In Chapter 5, the cytotoxicity of A $\beta$  was evaluated by measuring the metabolic activity of SH-SY5Y cells (measured by MTS assay) in the presence and absence of

vescalagin/castalagin (assessed 24h after the addition of A $\beta$  at a concentration of 25 $\mu$ M and the compounds at different concentration ratios).

In Chapter 6, the A $\beta$ <sub>6</sub>/A $\beta$ <sub>7</sub> cytotoxicity was evaluated by measuring the cellular metabolic activity by AlamarBlue®, 1 day and 5 days after the addition of A $\beta$ <sub>6</sub>/A $\beta$ <sub>7</sub> at a concentration of 25 $\mu$ M, in the presence and absence of Ga-terminated dendrimers (at different concentration ratios). In Chapter 7, the A $\beta$  cytotoxicity was evaluated by measuring the cell metabolic activity using AlamarBlue®, 1 day after the addition of A $\beta$  in the presence or absence of the GlcN and its analogues (at a concentration of 1mM).

Results are presented as mean  $\pm$  SEM of 6 independent experiments for each experimental condition. *p*-values were calculated using two-tailed t-test.

#### 2.2.25 CELL VIABILITY BY DNA QUANTIFICATION

The DNA content of SH-SY5Y cells was assessed by PicoGreen dsDNA Quantitation Reagent® P7589, from Invitrogen in Chapter 7. PicoGreen is a fluorescent probe that binds dsDNA and forms a highly luminescent complex. Samples were collected into microtubes with 1mL of ultrapure water and stored at -80°C. Samples were thawed and sonicated (VCX-130PB-220, Sonics) before quantification (following the manufacturer protocol). For the fluorescence acquisition (excitation wavelength of 485/20nm and an emission of 528/20nm) we used a Synergy HT microplate reader (Bio-Tek Instruments). *p*-values were calculated using one-tailed t-test. Results are presented as mean  $\pm$  SEM. Samples and standards were made in triplicate.

#### 2.2.26 CELL VIABILITY BY LIVE/DEAD ASSAY

Cell viability was also evaluated by Live/Dead assay using Calcein-AM (1 $\mu$ g/mL) to stain live cells (green) and propidium iodide (PI, 1 $\mu$ L/mL) to stain dead cells (red). This procedure allows the fast visualization of the distribution of live and dead cells in 2D cell cultures: dead cells have the cellular membrane compromised, allowing PI to cross and bind to double stranded DNA; Calcium-AM is a cell-permeant non-fluorescent dye able to cross the cellular membrane of live cells, which, when bound to calcium is able to fluoresce, after being hydrolysed in the presence of intracellular nonspecific esterases. In Chapters 4 to 7, cells were incubated for 20min with both dyes and then observed under a fluorescence microscope (Axio Imager Z1m, Zeiss).

In Chapter 3, the viability of each bacteria strain was evaluated after being in contact with cork-based compounds/extracts. Samples were incubated using the Live/Dead BacLight Viability Kit (L23101,

Life Technologies) following the manufacturer's instructions. Samples were analysed by an Inverted Fluorescence Microscope (Axio Observer, Zeiss, Germany).

#### 2.2.27 INTRACELLULAR REACTIVE OXYGEN SPECIES (ROS)

Intracellular ROS were evaluated using DCFH-DA probe. This probe is cell-permeable and it is deacetylated by cellular esterases to a non-fluorescent compound, which is later oxidized by ROS into 2',7'-dichlorofluorescein (DCF, a fluorescent product) that can be monitored by several fluorescence-based techniques.[50] In this case, cells, 10 000 per well, were seeded in 96-well black plates according to the above-mentioned cell culture conditions. After irradiation, cells were incubated with 25µM of DCFH-DA (2',7'-dichlorodihydrofluorescein diacetate) and its fluorescence recorded in a microplate reader after 90min (at an emission wavelength of 520nm and at an excitation wavelength of 490nm). Cells in DPBS were used as negative control. Results are expressed in relation to the positive control (100% of ROS), *i.e.* irradiated cells in the absence of cork-based extracts.

#### 2.2.28 TUNEL ASSAY

The TUNEL (terminal deoxynucleotidyl transferase dUTP nick end labeling) is an *in-situ* cell death detection kit (Roche). It was used to detect apoptotic cell death at the single-cell level by fluorescence microscopy. The DNA fragments (double-strand DNA breaks) can be labelled at the 3'-hydroxyl termini in the last phase of apoptosis.[51] Cells were fixed with formalin 10% and permeabilized using 0.1% Triton X-100 in 0.1% sodium citrate for 5min. The TUNEL reaction mixture was then added to each sample and incubated for 1h at 37°C. The negative control was only incubated with labelling solution without terminal transferase and the positive control was incubated with recombinant DNase I to induce DNA strand breaks. Finally, cells were stained with DAPI at a concentration of 1:1000 for 20min and analysed by fluorescence microscopy (Axio Imager Z1m, Zeiss).

#### 2.2.29 PROTEIN EXPRESSION BY IMMUNOCYTOCHEMISTRY

The cell morphology and the expression of specific proteins was accessed by immunocytochemistry in Chapters 4 to 7.

In Chapter 4 we used Giemsa staining to evaluate the morphology of L929 cells. Giemsa allows de identification of shranked cells, condensed chromatin and pycnotic nuclei.[52] In this case, cells were fixed with cold methanol, washed, stained with Giemsa solution, mounted and analysed by microscopy (Axio Imager Z1m, Zeiss).

In Chapters 5 and 6, immunostaining was used to evaluate the morphology (cytoskeleton organization and nuclei) and the accumulation of A $\beta$  at the SH-SY5Y cell surface. Thus, the expression of A $\beta$  was accessed using a primary antibody (Oligomer Polyclonal Antibody, clone A11, Rabbit, 1:200 dilution in 1% w/v BSA/PBS, Life Technologies) against A $\beta$  oligomeric forms (in chapter 6) or a primary antibody against A $\beta$  fibrillar aggregates (Biotin anti- $\beta$ -Amyloid, 1-16 Antibody, Mouse IgG1, 1:200 dilution in 1% w/v BSA/PBS, Biolegend), in Chapters 5 and 6. Accordingly, the fluorescence images were collected after 1 and 5 days of cell culture. Samples were washed twice with PBS, fixed in 10% neutral buffered formalin for 30min at 4 °C, permeabilized with 0.1% Triton X-100 in PBS for 5min, and blocked with 3% BSA in PBS for 30min at RT. After the primary antibody (incubated during 1h), it was added a secondary antibody rabbit anti-mouse Alexafluor-488 (1:500 dilution in 1% w/v BSA/PBS, anti-mouse, Invitrogen). A phalloidin–TRITC conjugate was used (1:200 dilution in PBS for 30min, Sigma) to assess the cytoskeleton organization. Nuclei were counterstained with 1mg/mL of 4,6-diamidino-2-phenylindole (DAPI, Sigma) for 30min. Samples were washed with PBS and placed in an imaging dish for confocal microscopy (Leica, TCS SP8).

In Chapter 8, the cytoskeleton organization and formation of focal adhesion was visualized for cells studied by QCM-D (1 h) and live imaging (1, and 3 hrs). The substrates with the cultured cells were removed from the respective equipment, washed twice with PBS, fixed with 10% neutral buffered formalin for 30 min at 4 °C, permeabilized with 0.1% Triton X-100 in PBS for 5 min, and blocked with 3% BSA in PBS for 30 min at room temperature. Cytoskeleton organization was visualized by phalloidin–TRITC conjugate (1:200 in PBS for 30 min, Sigma). Nuclei were counterstained with 4,6-diamidino-2-phenylindole (DAPI; 1:200 in PBS for 30 min). Formation of actin cap and normal focal adhesions was assessed using a primary antibody against paxillin (1:250 in 1% w/v BSA/PBS, VWR), followed by donkey anti-rabbit Alexafluor-488 (1:500 in 1% w/v BSA/PBS, Alfacene). Samples were washed with PBS, mounted with Vectashield (Vector) on glass slides and observed under an Imager Z1 fluorescence microscope (Zeiss). Photographs were taken with an Axio Cam MRm (Zeiss).

### 2.2.30 THIOFLAVIN-T (ThT) STUDIES

The fluorescent dye ThT changes its fluorescence spectrum when bound to the cross- $\beta$ -sheets of different amyloids, shifting its emission spectra by increasing the emission wavelength of the formed amyloid-ThT complexes.[53] ThT enables a high-throughput analysis, with real time characterization of the aggregation kinetics. Fibril formation was followed by ThT assay during the A $\beta$  supramolecular assembly, in Chapters 5 to 7. A $\beta$  stock samples were prepared as described in section 2-2.3 and fibril formation was induced

(under a cold-water bath) by fast mixing of 2 $\mu$ L of A $\beta$  in DMSO with 98 $\mu$ L of Phosphate Buffer (5mM, with 0.1% of sodium azide, at pH 7.2). ThT fluorescence was measured by mixing the A $\beta$  solution (final concentration of 25 $\mu$ M) with ThT (final concentration of 40 $\mu$ M) and different concentrations of vescalagin/castalagin (in Chapter 5), Ga-terminated dendrimers (in Chapter 6), and GlcN analogues (in Chapter 7). ThT fluorescence was then recorded in a fluorescence spectrometer (Jasco, FP-8500, Japan) over time, using an excitation wavelength of 435nm and an emission wavelength of 465nm. Each experiment was repeated in triplicate. The experiments for the disassembly of the A $\beta$  fibrils (in Chapters 5 and 6) were performed with A $\beta$  fibrillar form, over time, using the same experimental protocol.

In Chapter 6, ThT was also used to quantify the  $\beta$ -sheet content under cell culture. Cells were cultured with A $\beta_42$ /A $\beta_40$  with different concentrations of Ga-terminated dendrimers during 24h. Afterwards, 1% Thioflavin-T (in sterile DPBS) were added to the wells. After 20min of incubation, the ThT fluorescence intensity was measured using a fluorescence spectrometer (Jasco, FP-8500, Japan) using an excitation wavelength of 435nm and an emission wavelength of 465nm, with a bandwidth of 10nm. Each experimental condition was repeated in triplicate and using data from at least two independent experiments.

### 2.2.31 PROTEIN EXPRESSION BY WESTERN-BLOTTING (WB)

WB is used to separate specific protein molecules by size by gel electrophoresis. Upon separation, the proteins are transferred from the gel onto a blotting membrane, and subsequently exposed to the corresponding primary and secondary antibodies for identification.

WB was used to identify specific sizes of A $\beta$  aggregates in the presence and absence of vescalagin/castalagin (in Chapter 5), Ga-terminated dendrimers (in Chapter 6) and GlcN analogues (in Chapter 7) at different A $\beta$ :compound concentration ratios, allowing the visualization of the relative amount of remodelled A $\beta$  peptide (by size). Samples were dissolved on Laemmli buffer (1x) without reducing agent (10 $\mu$ g A $\beta$  per lane). Afterwards, samples were electrophoretically resolved in a 12% Bis-Tris Gel Invitrogen NuPAGE, with MES SDS Running Buffer and were transferred to nitrocellulose membranes using iBlot 2 System and blocked with 4% bovine serum albumin (BSA) in TBS containing 0.1% Tween-20 (TBS-T). The membranes were then incubated at 4 °C with the 6E10 (anti-A $\beta$  1-16 antibody – 1:1000) overnight, followed by IRDye 800CW Goat anti-Mouse IgG Secondary Antibody (RT, during 1.5h; 1:10000).

In Chapter 7, proteins were extracted from cell lysates (25 $\mu$ g of protein) of SH-SY5Y cells, electrophoretically resolved in 10% Bis-Tris Gel Invitrogen NuPAGE, with MES SDS Running Buffer gel (gel loading buffer without DTT), followed by a transference to a nitrocellulose membrane using the same iBlot

2 System. Membranes were first blocked with 5% BSA in Tris-buffered saline added with 0.1% Tween 20 (TBST) buffer for 1.5h followed by the overnight incubation with primary antibodies at 1:250 dilutions in a shaker at 4°C: Anti-phospho-IRS1 (pSer612) (Sigma-Aldrich); AKT1 total (Cell Signalling Technology, Inc); AKT1 (phospho S473, abcam); Annexin I (EH17a, Santa Cruz Biotechnology, Inc); and  $\beta$ -Actin antibodies (Cell Signaling Technology, Inc).

All WB membranes, were washed three times with TBST, and incubated with in IRDye 800CW Goat anti-Mouse (or Rabbit) IgG Secondary Antibody (1:15000 dilution in TBS-T).

Finally, all the WB lanes were detected using an Odyssey Fc Imaging System (LI-COR Inc., Nebraska USA). The comparisons between bands in different lanes were quantified using Fiji software. For the cell lysates, bands were quantified by densitometry and normalized to  $\beta$ -actin.

### 2.2.32 ATOMIC FORCE MICROSCOPE (AFM) STUDIES

AFM uses a cantilever with a very accurate and sensitive tip that is used to scan the surface of a sample. AFM can be operated under different modes, such as contact, intermittent contact and non-contact for morphological analysis and contact mode for force spectroscopy experiments. We used AFM to evaluate the remodelling of the A $\beta$  species caused by the presence of the biomolecules used in this thesis (in Chapters 5 to 7).

AFM topographical images we acquired using non-contact mode. In brief, freshly cleaved mica sheets were washed with one drop of 1mM HCl for 20 seconds, rinsed with ultra-pure water (five times) and dried under a gentle nitrogen flux. Afterwards, A $\beta$  solution (prepared as previously described in section 2-2.3) and mixed with vescalagin/castalagin (in Chapter 5), Ga-terminated dendrimers (in Chapter 6) and GlcN analogues (in Chapter 7). After the defined period of incubation, a 20 $\mu$ L sample were spotted onto the mica during 3min, washed with water and dried under a gentle nitrogen flux. AFM images were recorder using a JPK Nanowizard 3 (JPK, Germany) in air, at RT under AC mode. The scans were acquired at a 512x512 pixels resolution using ACTA-SS probes ( $k\sim 37$ N/m, AppNano, USA), a drive frequency of  $\sim 254$ kHz, a setpoint of  $\sim 0.5$ V and a scanning speed of 1.0Hz.

In Chapter 8, the substrates used in the MP-SPR experiments, were removed from the SPR chamber and further analyzed with an atomic force microscope NanoWizard 3 (JPK Instruments, Germany). The measurements were performed in air-dry state in AC mode. Different areas of each substrates with dimensions of 5x5  $\mu\text{m}^2$  and 1x1  $\mu\text{m}^2$  were scanned in order to have representative data. The data were analyzed with the JPK data processing software. The AFM images were acquired using RFESP tips (Bruker, Germany) with a spring constant of 3 N/m and a resonance frequency of 75 kHz.



In Chapter 6, cell nanomechanical analysis was performed using a JPK Nanowizard 3 (JPK, Germany) under PBS at 37°C. Force curves were acquired using sQube cantilevers (with tips of borosilicate spheres of 5µm diameter, CP-qp-CONT-BSG, sQube), presenting a  $k \sim 0.1 \text{ N/m}$ . All cantilevers were calibrated before performing the analysis using the JPK non-contact method. For each experimental condition, at least 15 fixed cells were analysed and it was acquired at least 10 curves per cell. All force curves were fitted using the Hertz model to obtain the cellular Young's modulus. For the cell height analysis, at least 10 cells per experimental condition were analysed under the JPK QI Imaging Mode, using the cantilevers qpBioAC-CB1 (NanoSensors, Germany). To obtain cell height data, cellular cross-sections were retrieved from the AFM height Images. All the presented height data are averages of 10 cells with the corresponding standard deviations.

### 2.2.33 MEASUREMENTS OF CYTOSOLIC $\text{Ca}^{2+}$ LEVELS

The amount of free  $\text{Ca}^{2+}$  in the cytosol can be measured using Ca-binding fluorescence probes, such as Fluo3-AM and Calcein-AM. Both probes exhibit an increase in fluorescence upon binding to the free  $\text{Ca}^{2+}$  at the cytosol of the cells.

In Chapter 7, these two probes were used to assess the  $\text{Ca}^{2+}$  homeostasis in SH-SY5Y cells in the presence and absence of Aβ peptide, as well in the presence of Aβ:GlcN analogues mixtures. In brief, each well was loaded with 5.0µM of Fluo3-AM for 30min in Krebs-Ringer-Hepes glucose buffer and then washed, and allowed to equilibrate for 30min. The  $\text{Ca}^{2+}$  levels were measured at, approximately, 520nm by scanning confocal fluorescence microscopy (Leica, TCS SP8), after excitation at 488nm. The fluorescence results were normalized by the number of cells in each acquired image (15 images per experimental condition), in three different experiments. In the case of the Calcein-AM experiments, the probe was added to each well, in a concentration of 1.0µM, for a period of 30min in Krebs-Ringer-Hepes glucose buffer and then washed. Afterwards, using an inverted microscope (Axio Observer, Zeiss, Germany) the emitted fluorescence was recorded during 45min (pictures were acquired each 5min). Fluorescence was normalized by the number of cells in each acquired image (12 images per experimental condition) and compared with the vehicle (V). Results are average of three independent experiments.

The data recorded with both probes were analysed using Fiji ImageJ software.

### 2.2.34 ACETYLCHOLINESTERASE (ACHE) ACTIVITY

Acetylcholinesterase (AChE) is an enzyme whose primary function is to regulate the presence of the neurotransmitter acetylcholine in neuronal cells, muscles, and exocrine glands. The acetylcholine neurotransmitter and neuromodulator (of cognitive function and mechanisms related with memory) is

released at the synaptic cleft by neurons. AChE catalyses the breakdown of acetylcholine upon exerting its function. In this context, the overexpression of AChE usually detected in AD patients blocks its efficacy and hampering synaptic transmission.[54]

AChE activity was determined under SH-SY5Y cell culture. This was executed using an acetylcholinesterase assay kit (ab138871, abcam) in Chapter 7. The assay was performed according to the manufacturer's instructions. AChE activity was measured using Synergy HT microplate reader (Bio-Tek Instruments) at 410nm (absorption intensity). *p*-values were calculated using one-tailed t-test. Results are presented as mean  $\pm$  SEM. Samples and standards experiments were executed in triplicate.

### 2.2.35 QUARTZ CRYSTAL MICROBALANCE WITH DISSIPATION (QCM-D)

In Chapter 8, QCM-D was used to study the interaction of SAMs surfaces (mimicking glycosaminoglycans) and Fibronectin and for the *in situ* characterization of cell adhesion. Firstly, we did a real time characterization of protein adsorbed. The QCM-D experiments were performed with E4 instrument (Q-Sense, Sweden). All the assays were performed at 37 °C and thus, the used solutions were equilibrated at this temperature before being introduced into the measurement chamber. The QCM-D crystals with the SAMs were placed in the QCM-D flow chamber and a stable baseline was acquired by flowing a serum free  $\alpha$ -MEM. The Fn (10  $\mu$ g/mL in a serum free  $\alpha$ -MEM) was then added at flow rate of 50  $\mu$ L/min. Upon stabilization of the signal, the flow was stopped for 30 min to allow the protein to adsorb. Finally, the sensors were rinsed with  $\alpha$ -MEM to remove loosely bound material. The resonance frequency shift,  $\Delta f$ , and the dissipative shift,  $\Delta D$ , were recorded at several harmonics ( $n = 3, 5, 7, 9, 11$  and  $13$ ). The Voigt model was applied to calculate the adsorbed protein mass, using two overtones (7th and 9th). Immediately after the Fn deposition in the QCM-D, ASCs ( $0.20 \times 10^6$  cells/mL) were introduced into the chamber at a flow rate of 150  $\mu$ L/min. Upon signal change, the flow was stopped for 1h to allow cell attachment. Then, the sensors were rinsed with serum free  $\alpha$ -MEM at a rate of 300  $\mu$ L/min. The obtained data are presented as  $\Delta D/\Delta f$  (3<sup>rd</sup> overtone) plots.

### 2.2.36 CHARACTERIZATION OF CELLS SPREADING BY LIVE IMAGING

The substrates used on Chapter 8, namely gold coated glasses modified with single component and mixed SAMs. ASCs (6000 cells/cm<sup>2</sup>) were seeded (serum free  $\alpha$ -MEM) on these substrates under standard conditions either in the absence of Fn or on substrates previously coated with Fn by incubation with protein solution in serum free  $\alpha$ -MEM (10  $\mu$ g/mL) at 37 °C for 30 min. Live monitoring of cell spreading was performed at 37°C in an inverted microscope (Zeiss Axio Observer) equipped with a

temperature and CO<sub>2</sub> control device (5% CO<sub>2</sub>). Time-lapse images (20X) were captured every 1 min using Zen software. Cells were continuously observed for 5 h. Image stacks were analysed with image processing software Fiji (<http://fiji.sc/wiki/index.php/Fiji>). The typical cell behaviour for each substrate is shown by images taken at 5 min intervals and up to 45 min culture time as the most significant changes in the cell spreading were observed immediately after seeding.

## References

1. Silva, S., et al., Cork: properties, capabilities and applications. *International Materials Reviews*, 2005. 50(6): p. 345-365.
2. Fernandes, E.M., et al., Bionanocomposites from lignocellulosic resources: Properties, applications and future trends for their use in the biomedical field. *Progress in Polymer Science*, 2013. 38(10-11): p. 1415-1441.
3. Aroso, I.M., et al., Cork: current technological developments and future perspectives for this natural, renewable, and sustainable material. *ACS Sustainable Chemistry & Engineering*, 2017. 5(12): p. 11130-11146.
4. Pereira, H., Variability of the chemical composition of cork. *BioResources*, 2013. 8(2): p. 2246-2256.
5. Cadahía, E., et al., Changes in tannic composition of reproduction cork *Quercus suber* throughout industrial processing. *Journal of Agricultural and Food Chemistry*, 1998. 46(6): p. 2332-2336.
6. El Gharas, H., Polyphenols: food sources, properties and applications – a review. *International Journal of Food Science & Technology*, 2009. 44(12): p. 2512-2518.
7. Papuc, C., et al., Plant Polyphenols as Antioxidant and Antibacterial Agents for Shelf-Life Extension of Meat and Meat Products: Classification, Structures, Sources, and Action Mechanisms. *Comprehensive Reviews in Food Science and Food Safety*, 2017. 16(6): p. 1243-1268.
8. Dupenhoat, C.L.M.H., et al., Structural Elucidation of New Dimeric Ellagitannins from *Quercus-Robur L* - Roburin-a, Roburin-B, Roburin-C, Roburin-D, and Roburin-E. *Journal of the Chemical Society-Perkin Transactions 1*, 1991(7): p. 1653-1660.
9. Aroso, I.M., et al., Hydroalcoholic extracts from the bark of *Quercus suber L.* (Cork): optimization of extraction conditions, chemical composition and antioxidant potential. *Wood Science and Technology*, 2017. 51(4): p. 855-872.
10. Tomalia, D.A. Starburst dendrimers—Nanoscopic supermolecules according to dendritic rules and principles. in *Macromolecular Symposia*. 1996. Wiley Online Library.
11. Bosman, d.A., H. Janssen, and E. Meijer, About dendrimers: structure, physical properties, and applications. *Chemical reviews*, 1999. 99(7): p. 1665-1688.
12. Grayson, S.M. and J.M.J. Fréchet, Convergent Dendrons and Dendrimers: from Synthesis to Applications. *Chemical Reviews*, 2001. 101(12): p. 3819-3868.

13. Svenson, S. and D.A. Tomalia, Dendrimers in biomedical applications—reflections on the field. *Advanced Drug Delivery Reviews*, 2012. 64: p. 102-115.
14. D'Emanuele, A. and D. Attwood, Dendrimer–drug interactions. *Advanced drug delivery reviews*, 2005. 57(15): p. 2147-2162.
15. Blanco, A. and G. Blanco, Carbohydrate Metabolism, in *Medical Biochemistry*, A. Blanco and G. Blanco, Editors. 2017, Academic Press. p. 283-323.
16. Pomin, V.H. and B. Mulloy, *Glycosaminoglycans and Proteoglycans*. Pharmaceuticals (Basel, Switzerland), 2018. 11(1): p. 27.
17. Nair, L.S. and C.T. Laurencin, Biodegradable polymers as biomaterials. *Progress in polymer science*, 2007. 32(8-9): p. 762-798.
18. Matheson, A.J. and C.M. Perry, Glucosamine. *Drugs & Aging*, 2003. 20(14): p. 1041-1060.
19. Zhang, J. and N. Yan, Production of Glucosamine from Chitin by Co-solvent Promoted Hydrolysis and Deacetylation. *ChemCatChem*, 2017. 9(14): p. 2790-2796.
20. Chen, J.-K., C.-R. Shen, and C.-L. Liu, N-acetylglucosamine: production and applications. *Marine drugs*, 2010. 8(9): p. 2493-2516.
21. Hanover, J.A., Glycan-dependent signaling: O-linked N-acetylglucosamine. *The FASEB Journal*, 2001. 15(11): p. 1865-1876.
22. Höök, M., et al., Cell-surface glycosaminoglycans. *Annual review of biochemistry*, 1984. 53(1): p. 847-869.
23. Hascall, V.C., Interaction of cartilage proteoglycans with hyaluronic acid. *Journal of supramolecular structure*, 1977. 7(1): p. 101-120.
24. Love, D.C. and J.A. Hanover, The hexosamine signaling pathway: deciphering the "O-GlcNAc code". *Sci. Stke*, 2005. 2005(312): p. re13-re13.
25. Foot, M. and M. Mulholland, Classification of chondroitin sulfate A, chondroitin sulfate C, glucosamine hydrochloride and glucosamine 6 sulfate using chemometric techniques. *Journal of pharmaceutical and biomedical analysis*, 2005. 38(3): p. 397-407.
26. Soares da Costa, D., R.L. Reis, and I. Pashkuleva, Sulfation of glycosaminoglycans and its implications in human health and disorders. *Annual review of biomedical engineering*, 2017. 19: p. 1-26.
27. Masters, C.L., et al., Alzheimer's disease. *Nat Rev Dis Primers*, 2015. 1: p. 15056.
28. Eisenberg, D. and M. Jucker, The Amyloid State of Proteins in Human Diseases. *Cell*, 2012. 148(6): p. 1188-1203.
29. Cohen, S.I., et al., Proliferation of amyloid-beta42 aggregates occurs through a secondary nucleation mechanism. *Proc Natl Acad Sci U S A*, 2013. 110(24): p. 9758-63.
30. Hardy, J., Membrane damage is at the core of Alzheimer's disease. *The Lancet Neurology*, 2017. 16(5): p. 342.
31. Reimand, J., et al., Amyloid-beta CSF/PET discordance vs tau load 5 years later: It takes two to tangle. *medRxiv*, 2020.

32. Pontecorvo, M.J., et al., Relationships between flortaucupir PET tau binding and amyloid burden, clinical diagnosis, age and cognition. *Brain*, 2017. 140(3): p. 748-763.
33. Zhang, F., et al., beta-amyloid redirects norepinephrine signaling to activate the pathogenic GSK3beta/tau cascade. *Sci Transl Med*, 2020. 12(526).
34. Hanseeuw, B.J., et al., Association of Amyloid and Tau With Cognition in Preclinical Alzheimer Disease: A Longitudinal Study. *JAMA Neurol*, 2019.
35. Baumgart, M., et al., Summary of the evidence on modifiable risk factors for cognitive decline and dementia: A population-based perspective. *Alzheimer's & Dementia*, 2015. 11(6): p. 718-726.
36. Scheuner, D., et al., Secreted amyloid  $\beta$ -protein similar to that in the senile plaques of Alzheimer's disease is increased in vivo by the presenilin 1 and 2 and APP mutations linked to familial Alzheimer's disease. *Nature medicine*, 1996. 2(8): p. 864-870.
37. Ando, K., et al., Inside Alzheimer brain with CLARITY: senile plaques, neurofibrillary tangles and axons in 3-D. *Acta Neuropathologica*, 2014. 128(3): p. 457-459.
38. Lan, M.A., et al., Myoblast proliferation and differentiation on fibronectin-coated self assembled monolayers presenting different surface chemistries. *Biomaterials*, 2005. 26(22): p. 4523-4531.
39. Keselowsky, B.G., D.M. Collard, and A.J. Garcia, Surface chemistry modulates fibronectin conformation and directs integrin binding and specificity to control cell adhesion. *Journal of Biomedical Materials Research Part A*, 2003. 66A(2): p. 247-259.
40. Llopis-Hernandez, V., et al., Role of Surface Chemistry in Protein Remodeling at the Cell-Material Interface. *Plos One*, 2011. 6(5).
41. Rico, P., et al., Substrate-Induced Assembly of Fibronectin into Networks: Influence of Surface Chemistry and Effect on Osteoblast Adhesion. *Tissue Engineering Part A*, 2009. 15(11): p. 3271-3281.
42. Keselowsky, B.G., D.M. Collard, and A.J. Garcia, Integrin binding specificity regulates biomaterial surface chemistry effects on cell differentiation. *Proceedings of the National Academy of Sciences of the United States of America*, 2005. 102(17): p. 5953-5957.
43. Altankov, G., K. Richau, and T. Groth, The role of surface zeta potential and substratum chemistry for regulation of dermal fibroblasts interaction. *Materialwissenschaft Und Werkstofftechnik*, 2003. 34(12): p. 1120-1128.
44. Mrksich, M. and G.M. Whitesides, Using self-assembled monolayers to understand the interactions of man-made surfaces with proteins and cells. *Annual Review of Biophysics and Biomolecular Structure*, 1996. 25: p. 55-78.
45. Faucheux, N., et al., Self-assembled monolayers with different terminating groups as model substrates for cell adhesion studies. *Biomaterials*, 2004. 25(14): p. 2721-2730.
46. Amaral, S.P., et al., Efficient multigram synthesis of the repeating unit of gallic acid-triethylene glycol dendrimers. *Org Lett*, 2011. 13(17): p. 4522-5.

47. Stine, W.B., et al., Preparing synthetic Abeta in different aggregation states. *Methods Mol Biol*, 2011. 670: p. 13-32.
48. da Costa, D.S., et al., Sulfonic groups induce formation of filopodia in mesenchymal stem cells. *Journal of Materials Chemistry*, 2012. 22(15): p. 7172-7178.
49. *Proceedings Of The Biochemical Society. The Biochemical journal*, 1955. 60(4): p. xxxi-xlii.
50. Greenfield, N. and G.D. Fasman, Computed circular dichroism spectra for the evaluation of protein conformation. *Biochemistry*, 1969. 8(10): p. 4108-16.
51. Micsonai, A., et al., Accurate secondary structure prediction and fold recognition for circular dichroism spectroscopy. *Proc Natl Acad Sci U S A*, 2015. 112(24): p. E3095-103.
52. Liang, H., et al., Surface plasmon resonance instrument as a refractometer for liquids and ultrathin films. *Sensors and Actuators B: Chemical*, 2010. 149(1): p. 212-220.
53. Teixeira, R., R.L. Reis, and I. Pashkuleva, Influence of the sulfation degree of glycosaminoglycans on their multilayer assembly with poly-L-lysine. *Colloids Surf B Biointerfaces*, 2016. 145: p. 567-575.
54. Santos, S.A., et al., Chemical composition and antioxidant activity of phenolic extracts of cork from *Quercus suber* L. *Industrial Crops and Products*, 2010. 31(3): p. 521-526.
55. Litescu, S.C., et al., Chapter 25 - The Use of Oxygen Radical Absorbance Capacity (ORAC) and Trolox Equivalent Antioxidant Capacity (TEAC) Assays in the Assessment of Beverages' Antioxidant Properties, in *Processing and Impact on Antioxidants in Beverages*, V. Preedy, Editor. 2014, Academic Press: San Diego. p. 245-251.
56. Huang, D., et al., High-throughput assay of oxygen radical absorbance capacity (ORAC) using a multichannel liquid handling system coupled with a microplate fluorescence reader in 96-well format. *Journal of agricultural and food chemistry*, 2002. 50(16): p. 4437-4444.
57. Singleton, V.L., R. Orthofer, and R.M. Lamuela-Raventós, [14] Analysis of total phenols and other oxidation substrates and antioxidants by means of folin-ciocalteu reagent, in *Methods in enzymology*. 1999, Elsevier. p. 152-178.
58. Wilkins, T.D. and T. Thiel, Modified broth-disk method for testing the antibiotic susceptibility of anaerobic bacteria. *Antimicrobial agents and chemotherapy*, 1973. 3(3): p. 350-356.
59. Andrews, J.M., Determination of minimum inhibitory concentrations. *J Antimicrob Chemother*, 2001. 48 Suppl 1: p. 5-16.
60. Kaiser, T.D.L., et al., Modification of the Congo red agar method to detect biofilm production by *Staphylococcus epidermidis*. *Diagnostic Microbiology and Infectious Disease*, 2013. 75(3): p. 235-239.
61. Karlsson, M., et al., What does the commonly used DCF test for oxidative stress really show? *Biochemical Journal*, 2010. 428(2): p. 183-190.
62. Kyrylkova, K., et al., Detection of apoptosis by TUNEL assay, in *Odontogenesis*. 2012, Springer. p. 41-47.

63. Goto, K., et al., Simple differential Giemsa staining of sister chromatids after treatment with photosensitive dyes and exposure to light and the mechanism of staining. *Chromosoma*, 1975. 53(3): p. 223-230.
64. Biancalana, M. and S. Koide, Molecular mechanism of Thioflavin-T binding to amyloid fibrils. *Biochim Biophys Acta*, 2010. 1804(7): p. 1405-12.
65. Coyle, J., D. Price, and M. DeLong, Alzheimer's disease: a disorder of cortical cholinergic innervation. *Science*, 1983. 219(4589): p. 1184-1190.

## SECTION III



## Chapter 3

**Vescalagin and castalagin present bactericidal activity towards Methicillin-resistant bacteria**

## CHAPTER 3

### Vescalagin and castalagin present bactericidal activity towards Methicillin-resistant bacteria <sup>2</sup>

#### ABSTRACT

Polyphenols have been extensively exploited in the biomedical field due to their wide range of bioactive properties and historical use as traditional medicines. They typically present anti-oxidant, anti-microbial, anti-amyloidogenic and/or anti-tumour activities. In particular, cork water extracts and their components, have been previously reported to present anti-oxidant and anti-amyloidogenic properties. Based on this knowledge, we tested cork water extract (CWE), cork water enriched extract (CWE-E), vescalagin/castalagin (two of the main polyphenols present in CWE and CWE-E) for their anti-bacterial activity against four bacterial strains, namely, Methicillin-resistant *Staphylococcus epidermidis* (MRSE), *Staphylococcus aureus* (SA), Methicillin-resistant *Staphylococcus aureus* (MRSA) and *Pseudomonas aeruginosa* (PA). Vescalagin and castalagin presented bactericidal activity against all the tested bacterial strains, in particular towards the Methicillin-resistant ones, *i.e.* MRSA and MRSE, and the ability to inhibit the formation of biofilms. Moreover, vescalagin/castalagin seem to modulate the normal assembly of the peptidoglycans at the bacteria surface, promoting the disruption of their cell wall leading to bacterial cell death.

**Keywords:** Anti-bacterial effect, Vescalagin/castalagin, Methicillin-resistant bacteria.

---

<sup>2</sup> This Chapter is based on the publication: "Araújo A. R., C. A., Reis, R. L. & Pires, R. A, (2020), Vescalagin and castalagin present bactericidal activity towards Methicillin-resistant bacteria (submitted)"

### 3.1 MAIN TEXT

Pathogenic bacteria are a serious health concern in modern society, as they present an increasing resistance to the most common antibiotics.[1] They are associated with chronic infections and severe inflammation due to their ability to create a physical and chemical barrier (through the extracellular matrix) to external factors, enhancing their resistance to therapeutic strategies.[2] They grow under both static and continuous flow conditions, in a dense layer of cells within an elaborate matrix, that harbours various types of biopolymers including phenol-soluble modulins (PSMs), alginate, exopolysaccharides, extracellular DNA, different proteins able to generate amyloid-like fibres (*i.e.* curli or fimbriae), which, in turn, are used by bacteria to aggregate, form microcolonies and generate biofilms.[3-5] Biofilms are extremely common, being present in water pipes (inner surfaces), on dental plaque, in lung infections, and general infections related to the use of medical devices.[6]

Importantly, bacteria are divided into Gram-positive and Gram-negative, a classification which is related with the chemical/physical composition of the cell membrane that protect their cytoplasm from external aggression.[7] While Gram-positive bacteria have a thick layer of peptidoglycans,[8] in the Gram-negative bacteria this layer is thinner, however they present an additional outer membrane that contains a unique type of component, *i.e.* lipopolysaccharides, and an inner membrane composed by proteins and phospholipids.[3, 9, 10]

Polyphenols have been studied as alternative anti-bacterial agents.[11] They are essential component of plants where they can be found in a series of different roles.[12] They are not involved in the normal growth and maturation of plants (as they are secondary metabolites), however, they have a critical role in the plant's defence mechanisms against viruses, bacteria or fungi.[13] The anti-oxidant and anti-microbial activities of these molecules are related to the number of phenyl rings and the number of conjugated hydroxyl groups (*e.g.* galloyl units).[14] Polyphenols (*e.g.* epigallocatechin gallate (EGCG), resveratrol, etc.) or tannins have been tested for a range of different pathologies (*i.e.* inflammation, cardiovascular diseases, cancer, neurodegenerative disorders, among others), or as molecules that are able to enhance the human immune response mechanisms.[15-17]

Cork is a relevant natural source of polyphenols. In fact, we previously demonstrated that it is possible to extract a series of phenolic compounds using hot water, *i.e.* cork water extract (CWE), with important anti-oxidant activity.[18]

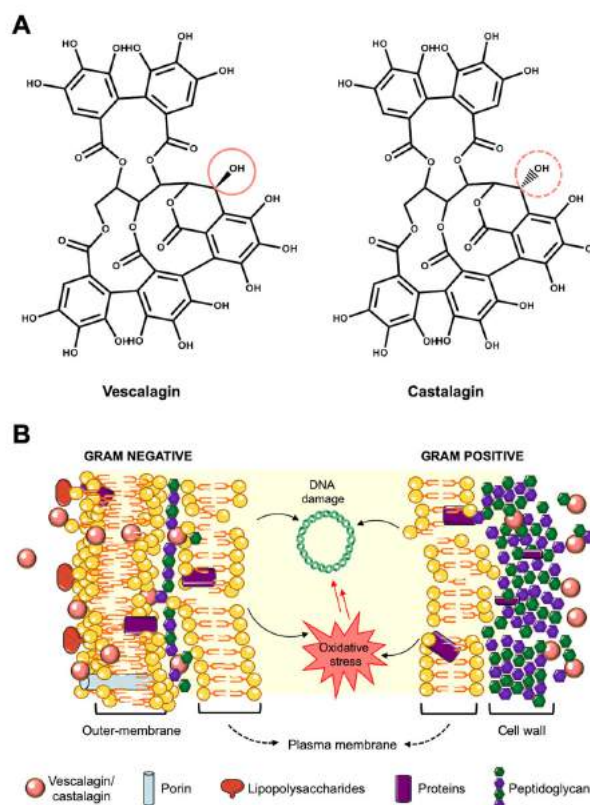


**Figure 3-1.** (A) Chemical structure of the polyphenols vescalagin and castalagin purified from CWE. (B) Schematic presentation of the mechanism of action of vescalagin/castalagin: i) Gram-negative: anti-bacterial activity through the diffusion into a region near the peptidoglycans layer; ii) Gram-positive: direct binding of vescalagin/castalagin to the peptidoglycan of the bacterial cell wall and its subsequent disruption.

Based on these results, we also showed that it is possible to use CWE or vescalagin/castalagin (isolated from CWE) to protect DNA from UV-mediated damage and subsequent cell death,[19] or as anti-amyloidogenic agents.[20] In the context of anti-bacterial activity, the mechanism of action of most polyphenols is reported to be related with their ability to target the bacterial membrane, interacting with the lipids and its subsequent permeabilization.[21] Of note, in a previous study, we demonstrated that vescalagin/castalagin were able to interact with the amyloidogenic peptide  $A\beta 42$ , inhibiting the generation of cytotoxic supramolecular forms and modulating its activity. Importantly, amyloids are highly abundant in the matrices of biofilms of diverse bacterial species, sharing a common structural feature, *i.e.* cross- $\beta$ -sheets.[22] This bacterial amyloid-like fibres mediate adhesion and promote biofilm formation, being a relevant target to inhibit the formation of biofilms.[23]

Herein, we used the knowledge from our previous results and explore the anti-bacterial capacity of cork-based polyphenols, namely the CWE, vescalagin and castalagin. We also tested the enrichment of CWE in vescalagin, through the use of an additional subsequent extraction with ethanol (CWE-E). We tested these extracts/polyphenols against four different pathogenic bacteria strains, namely: Methicillin-resistant *Staphylococcus epidermidis* (MRSE, ATCC 35984), *Staphylococcus aureus* (SA, ATCC 25923),

Methicillin-resistant *Staphylococcus aureus* (MRSA, ATCC 700698), and *Pseudomonas aeruginosa* (PA, ATCC 27853).

### 3.2 RESULTS AND DISCUSSION

We started by extracting CWE and CWE-E, as well as isolating the polyphenols vescalagin/castalagin (characterization presented in S. Fig. 3-1, 3-5). We then evaluated their anti-oxidant activity using the DPPH assay (S. Fig. 3-6) to understand if there was a relationship between anti-oxidant and anti-bacterial activities. The second ethanol extraction, yielding CWE-E from the CWE extract, allowed an enrichment in the vescalagin content, and this is reflected in the anti-oxidant potential of the CWE-E (~10% higher than the original CWE). Of note, the purified vescalagin presented ~30% higher anti-oxidant activity than CWE, while in the case of castalagin it was observed a ~37% increment. These results could be directly related to anti-bacterial activity: i) due to the anti- and pro-oxidant capacity of the galloyl moieties present in the molecular structure of the polyphenols (these molecules can oxidise readily in aqueous solution, acting as pro-oxidants, *i.e.* producing reactive oxygen species and a complex mixture of quinones, which are potentially cytotoxic)[24], thus, leading to the formation of peroxides and their restructuring to form o-diphenols (increasing the free-radical scavenging capacity);[25] ii) the formation of o-diphenols is linked with the polyphenols ability to complex with proteins (at the surface of the cell wall);[26] iii) polyphenols are reported to interact with the polar regions of the lipid bilayer, promoting lipid peroxidation, and therefore, inhibiting bacterial growth;[13] and iv) it has been reported that their anti-oxidant activity is linked to the ability of these molecules to promote metal-ion deficiency based on their chelating ability, leading to the inhibition of bacterial enzymatic activity due to substrate deprivation.[27]

To evaluate if the cork-derived extracts/polyphenols are able to act as antibacterial agents we started by disc diffusion tests (S. Fig. 3-7, 3-8 and S. Table 3-1). The results showed that vescalagin/castalagin presented clear anti-bacterial activity towards all the Gram-positive bacteria. We then evaluated their minimum inhibitory concentration (MIC – Table 3-1) and minimum bactericidal concentration (MBC – S. Table 3-2) towards the same bacterial strains, *i.e.* MRSE, SA and MRSA. In general, all the tested bacteria are affected by the presence of the cork extracts/polyphenols. Importantly, vescalagin/castalagin seems to be the components present in the CWE/CWE-E that present higher anti-bacterial activity, with MIC values between 0.125 and 0.250 mg/mL and MBCs between 0.250 and 1.000 mg/mL. Of note, it was observed a higher sensitivity of the Methicillin-resistant strains to vescalagin/castalagin than the non-resistant strains.

In the case of the Gram-negative bacterium PA, it presented a higher MIC/MBC (only measured for the purified compounds, *i.e.* vescalagin/castalagin, Table 3-1 and S. Table 3-2). It seems that the outer membrane of the Gram-negative bacteria renders additional resistance to the tested compounds. In contrast, our results are consistent with the high efficiency of vescalagin/castalagin to disrupt the peptidoglycan layer of the cell wall from the Gram-positive bacteria. In addition, overall for both Gram-positive and Gram-negative bacteria, we observed a direct relation between anti-oxidant and anti-bacterial activity, as CWE-E presented lower MBCs than CWE, which correlates with its significantly higher anti-oxidant activity, suggesting that it is contributing to its capacity to promote bacterial cell death.

**Table 3-1. Minimum inhibitory concentration (MIC, mg/mL) of each extract/polyphenol, *i.e.* CWE, CWE-E, vescalagin and castalagin, towards the four tested strains of bacteria, namely: Methicillin-resistant *Staphylococcus epidermidis* (MRSE), *Staphylococcus aureus* (SA), Methicillin-resistant *Staphylococcus aureus* (MRSA), and *Pseudomonas aeruginosa* (PA).**

Strain of bacteria	Extract/Polyphenol – MIC (mg/mL)			
	CWE	CWE-E	Vescalagin	Castalagin
MRSE	0.500	0.500	0.125	0.250
SA	2.000	1.000	0.500	0.500
MRSA	2.000	1.000	0.125	0.125
PA	NI	NI	1.000	1.000

NI: No inhibition at concentrations up to 2.50mg/mL.

We then used the Live/Dead assay (Figures 3-2 and S. Fig. 3-8) to confirm the MIC/MBC results. In this case, it is clear that vescalagin and castalagin effectively suppress the bacteria proliferation at the MIC concentrations (see Table 3-1). Overall, and in accordance with the disc diffusion, MIC and MBC results, it is surprising that vescalagin and castalagin present lower MICs and MBCs against MRSE and MRSA than SA (Table 3-1). Hence, we hypothesise that the mechanism of action of vescalagin/castalagin is partially linked to their capacity to interact with the proteins at the surface of the bacteria cell wall responsible for the Methicillin resistance. If we compare the MRSA and SA bacterial strains, their main difference is based on the capacity of MRSA (and not SA) to produce an additional penicillin-binding protein, PBP2a (as a result of an extensive use of  $\beta$ -lactam class of antibiotics these strains became resistant to an entire class of  $\beta$ -lactam-based antibiotics).

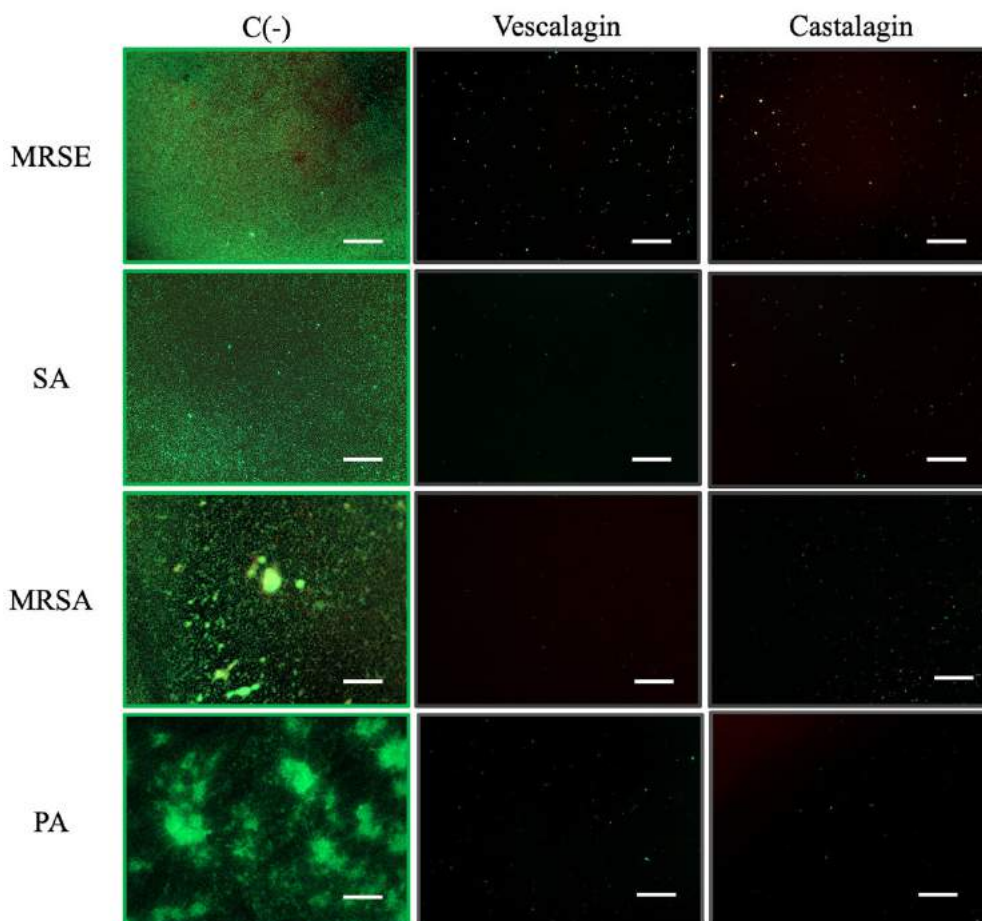


Figure 3-2. Representative Live/Dead images (in green live cells and in red dead cells) showing the antibacterial activity of vescalagin and castalagin (at their MIC concentration) towards Methicillin-resistant *Staphylococcus epidermidis* (MRSE), *Staphylococcus aureus* (SA), Methicillin-resistant *Staphylococcus aureus* (MRSA) and *Pseudomonas aeruginosa* (PA); scale bar = 200 $\mu$ m.

While PBPs make MRSA and MRSE resistant to common antibiotics, they are also responsible for the final step of the synthesis of peptidoglycans (covalently cross-linked units of N-acetylglucosamine and N-acetylmuramic acid).[4] Specifically, the serine nucleophile of the PBP2a active site change its supramolecular assembly to diminish the reactivity against  $\beta$ -lactam. Also, the loop in the PBP2a protein protect its active site from the  $\beta$ -lactam antibiotics.[28] In addition, some Methicillin-resistant cell-wall-anchored proteins are composed of several connecting subdomains folded into  $\beta$ -sheet rich regions.[29] These supramolecular arrangements can explain the lower MIC values for vescalagin towards Methicillin-resistant, due to its proven higher anti-amyloidogenic capacity when compared with castalagin.[20, 30]

In the case of PA, the efficacy of CWE, CWE-E and vescalagin/castalagin is lower. It is important to consider that PA is the only Gram-negative bacterium that we tested. This lower activity of the cork-derived extracts/polyphenols is, as previously suggested, probably due the different organization of its outer membrane. However, it is also important to consider that PA is associated with serious illnesses

(*e.g.* infections such as ventilator-associated pneumonia) and presents complex antibiotic resistance mechanisms,[31] that might be also at play in its resistance towards vescalagin/castalagin.

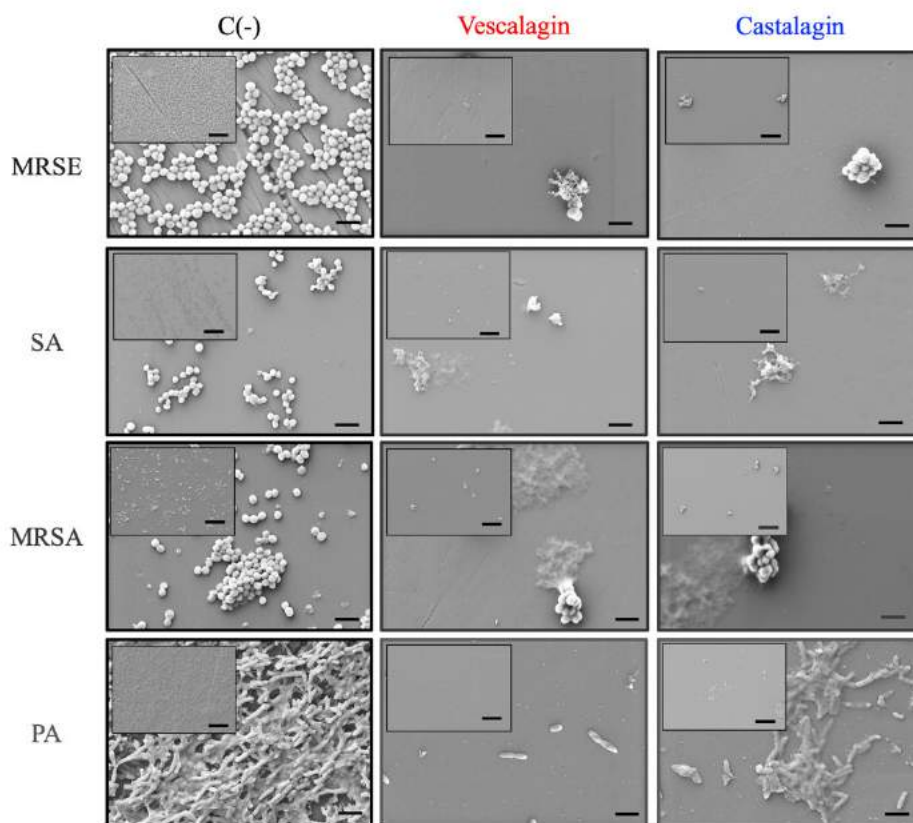


Figure 3-3. Representative SEM images showing a deterioration of cell wall of each strain of bacteria, namely, Methicillin-resistant *Staphylococcus epidermidis* (MRSE); *Staphylococcus aureus* (SA), Methicillin-resistant *Staphylococcus aureus* (MRSA) and *Pseudomonas aeruginosa* (PA); scale bar = 5 $\mu$ m (insets = 20 $\mu$ m); experiments executed at the corresponding MIC concentration.

The formation of biofilms increases the capacity of bacteria to resist to external aggressions. To evaluate if the extracts/polyphenols were able to act under these circumstances and if they were able to target proteins that mediate adhesion and biofilm formation, we used scanning electron microscopy (SEM) to visualize the bacteria in the presence and absence of the extracts/polyphenols. Both vescalagin and castalagin clearly reduced the number of bacteria, and altered their morphology by promoting the disruption of the bacterial cell wall. In addition, their extracellular matrix also appears unstructured, confirming the MIC/MBC data.

To evaluate if vescalagin/castalagin could interfere with the formation of  $\beta$ -sheet rich structures essential for cell survival we used the Congo red agar (CRA) assay,[32] as it is usually sensitive to the presence of amyloid-like protein structures. Congo red is able to bind to these types of supramolecular structures, namely the ones generated by: polysaccharide intercellular adhesin, *i.e.* PIA or PSMs (in *Staphylococcus* strains); and exopolysaccharides, such as Pel and Psl in PA. [33-37] In general, the



formation of light-coloured colonies of MRSE, MRSA and SA is associated with the inexistence of biofilm (and reduced concentration of  $\beta$ -sheet structures), while darker ones is consistent with formation of biofilm (rich in  $\beta$ -sheet structures).[38]

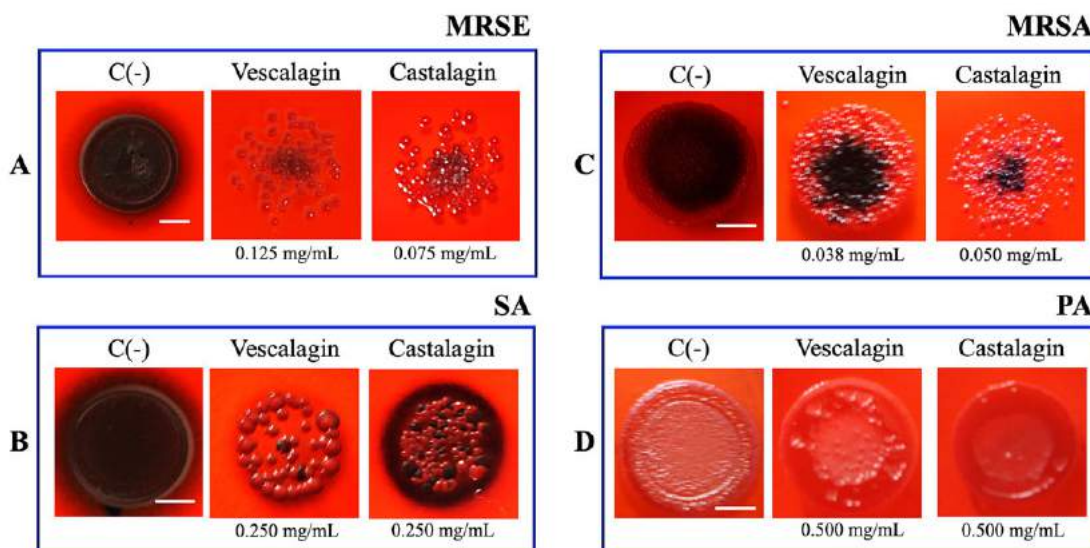


Figure 3-4. Representative Congo red assay images showing a decrease in the dark pigmentation consistent with a decrease of amyloid-like protein presentations for the tested strains of bacteria, namely: (A) Methicillin-resistant *Staphylococcus epidermidis* (MRSE); (B) *Staphylococcus aureus* (SA); (C) Methicillin-resistant *Staphylococcus aureus* (MRSA). For (D) *Pseudomonas aeruginosa* (PA); scale bar = 5mm.

In the CRA assay, we used a concentration below the MIC values (presented in Table 3-1) because at those concentrations and above it was observed a strong (and dose-dependent) inhibition of the colony formation, being difficult to extract relevant conclusions (S. Fig. 3-11, 3-14). The CRA assay (Figure 3-4) showed that both vescalagin and castalagin caused a strong inhibition of the formation of biofilm (and cross  $\beta$ -sheet structures) by the MRSE, SA and MRSA strains. In the case of PA, its biofilm is stained light red by Congo red (Figure 3-4D). Reports have shown the formation of biofilms on CRA is difficult to produce, and this test might not be suitable for identifying the exopolysaccharide layer produced by non-fermenting Gram-negative bacteria, such as PA.[39, 40] We obtained a light pink colour mesh, probably due to the interference in the cell-to-cell communication process (*i.e.* quorum sensing). Under these conditions, it has been reported that PA cannot catabolize glucose, and is thus unable to synthesise the biofilm components.[41, 42] Our results are also consistent with the ability of vescalagin/castalagin to efficiently remodel the adherence proteins (*i.e.* PIA and PSMs) leading to bacterial cell death and reduction of the biofilm formation by PA.

Interestingly, vescalagin/castalagin is more efficient to inhibit the growth and kill Methicillin-resistant strains. In fact, Stapleton *et al*[43] showed that, at low concentrations (*i.e.* 0.025 mg/mL), EGCG can reduce MRSA, by its direct binding to the peptidoglycan layer, at the N-acetylglucosamine and N-

acetylmuramic acid residues, but only if it acts synergistically with the  $\beta$ -lactam oxacillin (antibiotic of the penicillin class).[43] In addition, the MIC concentration obtained for vescalagin is four times lower than the one found for EGCG against the other Methicillin-resistant bacterium, *i.e.* MRSE.[44] As mentioned before, these strains express the PBP2a protein that acts as crosslinker of the peptidoglycan layer. Therefore, it is likely that vescalagin/castalagin is a strong PBP2a inhibitor, as well as it might also act as a modulator of the normal assembly of peptidoglycan, exopolysaccharides and proteins, which leads to an inhibition of biofilm formation and the survival of the Methicillin-resistant strains. In fact, a molecular docking study[45] demonstrated that the presence of a carboxylic acid (COOH), but as well of two hydroxyls (OH) groups in the *para* and *ortho* positions (as in the case of vescalagin and castalagin) seems to play an important role in the capacity of phenolic compounds to inhibit the MRSA survival.

Finally, we tested the cytocompatibility of the cork-derived extracts/polyphenols towards the L929 cell line, by direct contact method during 24h. We used concentrations down to the MIC values (S. Fig. 3-15, 3-18) envisioning the exploitation of their anti-bacterial activity. Vescalagin is cytocompatible at a concentration of 0.125 mg/mL, which is its MIC value (Table 3-1) for the MRSA and MRSE strains without eliciting cytotoxicity to eukaryotic cells. In the case of castalagin, it was also found to be cytocompatible at a concentration of 0.125 mg/mL, which is the MIC value only for MRSA.

Overall, we show that, at a concentration of 0.125 mg/mL of vescalagin and castalagin it is possible to inhibit bacterial growth for Methicillin-resistant *Staphylococcus* strains.

### 3.3 CONCLUSIONS

We investigated the potential of cork-derived extracts/polyphenols, *i.e.* CWE, CWE-E, vescalagin and castalagin, as antibacterial agents against three Gram-positive bacterial strains, *i.e.* MRSE, SA and MRSA; as well as one Gram-negative bacterial strain, *i.e.* PA. Both vescalagin and castalagin exhibited anti-oxidant activity, which at the same time might be related with their capability to act against bacteria machinery in a process that is still not completely understood.

Vescalagin/castalagin presented anti-bacterial activity, and showed to be more effective against Methicillin-resistant bacterial strains. Despite the need of more in-depth studies regarding their mode of action, vescalagin/castalagin seems to present a significant impact in the PBP2a-mediated stabilization of the peptidoglycan layer of Methicillin-resistant bacteria. They seem to be also able to reduce the formation of  $\beta$ -sheet supramolecular arrangements necessary to maintain the bacterial cell wall integrity and biofilm formation.

In general, our results can pave the way to the development of anti-bacterial vescalagin/castalagin-based methodologies and their future biomedical application.

### 3.4 REFERENCES

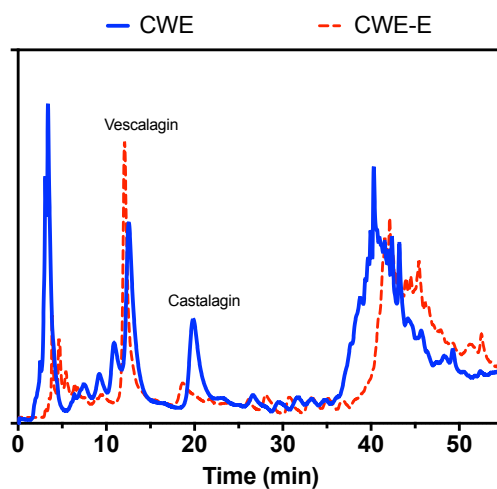
1. Nicoloff, H., et al., The high prevalence of antibiotic heteroresistance in pathogenic bacteria is mainly caused by gene amplification. *Nature Microbiology*, 2019. 4(3): p. 504-514.
2. Wolf-Rainer, A., Controlling Biofilms of Gram-Positive Pathogenic Bacteria. *Current Medicinal Chemistry*, 2006. 13(13): p. 1509-1524.
3. Flemming, H.-C. and J. Wingender, The biofilm matrix. *Nature Reviews Microbiology*, 2010. 8(9): p. 623-633.
4. Abee, T., et al., Biofilm formation and dispersal in Gram-positive bacteria. *Current opinion in biotechnology*, 2011. 22(2): p. 172-179.
5. Reichhardt, C., et al., Congo Red Interactions with Curli-Producing *E. coli* and Native Curli Amyloid Fibers. *PLOS ONE*, 2015. 10(10): p. e0140388.
6. Schembri, M.A., M. Givskov, and P. Klemm, An Attractive Surface: Gram-Negative Bacterial Biofilms. *Science's STKE*, 2002. 2002(132): p. re6-re6.
7. Silhavy, T.J., D. Kahne, and S. Walker, The bacterial cell envelope. *Cold Spring Harbor perspectives in biology*, 2010. 2(5): p. a000414-a000414.
8. Gregersen, T., Rapid method for distinction of Gram-negative from Gram-positive bacteria. *European journal of applied microbiology and biotechnology*, 1978. 5(2): p. 123-127.
9. Fischetti, V.A., Surface proteins on Gram-positive bacteria. *Gram-positive pathogens*, 2019: p. 19-31.
10. Bouarab-Chibane, L., et al., Antibacterial Properties of Polyphenols: Characterization and QSAR (Quantitative Structure–Activity Relationship) Models. *Frontiers in Microbiology*, 2019. 10(829).
11. Álvarez-Martínez, F.J., et al., Antimicrobial capacity of plant polyphenols against gram-positive bacteria: A comprehensive review. *Current Medicinal Chemistry*, 2019.
12. Tanaka, T., Y. Matsuo, and I. Kouno, Chemistry of Secondary Polyphenols Produced during Processing of Tea and Selected Foods. *International Journal of Molecular Sciences*, 2010. 11(1): p. 14-40.
13. Papuc, C., et al., Plant Polyphenols as Antioxidant and Antibacterial Agents for Shelf-Life Extension of Meat and Meat Products: Classification, Structures, Sources, and Action Mechanisms. *Comprehensive Reviews in Food Science and Food Safety*, 2017. 16(6): p. 1243-1268.
14. Porat, Y., A. Abramowitz, and E. Gazit, Inhibition of amyloid fibril formation by polyphenols: structural similarity and aromatic interactions as a common inhibition mechanism. *Chem Biol Drug Des*, 2006. 67(1): p. 27-37.

15. Velandar, P., et al., Natural product-based amyloid inhibitors. *Biochem Pharmacol*, 2017. 139: p. 40-55.
16. Ngougoure, V.L., et al., Natural polyphenols binding to amyloid: a broad class of compounds to treat different human amyloid diseases. *Mol Nutr Food Res*, 2015. 59(1): p. 8-20.
17. Nedumpully-Govindan, P., et al., Stabilizing Off-pathway Oligomers by Polyphenol Nanoassemblies for IAPP Aggregation Inhibition. *Sci Rep*, 2016. 6: p. 19463.
18. Aroso, I.M., et al., Hydroalcoholic extracts from the bark of *Quercus suber* L. (Cork): optimization of extraction conditions, chemical composition and antioxidant potential. *Wood Science and Technology*, 2017. 51(4): p. 855-872.
19. Araújo, A.R., et al., Cork extracts reduce UV-mediated DNA fragmentation and cell death. *RSC Advances*, 2015. 5(116): p. 96151-96157.
20. Araújo, A.R., et al., Vescalagin and castalagin reduce the toxicity of amyloid-beta42 oligomers through the remodelling of its secondary structure. *Chemical Communications*, 2020.
21. Hengge, R., Targeting Bacterial Biofilms by the Green Tea Polyphenol EGCG. *Molecules*, 2019. 24(13).
22. Larsen, P., et al., Amyloid adhesins are abundant in natural biofilms. *Environmental microbiology*, 2007. 9(12): p. 3077-3090.
23. Serra, D.O., et al., The green tea polyphenol EGCG inhibits *E. coli* biofilm formation by impairing amyloid curli fibre assembly and downregulating the biofilm regulator CsgD via the sigma(E) -dependent sRNA RybB. *Mol Microbiol*, 2016. 101(1): p. 136-51.
24. Halliwell, B., Are polyphenols antioxidants or pro-oxidants? What do we learn from cell culture and in vivo studies? *Archives of Biochemistry and Biophysics*, 2008. 476(2): p. 107-112.
25. El Gharras, H., Polyphenols: food sources, properties and applications – a review. *International Journal of Food Science & Technology*, 2009. 44(12): p. 2512-2518.
26. Ricardo-da-Silva, J.M., et al., Interaction of grape seed procyanidins with various proteins in relation to wine fining. *Journal of the Science of Food and Agriculture*, 1991. 57(1): p. 111-125.
27. Naqvi, S.A.R., et al., Antioxidants: Natural Antibiotics, in *Antioxidants*. 2019, IntechOpen.
28. Mahasenan, K.V., et al., Conformational Dynamics in Penicillin-Binding Protein 2a of Methicillin-Resistant *Staphylococcus aureus*, Allosteric Communication Network and Enablement of Catalysis. *Journal of the American Chemical Society*, 2017. 139(5): p. 2102-2110.
29. Bowden, M.G., et al., Identification and preliminary characterization of cell-wall-anchored proteins of *Staphylococcus epidermidis*. *Microbiology*, 2005. 151(5): p. 1453-1464.
30. Vivas, N., et al., Conformational interpretation of vescalagin and castalagin physicochemical properties. *J Agric Food Chem*, 2004. 52(7): p. 2073-8.
31. Lambert, P., Mechanisms of antibiotic resistance in *Pseudomonas aeruginosa*. *Journal of the royal society of medicine*, 2002. 95(Suppl 41): p. 22.
32. Freeman, D., F. Falkiner, and C. Keane, New method for detecting slime production by coagulase negative staphylococci. *Journal of clinical pathology*, 1989. 42(8): p. 872-874.

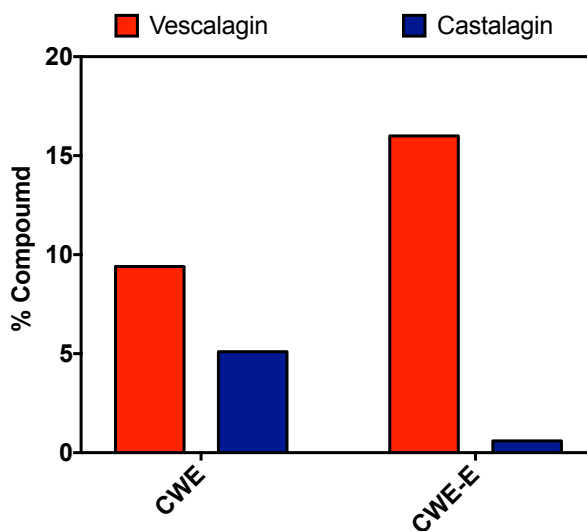
33. Rabin, N., et al., Agents that inhibit bacterial biofilm formation. *Future medicinal chemistry*, 2015. 7(5): p. 647-671.
34. Hammer, N.D., J.C. Schmidt, and M.R. Chapman, The curli nucleator protein, CsgB, contains an amyloidogenic domain that directs CsgA polymerization. *Proceedings of the National Academy of Sciences of the United States of America*, 2007. 104(30): p. 12494-12499.
35. Sgarbossa, A., Natural biomolecules and protein aggregation: emerging strategies against amyloidogenesis. *Int J Mol Sci*, 2012. 13(12): p. 17121-37.
36. Rohde, H., et al., Structure, function and contribution of polysaccharide intercellular adhesin (PIA) to *Staphylococcus epidermidis* biofilm formation and pathogenesis of biomaterial-associated infections. *European Journal of Cell Biology*, 2010. 89(1): p. 103-111.
37. Colvin, K.M., et al., The Pel and Psl polysaccharides provide *Pseudomonas aeruginosa* structural redundancy within the biofilm matrix. *Environmental Microbiology*, 2012. 14(8): p. 1913-1928.
38. Kaiser, T.D.L., et al., Modification of the Congo red agar method to detect biofilm production by *Staphylococcus epidermidis*. *Diagnostic Microbiology and Infectious Disease*, 2013. 75(3): p. 235-239.
39. Cao, H., et al., Comparative genome and transcriptome analysis reveals distinctive surface characteristics and unique physiological potentials of *Pseudomonas aeruginosa* ATCC 27853. *BMC genomics*, 2017. 18(1): p. 459.
40. Hrv, R., R. Devaki, and V. Kandi, Evaluation of Different Phenotypic Techniques for the Detection of Slime Produced by Bacteria Isolated from Clinical Specimens. *Cureus*, 2016. 8(2): p. e505-e505.
41. Plyuta, V., et al., Effect of plant phenolic compounds on biofilm formation by *Pseudomonas aeruginosa*. *APMIS*, 2013. 121(11): p. 1073-1081.
42. Mukherjee, S., et al., Photosensing and quorum sensing are integrated to control *Pseudomonas aeruginosa* collective behaviors. *PLOS Biology*, 2019. 17(12): p. e3000579.
43. Stapleton, P.D. and P.W. Taylor, Methicillin resistance in *Staphylococcus aureus*: mechanisms and modulation. *Science progress*, 2002. 85(Pt 1): p. 57-72.
44. Blanco, A.R., et al., Epigallocatechin Gallate Inhibits Biofilm Formation by Ocular *Staphylococcal* Isolates. *Antimicrobial Agents and Chemotherapy*, 2005. 49(10): p. 4339-4343.
45. Alves, M.J., et al., Antimicrobial activity of phenolic compounds identified in wild mushrooms, SAR analysis and docking studies. *Journal of applied microbiology*, 2013. 115(2): p. 346-357.

## SUPPLEMENTARY INFORMATION

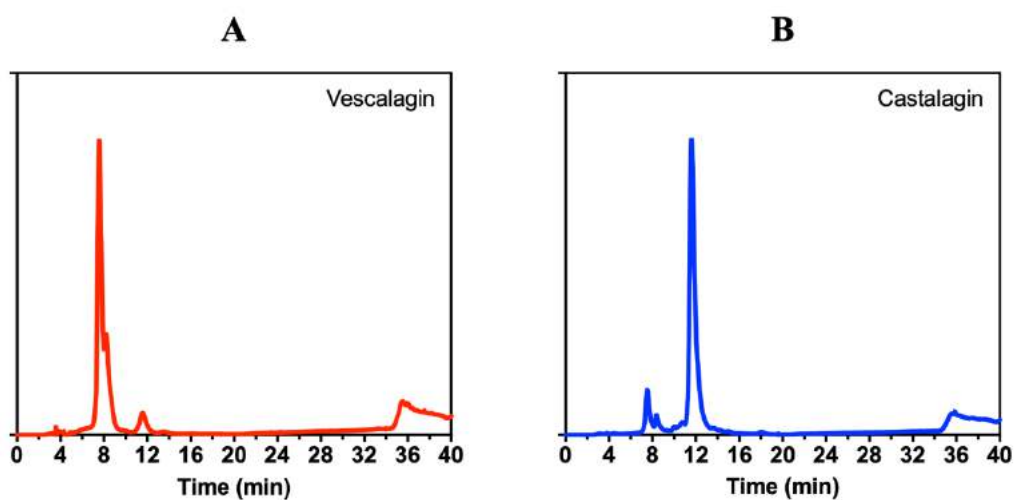
- Characterization of extracts and polyphenols obtained from cork powder

HPLC characterization

Supplementary Fig. 3-1. Preparative HPLC chromatograms of cork water extract (CWE) and cork water extract ethanol (CWE-E) with the identification of the peaks that correspond to vescalagin and castalagin.

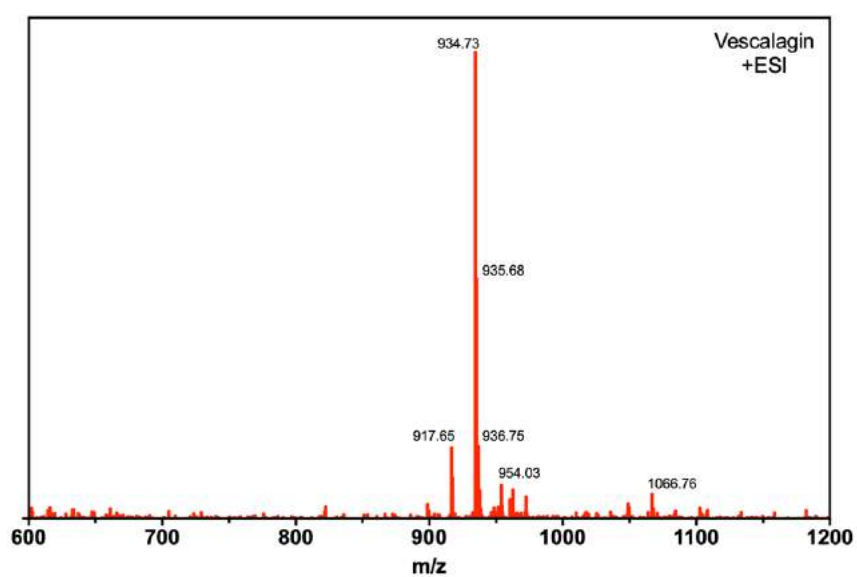


Supplementary Fig. 3-2. Quantification of vescalagin and castalagin present in CWE and CWE-E.

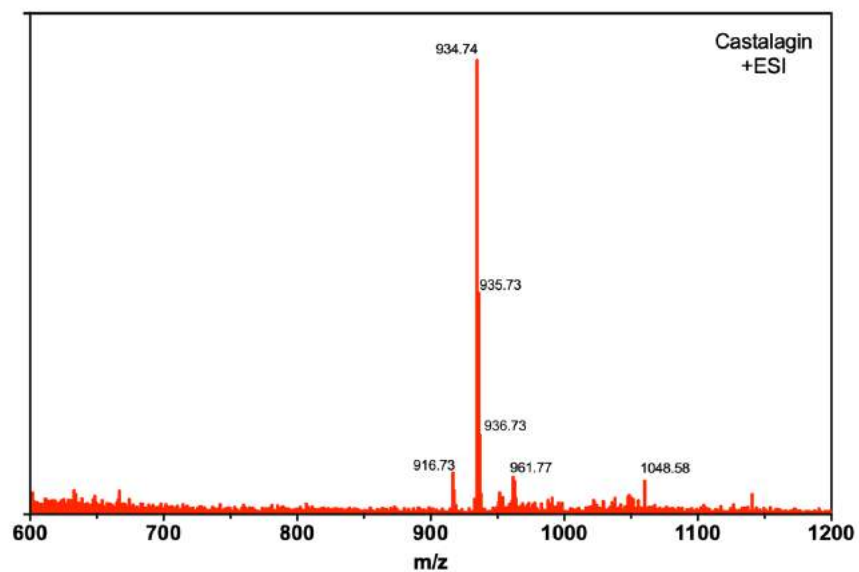


Supplementary Fig. 3-3. HPLC chromatograms showing the purified compounds: (A) vescalagin and (B) castalagin.

ESI-MS ( $m/z$ ):  $[M+H]^+$  935

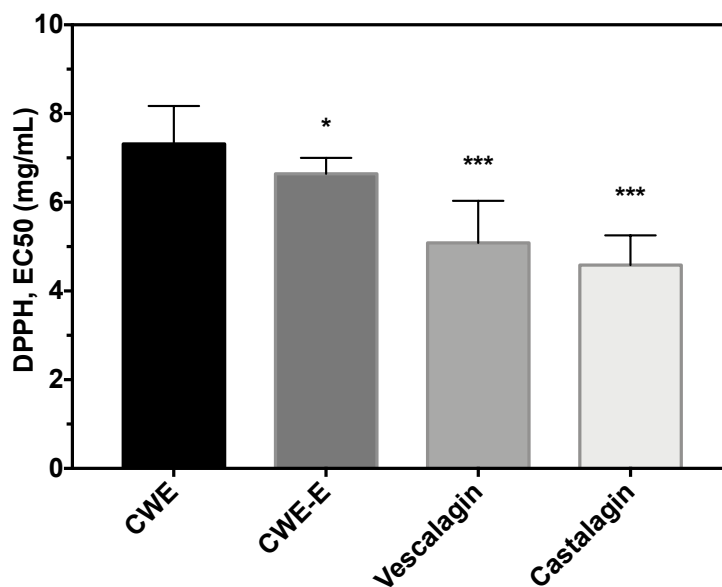


Supplementary Fig. 3-4. Positive ESI-MS spectrum of vescalagin.



Supplementary Fig. 3-5. Positive ESI-MS spectrum of castalagin.

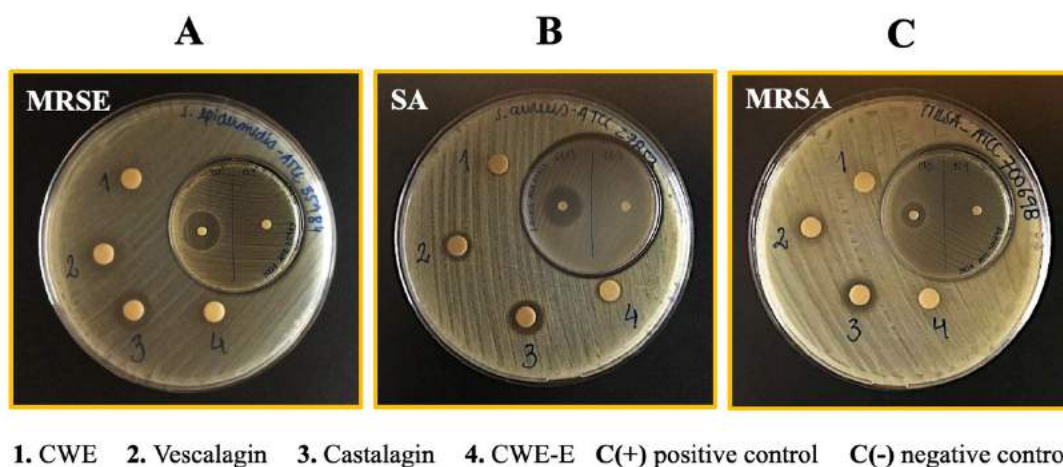
### Anti-oxidant activity



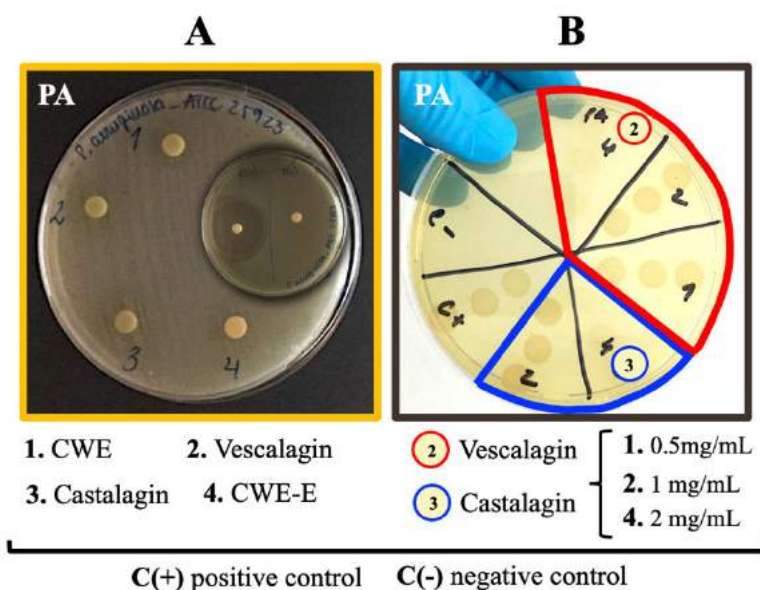
Supplementary Fig. 3-6. DPPH assay. Free radical scavenging activity of the cork-based compounds. Error bars = SD, \* $p < 0.05$ , \*\* $p < 0.01$  and \*\*\* $p < 0.001$  vs CWE ; $n = 3$ .



- Anti-bacterial activity of the cork-derived extracts/polyphenols



Supplementary Fig. 3-7. Disc diffusion assay in agar media showing the zone of inhibition for each extract/polyphenol against the tested bacteria, namely: (A) Methicillin-resistant *Staphylococcus epidermidis* (MRSE); (B) *Staphylococcus aureus* (SA); (C) Methicillin-resistant *Staphylococcus aureus* (MRSA); C(-): water; and C(+): gentamicin; n=3.



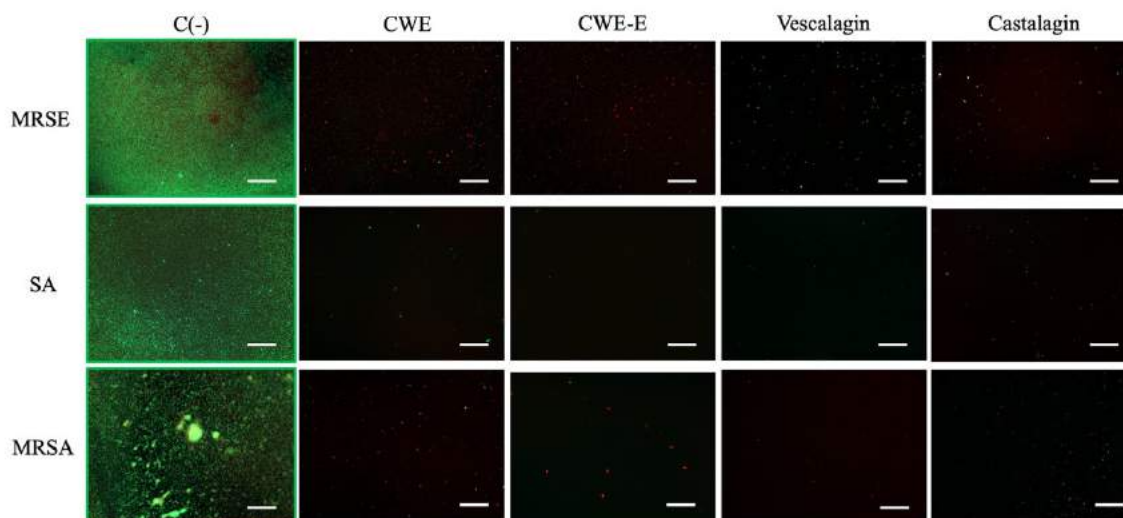
Supplementary Fig. 3-8. Disc diffusion assay in agar media showing the zone of inhibition for each extract/polyphenol against *Pseudomonas Aeruginosa* (PA); C(-): water; and C(+): gentamicin. (B) *Pseudomonas Aeruginosa* (PA) growth in liquid media followed by Muller-Hinton Agar plate spreading, showing an inhibition zone for vescalagin and castalagin at 2mg/mL; C(-): water; and C(+): gentamicin; n=3. In this case, vescalagin/castalagin were serially diluted and dispensed into a 96-well plate (which had been inoculated with the bacterial suspension), and after 24h were spread onto a Muller-Hinton Agar plate.

Supplementary Table 3-1. Quantification of disc diffusion assay for vescalagin and castalagin, towards Gram-positive bacteria, namely: Methicillin-resistant *Staphylococcus epidermidis* (MRSE), *Staphylococcus aureus* (SA), and Methicillin-resistant *Staphylococcus aureus* (MRSA)

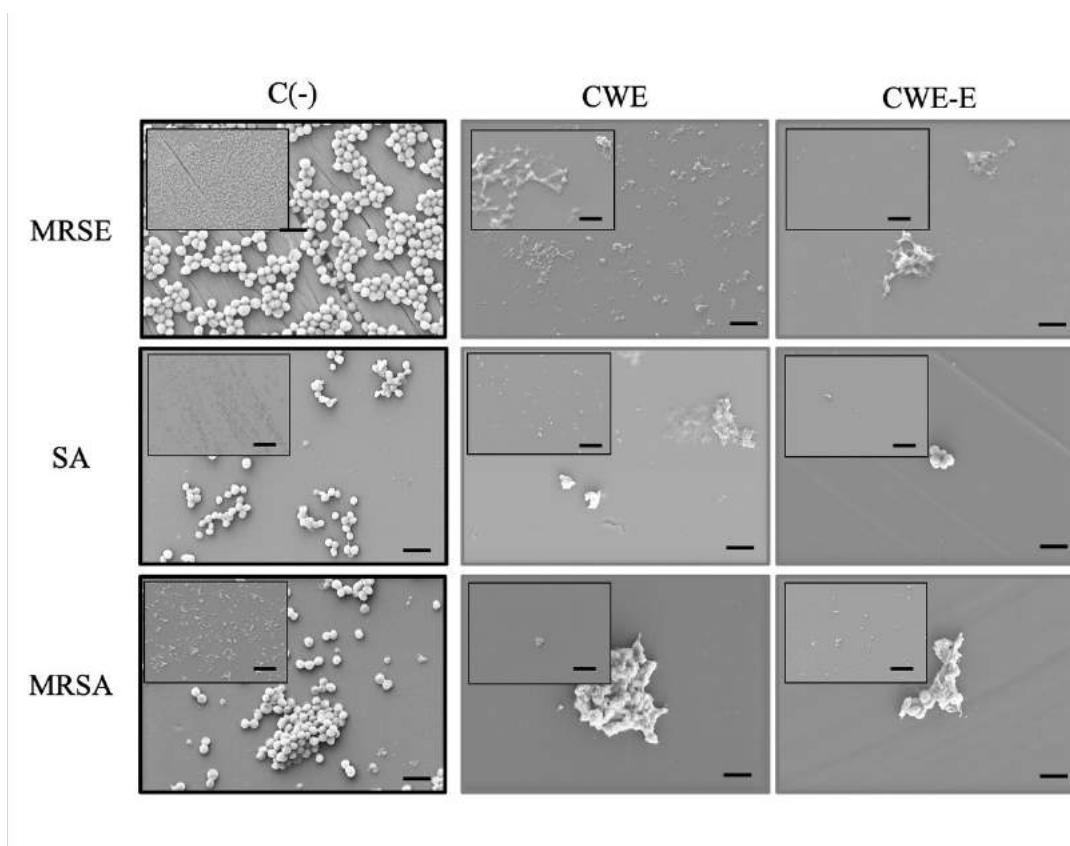
Strain of bacterium	Polyphenol/Control - Diameter of inhibition zone (mm)			
	Vescalagin	Castalagin	C(+)	C(-)
MRSE	10.2 ± 1.3	10.2 ± 1.0	21.7 ± 1.5	-
SA	11.0 ± 0.6	10.7 ± 1.2	29.5 ± 1.1	-
MRSA	9.0 ± 0.6	9.2 ± 0.4	17.2 ± 0.7	-

Supplementary Table 3-2. Minimum bactericidal concentration (MBC, mg/mL) of each extract/polyphenol (i.e. CWE, CWE-E, vescalagin and castalagin), towards the four tested strains of bacteria, namely: Methicillin-resistant *Staphylococcus epidermidis* (SE), *Staphylococcus aureus* (SA), Methicillin-resistant *Staphylococcus aureus* (MRSA), and *Pseudomonas aeruginosa* (PA).

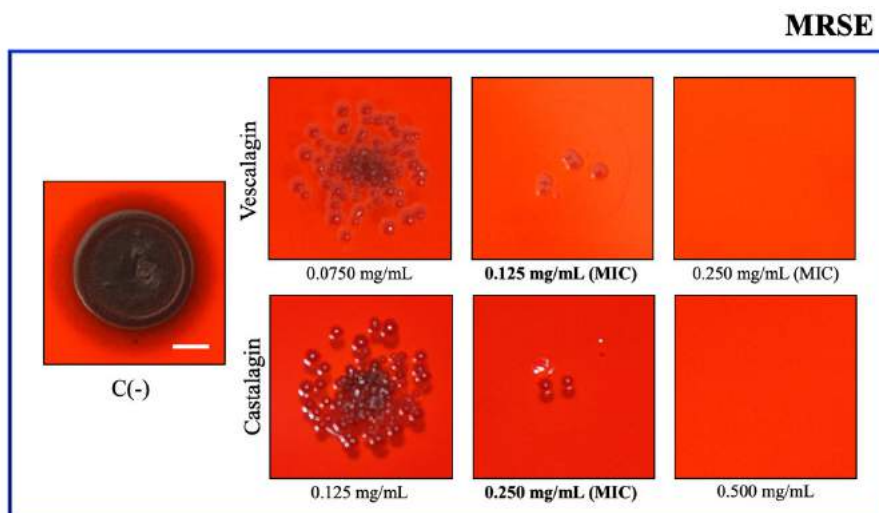
Strain of bacteria	Extract/Polyphenol – MBC (mg/mL)			
	CWE	CWE-E	Vescalagin	Castalagin
MRSE	1.00	0.50	0.25	1.00
SA	4.00	2.00	1.00	1.00
MRSA	4.00	2.00	0.25	0.25
PA	-	-	2.00	2.00



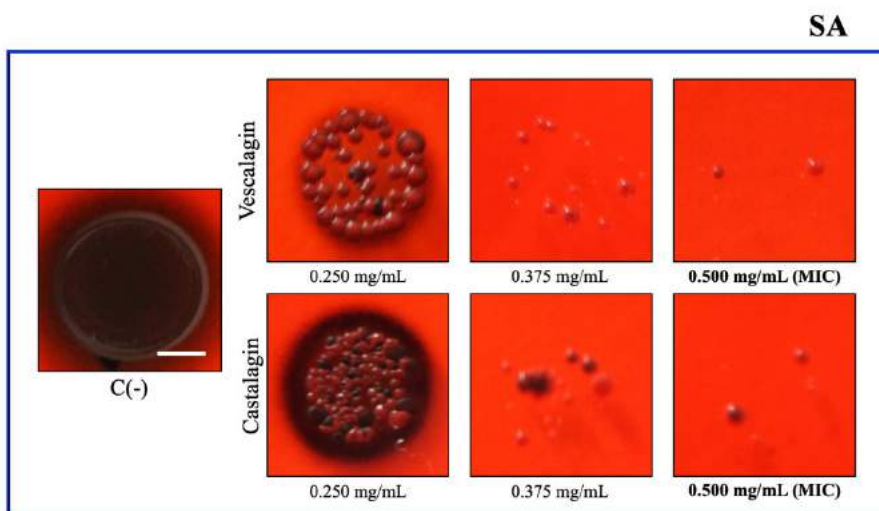
Supplementary Fig. 3-9. Live/Dead assay using BacLight Viability Kit showing the ability of the extracts/polyphenols (at the respective MIC concentration) to drastically reduce the viability of Methicillin-resistant *Staphylococcus epidermidis* (MRSE), *Staphylococcus aureus* (SA) and Methicillin-resistant *Staphylococcus aureus* (MRSA); scale bar = 200 $\mu$ m; n=3.



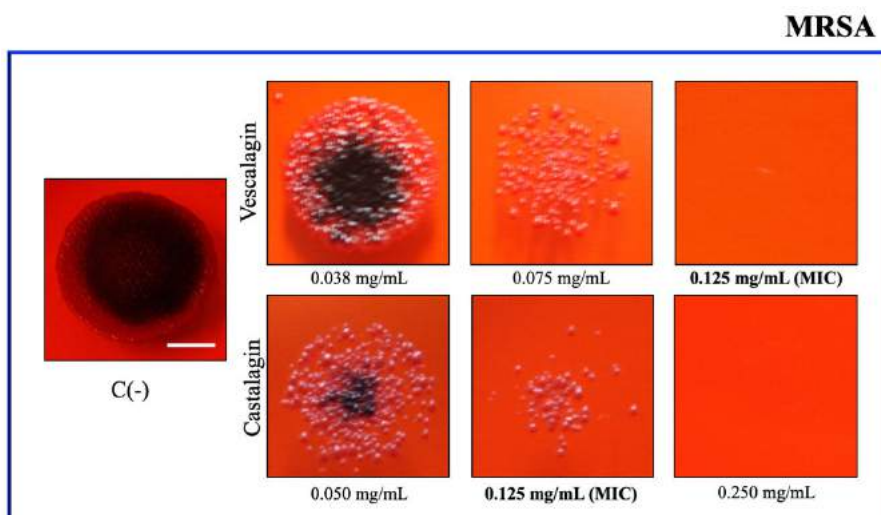
Supplementary Fig. 3-10. Representative SEM images showing a deterioration of the cell wall caused by CWE and CWE-E on each strain of bacteria, namely: Methicillin-resistant *Staphylococcus epidermidis* (MRSE); *Staphylococcus aureus* (SA); and Methicillin-resistant *Staphylococcus aureus* (MRSA); scale bar = 20 $\mu$ m (insets = 5 $\mu$ m); MIC concentrations of each individual extract was used; n=3.



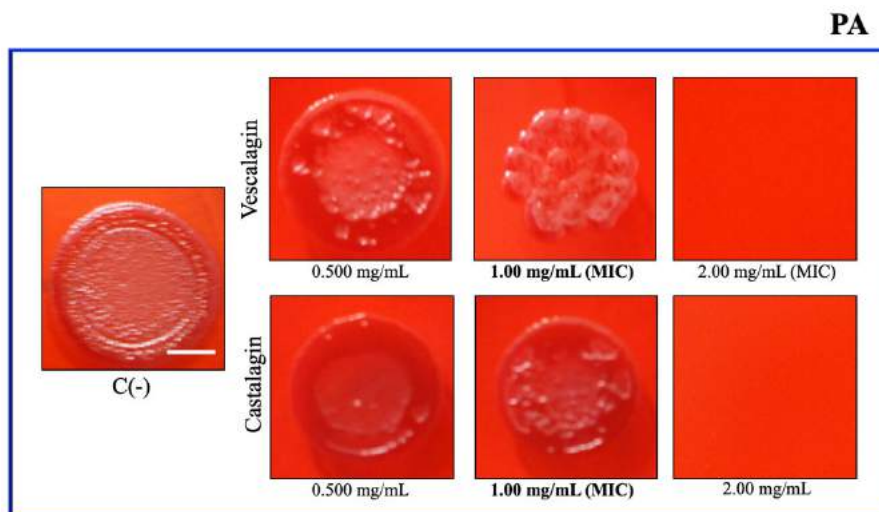
Supplementary Fig. 3-11. Congo red agar assay for vescalagin/castalagin on Methicillin-resistant *Staphylococcus epidermidis* (MRSE). Reduction of darker pigmentation indicates reduced formation of biofilm and lower concentration of amyloid-like protein structures; scale bar = 5mm; n=3.



Supplementary Fig. 3-12. Congo red agar assay for vescalagin/castalagin on *Staphylococcus aureus* (SA). Reduction of darker pigmentation indicates reduced formation of biofilm and lower concentration of amyloid-like protein structures; scale bar = 5mm; n=3.

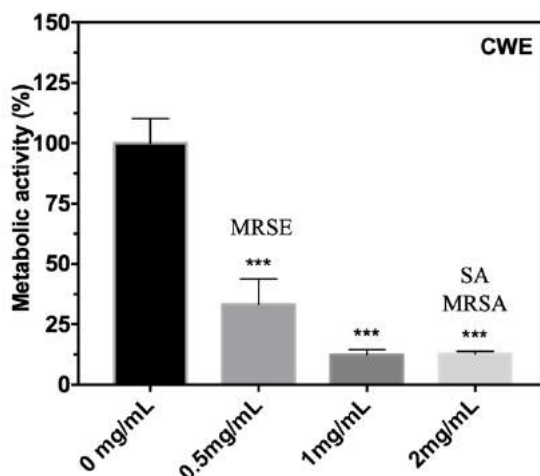


Supplementary Fig. 3-13. Congo red agar assay for vescalagin/castalagin on Methicillin-resistant *Staphylococcus aureus* (MRSA). Reduction of darker pigmentation indicates reduced formation of biofilm and lower concentration of amyloid-like protein structures; scale bar = 5mm; n=3.

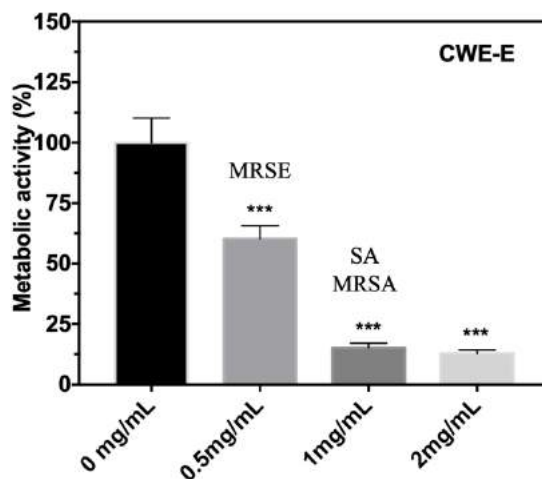


Supplementary Fig. 3-14. Congo red agar assay for vescalagin/castalagin on *Pseudomonas aeruginosa* (PA). Scale bar = 5mm; n=3.

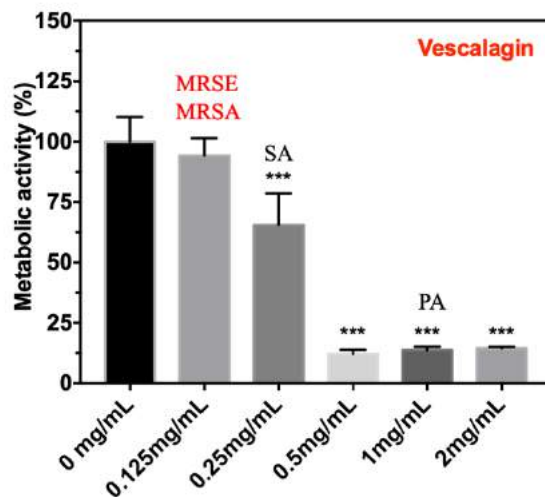
- Assessment of the cytocompatibility of the cork-derived extracts/polyphenols



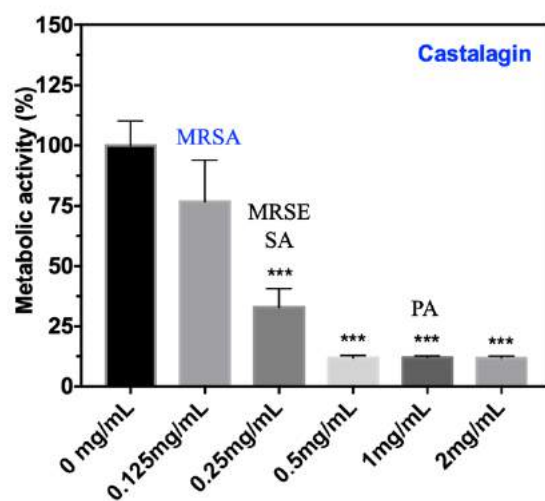
Supplementary Fig. 3-15. Cytocompatibility of CWE towards the L929 cell line, measured by their metabolic activity using AlamarBlue®. CWE was directly added to the cell culture medium. It is also shown the corresponding MIC concentrations for each strain of bacteria, i.e. Methicillin-resistant *Staphylococcus epidermidis* (MRSE, 0.5mg/mL), *Staphylococcus aureus* (SA, 2mg/mL) and Methicillin-resistant *Staphylococcus aureus* (MRSA, 2mg/mL). L929 cells were incubated during 24h. \*  $p < 0.05$ , \*\*  $p < 0.01$ , \*\*\*  $p < 0.001$  (vs 0mg/mL of CWE);  $n=3$ .



Supplementary Fig. 3-16. Cytocompatibility of CWE-E towards the L929 cell line, measured by their metabolic activity using AlamarBlue®. CWE-E was directly added to the cell culture medium. It is also shown the corresponding MIC concentrations for each strain of bacteria, i.e. Methicillin-resistant *Staphylococcus epidermidis* (MRSE, 0.5mg/mL), *Staphylococcus aureus* (SA, 1mg/mL) and Methicillin-resistant *Staphylococcus aureus* (MRSA, 1mg/mL). L929 cells were incubated during 24h. \*  $p < 0.05$ , \*\*  $p < 0.01$ , \*\*\*  $p < 0.001$  (vs 0mg/mL of CWE-E);  $n=3$ .



Supplementary Fig. 3-17. Cytocompatibility of vescalagin towards the L929 cell line, measured by their metabolic activity using AlamarBlue®. Vescalagin was directly added to the cell culture medium. It is also shown the MIC concentrations for each strain of bacteria, i.e. Methicillin-resistant *Staphylococcus epidermidis* (MRSE, 0.125mg/mL), *Staphylococcus aureus* (SA, 0.250mg/mL), Methicillin-resistant *Staphylococcus aureus* (MRSA, 0.125mg/mL) and *Pseudomonas aeruginosa* (PA, 1.00mg/mL). L929 cells were incubated during 24h. \*  $p < 0.05$ , \*\*  $p < 0.01$ , \*\*\*  $p < 0.001$  (vs 0mg/mL of vescalagin);  $n=3$ .



Supplementary Fig. 3-18. Cytocompatibility of castalagin towards the L929 cell line, measured by their metabolic activity using AlamarBlue®. Castalagin was directly added to the cell culture medium. It is also shown the MIC concentrations for each strain of bacteria, i.e. Methicillin-resistant *Staphylococcus epidermidis* (MRSE, 0.250mg/mL), *Staphylococcus aureus* (SA, 0.250mg/mL), Methicillin-resistant *Staphylococcus aureus* (MRSA, 0.125mg/mL) and *Pseudomonas aeruginosa* (PA, 1.00mg/mL). L929 cells were incubated during 24h. \*  $p < 0.05$ , \*\*  $p < 0.01$ , \*\*\*  $p < 0.001$  (vs 0mg/mL of castalagin);  $n=3$ .

## Chapter 4

**Cork extracts reduce UV-mediated DNA  
fragmentation and cell death**



## CHAPTER 4

### Cork extracts reduce UV-mediated DNA fragmentation and cell death<sup>3</sup>

#### ABSTRACT

UV radiation is known to induce the premature aging of human skin and to contribute to the occurrence of different skin cancers. High doses of UVA (able to penetrate through the epidermis into the dermis) and/or UVB radiation (only affecting the epidermis) leads to cellular oxidative damage compromising the recovery of the normal functions of the cells. This cellular damage is mainly driven by the generation of reactive oxygen species (ROS) that alter the redox status of the intracellular milieu, affecting the cellular metabolic activity, leading to DNA damage, apoptosis and, consequently, to a drastic decrease in the number of live cells, compromising the function of the skin. A series of polyphenolic fractions were extracted from the outer bark (cork) of *Quercus suber* L., and tested for their capacity to reduce the cellular damage promoted by the ROS produced during UV exposure. This was evaluated after exposing L929 fibroblasts to UV radiation in the presence and absence of the cork extracts. In all the cases the extracts at the concentration of 75µg/ml demonstrated the capacity to preserve cell metabolic activity and their typical morphology, as well as, to avoid DNA fragmentation after exposure to UV radiation. We were also able to correlate these findings with the intracellular reduction of ROS species and the presence of higher proportions of castalagin and vescalagin in the extracts. Our data proves that cork is a relevant source of antioxidant compounds able to act in the cellular environment, protecting cells against oxidation, reducing the number of ROS species and limiting the negative impact of UV radiation. These extracts can be further exploited in the preparation of anti-UV formulations for skin protection.

**Keywords:** Anti-UV radiation, Cork extracts, DNA fragmentation, Anti-oxidant properties.

---

<sup>3</sup> This Chapter is based on the publication: "Araújo A. R., Pereira D. M., Aroso I. M., Santos T., Batista M. T., Cerqueira M. T., Marques A. P., Reis R. L., and Pires R. A., "Cork extracts reduce UV-mediated DNA fragmentation"

## 4.1 INTRODUCTION

At the sea level, the solar radiation is composed by  $\sim 3\%$  of Ultra-Violet (UV) light (100-400nm),  $\sim 44\%$  of visible light (400-700nm), and  $\sim 53\%$  of infra-red light (700-1440nm)[1]. The UV section of the solar spectrum is composed by three types of UV rays, such as: UVA (315-400nm); UVB (280-315nm); and UVC (<280nm)[2]. The ozone layer is able to adsorb the UVC wavelengths and a significant part of the UVB radiation that reaches the Earth. However, the small quantity of UVB that cross the ozone barrier is enough to interfere with the physiological balance (homeostasis) of tissues and cells[3]. In the case of the UVA radiation, it has been associated to skin premature aging or long-term skin damage[4] (e.g. wrinkles), as well as with skin cancer in individuals that presented a history of long periods of sunlight exposure. In fact, several epidemiological studies link the combined UVA and UVB exposure to an increased risk of occurrence of skin cancer[5, 6].

At the cellular level, UV irradiation induces the direct or indirect DNA degradation. This has been reported for the UVB range and for the high-energy artificial UVC radiation, through the dimerization of the pyrimidines nucleobases[7]. Apoptosis is one of the hallmarks of UV cell damage[5, 8]. This UV-mediated cell death is the result of several biochemical processes, such as: formation of pyrimidine dimers and photoproducts[8, 9], activation of death receptors (including CD95, i.e. Fas/APO-1)[10], and formation of reactive oxygen species (ROS)[9, 11]. ROS, such as, superoxide radical ( $\bullet O_2$ ), hydrogen peroxide ( $H_2O_2$ ) and hydroxyl radical ( $\bullet OH$ ), are known as key mediators of DNA and protein oxidative damage in skin cells. However, they also act in the oxidation of membrane lipids via the generation of lipids' peroxides and in the fast reduction in the activity of several endogenous skin enzymes, such as, reductase and catalase, as well as lowering the concentration of cellular antioxidants (e.g. glutathione)[12, 13].

The reported relation between UV-mediated skin damage and the increment of ROS in the cellular milieu, lead several authors to propose the use of phenolic compounds to neutralize the ROS species generated by the UV radiation[14-17] and to protect the skin cells from mutations or death[18-20]. Cork (the outer bark of *Quercus suber L.*) is a suberized cellular tissue that present  $\sim 15\%$  of extractives[21], which can be easily obtained using suitable solvents[21-23]. Several studies on the chemical composition of such extracts have reported the presence of phenolic acids, such as, gallic, protocatechuic, caffeic, and ferulic acids, which as natural antioxidants (AO) have been proven relevant in the biomedical area[22, 24]. Moreover, antibacterial, antiviral, anticarcinogenic, anti-inflammatory and antiallergic activities have been also attributed to these phenolic compounds[25].

Considering the presence of these AOs in cork and the above-mentioned correlation between UV-mediated cell damage and the increased concentration of ROS in the cellular environment, we hypothesized that the cork polyphenols had the capacity to reduce the ROS oxidative damage generated in skin cells by UV radiation. In this context we evaluated the capacity of cork's AOs to reduce the negative impact of UVA and UVB radiation on cell function. This study was centred in the use of L929 fibroblast cell line due to the fact that fibroblasts are one of the main cell type present in skin, namely in the dermis, which is responsible for the generation of connective tissue, and for the skin's recovery from injury (since they synthesize most of the dermis's extracellular matrix)[26-30]. The cork extracts were characterized by HPLC to quantify the most abundant compounds. Its total content in phenolic acids was determined and then correlated with the AO activity of the extracts. The AO activity of the cork extracts and consequently their capacity to act as anti-UV agents was confirmed by their capacity to preserve cells' viability; depicting their typical morphology and, more importantly, to prevent DNA fragmentation.

## 4.2 MATERIALS AND METHODS

Unless otherwise stated, chemicals were acquired from Sigma-Aldrich and used without further purification

### 4.2.1 MATERIALS

Two different raw extracts were obtained by maintaining cork powder (Amorim Cork Composites, Portugal) in contact with water (producing the CWE) or a mixture of water and ethanol (50:50 v/v, producing the CWEE), under reflux conditions, for a period of 6h. After cooling, the liquid fraction was recovered by filtration, the solvent was partially removed by vacuum evaporation, and the final solid extracts were recovered upon freeze-drying. The CWEE was loaded to a chromatographic column, packed with Sephadex LH-20 as stationary phase and stabilized in water. The elution was performed using water, followed by mixtures of water and increasing percentages of ethanol, yielding fCWEE.

### 4.2.2 CHEMICAL CHARACTERIZATION OF CORK EXTRACTS

#### Reagents

Folin-Ciocalteu phenol reagent, gallic acid, 2,2-diphenyl-1-picrylhydrazyl (DPPH), 2,2-azobis (2-methylpropionamide) dihydrochloride (AAPH), fluorescein sodium salt and 6-hydroxy-2,5,7,8-

tetramethylchromane-2-carboxylic acid (trolox) and ellagic acid were purchased from Sigma-Aldrich while methanol was acquired from Fluka. All reagents were used as received. Vescalagin and castalagin were obtained internally by preparative HPLC and identified by mass spectrometry.

### **Total phenolic content (TPC) and antioxidant (AO) activity**

The TPC was determined according to the Folin-Ciocalteu method[31] and adapted from Santos *et al*[23]. Briefly, 50 $\mu$ l of sample solution (1mg/ml) was added to 500 $\mu$ l of Folin reagent (diluted 1:10) and 450 $\mu$ l of sodium carbonate solution (75g/l). After heating to 50°C for 5min, the absorbance at 756nm was read in a microplate reader (Synergy HT, BioTek, USA). The TPC was calculated from a calibration curve obtained with gallic acid standards and expressed as mg of gallic acid equivalents per g of extract.

The AO activity was determined by the DPPH radical scavenging activity and the oxygen radical absorbance capacity (ORAC) assays. The DPPH scavenging was determined following the methodology reported by Santos *et al*[23]. Briefly, 50 $\mu$ l of suitable sample dilutions was added to 900 $\mu$ l of DPPH (6.2mg in 100ml methanol, initial absorbance of 1.02 $\pm$ 0.03) and the absorbance was measured at 517nm in the microplate reader. The EC50 was calculated as the concentration of extract necessary to reduce the initial absorbance by 50%. The ORAC assay was adapted from the methodology described by Huang *et al*[32]. The reaction mixture consisted of 25 $\mu$ l of sample or trolox (as standard), 25 $\mu$ l of 250mM AAPH and 150 $\mu$ l of fluorescein at a concentration of 0.025 $\mu$ M. Fluorescence measurements (excitation wavelength at 485nm and emission wavelength at 520nm) were performed in the microplate reader at 37°C, with readings taken at 2min intervals and with agitation in between each measurement. The results are expressed as mg of trolox equivalents (TE) per g of extract.

### **High Performance Liquid Chromatography (HPLC) analysis**

The HPLC analysis was used to quantify the proportion of castalagin, vescalagin, gallic acid and ellagic acid present in CWE, CWEE and fCWEE. The analysis were performed on a Knauer apparatus equipped with a photodiode array detector (PDA) model Smartline UV detector 2600 and using an Atlantis T3 5 $\mu$ m (4.6x250mm) column protected by an Atlantis T3 5 $\mu$ m (4.6x20mm) guard column. The mobile phase consisted of water:methanol:acetic acid 88:10:2 (v/v/v) (A) and methanol:acetic acid 98:2 (v/v) (B) and the elution program was as follows: 0% B (0-2min), 0-100% B (2-50min), 100% B (50-60min), 100-0% B (60-70min) and 0% B (70-80min). The flow rate was 1ml.min<sup>-1</sup> and the injection volume was 100 $\mu$ l. The identification was performed by mass spectrometry or PDA and the quantification was performed using calibration curves of the standards, i.e. vescalagin and castalagin purified in our lab by semi-preparative

HPLC (Atalntis T3 column, 25x250mm and injection volume of 2mL) using the same eluent gradients as the analytical program; and gallic acid and ellagic acid obtained from Sigma-Aldrich.

### Cell culture

L929 cells (passages 10 to 12) were maintained in DMEM, supplemented with 10% FBS (ALFAGENE) and 1% penicillin/streptomycin (ALFAGENE). Cells were plated at a concentration of 45000 cells/ml, in 24 well plates; incubated at 37°C under 5% CO<sub>2</sub> with the sample extracts at the 75µg/ml (for each extract) for 24h. Afterwards, the cell-culture plates were positioned over an ice dish and irradiated with a 400 W HPA lamp (Hapro Summer Glow HB 404, Germany) during 15min. The UV dose during exposure was measured using a radiometer (UVP UVX, USA) at different wavelengths: 365nm (UVA), 302nm (UVB) and 254nm (UVC). Only UVA and UVB were detected at an exposure dose of 17.1J/cm<sup>2</sup> and 4.1J/cm<sup>2</sup>, respectively. After an additional 24h of cell culture under standard conditions, cells were evaluated for several parameters as described in the next subsections.

### Viability and metabolic assays

Cellular metabolic activity was assessed using a commercial MTS assay kit (Promega, USA). Briefly, a tetrazolium derivative, subsequently reduced to a water-soluble brown formazan product by viable cells, was added to the culture wells. After an incubation period of 3h, the absorbance at 490nm was read in the microplate reader and the results expressed in relation to control, i.e. cells without UV irradiation.

Cell viability was evaluated by Live/Dead assay respectively after calcein AM-propidium iodide (PI) staining. Cells were incubated for 20min with both dyes and then observed under a fluorescence microscope (Axio Imager Z1m, Zeiss). Viable cells were stained green and dead cells were stained red.

Giemsa staining was used to evaluate the morphology of the cells. Cells were fixed with cold methanol, washed, stained with Giemsa solution, mounted and analysed by microscopy (Axio Imager Z1m, Zeiss).

### Reactive oxygen species

Intracellular ROS were evaluated as described before by Pereira *et al*[33]. Cells, 10000 per well, were seeded in 96-well black plates according to the above-mentioned cell culture conditions. After irradiation, cells were incubated with 25µM of DCDHF-DA (2',7'-dichlorodihydrofluorescein diacetate, succinimidyl ester) and its fluorescence recorded in a microplate reader after 90min (at an emission wavelength of 520nm and at an excitation wavelength of 490nm). Cells in DPBS were used as negative control. Results

are expressed in relation to the positive control (100% of ROS), i.e. irradiated cells in the absence of cork extracts.

### Tunel assay

The in situ cell death detection kit (Roche) was used to detect apoptotic cell death at the single-cell level by fluorescence microscopy. Cells were fixed with formalin 10% and permeabilized using 0.1% Triton X-100 in 0.1% sodium citrate for 5min. The Tunel reaction mixture was then added to each sample and incubated for 1h at 37°C. The negative control was only incubated with labelling solution without terminal transferase and the positive control was incubated with recombinant DNase I to induce DNA strand breaks. Finally, cells were stained with DAPI at a concentration of 1:1000 for 20min and analysed by fluorescence microscopy (Axio Imager Z1m, Zeiss).

### Statistical Analysis

All the quantitative results were obtained after analysis of at least six measurements per sample. Initially, a Shapiro–Wilk test was used to ascertain the normality of the data. All the collected data followed a normal distribution, and the results were presented as mean  $\pm$  standard deviation (SD). Student's t-tests for independent samples were performed to test differences among the samples. Throughout the following discussion, the differences were considered significant if  $p < 0.05$ .

## 4.3 RESULTS AND DISCUSSION

### Chemical composition of cork extracts

Cork powder was extracted with water (CWE) and a mixture of water:ethanol (50:50) (CWEE). Both CWE and CWEE were characterized for their extraction yield, TPC and AO activity (Table 4-1). The latter one seems to be related with the anti-UV activity due to the fact that the protection of tissues from damage by UV radiation is usually associated with the capacity to quench oxygen radical species and scavenge those radicals.

**Table 4-1. Yield of extraction, TPC and AO activity of the cork extracts (CWE and CWEE) and chromatographically fractionated sample (fCWEE)\***

Sample	Yield (%m/m)	TPC (mgGA <sub>cat</sub> / g <sub>extract</sub> )	DPPH, EC50 ( $\mu$ g/ml)	ORAC (mgTE <sub>cat</sub> / g <sub>extract</sub> )
CWE	6.7 $\pm$ 1.0	486 $\pm$ 6	6.33 $\pm$ 0.38	1.21 $\pm$ 0.25
CWEE	9.3 $\pm$ 0.2	570 $\pm$ 39	5.32 $\pm$ 0.45	2.11 $\pm$ 0.24
fCWEE	28 <sup>†</sup>	866 $\pm$ 30	4.04 $\pm$ 0.25	2.23 $\pm$ 0.32

\*m/m of the CWEE sample; \*\*all values are presented as average  $\pm$  standard deviation.

Our results revealed that the use of a mixture of water and ethanol (50:50 v/v; CWEE) generates higher yields of extraction and an extract with higher TPC and AO activity than the extract obtained only

with water, i.e. CWE (as indicated by both DPPH and ORAC assays). This data led us to fractionate the CWEE using chromatographic techniques, yielding fCWEE.

This fractionated sample (fCWEE), presented a significantly higher TPC and lower EC<sub>50</sub>. However, no significant differences were observed between AO activity of CWEE and fCWEE in the ORAC assay. This latter assay measures the efficiency of a given AO molecule to capture ROS, with origin on the thermal decomposition of AAPH and in the presence of fluorescein that functions as a probe. Therefore, the AO efficiency depends not only on the chemical ability to react with ROS (through a hydrogen bond transfer reaction) but also to do so on a timely manner. On the other hand, the DPPH assay is based on the reaction of the AO molecule with the stable radical DPPH•, through an electron transfer reaction. Therefore, the fractionation of CWEE into fCWEE results in a sample with a higher capacity to act as AO through radical scavenging. However, this fractionation did not impart a noticeable improvement in the capacity of the extract to neutralize the ROS by hydrogen atom transfer.

In order to establish a link between the chemical composition and the detected AO activity, we acquired the HPLC chromatographic profile of each sample (S. Fig. 4-1), leading us to conclude that the 3 samples are mostly composed of ellagitannins and phenolic acids, namely: vescalagin, castalagin, gallic acid and ellagic acid (identification by PDA and MS presented in S. Table 4-1). HPLC was also used to quantify their weight percentage in the composition of the extracts (results presented in Table 4-2).

**Table 4-2. Quantitative analysis of the cork extracts (CWE and CWEE) and the fractioned sample (fCWEE), expressed as mg of compound/g of extract.**

Sample	Compounds			
	Vescalagin	Castalagin	Gallic Acid	Ellagic Acid
CWE	32.1	40.3	4.2	6.5
CWEE	22.4	46.9	2.9	26.7
fCWEE	140.9	200.3	3.8	3.4

The highest content on ellagic acid was observed for CWEE, while gallic acid was more abundant in the CWE. The content on castalagin was slightly higher in CWEE, while vescalagin was found in higher amounts in CWE. This result reflects the lower solubility of vescalagin in ethanol than that of castalagin[34]. In sample fCWEE the concentration of vescalagin and castalagin increased by 4 and 6 times, respectively, in relation to the unfractioned sample (CWEE). In addition, the content on ellagic acid decreased from 26.7 to 3.4mg/g of extract. Combining this characterization with the results obtained for the AO activity (Table 4-1), our data suggests that vescalagin and castalagin (the main components of fCWEE) are responsible for the improvement of the DPPH AO activity, i.e. they are efficient in stabilizing

free radicals through an electron transfer mechanism. However, they do not seem to be as effective AOs through mechanisms related with hydrogen atom transfer (ORAC assay).

### Cork extracts protect L929 cells from UV-induced cell death

In order to evaluate the capacity of the cork extracts to protect the L929 fibroblasts from UV-induced cell death, we conducted initial experiments to determine the cytotoxicity limit of the extracts (S. Figure 4-2) and the timeframe of UV exposure capable of inducing a noticeable reduction of cellular metabolic activity (Figure 4-1). This initial screening revealed that cork extracts, at a concentration of 75 $\mu$ g/ml, did not elicit any noticeable cytotoxicity. Thus, this concentration was established for all the subsequent biological tests. Regarding the time of UV exposure, a 15min timeframe (in the absence of cork extracts, that corresponds to a dose of 17.1J/cm<sup>2</sup> of UVA and 4.1J/cm<sup>2</sup> of UVB) lead to a reduction of the cell metabolic activity to, approximately, 60%, leading us to select this timeframe for the whole set of experiments. Longer time periods (e.g. 30min) already generated irreversible loss of cell viability[35].

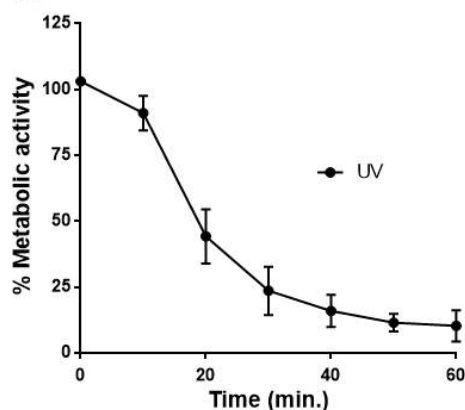


Figure 4-1. Metabolic activity of L929 cells measured 27h after exposure to UV radiation for different timeframes/UV doses (upon UV exposure, cells were pre-incubated for 24h in the absence of cork extracts, and an additional 3h for MTS incubation). Results are expressed in relation to the negative control C-, i.e., 100% corresponds to the metabolic activity of non-exposed cells that were pre-incubated in the absence of cork extracts. Statistical significance corresponds to \*\*p < 0.01 or \*\*\*p < 0.001.

The structural diversity of the compounds (and their proportions) detected in the 3 samples (as well as their different TPC and AO activity) could lead us to expect differences in the biological AO potential and anti-UV activity. However, while the presence of the cork samples significantly reduce the negative impact of the UV-mediated cell damage, our data also indicates that, in the cellular environment, the variations observed between the 3 cork samples in the metabolic activity are not statistically significant.



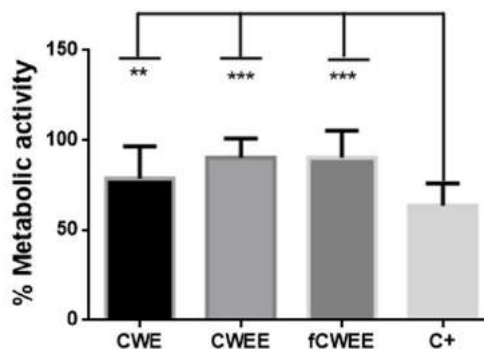


Figure 4-2. Metabolic activity of L929 cells pre-incubated with 75µg/ml of each cork extract for 24h, followed by a UVA dose of 17.1J/cm<sup>2</sup> in combination with a UVB dose of 4.1J/cm<sup>2</sup>. C+ corresponds to the control sample prepared in the absence of cork extracts. Results are expressed and normalized in relation to C-, i.e. 100% corresponds to the metabolic activity of non-exposed cells that were pre-incubated in the absence of cork extracts. Statistical significance corresponds to \*\*p < 0.01 and \*\*\*p < 0.001.

As it can be seen in Figure 4-2, under the selected conditions (UVA dose of 17.1J/cm<sup>2</sup>, UVB dose of 4.1J/cm<sup>2</sup> and 75µg/ml of each cork extract), the ≈40% loss of viability caused by UV-irradiation was partially avoided (between 40% and 60%) when the cells were pre-incubated with CWE, CWEE and fCWEE. No significant differences were detected between the different samples.

#### Cork extracts prevent the UV-triggered increase in cellular ROS

The increment of oxidative stress promoted by the UV radiation is known to promote the generation of ROS. These species play a pivotal role in cellular damage, arising from their interaction with the cellular macromolecules.

As depicted in Figure 4-3, the UV irradiation significantly increased the amount of intracellular ROS in the L929 cell culture. However, the pre-incubation of the cells with the cork extracts lowered the ROS levels in the intracellular environment by ≈50% (higher efficiency observed with CWEE and fCWEE). These results are in accordance with the performed AO tests that also indicated a higher AO activity in the case of the CWEE and fCWEE. It is important to notice that in a non-irradiated state (C-), the amount of ROS detected in the medium is within the range of the physiological concentration originated from the normal metabolism of cells.

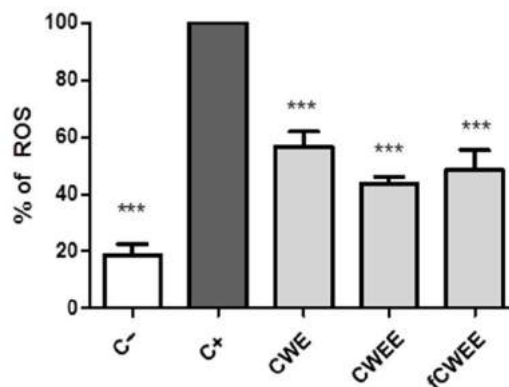
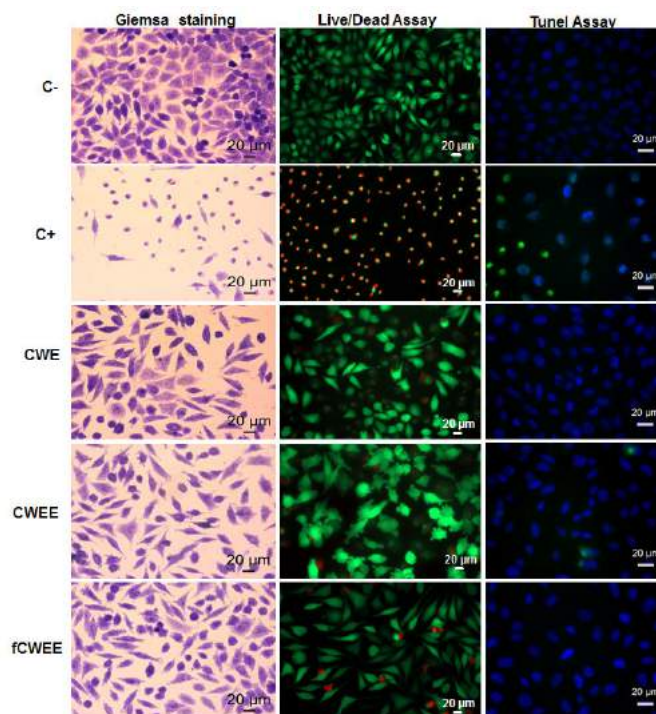


Figure 4-3. Intracellular ROS levels assessed with the DCDHF-DA probe. Results are expressed in relation to the positive control C+ (100% of ROS), i.e. UV-exposed cells in the absence of cork extracts. C- corresponds to cells not exposed to the UV radiation and pre-incubated in the absence of cork extracts. Statistical significance corresponds to \*\*\* $p < 0.001$  in relation to C+.

#### Cell morphology and viability after UV irradiation

UV irradiation also elicited marked changes in the cellular morphology compatible with cell death (Figure 4-4). Shranked cells, condensed chromatin and pycnotic nuclei were clearly observed in the positive control. The majority of these features were not observed in the cells pre-incubated with cork extracts and exposed to UV (the same results were obtained with the cells pre-incubated with cork extracts and without UV exposure, S. Fig. 4-3). The only exception was observed for the cells pre-incubated with CWEE (and UV exposed) where several irregularities in the membrane of the cells were observed. The purified fraction fCWEE improved this scenario. In this case, the cells show a normal morphology. This observation seems to be related with the increase in the proportion of vescalagin and castalagin (Table 4-2) after the fractionation of CWEE. This can be also related with the improvement on the AO activity of the fCWEE (Table 4-1 – DPPH and ORAC assay) protecting the cells from UV-mediated oxidative damage. The Live/Dead assay also confirmed that in the positive control the majority of the cells were dead, while the percentage of these in the presence of the extracts was similar to what was observed for the negative control. Thus, a significant cell death induced by UV irradiation was avoided by pre-incubation with the cork extracts.



**Figure 4-4.** Assessment of the morphology (Giemsa staining), viability (Live (green)/Dead (red)) and apoptosis level (Tunel assay, nuclei (blue) and DNA fragmentation (green)) upon UV irradiation, in the absence (C+) and presence of cork extract (at a concentration of 75 μg/ml). C- corresponds to cells cultured in the absence of cork extracts and not exposed to UV radiation.

The Tunel assay allowed us to evaluate the presence of significant DNA fragmentation and of apoptotic cells. In this case, limited UV-mediated DNA damage was observed in the presence cork extracts, in opposition to what was observed for the positive control (i.e. cells irradiated in the absence of cork samples).

Overall, CWEE exhibited a lower capacity to: maintain the cell typical morphology; rescue cell viability; and prevent DNA fragmentation. Its fractionated sample, fCWEE, was able to act as a more efficient anti-UV extract potentially due to the higher AO activity resulting from the higher content of vescalagin and castalagin. Although lower AO activity was detected for the CWE, its capacity to avoid cell death, and to protect DNA from fragmentation, suggests that the activity of these extracts is not only driven by their AO capacity[36]. Other biochemical mechanisms, whose origin is still unclear, may have a pivotal role in the case of the CWE activity. In fact, while UV radiation has been linked primarily to generation of ROS species, it is also reported its capacity to break single-strand DNA; disrupt DNA synthesis; deplete the intracellular glutathione; induce the peroxidation of biomembrane lipids. CWE might interfere with some of these events in a way that is still to be evaluated[13, 37, 38].

#### 4.4 CONCLUSIONS

A series of cork fractions (obtained by water or a water:ethanol 50:50 mixture) were tested for their capacity to prevent UV-mediated cellular damage. Their capacity to reduce the concentration of ROS in the cellular milieu was correlated to their AO capacity. Our data showed that the sample with highest AO activity (fCWEE), and highest proportion of vescalagin and castalagin, is the one that is able to better prevent UV-mediated cellular damage. However, the CWE fraction, the one with lower AO activity, also presented protection against UV-mediated cell death, morphological modification and DNA fragmentation at levels similar to the ones presented by the fCWEE sample. It seems that CWE is also able to reduce the UV-mediated cell damage, although through ROS-independent pathways. Therefore, CWE and fCWEE are vescalagin/castalagin-rich extracts that can be exploited in the preparation of pharmaceutical or cosmetic skin-care products with the capacity to prevent UV-mediated cellular damage.

#### 4.5 REFERENCES

1. Frederick, J.E., H.E. Snell, and E.K. Haywood, Solar Ultraviolet-Radiation at the Earth's Surface. *Photochemistry and Photobiology*, 1989. 50(4): p. 443-450.
2. de Gruijl, F.R., Skin cancer and solar UV radiation. *European Journal of Cancer*, 1999. 35(14): p. 2003-2009.
3. de Gruijl, F.R., H.J. van Kranen, and L.H.F. Mullenders, UV-induced DNA damage, repair, mutations and oncogenic pathways in skin cancer. *Journal of Photochemistry and Photobiology B: Biology*, 2001. 63(1-3): p. 19-27.
4. Wu, Z.H., et al., [UV-induced DNA damage and protective effects of antioxidants on DNA damage in human lens epithelial cells studied with comet assay]. *Zhonghua Yan Ke Za Zhi*, 2006. 42(11): p. 1002-7.
5. Tucker, M.A., Is sunlight important to melanoma causation? *Cancer Epidemiology Biomarkers & Prevention*, 2008. 17(3): p. 467-468.
6. Greinert, R., Skin Cancer: New Markers for Better Prevention. *Pathobiology*, 2009. 76(2): p. 64-81.
7. Pfeifer, G.P. and A. Besaratinia, UV wavelength-dependent DNA damage and human non-melanoma and melanoma skin cancer. *Photochemical & Photobiological Sciences*, 2012. 11(1): p. 90-97.
8. Katiyar, S.K., S.K. Mantena, and S.M. Meeran, Silymarin Protects Epidermal Keratinocytes from Ultraviolet Radiation-Induced Apoptosis and DNA Damage by Nucleotide Excision Repair Mechanism. *Plos One*, 2011. 6(6).

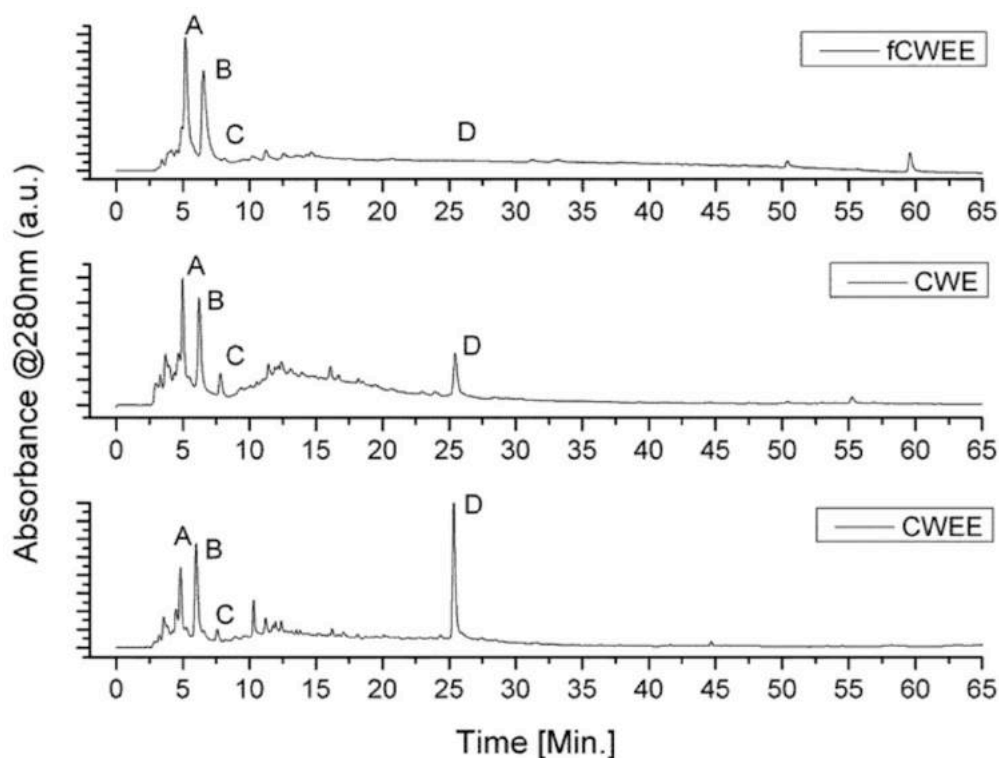
9. Kulms, D., et al., Nuclear and cell membrane effects contribute independently to the induction of apoptosis in human cells exposed to UVB radiation. *Proceedings of the National Academy of Sciences of the United States of America*, 1999. 96(14): p. 7974-7979.
10. Aragane, Y., et al., Ultraviolet light induces apoptosis via direct activation of CD95 (FAS/APO-1) independently from its ligand CD95L. *Journal of Investigative Dermatology*, 1998. 110(4): p. 490-490.
11. Scharffetter-Kochanek, K., et al., UV-induced reactive oxygen species in photocarcinogenesis and photoaging. *Biological Chemistry*, 1997. 378(11): p. 1247-1257.
12. Ichihashi, M., et al., UV-induced skin damage. *Toxicology*, 2003. 189(1-2): p. 21-39.
13. Liebel, F., et al., Irradiation of Skin with Visible Light Induces Reactive Oxygen Species and Matrix-Degrading Enzymes. *Journal of Investigative Dermatology*, 2012. 132(7): p. 1901-1907.
14. Huang, C.-C., et al., Protective effects of (–)-epicatechin-3-gallate on UVA-induced damage in HaCaT keratinocytes. *Archives of Dermatological Research*, 2005. 296(10): p. 473-481.
15. Psotova, J., et al., Photoprotective properties of *Prunella vulgaris* and rosmarinic acid on human keratinocytes. *Journal of Photochemistry and Photobiology B-Biology*, 2006. 84(3): p. 167-74.
16. Svobodová, A., et al., Attenuation of UVA-induced damage to human keratinocytes by silymarin. *Journal of Dermatological Science*, 2007. 46(1): p. 21-30.
17. Silva, J.P., A.C. Gomes, and O.P. Coutinho, Oxidative DNA damage protection and repair by polyphenolic compounds in PC12 cells. *European Journal of Pharmacology*, 2008. 601(1-3): p. 50-60.
18. Aboul-Enein, H.Y., et al., Scavenging effects of phenolic compounds on reactive oxygen species. *Biopolymers*, 2007. 86(3): p. 222-30.
19. Svobodova, A., J. Psotova, and D. Walterova, Natural phenolics in the prevention of UV-induced skin damage. A review. *Biomed Pap Med Fac Univ Palacky Olomouc Czech Repub*, 2003. 147(2): p. 137-45.
20. Stahl, W. and H. Sies, Photoprotection by dietary carotenoids: Concept, mechanisms, evidence and future development. *Molecular Nutrition & Food Research*, 2012. 56(2): p. 287-295.
21. Cordeiro, N., et al., Cork suberin as a new source of chemicals. 1. Isolation and chemical characterization of its composition. *International Journal of Biological Macromolecules*, 1998. 22(2): p. 71-80.
22. Fernandes, A., et al., Antioxidant and Biological Properties of Bioactive Phenolic Compounds from *Quercus suber* L. *Journal of Agricultural and Food Chemistry*, 2009. 57(23): p. 11154-11160.
23. Santos, S.A.O., et al., Chemical composition and antioxidant activity of phenolic extracts of cork from *Quercus suber* L. *Industrial Crops and Products*, 2010. 31(3): p. 521-526.
24. Fernandes, A., et al., Analysis of phenolic compounds in cork from *Quercus suber* L by HPLC-DAD/ESI-MS. *Food Chemistry*, 2011. 125(4): p. 1398-1405.

25. Hooper, L. and A. Cassidy, A review of the health care potential of bioactive compounds. *Journal of the Science of Food and Agriculture*, 2006. 86(12): p. 1805-1813.
26. Agyare, C., et al., Ellagitannins from *Phyllanthus muellerianus* (Kuntze) Exell.: Geraniin and furosin stimulate cellular activity, differentiation and collagen synthesis of human skin keratinocytes and dermal fibroblasts. *Phytomedicine*, 2011. 18(7): p. 617-624.
27. Alonso-Lebrero, J.L., et al., Photoprotective properties of a hydrophilic extract of the fern *Polypodium leucotomos* on human skin cells. *Journal of Photochemistry and Photobiology B-Biology*, 2003. 70(1): p. 31-37.
28. Basu-Modak, S., et al., Epicatechin and its methylated metabolite attenuate UVA-induced oxidative damage to human skin fibroblasts. *Free Radic Biol Med*, 2003. 35(8): p. 910-21.
29. Rittié, L. and G.J. Fisher, UV-light-induced signal cascades and skin aging. *Ageing Research Reviews*, 2002. 1(4): p. 705-720.
30. Seo, M.Y., et al., Anti-aging effect of rice wine in cultured human fibroblasts and keratinocytes. *Journal of Bioscience and Bioengineering*, 2009. 107(3): p. 266-271.
31. Singleton, V.L., Citation Classic - Colorimetry of Total Phenolics with Phosphomolybdic-Phosphotungstic Acid Reagents. *Current Contents/Agriculture Biology & Environmental Sciences*, 1985(48): p. 18-18.
32. Huang, D.J., et al., High-throughput assay of oxygen radical absorbance capacity (ORAC) using a multichannel liquid handling system coupled with a microplate fluorescence reader in 96-well format. *Journal of Agricultural and Food Chemistry*, 2002. 50(16): p. 4437-4444.
33. Pereira, D.M., et al., Palmitic Acid and Ergosta-7,22-dien-3-ol Contribute to the Apoptotic Effect and Cell Cycle Arrest of an Extract from *Marthasterias glacialis* L. in Neuroblastoma Cells. *Marine Drugs*, 2014. 12(1): p. 54-68.
34. Vivas, N., et al., Conformational interpretation of vescalagin and castalagin physicochemical properties. *J Agric Food Chem*, 2004. 52(7): p. 2073-8.
35. Giampieri, F., et al., Photoprotective Potential of Strawberry (*Fragaria x ananassa*) Extract against UV-A Irradiation Damage on Human Fibroblasts. *Journal of Agricultural and Food Chemistry*, 2012. 60(9): p. 2322-2327.
36. Nichols, J.A. and S.K. Katiyar, Skin photoprotection by natural polyphenols: anti-inflammatory, antioxidant and DNA repair mechanisms. *Archives of Dermatological Research*, 2010. 302(2): p. 71-83.
37. Marrot, L. and J.-R. Meunier, Skin DNA photodamage and its biological consequences. *Journal of the American Academy of Dermatology*, 2008. 58(5, Supplement 2): p. S139-S148.
38. Trachootham, D., et al., Redox Regulation of Cell Survival. *Antioxidants & Redox Signaling*, 2008. 10(8): p. 1343-1374.

## SUPPLEMENTARY INFORMATION

## ▪ HPLC characterization of samples CWE, CWEE and fCWEE

The chromatographic analysis of the cork extracts CWE, CWEE and fCWEE is presented in S. Fig. 4-1. The main peaks, indicated by the letters, are assigned, respectively, to A – Vescalagin, B – Castalagin, C – Gallic acid and D – Ellagic acid. The identification was performed by comparison of the retention time and spectroscopic data from the photodiode array (PDA) with that of the standards compounds. The quantification was performed from calibration curves obtained with standard solutions of the pure compounds. The vescalagin and castalagin was previously isolated in our lab and their HPLC-ESI/MS analysis is presented in S. Table 4-1.



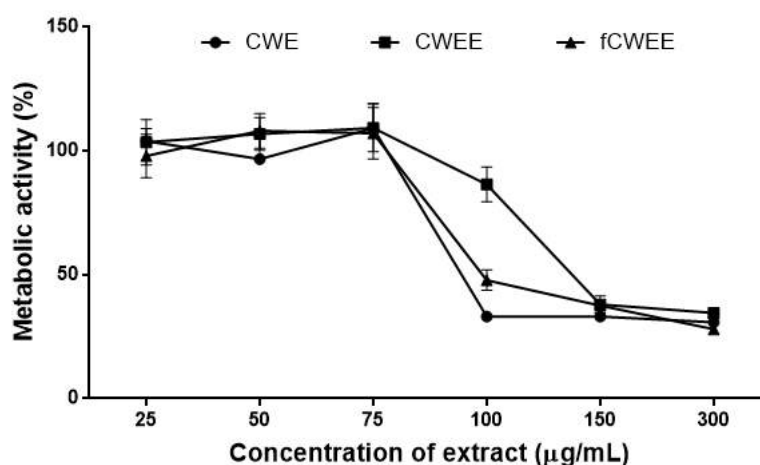
Supplementary Fig. 4-1. HPLC chromatographic profiles of samples CWE, CWEE and fCWEE obtained using UV detection at  $\lambda=280\text{nm}$ ; the letters indicate the most relevant peaks assigned and identified as: A – vescalagin; B – castalagin; C – gallic acid and D – ellagic acid.

Supplementary Table 4-1. HPLC-ESI/MS analysis and identification of main cork extract compounds

Retention time (min)	PDA – $\lambda$ max (nm)	HPLC-ESI/MS tandem			Compound
		[M-H] <sup>-</sup>	MS <sup>2</sup>	MS <sup>3</sup>	
5.1	251	933	915 871 569 613	871 897 569 613	Vescalagin (A)
6.5	254	933	915 631 569	613 569	Castalagin (B)
7.8	272	-	-	-	Gallic acid (C)
25.4	255; 366	-	-	-	Ellagic acid (D)

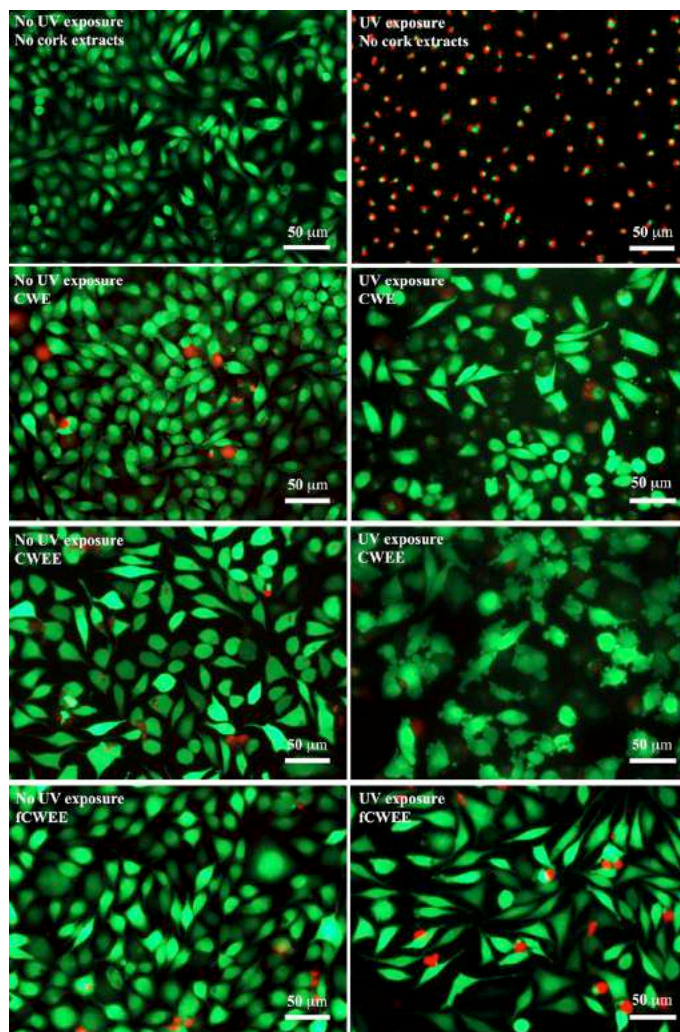
- Cytotoxicity evaluation of cork extracts in L929 cells

The cytotoxicity of each extract was assessed by MTS assay. The range of concentration used for study the work concentration was from 300  $\mu\text{g/ml}$  until 25  $\mu\text{g/ml}$ . Once cells were confluent, each extract was added to the culture medium. After 24h the metabolic activity was determined. The data (S. Fig. 4-2) showed no cytotoxicity up to a working concentration of 75  $\mu\text{g/ml}$  for the three extracts.



Supplementary Fig. 4-2. Metabolic activity of L929 cells cultured with 300, 150, 100, 75, 50 and 25  $\mu\text{g/ml}$  of each cork extract for 24h.





Supplementary Fig. 4-3. Assessment of viability of the cells cultured in the absence and presence of cork extracts as well as in the presence or absence of UV-exposure. Live cells are stained in green and dead cells are stained in red.

## Chapter 5

Vescalagin and castalagin reduce the toxicity of amyloid-beta42 oligomers through the remodelling of its secondary structure

## CHAPTER 5

### Vescalagin and castalagin reduce the toxicity of amyloid-beta 42 oligomers through the remodelling of its secondary structure<sup>4</sup>

#### ABSTRACT

The isomers vescalagin and castalagin protect SH-SY5Y cells from A $\beta$ 42-mediated death. This is achieved better by vescalagin due to the spatial organization of its OH group at the C1 position of the glycosidic chain, improving its capacity to remodel the secondary structure of toxic A $\beta$ 42 oligomers.

**Keywords:** Alzheimer Disease, Vescalagin/castalagin, Galloyl group, amyloid- $\beta$  peptide

---

<sup>4</sup> This Chapter is based on the publication: "Araújo A. R., Gigante S. C., Taboada P., Reis R. L., and Pires R. A., "Vescalagin and castalagin reduce the toxicity of amyloid-beta42 oligomers through the remodelling of its secondary structure", Chemical Communications (RSC), doi:10.1039/D0CC00192A, 2020."

## 5.1 MAIN TEXT

Alzheimer's Disease (AD) is the most common cause of dementia, characterized by cognitive impairment and memory loss.<sup>1</sup> The most characteristic hallmarks of AD are the presence of intracellular neurofibrillary tangles (of hyperphosphorylated Tau protein) in the affected neurons, and the deposition of extracellular plaques of amyloid- $\beta$  (A $\beta$ ) peptides in the hippocampus and entorhinal cortex. In the case of the amyloid deposits, they are usually composed of A $\beta$  of different lengths, *i.e.* between 38 and 43 amino acids. A $\beta$  is produced by neurons during the sequential proteolytic cleavage of amyloid precursor protein (APP).<sup>2</sup> A $\beta$  (1-42) (A $\beta$ 42) is the less abundant species, however, it is the most amyloidogenic due to its higher propensity to self-assemble into supramolecular aggregates, which has been linked with the predominance of hydrophobic amino acid residues at its C-terminus.<sup>3</sup> A $\beta$ 42 can exist in several forms, *e.g.* monomers, oligomers or fibrils, however, its oligomeric species are reported to be the most cytotoxic<sup>4</sup>. They comprise different levels of association, such as dimers, trimers and higher hierarchical assemblies that lead to the formation of protofibrils, the intermediates of the A $\beta$  fibril formation and elongation.<sup>5,6</sup> It has been also reported that these oligomeric structures spread out through the brain and trigger the hyperphosphorylation of Tau leading to the formation of the neurofibrillary tangles.<sup>7,8</sup> Despite the strong body of evidence that supports the pivotal role of oligomers on A $\beta$  toxicity, there is no agreement in the literature on their supramolecular organization. While some authors report them as being unstructured<sup>9</sup>, others show that they present an anti-parallel  $\beta$ -sheet structure (in contrast to the parallel organization of the fibrils).<sup>10</sup>

Polyphenolic compounds are able to interact with A $\beta$ 42<sup>11-14</sup>. This interaction is mainly driven by: the binding of the polyphenols' aromatic rings with the amino and sulfhydryl groups of the peptide; or directly through  $\pi$ - $\pi$  stacking between the same aromatic rings and the A $\beta$ 42 aromatic aminoacidic residues (*e.g.* phenylalanine).<sup>15</sup> Based on these studies we evaluated the capacity of two cork polyphenols, *i.e.* vescalagin (**1**) and castalagin (**2**) (chemical structures presented in Fig. 5-1) to remodel the supramolecular organization of oligomeric A $\beta$ 42 into non-cytotoxic forms. The extraction and identification of each compound was optimized and performed following a previous work<sup>16</sup> (chemical characterization is presented in S. Fig. 5-1, 5-7).

We started by evaluating the capacity of **1** and **2** to reduce the fibrillization of A $\beta$ 42 using the Thioflavin-T (ThT) assay. ThT binds to  $\beta$ -sheet-rich structures mainly through  $\pi$ - $\pi$  interactions and displays enhanced fluorescence in the presence of amyloid fibrils.<sup>17,18</sup> Initial ThT fluorescence was monitored for A $\beta$ 42 alone, showing the characteristic sigmoidal curve of peptide fibrillization (Fig. 5-2A and S. Fig. 5-

12). To guarantee that there is no interference from the fluorescence of **1** and **2** in the results, their spectra were acquired in the absence of A $\beta$ 42 (S. Fig. 5-8 and 5-9). At the excitation/emission wavelengths used for the ThT analysis, no fluorescence was observed for **1** and **2** showing that the ThT data is devoid of interference from the polyphenols themselves. After guaranteeing that the experimental conditions were set to provide meaningful data, A $\beta$ 42 (25 $\mu$ M in the monomeric form) was incubated at room temperature with ThT (25 $\mu$ M) and its fluorescence associated with the A $\beta$ 42 secondary structure in the presence of **1** or **2** (A $\beta$ 42:polyphenol molar ratios of 1:0.5; 1:1 and 1:2) was followed over 140h (apx. 6 days). From Fig. 5-2A and S. Fig. 5-13, it is clear the reduction of A $\beta$ 42 fibrillization in the presence of **1** or **2** in a concentration dependent manner, where **1** was able to completely inhibit aggregation at an A $\beta$ 42:polyphenol ratio of 1:1, while **2** could only achieve this outcome at a ratio of 1:2.

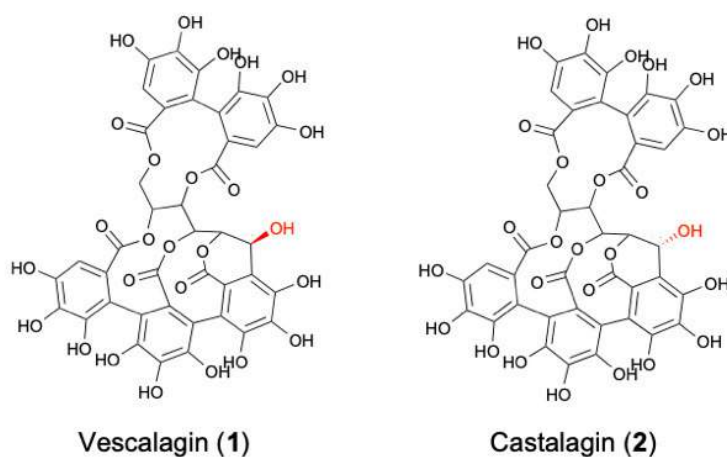


Figure 5-1. Chemical structure of the polyphenols vescalagin (**1**) and castalagin (**2**) extracted and purified from cork powder.

We also tested the capacity of **1** and **2** to disassemble the A $\beta$ 42 pre-formed fibrils (Fig. 5-2B and S. Fig. 5-14). In this case, **1** and **2** were added at the plateau phase (after apx. 6 days of peptide incubation). The ThT fluorescence decreased immediately after the addition of the polyphenols (t=0-24h). Incubation of fibrils with an equimolar concentration of **1** reduced markedly the ThT fluorescence to apx. 20% at t~20min and to apx. 3% after 1h (S. Fig. 5-14A). An almost coincident curve was recorded when a higher ratio of **1** was used (*i.e.* 1:2). In the case of **2** the ThT fluorescence reduced to apx. 50% at t~20min and to apx. 20% after 1h (S. Fig. 5-14B). In both cases, assembly and disassembly, **1** seems to be more efficient in disrupting the  $\beta$ -sheet rich supramolecular assemblies of A $\beta$ 42. Despite the reduction on ThT fluorescence, this method is not completely reliable to guarantee that no cytotoxic assemblies are

formed. In fact, there are some reports in the literature that show that oligomer-specific antiparallel  $\beta$ -sheets do not exhibit ThT fluorescence, showing that this technique should not be considered on its own to evaluate the remodelling of A $\beta$ 42 into non-cytotoxic forms. Considering these methodological constraints, we needed a complementary technique to ensure that we are indeed reducing the presence of A $\beta$ 42 oligomers. We then evaluated by Western Blot (WB) if there was an observable reduction of the size of the peptide aggregates in the presence of **1** and **2** both during A $\beta$ 42 assembly and disassembly (Figs. 5-2C-D and S. Fig. 5-15, 5-19). Overall, during assembly (*i.e.* 7 days of incubation, Fig. 5-2C and S. Fig. 5-15, 5-16) there is a clear reduction of A $\beta$ 42 oligomers (between 2-3 peptide units, *i.e.* 15-10kDa) from ~35% to ~18% in the presence of **1**. In contrast, in the presence of **2**, only at the highest ratio 1:2, it starts to be observed a reduction of the oligomeric species, to ~27%. Importantly, we also observe a significant loss of larger A $\beta$ 42 species (of different sizes: 250-55kDa) for all the tested ratios (Fig. 5-2C). In the case of the A $\beta$ 42 disassembly (Figs. 5-2D and S. Fig. 5-17, 5-18) the presence of **2** seems to be more effective in the reduction of the fibrillar/larger species. In addition, overall both during assembly and disassembly, it is always detected a reduction of the A $\beta$ 42 species detected by the 6E10 monoclonal antibody. These results are consistent with a remodelling of the supramolecular organization of A $\beta$ 42 into structures that are not able to be detected by immunostaining with 6E10 (reported to detect different types of supramolecular A $\beta$ 42 assemblies).<sup>5</sup> Possible explanations are related with the 6E10 binding sites that, either are being occupied by the polyphenols, either the remodelled aggregates do not expose them on their surface. In any case, it is clear that **1** and **2** are able to partially alter the A $\beta$ 42 supramolecular assemblies into forms that are not detectable by ThT nor by the 6E10 antibody.

While ThT and WB assays confirmed the capacity of **1** and **2** to alter the aggregation pathway of A $\beta$ 42, it is important to look for the structural features that guide the observed remodelling. We then used circular dichroism (CD) to confirm if the peptide secondary structure is actually affected by the presence of **1** and **2**. After 7 days of incubation, we observed that A $\beta$ 42 alone presents a characteristic negative peak, at apx. 218 nm and a positive peak at ~197nm (S. Fig. 5-20). This spectral profile has been previously reported for the  $\beta$ -sheet conformation of oligomers.<sup>19, 20</sup> Surprisingly, the addition of **1** or **2** (at the different ratios) does not change the overall spectral profile. However, both peaks present a blue shift after the addition of **1** or **2**, showing that they promote an alteration of the  $\beta$ -sheet conformation of the A $\beta$ 42 supramolecular assemblies (S. Fig. 5-20).

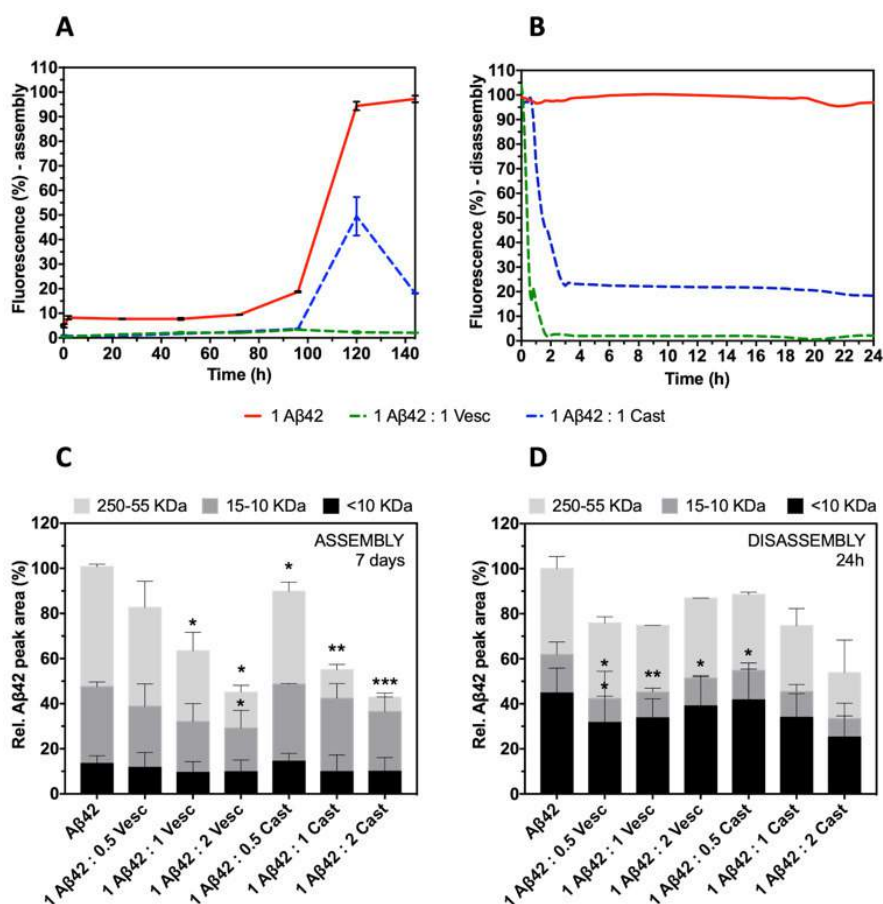


Figure 5-2. Aggregation of A $\beta$ 42 (25 $\mu$ M) followed by ThT fluorescence upon incubation over 140h under different A $\beta$ 42:polyphenol molar ratios, i.e. 1:0.5, 1:1 and 1:2. B. Disassembly of the fibrillar A $\beta$ 42 (25 $\mu$ M) followed by ThT fluorescence using the same A $\beta$ 42:polyphenol ratios. All measurements were recorded under constant agitation at 37 $^{\circ}$ C and were monitored during 24h. Error bars = SD; n = 3. C-D. Relative densitometric bar graphs of C. A $\beta$ 42 (25 $\mu$ M) assembly and D. A $\beta$ 42 (25 $\mu$ M) disassembly quantified by WB (using the antibody 6E10); experiments conducted at 37 $^{\circ}$ C in phosphate buffer, during C. 7days or D. 24h; Error bars = SD, \* p < 0.05, \*\* p < 0.01 and \*\*\* p < 0.001 vs control 25 $\mu$ M A $\beta$ 42; n = 3.

To evaluate if this shift was concomitant with a redistribution of the different types of the peptide secondary structure we fitted the CD spectra with BeStSel method for secondary structure estimation (S. Table 5-1).<sup>21</sup> The results showed that A $\beta$ 42 fibrils during the disassembly experiments (24h) are mainly composed by parallel  $\beta$ -sheet assemblies (Fig. 5-3A).<sup>21</sup> We also found that both **1** and **2** decrease the parallel  $\beta$ -sheets content and promote a rearrangement of the peptide into helix, anti-parallel  $\beta$ -sheets and other types of secondary structures. Importantly, only **1** is able to eliminate the parallel arrangement without any anti-parallel organization. The remodelling of A $\beta$ 42 promoted by **2** leads to the appearance of anti-parallel  $\beta$ -sheets. In the case of the assembly experiments, the CD quantification (S. Table 5-1) is consistent with the ThT and WB analysis (Figs. 5-2A and 5-2C), showing a higher capacity of **1** to reduce the  $\beta$ -sheet content of A $\beta$ 42, when compared to **2**.

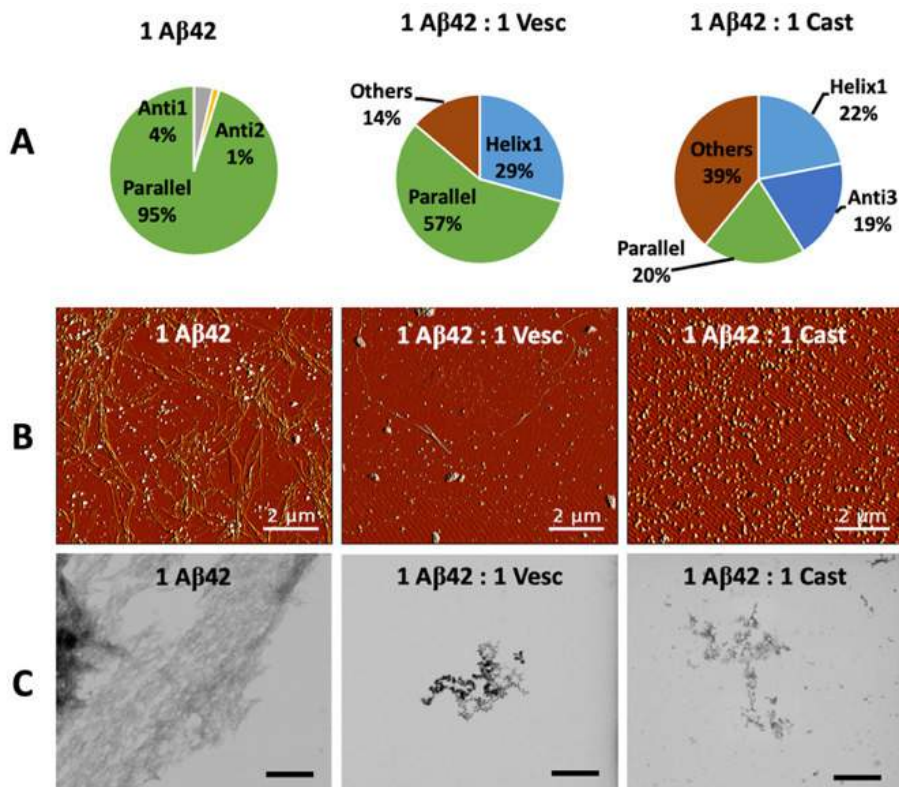


Figure 5-3. Loss of parallel  $\beta$ -sheets by A $\beta$ 42 (25 $\mu$ M) monitored by CD upon incubation with **1** and **2** under constant agitation at 37°C, during 24h. CD data were fitted using BeStSel - RMSD: 1.0283; NRMSD: 0.04966. B-C. **1** and **2** (25 $\mu$ M) induced the refolding of A $\beta$ 42 (25 $\mu$ M) into spherical assemblies detected by AFM and STEM, respectively. Scale bars 2 $\mu$ m (AFM) and 500nm (STEM).

The morphology of the generated assemblies was also monitored by AFM and STEM. Both **1** and **2** are highly efficient in remodelling the A $\beta$ 42 fibrils (Figs. 5-3B-C and S. Fig. 5-22, 5-23). Both during assembly (24h) and disassembly (7days) experiments peptide aggregates were detected instead of long fibrils. Of note is that the oligomers observed in the A $\beta$ 42 control, *i.e.* in the form of 10-15nm aggregates disappear in the presence of **1** or **2**, giving rise to non-fibrillar larger aggregates. AFM images (S. Fig. 5-22) also confirmed that the remodelling of the A $\beta$ 42 morphology is concentration-dependent.

Finally, considering that the association of the exposed hydrophobic peptide domains are the main driving forces for the intramolecular interactions, we evaluated the peptide-ligand binding energies (for both **1** and **2**) at the thermodynamic level using isothermal titration calorimetry (ITC)<sup>22</sup> (Table 5-1 and S. Fig. 5-24). In both cases  $\Delta G$  is negative, indicating a tendency for the interaction to occur and that the formed peptide:ligand complex is thermodynamically stable. Our results show negative values for the other two thermodynamic parameters, *i.e.*  $\Delta H$  and  $\Delta S$ . The enthalpic property, *i.e.*  $\Delta H$ , is a measure of the average energy released along the interaction process between the peptide and the ligand.<sup>23</sup> In this context, the negative value of  $\Delta H$  (similarly to the results obtained for  $\Delta G$ ) show that the formation of



peptide:ligand complexes are energetically favourable; however, the negative values for  $\Delta S$  indicate that the complexes are entropically unfavourable.

**Table 5-1.** ITC analysis of the interaction between A $\beta$ 42 and **1** or **2** under a A $\beta$ 42:polyphenol ratio of 1:1:  $K_1$  (mol<sup>-1</sup>)= 1.26e6 $\pm$ 0.18;  $K_2$  (mol<sup>-1</sup>)= 4.54e6 $\pm$ 0.56 using a one binding site model.

	$\Delta H$ (cal mol <sup>-1</sup> )	$\Delta G$ (cal mol <sup>-1</sup> )	$\Delta S$ (cal mol <sup>-1</sup> K <sup>-1</sup> )
A $\beta$ 42: <b>1</b> ratio 1:1	-9.28e4 $\pm$ 0.91	-11051 $\pm$ 502	-274 $\pm$ 61
A $\beta$ 42: <b>2</b> ratio 1:1	-4.58e4 $\pm$ 0.22	-9082 $\pm$ 290	-123 $\pm$ 45

This outcome can be explained by a progressive rupture of the hydration layer and release of counterions caused by the ring torsional degrees of freedom of each compound. In the case of **1** and **2**, there is a covalent link between their aromatic rings generating a significant structural rigidity that is probably reflected in their interaction with A $\beta$ 42. This rigidity might affect the hydrophobic interactions (*e.g.*  $\pi$ - $\pi$  stacking) promoting an increase on hydrogen bonding between the polyphenols and A $\beta$ 42. In fact, **1** is reported to be more hydrophilic than **2** and with increased capacity to participate in hydrogen bonding due to the spatial organization of its OH at position C1 of the glycosidic chain.<sup>24</sup> In addition, the interaction can also comprise charge shielding effects and/or molecular rearrangements of the ligand/peptide complexes. Interestingly, ITC data is consistent with the ThT, WB and CD results by suggesting that the complexes formed between compound **1** and A $\beta$ 42 are more stable and energetically more favourable.

Our data suggests that both **1** and **2** are interacting with A $\beta$ 42, remodelling its supramolecular organization and morphological presentation, reducing the concentration of oligomers. To evaluate if compounds **1** and **2** are in fact able to reduce the A $\beta$ 42-mediated cell death we performed a cytotoxicity assay using SH-SY5Y cells. To this end, A $\beta$ 42 (in the monomeric form) was incubated with SH-SY5Y cells and their viability was quantified after 24h using standardized MTS and Live/Dead assays. When A $\beta$ 42 was added at a concentration of 25 $\mu$ M, there was a decrease on cell viability to ~50% (S. Fig. 5-25). Maintaining this concentration of A $\beta$ 42, we added different concentrations of **1** and **2** (*i.e.* 12.5 $\mu$ M, 25 $\mu$ M and 50 $\mu$ M). Cellular metabolic activity is recovered to ~100%, after 24h (S. Fig. 5-29A) for all the tested conditions. In addition, Live/Dead assay (Figs. 5-4A) confirmed the same tendency showing that both **1** and **2** are able to rescue cell viability after 24h of incubation. Quantification of the percentage of live cells (S. Fig. 5-28) revealed that the cytotoxicity of A $\beta$ 42 resulted in less than 50% of live cells, however, **1** and **2** were able to rescue cells from death to a level similar to the control experiments, *i.e.* ~100% of live

cells. To understand if A $\beta$ 42 was still present in the cellular space, we visualized the peptide by immunofluorescence (using the 6E10 monoclonal antibody, Figs. 5-4B and S. Fig. 5-30). The results clearly show a marked reduction in the fluorescence for A $\beta$ 42 when **1** (but not **2**) is added to the culture medium, showing that **1** is clearly more effective than **2** in reducing the presence of A $\beta$ 42 aggregates in the cell culture. Of note, in the case of **1** (but not of **2**) the reduction in fluorescence is also concentration-dependent, being able to reduce the fluorescence to  $\sim$ 35% (S. Fig. 5-29B).

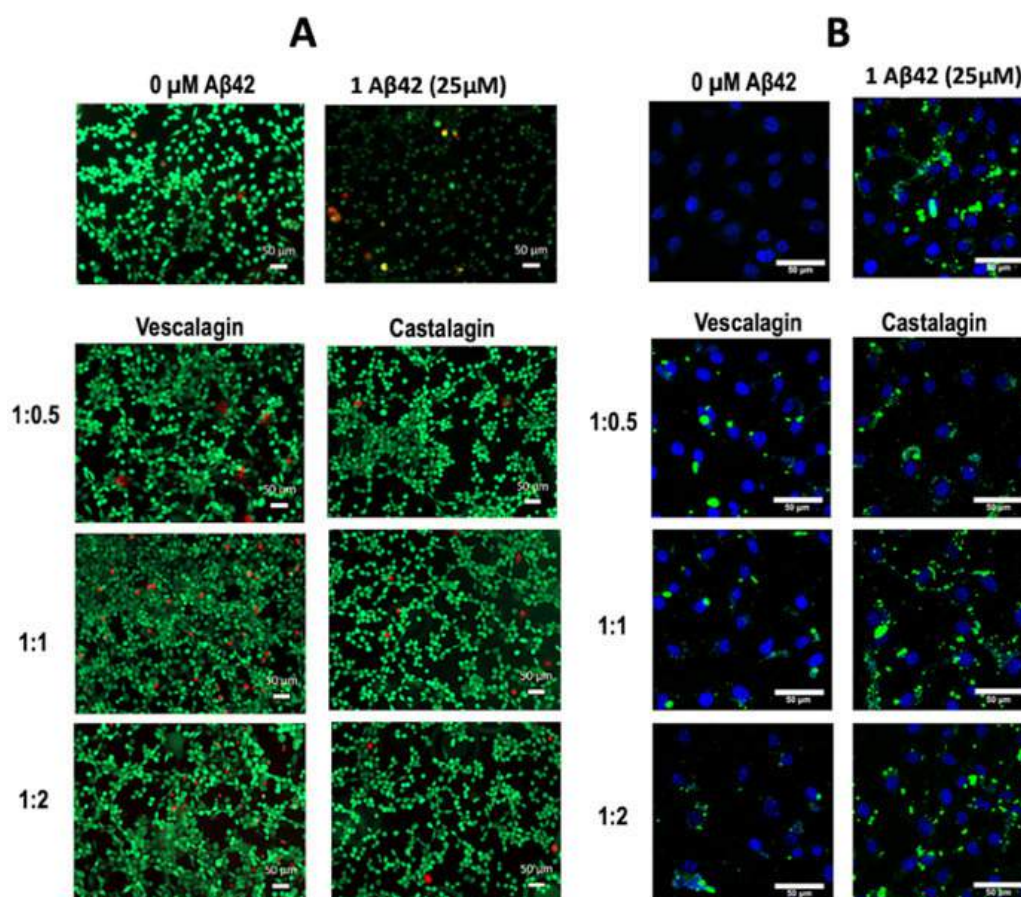


Figure 5-4. Live/Dead assay using SH-SY5Y cells incubated with different A $\beta$ 42:polyphenol ratios during 24h (green: live cells; red: dead cells). B. Immunofluorescence analysis of A $\beta$ 42 aggregates in the SH-SY5Y cell culture visualized by confocal microscopy (mAb 6E10, green) after incubation with **1** or **2** for 24h (A $\beta$ 42: green, cell nuclei: blue). Scale bar = 50  $\mu$ m.

Overall, our data suggests that there is a higher propensity of **1** to interact with A $\beta$ 42 when compared with **2**. While being surprising, as the structural difference between **1** and **2** is only in the spatial organization of their OH group at the C1 position of the glycosidic chain, it has been already reported that this difference leads to higher reactivity, increased polarity and lower lipophilicity of **1** compared to **2**.<sup>24</sup> Overall, **1** is able not only to rearrange the A $\beta$ 42 secondary structure, leading to the formation of non-cytotoxic structures (without their typical antiparallel  $\beta$ -sheets arrangement). Taken together, the ability of **1** to modulate the A $\beta$ 42 aggregation pathway eliminating the characteristic cytotoxic

oligomers is a step forward in the development of compounds with the capacity to control the trigger and/or progression of AD. Despite the higher activity of **1**, it is clear that **2** is also able to interact with A $\beta$ 42 and reduce its cytotoxicity towards the neuroblastoma cell line SH-SY5Y.

## 5.2 REFERENCES

1. Merluzzi, A. P.; Carlsson, C. M.; Johnson, S. C.; Schindler, S. E.; Asthana, S.; Blennow, K.; Zetterberg, H.; Bendlin, B. B., Neurodegeneration, synaptic dysfunction, and gliosis are phenotypic of Alzheimer dementia. *Neurology* 2018, 91 (5), e436-e443.
2. Selkoe, D. J., Translating cell biology into therapeutic advances in Alzheimer's disease. *Nature* 1999, 399 (6738), A23-A31.
3. Gremer, L.; Scholzel, D.; Schenk, C.; Reinartz, E.; Labahn, J.; Ravelli, R. B. G.; Tusche, M.; Lopez-Iglesias, C.; Hoyer, W.; Heise, H.; Willbold, D.; Schroder, G. F., Fibril structure of amyloid-beta(1-42) by cryo-electron microscopy. *Science* 2017, 358 (6359), 116-119.
4. Sengupta, U.; Nilson, A. N.; Kaye, R., The Role of Amyloid-beta Oligomers in Toxicity, Propagation, and Immunotherapy. *EBioMedicine* 2016, 6, 42-49.
5. Kaye, R.; Head, E.; Sarsoza, F.; Saing, T.; Cotman, C. W.; Necula, M.; Margol, L.; Wu, J.; Breydo, L.; Thompson, J. L.; Rasool, S.; Gurlo, T.; Butler, P.; Glabe, C. G., Fibril specific, conformation dependent antibodies recognize a generic epitope common to amyloid fibrils and fibrillar oligomers that is absent in prefibrillar oligomers. *Mol Neurodegener* 2007, 2, 18.
6. Necula, M.; Kaye, R.; Milton, S.; Glabe, C. G., Small molecule inhibitors of aggregation indicate that amyloid beta oligomerization and fibrillization pathways are independent and distinct. *J Biol Chem* 2007, 282 (14), 10311-24.
7. Andrieu, S.; Coley, N.; Lovestone, S.; Aisen, P. S.; Vellas, B., Prevention of sporadic Alzheimer's disease: lessons learned from clinical trials and future directions. *Lancet Neurol* 2015, 14 (9), 926-944.
8. Godyn, J.; Jonczyk, J.; Panek, D.; Malawska, B., Therapeutic strategies for Alzheimer's disease in clinical trials. *Pharmacol Rep* 2016, 68 (1), 127-38.
9. Ehrnhoefer, D. E.; Bieschke, J.; Boeddrich, A.; Herbst, M.; Masino, L.; Lurz, R.; Engemann, S.; Pastore, A.; Wanker, E. E., EGCG redirects amyloidogenic polypeptides into unstructured, off-pathway oligomers. *Nat Struct Mol Biol* 2008, 15 (6), 558-566.
10. Abeyawardhane, D. L.; Fernandez, R. D.; Murgas, C. J.; Heitger, D. R.; Forney, A. K.; Crozier, M. K.; Lucas, H. R., Iron Redox Chemistry Promotes Antiparallel Oligomerization of alpha-Synuclein. *J Am Chem Soc* 2018, 140 (15), 5028-5032.
11. Marambaud, P.; Zhao, H.; Davies, P., Resveratrol promotes clearance of Alzheimer's disease amyloid-beta peptides. *J Biol Chem* 2005, 280 (45), 37377-82.

12. Ramassamy, C., Emerging role of polyphenolic compounds in the treatment of neurodegenerative diseases: a review of their intracellular targets. *Eur J Pharmacol* 2006, 545 (1), 51-64.
13. Ehrnhoefer, D. E.; Bieschke, J.; Boeddrich, A.; Herbst, M.; Masino, L.; Lurz, R.; Engemann, S.; Pastore, A.; Wanker, E. E., EGCG redirects amyloidogenic polypeptides into unstructured, off-pathway oligomers. *Nat Struct Mol Biol* 2008, 15 (6), 558-566.
14. Palhano, F. L.; Lee, J.; Grimster, N. P.; Kelly, J. W., Toward the molecular mechanism(s) by which EGCG treatment remodels mature amyloid fibrils. *J Am Chem Soc* 2013, 135 (20), 7503-10.
15. Wright, J. S.; Johnson, E. R.; DiLabio, G. A., Predicting the activity of phenolic antioxidants: theoretical method, analysis of substituent effects, and application to major families of antioxidants. *J Am Chem Soc* 2001, 123 (6), 1173-83.
16. Araujo, A. R.; Pereira, D. M.; Aroso, I. M.; Santos, T.; Batista, M. T.; Cerqueira, M. T.; Marques, A. P.; Reis, R. L.; Pires, R. A., Cork extracts reduce UV-mediated DNA fragmentation and cell death. *Rsc Adv* 2015, 5 (116), 96151-96157.
17. Porat, Y.; Abramowitz, A.; Gazit, E., Inhibition of amyloid fibril formation by polyphenols: structural similarity and aromatic interactions as a common inhibition mechanism. *Chem Biol Drug Des* 2006, 67 (1), 27-37.
18. Jarrett, J. T.; Lansbury, P. T., Seeding "one-dimensional crystallization" of amyloid: A pathogenic mechanism in Alzheimer's disease and scrapie? *Cell* 1993, 73 (6), 1055-1058.
19. Bieschke, J.; Russ, J.; Friedrich, R. P.; Ehrnhoefer, D. E.; Wobst, H.; Neugebauer, K.; Wanker, E. E., EGCG remodels mature alpha-synuclein and amyloid-beta fibrils and reduces cellular toxicity. *Proc Natl Acad Sci U S A* 2010, 107 (17), 7710-5.
20. Barrow, C. J.; Yasuda, A.; Kenny, P. T.; Zagorski, M. G., Solution conformations and aggregational properties of synthetic amyloid beta-peptides of Alzheimer's disease. Analysis of circular dichroism spectra. *J Mol Biol* 1992, 225 (4), 1075-93.
21. Micsonai, A.; Wien, F.; Kernya, L.; Lee, Y. H.; Goto, Y.; Refregiers, M.; Kardos, J., Accurate secondary structure prediction and fold recognition for circular dichroism spectroscopy. *Proc Natl Acad Sci U S A* 2015, 112 (24), E3095-103.
22. Chandler, D., Interfaces and the driving force of hydrophobic assembly. *Nature* 2005, 437 (7059), 640-7.
23. de Ruiter, A.; Oostenbrink, C., Free energy calculations of protein-ligand interactions. *Curr Opin Chem Biol* 2011, 15 (4), 547-52.
24. Vivas, N.; Laguerre, M.; Planet de Boissel, I.; Vivas de Gaulejac, N.; Nonier, M. F., Conformational interpretation of vescalagin and castalagin physicochemical properties. *Journal of agricultural and food chemistry* 2004, 52 (7), 2073-8.

## SUPPLEMENTARY INFORMATION

▪ **Materials and methods**Purification and characterization of vescalagin (1) and castalagin (2)

The extraction, purification and identification of vescalagin (**1**) and castalagin (**2**) was optimized and performed following a previous work.<sup>3</sup> Briefly, **1** and **2** were obtained from a raw extract from cork powder (Amorim Cork Composites, Portugal) collected by contact with water under reflux for 6h. After cooling, the liquid fraction was filtered and the solvent was partially removed by vacuum evaporation. The final solid extracts were recovered by freeze-drying. The cork water extract was loaded into a semi-preparative chromatographic column, Waters Atlantis OBD Prep T3 (5 $\mu$ m 19x250mm) and **1** and **2** were collected at their respective retention times using the mobile phases A - water:acetic acid 98:2 (v/v) and B - water:acetonitrile:acetic acid 78:20:2 (v/v/v), under the following gradient: 100% A (t=0min) – 100% A (t=15min) – 70% A : 30% B (t=30min) – 100% B (t=35min) – 100% B (t=50min) – 100% A (t=52min) – 100% A (t=57min). The flow rate was maintained at 5ml.min<sup>-1</sup> and the injection volume was 5mL. The purity of **1** and **2** was determined by HPLC (KANUER, Germany) using a 250 mm x 4.6 mm reverse-phase C18 Atlantis column (Waters, UK), a flow of 1 mL/min, using the same mobile phases and gradients (S. Figs. 5-1, 5-3). Mass spectra were acquired on an electrospray ionization (ESI) mass spectrometer (MS) Water Micromass Quattro (Waters, USA) under positive-ion mode (S. Figs. 5-4, 5-5). <sup>1</sup>H NMR spectra of both **1** and **2** were recorded on a Bruker Avance III spectrometer (Bruker, Germany) at 25°C in D<sub>2</sub>O. The chemical shifts ( $\delta$ ) are reported in ppm downfield to the solvent signal (S. Figs. 5-6, 5-7).

Peptide preparation

Human amyloid  $\beta$ -peptide (1-42) was obtained by custom synthesis from GeneCust® Europe (Dudelange, Luxembourg). Stock solutions of 0.45mg were prepared by dissolving 10mg of amyloid  $\beta$ -peptide (1-42, A $\beta$ 42) in 2.2 mL of HFIP (Fluorochem Ltd, UK) according to the protocol described by Stine *et al.* Briefly, A $\beta$ 42 was dissolved in HFIP (5mg/mL) during 30min at room temperature. HFIP was allowed to evaporate in open tubes overnight in the fume hood, and afterwards during an additional 1h under vacuum. A solution of A $\beta$ 42 (5mM) in DMSO (*i.e.* 20 $\mu$ l of fresh dry DMSO to 0.45mg of A $\beta$ 42) was sonicated for 10min in an ultra-sound bath. Immediately afterwards, ice-cold water (monomeric form) or

10mM HCl (fibrillar form) was added to a final concentration of 100 $\mu$ M of Ab42. Finally, the Ab42 solution was vortex for 15s prior to use.

### A $\beta$ 42 peptide aggregation studies

**Thioflavin T (ThT).** Fibril formation was followed by ThT assay (assembly, Figs. 5-2A and S5-13) during 196h. A $\beta$ 42 peptide stock solution was prepared as described above, and fibril formation was induced (under a cold-water bath) by fast mixing of 2 $\mu$ L of A $\beta$ 42 DMSO with 98 $\mu$ L of Phosphate Buffer (5mM, with 0.1% of sodium azide, pH 7.2). ThT fluorescence was measured by mixing A $\beta$ 42 solution (final concentration of 25 $\mu$ M) with ThT (final concentration of 40 $\mu$ M) and different concentrations of **1** and **2**, *e.g.* concentration ratios A $\beta$ 42:polyphenol of 1:0.5; 1:1 and 1:2. The ThT fluorescence was then recorded in a Fluorescence Spectrometer (Jasco, FP-8500, Japan) during 196h using an excitation wavelength of 435nm and an emission wavelength of 465nm. Each experiment was repeated in triplicate. The experiments for the disassembly of the A $\beta$ 42 fibrils (Figs. 5-2B and S. Fig. 5-14) were performed with A $\beta$ 42 fibrillar form, for 24h using the same experimental protocol.

**Western Blot (WB).** WB analysis of the A $\beta$ 42 aggregated forms in the presence and absence of **1** and **2** (at different A $\beta$ 42:polyphenol ratios of 1:0.5; 1:1 and 1:2 for 24h or 7 days) allowed the visualization of the relative amount of remodelled peptide. Samples were dissolved on Laemmli buffer (1x) without reducing agent (10 $\mu$ g A $\beta$ 42 per lane). Afterwards, samples were electrophoretically resolved in a 12% Bis-Tris Gel Invitrogen NuPAGE, with MES SDS Running Buffer and were transferred to nitrocellulose membranes using iBlot 2 System and blocked with 4% bovine serum albumin (BSA) in TBS containing 0.1% Tween-20 (TBS-T). The membranes were then incubated at 4 °C with the 6E10 (anti-A $\beta$  1-16 antibody – 1:1000) overnight, followed by IRDye 800CW Goat anti-Mouse IgG Secondary Antibody (RT, during 1.5h;1:10000). After each antibody incubation, the membranes were washed with TBS-T. Signal were detected (acquisition time: 2min) in Odyssey Fc Imaging System (LI-COR Inc., Nebraska USA).

**Circular Dichroism (CD).** CD was performed using a 1mm path length cell at 37°C in a CD spectrometer (Jasco, J1500, Japan). Spectra (S. Figs. 5-20, 5-21) were recorded in the range between 190–260nm with a scan rate of 10nm/min and a response time of 1s. Three scans were accumulated for each spectrum. For all the CD experiments, the A $\beta$ 42 concentration was 25 $\mu$ M, and the A $\beta$ 42/polyphenol ratios were 1:0.5 and 1:1. Results are expressed as  $\theta$  [mdeg].

**Isothermal Titration Calorimetry (ITC).** ITC was used to evaluate the interactions between **1** and **2** and A $\beta$ 42. ITC measurements were performed using a MicroCal VP-ITC (MicroCal Inc., Northampton, MA,

USA). Samples were degassed in a ThermoVac system (MicroCal) prior to use. **1** (or **2**) was titrated into an A $\beta$ 42 solution (10 $\mu$ M) in PBS. A first injection of 2 $\mu$ L (neglected in the analysis) followed by other 27 injections of 10 $\mu$ L each were performed under continuous stirring at 286 rpm. All the measurements were done at 25°C. PBS buffer was titrated to peptide solution to establish the baseline analysis. ITC experiment offers the basic thermodynamic profile for the established interactions, including three key binding parameters: Gibbs energy (that can be calculated from the equilibrium association constant K), enthalpy and entropy of interaction:

$$\Delta G = - RT \ln K = RT \ln k_d$$

where K is the equilibrium association constant,  $k_d$  is the equilibrium dissociation constant, T is the thermodynamic or absolute temperature and R is the gas constant.

The binding Gibbs energy change can be calculated from the enthalpic and entropic contributions by means of:

$$\Delta G = \Delta H - T\Delta S$$

to obtain such thermodynamic parameters, the raw data of ligand interaction were analysed by fitting the heat isotherms by a nonlinear least-squares analysis to a one-binding-site model.

**Atomic Force Microscopy (AFM).** For the acquisition of AFM images (Figs. 5-3B, S. Figs. 5-22, 5-23), freshly cleaved mica was functionalized with a drop of (3-Aminopropyl)triethoxysilane (APTES, 200 $\mu$ L), during 30 min at room temperature. Then, micas were rinsed with deionized water and dried under a nitrogen flux. Each sample, A $\beta$ 42 peptide (10 $\mu$ M) in the presence and absence of **1** and **2**, were spotted onto the functionalized mica during 30min, and then washed with water and dried under nitrogen.

AFM images were acquired using a JPK Nanowizard 3 (JPK, Germany) in air at room temperature under AC mode. The scans were acquired at a 512 x 512 pixels resolution using ACTA-SS probes ( $k \sim 37$ N/m, AppNano, USA), a drive frequency of  $\sim 254$ kHz, a setpoint of  $\sim 0.5$ V and a scanning speed of 1.0Hz.

#### Cell toxicity assays

Neuroblastoma SH-SY5Y cells were cultured at 37°C in a humidified 95/5% air/CO<sub>2</sub> atmosphere using Dulbecco's modified Eagles medium F-12 (Gibco, UK) supplemented with 10% FBS (Gibco, UK) and 1% ATB (Gibco, UK) solution. Cell medium were replaced each 2 days and cells were sub-cultured once they reached 90% confluence. Cells were plated at a density of 25 000 cells per well on 96-well plates containing DMEM/F-12 media (for MTS assay) and plated at a density of 50 000 cells per well on 24-well

plates containing DMEM/F-12 media (for the live/dead assay). A typical experiment included the culture of the neuroblastoma cell line (SHSY-5Y) during 24h in the absence or presence of **1** or **2** at different concentrations. Afterwards, A $\beta$ 42 were added to the culture medium, and, after an additional 24h, the cells were evaluated for their metabolic activity. Both **1** and **2** were sterilized by autoclaving before use. A $\beta$ 42 peptide was sterilized by UV and immediately added to the cells after being reconstituted in DMSO (0.02%) and diluted into DMEM/F-12 media.

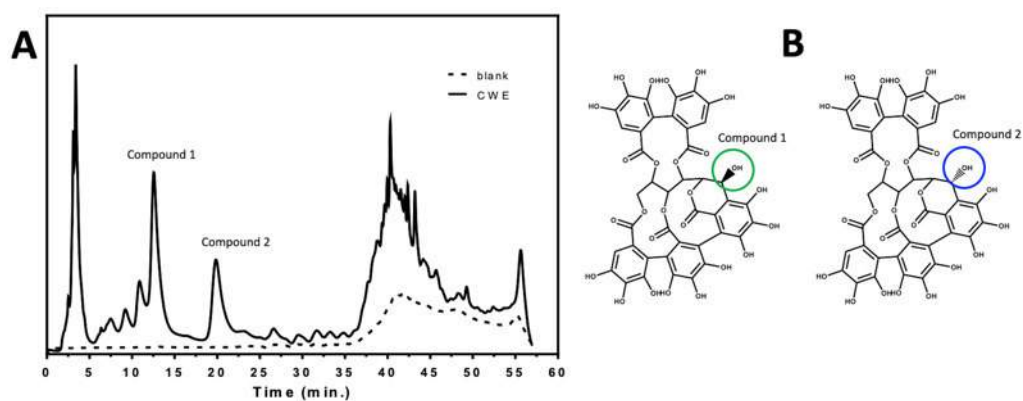
**MTS assay.** The A $\beta$ 42 cytotoxicity (Figs. S5-25, S5-26 and S5-29) was measured using a colorimetric assay for assessing cell metabolic activity, 24h after the addition of A $\beta$ 42 at a concentration of 25 $\mu$ M. The absorbance of the metabolic activity was assessed by MTS (CellTiter 96® AQueous One Solution Cell Proliferation Assay, Promega) according to the supplier's instructions. The relative metabolic activity (%) of the SH-SY5Y cells was determined for each experimental condition. The optical density (OD) was recorded at 490nm with a Synergy HT microplate reader (Bio-Tek Instruments). *p*-values were calculated using two-tailed t-test. Results are presented as mean  $\pm$  SEM of 6 independent experiments for each experimental condition.

**Live/Dead assay.** Cell viability was also evaluated by Live/Dead assay using calcein AM to stain live cells and propidium iodide (PI) to stain dead cells (Figs. 5-4A and S. Fig. 5-27). Viable cells were stained in green and dead cells were stained in red. Shortly, cells were incubated for 20min with both dyes and then observed under a fluorescence microscope (Axio Imager Z1m, Zeiss).

**Protein expression.** For immunostaining, fluorescence images (Figs. 5-4B and S. Fig. 5-30), after 24h of culture, the samples were washed twice with PBS, fixed in 10% neutral buffered formalin for 30min at 4 ° C, permeabilised with 0.1% Triton X-100 in PBS for 5min, and blocked with 3% BSA in PBS for 30min at room temperature. To evaluate the accumulation of A $\beta$ 42 in its different forms, a primary antibody against A $\beta$ 42 (1-16) (Biotin anti- $\beta$ -Amyloid, 1-16 Antibody, Mouse IgG1 1:200 in 1% w/v BSA/PBS, Biolegend) was employed, followed by rabbit anti-mouse Alexafluor-488 (1:500 in 1% w/v BSA/PBS, anti-mouse, Invitrogen). A phalloidin-TRITC conjugate was used (1:200 in PBS for 30min, Sigma) to assess cytoskeleton organisation. Nuclei were counterstained with 1mg/mL of 4,6-diamidino-2-phenylindole (DAPI; Sigma) for 30min. Samples were washed with PBS, mounted with Vectashield® (Vector) on glass slides and observed under a confocal laser scanning microscope (Leica TCS SP8, Leica Microsystems).

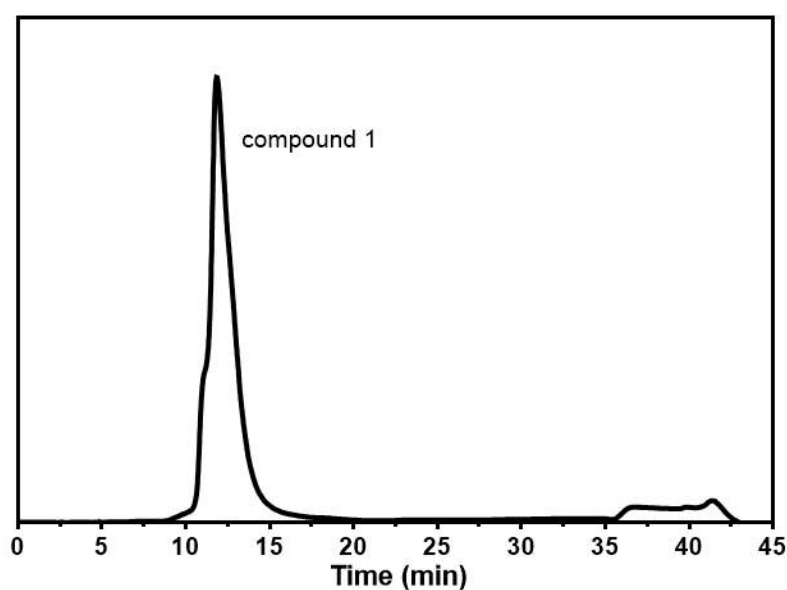


- Purification and characterization of vescalagin (1) and castalagin (2)

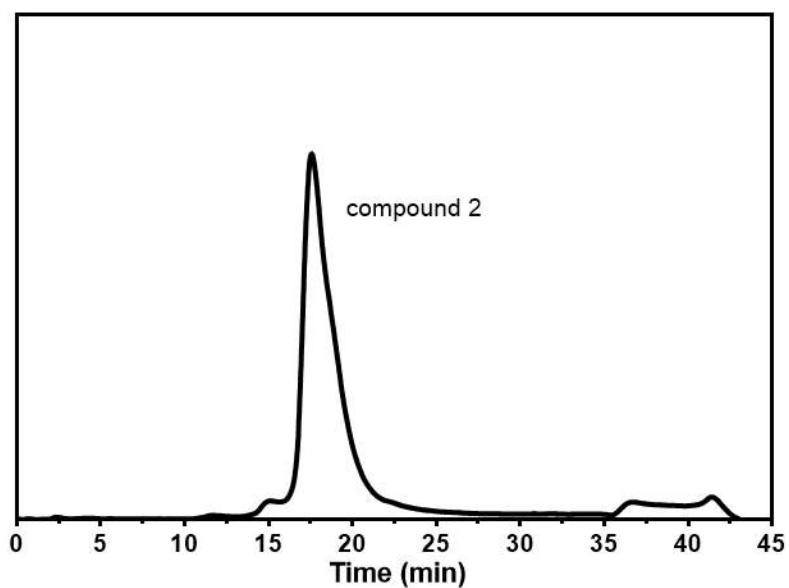


Supplementary Fig. 5-1. A. Preparative HPLC chromatogram of cork water extract with the identification of the peaks that correspond to vescalagin (1) and castalagin (2). B. Chemical structure of both isomers, vescalagin (1) and castalagin (2), with the position C1 (that identifies the main structural difference between 1 and 2) highlighted.

HPLC characterization of purified 1 and 2.

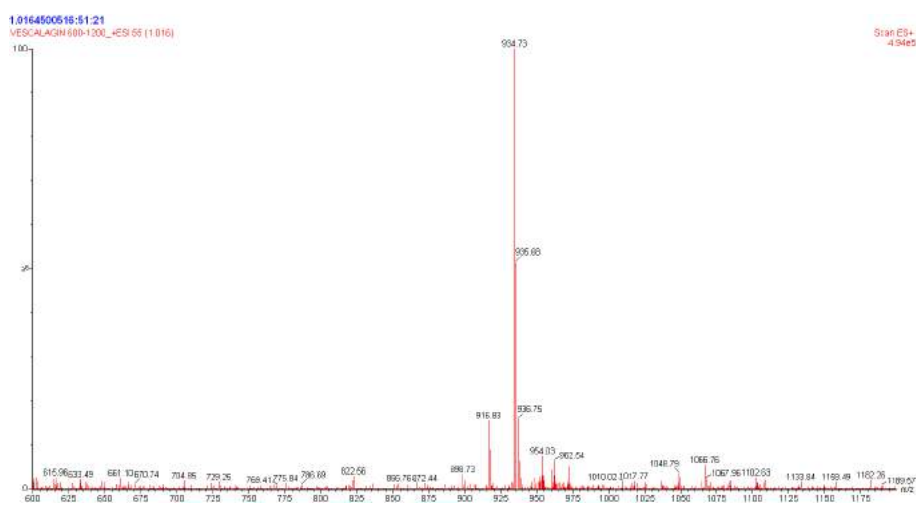


Supplementary Fig. 5-2. HPLC run showing the purified compound 1 - vescalagin.

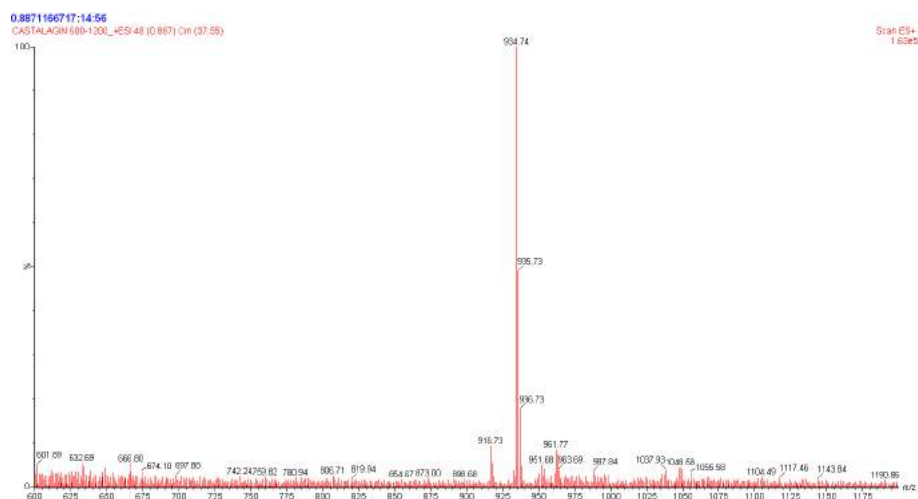


Supplementary Fig. 5-3. HPLC run showing the purified compound 2 - castalagin.

ESI-MS ( $m/z$ ): [M]<sup>+</sup> 935



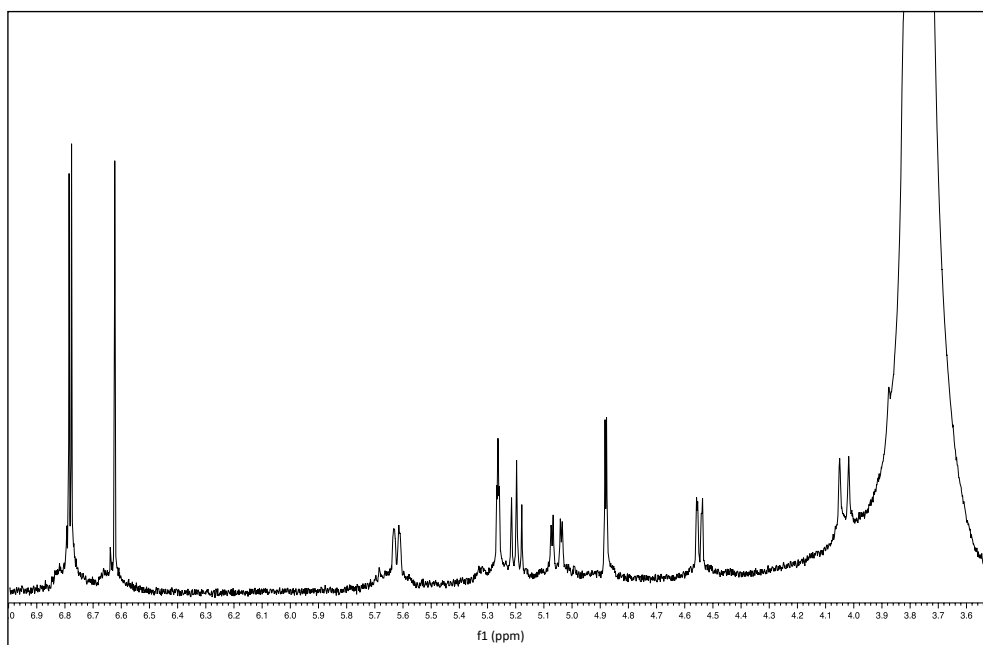
Supplementary Fig. 5-4. Positive ESI-MS spectrum of vescalagin (1).



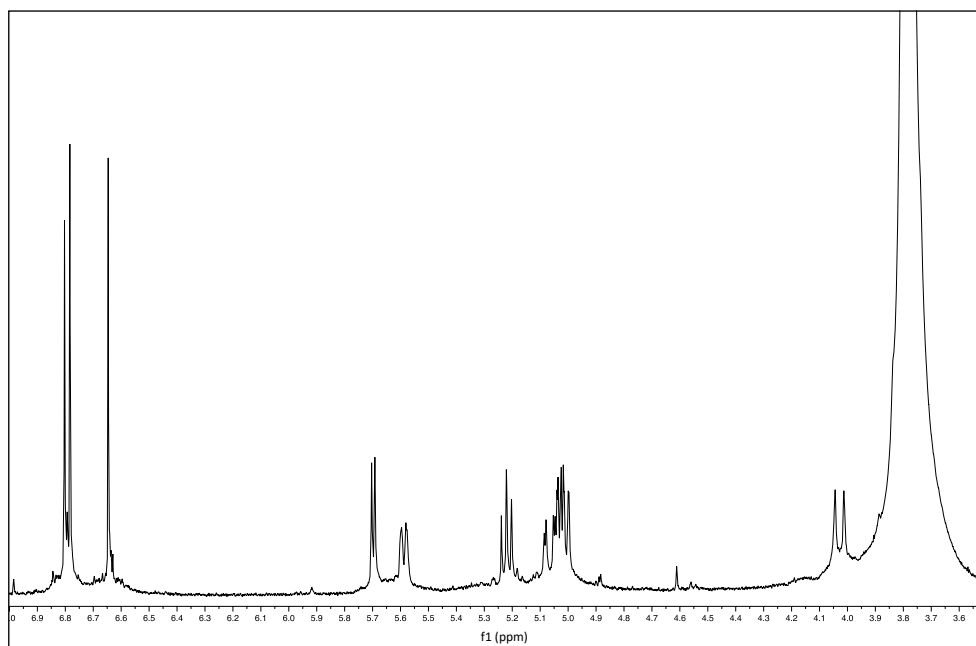
Supplementary Fig. 5-5. Positive ESI-MS spectrum of castalagin (2).

$^1\text{H}$  NMR (400 MHz,  $\text{D}_2\text{O}$ , 298 K)

$^1\text{H}$  NMR spectra was recorded on Bruker Avance III spectrometer (Bruker, Germany) at 25 °C in  $\text{D}_2\text{O}$  (S. Figs. 6-S7). The assignments reported below were made following the ones reported by Puech et al.[3] and Douat et al.[4]



Supplementary Fig. 5-6.  $^1\text{H}$  NMR spectra of vescalagin (1).



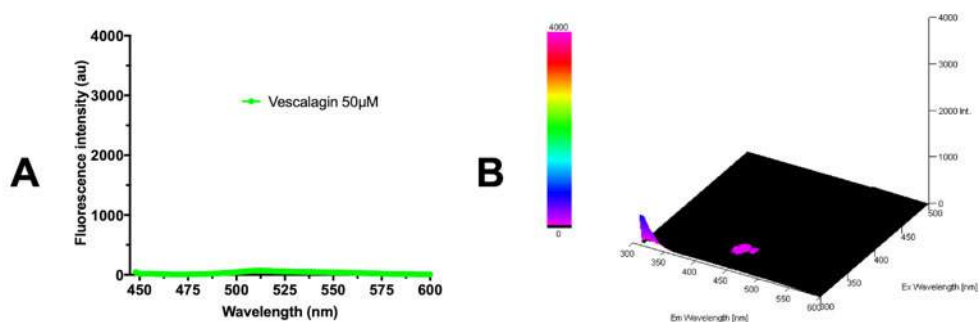
Supplementary Fig. 5-7.  $^1\text{H}$  NMR spectra of castalagin (2).

***Vescalagin (1)***

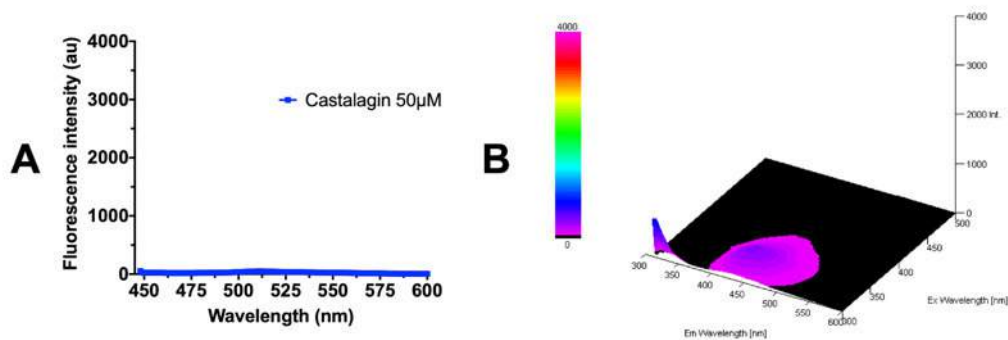
$^1\text{H}$  NMR (400 MHz, DMSO- $d_6$ , 298 K):  $\delta$  6.91 (s, 1H);  $\delta$  6.51 (s, 1H);  $\delta$  6.36 (s, 1H);  $\delta$  4.93 (m, 1H, H-5);  $\delta$  4.90 (m, 1H, H-2);  $\delta$  4.88 (m, 1H, H-4);  $\delta$  4.87 (m, 1H, H-1);  $\delta$  4.85 (m, 1H, H-3);  $\delta$  4.03 (dd, 1H,  $J=4.0, 6.5\text{Hz}$ , H-6);  $\delta$  3.89 (dd, 1H,  $J=4.0, 6.5\text{Hz}$ , H-6').

***Castalagin (2)***

$^1\text{H}$  NMR (400 MHz, DMSO- $d_6$ , 298 K):  $\delta$  6.62 (s, 1H);  $\delta$  6.51 (s, 1H);  $\delta$  6.37 (s, 1H);  $\delta$  4.92 (m, 1H, H-1);  $\delta$  4.90 (d, 1H,  $J=7.1\text{ Hz}$ , H-6);  $\delta$  4.82 (m, 1H, H-5);  $\delta$  4.80 (m, 1H, H-4);  $\delta$  4.78 (m, 1H, H-2);  $\delta$  4.77 (m, 1H, H-3);  $\delta$  3.96 (d, 1H,  $J=12\text{Hz}$ , H-6').

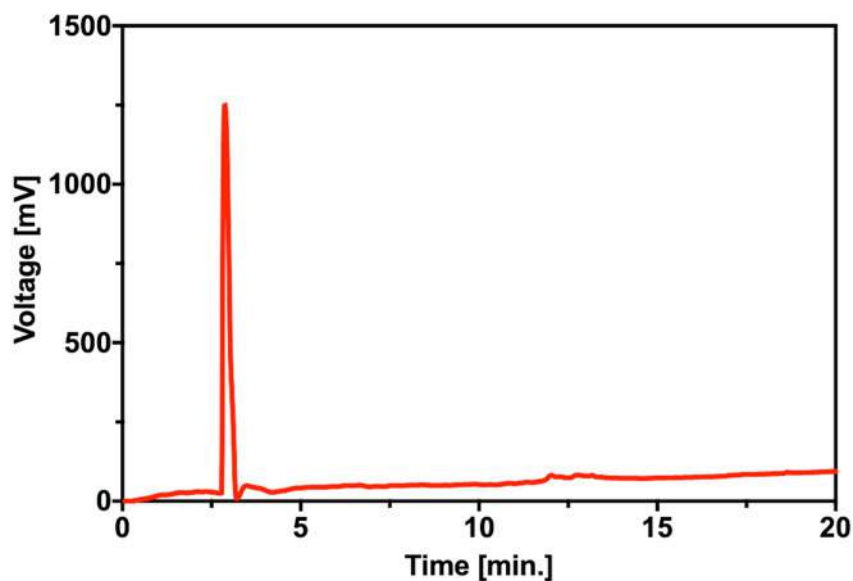


Supplementary Fig. 5-8. A. Fluorescence spectrum of vescalagin (1, 50  $\mu\text{M}$ ) acquired using a  $\lambda_{\text{ex}} = 435$  nm and a  $\lambda_{\text{em}} = 445$ -600 nm; B. 3D fluorescence spectra for vescalagin (1, 50  $\mu\text{M}$ ) using the following acquisition parameters:  $\lambda_{\text{ex}} = 300$ -500 nm;  $\lambda_{\text{em}} = 300$ -600 nm; excitation bandwidth = 5nm; emission bandwidth = 10nm; response = 2s.

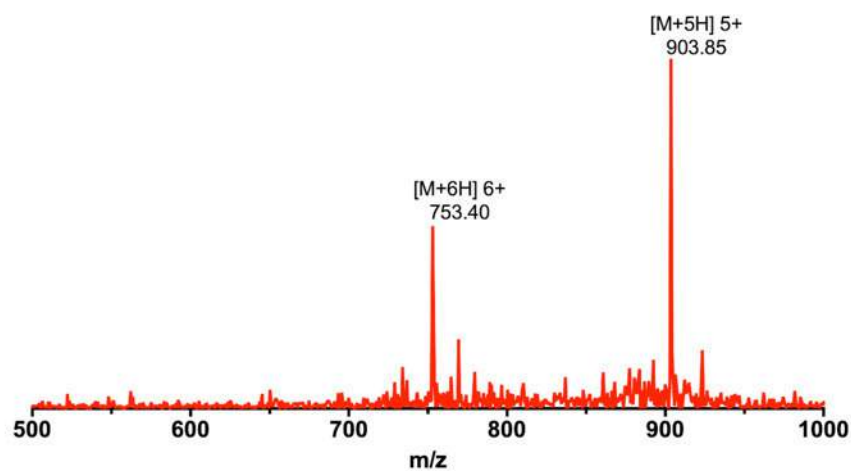


Supplementary Fig. 5-9. A. Fluorescence spectrum of castalagin (2, 50  $\mu\text{M}$ ) acquired using a  $\lambda_{\text{ex}} = 435$  nm and a  $\lambda_{\text{em}} = 445$ -600 nm; B. 3D fluorescence spectra for castalagin (2, 50  $\mu\text{M}$ ) using the following acquisition parameters:  $\lambda_{\text{ex}} = 300$ -500 nm;  $\lambda_{\text{em}} = 300$ -600 nm; excitation bandwidth = 5nm; emission bandwidth = 10nm; response = 2s.

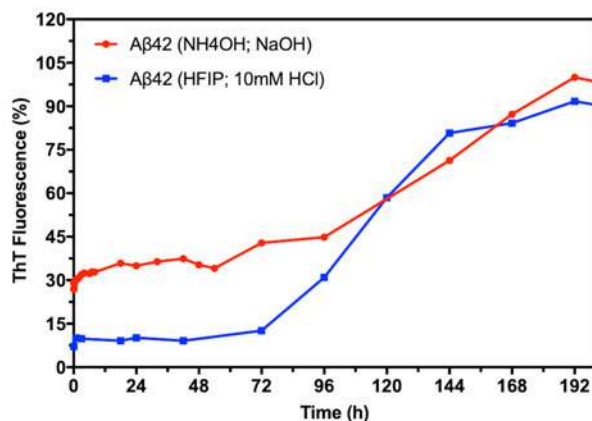
- A $\beta$ 42 peptide aggregation studies



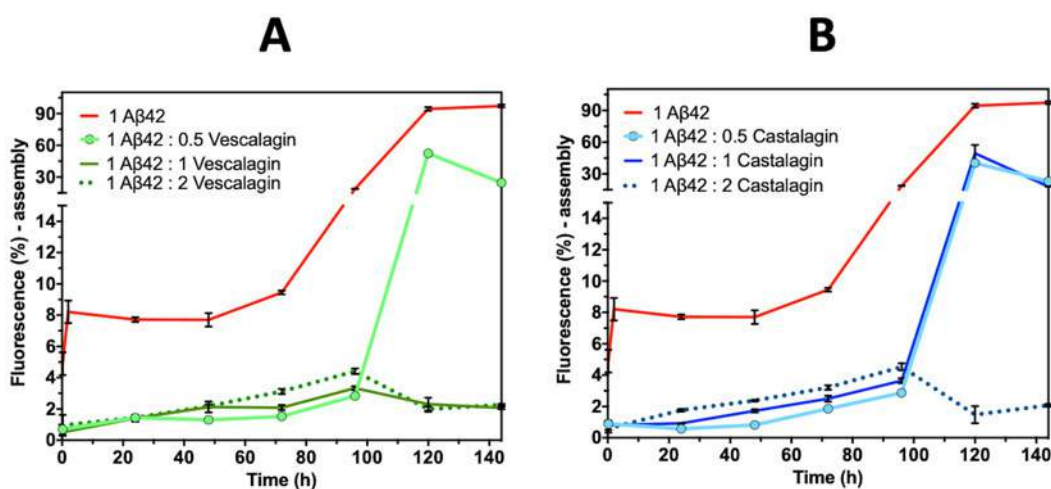
Supplementary Fig. 5-10. HPLC run of the A $\beta$ 42 peptide used throughout the present work. A sample of peptide was dissolved in acetonitrile (0.02% DMSO) and the HPLC run was performed using a reverse phase C18 column (4.6x250mm, Waters, UK), a mixture of eluents (A – acetonitrile, 0.1% trifluoroacetic acid, and B – water, 0.1% trifluoroacetic acid), starting with 10% A (t=0min) and ending with 100% B (t=20min); using a flow rate of 1.0mL/min; column.



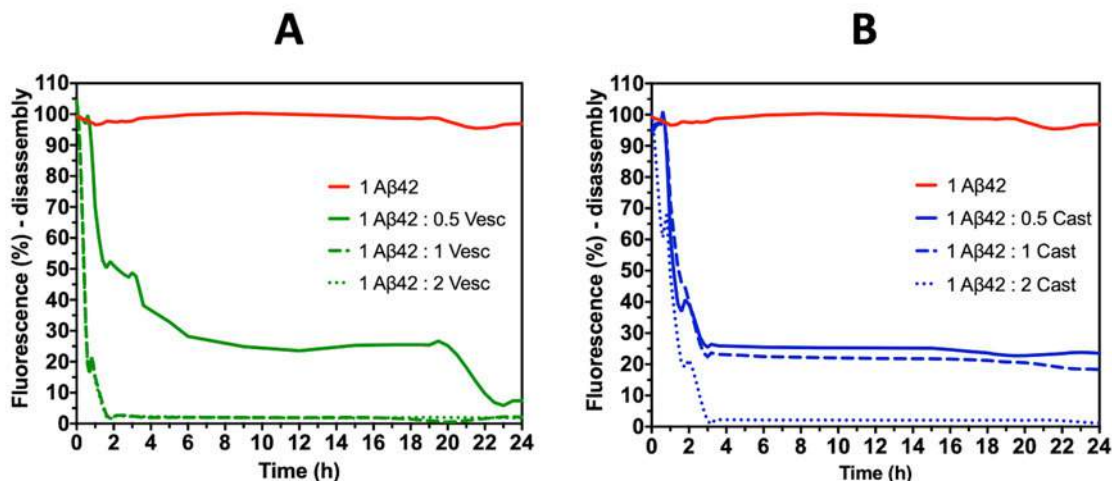
Supplementary Fig. 5-11. Positive ESI-MS spectrum of A $\beta$ 42 sample used throughout the present work, showing the characteristic [M+5H]<sup>5+</sup> and [M+6H]<sup>6+</sup> peaks of A $\beta$ 42.



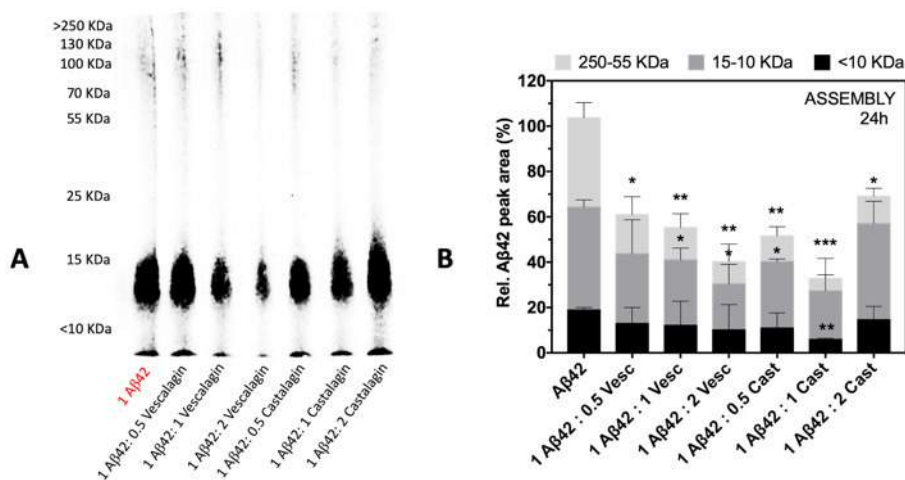
Supplementary Fig. 5-12. A $\beta$ 42 aggregation kinetics monitored by the ThT binding assay. A $\beta$ 42 samples were prepared by two methods: Method 1 (red line) - A $\beta$ 42 was dissolved in 10% (w/v) NH<sub>4</sub>OH at a concentration of 0.5mg/ml. The peptide was incubated for 10min at room temperature followed by sonication (5min). The NH<sub>4</sub>OH was removed by lyophilization overnight. Immediately prior to use, the A $\beta$ 42 was dissolved in 60mM NaOH; Method 2 (blue line) - A $\beta$ 42 was dissolved in HFIP (5mg/ml) at room temperature, during 30min. We allowed HFIP to evaporate in open tubes overnight in the fume hood, and then during 1h under vacuum. An aliquot of 5mM A $\beta$ 42 in DMSO (20 $\mu$ l of fresh dry DMSO to 0.45mg of A $\beta$ 42) was sonicated for 10min in a bath sonicator. Immediately after, ice-cold water was added to a final concentration of 100 $\mu$ M of A $\beta$ 42, followed by vortexing during 15s. ThT fluorescence was monitored in 0.1mM phosphate buffer, pH 7.2, 0.02% NaN<sub>3</sub> (using 25 $\mu$ M of A $\beta$ 42).



Supplementary Fig. 5-13. A $\beta$ 42 assembly kinetics (Method 2) using the ThT assay. A. Assembly of A $\beta$ 42 in the presence of different concentrations of 1. B. Assembly of A $\beta$ 42 in the presence of different concentrations of 2. Compounds were added at the lag phase of the A $\beta$ 42 aggregation profile and fluorescence was measured over 140h. Both experiments (A-B) were performed at room temperature. ThT fluorescence data collected using the following parameters:  $\lambda_{ex}$  = 435nm,  $\lambda_{em}$  = 465nm; excitation bandwidth = 5nm; emission bandwidth = 10nm; response = 2s.

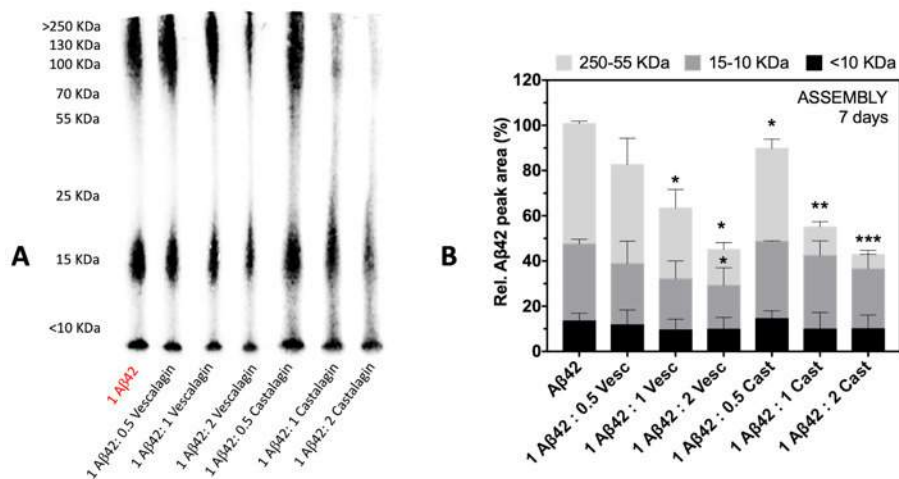


Supplementary Fig. 5-14. A $\beta$ 42 disassembly kinetics (Method 2) using the ThT assay. A. Disassembly of A $\beta$ 42 in the presence of different A $\beta$ 42:polyphenol ratios for 1. B. Disassembly of A $\beta$ 42 in the presence of different A $\beta$ 42:polyphenol ratios for 2. Compounds were added at the plateau phase of the A $\beta$ 42 aggregation profile and fluorescence was measured over 24h. Both experiments (A-B) were performed at room temperature. ThT fluorescence data collected using the following parameters:  $\lambda_{ex}$  = 435nm,  $\lambda_{em}$  = 465nm; excitation bandwidth = 5nm; emission bandwidth = 10nm; response = 2s.

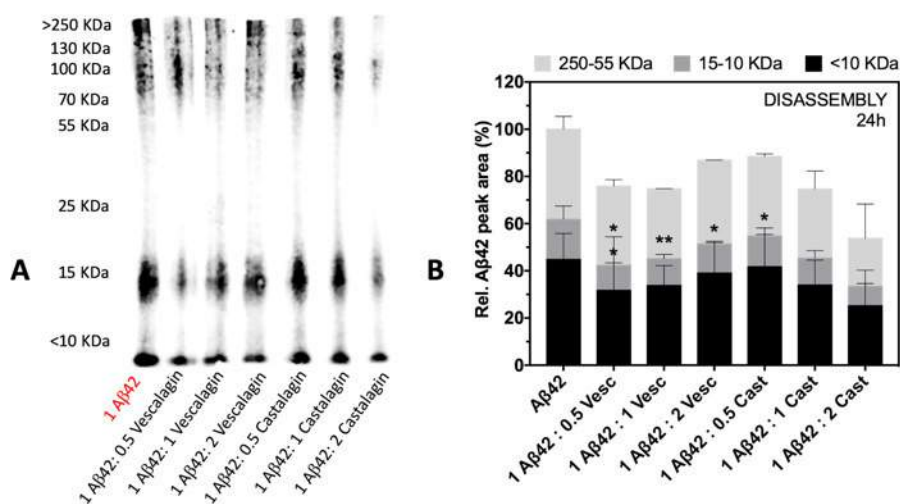


Supplementary Fig. 5-15. A. Representative WB image and B. relative densitometric bar graphs of the A $\beta$ 42 assembly in the presence of vescalagin (1) and castalagin (2). Both compounds were incubated during 24h (under A $\beta$ 42:polyphenol ratios of 1:0.5, 1:1 and 1:2). WBs were performed in a NuPAGE 12% Bis-Tris Gels, using MES running buffer, and incubated with 6E10 (anti-A $\beta$ 1-16) antibody.

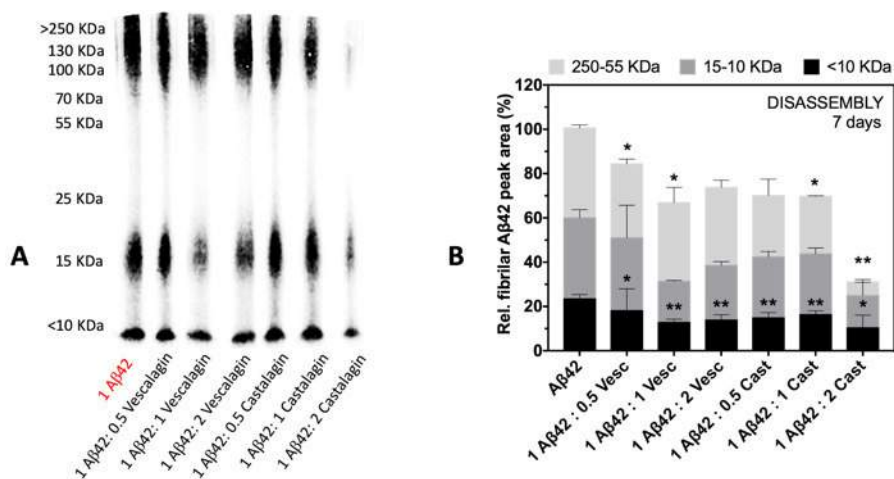




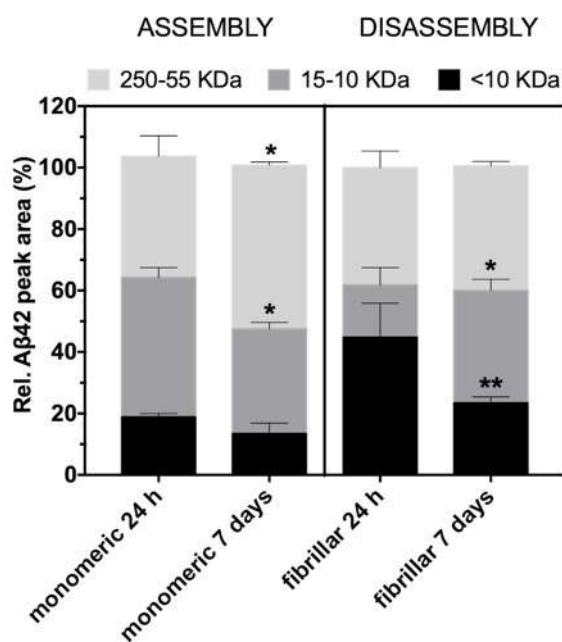
Supplementary Fig. 5-16. A. Representative WB image and B. relative densitometric bar graphs of the Aβ42 assembly in the presence of vescalagin (1) and castalagin (2). Both compounds were incubated during 7 days (under Aβ42:polyphenol ratios of 1:0.5, 1:1 and 1:2). WBs were performed in a NuPAGE 12% Bis-Tris Gels, using MES running buffer, and incubated with 6E10 (anti-Aβ1-16) antibody.



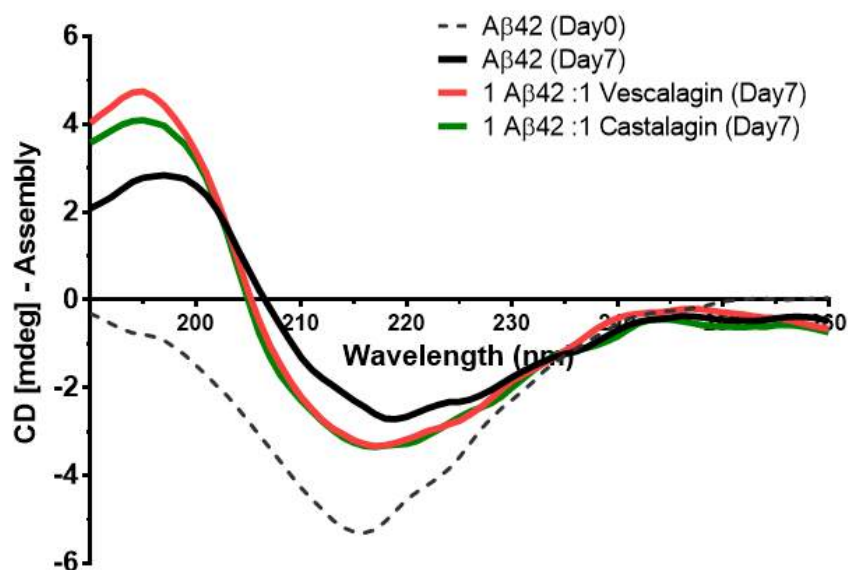
Supplementary Fig. 5-17. A. Representative WB image and B. relative densitometric bar graphs of the Aβ42 disassembly in the presence of vescalagin (1) and castalagin (2). Both compounds were incubated during 24h (under Aβ42:polyphenol ratios of 1:0.5, 1:1 and 1:2). WBs were performed in a NuPAGE 12% Bis-Tris Gels, using MES running buffer, and incubated with 6E10 (anti-Aβ1-16) antibody.



Supplementary Fig. 5-18. A. Representative WB image and B. relative densitometric bar graphs of the Aβ42 disassembly in the presence of vescalagin (1) and castalagin (2). Both compounds were incubated during 7 days (under Aβ42:polyphenol ratios of 1:0.5, 1:1 and 1:2). WBs were performed in a NuPAGE 12% Bis-Tris Gels, using MES running buffer, and incubated with 6E10 (anti-Aβ1-16) antibody.



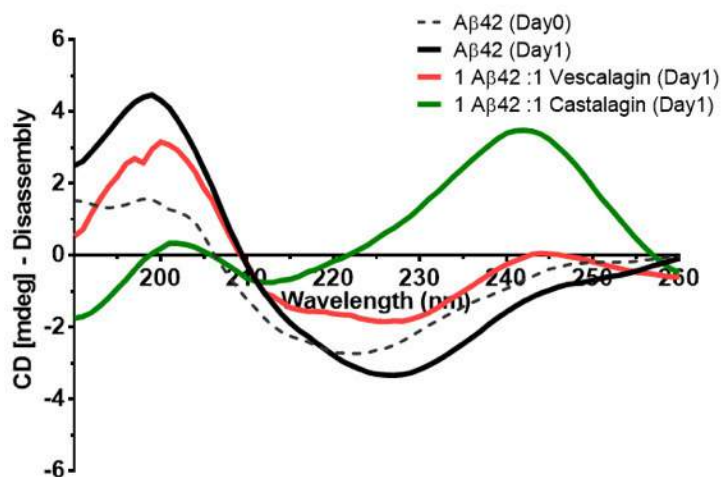
Supplementary Fig. 5-19. Relative densitometric bar graphs of Aβ42 assembly and disassembly for 24h and 7 days, respectively. WBs were performed in a NuPAGE 12% Bis-Tris Gels, using MES running buffer, and incubated with 6E10 (anti-Aβ1-16) antibody.



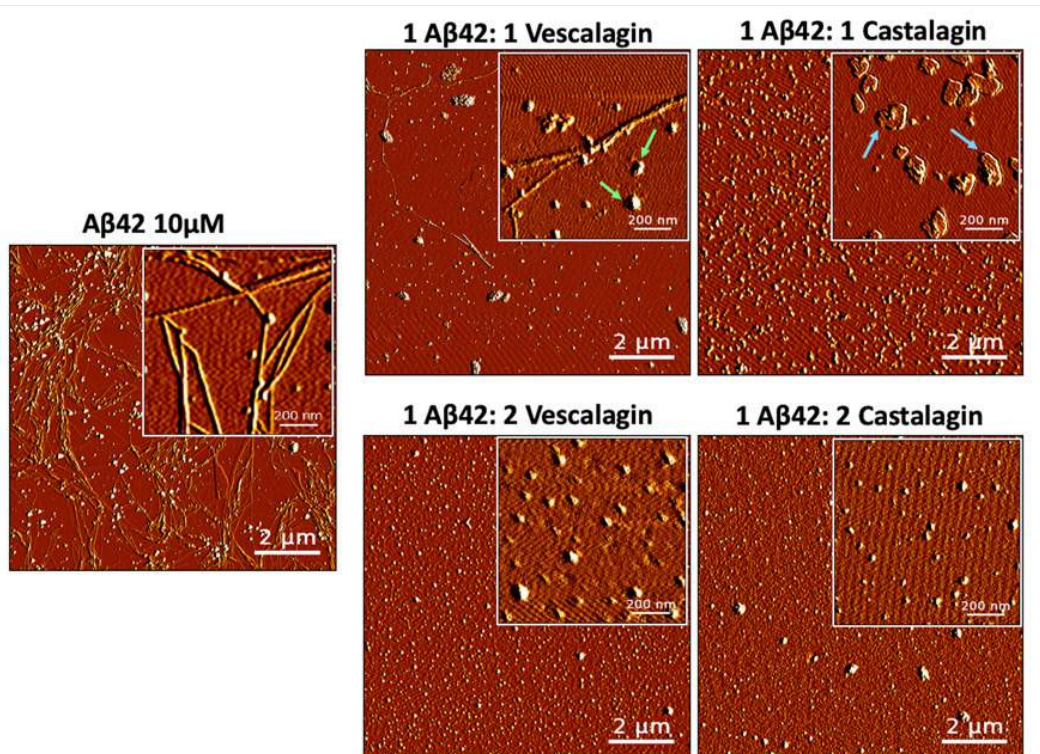
Supplementary Fig. 5-20. CD spectra of A $\beta$ 42 peptide (25 $\mu$ M) in the presence and absence of vescalagin (1) or castalagin (2) during 7 days. Amyloid-aggregates have a  $\beta$ -sheet-rich secondary structure after 7 days. In all the cases, incubation was made at 37°C, under constant agitation. The interaction between the A $\beta$ 42 and 1 or 2 results in a blue shift in the characteristic curves of the  $\beta$ -sheet-rich structures of A $\beta$ 42, especially for the one at ~220nm.

Supplementary Table 5-1. Secondary structure of A $\beta$ 42 during assembly (aggregation from the monomeric form) and disassembly (disaggregation of the pre-formed fibrils) in the presence of vescalagin (1) and castalagin (2). Values are in percentage obtained by fitting the CD spectra using the BeStSel method.<sup>5</sup> Parallel  $\beta$ -sheets are usually reported to be the major structure present in A $\beta$ 42 fibrils, while antiparallel  $\beta$ -sheets are usually assigned to on- and off-pathway A $\beta$ 42 oligomeric structures (including cytotoxic and non-cytotoxic forms).

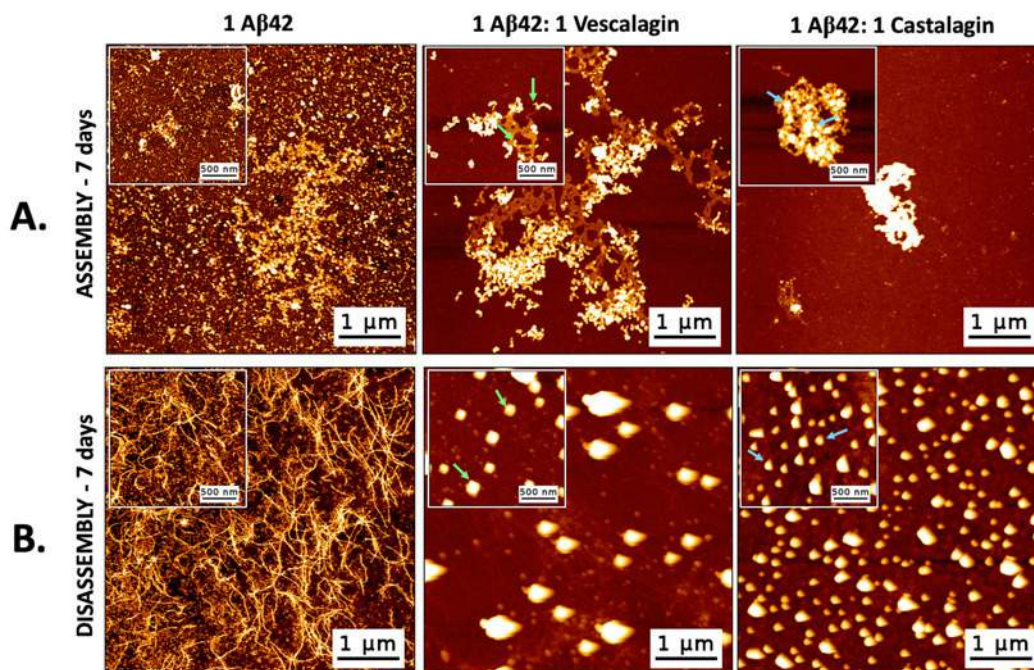
<i>Assembly of A<math>\beta</math>42</i>				
Secondary structure	A $\beta$ 42 (Day 0)	A $\beta$ 42 (Day 7)	A $\beta$ 42 + 1 (Day 7)	A $\beta$ 42 + 2 (Day 7)
Parallel $\beta$ -sheets	28.0	21.3	45.7	78.5
Antiparallel $\beta$ -sheets	14.0	30.5	0.0	0.0
Others	38.6	48.2	54.3	21.5
<i>Disassembly of A<math>\beta</math>42</i>				
Secondary structure	A $\beta$ 42 (Day 0)	A $\beta$ 42 (Day 1)	A $\beta$ 42 + 1 (Day 1)	A $\beta$ 42 + 2 (Day 1)
Parallel $\beta$ -sheets	42.8	93.9	63.6	49.6
Antiparallel $\beta$ -sheets	13.6	6.1	0.0	11
Others	43.6	0.0	36.4	39.4



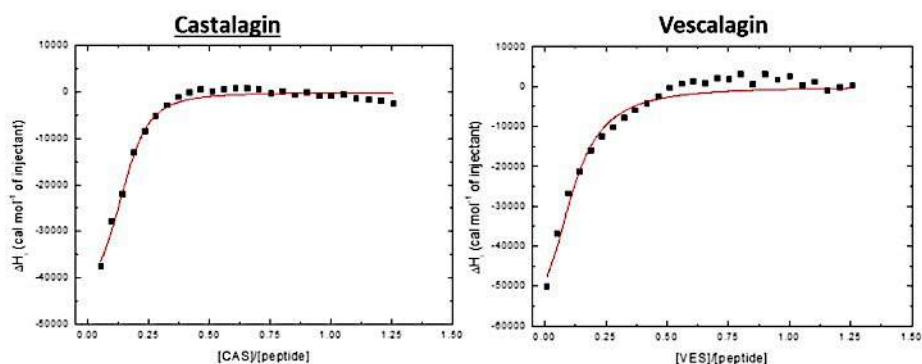
Supplementary Fig. 5-21. CD spectra of Aβ42 pre-formed fibrils in the absence and presence of vescalagin (1) or castalagin (2) during 1 day. In all the cases, incubation was made at 37°C, under constant agitation.



Supplementary Fig. 5-22. AFM images of Aβ42 fibrils formed for 10 days (10 μM). Vescalagin (1) and castalagin (2) were added into an Aβ42 solution (ratios Aβ42:polyphenol of 1:1 and 1:2) and left to incubate for 24h under constant agitation. Both compounds directly modified Aβ42 fibrils and oligomers (green arrows: aggregates with ≈30 nm; blue arrows: ≈70 nm); scale bars 2 μm and 200 nm.

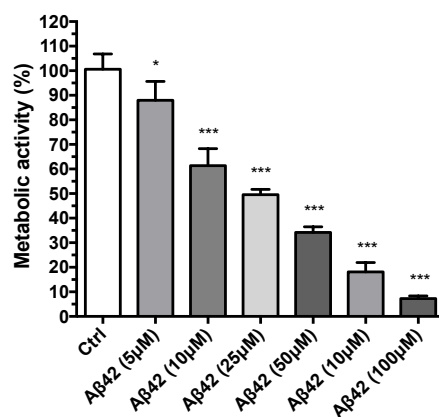


Supplementary Fig. 5-23. AFM representative images of A $\beta$ 42 (25  $\mu$ M). A. Assembly of A $\beta$ 42: vescalagin (1) and castalagin (2) were added into an A $\beta$ 42 monomeric solution (ratio of A $\beta$ 42:polyphenol of: 1:1) and left to incubate for 7 days; B. Disassembly of A $\beta$ 42: vescalagin (1) and castalagin (2) were added into a solution of A $\beta$ 42 pre-formed fibrils (ratio of A $\beta$ 42:polyphenol of: 1:1) and left to incubate for 7 days. Scale bar = 1  $\mu$ m and 500 nm. Green arrows: aggregates generated in the presence of vescalagin (1) with  $\approx$ 50nm (assembly) and  $\approx$ 200nm (disassembly). Blue arrows: aggregates generated in the presence of castalagin (2) with  $\approx$ 80nm (assembly) and  $\approx$ 100nm (disassembly). Scale bars = 2  $\mu$ m and 200 nm.

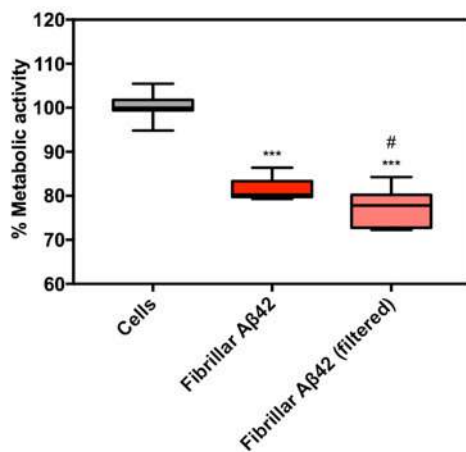


Supplementary Fig. 5-24. Isothermal titration calorimetry (ITC) curves for the binding of vescalagin (1) and castalagin (2) to A $\beta$ 42 peptide:  $K_1$  ( $\text{mol}^{-1}$ ) =  $1.26\text{E}6 \pm 0.18\text{E}6$ ;  $K_2$  ( $\text{mol}^{-1}$ ) =  $4.54\text{E}6 \pm 0.56\text{E}6$ .

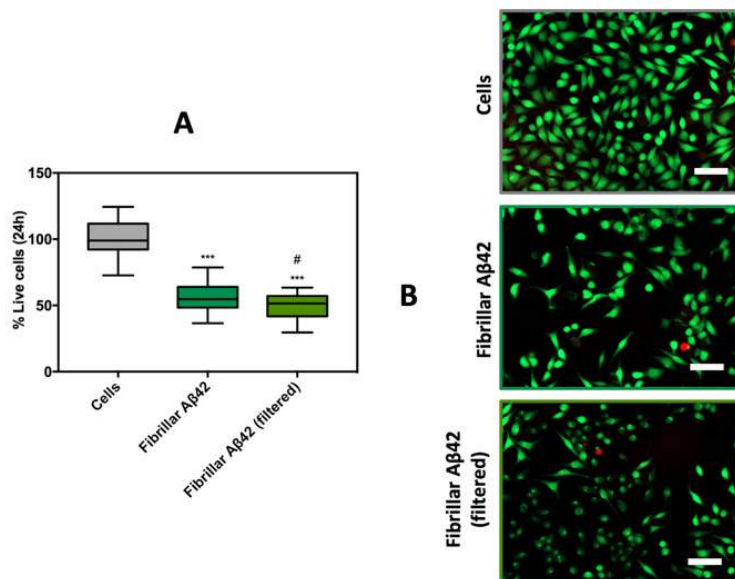
- Cell toxicity assays



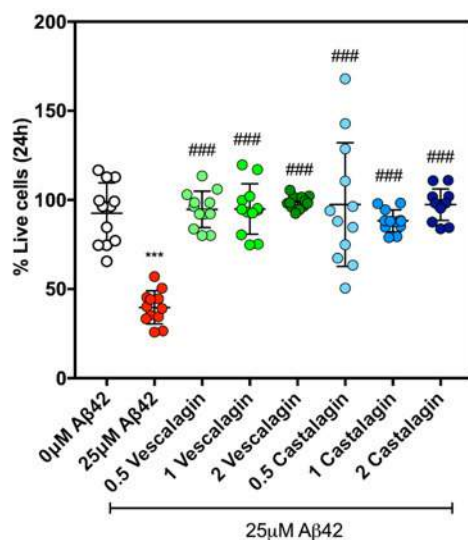
Supplementary Fig. 5-25. SH-SY5Y cell viability in the presence of Aβ42 fibrils during 24h. Cells were incubated during 24h with different concentrations of freshly prepared Aβ42. \* p < 0.05, \*\* p < 0.01, \*\*\* p < 0.001 (vs. control); n=3.



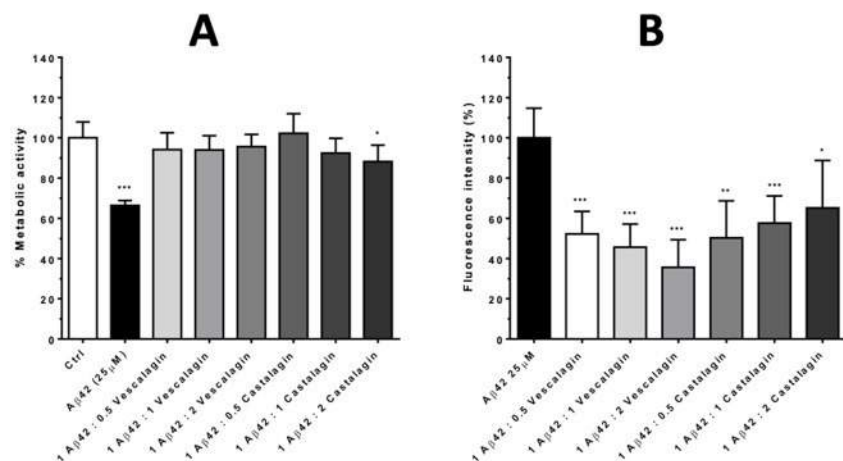
Supplementary Fig. 5-26. MTS assay: SH-SY5Y metabolic activity in the presence of a solution of A $\beta$ 42 pre-formed fibrils (25 $\mu$ M) and filtered A $\beta$ 42 (25 $\mu$ M) during 24h. Fibrillar A $\beta$ 42 was filtered with a 0.22 $\mu$ m filter. \*\*\* p < 0.001 (vs cells: without A $\beta$ 42) n=3; \*p < 0.05 (vs fibrillar A $\beta$ 42); n=3.



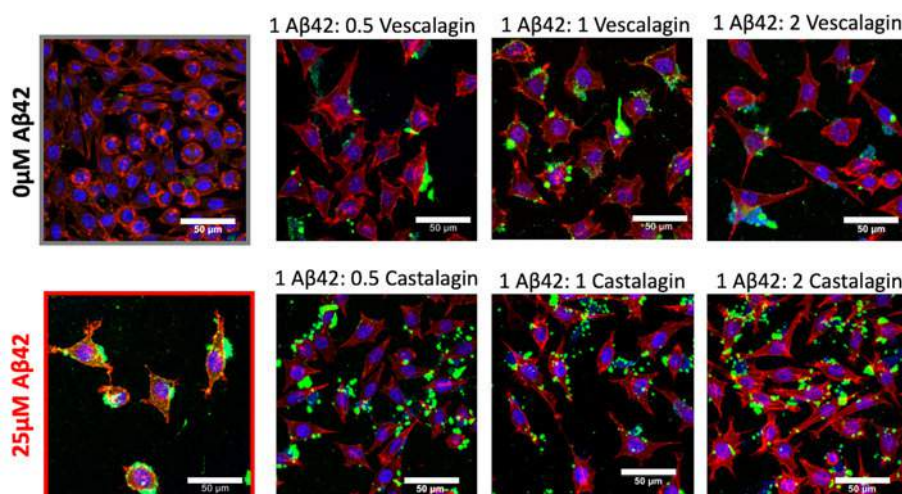
Supplementary Fig. 5-27. Fluorescence quantification of live cells stained in green (calcein) in the presence of a solution of A $\beta$ 42 pre-formed fibrils (25 $\mu$ M) and filtered fibrillar A $\beta$ 42 (25 $\mu$ M), during 24h. Fibrillar A $\beta$ 42 was filtered with a 0.22 $\mu$ m filter. \*\*\* p < 0.001 (vs cells: without A $\beta$ 42); n=3; \*p < 0.05 (vs fibrillar A $\beta$ 42); n=3. B. Representative images of the Live/dead assay. Scale bar = 50  $\mu$ m.



Supplementary Fig. 5-28. Live/Dead assay of SH-SY5Y: A. fluorescence quantification of live cells stained in green (calcein) in the presence of a solution of A $\beta$ 42 pre-formed fibrils (25 $\mu$ M) and vescalagin (1) or castalagin (2) at different molar ratios (A $\beta$ 42:polyphenol 1:0.5; 1:1; 1:2) during 24h. \*\*\* p < 0.001 (vs control); ### p < 0.001 (vs 25 $\mu$ M A $\beta$ 42); n=3.



Supplementary Fig. 5-29. A. MTS assay: SH-SY5Y cell viability in the presence of A $\beta$ 42 (25 $\mu$ M) and vescalagin (1) or castalagin (2) at different molar ratios (A $\beta$ 42:polyphenol 1:0.5; 1:1; 1:2) during 24h. \*  $p < 0.05$ , \*\*  $p < 0.01$ , \*\*\*  $p < 0.001$  (vs control);  $n=4$ . B. Fluorescence intensity of the A $\beta$ 42 immunostaining (6E10 antibody) after SH-SY5Y cell culture in the absence and presence of vescalagin (1) and castalagin (2), at different A $\beta$ 42:polyphenol ratios, 1:0.5, 1:1 and 1:2, for 24h. Fluorescence was quantified using the image processing package Fiji (<http://fiji.sc/wiki/index.php/Fiji>).



Supplementary Fig. 5-30. Representative fluorescence microscopy images of SH-SY5Y cells treated with different molar ratios of A $\beta$ 42:polyphenol, i.e. 1:0.5, 1:1 and 1:2, of vescalagin (1) and castalagin (2), as well as A $\beta$ 42 (25 $\mu$ M) during 24h. Immunostaining of A $\beta$ 42 (6E10, A $\beta$ 1-16) (green), actin (red) and nuclei (blue). Scale bar = 50  $\mu$ m.

#### References

1. A. R. Araujo, D. M. Pereira, I. M. Aroso, T. Santos, M. T. Batista, M. T. Cerqueira, A. P. Marques, R. L. Reis and R. A. Pires, *Rsc Advances*, 2015, 5, 96151-96157.
2. W. B. Stine, L. Jungbauer, C. Yu and M. J. LaDu, *Methods in molecular biology* (Clifton, N.J.), 2011, 670, 13-32.
3. J. L. Puech, C. Mertz, V. Michon, C. Le Guerneve, T. Doco and C. Herve Du Penhoat, *J Agric Food Chem*, 1999, 47, 2060-2066.



4. C. Douat, E. Berni, R. Jacquet, L. Pouysegu, D. Deffieux and S. Quideau, *Eur J Org Chem*, 2014, DOI: DOI 10.1002/ejoc.201402444, 4963-4972.
5. A. Micsonai, F. Wien, L. Kernya, Y. H. Lee, Y. Goto, M. Refregiers and J. Kardos, *Proceedings of the National Academy of Sciences of the United States of America*, 2015, 112, E3095-3103.

## Chapter 6

Functional gallic acid-based dendrimers as  
synthetic nanotools to remodel  
amyloid-beta 42 into  
non-cytotoxic forms

## CHAPTER 6

### Functional gallic acid-based dendrimers as synthetic nanotools to remodel amyloid-beta 42 into non-cytotoxic forms <sup>5</sup>

#### ABSTRACT

The molecular self-assembly of amyloid- $\beta$  ( $A\beta$ ) generates cytotoxic oligomeric species that have been linked to the onset and progression of Alzheimer's Disease (AD). As many fundamental molecular pathways that control  $A\beta$  aggregation are yet to be unravelled, an important strategy to control the  $A\beta$  cytotoxicity is the development of bioactive synthetic nanotools capable of interacting with the heterogeneous ensemble of  $A\beta$  species and remodel them into non-cytotoxic forms. In this work, we have synthesised nanosized, functional gallic acid (Ga)-based dendrimers with a precise number of Ga at their surface. We show these Ga-terminated dendrimers are able to interact with the monomeric/oligomeric  $A\beta$  species at their Glu, Ala and Val residues by H-bonding, promoting their remodelling into non-cytotoxic aggregates in a process controlled by the Ga units.

**Keywords:** Alzheimer Disease, Dendrimers, Galloyl group, amyloid- $\beta$  peptide.

---

<sup>5</sup> This Chapter is based on the publication: "Araújo A. R., Correa J., Dominguez-Arca V., Reis, R. L., Fernandez-Megia E. & Pires, R. A, (2020), Functional gallic acid-based dendrimers as synthetic nanotools to remodel amyloid-beta 42 into non-cytotoxic forms (submitted)"

## 6.1 MAIN TEXT

Pathological protein/peptide aggregation is at the basis of several neurodegenerative processes, such as the ones that lead to Alzheimer's Disease (AD).[1] In AD, amyloid- $\beta$  ( $A\beta$ ) peptides of different lengths (between 38 to 43 amino acids) are at the onset and progression of the disease. These amyloidogenic  $A\beta$  species are highly prone to aggregate into a diverse set of supramolecular assemblies, that range from long fibrils to short oligomers.  $A\beta$  peptides are produced from the sequential cleavage of the amyloid precursor protein (APP) promoted by the  $\gamma$ -secretase complex.[2] The resulting peptides are reported to produce thermodynamically unstable oligomers ( $A\beta_o$ ) with a high propensity to self-assemble into stable  $\beta$ -sheet structures that present a fibril-like morphology ( $A\beta_f$ ). These high molecular weight fibrils have been shown to be relatively inactive, but lower molecular weight aggregates (*i.e.*  $A\beta_o$ ) have emerged as potent cytotoxins with the ability to trigger neuronal cell death, both *in vitro* and *in vivo*. [3] In fact, these  $A\beta_o$  species can diffuse through the intracellular and pericellular spaces and interact with a series of cellular motifs, triggering, for example, the hyperphosphorylation of Tau, hampering its ability to maintain the microtubules of neurons, which leads to their disassembly and neuronal cell death.[4] The growth of  $A\beta_f$  in the cellular milieu occurs at the cell surface through an autocatalytic process, usually referred to as secondary nucleation, which is mediated by the  $A\beta_o$  species.[5, 6] These  $A\beta_o$  differ from  $A\beta_f$  in the intermolecular arrangement of the  $\beta$ -strands (antiparallel arrangement for  $A\beta_o$ , parallel  $\beta$ -sheet conformation usually for  $A\beta_f$ ). [7, 8] These supramolecular assemblies are typically maintained through H-bonding between the backbones of two peptide monomers, as well as by  $\pi$ - $\pi$  stacking between the aromatic amino acid residues of the  $A\beta$  sequence, making them as key targets for the inhibition of the  $A\beta$  supramolecular assembly.[9] Natural polyphenols (*e.g.* EGCG[10], resveratrol[11] or vesicalagin[12]) have been reported to remodel the supramolecular structure of amyloidogenic proteins/peptides. They usually interfere with the H-bonding and hydrophobic interactions (*e.g.*  $\pi$ - $\pi$  stacking) between the protein/peptide chains generating disordered assemblies of low toxicity.[10] This interference is reported to be mediated by gallic acid (Ga) and other phenolic units in their structures. Based on this bioactive potential, we have mimicked these polyphenols by designing three nano-sized dendrimers functionalized with an increasing number of Ga units (Figure 6-1A-C).

To this end, gallic acid-triethylene glycol (GATG) dendrimers[13-15] of the 2G family have been decorated with peripheral Ga units to afford 2G0-GaOH (two Ga units) and 2G1-GaOH (six Ga units). Since dendrimers with a larger number of Ga like 2G2-GaOH (eighteen Ga units) revealed highly hydrophobic and insoluble in water, a strategy for a higher number of Ga was devised with a dendrimer of the 3G

family such as 3G1-GaOH (nine Ga units). Functional Ga-based dendrimers were obtained in very good yields. Their chemical characterization is described in the Supporting Information (SI) with convincing evidence by  $^1\text{H}$ ,  $^{13}\text{C}$  NMR and IR spectroscopy. Furthermore, their purity and monodispersity were verified by gel permeation chromatography (GPC) (S. Figs. 6-1 and 6-24).

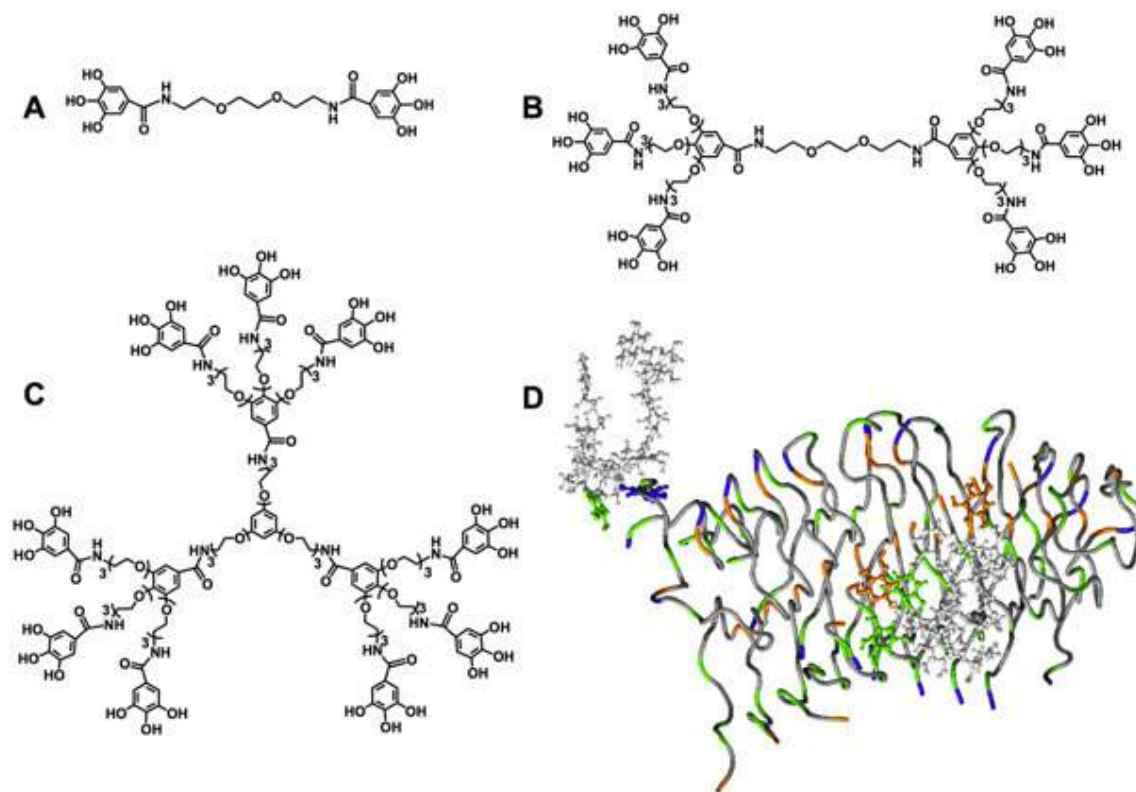


**Figure 6-1.** Chemical structure of Ga-terminated dendrimers: A. 2G0-GaOH, B. 2G1-GaOH and C. 3G1-GaOH. D. Optimized geometry from MD simulations (2G1-GaOH interacts with A $\beta$  at its Glu (blue), Val (green) and Ala (orange) residues). Remaining A $\beta$  residues, as well as the portion of 2G1-GaOH that does not interact with A $\beta$ , are shown in grey

We then assessed the ability of 2G0-GaOH, 2G1-GaOH and 3G1-GaOH to modulate the supramolecular assembly of A $\beta$  and to promote the formation of non-cytotoxic aggregates. We started modelling the potential of the dendrimers to disassemble A $\beta$  by coarse-grain by all atom molecular dynamics (MD) simulations (*i.e.* 2MXU PDB structure[16]). Since the dynamic character of A $\beta$  largely limits the reproducibility of data obtained during the relative short timeframes of the simulations,[17] preformed fibrils were used for this analysis. We assessed the stability of A $\beta$  in the presence and absence of dendrimers (Figures 6-1D and S. Fig 6-25, 6-29, S. Table 6-1). All dendrimers exhibited strong and stable H-bondings with Glu, Ala and Val residues of A $\beta$ . The placement of dendrimers in close proximity to Glu 11, Glu 22 and Ala 21 increases the spacing between the A $\beta$  strands (Figure 6-1D for the Glu in blue and Ala residue in orange), compromising the formation of  $\beta$ -sheets and other secondary conformations maintained by the H-bonding network.[18] All the tested compounds increased the solvent-

accessible surface area (SASA, S. Table 6-1) of A $\beta$ , as a consequence of the perturbation of its secondary structure. Analysing the number of H-bonds generated during the simulations, 2G1-GaOH presented the highest number of H-bonds with A $\beta$ . Of note, although water was used as solvent for all the MD simulations, the limited solubility in aqueous medium of 2G1-GaOH, and particularly 3G1-GaOH, probably leads to an underestimation of the H-bond number and SASA calculations. In general, the MD simulations showed that dendrimers are able to interact with A $\beta$ , being 2G1-GaOH the most effective modulator of its supramolecular structure.

We then tested the ability of dendrimers to interfere the assembly of A $\beta$  *in vitro*, using the Thioflavin-T (ThT) fluorescence assay. Fluorescence spectra of the dendrimers revealed no major interference with the ThT emission spectrum (S. Figs 6-30 to 6-33). We analysed the dendrimers under both assembly (A $\beta$ ) and disassembly (A $\beta$ ) conditions (S. Figs. 6-34 to 6-35) to screen their potential to block the A $\beta$  supramolecular assembly, as well as to disrupt the pre-assembled A $\beta$  structures. The supramolecular assembly of A $\beta$  over time presents the typical sigmoidal curve (characteristic of secondary nucleation and fibril elongation)[19], which is abolished in the presence of all dendrimers at any of the concentrations tested (S. Fig. 6-34). After the exponential growth phase of A $\beta$  (at day 3-4), the fluorescence reaches a plateau (at day 7). Interestingly, the impact of the dendrimers in the disassembly pathway (A $\beta$ , S. Fig. 6-35) is dependent on the number of Ga units per dendrimer and their concentration, a result consistent with the disruption of the interstrand H-bonding of the  $\beta$ -sheets. These interactions lead to a new thermodynamic equilibrium, *i.e.* formation of off-pathway aggregates that are not recognized by ThT. In fact, it is known ThT does not bind to  $\beta$ -sheet rich globular proteins due to their highly twisted  $\beta$ -sheets with a lower content of  $\beta$ -strands.[20]

We used circular dichroism (CD) spectroscopy to evaluate the types of  $\beta$ -sheets present in the A $\beta$  supramolecular species generated upon interaction with the dendrimers. All dendrimers perturbed the A $\beta$  secondary structure (Figures S6-36, S6-43), probably due to the formation of off-pathway oligomers. All the CD spectra were fitted using the BeStSel method[21] for secondary structure estimation (S. Fig. 6-44). After 1 day of incubation, it was already visible a decrease in the antiparallel  $\beta$ -sheets for all the A $\beta$ :dendrimer ratios, which were further reduced over 5 days of incubation, especially for 2G1-GaOH. In the disassemble experiments A $\beta$ :dendrimers, the 2G1-GaOH dendrimer was able to abolish the antiparallel  $\beta$ -sheet content to undetectable levels after 5 days of incubation. These results are in accordance with the ThT data, indicating a clear direct relationship between the ability of the dendrimers to interfere with the assembly of A $\beta$  and the number of Ga units per dendrimer as well as their concentration. These findings support the capacity of 2G1-GaOH to inhibit the catalytic mechanism that

combines the growth of insoluble amyloid fibrils and the generation of soluble oligomeric aggregates, and consequently secondary nucleation.

Next, we evaluated the morphological changes of the  $A\beta_i$  aggregates upon contact with the dendrimers by AFM (S. Fig. 6-45) and STEM (S. Fig. 6-46). As expected, a reduction on the number of small aggregates is observed (*i.e.* oligomers); elongated fibrils are replaced by unstructured aggregates (condensed and less organized) as a result of the interaction between  $A\beta_i$  and the dendrimers. Western blot (with 6E10 antibody) allowed the quantification of the aggregates of different size, *i.e.* monomers, oligomers and fibrils, produced during the assembly ( $A\beta_o$ ) and disassembly ( $A\beta_f$ ) processes (Figure 6-2). In both cases, 2G1-GaOH shows the highest reduction in the oligomeric and monomeric species after 1 and 5 days of incubation (S. Fig. 6-47, 6-49). The antibody 6E10 is specific for the 1-16 amino acids of the  $A\beta$  sequence, requiring an intact N-terminal epitope which encloses the amino acid sequence 3-8: Glu-Phe-Arg-His-Asp-Ser. From the MD simulations, we found that dendrimers exhibit strong and stable H-bonding interactions with Glu11 residue so, these results are compatible with the ability of 2G1-GaOH to interact directly with the  $A\beta$  N-terminal, blocking the epitope recognized by 6E10 antibody.

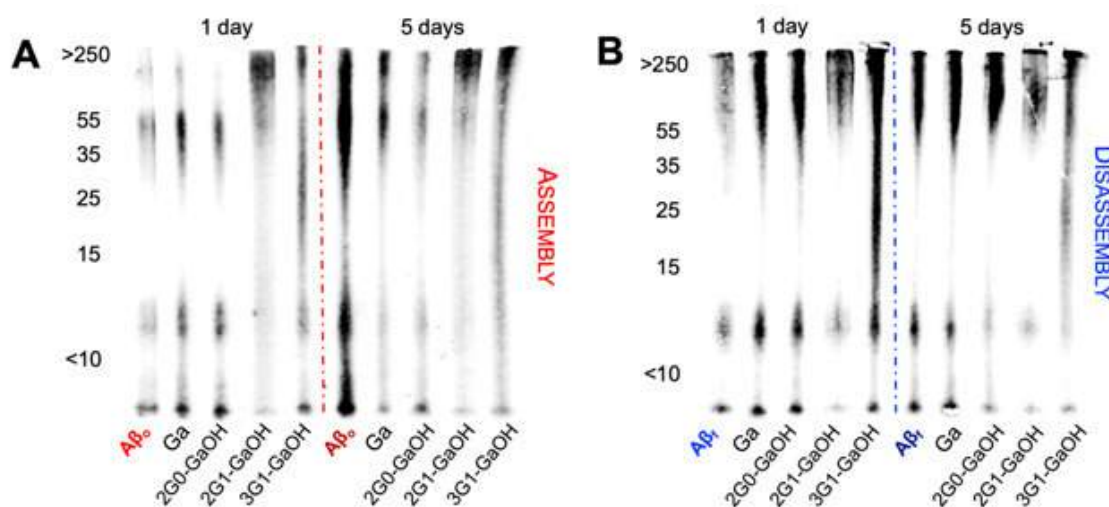


Figure 6-2. Relative densitometric bar graphs of  $A\beta_o$  (A) and  $A\beta_f$  (B) quantified by WB (using the antibody 6E10). Experiments performed using  $25\mu\text{M}$  of  $A\beta$ , 1:1 molar ratio of  $A\beta$  and dendrimers, at  $37^\circ\text{C}$  in PBS, for 1 and 5 days.

After showing that the dendrimers (and particularly 2G1-GaOH) are able to modulate the supramolecular assembly of  $A\beta$ , both under assembly and disassembly conditions, we selected a neuroblastoma cell line (SH-SY5Y) to evaluate the impact of this activity under cell culture conditions. All the dendrimers were cytocompatible and able to rescue cells from the cytotoxicity of  $A\beta_i$  and  $A\beta_o$ . (measured by AlamarBlue and live/dead assay and observed under confocal microscopy, at 1 and 5 days of cell culture conditions, S. Fig. 6-50, 6-52). Not surprisingly, when ThT was used to quantify the  $\beta$ -sheets present under cell culture conditions for both the assembly ( $A\beta_o$ ) and disassembly ( $A\beta_f$ )

experiments, ThT fluorescence reduced by  $\sim 50\%$  in the presence of 2G1-GaOH and  $A\beta$ . after 24 h of incubation (Figure S6-53A). Next, we used the 6E10 (stains  $A\beta_f$ , Figures 6-3 and S. Fig. 6-54, 6-55) and A11 (stains  $A\beta_o$ , S. Fig. 6-56, 6-57) antibodies to assess the presence of  $A\beta$  species in the pericellular space. We noticed that  $A\beta$  tend to aggregate ( $A\beta_f$  stained by 6E10) over the cell membrane while the smaller species ( $A\beta_o$  stained by A11) are internalized by the cells. For both pathways, the 2G1-GaOH dendrimer reduced the amount of  $A\beta$  supramolecular assemblies in the cellular environment (Figures 6-3A and 6-3C). Recent reports[22, 23] have shown that  $A\beta$  species interact with the phospholipid bilayer changing the lipid environment. It has been proposed that the transformation of the  $A\beta$  secondary structure results in hydrophobic segments being exposed which increase their tendency to attach onto the membrane. This interaction with the cell membrane disturbs the cytoskeletal organization (*i.e.* assembly of actin filaments and microtubules) influencing the cell mechanical properties, which results in changes in cellular morphology and mechanics (*e.g.* height and Young's modulus).[24, 25] Therefore, we used Bio-AFM to measure the nanomechanical properties of the cells in the presence and absence of  $A\beta$  and dendrimers (Figures 6-4 and S. Fig. 6-58, 6-59). Our results indicate that the presence of  $A\beta_f$  increases the stiffness of the cell body, while  $A\beta_o$  (being more toxic) decreases the Young's modulus and cell height probably via Tau hyperphosphorylation leading to the disassembly of microtubules. In all cases the presence of dendrimers ameliorated the perturbations promoted by  $A\beta$ .

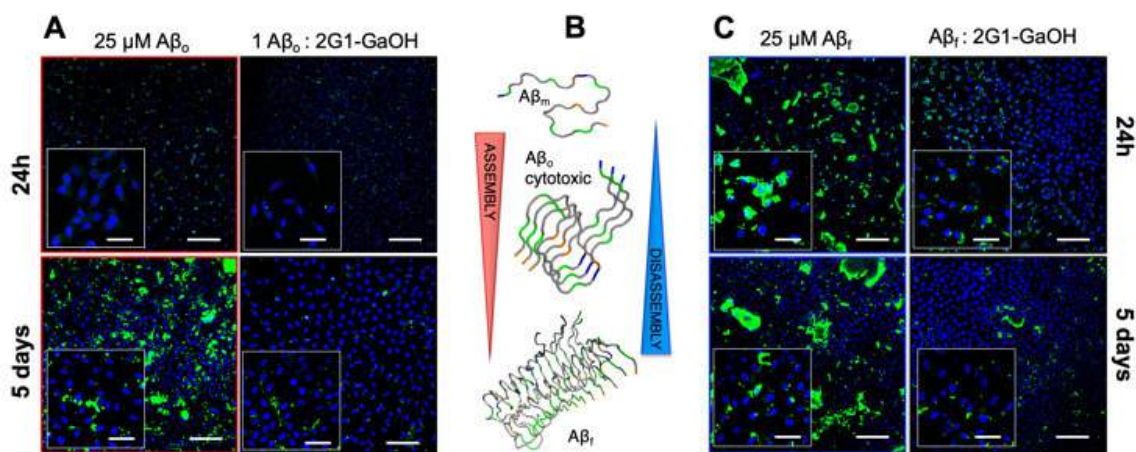


Figure 6-3. Immunofluorescence analysis of  $A\beta_o$  (A., assembly) and  $A\beta_f$  (C., disassembly) species in the SH-SY5Y cell culture (mAb 6E10) after incubation with 2G1-GaOH for 1 and 5 days ( $A\beta$ : green, cell nuclei: blue). Scale bar = 200  $\mu\text{m}$  (insets = 50  $\mu\text{m}$ ). B.  $A\beta$  peptide aggregation pathway.

In conclusion, we have developed a strategy, that based on Ga-terminated dendrimers, allows to inhibit the primary and secondary nucleation of  $A\beta$  fibrillization, as well as to disrupt the  $A\beta$  pre-formed fibrils. As in the case of natural polyphenols, the activity of the dendrimers was found to be proportional to the number of Ga units. The multivalent presentation of these chemical motifs increases their capacity



to remodel the A $\beta$  secondary structure. 2G1-GaOH dendrimer (six Ga units) displays an adequate balance between number of Ga units and hydrophilicity, maximizing the interaction with the Glu, Ala, and Val peptide residues through H-bonding, while reducing the A $\beta$  cytotoxicity *in vitro*.

The strategy herein presented can be extended to the development of dendrimers with alternative structural cores and other multivalent scaffolds aimed at abolishing the toxicity of A $\beta$  assemblies in the context of AD. Finally, we believe that these dendrimers represent relevant synthetic nanotools to study the assembly mechanisms of different A $\beta$  peptide sequences, as well as to find structure-activity relationships of the A $\beta$  cytotoxic oligomeric populations that have been linked to AD.

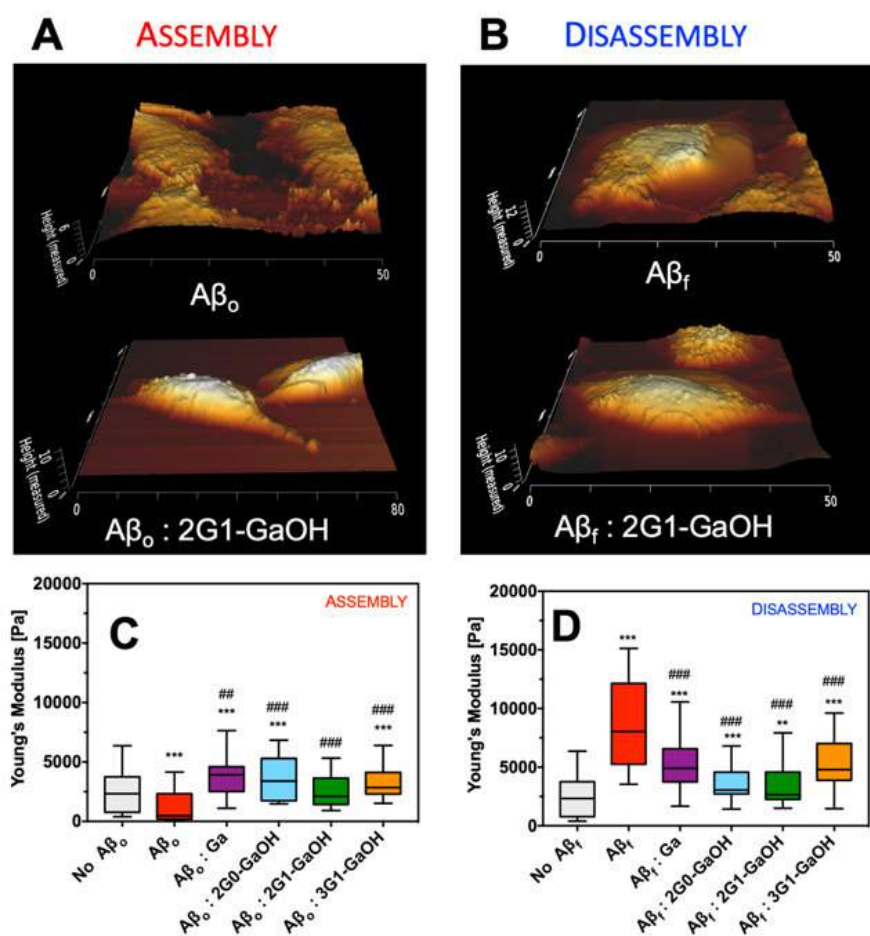


Figure 6-4. Representative Bio-AFM topographic images of SH-SY5Y cells (A. and B.) cultured in the presence of A $\beta$  and a 1:1 molar ratio of 2G1-GaOH. C. Cell height profile and D. Young's modulus of SH-SY5Y cells as a function of the presence of A $\beta$  and dendrimers (molar ratio 1:1). Experiments were recorded after 24h of incubation; A $\beta$  concentration was set at 25 $\mu$ M.

## 6.2 REFERENCES

1. Masters, C.L., et al., Alzheimer's disease. Nat Rev Dis Primers, 2015. 1: p. 15056.
2. Hardy, J.A. and G.A. Higgins, Alzheimer's disease: the amyloid cascade hypothesis. Science, 1992. 256(5054): p. 184-5.

3. Knowles, T.P., M. Vendruscolo, and C.M. Dobson, The amyloid state and its association with protein misfolding diseases. *Nat Rev Mol Cell Biol*, 2014. 15(6): p. 384-96.
4. Panza, F., et al., A critical appraisal of amyloid- $\beta$ -targeting therapies for Alzheimer disease. *Nature Reviews Neurology*, 2019. 15(2): p. 73-88.
5. Michaels, T.C.T., et al., Dynamics of oligomer populations formed during the aggregation of Alzheimers A $\beta$  42 peptide. *bioRxiv*, 2020: p. 2020.01.08.897488.
6. Cohen, S.I., et al., Proliferation of amyloid-beta42 aggregates occurs through a secondary nucleation mechanism. *Proc Natl Acad Sci U S A*, 2013. 110(24): p. 9758-63.
7. Lansbury, P.T., Jr., et al., Structural model for the beta-amyloid fibril based on interstrand alignment of an antiparallel-sheet comprising a C-terminal peptide. *Nat Struct Biol*, 1995. 2(11): p. 990-8.
8. Huang, D., et al., Antiparallel beta-Sheet Structure within the C-Terminal Region of 42-Residue Alzheimer's Amyloid-beta Peptides When They Form 150-kDa Oligomers. *J Mol Biol*, 2015. 427(13): p. 2319-28.
9. Porat, Y., A. Abramowitz, and E. Gazit, Inhibition of amyloid fibril formation by polyphenols: structural similarity and aromatic interactions as a common inhibition mechanism. *Chem Biol Drug Des*, 2006. 67(1): p. 27-37.
10. Lopez del Amo, J.M., et al., Structural properties of EGCG-induced, nontoxic Alzheimer's disease Abeta oligomers. *J Mol Biol*, 2012. 421(4-5): p. 517-24.
11. Marambaud, P., H. Zhao, and P. Davies, Resveratrol promotes clearance of Alzheimer's disease amyloid-beta peptides. *J Biol Chem*, 2005. 280(45): p. 37377-82.
12. Araújo, A.R., et al., Vescalagin and castalagin reduce the toxicity of amyloid-beta42 oligomers through the remodelling of its secondary structure. *Chemical Communications*, 2020: p. DOI:10.1039/D0CC00192A.
13. Amaral, S.P., et al., Efficient multigram synthesis of the repeating unit of gallic acid-triethylene glycol dendrimers. *Org Lett*, 2011. 13(17): p. 4522-5.
14. Vukojicic, P., et al., Multivalent Affidendrons with High Affinity and Specificity toward *Staphylococcus aureus* as Versatile Tools for Modulating Multicellular Behaviors. *ACS Appl Mater Interfaces*, 2019. 11(24): p. 21391-21398.
15. Amaral, S.P., et al., Tuning the Size of Nanoassemblies: A Hierarchical Transfer of Information from Dendrimers to Polyion Complexes. *Angewandte Chemie-International Edition*, 2018. 57(19): p. 5273-5277.
16. Xiao, Y., et al., Abeta(1-42) fibril structure illuminates self-recognition and replication of amyloid in Alzheimer's disease. *Nat Struct Mol Biol*, 2015. 22(6): p. 499-505.
17. Cohen, S.I.A., et al., Distinct thermodynamic signatures of oligomer generation in the aggregation of the amyloid-beta peptide. *Nat Chem*, 2018. 10(5): p. 523-531.

18. Rosenman, D.J., et al.,  $A\beta$  monomers transiently sample oligomer and fibril-like configurations: Ensemble characterization using a combined MD/NMR approach. *Journal of molecular biology*, 2013. 425(18): p. 3338-3359.
19. Wright, J.S., E.R. Johnson, and G.A. DiLabio, Predicting the activity of phenolic antioxidants: theoretical method, analysis of substituent effects, and application to major families of antioxidants. *J Am Chem Soc*, 2001. 123(6): p. 1173-83.
20. Biancalana, M. and S. Koide, Molecular mechanism of Thioflavin-T binding to amyloid fibrils. *Biochim Biophys Acta*, 2010. 1804(7): p. 1405-12.
21. Micsonai, A., et al., Accurate secondary structure prediction and fold recognition for circular dichroism spectroscopy. *Proc Natl Acad Sci U S A*, 2015. 112(24): p. E3095-103.
22. Fabiani, C. and S.S. Antollini, Alzheimer's Disease as a Membrane Disorder: Spatial Cross-Talk Among Beta-Amyloid Peptides, Nicotinic Acetylcholine Receptors and Lipid Rafts. *Front Cell Neurosci*, 2019. 13(309): p. 309.
23. Hardy, J., Membrane damage is at the core of Alzheimer's disease. *The Lancet Neurology*, 2017. 16(5): p. 342.
24. Fang, Y., et al., Investigating dynamic structural and mechanical changes of neuroblastoma cells associated with glutamate-mediated neurodegeneration. *Sci Rep*, 2014. 4: p. 7074.
25. Gao, Q., et al., Biophysical Characteristics of Human Neuroblastoma Cell in Oligomeric beta-Amyloid (1-40) Cytotoxicity. *IEEE Trans Nanobioscience*, 2018. 17(1): p. 70-77.

## SUPPLEMENTARY INFORMATION

### ▪ Materials and Methods

All chemicals were purchased from Sigma-Aldrich or Acros Organics and were used without further purification. All solvents were of HPLC grade, purchased from Scharlab and Fisher Chemical and used without further purification. DMSO and Et<sub>3</sub>N were dried under 4Å molecular sieves. H<sub>2</sub>O of Milli-Q grade was obtained from a Millipore water purification system. 2[G1]-NH<sub>2</sub>·HCl and 3[G1]-NH<sub>2</sub>·HCl were prepared following previously reported procedures by our group.<sup>1</sup>

**Column Chromatography.** Automated column chromatography was performed on a MPLC Teledyne ISCO CombiFlash RF 200 psi with RediSep Rf columns refilled with silica 40 mm (from VWR Chemicals) or neutral aluminum oxide 60 mesh (from Alfa Aesar). Samples were adsorbed onto silica 40 mm or neutral aluminum oxide 60 mesh into solid cartridges.

**NMR Spectroscopy.** NMR spectra were recorded on a Varian Mercury 300 MHz spectrometer. Chemical shifts are reported in ppm ( $\delta$  units) downfield from the HOD peak (CD<sub>3</sub>OD), internal tetramethylsilane (CDCl<sub>3</sub>), or residual solvent peak (DMSO-*d*<sub>6</sub>). Mestre Nova 9.0 software (Mestrelab Research) was used for spectral processing.

**Infrared Spectroscopy.** FT-IR spectra were recorded on a Perkin-Elmer Spectrum Two spectrophotometer equipped with a UATR accessory or Bruker Vertex 70v using KBr pellets.

**Mass Spectrometry (MS).** Mass spectra were recorded on a Bruker Microtof spectrometer coupled to a HPLC Agilent 1100 using atmospheric-pressure chemical ionization (APCI). Samples were injected via flow injection analysis (FIA) using a MeOH/aqueous solution of formic acid 0.1% 1:1, flow 0.2 mL/min.

**Gel Permeation Chromatography (GPC).** GPC experiments were performed on an Agilent 1100 series separation module using a PSS SDV pre-column (5 mm, 8 x 50 mm), a PSS SDV Linear S column (5 mm, 8 x 300 mm), and a PSS SDV Lux Linear M column (5 mm, 8 x 300 mm) equipped with an Agilent 1100 series refractive index and UV detectors. THF was used as eluent at 1 mL/min. The samples were filtered through a 0.45  $\mu$ m PTFE filter before injection.

**Peptide preparation.** Human amyloid  $\beta$ -peptide (1-42) was obtained by custom synthesis from GeneCust Europe (Luxembourg). Stock solutions of 0.45mg were prepared by dissolving 10mg of amyloid  $\beta$ -peptide (1-42, A $\beta$ ) in 2.217mL of HFIP (Fluorochem Ltd, UK) according to the protocol described by Stine *et al.*

In brief, A $\beta$  was dissolved in HFIP (5mg/mL) during 30min at room temperature. HFIP was allowed to evaporate in open tubes overnight in the fume hood, and afterwards during an additional 1h under vacuum. A $\beta$  aliquots were then stored at -20°C and reconstituted immediately before use: i) for the monomeric A $\beta$  (A $\beta$ <sub>o</sub>) studies, it was added 20 $\mu$ L of DMSO (sonicated for 10min in an ultra-sound bath) and immediately afterwards, ice-cold water was added (followed by 15s of vortex) to a final concentration of 100 $\mu$ M; ii) for the fibrillar A $\beta$  (A $\beta$ <sub>i</sub>) experiments it was added 20 $\mu$ L of DMSO (sonicated for 10min in an ultra-sound bath) and immediately afterwards it was added 10mM HCl at room temperature, diluting to a final concentration of 100 $\mu$ M of A $\beta$ , followed by vortex for 15s, and then incubated for 24h at 37 °C.

**Thioflavin T (ThT).** Fibril formation for A $\beta$ <sub>o</sub> was followed by ThT assay (assembly – S. Fig. 6-35) during 6 days. A $\beta$  peptide stock solution was prepared as described above. ThT fluorescence was monitored by mixing A $\beta$ <sub>o</sub> solution (final concentration of 25 $\mu$ M on Phosphate Buffer 5mM, with 0.1% of sodium azide, pH 7.2) with ThT (final concentration of 40 $\mu$ M) and different concentrations of Ga, 2G0-GaOH, 2G1-GaOH and 3G1-GaOH, *i.e.* concentration ratios A $\beta$ :dendrimers of 1:0.5; 1:1 and 1:2. The ThT fluorescence was then recorded in a Fluorescence Spectrometer (Jasco, FP-8500, Japan) during 6 days using an excitation wavelength of 435nm and an emission wavelength of 465nm. Each experiment was repeated in triplicate. The experiments for the disassembly of the A $\beta$  fibrils, *i.e.* A $\beta$ <sub>i</sub> (S. Fig. 6-36) were performed with A $\beta$  fibrillar form (A $\beta$ <sub>i</sub>), for 5 days using the same experimental protocol.

**Circular Dichroism (CD).** CD was performed using a 1mm path length cell at 37°C in a CD spectrometer (Jasco, J1500, Japan). Spectra (S. Figs. 6-37, 6-40) were recorded in the range between 190–260nm with a scan rate of 10nm/min and a response time of 1s. Three scans were accumulated for each spectrum. For all the CD experiments, the A $\beta$ <sub>o</sub>/A $\beta$ <sub>i</sub> concentration was 25 $\mu$ M with or without each dendrimer for the different ratios: 1:0.5; 1:1 and 1:2. Results are expressed as  $\theta$  [mdeg] – S. Figs. 6-41, 6-44.

**Atomic Force Microscopy (AFM).** For the acquisition of AFM images (S. Fig. 6-46), freshly cleaved mica was functionalized with a drop of (3-Aminopropyl)triethoxysilane (APTES, 200 $\mu$ L), during 30 min at room temperature. Afterwards, the micas were rinsed with deionized water and dried under a nitrogen flux. Each sample, A $\beta$ <sub>i</sub> peptide (30 $\mu$ M) in the presence and absence of dendrimers, were spotted onto the functionalized mica during 30min, washed with water and dried under nitrogen.

AFM images were acquired using a JPK Nanowizard 3 (JPK, Germany) in air at room temperature under AC mode. The scans were acquired at a 512 x 512 pixels resolution using ACTA-SS probes ( $k \sim 37\text{N/m}$ , AppNano, USA), a drive frequency of  $\sim 254\text{kHz}$ , a setpoint of  $\sim 0.5\text{V}$  and a scanning speed of  $1.0\text{Hz}$ .

**Scanning transmission electron microscopy (STEM).** For the acquisitions of the STEM images, (S. Fig. 6-47),  $A\beta_r$  peptide ( $30\mu\text{M}$ ) in the presence and absence of dendrimers, were spotted onto the a TEM grids, Carbon Type-B 400M Cu (IESMAT, Spain), during 3min, followed by the classic staining with UranylLess ( $10\mu\text{L}$  each sample, for 2 minutes) (EMS, UK). All samples were washed with water and dried under nitrogen. STEM images were obtained using a High-Resolution Field Emission Scanning Electron Microscope (SEM - Auriga Compact, Zeiss, Germany). The scans were acquired at a resolution of  $2048 \times 1536$  pixels, EHT =  $3000\text{kV}$ , WD =  $2.9\text{ mm}$  and magnification =  $5000\text{K}$  (Fig. S6-47).

**Western Blot (WB).** To access the effect of the dendrimers in the  $A\beta$  species sizes, produced afterword's for the different ratios: 1:0.5; 1:1 and 1:2 (during 1 day and 5 days) we run a 12% Bis-Tris Gel Invitrogen NuPAGE, with MES SDS Running Buffer gel (gel loading buffer without DTT), followed by a membrane transference to a nitrocellulose membranes using iBlot 2 System. Next, the nitrocellulose membranes were blocked with 4% BSA for 1.5 hours in TBS-T (TBS with 0.1% Tween 20%). After the blocking, the membranes were incubated (overnight at  $4^\circ\text{C}$ ) with the 6E10 antibody ( $A\beta$  1-16 – 1:1000 dilution in 4% of BSA in TBS-T). After washed 3 times in TBS-T, the membranes were incubated (during 1.5h at RT) in IRDye 800CW Goat anti-Mouse IgG Secondary Antibody (1:10000 dilution in TBS-T). Finally, the WB lanes were detected using an Odyssey Fc Imaging System (LI-COR Inc., Nebraska USA). The comparisons between bands in different lanes were quantified using Fiji software (Figs. 6-2 and S. Fig. 6-48, 6-50).

**Cell studies.** Neuroblastoma SH-SY5Y cells were cultured at  $37^\circ\text{C}$  in a humidified 95/5% air/ $\text{CO}_2$  atmosphere using Dulbecco's modified Eagles medium F-12 (Gibco, UK) supplemented with 10% FBS (Gibco, UK) and 1% ATB (Gibco, UK) solution. Cell medium were replaced each 2 days and cells were sub-cultured once they reached 90% confluence. Cells were plated at a density of 25 000 cells per well on 96-well plates containing DMEM/F-12 media (for MTS assay) and plated at a density of 50 000 cells per well on 24-well plates containing DMEM/F-12 media (for the Live/Dead assay). A typical experiment included the culture of the neuroblastoma cell line (SH-SY5Y) during 24h or 5 days in the absence or presence of dendrimers at different concentrations. Afterwards,  $A\beta_r/A\beta_i$  were added to the culture medium and, after an additional 24h, the cells were evaluated for their metabolic activity. The dendrimers

and A $\beta_6$ /A $\beta_7$  peptide were reconstituted in DMSO (0.02%), diluted into DMEM/F-12 media, sterilized by UV and immediately added to the cells.

**AlamarBlue® assay.** The A $\beta_6$ /A $\beta_7$  cytotoxicity (S. Figs. 6-51, 6-52A and 6-53A) was evaluated by measuring the cell metabolic activity, 24h after the addition of A $\beta_6$ /A $\beta_7$  at a concentration of 25 $\mu$ M using AlamarBlue® (indicator dye BUF012B, Bio-Rad) according to the manufacturer's instructions. The fluorescence intensity of each experimental condition was measured using an excitation wavelength of 530nm and an emission wavelength of 590nm with a Synergy HT microplate reader (Bio-Tek Instruments). *p*-values were calculated using two-tailed t-test. Results are presented as mean  $\pm$  SEM of 6 independent experiments for each experimental condition.

**Live/Dead assay.** Cell viability was also evaluated by Live/Dead assay using calcein AM (Life Technologies) to stain live cells and propidium iodide (PI, Biotium, Inc.) to stain dead cells (S. Figs. 6-52B and 6-53B). Viable cells were stained in green and dead cells were stained in red. Briefly, cells were incubated for 20min with both dyes and then observed under a fluorescence microscope (Axio Imager Z1m, Zeiss, Germany).

**Quantification of the  $\beta$ -sheet content under cell culture determined by ThT assay.** Cells were cultured with A $\beta_6$ /A $\beta_7$  within dendrimers during 24h. Afterwards, 1% Thioflavin T (in sterile D-PBS) were added to the wells. After 20min, the ThT fluorescence intensity was measured using a fluorescence spectrometer (Jasco, FP-8500, Japan), using an excitation wavelength of 435nm and an emission wavelength of 465nm, with a bandwidth of 10nm. Each condition was repeated in triplicate and using data from two independent experiments<sup>3</sup> (S. Fig. 6-54).

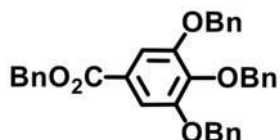
**Protein expression.** For immunostaining, fluorescence images (Figs. 6-3 and S. Fig. 6-48, 6-50) were collected after 1 day of cell culture. Samples were washed twice with PBS, fixed in 10% neutral buffered formalin for 30min at 4 °C, permeabilized with 0.1% Triton X-100 in PBS for 5min, and blocked with 3% BSA in PBS for 30min at room temperature. To evaluate the accumulation of A $\beta_6$ , a primary antibody (Oligomer Polyclonal Antibody, clone A11, Rabbit, 1:200 dilution in 1% w/v BSA/PBS, Life Technologies) against A $\beta$  oligomeric forms or a primary antibody against A $\beta_7$  aggregates (Biotin anti- $\beta$ -Amyloid, 1-16 Antibody, Mouse IgG1, 1:200 dilution in 1% w/v BSA/PBS, Biolegend) was employed, followed by the secondary antibody rabbit anti-mouse Alexafluor-488 (1:500 dilution in 1% w/v BSA/PBS, anti-mouse, Invitrogen). For the  $\beta$ III-tubulin expression it was used an anti- $\beta$  III Tubulin Mouse IgG (1:500 dilution in 1% w/v BSA/PBS, Abcam). A phalloidin-TRITC conjugate was used (1:200 dilution in PBS for 30min,

Sigma) to assess the cytoskeleton organization. Nuclei were counterstained with 1mg/mL of 4,6-diamidino-2-phenylindole (DAPI, Sigma) for 30min. Samples were washed with PBS and placed in an imaging dish for confocal microscope (Leica, TCS SP8).

**Bio-AFM experiments.** Cell nanomechanical analysis was performed using a JPK Nanowizard 3 (JPK, Germany) under PBS at 37°C. Force curves were acquired using sQube cantilevers (with tips of borosilicate spheres of 5µm diameter, CP-qp-CONT-BSG, sQube), presenting a  $k \sim 0.1$  N/m. All cantilevers were calibrated before performing the analysis using the JPK non-contact method. For each experimental condition, at least 15 fixed cells were analysed and it was acquired at least 10 curves per cell. All force curves were fitted using the Hertz model to obtain the Young's modulus (Figs. 6-4D, S. Fig. 6-59).

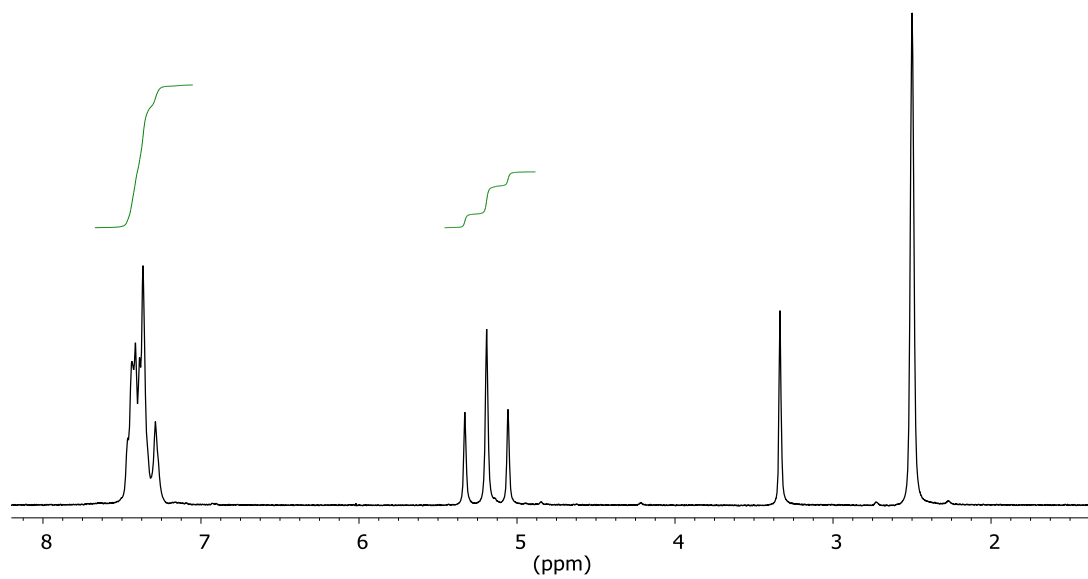
For the cell height analysis, at least 10 cells per experimental condition were analysed under the JPK QI Imaging Mode, using the cantilevers qpBioAC-CB1 (NanoSensors, Germany). To obtain cell height data cellular cross-sections were retrieved from the AFM Height Images. All the presented data are averages of 10 cells with the corresponding standard deviations (Figs. 6-4C and S. Fig. 6-60).

- **Synthesis and Characterization of New Compounds**

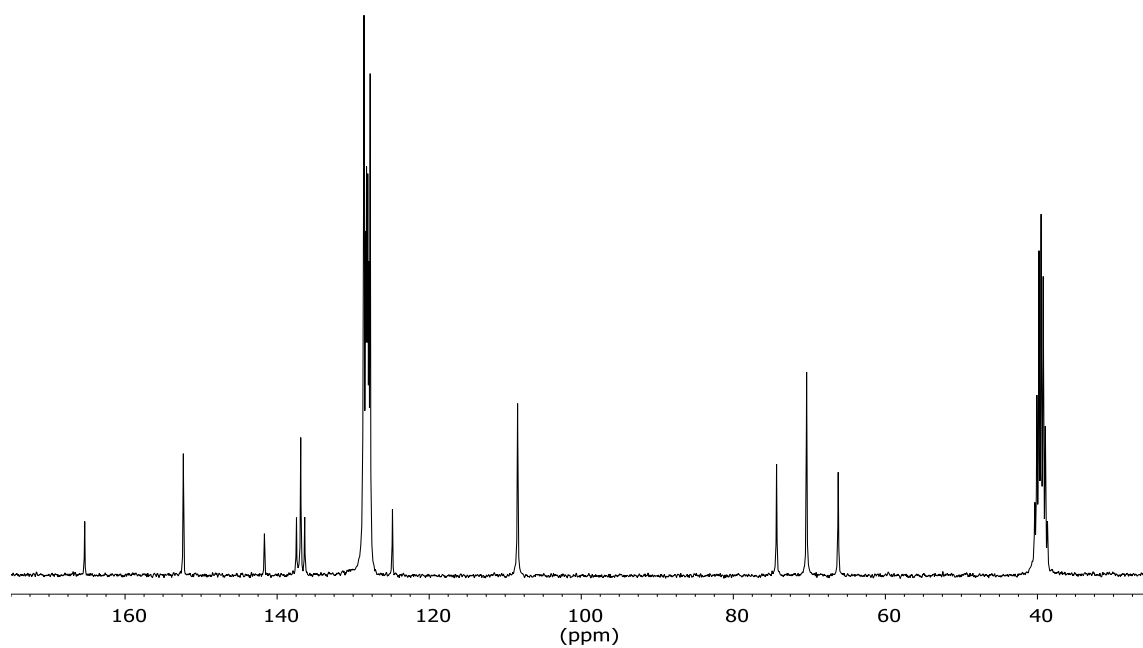


**Benzyl 3,4,5-tris(benzyloxy)benzoate.**  $K_2CO_3$  (12.04 g, 87.15 mmol), benzyl bromide (14.91 g, 87.15 mmol) and NaI (2.61 g, 17.43 mmol) were added to a stirred solution of gallic acid (3.0 g, 17.43 mmol) in MeOH (180 mL). The reaction was refluxed for 16 h, cooled down to RT and then,  $H_2O$  (30 mL) was added. After evaporation, the mixture was diluted with  $H_2O$  (50 mL) and extracted with EtOAc (3 x 20 mL). The combined organic layers were dried and concentrated to give a crude product that was recrystallized from EtOH to give benzyl 3,4,5-tris(benzyloxy)benzoate as a white solid (8.19 g, 88%).  $^1H$  NMR (300 MHz,  $DMSO-d_6$ )  $\delta$ : 7.63-7.17 (m, 22H), 5.33 (s, 2H), 5.17 (s, 4H), 5.06 (s, 2H).  $^{13}C$  NMR (75 MHz,  $DMSO-d_6$ )  $\delta$ : 165.3, 152.3, 141.7, 137.5, 136.9, 136.4, 128.7, 128.6, 128.4, 128.2, 128.1, 127.9, 127.8, 124.8, 108.4, 74.3, 70.4, 66.2. HRMS (APCI-FIA-TOF, positive mode,  $m/z$ ): 531.2166. Calcd for  $[M+H]^+$ ,  $C_{35}H_{31}O_5$ : 531.2171. IR (neat, ATR)  $\nu_{max}$ : 3091, 3033, 1713, 1590, 1498, 1109  $cm^{-1}$ .

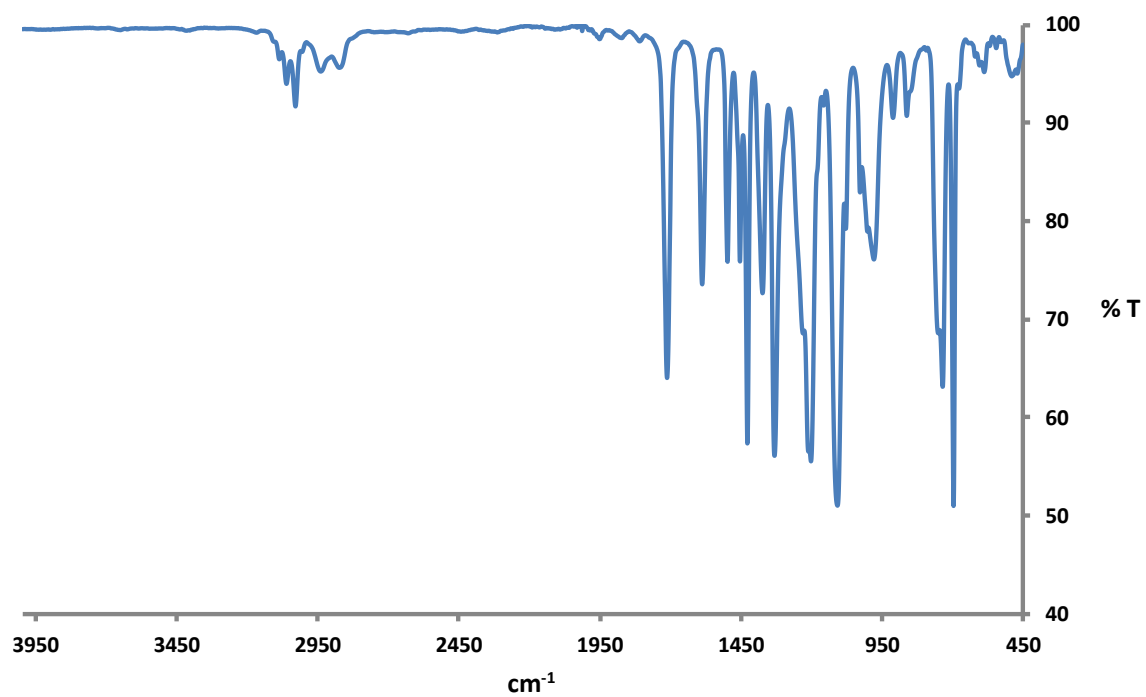




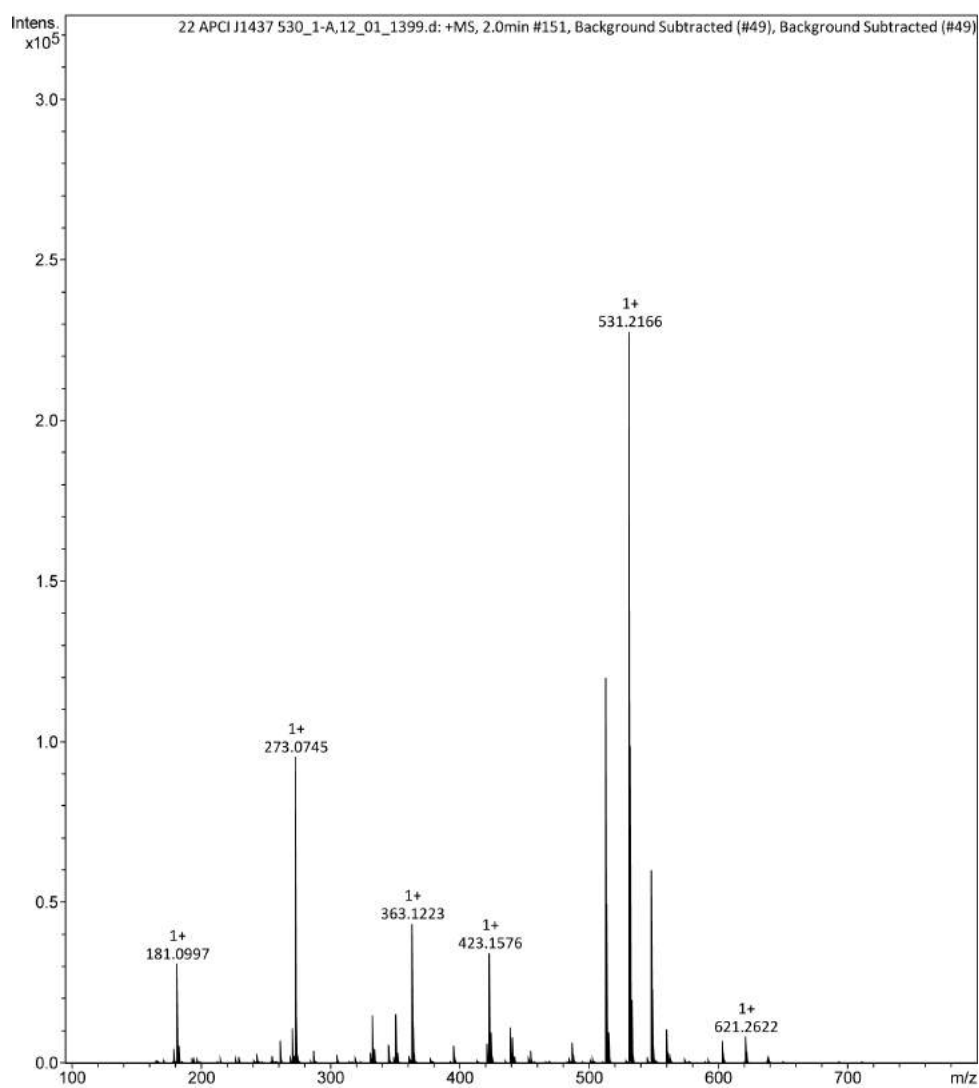
Supplementary Fig. 6-1.  $^1\text{H}$  NMR spectrum ( $\text{DMSO-d}_6$ ) of benzyl 3,4,5-tris(benzyloxy)benzoate.



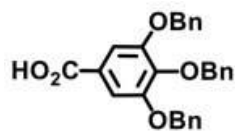
Supplementary Fig. 6-2.  $^{13}\text{C}$  NMR spectrum ( $\text{DMSO-d}_6$ ) of benzyl 3,4,5-tris(benzyloxy)benzoate.



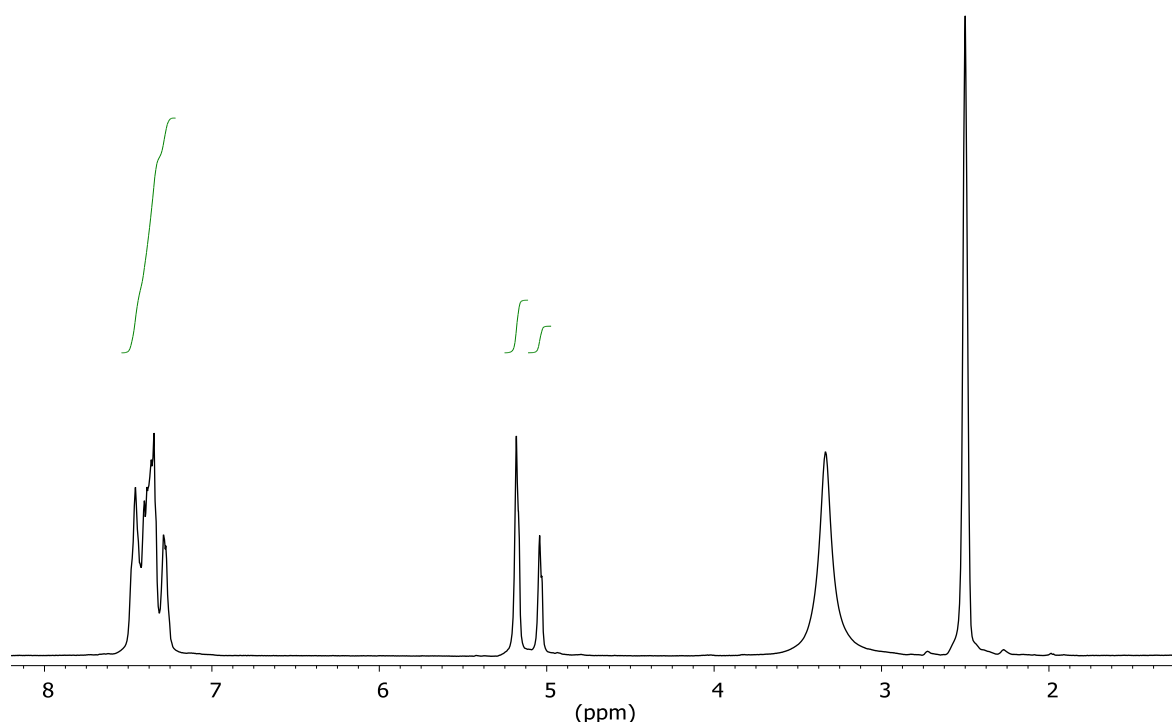
Supplementary Fig. 6-3. IR spectrum of benzyl 3,4,5-tris(benzyloxy)benzoate.



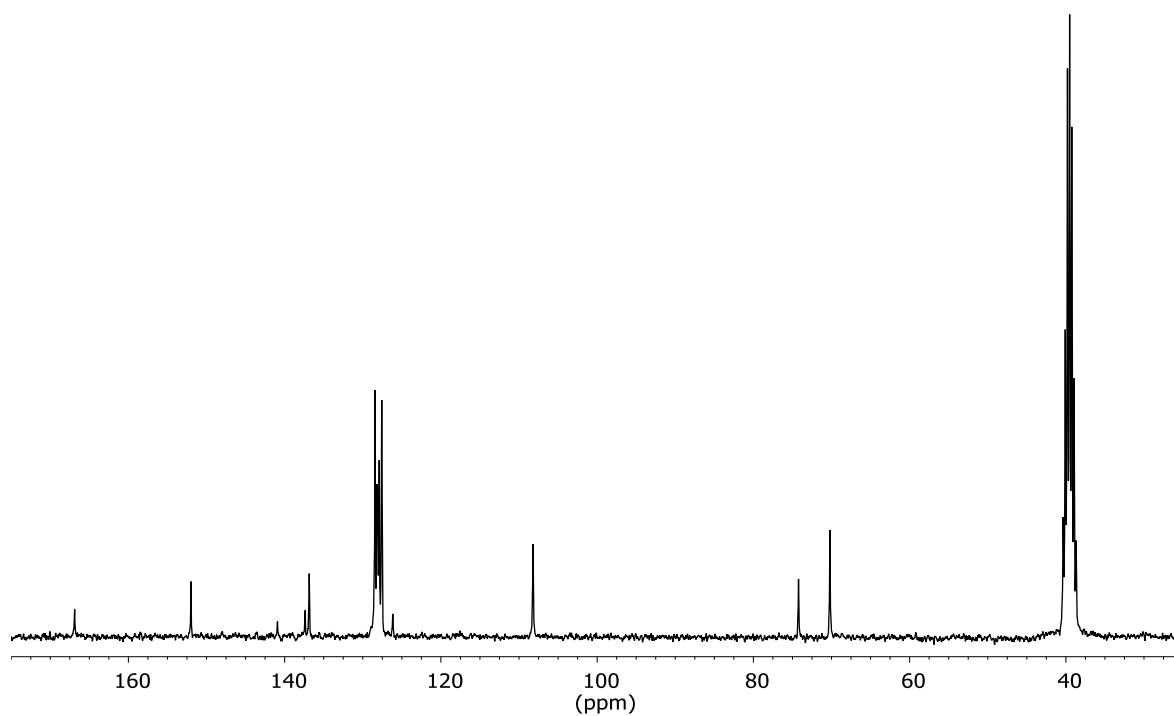
Supplementary Fig. 6-4. HR-MS of benzyl 3,4,5-tris(benzyloxy)benzoate.



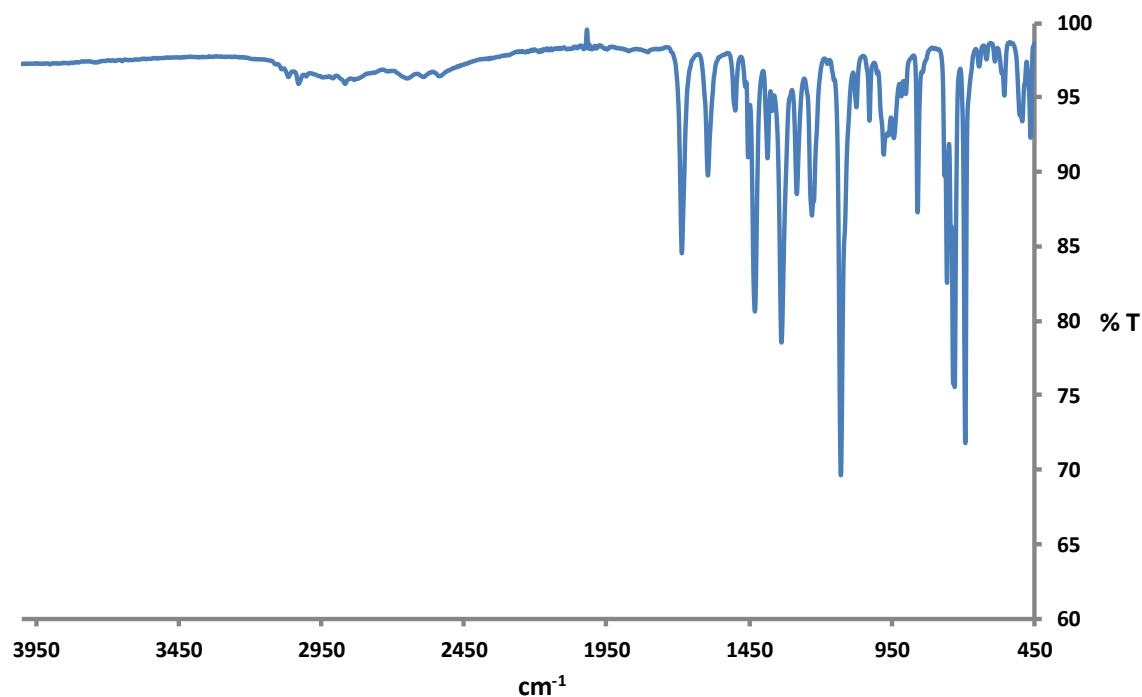
**3,4,5-Tris(benzyloxy)benzoic acid.** A stirred solution of benzyl 3,4,5-tris(benzyloxy)benzoate (5.69 g, 10.7 mmol) in a 3M KOH solution in MeOH (285 mL) was refluxed overnight. The mixture was cooled down to RT and acidified (pH= 3-4) by addition of 3M HCl. The resulting precipitate was filtered, dissolved in EtOAc (80 mL) and washed with H<sub>2</sub>O (40 mL). The aqueous phase was extracted with CH<sub>2</sub>Cl<sub>2</sub> (3 x 30 mL). The combined organic phase was dried and concentrated. The crude product was purified by automated MPLC (gradient from hexane to EtOAc, silica, 40 min) to afford 3,4,5-tris(benzyloxy)benzoic acid as a white solid (4.20 g, 89%). <sup>1</sup>H NMR (300 MHz, DMSO-*d*<sub>6</sub>) δ: 7.53-7.22 (m, 17H), 5.18 (s, 4H), 5.03 (s, 2H). <sup>13</sup>C NMR (75 MHz, DMSO-*d*<sub>6</sub>) δ: 166.9, 152.0, 140.9, 136.9, 128.4, 128.2, 128.1, 127.9, 127.6, 126.2, 108.2, 74.2, 70.2. HRMS (APCI-FIA-TOF, positive mode, *m/z*): 441,1694. Calcd for [M+H]<sup>+</sup>, C<sub>28</sub>H<sub>25</sub>O<sub>5</sub>: 441.1702. IR (neat, ATR) ν<sub>max</sub>: 3029, 1686, 1595, 1128 cm<sup>-1</sup>.



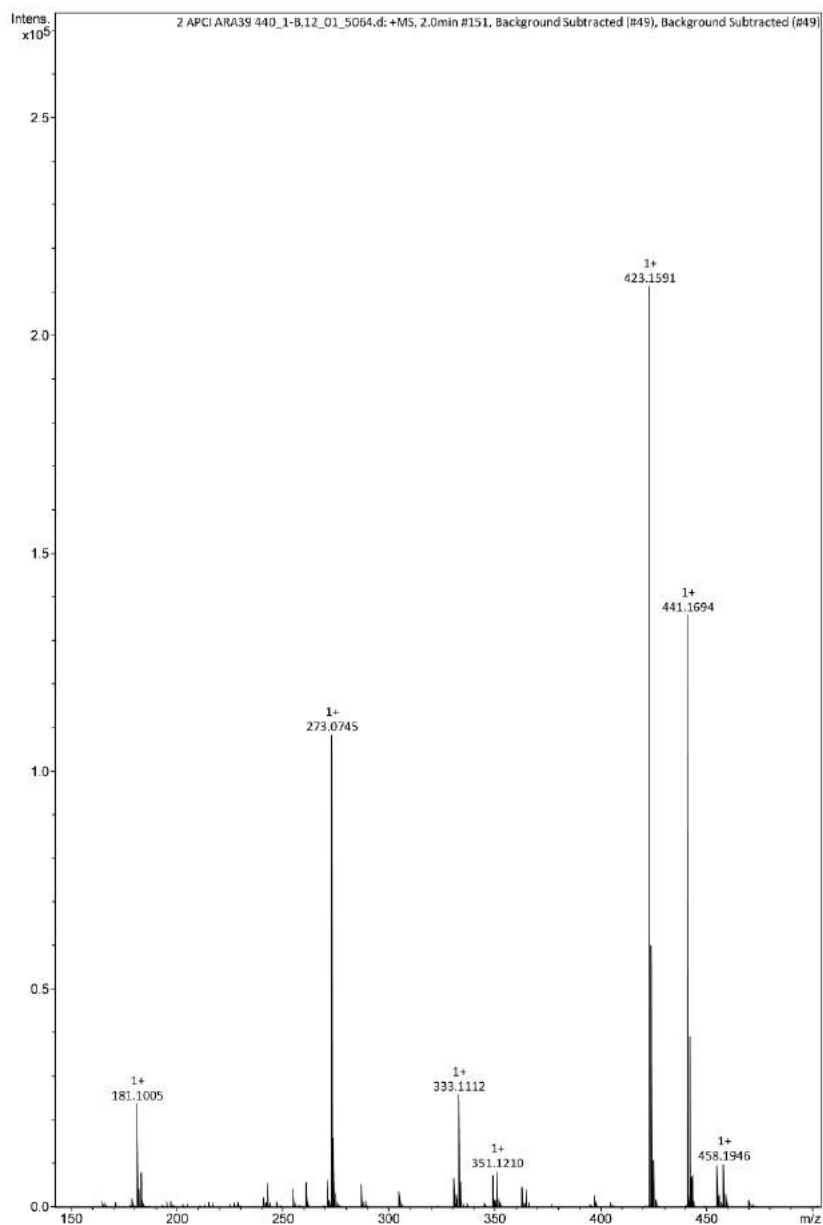
Supplementary Fig. 6-5. <sup>1</sup>H NMR spectrum (DMSO-*d*<sub>6</sub>) of 3,4,5-tris(benzyloxy)benzoic acid.



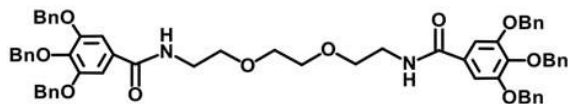
Supplementary Fig. 6-6.  $^{13}\text{C}$  NMR spectrum ( $\text{DMSO-d}_6$ ) of 3,4,5-tris(benzyloxy)benzoic acid.



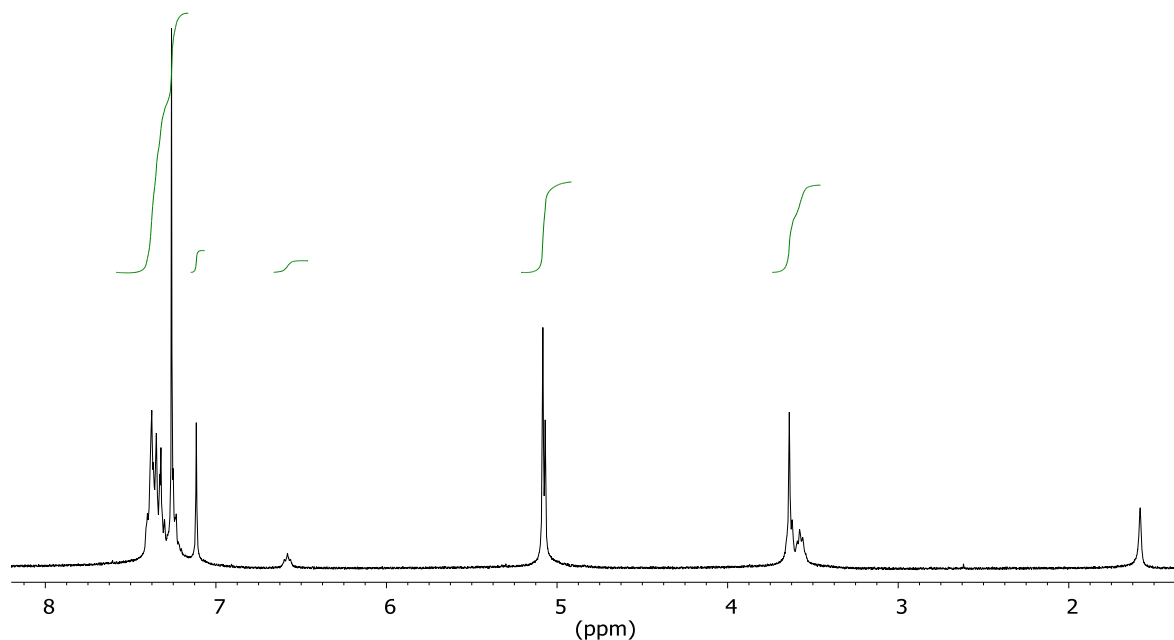
Supplementary Fig. 6-7. IR spectrum of 3,4,5-tris(benzyloxy)benzoic acid.



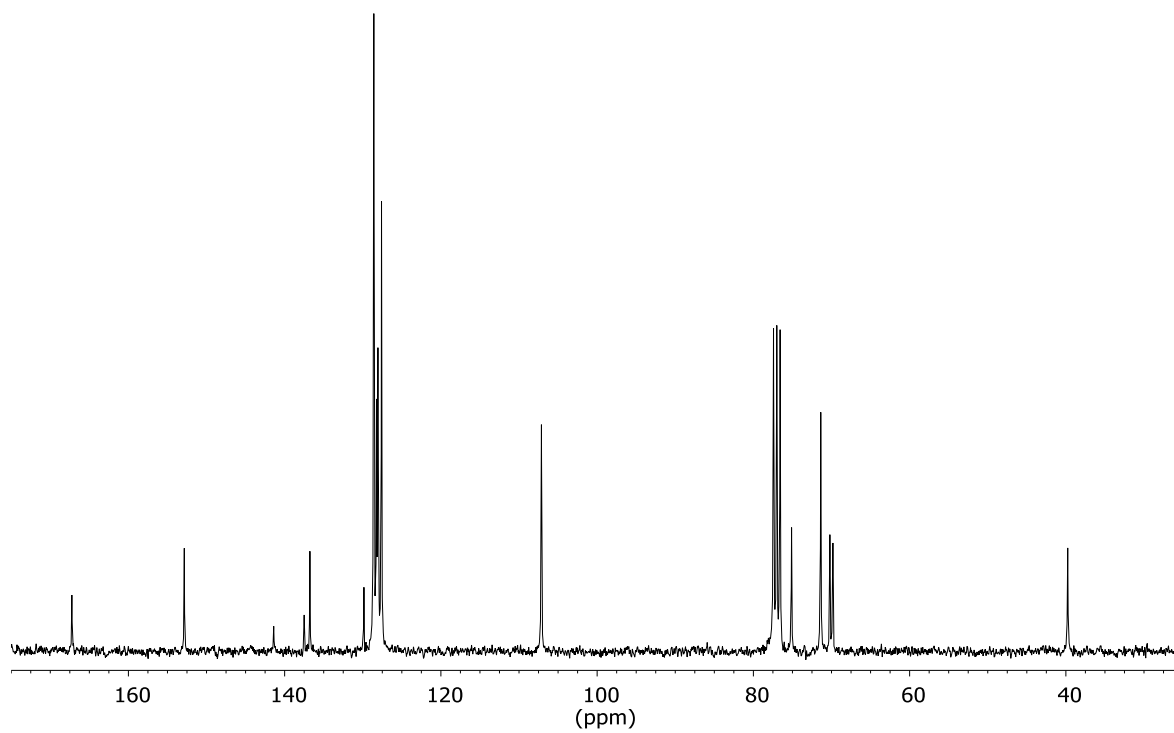
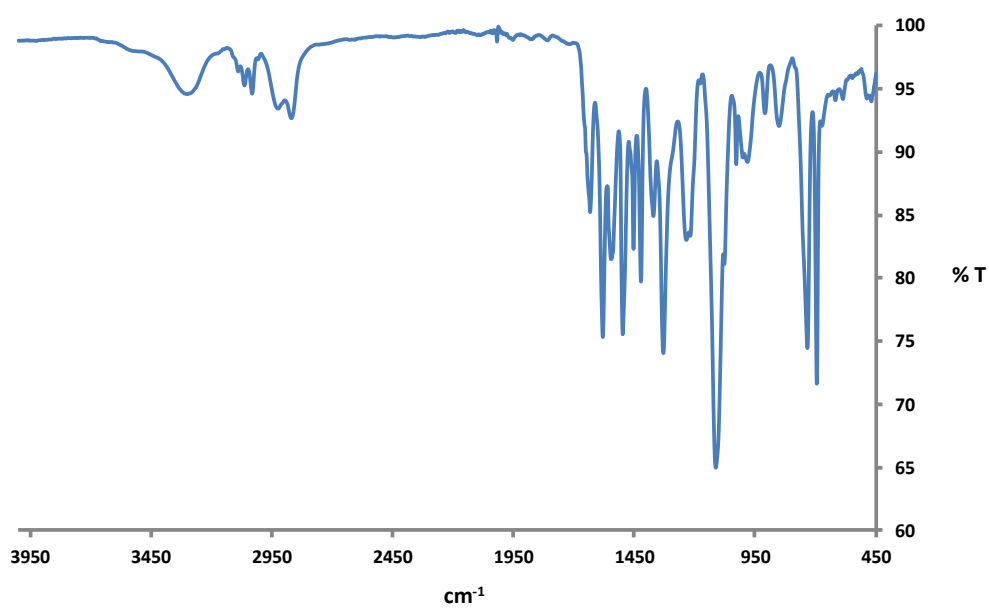
Supplementary Fig. 6-8. HR-MS of 3,4,5-tris(benzyloxy)benzoic acid.



**2G0-GaOBn.** 3,4,5-Tris(benzyloxy)benzoic acid (334 mg, 0.76 mmol), HOBT (103 mg, 0.76 mmol) and EDC (145 mg, 0.76 mmol) were added to a solution of 2,2'-(ethylenedioxy)bis(ethylamine) (45 mg, 0.30 mmol) in DMSO (6 mL). After 20 h of stirring at RT, the reaction mixture was distributed between EtOAc (30 mL) and brine (30 mL). The aqueous phase was extracted with EtOAc (3 x 30 mL). The combined organic phase was washed with H<sub>2</sub>O (30 mL), dried and evaporated under vacuum. The crude product was purified by automated MPLC (gradient from hexane to 100% EtOAc and then to 100% CH<sub>2</sub>Cl<sub>2</sub>, neutral alumina, 25 min) to afford 2G0-GaOBn (255 mg, 85%) as a white solid. <sup>1</sup>H NMR (300 MHz, CDCl<sub>3</sub>) δ: 7.47-7.18 (m, 30H), 7.11 (s, 4H), 6.62-6.53 (m, 2H), 5.08 (s, 8H), 5.07 (s, 4H), 3.69-3.50 (m, 12H). <sup>13</sup>C NMR (75 MHz, CDCl<sub>3</sub>) δ: 167.2, 152.8, 141.4, 137.5, 136.8, 129.9, 128.6, 128.2, 128.1, 128.0, 127.6, 107.1, 75.1, 71.4, 70.2, 69.8, 39.8. IR (neat, ATR) ν<sub>max</sub>: 3310, 3064, 3033, 1634, 1581, 1112 cm<sup>-1</sup>.

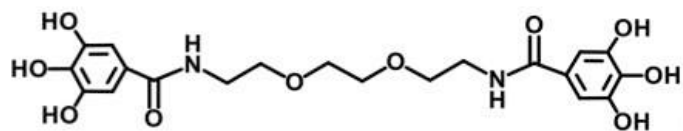


Supplementary Fig. 6-9. <sup>1</sup>H NMR spectrum (CDCl<sub>3</sub>) of 2G0-GaOBn.

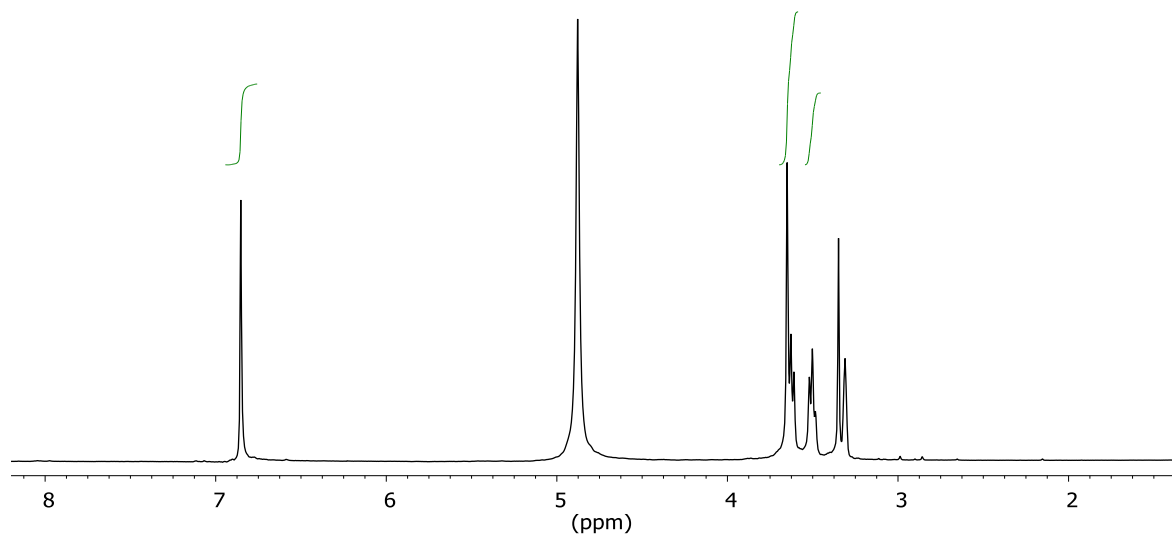
Supplementary Fig. 6-10.  $^{13}\text{C}$  NMR spectrum ( $\text{CDCl}_3$ ) of 2G0-GaOBn.

Supplementary Fig. 6-11. IR spectrum of 2G0-GaOBn.

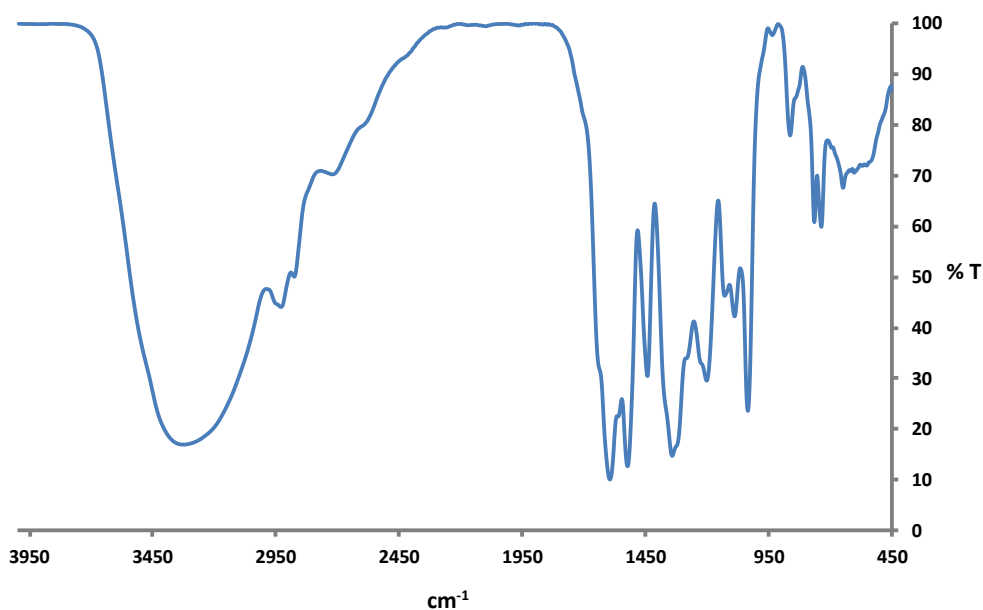




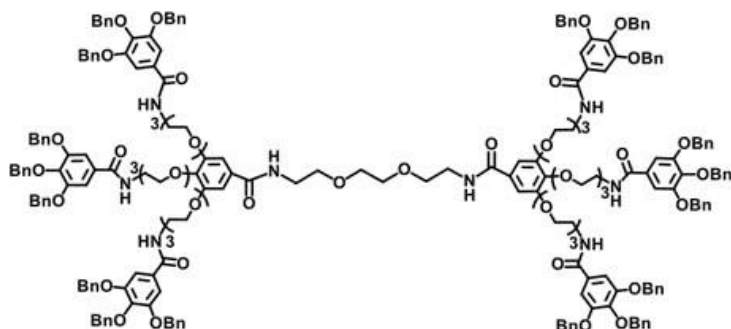
**2G0-GaOH.** Pd/C (16 mg, 10%) was added to a solution of 2G0-GaOBn (160 mg, 0.16 mmol) in a mixture of DMF-MeOH 3:1 (4 mL). The resulting mixture was stirred under H<sub>2</sub> (1 atm) for 20 h. The catalyst was removed by filtration through Celite. The filtrate was concentrated and then purified by short column chromatography (MeOH-CH<sub>2</sub>Cl<sub>2</sub>-H<sub>2</sub>O 3:3:0.2, silica) to give 2G0-GaOH as a green solid (71 mg, 98%). <sup>1</sup>H NMR (300 MHz, CD<sub>3</sub>OD) δ: 6.85 (s, 4H), 3.67-3.57 (m, 8H), 3.50 (t, *J*=5.5 Hz, 4H). IR (KBr)  $\nu_{\text{max}}$ : 3319, 1636, 1592, 1338, 1033 cm<sup>-1</sup>.



Supplementary Fig. 6-12. <sup>1</sup>H NMR spectrum (CD<sub>3</sub>OD) of 2G0-GaOH.

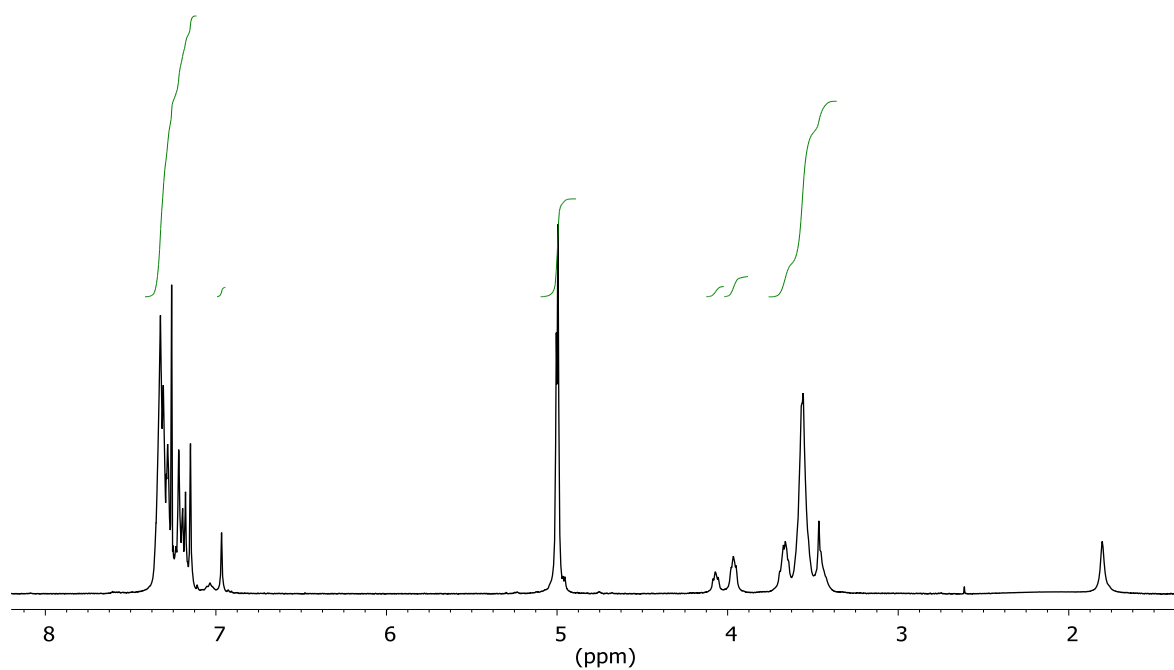


Supplementary Fig. 6-13. IR spectrum of 2G0-GaOH.

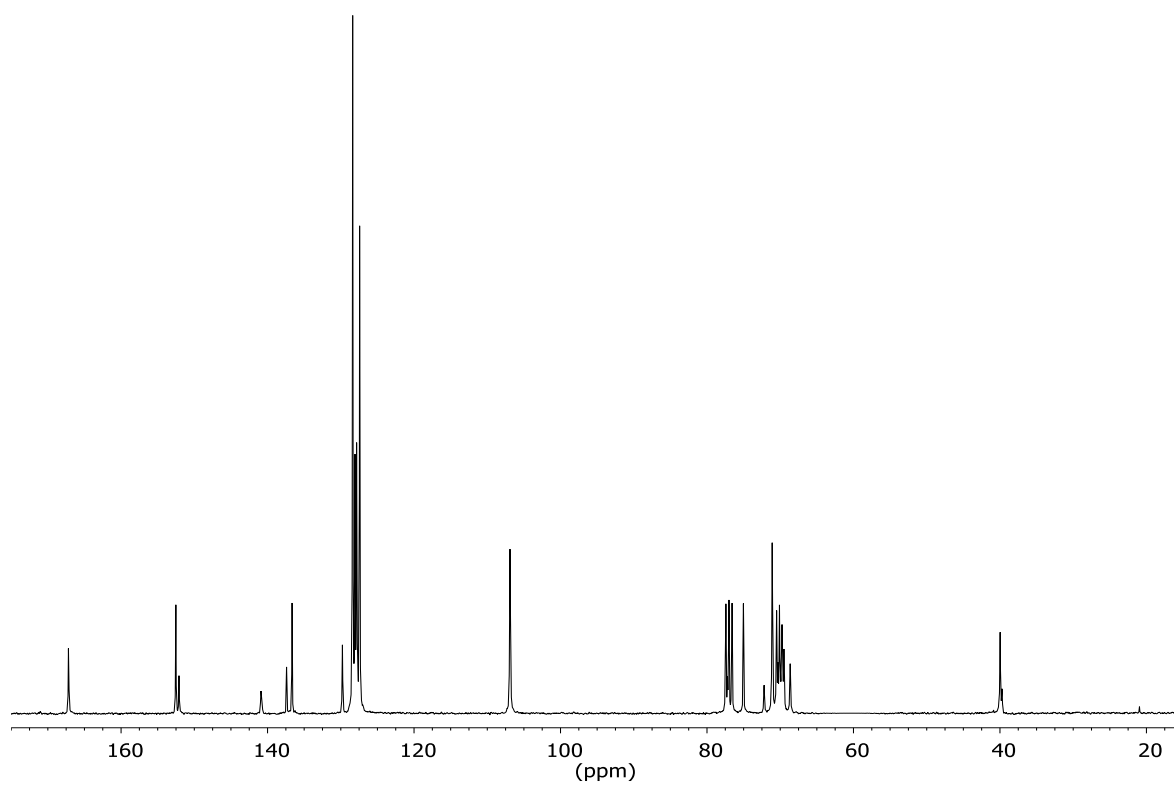
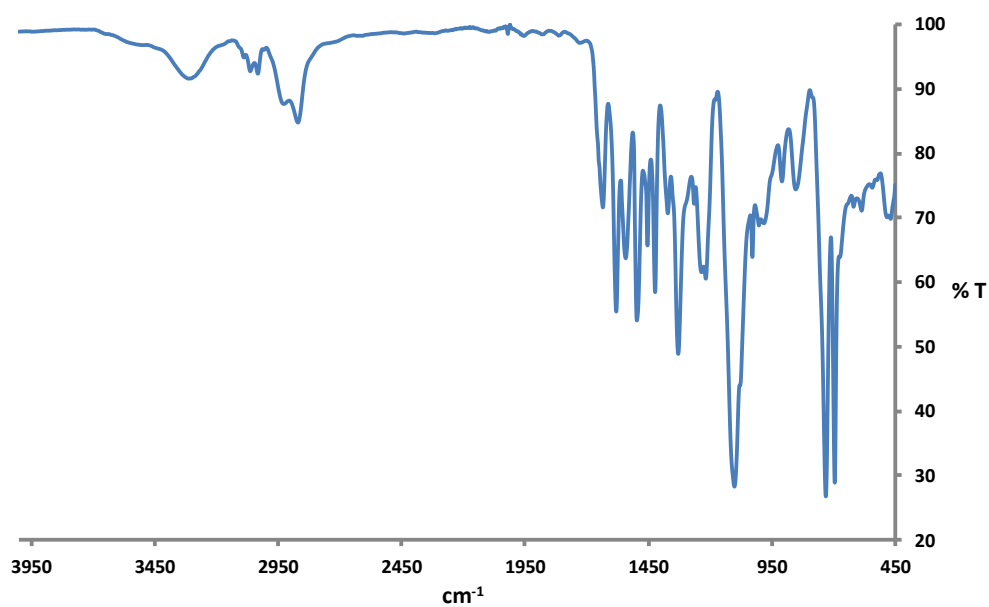


**2G1-GaOBn.** 3,4,5-Tris(benzyloxy)benzoic acid (466 mg, 1.06 mmol), Et<sub>3</sub>N (0.224 mL, 1.06 mmol), HOBT (143 mg, 1.06 mmol) and EDC (210 mg, 1.06 mmol) were added to a solution of 2[G1]-NH<sub>2</sub>·HCl (205 mg, 0.14 mmol) in DMSO (8 mL). After 24 h of stirring at rt, the reaction mixture was distributed between EtOAc (50 mL) and brine (50 mL). The aqueous phase was extracted with EtOAc (3 x 50 mL). The combined organic phase was washed with 0.1M HCl (30 mL) and H<sub>2</sub>O (50 mL), dried and evaporated under vacuum. The crude product was purified by automated MPLC (gradient from EtOAc to 25% MeOH, neutral alumina, 25 min) to afford 2G1-GaOBn (428 mg, 75%) as a pale yellow solid. <sup>1</sup>H NMR (300 MHz, CDCl<sub>3</sub>) δ: 7.40-7.10 (m, 102H), 6.97 (s, 4H), 5.03-4.94 (m, 36H), 4.07 (t, *J*=3.5 Hz, 4H), 3.96 (t, *J*=3.7 Hz, 8H), 3.75-3.38 (m, 72H). <sup>13</sup>C NMR (75 MHz, CDCl<sub>3</sub>) δ: 167.2, 167.1, 152.5, 152.1, 140.9, 137.4,

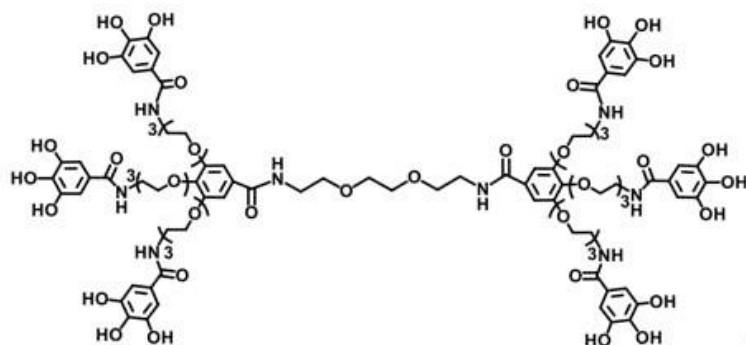
136.7, 129.8, 128.4, 128.1, 127.8, 127.7, 127.4, 106.9, 75.0, 72.2, 71.1, 70.5, 70.3, 70.1, 70.0, 69.8, 69.6, 69.5, 68.6, 40.7, 39.7. IR (neat, ATR)  $\nu_{\text{max}}$ : 3314, 3065, 3032, 1634, 1580, 1100  $\text{cm}^{-1}$ .



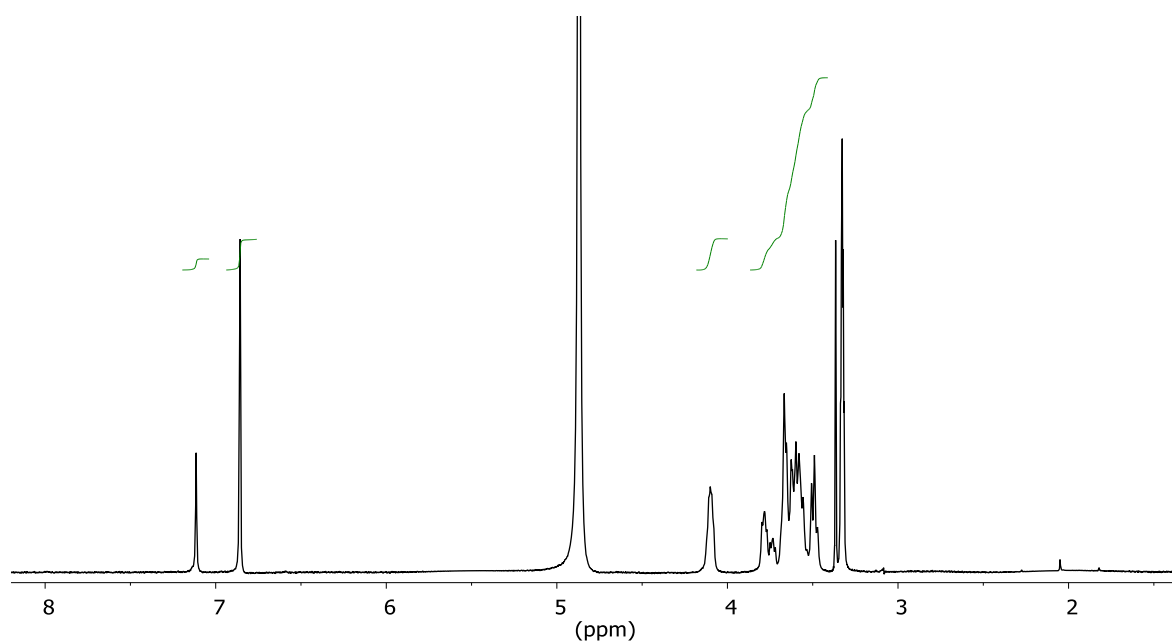
Supplementary Fig. 6-14.  $^1\text{H}$  NMR spectrum ( $\text{CDCl}_3$ ) of 2G1-GaOBn.

Supplementary Fig. 6-15.  $^{13}\text{C}$  NMR spectrum ( $\text{CDCl}_3$ ) of 2G1-GaOBn.

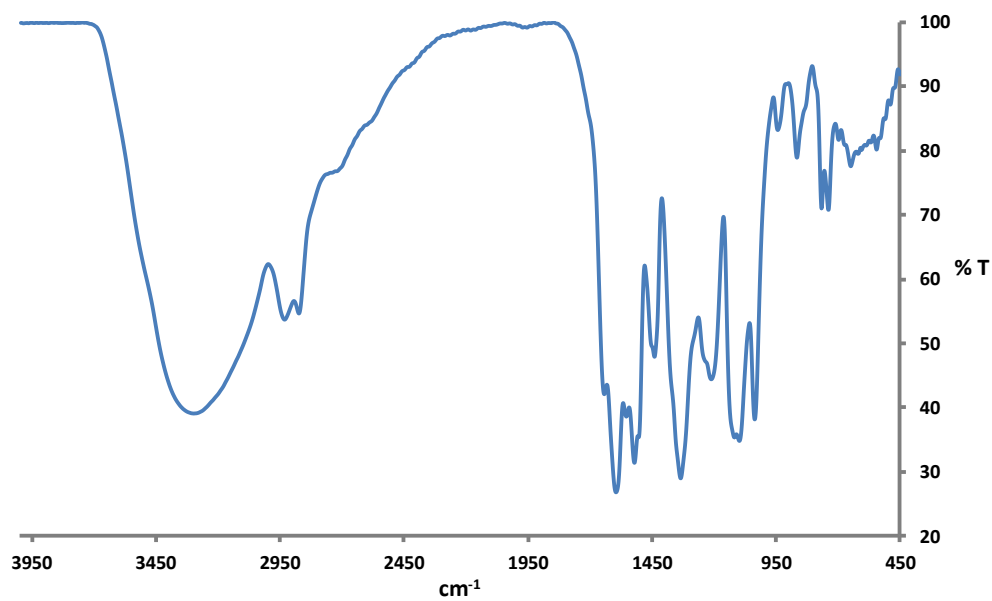
Supplementary Fig. 6-16. IR spectrum of 2G1-GaOBn.



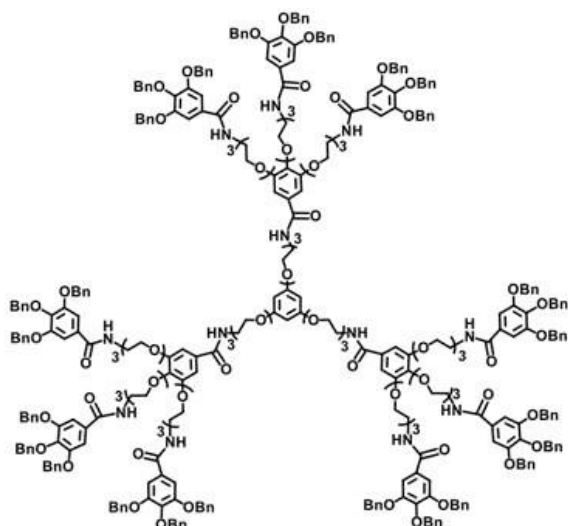
**2G1-GaOH.** Pd/C (60 mg, 20%) was added to a solution of 2G1-GaOBn (300 mg, 0.075 mmol) in a mixture of EtOAc-MeOH 1:1 (8 mL). The resulting mixture was stirred under H<sub>2</sub> (1 atm) for 14 h. The catalyst was removed by filtration through Celite. The filtrate was concentrated and then purified by short column chromatography (MeOH-CH<sub>2</sub>Cl<sub>2</sub>-H<sub>2</sub>O 3:3:0.2, silica) to give 2G1-GaOH as a green solid (133 mg, 82%). <sup>1</sup>H NMR (300 MHz, CD<sub>3</sub>OD) δ: 7.11 (s, 4H), 6.86 (s, 12H), 4.14-4.05 (m, 12H), 3.82-3.46 (m, 72H). IR (KBr) ν<sub>max</sub>: 3296, 1625, 1593, 1330, 1116, 1097 cm<sup>-1</sup>.



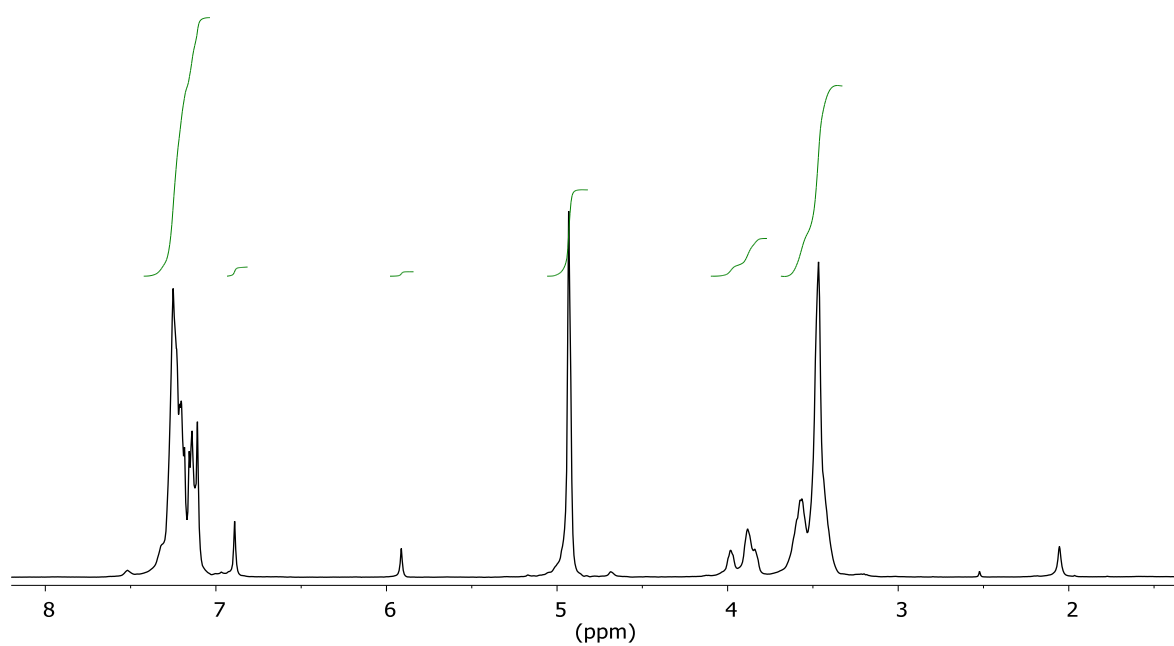
Supplementary Fig. 6-17. <sup>1</sup>H NMR spectrum (CD<sub>3</sub>OD) of 2G1-GaOH.



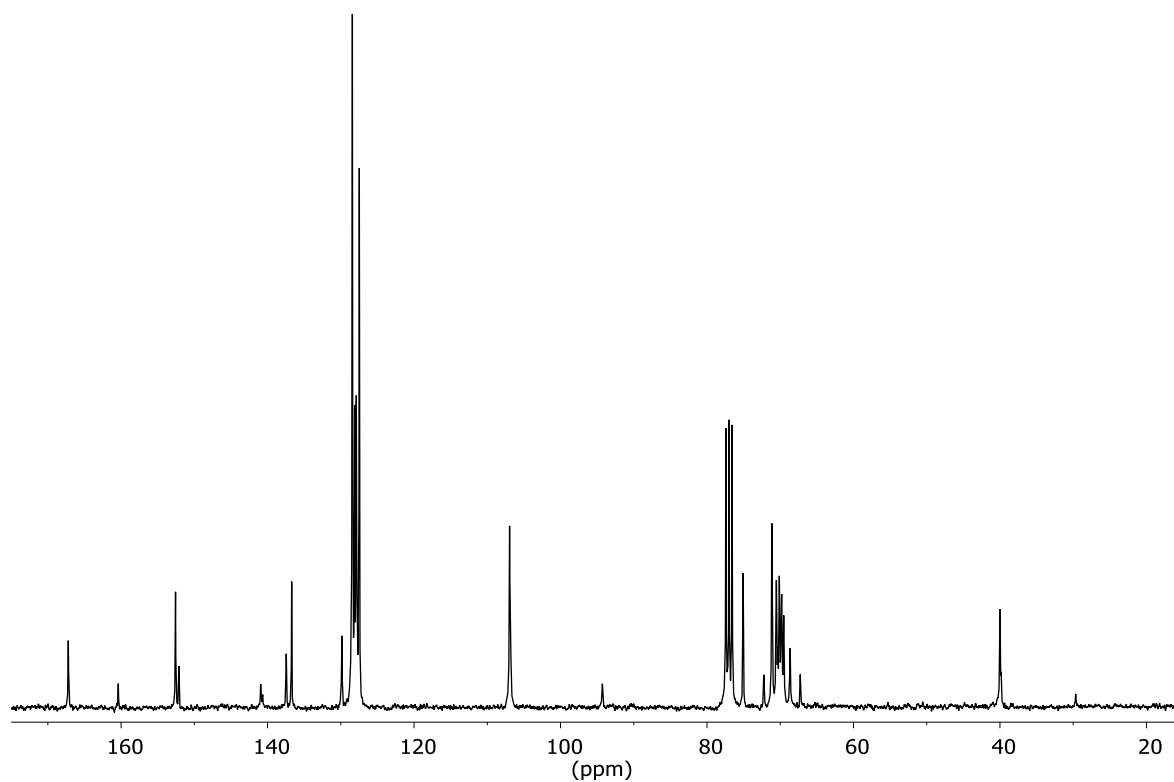
Supplementary Fig. 6-18. IR spectrum of 2G1-GaOH.



**3G1-GaOBn.** 3,4,5-Tris(benzyloxy)benzoic acid (268 mg, 0.61 mmol), Et<sub>3</sub>N (0.128 mL, 0.61 mmol), HOBT (82 mg, 0.61 mmol) and EDC (120 mg, 0.61 mmol) were added to a solution of 3G1-NH<sub>2</sub>·HCl (134 mg, 0.05 mmol) in DMSO (4.9 mL). After 36 h of stirring at rt, the reaction mixture was distributed between EtOAc (50 mL) and brine (50 mL). The aqueous phase was extracted with EtOAc (3 x 50 mL). The combined organic phase was washed with 0.1M HCl (30 mL) and H<sub>2</sub>O (50 mL), dried and evaporated under vacuum. The crude product was purified by automated MPLC (gradient from EtOAc to 25% MeOH, neutral alumina, 25 min) to afford 3G1-GaOBn (413 mg, 84%) as a pale yellow solid. <sup>1</sup>H NMR (300 MHz, CDCl<sub>3</sub>) δ: 7.37-7.08 (m, 153H), 6.89 (s, 6H), 4.93 (bs, 54H), 4.04-3.81 (m, 24H), 3.67-3.33 (m, 120H). <sup>13</sup>C NMR (75 MHz, CDCl<sub>3</sub>) δ: 167.2, 160.4, 152.6, 152.1, 140.9, 137.5, 136.7, 129.9, 129.8, 128.4, 128.1, 127.9, 127.5, 107.0, 106.8, 94.3, 75.1, 72.2, 71.2, 71.1, 70.5, 70.3, 70.1, 69.8, 69.5, 68.6, 67.3, 40.0. IR (neat, ATR) ν<sub>max</sub>: 3319, 3069, 3034, 1635, 1581, 1108 cm<sup>-1</sup>.

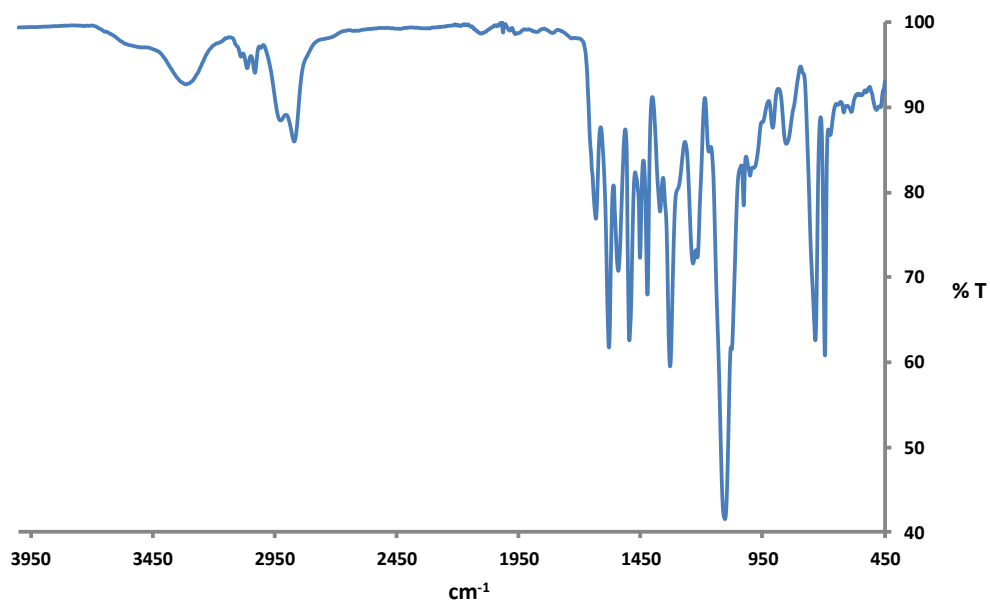


Supplementary Fig. 6-19.  $^1\text{H}$  NMR spectrum ( $\text{CDCl}_3$ ) of 3G1-GaOBn.

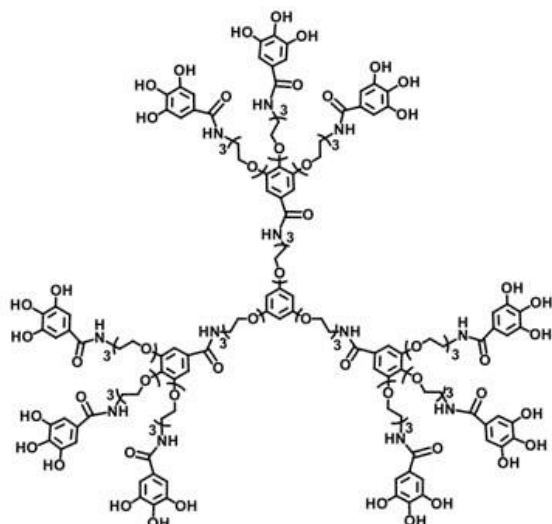


Supplementary Fig. 6-20.  $^{13}\text{C}$  NMR spectrum ( $\text{CDCl}_3$ ) of 3G1-GaOBn.

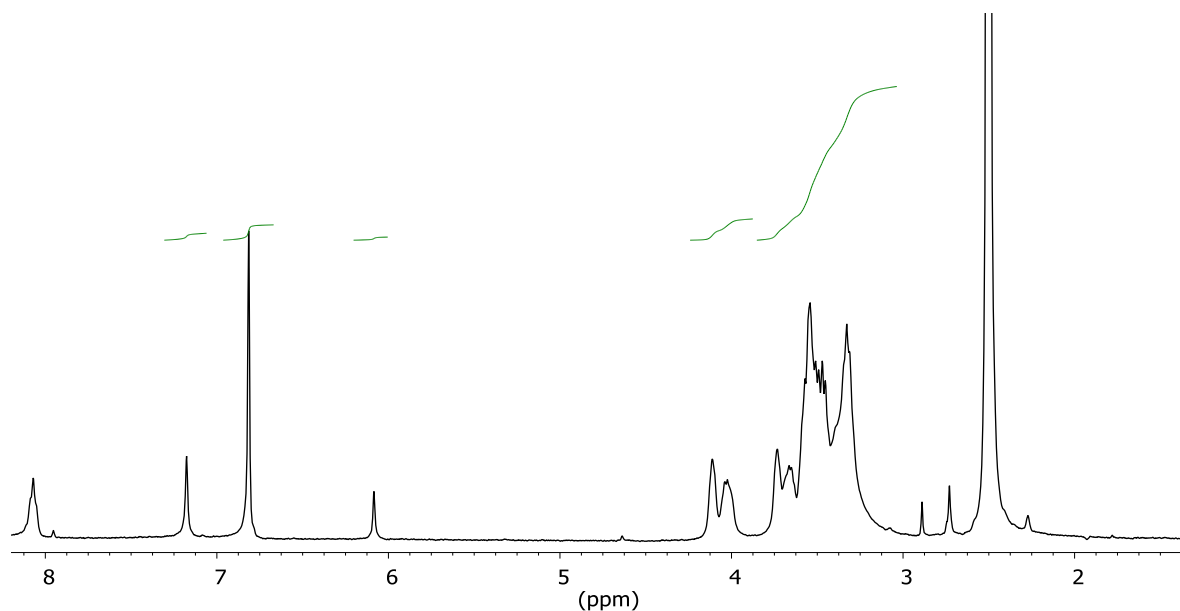




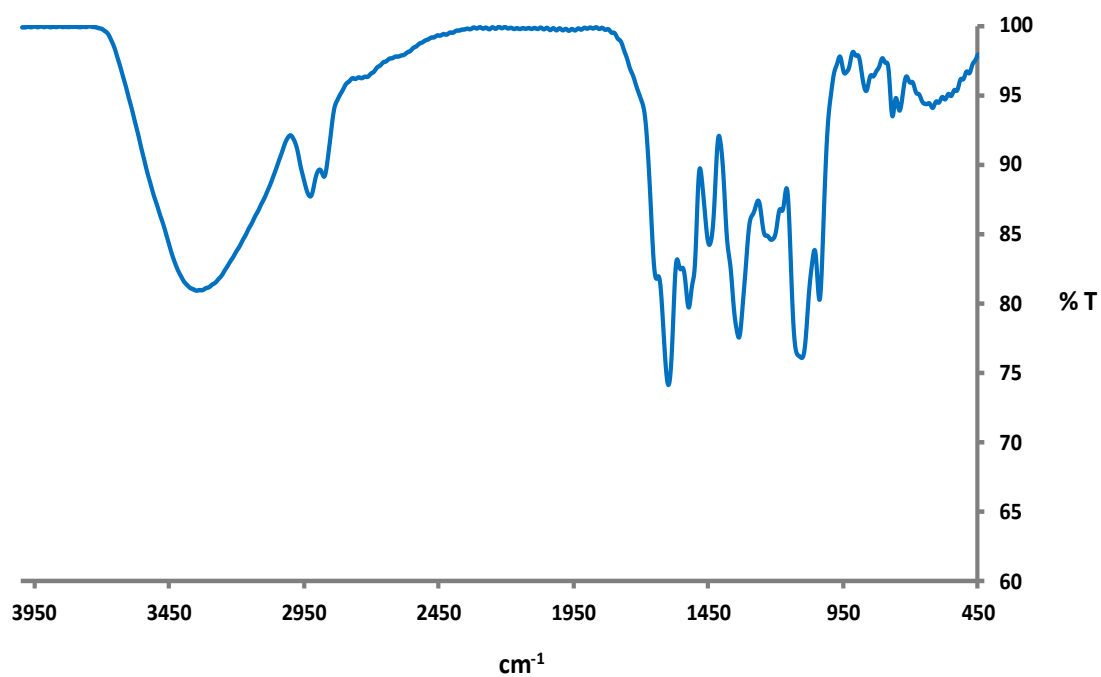
Supplementary Fig. 6-21. IR spectrum of 3G1-GaOBn.



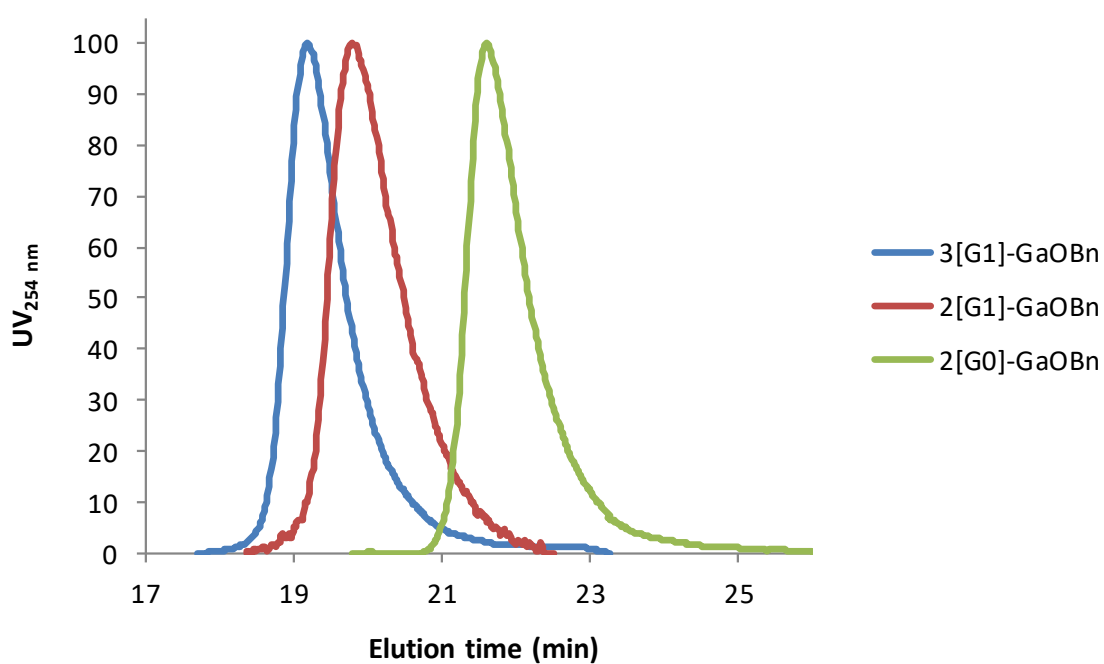
**3G1-GaOH.** Pd/C (10 mg, 20%) was added to a solution of 3G1-GaOBn (49 mg, 0.008 mmol) in a mixture of DMF-MeOH 4:1 (3 mL). The resulting mixture was stirred under H<sub>2</sub> (1 atm) for 24 h. The catalyst was removed by filtration through Celite. The filtrate was concentrated and then purified by short column chromatography (MeOH-CH<sub>2</sub>Cl<sub>2</sub>-H<sub>2</sub>O 3:3:0.2, silica) to give 3G1-GaOH as a green solid (26 mg, 90%). <sup>1</sup>H NMR (300 MHz, DMSO-d<sub>6</sub>) δ: 7.17 (s, 6H), 6.81 (s, 18H), 6.07 (s, 3H) 4.18-3.94 (m, 24H), 3.80-3.20 (m, 120H). IR (KBr) ν<sub>max</sub>: 3334, 1629, 1597, 1336, 1109, 1097 cm<sup>-1</sup>.



Supplementary Fig. 6-22. <sup>1</sup>H NMR spectrum (DMSO-d<sub>6</sub>) of 3G1-GaOH.



Supplementary Fig. 6-23. IR spectrum of 3G1-GaOH.



Supplementary Fig. 6-24. GPC elugrams of x[Gn]-GaOBn (THF).

### ▪ Molecular Simulations

All simulations were carried out during 120ns. The systems were formed with A $\beta$ <sub>42</sub> fibril (2MXU pdb file<sup>4</sup>) composed by 12 peptide chains (11-42 residues) and 1:1 ratio of each of dendrimer:

2MXU solvated and neutralized;

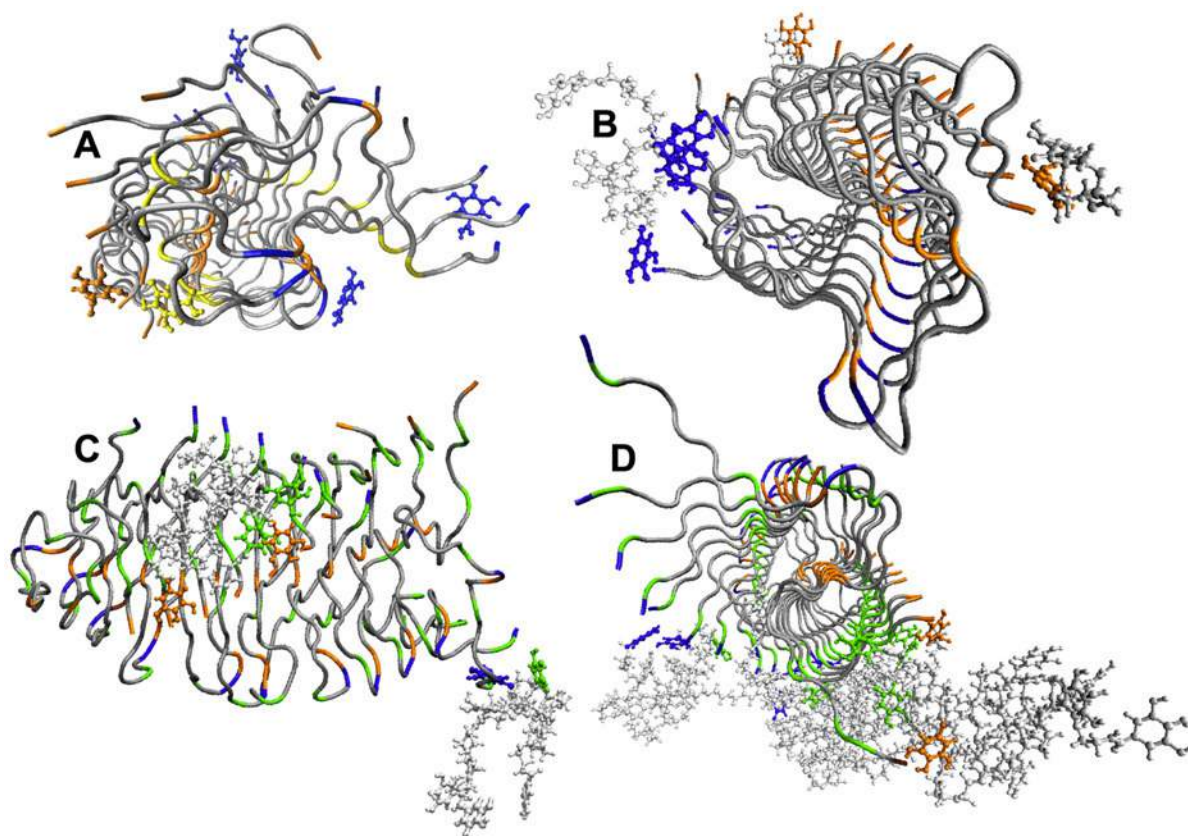
2MXU + 12 Ga solvated and neutralized;

2MXU + 12 2G0-GaOH solvated and neutralized;

2MXU + 12 2G1-GaOH solvated and neutralized;

2MXU + 12 3G1-GaOH solvated and neutralized.

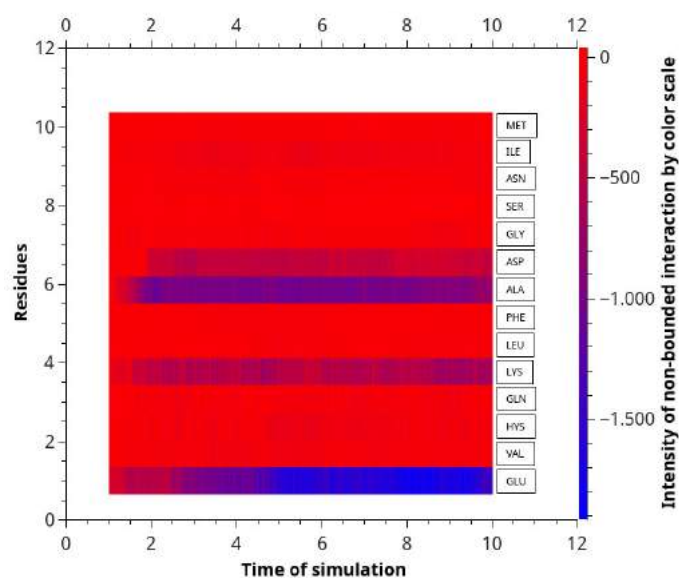
2G0-GaOH, 2G1-GaOH and 3G1-GaOH were parametrized and their topologies were built by merging dendrons whose topology was built using ATB<sup>5</sup>. The final system was minimized and simulated using GROMACS with the force field Gromos54a7<sup>6</sup>.



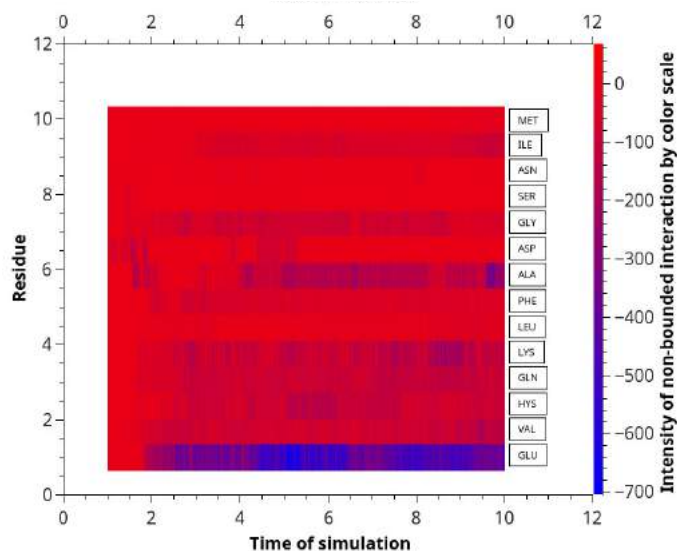
Supplementary Fig. 6-25. Optimized geometry for Ga (A), 2G0-GaOH (B), 2G1-GaOH (C) and, 3G1-GaOH (D) dendrimers interacting with the A $\beta$ <sub>42</sub> at its Glu (blue), Val (green) and Ala (orange) residues. A $\beta$ <sub>42</sub> remaining residues are shown in grey.

Supplementary Table 6-1 MD simulation analysis of the interaction between A $\beta$ <sub>i</sub> and dendrimers under a A $\beta$ <sub>i</sub>:dendrimers ratio of 1:1 showing the average number of H-bonds between the peptide chains of A $\beta$ <sub>i</sub> and the corresponding dendrimer, as well as the solvent-accessible surface area (SASA) of the region where dendrimers are interacting.

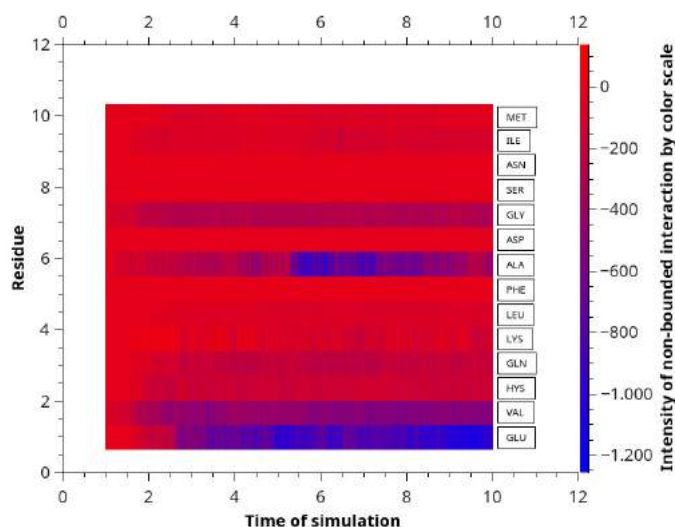
Disassembly 1:1	Number of H-Bonds	SASA (nm <sup>2</sup> )
A $\beta$ <sub>i</sub>	-	161.5 ±2.31
A $\beta$ <sub>i</sub> : Ga	44±3	164.7 ±1.81
A $\beta$ <sub>i</sub> : 2G0-GaOH	22±3	164.2 ±1.81
A $\beta$ <sub>i</sub> : 2G1-GaOH	46±5	164.9 ±2.02
A $\beta$ <sub>i</sub> : 3G1-GaOH	25±3	164.9 ±2.22



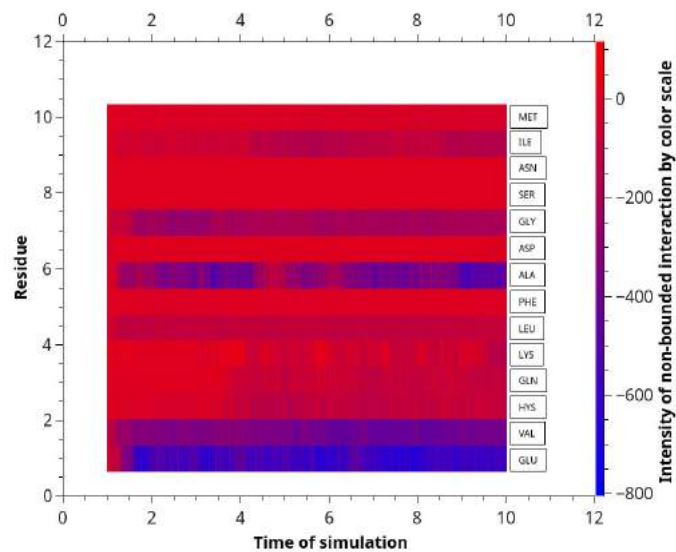
Supplementary Fig. 6-26. Dynamic interaction energy between A $\beta$ <sub>i</sub> (2MXU pdb file) and Ga (1:1 ratio). Preferential binding residues were calculated by the nonbonded interaction energy and the number of H-bonds between each A $\beta$ <sub>i</sub> residue and Ga. If the nonbonded interaction energy between dendrimer and a residue at a specific time point is less than -600 kJ/mol, this residue is considered as a strong single contact at this specific time point.



Supplementary Fig. 6-27. Dynamic interaction energy between A $\beta$  (2MXU pdb file<sup>4</sup>) and 2G0-GaOH (1:1 ratio). Preferential binding residues were calculated by the nonbonded interaction energy and the number of H-bonds between each A $\beta$  residue and the 2G0-GaOH. If the nonbonded interaction energy between dendrimer and a residue at a specific time point is less than -600 kJ/mol, this residue is considered as a strong single contact at this specific time point.

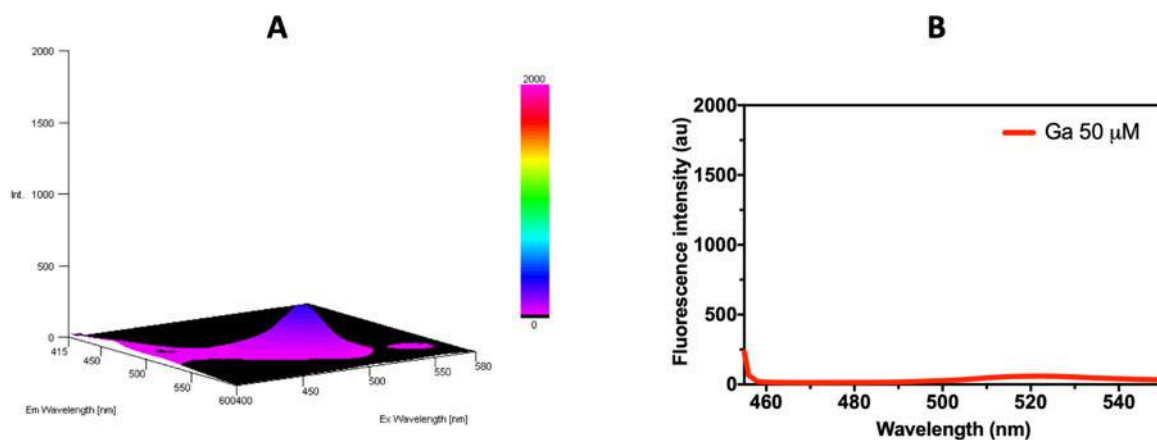


Supplementary Fig. 6-28. Dynamic interaction energy between A $\beta$  (2MXU pdb file<sup>4</sup>) and 2G1-GaOH (1:1 ratio). Preferential binding residues were calculated by the nonbonded interaction energy and the number of H-bonds between each A $\beta$  residue and the 2G1-GaOH. If the nonbonded interaction energy between dendrimer and a residue at a specific time point is less than -600 kJ/mol, this residue is considered as a strong single contact at this specific time point.

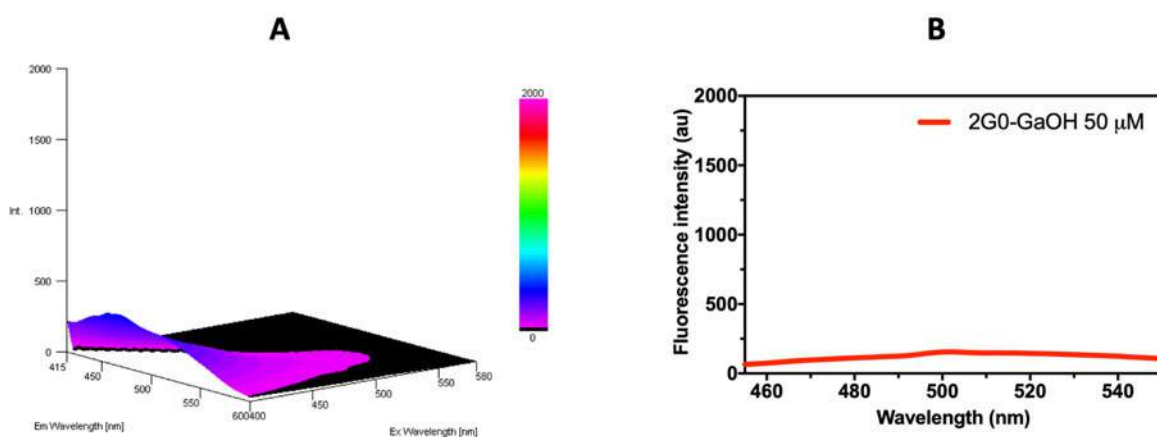


Supplementary Fig. 6-29. Dynamic interaction energy between A $\beta$ <sub>1-42</sub> (2MXU pdb file<sup>4</sup>) and 3G1-GaOH (1:1 ratio). Preferential binding residues were calculated by the nonbonded interaction energy and the number of H-bonds between each A $\beta$ <sub>1-42</sub> residue and 3G1-GaOH. If the nonbonded interaction energy between dendrimer and a residue at a specific time point is less than -600 kJ/mol, this residue is considered as a strong single contact at this specific time point.

▪ *In vitro Protein Aggregation Studies*

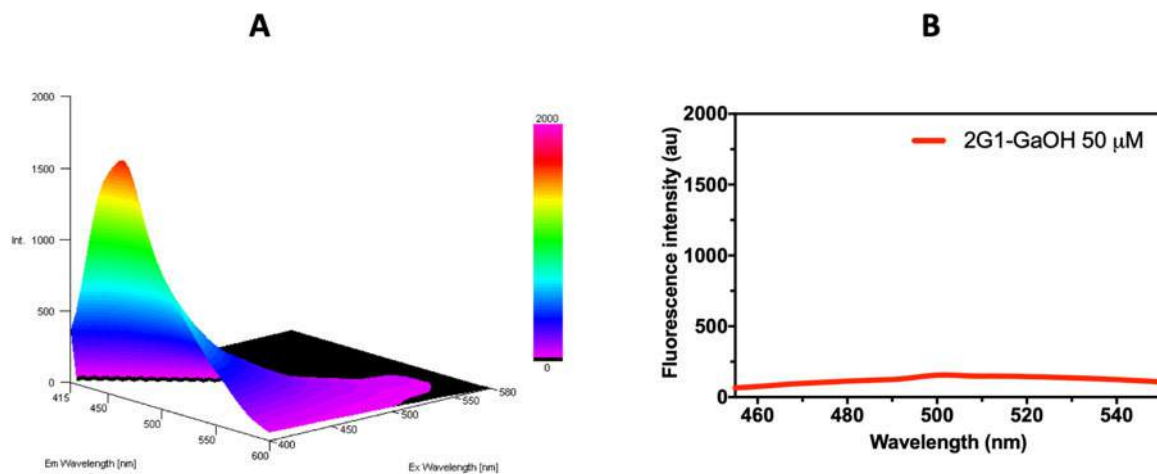


Supplementary Fig. 6-30. A. 3D fluorescence spectra of Gallic acid (Ga, 50  $\mu\text{M}$ ) using the following acquisition parameters:  $\lambda_{\text{ex}} = 400\text{-}580\text{ nm}$ ;  $\lambda_{\text{em}} = 415\text{-}600\text{ nm}$ ; B. Fluorescence spectrum of Ga (50  $\mu\text{M}$ ) acquired using a  $\lambda_{\text{ex}} = 435\text{ nm}$  and a  $\lambda_{\text{em}} = 445\text{-}600\text{ nm}$ ; excitation bandwidth = 5nm; emission bandwidth = 10nm; response = 2s.

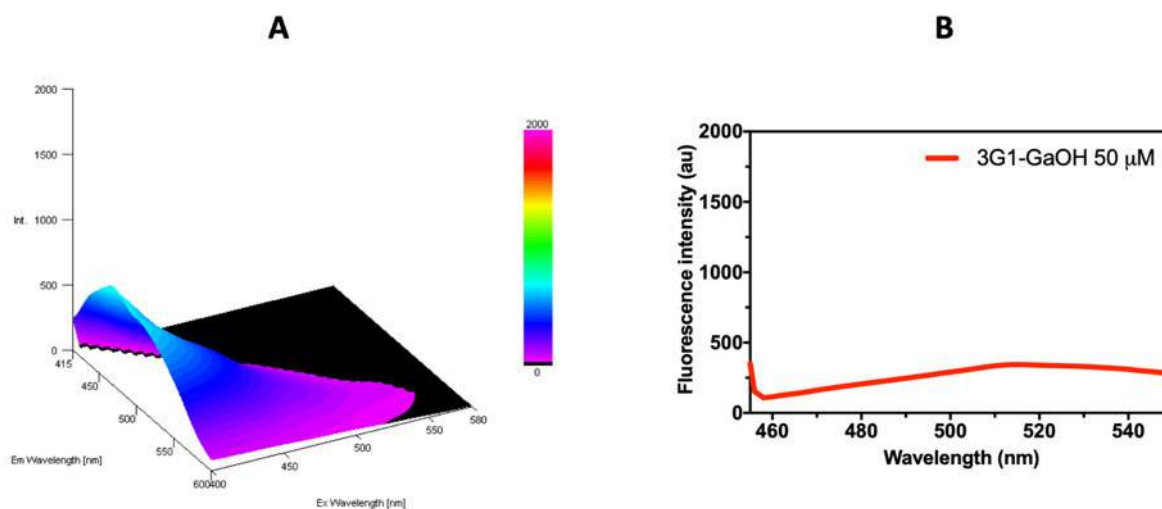


Supplementary Fig. 6-31. A. 3D fluorescence spectra of 2G0-GaOH (50  $\mu\text{M}$ ) using the following acquisition parameters:  $\lambda_{\text{ex}} = 400\text{-}580\text{ nm}$ ;  $\lambda_{\text{em}} = 415\text{-}600\text{ nm}$ ; B. Fluorescence spectrum of 2G0-GaOH (50  $\mu\text{M}$ ) acquired using a  $\lambda_{\text{ex}} = 435\text{ nm}$  and a  $\lambda_{\text{em}} = 445\text{-}600\text{ nm}$ ; excitation bandwidth = 5nm; emission bandwidth = 10nm; response = 2s.

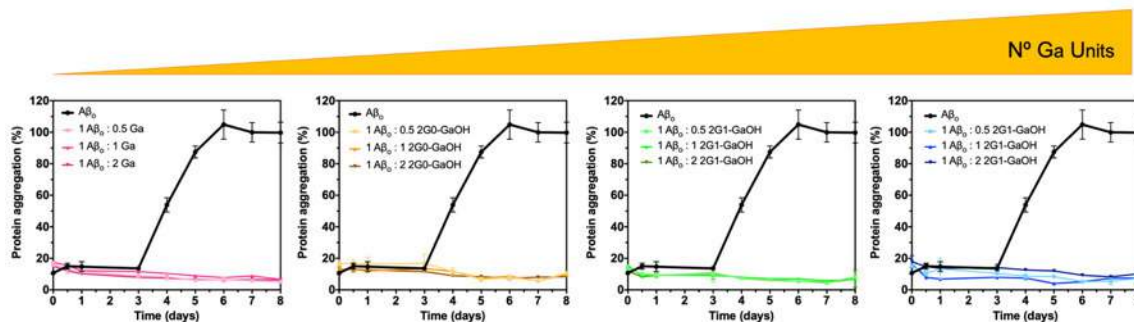




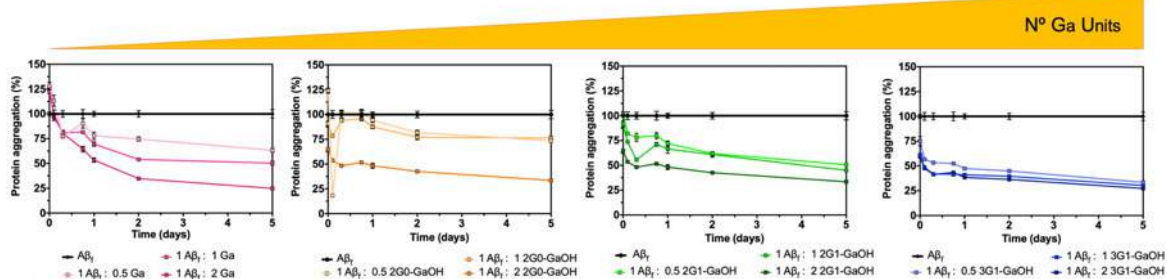
Supplementary Fig. 6-32. A. 3D fluorescence spectra of 2G1-GaOH (50 $\mu$ M) using the following acquisition parameters:  $\lambda_{ex}$  = 400-580 nm;  $\lambda_{em}$  = 415-600 nm; B. Fluorescence spectrum of 2G1-GaOH (50 $\mu$ M) acquired using a  $\lambda_{ex}$  = 435 nm and a  $\lambda_{em}$  = 445-600 nm; excitation bandwidth = 5nm; emission bandwidth = 10nm; response = 2s.



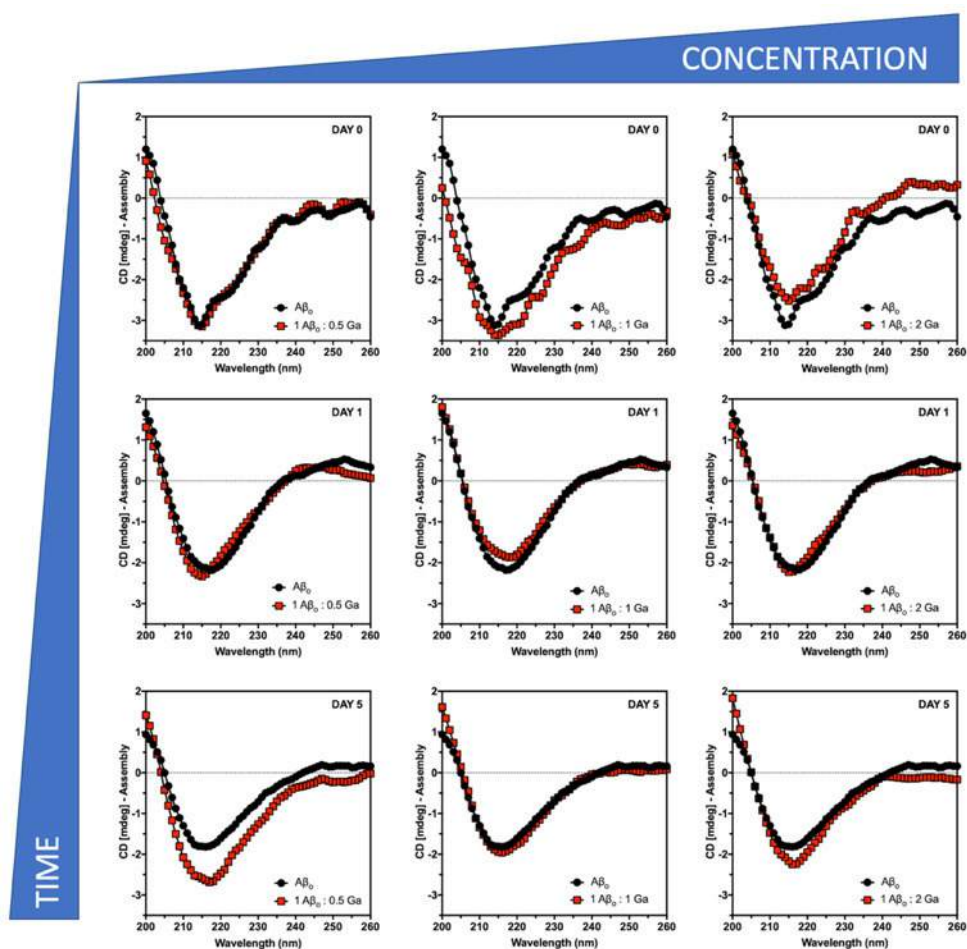
Supplementary Fig. 6-33. A. 3D fluorescence spectra of 3G1-GaOH (50 $\mu$ M) using the following acquisition parameters:  $\lambda_{ex}$  = 400-580 nm;  $\lambda_{em}$  = 415-600 nm; B. Fluorescence spectrum of 3G1-GaOH (50 $\mu$ M) acquired using a  $\lambda_{ex}$  = 435 nm and a  $\lambda_{em}$  = 445-600 nm; excitation bandwidth = 5nm; emission bandwidth = 10nm; response = 2s.



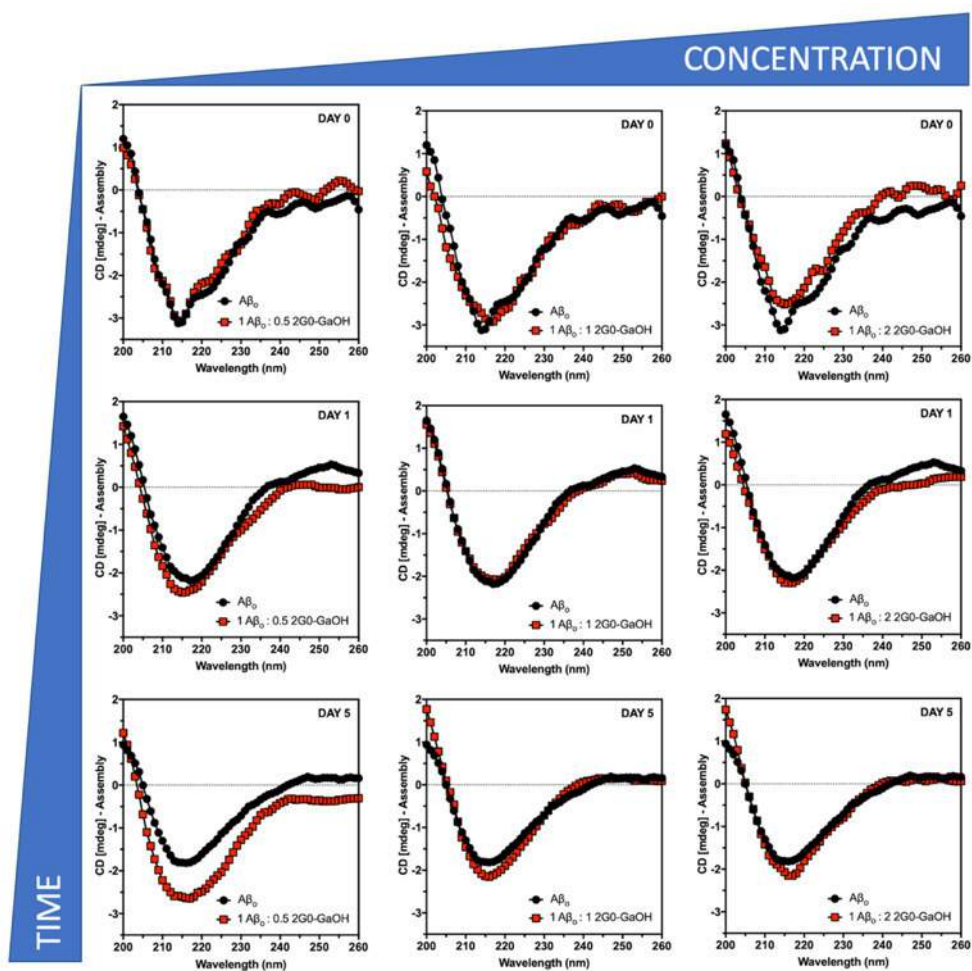
Supplementary Fig. 6-34. Inhibition of the A $\beta$  aggregation kinetics evaluated using the ThT assay. Ga, 2G0-GaOH, 2G1-GaOH and 3G1-GaOH inhibited the A $\beta$  fibril elongation at different molar ratios: 1:0.5, 1:1, and 1:2. Dendrimers were mixed with A $\beta$  in the lag-phase of the A $\beta$  fibril formation and fluorescence was measured over 6 days. All experiments were performed at room temperature.



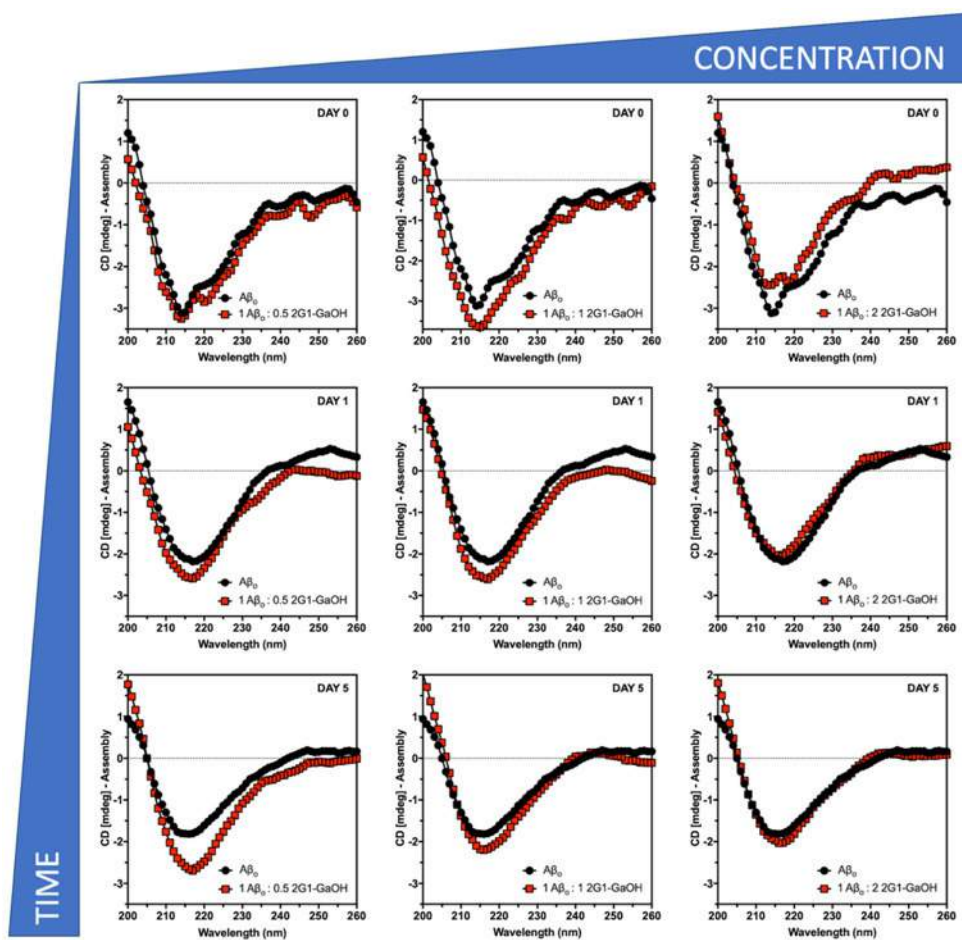
Supplementary Fig. 6-35. Disassembling of A $\beta$ fibrils evaluated using the ThT assay. Ga, 2G0-GaOH, 2G1-GaOH and 3G1-GaOH promoted the rupture of A $\beta$  fibrils at different A $\beta$ :dendrimer molar ratios: 1:0.5, 1:1, and 1:2. Compounds were mixed with A $\beta$  in the plateau phase and fluorescence was measured over 5 days. All experiments were performed at room temperature.



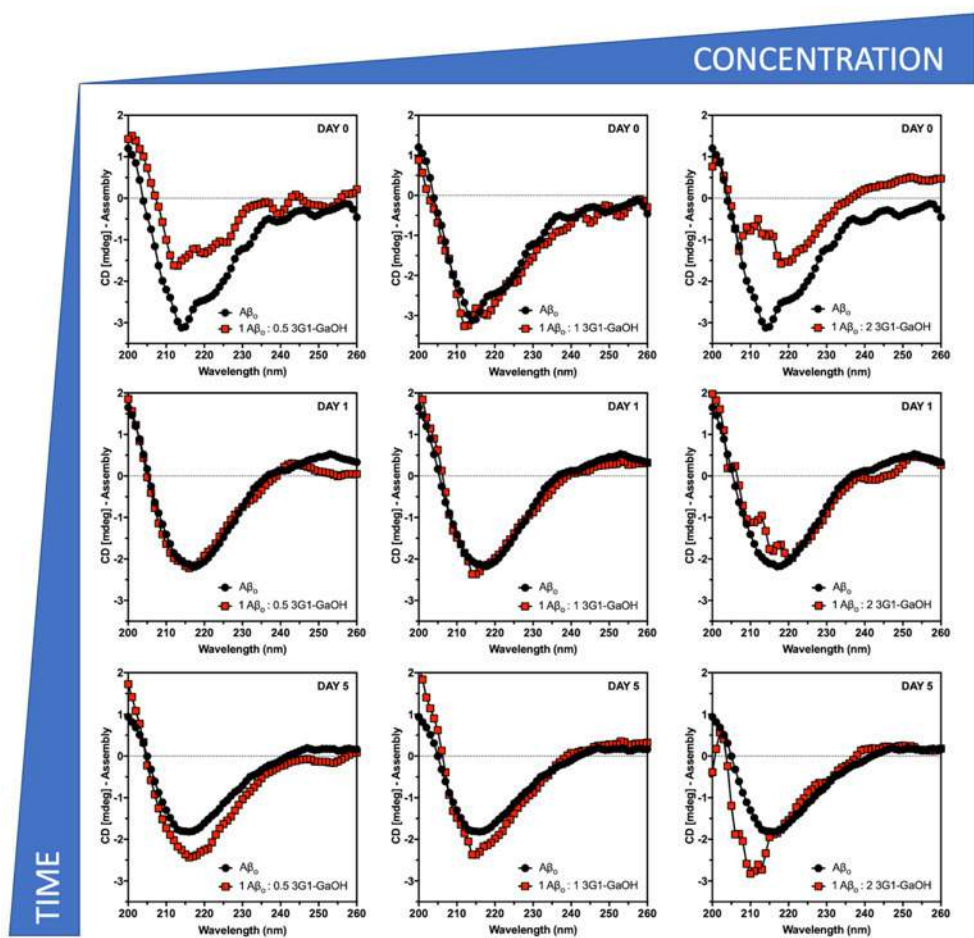
Supplementary Fig. 6-36. CD spectra of  $A\beta$  recorded for 5 days in the presence of different molar ratios of Ga. In all the cases, incubation was made at room temperature, under constant agitation.



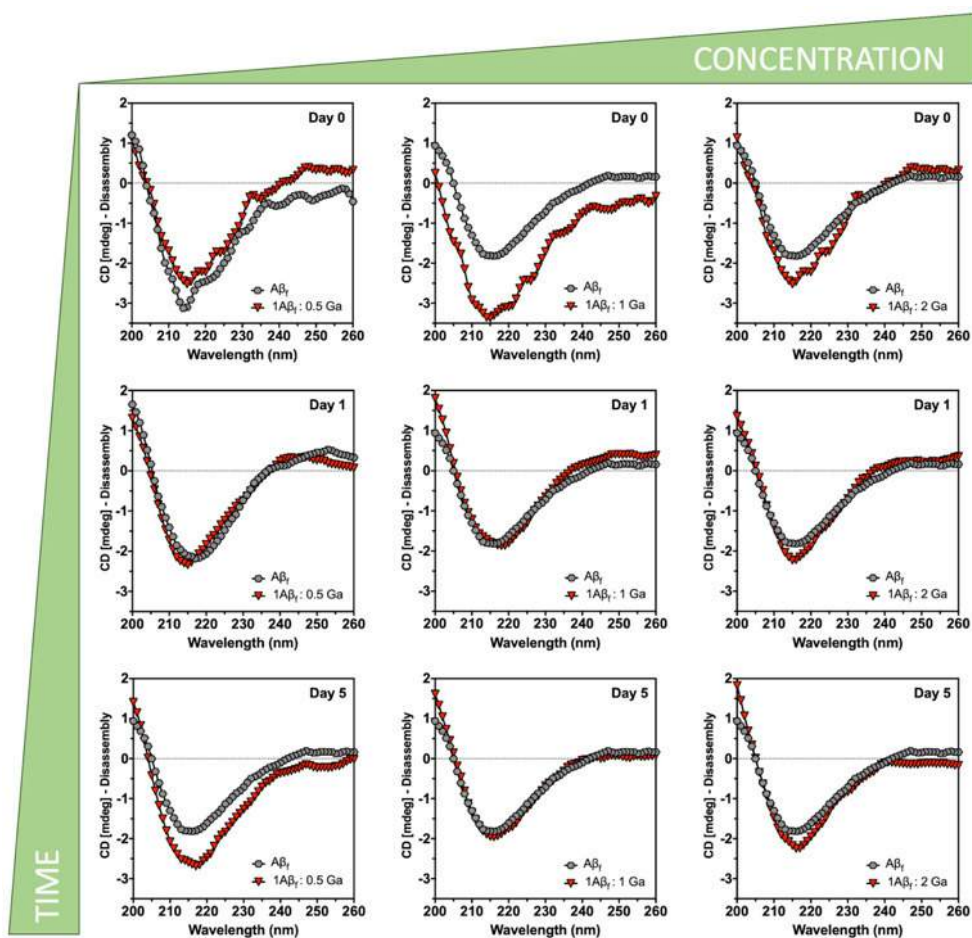
Supplementary Fig. 6-37. CD spectra of Aβ<sub>42</sub> recorded for 5 days in the presence of different molar ratios of 2G0-GaOH. In all the cases, incubation was made at room temperature, under constant agitation.



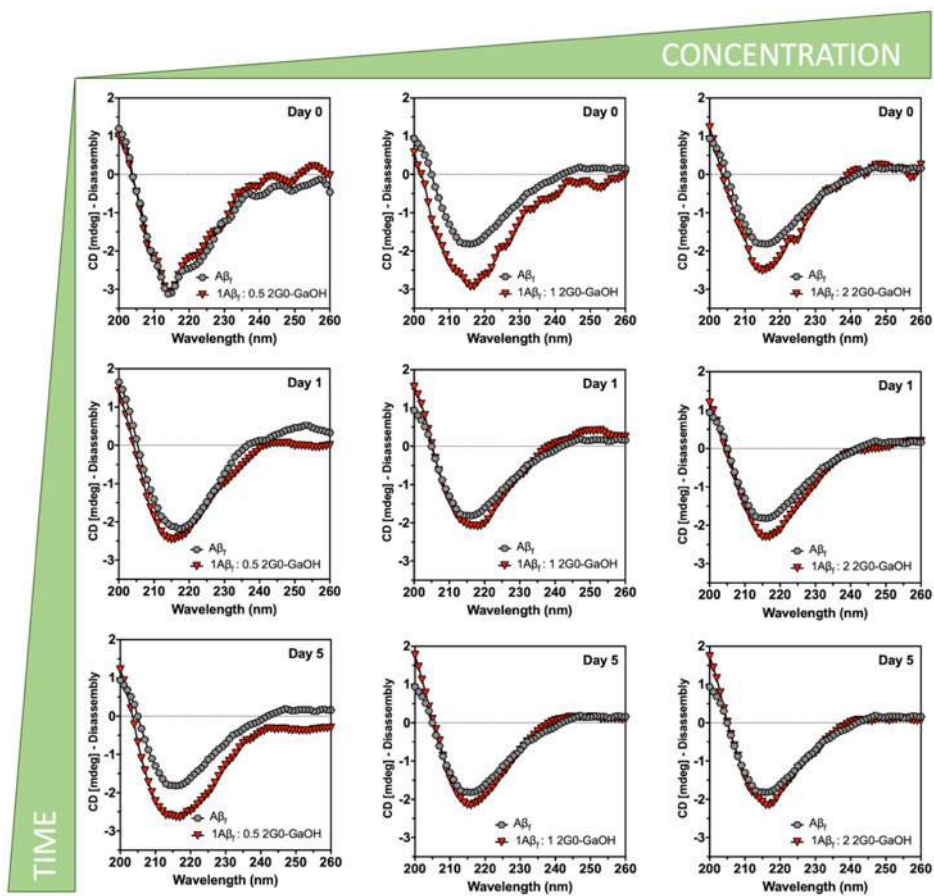
Supplementary Fig. 6-38. CD spectra of  $A\beta_42$  recorded for 5 days in the presence of different molar ratios of 2G1-GaOH. In all the cases, incubation was made at room temperature, under constant agitation.



Supplementary Fig. 6-39. CD spectra of Aβ<sub>40</sub> recorded for 5 days in the presence of different molar ratios of 3G1-GaOH. In all the cases, incubation was made at room temperature, under constant agitation.

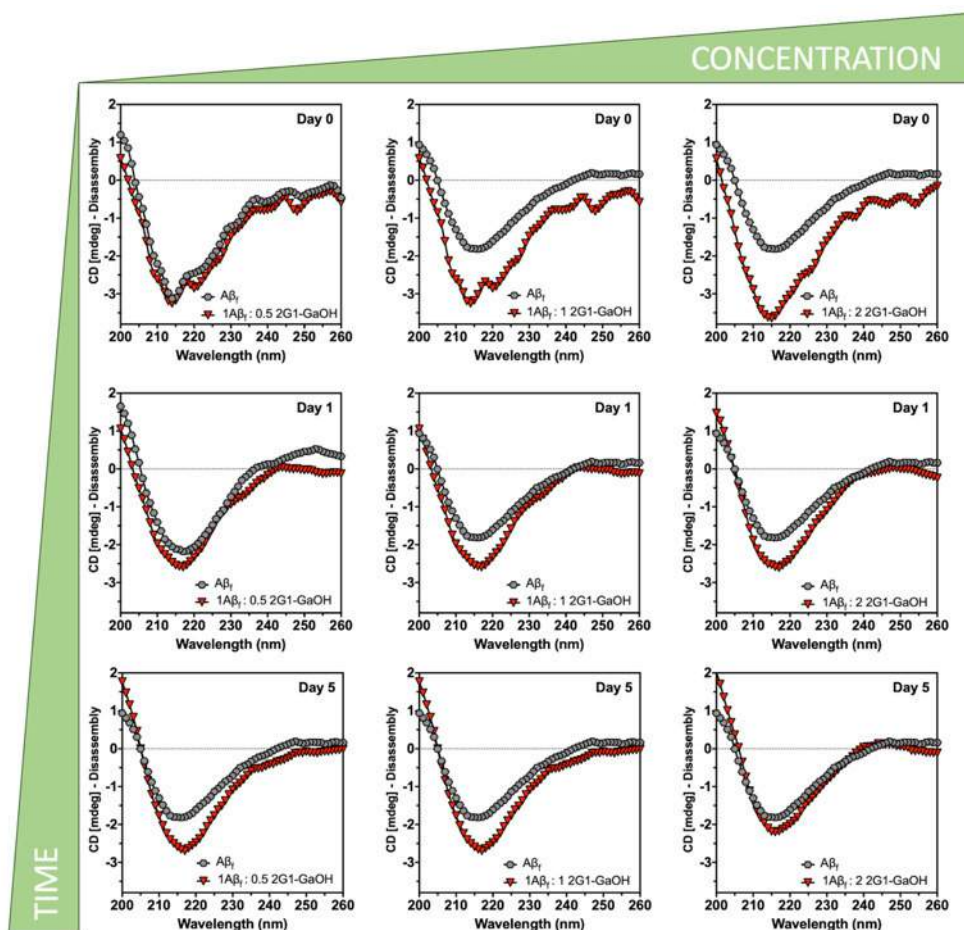


Supplementary Fig. 6-40. CD spectra of  $A\beta_1$  recorded for 5 days in the presence of different molar ratios of Ga. In all the cases, incubation was made at room temperature, under constant agitation.

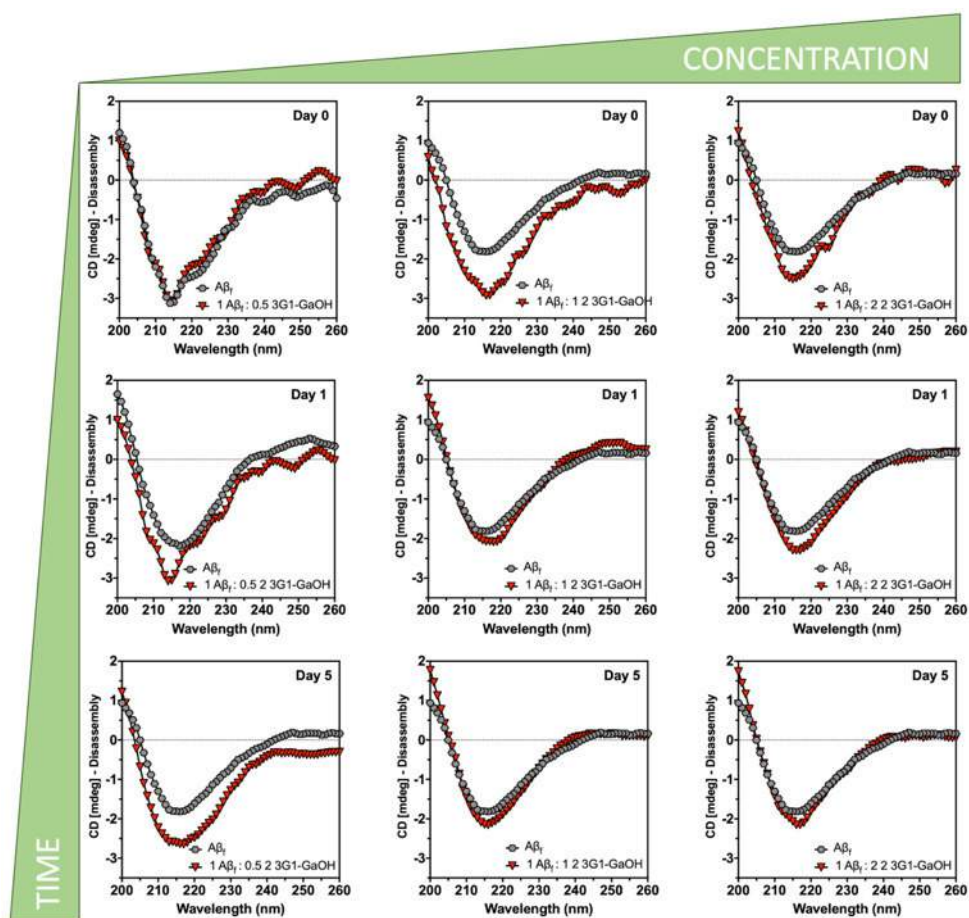


Supplementary Fig. 6-41. CD spectra of  $A\beta_1$  recorded for 5 days in the presence of different molar ratios of 2G0-GaOH. In all the cases, incubation was made at room temperature, under constant agitation.

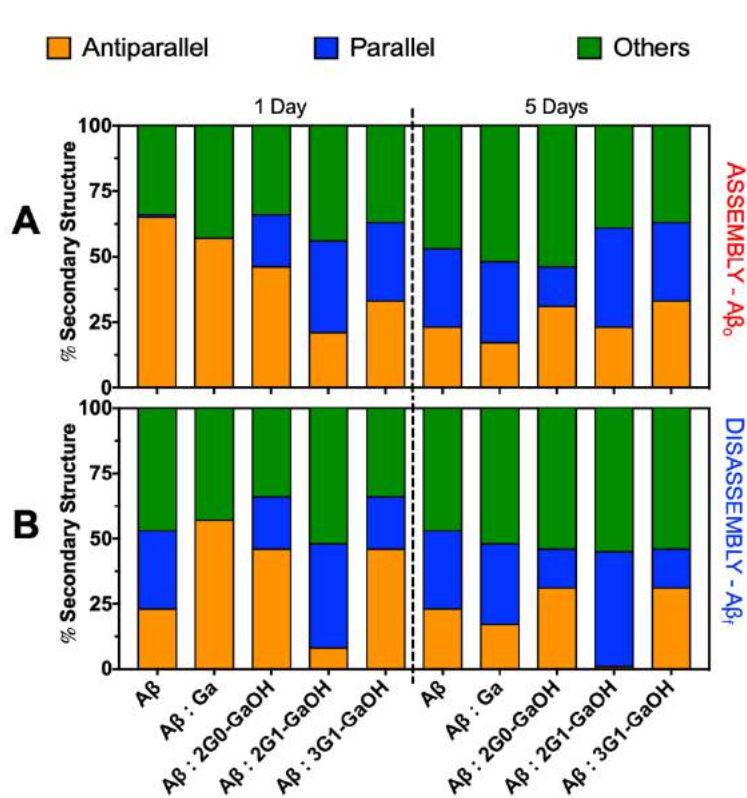




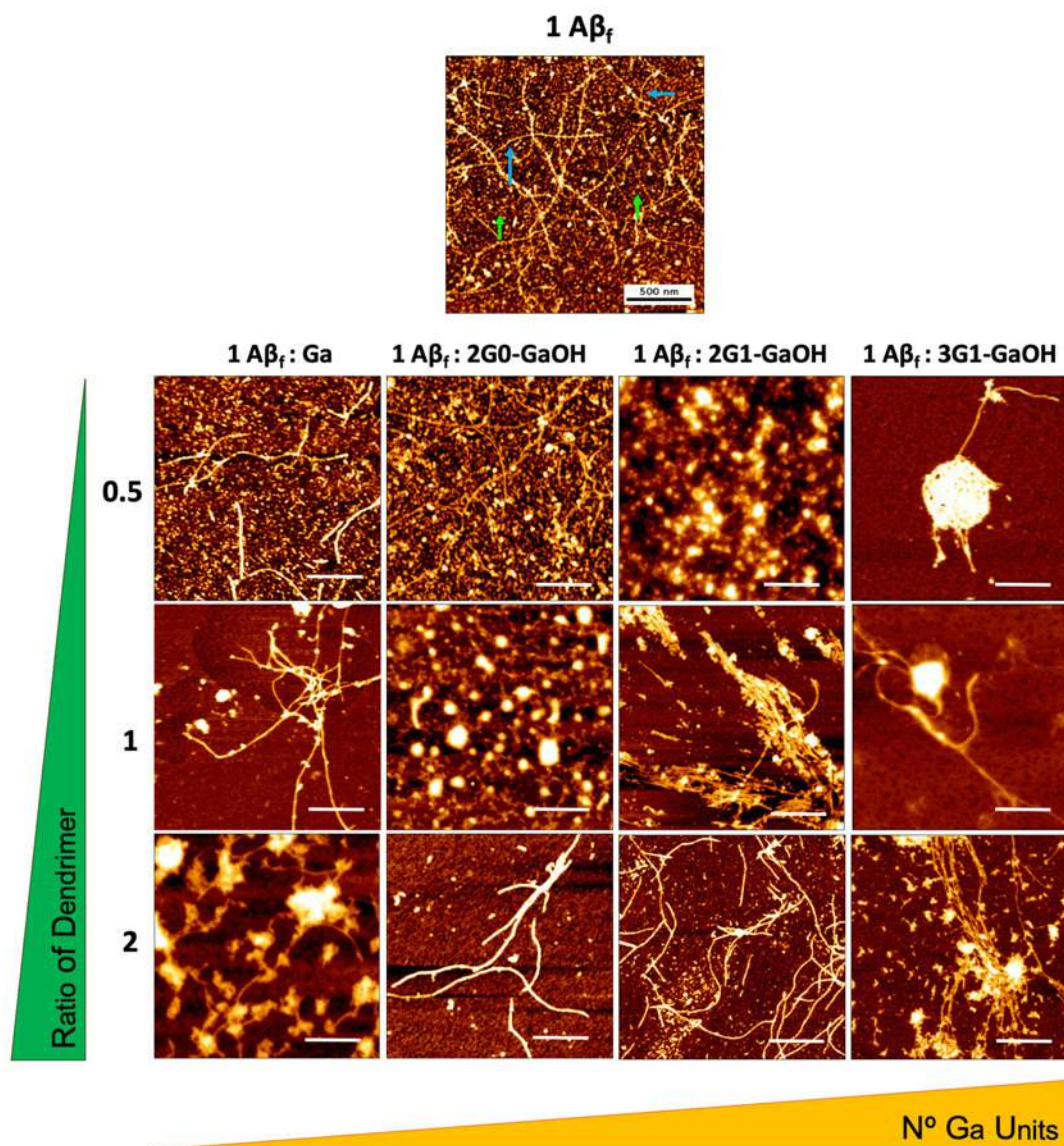
Supplementary Fig. 6-42. CD spectra of  $A\beta_1$  recorded for 5 days in the presence of different molar ratios of 2G1-GaOH. In all the cases, incubation was made at room temperature, under constant agitation.



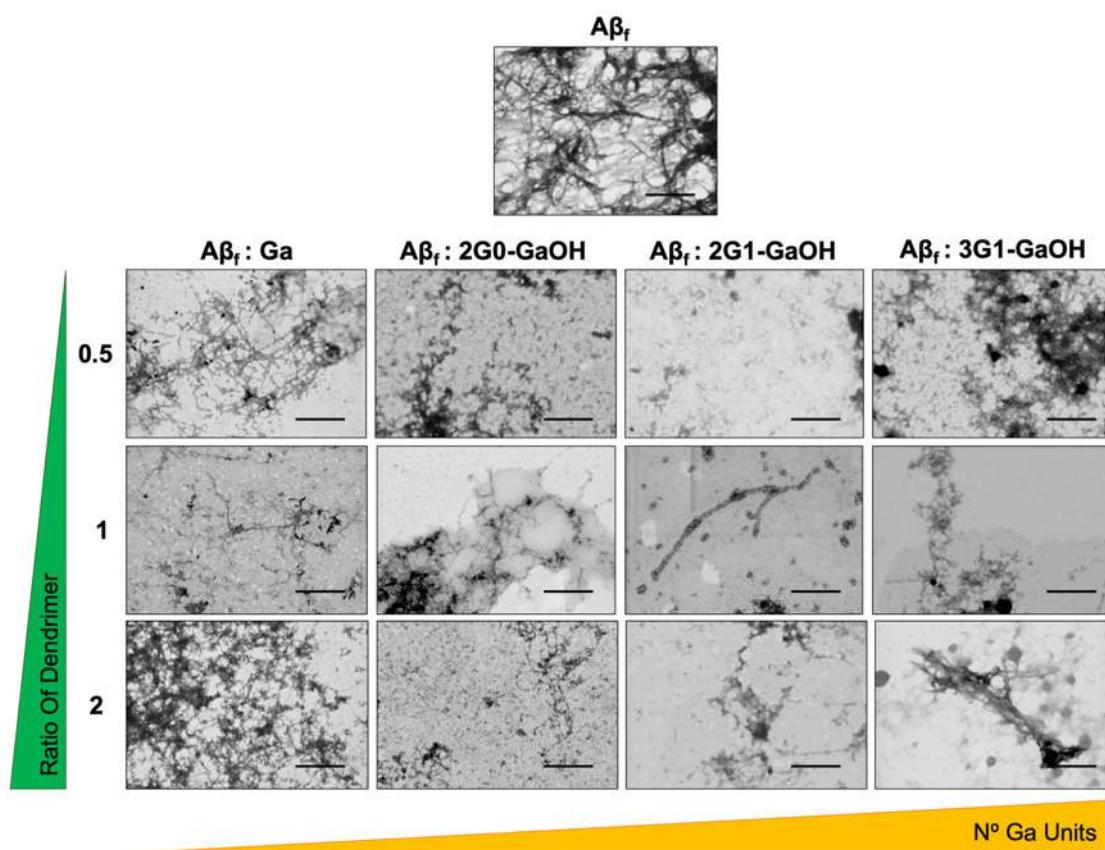
Supplementary Fig. 6-43. CD spectra of A $\beta$ <sub>42</sub> recorded for 5 days in the presence of different molar ratios of 3G1-GaOH. In all the cases, incubation was made at room temperature, under constant agitation.



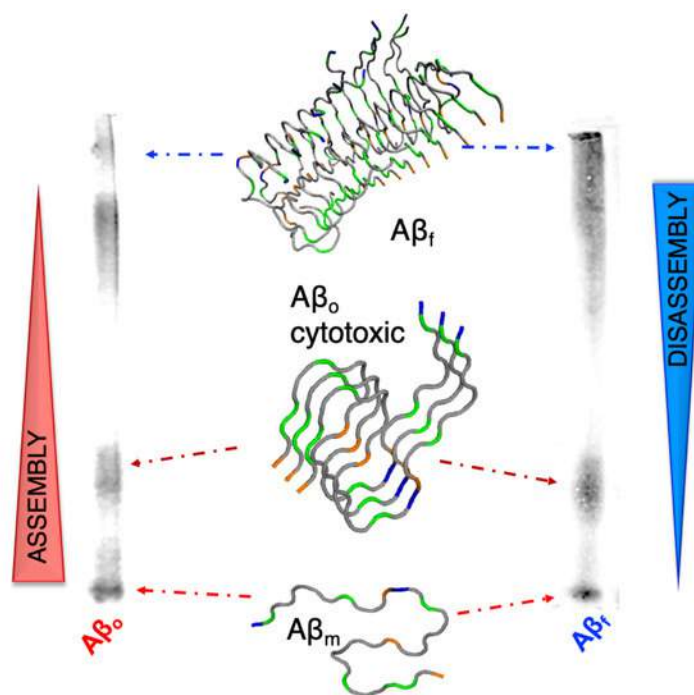
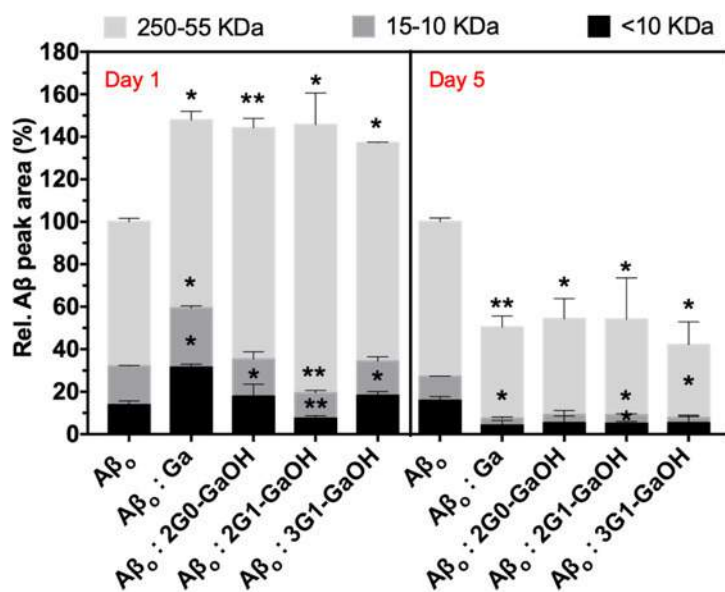
Supplementary Fig. 6-44. Loss of antiparallel  $\beta$ -sheets for the A. aggregation pathway (A $\beta$ ) and B. disaggregation of (A $\beta$ ) followed CD during 1 and 5 days. All experiments were done using a A $\beta$ :dendrimers ratio of 1:1; [A $\beta$ ]=25 $\mu$ M) under constant agitation at 37 °C. Error bars = SD; n = 3. CD data were fitted using BeStSel - RMSD: 1.0283; NRMSD: 0.04966.

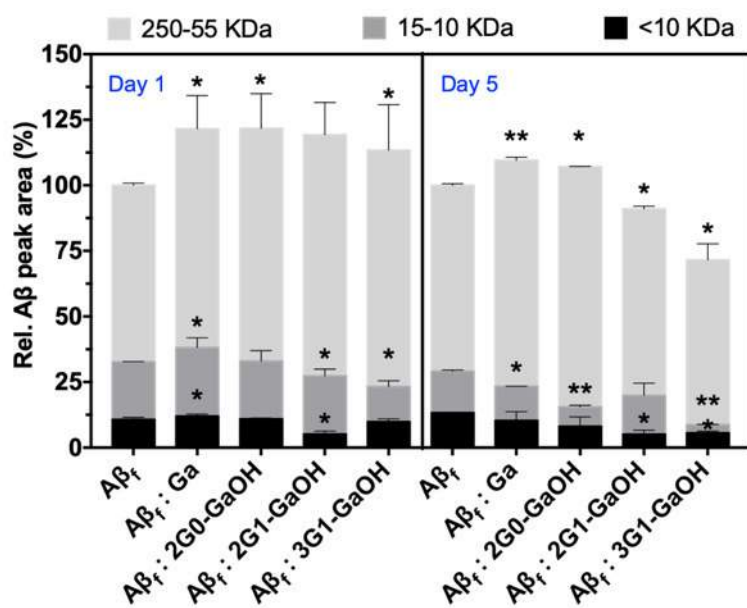


Supplementary Fig. 6-45. Representative AFM images of A $\beta$ . Each dendrimer was added into an A $\beta$  solution (at A $\beta$ :dendrimer concentration ratios of 1:0.5, 1:1 and 1:2) and left to incubate for 24h under constant agitation. Both compounds directly altered A $\beta$  presentation. Fibres marked with blue arrows and oligomers marked with green arrows in the A $\beta$  control sample. Scale bars = 500 nm.



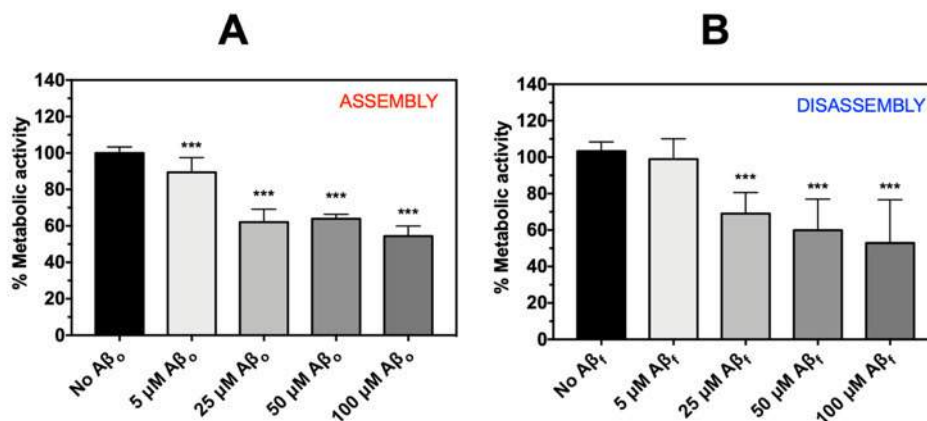
Supplementary Fig. 6-46. Representative STEM images of  $A\beta_1$  samples. Each dendrimer was added into an  $A\beta_1$  solution (under  $A\beta_1$ :dendrimer concentration ratios of 1:0.5, 1:1 and 1:2) and left to incubate for 24h under constant agitation. Both compounds directly altered  $A\beta_1$  morphological presentation. Scale bars = 500 nm.

Supplementary Fig. 6-47. A $\beta$  peptide assembly and disassembly pathways.Supplementary Fig. 6-48. Relative densitometric bar graphs of A $\beta$ . (25 $\mu$ M) assembly quantified by WB (using the antibody 6E10); experiments were executed at 37°C in PBS, during 1 and 5 days. Error bars = SD, \*  $p < 0.05$ , \*\*  $p < 0.01$  and \*\*\*  $p < 0.001$  vs control 25 $\mu$ M A $\beta$ ;  $n=3$ .

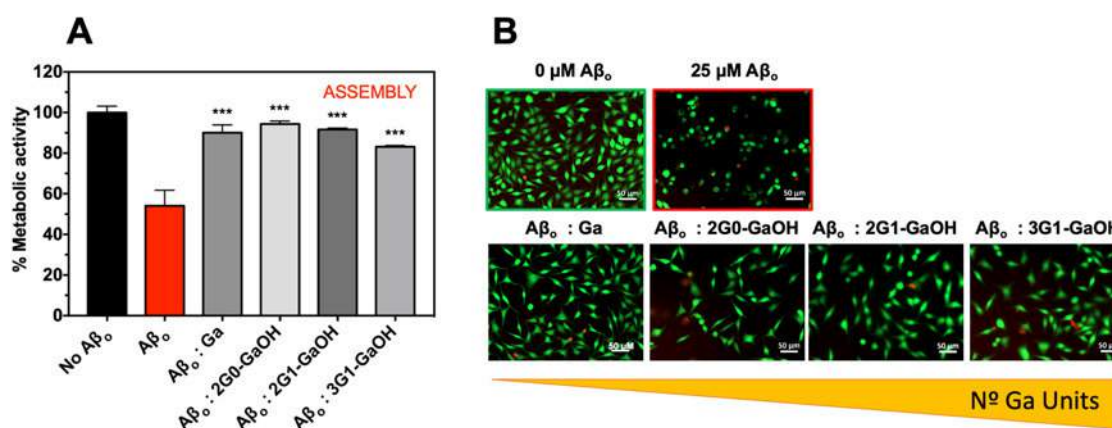


Supplementary Fig. 6-49. Relative densitometric bar graphs of Aβ<sub>1</sub> (25 μM) disassembly quantified by WB (using the antibody 6E10); experiments were executed at 37°C in PBS, during 1 and 5 days. Error bars = SD, \* p < 0.05, \*\* p < 0.01 and \*\*\* p < 0.001 vs control 25 μM Aβ<sub>1</sub>; n=3.

- Cells Studies

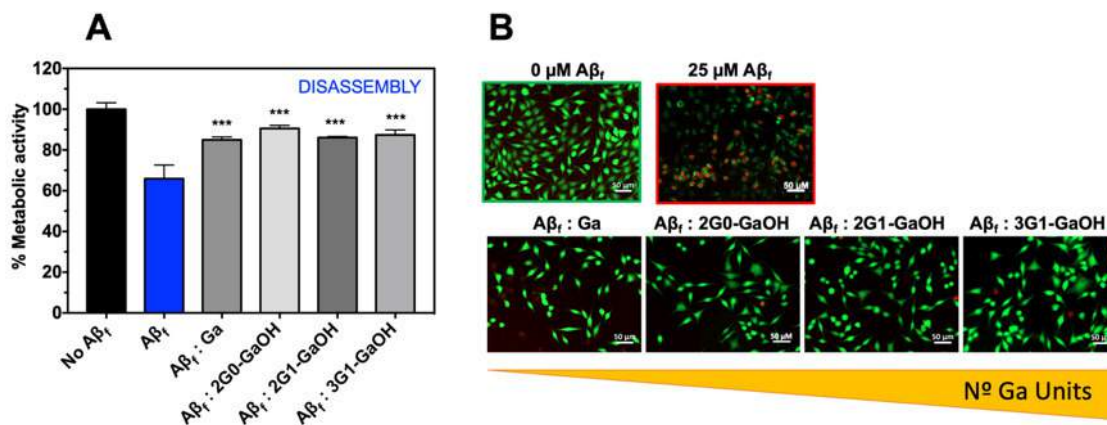


Supplementary Fig. 6-50. SH-SY5Y cell viability in the presence of Aβ oligomers (Aβ<sub>o</sub>) and Aβ fibrils (Aβ<sub>f</sub>) during 24h (using AlamarBlue® assay). Cells were incubated during 24h with different concentrations of Aβ. \* p < 0.05, \*\* p < 0.01, \*\*\* p < 0.001 (vs control); n=3.

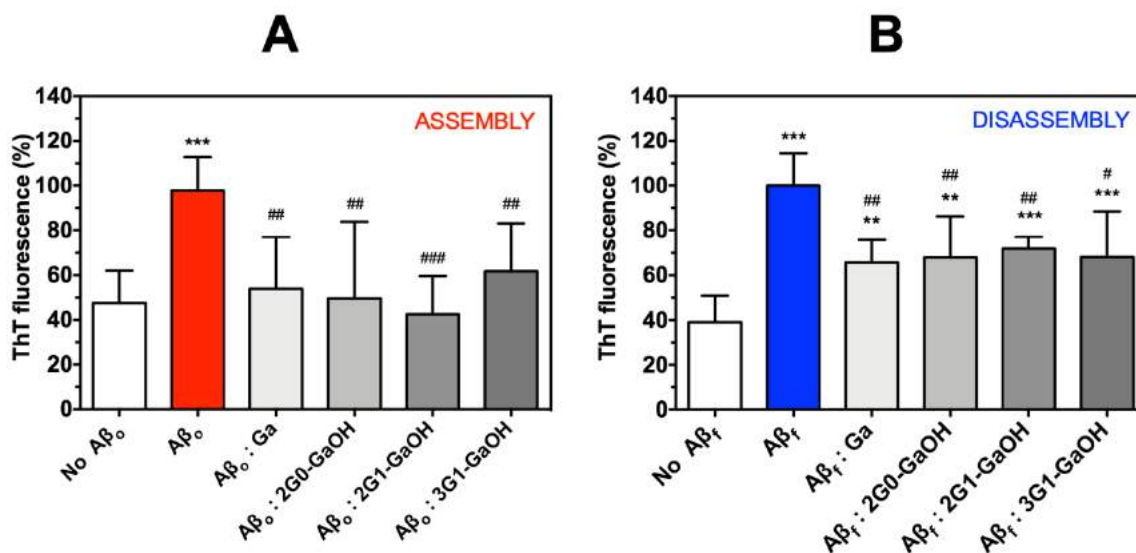


Supplementary Fig. 6-51. A. Metabolic activity measured by AlamarBlue® assay of SH-SY5Y in the presence of a solution of Aβ oligomeric species (25 μM) during 24h, for a Aβ:dendrimers concentration ratio of 1:1. \*\*\* p < 0.001 (vs No Aβ); n=3. B. Representative images of the Live/Dead assay. Scale bar = 50 μm.

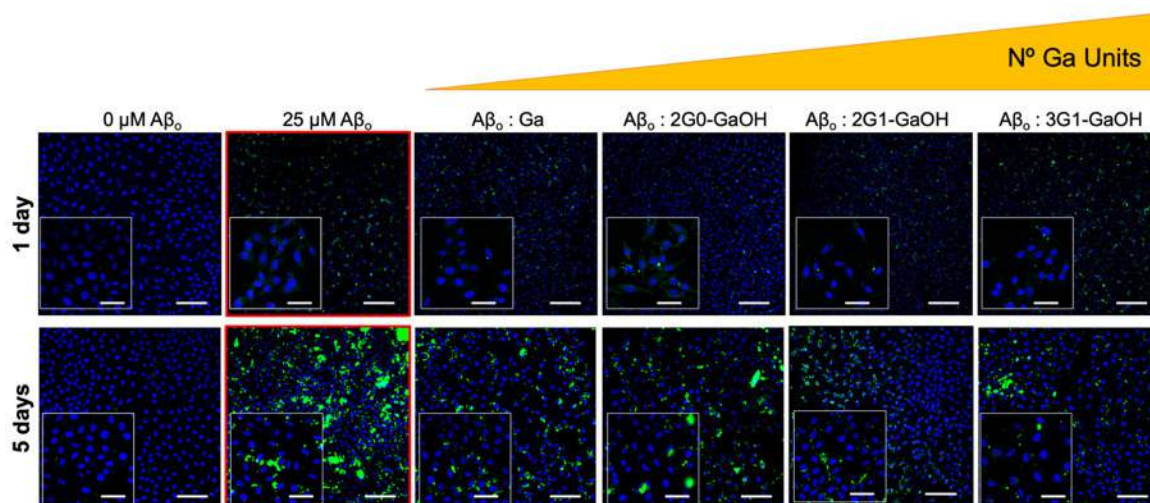




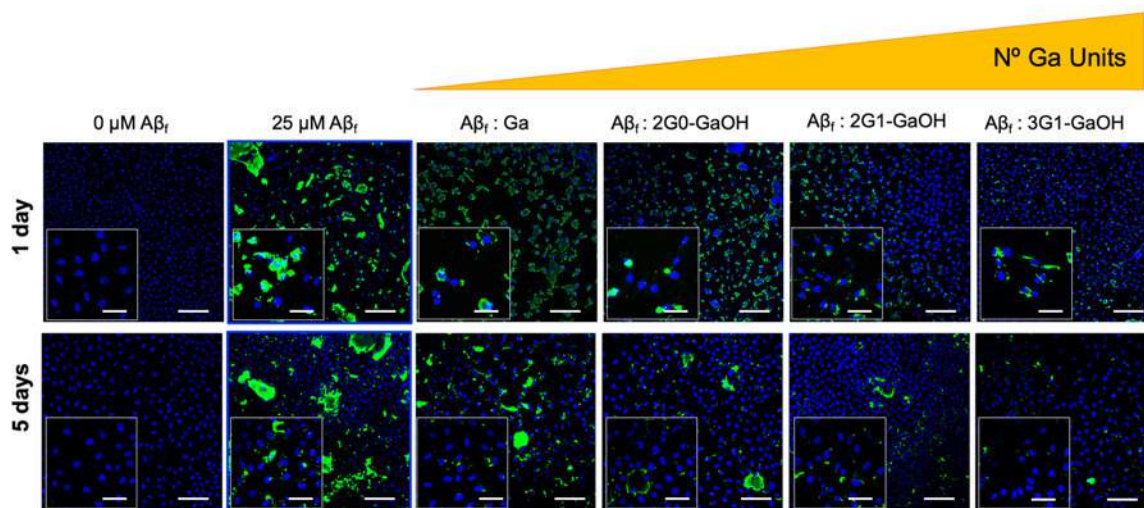
Supplementary Fig. 6-52. A. Metabolic activity measured by AlamarBlue® assay of SH-SY5Y in the presence of a solution of A $\beta_1$  pre-formed fibrils (25 $\mu$ M) during 24h, for a A $\beta_1$ :dendrimers concentration ratio of 1:1. \*\*\* p < 0.001 (vs No A $\beta_1$ ); n=3; B. Representative images of the Live/Dead assay. Scale bar = 50 $\mu$ m.



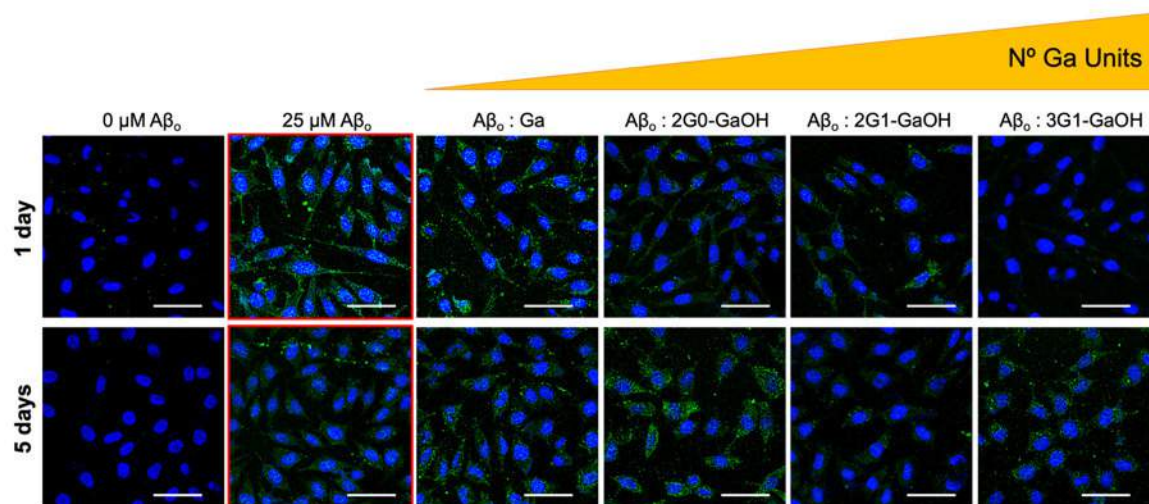
Supplementary Fig. 6-53. ThT fluorescence measurements in SH-SY5Y cell culture, after incubation with A $\beta_o$  (A) and A $\beta_f$  (B) species and dendrimers for a A $\beta$ :dendrimers concentration ratio of 1:1 ratio, during 1 day of culture. Error bars =SD, \*p < 0.05, \*\*p < 0.01 and \*\*\*p < 0.001 vs control 25 $\mu$ M A $\beta$ ; n=3; \*\*\*p<0.001 vs No A $\beta$ .



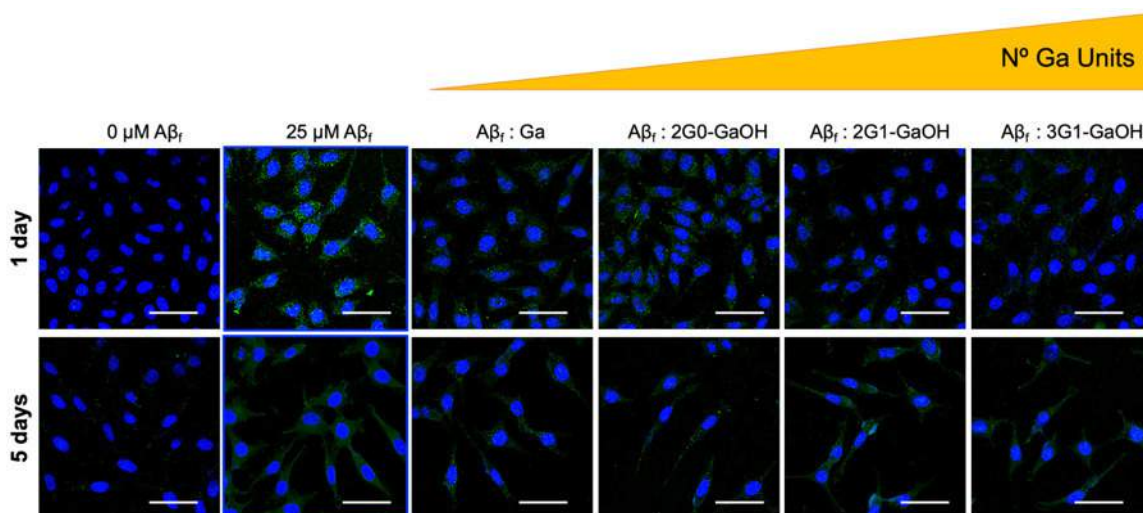
Supplementary Fig. 6-54. Immunofluorescence analysis of Aβ<sub>0</sub> species in the SH-SY5Y cell culture visualized by confocal microscopy (mAb 6E10, green) after incubation with dendrimers for a Aβ:dendrimer concentration ratio of 1:1, during 1 and 5 days (Aβ: green, cell nuclei: blue). Scale bar: 200 μm (50 μm for the insets).



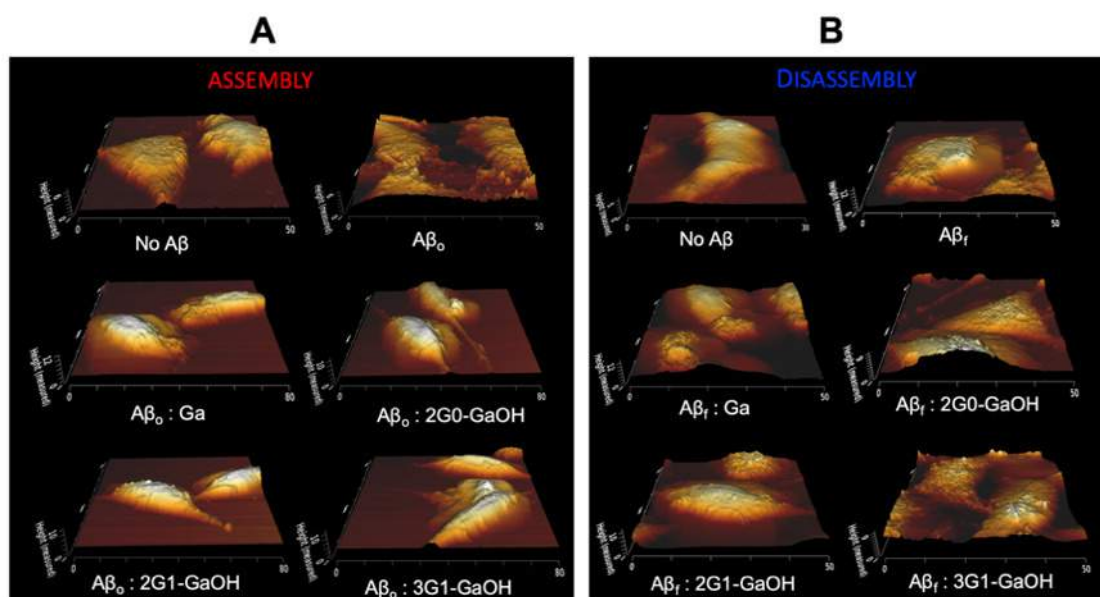
Supplementary Fig. 6-55. Immunofluorescence analysis of Aβ<sub>1</sub> species in the SH-SY5Y cell culture visualized by confocal microscopy (mAb 6E10, green) after incubation of dendrimers for a Aβ:dendrimers concentration ratio of 1:1, during 1 and 5 days (Aβ: green, cell nuclei: blue). Scale bar: 200 μm (50 μm for the insets).



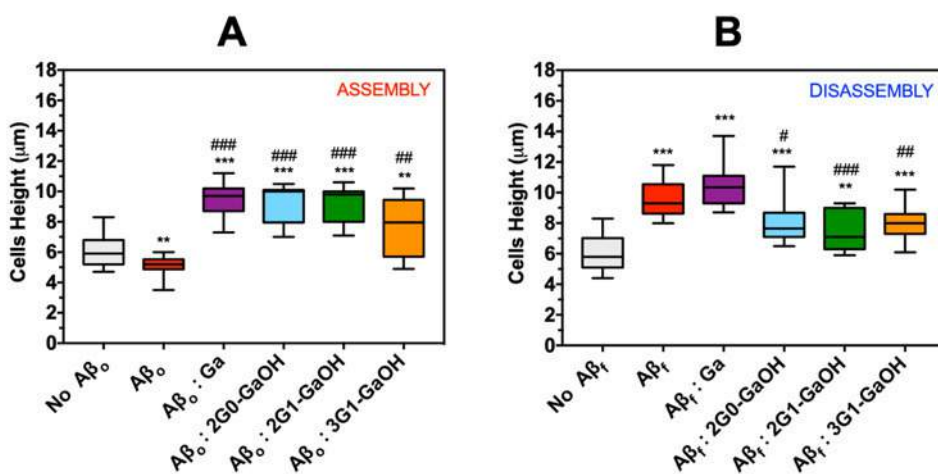
Supplementary Fig. 6-56. Immunofluorescence analysis of  $A\beta_o$  species in the SH-SY5Y cell culture visualized by confocal microscopy (A11 antibody, green) after incubation of dendrimers for a  $A\beta$ :dendrimers concentration ratio of 1:1, during 1 and 5 days ( $A\beta$ : green, cell nuclei: blue). A11 antibody specifically bind to oligomeric  $A\beta$  species. Scale bar: 50  $\mu\text{m}$



Supplementary Fig. 6-57. Immunofluorescence analysis of  $A\beta_r$  species in the SH-SY5Y cell culture visualized by confocal microscopy (A11 antibody, green) after incubation of dendrimers to a 1:1 ratio, for 1 and 5 days ( $A\beta$ : green, cell nuclei: blue). A11 antibody specifically bind to oligomeric  $A\beta$  species. Scale bar: 50  $\mu\text{m}$ .



Supplementary Fig. 6-58. Representative AFM topographic images of SH-SY5Y cells cultured during 24h in the presence of A $\beta$ . (A, assembly) and A $\beta$ <sub>t</sub> (B, disassembly) and Ga, 2G0-GaOH, 2G1-GaOH and 3G1-GaOH using a A $\beta$ :dendrimers ratio of 1:1.



Supplementary Fig. 6-59. Statistical comparison of the cells height profile from the nanomechanical properties obtained by AFM topographic images of normal SH-SY5Y cells with 1:1 ratio of A $\beta$ :dendrimers, under different conditions: A. Assembly pathway (A $\beta$ <sub>o</sub>) and B. Disassembly pathway (A $\beta$ <sub>t</sub>). All experiments were conducted after 24h of incubation with A $\beta$  (25 $\mu$ M).

## ▪ References

1. Amaral, S. P.; Tawara, M. H.; Fernandez-Villamarin, M.; Borrajo, E.; Martinez-Costas, J.; Vidal, A.; Riguera, R.; Fernandez-Megia, E., Tuning the Size of Nanoassemblies: A Hierarchical Transfer of Information from Dendrimers to Polyion Complexes. *Angew Chem Int Ed Engl* 2018, 57 (19), 5273-5277.
2. Stine, W. B.; Jungbauer, L.; Yu, C.; LaDu, M. J., Preparing synthetic Abeta in different aggregation states. *Methods in molecular biology* (Clifton, N.J.) 2011, 670, 13-32.
3. Garcia, A. M.; Kurbasic, M.; Kralj, S.; Melchionna, M.; Marchesan, S., A biocatalytic and thermoreversible hydrogel from a histidine-containing tripeptide. *Chem. Commun.* 2017, 53 (58), 8110-8113.
4. Xiao, Y.; Ma, B.; McElheny, D.; Parthasarathy, S.; Long, F.; Hoshi, M.; Nussinov, R.; Ishii, Y., Abeta(1-42) fibril structure illuminates self-recognition and replication of amyloid in Alzheimer's disease. *Nat Struct Mol Biol* 2015, 22 (6), 499-505.
5. Malde, A. K.; Zuo, L.; Breeze, M.; Stroet, M.; Poger, D.; Nair, P. C.; Oostenbrink, C.; Mark, A. E., An automated force field topology builder (ATB) and repository: version 1.0. *Journal of chemical theory and computation* 2011, 7 (12), 4026-4037.
6. Schmid, N.; Eichenberger, A. P.; Choutko, A.; Riniker, S.; Winger, M.; Mark, A. E.; van Gunsteren, W. F., Definition and testing of the GROMOS force-field versions 54A7 and 54B7. *European biophysics journal* 2011, 40 (7), 843.

## Chapter 7

# Glucosamine analogues as modulators of amyloid- $\beta$ toxicity

## CHAPTER 7

### Glucosamine analogues as modulators of amyloid- $\beta$ toxicity<sup>6</sup>

#### ABSTRACT

In Alzheimer's disease (AD), amyloid- $\beta$  (A $\beta$ ) oligomers are considered key mediators of synaptic dysfunction and cognitive impairment. These unstable intermediate A $\beta$  species can interfere with different cellular organelles leading to neuronal cell death, through: the formation of Ca<sup>2+</sup> permeable membrane pores; impairment in the levels of acetylcholine neurotransmitter; increased insulin resistance; promotion of pro-inflammatory cascades; among others. Based on a series of evidences that indicate the key role of glycosaminoglycans (GAGs) in amyloid plaque formation, we evaluated the capacity of four monosaccharides, *i.e.* glucosamine (GlcN), N-acetylglucosamine (GlcNAc), glucosamine-6-sulphate (GlcN6S) and glucosamine-6-phosphate (GlcN6P), to reduce these pathological hallmarks. The tested monosaccharides, in particular GlcN6S and GlcN6P, were able to interact with the oligomeric A $\beta$  species, reducing: neuronal cell death, A $\beta$ -mediated damage to the cellular membrane; acetylcholinesterase activity; insulin resistance and pro-inflammation levels.

**Keywords:** Alzheimer Disease, Glucosamine analogues, amyloid- $\beta$  peptide, Calcium imbalance.

---

<sup>6</sup> This Chapter is based on the publication: "Araújo A. R., Correa J., Reis, R. L. & Pires, R. A, (2020), Glucosamine analogues as modulators of amyloid- $\beta$  toxicity (submitted)"

## 7.1 MAIN TEXT

The aggregation of misfolded peptides/proteins is at the onset of different amyloid-based pathologies, including the most common neurodegenerative disorders, *e.g.* Alzheimer's disease (AD) or Parkinson disease, but also metabolic ones, *e.g.* Type-2 diabetes mellitus.[1] In the case of AD there are two main pathological hallmarks, namely: the deposition of extracellular senile plaques composed of misfolded amyloid- $\beta$  (A $\beta$ ) aggregates; and the presence of intracellular neurofibrillary tangles of hyperphosphorylated Tau in the affected neurons.[2] It has been under debate which one is the primary responsible for the onset of AD. While it has been reported that AD-mediated dementia only occurs in patients that present neurofibrillary tangles in the affected regions of the brain (*i.e.* medial temporal lobe and peripheral cortex)[3]; it has been also demonstrated that A $\beta$  is present above a certain threshold in the biological environment before the deposition of hyperphosphorylated Tau and the beginning of dementia.[4, 5] These observations lead to the present notion that the increased A $\beta$  deposition in the brain is at the onset of AD.

A $\beta$  is generated and released to the extracellular space after the sequential cleavage of the transmembrane amyloid precursor protein (APP) by  $\beta$ -site amyloid precursor protein cleaving enzyme 1 (BACE1), followed by the  $\gamma$ -secretase complex. The generated A $\beta$  monomers are highly prone to aggregate into cytotoxic supramolecular forms making them at the centre of the disease progression.[6, 7] Initial studies were reporting that high molecular weight A $\beta$  fibrils (adopting a parallel  $\beta$ -sheet conformation, as the ones detected in the senile plaques) were the main source of toxicity.[8] However, more recently, it has been reported that it's the diffusible oligomeric forms (organized under an antiparallel  $\beta$ -sheet conformation) that are perturbing the cellular homeostasis and are highly toxic.[9, 10] The presence of these A $\beta$  oligomers lead to the impairment of the normal function of the brain, mediated by its binding to different biochemical targets (*e.g.* APOE, G-proteins, or insulin receptor - IR) causing several abnormal downstream events, such as: i) membrane disruption; ii) Ca<sup>2+</sup> permeable pore formation in the cell membrane; iii) increased oxidative stress at the endoplasmic reticulum and mitochondrial dysfunction; iv) imbalance in the activity of neurotransmitters; and v) insulin resistance.[11-14] In addition, it is known that oligomeric A $\beta$  promotes the hyperphosphorylation of Tau and the subsequent microtubule dysfunction, which leads to early neuronal cell death and, ultimately, instigating the onset of dementia.[9] Moreover, the AD pathogenesis has been also linked to an altered metabolism of the phospholipids mediated by the overexpression of several genes (*e.g.* TREM2, PLCG2 or ABCA)[15, 16] involved in the clearance of A $\beta$ -mediated membrane damage.[17, 18] In fact, it has been reported



that during the A $\beta$  aggregation pathway, the A $\beta$  oligomers are able to interact with the cell membrane and initiate programmed neuronal cell death.[19] In fact, the dysregulation of cholesterol and lipid homeostasis (lipid, and lipoprotein dysregulation) in the brain is known to increase A $\beta$  production under a feedback loop.[20] Importantly, the damage caused at the membrane can initiate its disruption (imbalance of ions and oxidative stress) but can also alter the signalling of several other biochemical pathways, such as the insulin resistance cascade.[21] In the case of the A $\beta$ -mediated insulin signalling deficiency, it is considered a key aspect in the progression of AD. A $\beta$  interacts with IR impairing its function, promoting insulin-resistance, and the subsequent impairment of the glucose metabolism.[22]

Cytotoxic A $\beta$  oligomers are usually generated during the aggregation pathway that ultimately leads to the formation of fibrils. However, the fibrils themselves are under a dynamic equilibrium between assembly and disassembly, where oligomers are transiently present. In order to reduce their presence it has been suggested two main approaches: 1) the remodelling of the oligomeric structures into thermodynamically stable off-pathway non-cytotoxic forms;[23] or 2) the development of strategies that stabilize fibrils by blocking their disassembly into the cytotoxic A $\beta$  oligomers.[24] It is well established that glycosaminoglycans (GAGs, *i.e.* heparin and chondroitin sulphate)[25, 26] can modulate the supramolecular assembly of A $\beta$ , in particular by stabilizing the nanofibers and protecting them against disassembly and proteolytic degradation.[27] These interactions are described to occur mostly through electrostatic forces between the negatively charged saccharide units and the positively charged peptide domains.[28] In addition, it is known that A $\beta$  oligomers interact with the negatively charged membrane components (*e.g.* phospholipids and glycoproteins).

Based on these evidences, herein we evaluated if glucosamine (GlcN) and its analogues are able to modulate the toxicity of A $\beta$ . We selected four GlcN analogues, namely: GlcN with a positive charge; N-acetyl glucosamine (GlcNAc) with a neutral charge; and glucosamine-6-sulfate (GlcN6S) and glucosamine-6-phosphate (GlcN6P) with a negative charge (structures presented in S. Fig. 7-1). These saccharides were chosen in order to evaluate if the electrostatic forces were indeed the main drivers of their activity in the modulation of the A $\beta$  supramolecular assembly and cytotoxicity. Under these conditions we hypothesize that the negatively charged saccharides (available in the extracellular space) are able to compete with the cell membrane glycoproteins for A $\beta$  binding and sequestration. Finally, the sulphated GAGs are known to interact specifically with different proteins and, by comparison between the activity of GlcN6S and GlcN6P, we can assess if the presence of a sulphate moiety is able to provide additional benefits in the modulation of the A $\beta$  aggregation, toxicity, membrane disruption and insulin resistance, typically observed in the AD pathological scenario.

We started by screening the A $\beta$  aggregation kinetics for 10 days in the absence or presence of several concentrations (from 250 $\mu$ M up to 50mM) of each monosaccharide using the Thioflavin-T (ThT) assay (sensitive to the presence of parallel  $\beta$ -sheets). The A $\beta$  aggregation data (in the absence of monosaccharides) followed a typical profile presenting the secondary nucleation and fibril elongation regions, *i.e.* exponential growth and plateau phase, respectively (S. Fig. 7-2).[10] A strong ThT signal is observed during the formation/elongation of the A $\beta$  fibrils (composed of parallel  $\beta$ -sheets) in the presence of the monosaccharides, throughout the whole range of concentrations with the exception of the 50mM. All the monosaccharides seem to be able to enhance the secondary nucleation (*i.e.* formation of new fibres from oligomers nucleated on the surface of the existing ones), promoting a robust elongation of the A $\beta$  nanofibres.[29] Since fibrils are stated to be less cytotoxic, we selected the 1mM concentration of each monosaccharide to follow their ability to remodel the A $\beta$  supramolecular organization. We then used western blot (WB) with the 6E10 antibody to evaluate the size of peptide aggregates produced during the assembly pathway (Figures 7-1A-B and S. Fig. 7-7), for 1 and 5 days. The observed remodelling of the A $\beta$  aggregation seems to affect the section of the A $\beta$  sequence related with 6E10 epitope binding-site (*i.e.* the region between 1-16). This is more evident in the case of GlcN6S and GlcN6P (from day 1 of incubation until 5 days) due to the overall decrease of detected A $\beta$  structures. Importantly, the presence of GlcN6S generated a significant decrease in the amount of the cytotoxic A $\beta$  oligomeric forms (sizes of aggregates <15kDa) since day 1. To complement this data, we used circular dichroism (CD) analysis to assess the A $\beta$  secondary structure upon contact with the monosaccharides (S. Figs. 7-3 to 7-6) during 5 days.

It is clearly observed a series of alterations in the CD spectra (both in terms of intensity and profile) promoted by all the tested monosaccharides. In order to evaluate the impact of the observations in the A $\beta$  secondary structure we fitted all the CD spectra using the BestSel[30] deconvoluting algorithm. A $\beta$  oligomers, protofibrils and mature fibrils are organized under different secondary structures maintained by parallel or antiparallel  $\beta$ -sheets, which are dependent on the twisting angles between  $\beta$ -strands. By fitting the CD spectra with the BestSel deconvolution algorithm it is possible to predict the types of structures present in an ensemble of A $\beta$  supramolecular aggregates. Some reports show that antiparallel  $\beta$ -sheets are related to oligomeric cytotoxic forms.[31, 32] In contrast, the A $\beta$  parallel  $\beta$ -sheets are usually associated with the less toxic and more stable species, *e.g.* nanofibers detected in the extracellular senile plaques.[33]

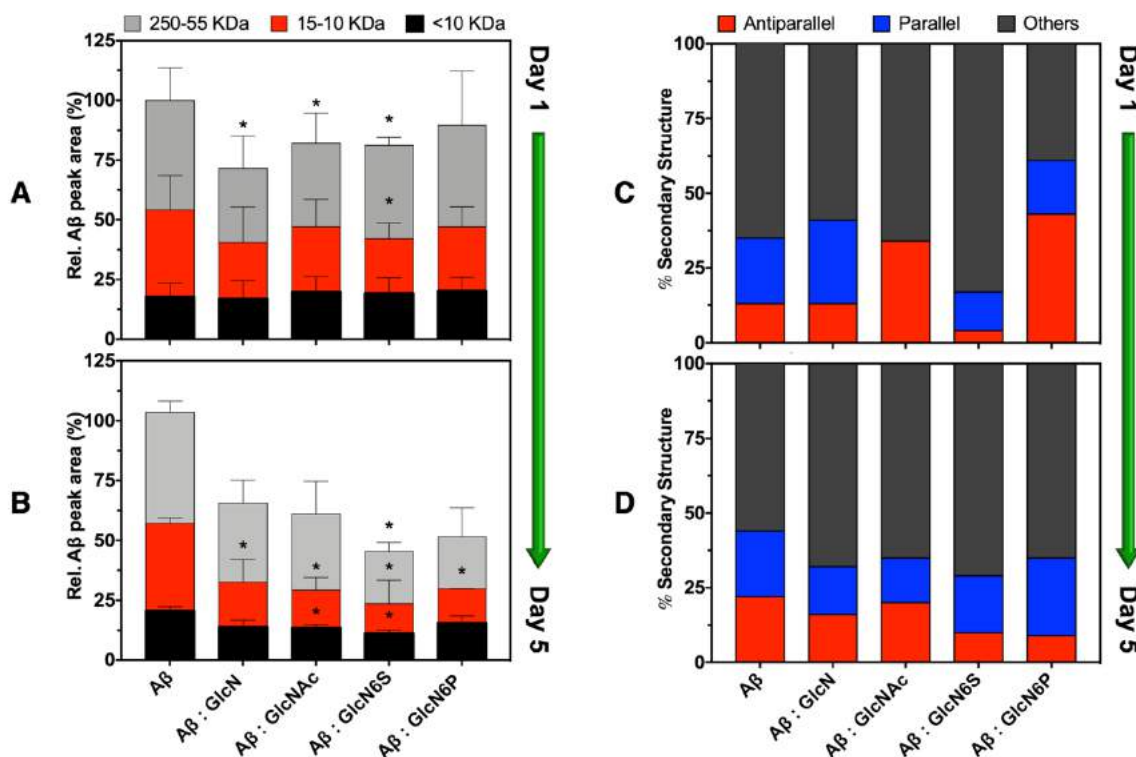


Figure 7-1. Relative densitometric bar graphs of A $\beta$  assembly quantified by WB after (A) 1 day or (B) 5 days of incubation, using the antibody 6E10. Loss of antiparallel  $\beta$ -sheets in the supramolecular organization of A $\beta$  followed by CD during (C) 1 and (D) 5 days. All experiments were executed using 25 $\mu$ M of A $\beta$  and 1mM of each monosaccharide, under constant agitation, at 37°C, in 0.1mM sodium phosphate buffer. Error bars = SD, \*\*\* p < 0.001, \*\* p < 0.01, \* p < 0.05 (all vs control of 25 $\mu$ M A $\beta$ ). In all the cases n=3. CD data was fitted using the BeStSel algorithm<sup>30</sup> - RMSD: 1.0283; NRMSD: 0.04966.

Our results (Figures 7-1C-D) are consistent with the ability of all the monosaccharides (but in particular of GlcN6S) to decrease the antiparallel  $\beta$ -sheets characteristic of the cytotoxic A $\beta$  oligomers. This observation is sustained over time, as after five days of incubation the reduction of the antiparallel arrangement is maintained.

We then used atomic force microscopy (AFM) to assess the impact of these structural observations in the morphological presentation of the A $\beta$  aggregates (Figures 7-2 and S. Fig. 7-8). It is clearly observed that all the monosaccharides, in particular GlcN6S and GlcN6P, are able to promote the supramolecular assembly of A $\beta$  generating large spherical aggregates, as well as fibrous structures. This process seems to be time dependent as the presence of these unstructured aggregates increases during the 5 days of incubation, being consistent with the results obtained from the ThT, WB and CD analysis.

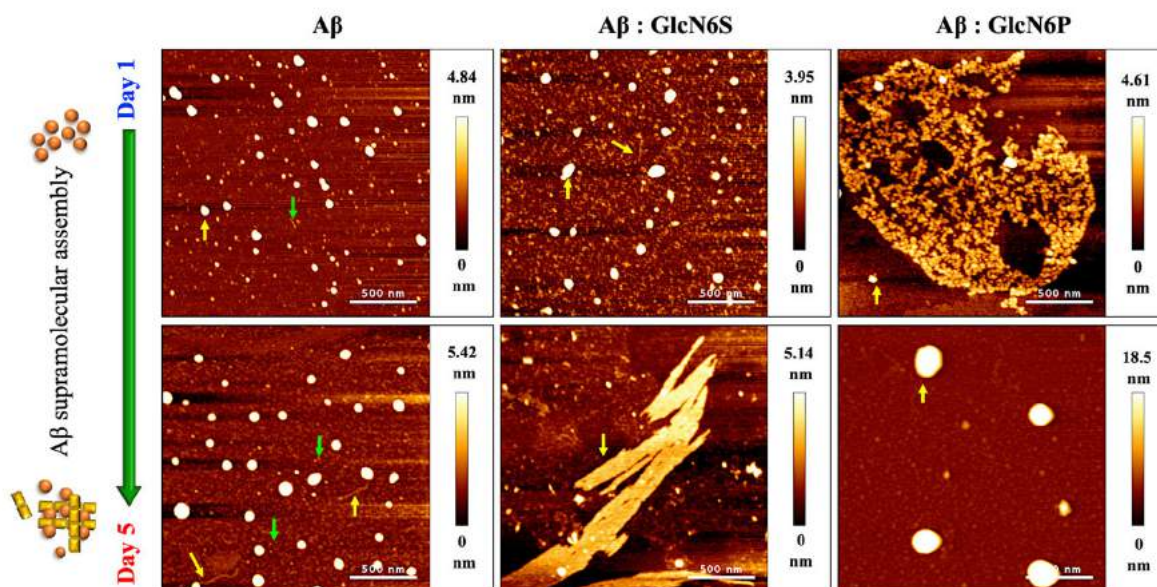


Figure 7-2. Representative AFM images of  $A\beta$  aggregates formed in the presence and absence of 1mM of GlcN6S and GlcN6P. All the samples were incubated for 1 or 5 days under constant agitation. Large aggregates and fibres marked with yellow arrows and oligomers marked with green arrows. Scale bars = 500 nm.

All the monosaccharides, but in particular GlcN6S and GlcN6P, interact with  $A\beta$ , remodelling its supramolecular forms. However, instead of reducing the presence of aggregates, it induced their formation but under morphological presentations that are distinct than the ones usually described for the  $A\beta$  oligomers. In order to evaluate if indeed these alterations were concomitant with reduction of  $A\beta$  toxicity, we evaluated the impact of the presence of the monosaccharides in the  $A\beta$ -mediated cell death using the neuroblastoma cell line (SH-SY5Y). An initial screening of all the monosaccharides under cell culture conditions, in the absence of  $A\beta$ , showed that, for the 1mM concentration, no major cytotoxic character was detected. Upon addition of the  $A\beta$ , all the monosaccharides were able to rescue cell viability confirmed both in terms of metabolic activity and DNA quantification (S. Fig. 7-9).

As mentioned before, several studies have revealed that one of the outcomes of the presence of  $A\beta$  in the pericellular space is the disruption of the cell membrane, leading to the influx of  $Ca^{2+}$  from the extracellular medium into the cytosol. This event is at the origin of a more complex cascade of biochemical changes that lead to an increased oxidative stress and neuronal cell death.[34] Based on this knowledge, we evaluated if the presence of the monosaccharides is able to produce alterations on the  $Ca^{2+}$  influx caused by the presence of  $A\beta$  and its different supramolecular forms. We used Fluo3-AM (Figures 7-3A and S. Fig. 7-10) and Calcein-AM (S. Fig. 7-11) as fluorescent  $Ca^{2+}$  probes (*i.e.* increase their fluorescence upon binding to the free  $Ca^{2+}$  present in the cytosol).[35, 36] The results obtained with both probes were comparable; as an example, in the presence of  $A\beta$  and GlcN6S it was observed a

reduction in the Fluo3-AM fluorescence of 41%, and of 60% for the Calcein-AM (both with no significant differences in relation with the control, *i.e.* cells cultured in the absence of both A $\beta$  and GlcN6S). In general, the presence of GlcN6S and GlcN6P protected the cell membrane from disruption and from the generation of additional Ca<sup>2+</sup> pores, maintaining the ionic balance in the intracellular environment.

There are other biochemical alterations that are commonly observed in AD. One example is an enhanced activity of acetylcholinesterase (AChE). AChE is an enzyme that regulates the level of the acetylcholine neurotransmitter (related with memory, motivation and movement) in the synaptic cleft.[34] AChE cleaves acetylcholine, affecting the communication between neurons.[37] It is usually overexpressed in AD leading to the use of inhibitors as part of the available clinical treatments. We were able to replicate this increase in AChE activity of SH-SY5Y cells in the presence of A $\beta$  (S. Fig. 7-12, V vs A $\beta$ ). We then tested if the presence of the monosaccharides were able to re-establish the basal level of AChE activity. Upon 1 day of incubation, GlcN6S significantly reduced the AChE activity to levels closer to the ones detected in the absence of A $\beta$ .

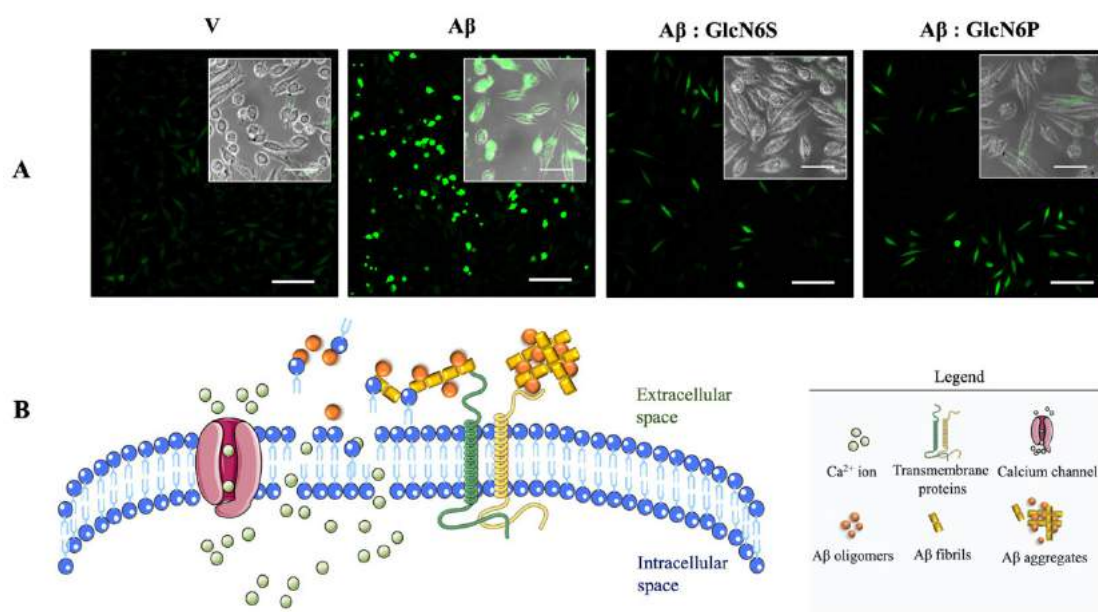


Figure 7-3. Representative fluorescence images of SH-SY5Y cells cultured for 24h in the presence of A $\beta$  (at a concentration of 25 $\mu$ M) and each monosaccharide (at 1mM) showing the levels of intracellular free Ca<sup>2+</sup> in the cytosol of the cells measured using two probes: (A) Fluo3-AM (confocal images). Scale bar = 100 $\mu$ m (insets = 50 $\mu$ m) (B) Graphical representation showing the Ca<sup>2+</sup> imbalance caused by the supramolecular A $\beta$  forms through their interaction with the lipid raft.

Moreover, the acetylcholine receptor location and function can be altered by changes in the cell membrane, since it is highly dependent of Ca<sup>2+</sup> channels and, may form a complex with A $\beta$  oligomers interfering in the protein kinase B (AKT) signalling pathway (related with glucose metabolism, apoptosis or cell proliferation).[11, 37] These results indicate that there might be other pathological events, such

as, insulin resistance and deficiency in insulin signalling, that might be attenuated by the presence of GlcN6S. Therefore, to test this hypothesis, we analysed the insulin signalling in SH-SY5Y cells, namely the phosphorylation of signalling proteins such as AKT into pAKT1 (S473) and Insulin Receptor Substrate 1 (IRS1) into pIRS1 (S612).[38]

As detailed in Figure 7-4D, insulin signalling involves its recognition by the IR. Insulin binds to  $\alpha$ -subunit of the IR, and the  $\beta$ -subunit becomes activated and auto-phosphorylate on its tyrosine residues, leading to the phosphorylation and activation of IRS1.[39]

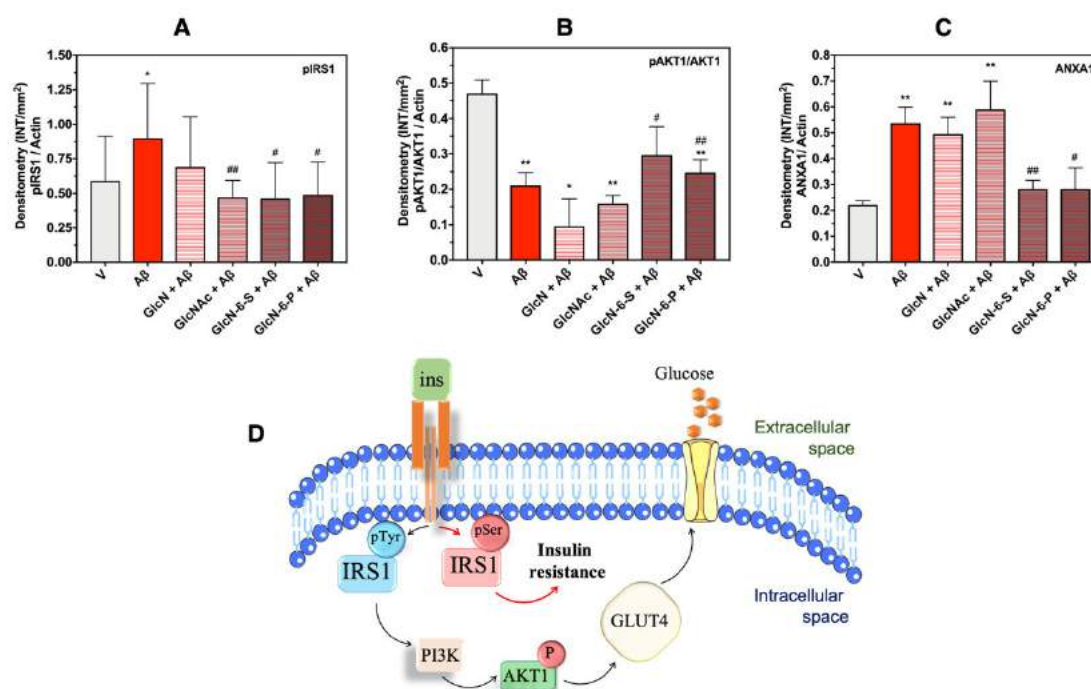


Figure 7-4. Ability of each monosaccharide to modulate the expression of (A) pIRS1; (B) pAKT1 and (C) Annexin 1 (ANXA1) by SH-SY5Y cells cultured for 1h in the absence/presence of A $\beta$ . Proteins were resolved by SDS-PAGE and visualized by western blotting. Protein levels were quantified by relative densitometric bar normalized to  $\beta$ -actin; n=3; \*\* p < 0.01 and \* p < 0.05 (both vs V, i.e. 0 $\mu$ M of A $\beta$ ); # p < 0.01 and # p < 0.05 (both vs 25 $\mu$ M of A $\beta$ ). (D) Schematic representation of the insulin signalling pathway affected by the A $\beta$  supramolecular forms.

Typically, under normal metabolism, the IR is phosphorylated in tyrosine residues. An increase in the phosphorylation on serine residues, hampers normal signal transduction, being usually associated with insulin resistance.[40] Therefore, the resistance pathway can be followed by tracking the phosphorylation of IRS1 at specific serine residues, such as serine 612 (S612).[41] Moreover, phosphorylation of AKT is related with the translocation of the glucose transporter (GLUT4) to the cell membrane, which occur later in the insulin signalling cascade. In this case, a reduction of pAKT leads to the inhibition of the phosphorylation of AS160, which is required for the insulin-stimulated translocation of the glucose transporter GLUT4 to the cell surface (Figure 4D).[38] Overall, in the presence of insulin

resistance it is expected an increased pIRS (S612) and a reduction of pAKT. We then used these markers to assess if the selected monosaccharides were able to modulate the insulin signalling, which is typically hampered in the presence of A $\beta$ .

The cell culture conditions used for the experiments included the presence of 10% of foetal bovine serum (FBS). FBS is reported to contain  $\sim 10\mu\text{U}/\text{mL}$  of insulin.[42] Therefore, IRS1 should be activated in the presence of FBS, without any additional insulin stimulus. Anyway, we tested the addition of four different concentration of insulin in SH-SY5Y cell culture, during 1h (S. Fig. 7-3).[13, 43] As expected, the presence of FBS alone is already stimulating the IRS1 pathway. Afterwards, we assessed the insulin pathway under standard culture conditions (*i.e.* no additional insulin stimulus), and also with the supplementation of insulin (at 5nM). Under standard culture conditions, the presence of A $\beta$  (25 $\mu\text{M}$ ) alone increases the expression of pIRS1 at S612 (after 1h of cell culture). The addition of each monosaccharide reduced its expression levels to close to the ones observed in the control experiment. However, GlcNAc, GlcN6S and GlcN6P were clearly more efficient (Figure 7-4A). Of note, the supplementation of GlcN in animal intravenous studies shows that GlcN-mediated hexosamine biosynthesis increases in insulin-sensitive tissues, a metabolic pathway that has been implicated in the development of insulin resistance and impairment of glucose metabolism (typical features of type 2 diabetes).[44, 45] Furthermore, we also evaluated the levels of insulin signalling by assessing the phosphorylation of AKT1 at S473 (pAKT1). In this case, we observed an increased expression of pAKT1 in the presence of GlcN6S and GlcN6P, indicating a trend to reach normal glucose metabolism (Figure 7-4B). Thus, in general, the expression of both pIRS1 (S612) and pAKT1, in the presence of GlcN6S and GlcN6P, supports the partial recovery of the homeostasis of insulin signalling.

Finally, most of the previously described AD-related pathological hallmarks are associated with inflammation. We then assessed the expression of Annexin 1 (ANXA1) as it is reported to be involved in the inflammatory response.[46] In addition, as ANXA1 is also a Ca<sup>2+</sup>-dependent phospholipid-binding protein and, at low Ca<sup>2+</sup> concentrations, the ANXA1 N-terminal domain is embedded within the Ca<sup>2+</sup> pore. The increment of Ca<sup>2+</sup> concentrations (imbalance) causes the overexpression of ANXA1 in the extracellular space, and may mediate multiple inflammatory responses of the cellular machinery.[47] Initial ANXA1 overexpression was detected in the presence of A $\beta$  alone (Figure 7-4C), which is in line with an increment of A $\beta$ -mediated inflammation. However, when GlcN6S and GlcN6P is used, ANXA1 expression is restored to normal levels of expression (comparing with V) indicating a reduction of the inflammatory pathway.

The results obtained by the quantification of pIRS1 (S612), pAKT1 and ANXA1 show that GlcN6P and GlcN6P are able to promote the re-establishment of the normal insulin signalling. Additionally, the

most important stimulus for insulin production is a postprandial increase of blood glucose level. Insulin is then released into the blood stream and binds to the insulin receptors present in the cells from the peripheral tissues promoting (at the end of the pathway) the translocation of GLUT4 to the cell membrane, and the subsequent transportation of glucose into the cell.[43] We then stimulated cells with an additional 5nM of insulin (S. Figs. 7-14, 7-15). We observed the recovery from the damage promoted by A $\beta$  itself that was enhanced by the presence of GlcN6S and GlcN6P, as shown by the decrease on the pIRS1 and ANXA1 expression levels.

Overall, we evaluated the capacity of four GlcN analogues in their ability to re-establish the homeostasis of a series of biochemical hallmarks of AD, namely, the remodelling of the A $\beta$  oligomers into non-cytotoxic forms, reduction of membrane dysfunction, levelling of the AChE enzymatic activity, reestablishment of the basal levels of insulin signalling and reduction of inflammation. We found that the sulphated (GlcN6S) and phosphated (GlcN6P) monosaccharides were able to promote the recovery from all these AD-related disfunctions. These observations are probably caused by the negative charge of these monosaccharides, which reduces their ability to be internalized by the cells (due to negative charge of the cell membrane), allowing them to interact electrostatically with the A $\beta$  oligomers.

Finally, we believe that GlcN6S and GlcN6P present relevant potential as single AD drug leads, or as bioactive moieties to be integrated into nanocarriers targeting the control of the onset and progression of AD. Our results are also consistent with the possible influence of the negatively charged groups in the GAGs in modulating the supramolecular assembly of different amyloidogenic peptides/proteins linked to neurodegenerative disorders and levelling their ensuing pathological biochemical cascades.



## 7.2 REFERENCES

1. Masters, C.L., et al., Alzheimer's disease. *Nat Rev Dis Primers*, 2015. 1: p. 15056.
2. Spires-Jones, Tara L. and Bradley T. Hyman, The Intersection of Amyloid Beta and Tau at Synapses in Alzheimer's Disease. *Neuron*, 2014. 82(4): p. 756-771.
3. Zhang, F., et al., beta-amyloid redirects norepinephrine signaling to activate the pathogenic GSK3beta/tau cascade. *Sci Transl Med*, 2020. 12(526).
4. Reimand, J., et al., Amyloid-beta CSF/PET discordance vs tau load 5 years later: It takes two to tangle. *medRxiv*, 2020.
5. Pontecorvo, M.J., et al., Relationships between flortaucipir PET tau binding and amyloid burden, clinical diagnosis, age and cognition. *Brain*, 2017. 140(3): p. 748-763.
6. Aguzzi, A. and T. O'Connor, Protein aggregation diseases: pathogenicity and therapeutic perspectives. *Nat Rev Drug Discov*, 2010. 9(3): p. 237-48.
7. Knowles, T.P., M. Vendruscolo, and C.M. Dobson, The amyloid state and its association with protein misfolding diseases. *Nat Rev Mol Cell Biol*, 2014. 15(6): p. 384-96.
8. Soto, C., et al., Inhibition of Alzheimer's amyloidosis by peptides that prevent  $\beta$ -sheet conformation. *Biochemical and biophysical research communications*, 1996. 226(3): p. 672-680.
9. Panza, F., et al., A critical appraisal of amyloid- $\beta$ -targeting therapies for Alzheimer disease. *Nature Reviews Neurology*, 2019. 15(2): p. 73-88.
10. Cohen, S.I., et al., Proliferation of amyloid-beta42 aggregates occurs through a secondary nucleation mechanism. *Proc Natl Acad Sci U S A*, 2013. 110(24): p. 9758-63.
11. Fabiani, C. and S.S. Antollini, Alzheimer's Disease as a Membrane Disorder: Spatial Cross-Talk Among Beta-Amyloid Peptides, Nicotinic Acetylcholine Receptors and Lipid Rafts. *Front Cell Neurosci*, 2019. 13(309): p. 309.
12. Gan, L., et al., Converging pathways in neurodegeneration, from genetics to mechanisms. *Nature Neuroscience*, 2018. 21(10): p. 1300-1309.
13. Najem, D., et al., A  $\beta$ -Induced Insulin Resistance and the Effects of Insulin on the Cholesterol Synthesis Pathway and A  $\beta$  Secretion in Neural Cells. *Neuroscience Bulletin*, 2016. 32(3): p. 227-238.
14. Garai, K., et al., The binding of apolipoprotein E to oligomers and fibrils of amyloid-beta alters the kinetics of amyloid aggregation. *Biochemistry*, 2014. 53(40): p. 6323-31.
15. Quazi, F. and R.S. Molday, Differential phospholipid substrates and directional transport by ATP-binding cassette proteins ABCA1, ABCA7, and ABCA4 and disease-causing mutants. *Journal of Biological Chemistry*, 2013. 288(48): p. 34414-34426.
16. Wang, Y., et al., TREM2 lipid sensing sustains the microglial response in an Alzheimer's disease model. *Cell*, 2015. 160(6): p. 1061-1071.
17. Hardy, J., Membrane damage is at the core of Alzheimer's disease. *The Lancet Neurology*, 2017. 16(5): p. 342.

18. Magno, L., et al., Alzheimer's disease phospholipase C-gamma-2 (PLCG2) protective variant is a functional hypermorph. *Alzheimer's Research & Therapy*, 2019. 11(1): p. 16.
19. Krausser, J., T.P.J. Knowles, and A. Šarić, Physical mechanisms of amyloid nucleation on fluid membranes. *bioRxiv*, 2019: p. 2019.12.22.886267.
20. Steen, E., et al., Impaired insulin and insulin-like growth factor expression and signaling mechanisms in Alzheimer's disease—is this type 3 diabetes? *Journal of Alzheimer's disease*, 2005. 7(1): p. 63-80.
21. Najem, D., et al., Insulin resistance, neuroinflammation, and Alzheimer's disease. *Reviews in the Neurosciences*, 2014. 25(4): p. 509-525.
22. Craft, S., Alzheimer disease: insulin resistance and AD—extending the translational path. *Nature reviews Neurology*, 2012. 8(7): p. 360.
23. Sandberg, A., et al., Stabilization of neurotoxic Alzheimer amyloid-beta oligomers by protein engineering. *Proceedings of the National Academy of Sciences of the United States of America*, 2010. 107(35): p. 15595-15600.
24. Cohen, S.I.A., et al., Distinct thermodynamic signatures of oligomer generation in the aggregation of the amyloid-beta peptide. *Nat Chem*, 2018. 10(5): p. 523-531.
25. Fraser, P.E., A.A. Darabie, and J.A. McLaurin, Amyloid-beta interactions with chondroitin sulfate-derived monosaccharides and disaccharides. implications for drug development. *J Biol Chem*, 2001. 276(9): p. 6412-9.
26. Jha, S., et al., Mechanism of Amylin Fibrillization Enhancement by Heparin. *Journal of Biological Chemistry*, 2011. 286(26): p. 22894-22904.
27. Iannuzzi, C., G. Irace, and I. Sirangelo, The effect of glycosaminoglycans (GAGs) on amyloid aggregation and toxicity. *Molecules*, 2015. 20(2): p. 2510-28.
28. Meisl, G., et al., Modulation of electrostatic interactions to reveal a reaction network unifying the aggregation behaviour of the Ab42 peptide and its variants. *Chemical science*, 2017.
29. Törnquist, M., et al., Secondary nucleation in amyloid formation. *Chemical Communications*, 2018. 54(63): p. 8667-8684.
30. Micsonai, A., et al., Accurate secondary structure prediction and fold recognition for circular dichroism spectroscopy. *Proc Natl Acad Sci U S A*, 2015. 112(24): p. E3095-103.
31. Cerf, E., et al., Antiparallel beta-sheet: a signature structure of the oligomeric amyloid beta-peptide. *Biochem J*, 2009. 421(3): p. 415-23.
32. Celej, María S., et al., Toxic prefibrillar  $\alpha$ -synuclein amyloid oligomers adopt a distinctive antiparallel  $\beta$ -sheet structure. *Biochemical Journal*, 2012. 443(3): p. 719-726.
33. Chen, G.-F., et al., Amyloid beta: structure, biology and structure-based therapeutic development. *Acta pharmacologica Sinica*, 2017. 38(9): p. 1205-1235.
34. Fabiani, C. and S.S. Antollini, Alzheimer's Disease as a Membrane Disorder: Spatial Cross-Talk Among Beta-Amyloid Peptides, Nicotinic Acetylcholine Receptors and Lipid Rafts. *Frontiers in Cellular Neuroscience*, 2019. 13(309).

35. Evangelisti, E., et al., Binding affinity of amyloid oligomers to cellular membranes is a generic indicator of cellular dysfunction in protein misfolding diseases. *Scientific reports*, 2016. 6: p. 32721.
36. Patel, H., C. Tscheka, and H. Heerklotz, Characterizing vesicle leakage by fluorescence lifetime measurements. *Soft Matter*, 2009. 5(15): p. 2849-2851.
37. Ma, K.G. and Y.H. Qian, Alpha 7 nicotinic acetylcholine receptor and its effects on Alzheimer's disease. *Neuropeptides*, 2019. 73: p. 96-106.
38. Świdarska, E., et al., Role of PI3K/AKT pathway in insulin-mediated glucose uptake, in *Blood Glucose Levels*. 2018, IntechOpen.
39. Olivares-Reyes, J.A., A. Arellano-Plancarte, and J.R. Castillo-Hernandez, Angiotensin II and the development of insulin resistance: implications for diabetes. *Molecular and cellular endocrinology*, 2009. 302(2): p. 128-139.
40. Arnold, S.E., et al., Brain insulin resistance in type 2 diabetes and Alzheimer disease: concepts and conundrums. *Nat Rev Neurol*, 2018. 14(3): p. 168-181.
41. Copps, K.D. and M.F. White, Regulation of insulin sensitivity by serine/threonine phosphorylation of insulin receptor substrate proteins IRS1 and IRS2. *Diabetologia*, 2012. 55(10): p. 2565-2582.
42. Gstraunthaler, G., Alternatives to the use of fetal bovine serum: serum-free cell culture. *ALTEX-Alternatives to animal experimentation*, 2003. 20(4): p. 275-281.
43. Di Camillo, B., et al., A rule-based model of insulin signalling pathway. *BMC systems biology*, 2016. 10(1): p. 38-38.
44. Marshall, S., V. Bacote, and R. Traxinger, Discovery of a metabolic pathway mediating glucose-induced desensitization of the glucose transport system. Role of hexosamine biosynthesis in the induction of insulin resistance. *Journal of Biological Chemistry*, 1991. 266(8): p. 4706-4712.
45. Simon, R.R., et al., A comprehensive review of oral glucosamine use and effects on glucose metabolism in normal and diabetic individuals. *Diabetes/metabolism research and reviews*, 2011. 27(1): p. 14-27.
46. Perretti, M. and F. D'acquistio, Annexin A1 and glucocorticoids as effectors of the resolution of inflammation. *Nature Reviews Immunology*, 2009. 9(1): p. 62-70.
47. Zhao, B., et al., Annexin A1 translocates to nucleus and promotes the expression of pro-inflammatory cytokines in a PKC-dependent manner after OGD/R. *Scientific reports*, 2016. 6: p. 27028-27028.
48. Stine, W.B., et al., Preparing synthetic A $\beta$  in different aggregation states. *Methods Mol Biol*, 2011. 670: p. 13-32.

## SUPPLEMENTARY INFORMATION

### ▪ Materials and Methods

All the chemicals used in this work were purchased from Sigma-Aldrich and were used without further purification. Water of Milli-Q grade was obtained from a Millipore water purification system. The monosaccharides used in this work (S. Fig. 7-1) were obtained from: glucosamine (GlcN) – Sigma-Aldrich; N-acetylglucosamine (GlcNAc) – Laborspirit; and glucosamine-6-sulphate (GlcN6S) and glucosamine-6-phosphate (GlcN6P) – Carbosynth.

**Peptide preparation.** Human amyloid- $\beta$  peptide (1-42, A $\beta$ ) was obtained by custom synthesis and acquired from GeneCust Europe (Luxembourg). A $\beta$  was prepared by dissolving 10mg of the peptide in (Fluorochem Ltd, UK) as reported by Stine *et al.*[48] Shortly, in a chemical fume hood, A $\beta$  was incubated during 30min in HFIP (5mg/mL, at room temperature). A $\beta$  aliquots of 100 $\mu$ L were allowed to evaporate in open vials overnight (in the fume hood). The vials were transferred to a vacuum system for 1h without heating to eliminate any residual traces of HFIP. A $\beta$  aliquots were kept at -20°C and reconstituted immediately before use. Oligomeric A $\beta$  was prepared by adding 20 $\mu$ L of DMSO (sonicated for 10min in an ultra-sound bath) followed by adding ice-cold water to a final concentration of 100 $\mu$ M with 15s of vortexing.

**Thioflavin-T (ThT).** The supramolecular assembly of A $\beta$  species was followed by ThT assay (assembly – S. Fig. 7-2) during 10 days. A $\beta$  peptide stock solution was prepared as described previously. A $\beta$  solution (final concentration of 25 $\mu$ M) in Phosphate Buffer 0.1mM (with 0.1% of sodium azide, pH 7.2) was mixed with different concentrations of each monosaccharide (from 50mM down to 0.250mM), and added to a ThT solution (final concentration of 40 $\mu$ M). During the 10 days, the ThT fluorescence was monitored in a Fluorescence Spectrometer (Jasco, FP-8500, Japan) using an excitation wavelength of 435nm and an emission wavelength of 465nm. Each individual experiment was repeated in triplicate.

**Circular Dichroism (CD).** The same set of experimental conditions were used for the CD analysis (25 $\mu$ M of A $\beta$  in the presence or absence of each monosaccharide, for the different concentrations – 50mM down to 0.250mM). The measurements were executed using a 1mm path length cell in a CD spectrometer (Jasco, J1500, Japan). The spectra (S. Fig. 73, 7-6) were acquired in a range between 190–260nm, a scan rate of 10nm/min, response time of 1s, with three accumulative scans for each spectrum. Results are expressed in  $\theta$  [mdeg].

**Western Blot (WB).** WB was used to quantify the sizes of the A $\beta$  species produced during the interaction with each monosaccharide (at a concentration of 1mM) during 1 and 5 days. WBs were run using the iBlot 2 System for membrane transfer after a 12% Bis-Tris Gel Invitrogen NuPAGE, with MES SDS Running Buffer gel (Laemmli loading buffer without DTT) SDS-page procedure. Next, the nitrocellulose membranes were blocked with 4% BSA for 1.5 hours in TBS-T (TBS with 0.1% Tween 20%), followed by an incubation period (overnight at 4°C) with the 6E10 antibody (A $\beta$  1-16 – 1:1000 dilution in 4% of BSA in TBS-T). Washed membranes (3 times in TBS-T) were incubated (during 1.5h at RT) in IRDye 800CW Goat anti-mouse IgG secondary antibody (1:10000 dilution in TBS-T). Finally, the membranes were revealed by an Odyssey Fc imaging system (LI-COR Inc., Nebraska USA). For the quantification of the obtained lanes we used the Fiji software (Figures 7-1A and S. Fig. 7-7).

**Atomic Force Microscopy (AFM).** Freshly cleaved mica sheets were washed with one drop of 1mM HCl for 20 seconds, rinsed with ultra-pure water (five times) and dried under a nitrogen flux. Afterwards, A $\beta$  peptide stock solution (25 $\mu$ M) was prepared as described previously and mixed with each monosaccharide (at a concentration of 1mM). After 1 or 5 days of incubation, a 20 $\mu$ L sample were spotted onto the mica during 3min, washed with water and dried under nitrogen. AFM images were recorder using a JPK Nanowizard 3 (JPK, Germany) in air at room temperature under AC mode. The scans were acquired at a 512x512 pixels resolution using ACTA-SS probes ( $k\sim$ 37N/m, AppNano, USA), a drive frequency of  $\sim$ 254kHz, a setpoint of  $\sim$ 0.5V and a scanning speed of 1.0Hz (Figures 7-2 and S. Fig. 7-8).

**Cell studies.** SH-SY5Y neuroblastoma cells were cultured at 37°C in a humidified 95/5% air/CO<sub>2</sub> atmosphere using Dulbecco's modified Eagles medium F-12 (Gibco, UK) supplemented with 10% FBS (Gibco, UK) and 1% ATB (Gibco, UK) solution. Medium was replaced each 2 days, and cells were used after reaching 80% of confluence. Cells were plated at a density of 25 000 cells per cm<sup>2</sup> containing DMEM/F-12 media for: i) AlamarBlue® assay; ii) DNA content; iii) Ca<sup>2+</sup> influx measurements; iv) and acetylcholinesterase quantification. All these experiments were executed after 1 day of culture in the presence and absence of A $\beta$ , with or without 1mM of each monosaccharide.

For the insulin resistance experiments, cells were cultured until they reach 70% of confluence. Then, the culture medium was replaced to a low-glucose medium (SILAC Advanced DMEM/F-12 Flex Media, no phenol red from Alfacene). After 12h of culture, A $\beta$ , insulin and each monosaccharide were added and cultured during 1h.

**AlamarBlue® assay.** The cytocompatibility of each monosaccharide (S. Fig. 7-9A) and A $\beta$  cytotoxicity (S. Fig. 7-9B) was evaluated by measuring the cell metabolic activity, 1 day after the addition of the monosaccharide (at a concentration of 1mM) or A $\beta$  (at a concentration of 25 $\mu$ M) using AlamarBlue® (indicator dye BUF012B, Bio-Rad) according to the manufacturer's instructions. The fluorescence intensity of each experimental condition was measured in a Synergy HT microplate reader (Bio-Tek Instruments) using an excitation wavelength of 530nm and an emission wavelength of 590nm. *p*-values were calculated using one-tailed t-test. Results are presented as mean  $\pm$  SEM of 6 independent experiments for each experimental condition (S. Fig. 7-9A, 7-9B).

**DNA content.** The DNA content was assessed by PicoGreen dsDNA Quantitation Reagent® P7589, from Invitrogen (S. Fig. 7-9C). Samples were collected into microtubes with 1mL of ultrapure water and stored at -80°C. Samples were thawed and sonicated (VCX-130PB-220, Sonics) before quantification (following the manufacture protocol). For the fluorescence acquisition (excitation wavelength of 485/20 nm and an emission of 528/20 nm) we used a Synergy HT microplate reader (Bio-Tek Instruments). *p*-values were calculated using one-tailed t-test. Results are presented as mean  $\pm$  SEM. Samples and standards were made in triplicate (S. Fig. 7-9C).

#### **Measurements of cytosolic Ca<sup>2+</sup> levels.**

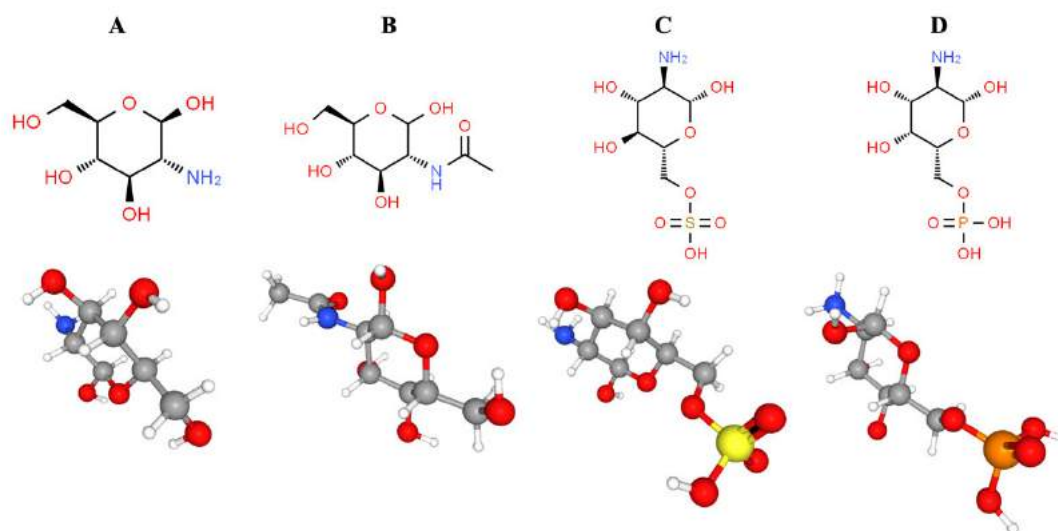
Fluo3-AM: The amount of free Ca<sup>2+</sup> in the cytosol was measured using the Fluo3-AM probe (Figure 7-3 and S. Fig. 7-10). Each well was loaded with 5.0 $\mu$ M Fluo3-AM for 30 min in Krebs-Ringer-Hepes glucose and then washed, and allowed to equilibrate for 30 min. The levels were measured at, approximately, 520nm by scanning confocal fluorescence microscopy (Leica, TCS SP8), after excitation at 488nm. The fluorescence results were normalized by the number of cells in each acquired image (15 images per experimental condition), in three different experiments, and were analysed using Fiji ImageJ software.

Calcein-AM: Each well was loaded with 1.0 $\mu$ M of Calcein-AM for 30 min in Krebs-Ringer-Hepes glucose and then washed. Afterwards, using an inverted microscope (Zeiss, Axio Observer) the emitted fluorescence was recorded during 45min (pictures were acquired each 5min). Fluorescence was normalized by the number of cells in each acquired image (12 images per experimental condition) comparing with the vehicle (V). Results are average of three independent experiments. Data was analysed using Fiji ImageJ software (S. Fig. 7-11).

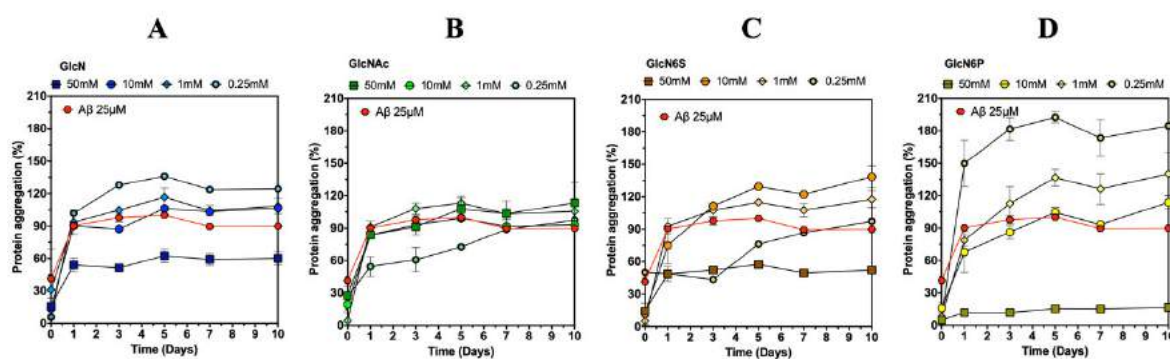
**Acetylcholinesterase (AChE) activity.** To determine AChE activity of the SH-SY5Y cell culture (Figure S12), an acetylcholinesterase assay kit (ab138871, abcam) was used. The assay was performed according to the manufacturer's instructions. AChE activity was measured using Synergy HT microplate reader (Bio-Tek Instruments) at 410nm (absorption intensity). *p*-values were calculated using one-tailed t-test. Results are presented as mean  $\pm$  SEM. Samples and standards were made in triplicate (S. Fig. 7-12).

**Insulin and inflammatory signalling pathway.** Immunoblot analysis was performed following Western Blot technique. Briefly, cell lysates (25 $\mu$ g of protein) were subjected to 10% Bis-Tris Gel Invitrogen NuPAGE, with MES SDS Running Buffer gel (gel loading buffer without DTT), followed by a membrane transference to a nitrocellulose membrane using iBlot 2 System. Membranes were first blocked with 5% BSA in Tris-buffered saline added with 0.1% Tween 20 (TBST) buffer for 1.5h followed by the overnight incubation with primary antibodies at 1:250 dilutions in a shaker at 4°C: Anti-phospho-IRS-1 (pSer612) (Sigma-Aldrich); AKT1 total (Cell Signalling Technology, Inc); AKT1 (phospho S473, abcam); Annexin I (EH17a, Santa Cruz Biotechnology, Inc); and  $\beta$ -Actin Antibody (Cell Signaling Technology, Inc). The membranes were then washed three times with TBST, and incubated with in IRDye 800CW Goat anti-Mouse (or Rabbit) IgG Secondary Antibody (1:15000 dilution in TBS-T). Finally, the WB lanes were detected using an Odyssey Fc Imaging System (LI-COR Inc., Nebraska USA). The comparisons between bands in different lanes were quantified using Fiji software (Figures 7-4 and S. Fig. 7-13, 7-15). Bands were quantified by densitometry and normalized to those of  $\beta$ -actin.

▪ In vitro protein aggregation studies

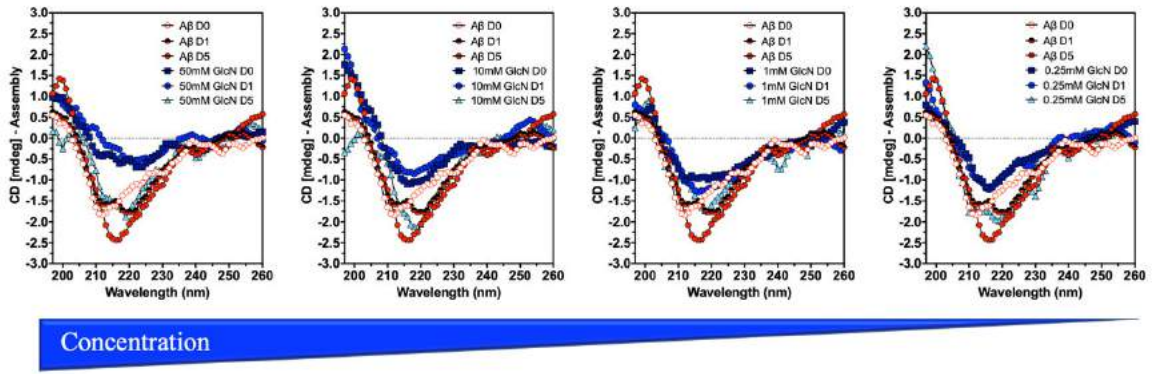


Supplementary Fig. 7-1. Chemical structure of the glucosamine and its analogues: (A) glucosamine (GlcN), (B) N-acetyl glucosamine (GlcNAc), (C) glucosamine-6-sulphate (GlcN6S), and (D) glucosamine-6-phosphate (GlcN6P).

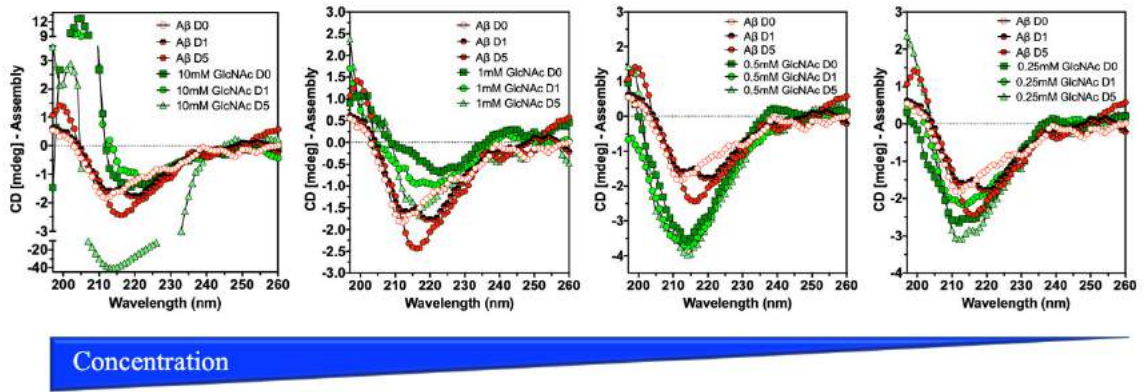


Supplementary Fig. 7-2. A $\beta$  aggregation kinetics evaluated using the ThT assay in the presence of the monosaccharides (at a concentration of 1mM): (A) GlcN, (B) GlcNAc, (C) GlcN6S, and (D) GlcN6P. The A $\beta$  fibril formation and fluorescence was measured over 10 days. All experiments were performed under constant agitation and at room temperature. In all the cases n=3.

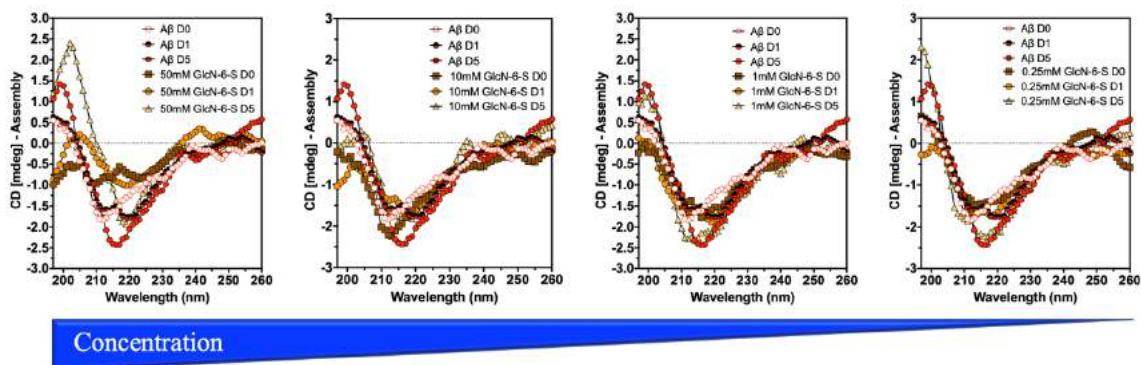




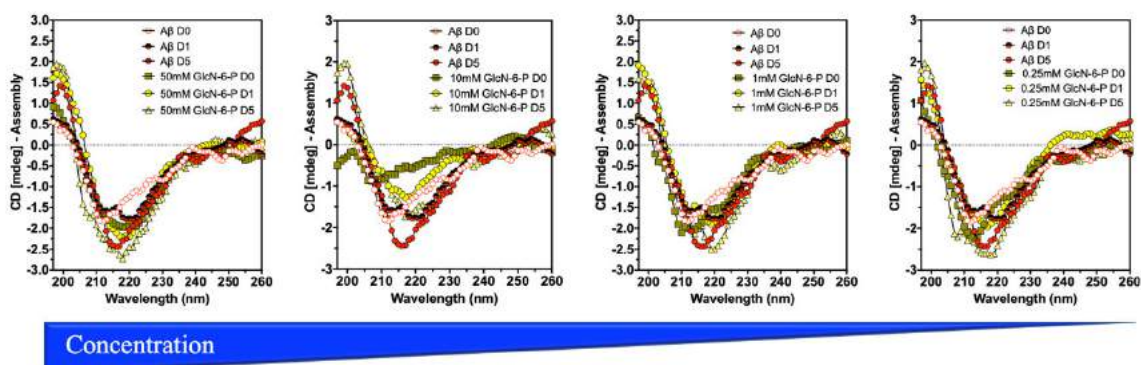
Supplementary Fig. 7-3. CD spectra of A $\beta$  measured during 5 days, in the presence of different concentrations of GlcN. All the experiments were executed in 0.1mM of sodium phosphate buffer (pH=7) under constant agitation and at room temperature.



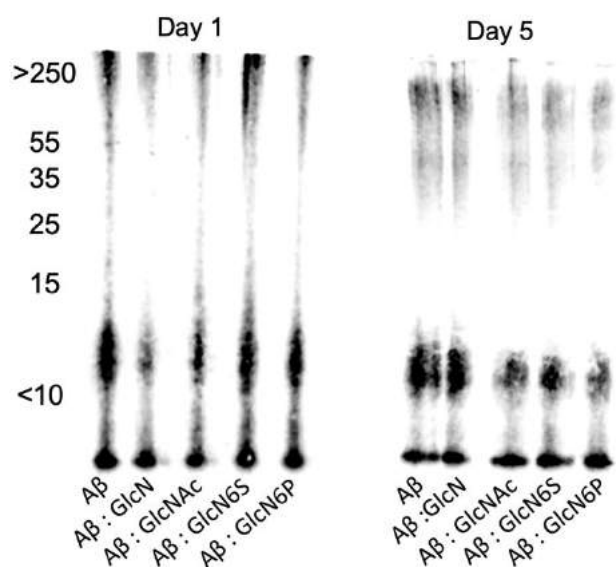
Supplementary Fig. 7-4. CD spectra of A $\beta$  measured during 5 days, in the presence of different concentrations of GlcNAc. All the experiments were executed in 0.1mM of sodium phosphate buffer (pH=7) under constant agitation, at room temperature.



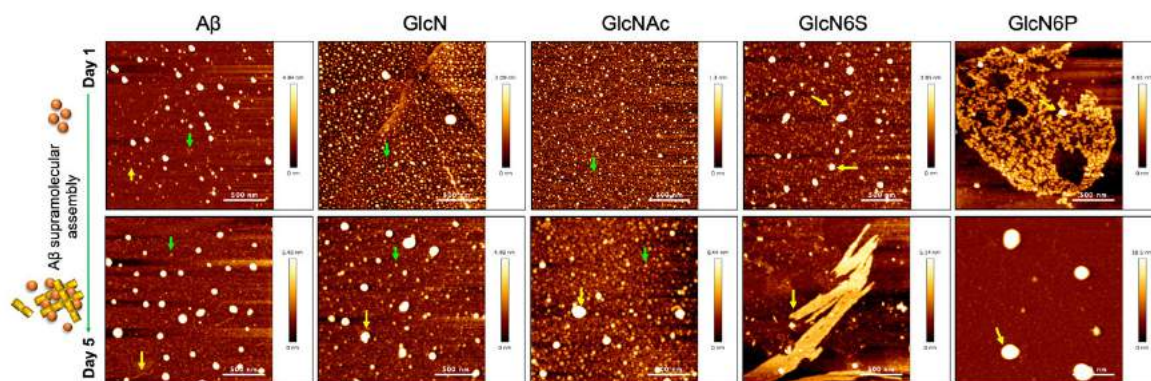
Supplementary Fig. 7-5. CD spectra of A $\beta$  measured during 5 days, in the presence of different concentrations of GlcN6S. All the experiments were executed in 0.1mM of sodium phosphate buffer (pH=7) under constant agitation and at room temperature.



Supplementary Fig. 7-6. CD spectra of A $\beta$  measured during 5 days, in the presence of different concentrations of GlcN6P. All the experiments were executed in 0.1mM of sodium phosphate buffer (pH=7) under constant agitation and at room temperature.

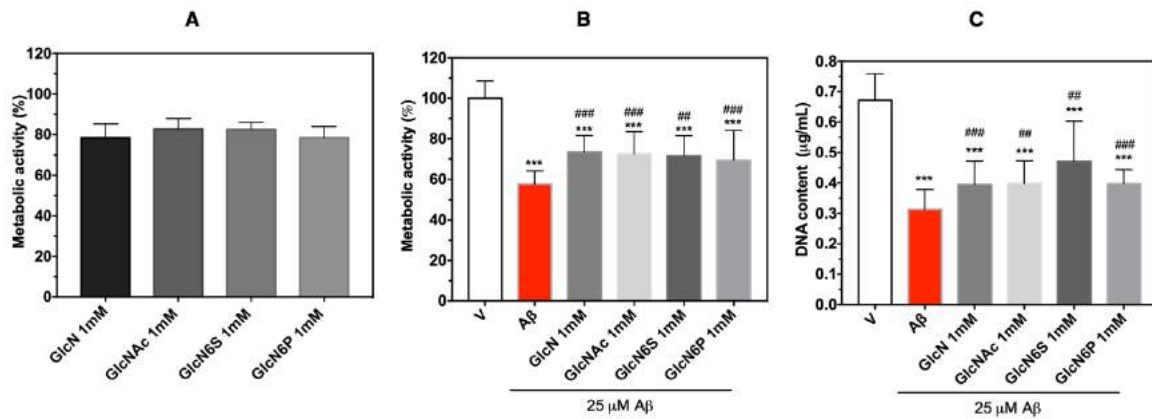


Supplementary Fig. 7-7. Representative WB membranes revealed using the 6E10 antibody for A $\beta$  in the absence and presence of 1mM of each monosaccharide. Experiments were executed for 1 and 5 days under constant agitation and at room temperature. In all the cases n=3.

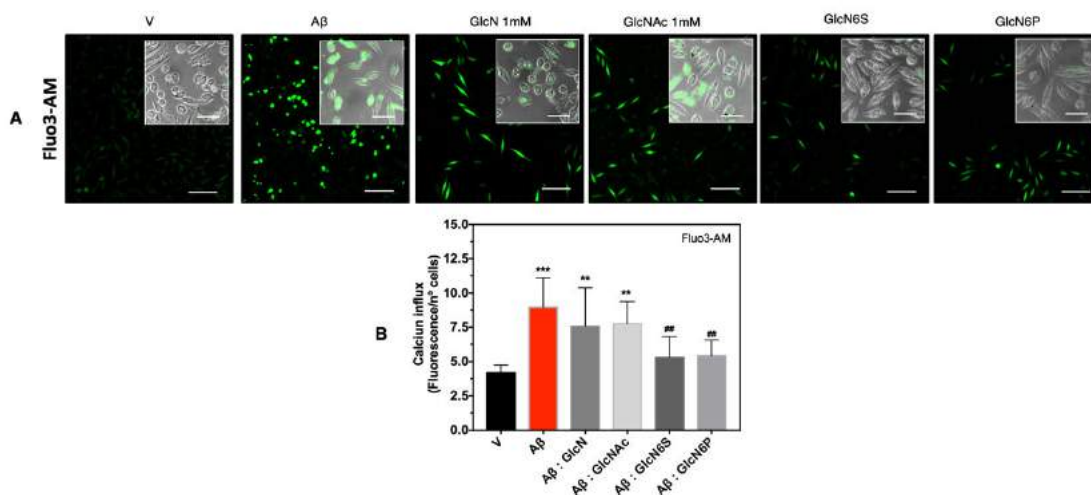


Supplementary Fig. 7-8. Representative AFM images of A $\beta$  (at a concentration of 25 $\mu$ M) incubated in the absence and presence of 1mM of GlcN, GlcNAc, GlcN6S and GlcN6P during 1 day and 5 days, under constant agitation. All compounds directly altered A $\beta$  supramolecular presentation. Large aggregates and fibres marked with yellow arrows and oligomers marked with green arrows. Scale bars = 500 nm.

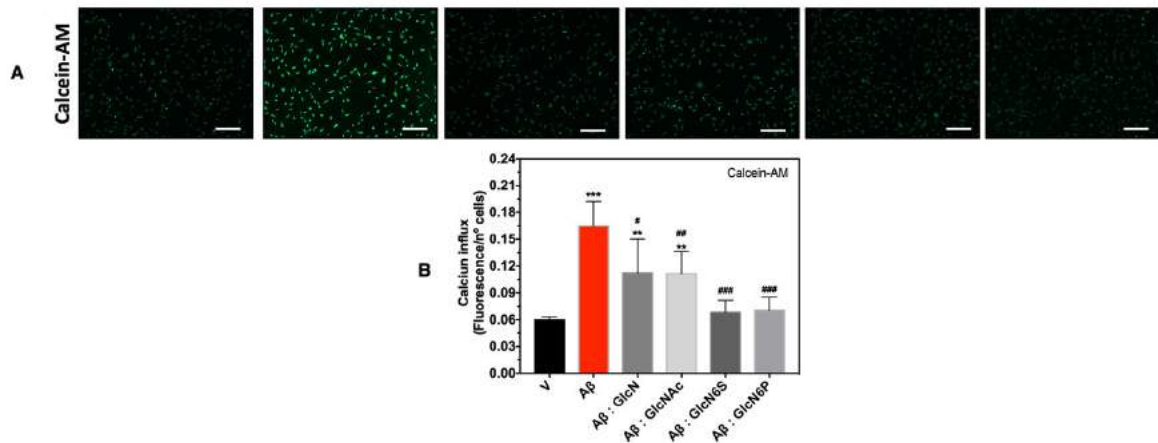
■ Cells Studies



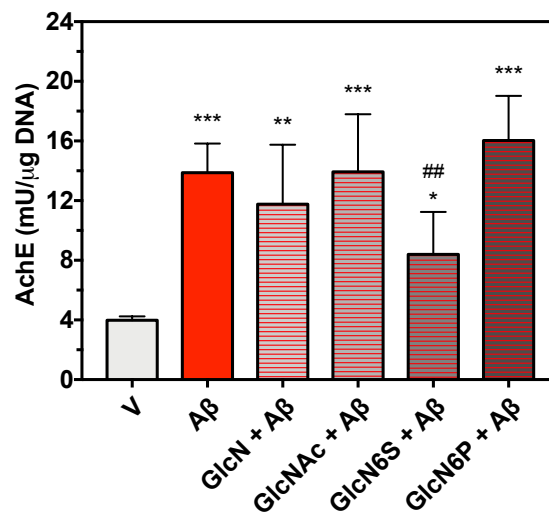
Supplementary Fig. 7-9. Metabolic activity of SH-SY5Y cells (using AlmarBlue® assay) in the presence of each monosaccharide (A) in the absence of A $\beta$  and (B) in the presence of 25  $\mu$ M of A $\beta$ . (C) Proliferation of SH-SY5Y cells, measured by quantification of the DNA content. Cells were incubated during 24h. \*\*\*  $p < 0.001$ , \*\*  $p < 0.01$ , \*  $p < 0.05$  (vs control). In all the cases  $n=3$ .



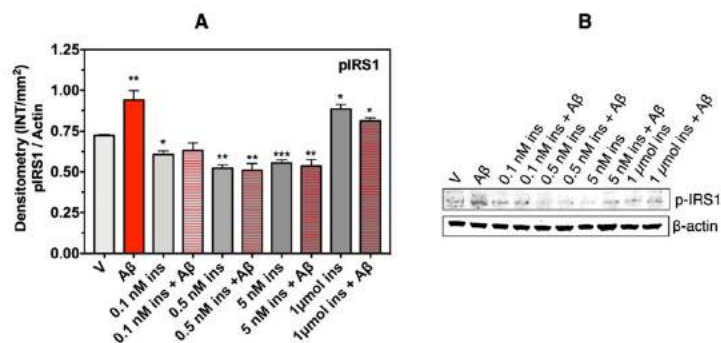
Supplementary Fig. 7-10. Representative images of SH-SY5Y cells treated for 24h with A $\beta$  (at a concentration of 25  $\mu$ M) and each monosaccharide (at a concentration of 1mM) showing the levels of intracellular free Ca $^{2+}$  in the cytosol of the cells using the Fluor3-AM probe (images acquired under confocal microscopy). Scale bars = 100  $\mu$ m (insets = 50  $\mu$ m). (B) Quantification of the fluorescence associated with intracellular Ca $^{2+}$  obtained from the confocal images. \*\*\*  $p < 0.001$  and \*\*  $p < 0.01$  (both vs control - 0  $\mu$ M of A $\beta$ ); \*  $p < 0.01$  (vs 25  $\mu$ M A $\beta$ ). In all the cases  $n=3$ .



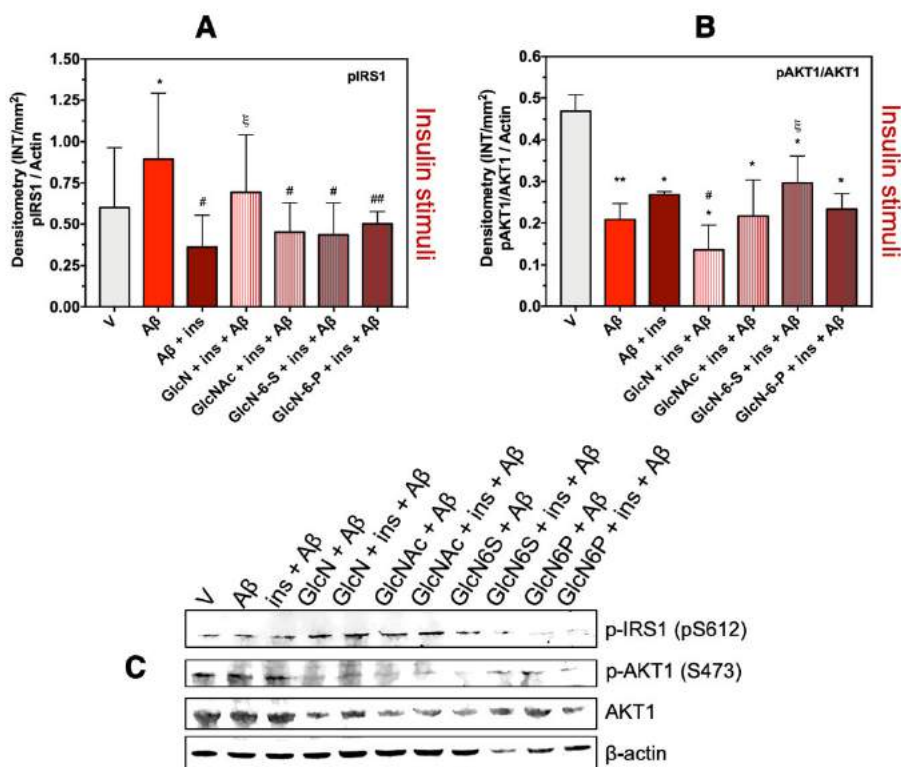
Supplementary Fig. 7-11. Representative images of SH-SY5Y cells treated for 1 day with A $\beta$  (at a concentration of 25 $\mu$ M) and each monosaccharide (at a concentration of 1mM) showing degree of membrane permeability using the probe Calcein-AM (images acquired by fluorescence inverted microscope). Scale bar = 200 $\mu$ m. (B) Quantification of the fluorescence associated with intracellular Ca<sup>2+</sup>. \*\*\* p < 0.001, \*\* p < 0.01 (both vs control - 0 $\mu$ M of A $\beta$ ); ### p < 0.001, # p < 0.01 and \* p < 0.05 (all vs 25 $\mu$ M A $\beta$ ). In all the cases n=3.



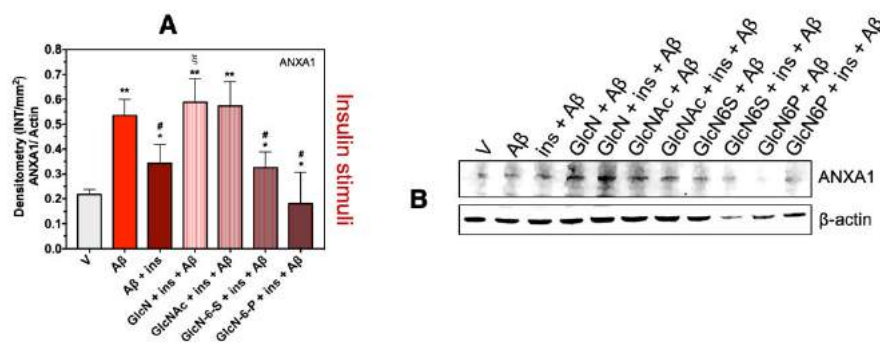
Supplementary Fig. 7-12. Quantification of the AChE enzymatic activity in the SH-SY5Y cells cultured for 1 day in the presence of A $\beta$  (at a concentration of 25 $\mu$ M) and of each monosaccharide (at a concentration of 1mM). \*\*\* p < 0.001, \*\* p < 0.01 and \* p < 0.05 (all vs control - 0 $\mu$ M of A $\beta$ ); ## p < 0.01 (vs 25 $\mu$ M A $\beta$ ). In all the cases n=3.



Supplementary Fig. 7-13. Relative densitometric bar graphs of pIRS1 (measured using the WB membrane) expressed by SH-SY5Y cells treated for 1h with A $\beta$  (at a concentration of 25 $\mu$ M) and different concentrations of insulin. In all the cases the results were normalized considering the  $\beta$ -actin expression. (B) Representative WB membranes used for the pIRS1, quantification and  $\beta$ -actin. \*\*\*  $p < 0.001$ , \*\*  $p < 0.01$  and \*  $p < 0.05$  (all vs control - 0 $\mu$ M of A $\beta$ ). In all the cases  $n=3$ .



Supplementary Fig. 7-14. Relative densitometric bar graphs of pIRS1 and pAKT1/AKT1 (measured using the WB membranes) expressed by SH-SY5Y cells treated for 1h with A $\beta$  (at a concentration of 25 $\mu$ M), insulin (using 5nM), and each monosaccharide (at a concentration of 1mM). In all the cases the results were normalized considering the  $\beta$ -actin expression. (B) Representative WB membranes of pIRS1 (S612), pAKT1 (S473), AKT1 total and  $\beta$ -actin expression. \*\*  $p < 0.01$  and \*  $p < 0.05$  (both vs control - 0 $\mu$ M of A $\beta$ ); \*  $p < 0.01$  and \*  $p < 0.05$  (both vs 25 $\mu$ M A $\beta$ );  $\xi$   $p < 0.05$  (vs 5nM of insulin). In all the case  $n=3$ .



Supplementary Fig. 7-15. Relative densitometric bar graphs of Annexin 1 (ANXA1, measured using the WB membranes) expressed by SH-SY5Y cells treated for 1h with A $\beta$  (at a concentration of 25 $\mu$ M), insulin (using 5nM), and each monosaccharide (at a concentration of 1mM). Results were normalized considering the  $\beta$ -actin expression. (B) Representative WB membranes of ANXA1 and  $\beta$ -actin expression. \*\*  $p < 0.01$  and \*  $p < 0.05$  (both vs control - 0 $\mu$ M of A $\beta$ ); #  $p < 0.05$  (vs 25 $\mu$ M A $\beta$ );  $\xi$   $p < 0.05$  (vs 5 nM of insulin). In all the cases  $n=3$ .

#### References

1. Stine, W. B.; Jungbauer, L.; Yu, C.; LaDu, M. J., Preparing synthetic Abeta in different aggregation states. *Methods in molecular biology* (Clifton, N.J.) 2011, 670, 13-32.

## Chapter 8

Surfaces mimicking glycosaminoglycans  
trigger different response of stem cells via  
distinct fibronectin adsorption and  
reorganization



## CHAPTER 8

### Surfaces mimicking glycosaminoglycans trigger different response of stem cells via distinct fibronectin adsorption and reorganization<sup>7</sup>

#### ABSTRACT

We report on the utility of a platform created by self-assembled monolayers to investigate the influence of the degree of sulfation of glycosaminoglycans (GAGs) on their interactions with fibronectin (Fn) and the impact of these interactions on the adhesion and morphology of human adipose derived stem cells (ASCs). We used the label-free QCM-D, AFM and SPR to follow the changes in the adlayer in close proximity to the substrates surface and QCM-D in combination with live imaging to characterize the adherent cells. Our results suggest that Fn interactions with GAGs are governed by both H-bonding and electrostatic forces. While very strong electrostatic interactions cause irreversible change in the protein conformation, the weaker H-bonding restricts only partially the protein flexibility, allowing Fn reorganization and exposure of its binding sites for ASCs adhesion. These findings imply that a delicate balance between these two types of forces must be considered in the design of biomaterials that mimic GAGs.

**Keywords:** Glycosaminoglycans; fibronectin; self-assembling monolayers; adipose-derived stem cells; quartz crystal microbalance with dissipation (QCM-D).

---

<sup>7</sup> This Chapter is based on the publication: "Araújo A. R Soares da Costa D., Amorim S., Reis R. L., Pires R. A., and Pashkuleva I., "Surfaces mimicking glycosaminoglycans trigger different response of stem cells via distinct fibronectin adsorption and reorganization", ACS Applied Materials & Interfaces, vol. 8, issue 42, pp. 28428 - 28436, doi:10.1021/acsami.6b04472, 2016"

## 8.1 INTRODUCTION

The extracellular matrix (ECM) comprises the closest cellular environment: it provides physical supports for cells but also displays significant biochemical information via the molecules secreted by them.[1-3] While the chemical composition, organization and turnover are unique for each cell, ECM of different tissues/cells share some common components, namely proteins and their glycoconjugates (proteoglycans and glycoproteins). Multivalent, supramolecular interactions between these insoluble macromolecules with soluble bioactive counterparts regulate the proper function of the ECM and thus, the development, function and homeostasis of all eukaryotic cells.[2] Besides the importance of these interactions, their study is quite complex not only because they are weak and therefore difficult to measure, but also because of the complex environment in which they occur. Previously, we have developed model surfaces that mimic glycosaminoglycans (GAGs) and we have validated them in studies with cells and growth factors.[4, 5] These substrates are created by self-assembly of alkanethiols with  $-SO_3H$  and  $-OH$  end groups – the main functionalities that are involved in GAGs supramolecular interactions with other bioentities in the physiological milieu. The main advantages of these surfaces are preparation simplicity, well defined surface chemistry and reproducibility.[5, 6] Moreover, the presentation of the functional groups on the surface (no steric hindrance) makes them available for multivalent interactions with an analyte and the compatibility with different characterization techniques (including label-free approaches, such as, surface plasmon resonance, SPR, and quartz crystal microbalance, QCM-D) allows the measurement of these interactions. Indeed, single component or mixed self-assembled monolayers (SAMs) have been widely used to elucidate the effect of surface chemistry, hydrophobicity and/or charge on protein adsorption and the following cellular behavior.[7-14]

In this study, we used SAMs to mimic GAGs with different sulfation degree (simulated by mixing alkanethiol with  $-SO_3H$  and  $-OH$  end groups at different ratios) and to characterize *in situ* their interactions with another ECM component – fibronectin (Fn). Because Fn plays a main role in cell adhesion and growth, we have further investigated the impact of the substrate-protein interactions on the cellular behavior using adipose derived stem cells (ASCs). The use of ASCs have a growing impact in tissue engineering and regenerative medicine fields because of several advantages that they have, such as, multipotential differentiation (similar to bone marrow stem cells), simpler isolation, and much easier access to subcutaneous adipose tissue when compared to bone marrow.[15]

## 8.2 EXPERIMENTAL SECTION

**Chemicals.** Unless otherwise stated, chemicals were purchased from Sigma Aldrich and used without further purification. Human plasma fibronectin (Fn) was purchased from Millipore Iberica.

**Materials.** Gold-coated quartz crystals (QSX301, Q-Sense, Sweden) were used for the QCM-D measurements. Gold-coated sensors (BioNavis, Finland) were used for the SPR characterization. The AFM images were acquired using RFESP tips (Bruker, Germany) with a spring constant of 3 N/m and a resonance frequency of 75 kHz. The substrates used for the live imaging were glass slides uniformly coated with gold (20 nm) by the e-beam physical vapour deposition (ATC Orion series UHV Evaporation system, AJA International Inc.). Titanium (3–5 nm film) was used as a primer improving the adhesion between the gold and the glass. All the substrates were cleaned (piranha solution, 10 min) prior use. The single component and mixed SAMs (S. Fig. 8-1) were formed on the substrates as previously described.[5] Briefly, the cleaned substrates (QCM crystals, SPR sensors and gold-coated glass) were immersed in 20 mM ethanol solution of  $\text{HS}(\text{CH}_2)_{11}\text{OH}$  (samples designated as  $\text{SO}_3\text{H } 0$ ),  $\text{HS}(\text{CH}_2)_{11}\text{SO}_3\text{H}$  (synthesised in our lab[5], designated as  $\text{SO}_3\text{H } 100$ ) or mixture of these at  $-\text{SO}_3\text{H} : -\text{OH}$  ratios of 1 : 3 and 3 : 1 in order to obtain 25% and 75% of  $-\text{SO}_3\text{H}$  groups on the surface (samples referred to as  $\text{SO}_3\text{H } 25$  and  $\text{SO}_3\text{H } 75$ , respectively). After 48 hrs, the coated substrates were washed several times with ethanol, dried under  $\text{N}_2$  and immediately used in the following studies.

**Adipose-derived Stem Cells (ASCs).** ASCs were isolated from human subcutaneous adipose tissue (age range between 20-36 years) obtained from lipoaspiration procedures under the scope of a cooperation agreement with Hospital da Prelada (Porto, Portugal). Aspirates were washed with PBS containing 10% Antibiotic/Antimycotic and then the adipose tissue was digested with a phosphate buffer saline (PBS) solution containing 0.1% collagenase from *Clostridium histolyticum* (Sigma-Aldrich) during 45min at  $37^\circ\text{C}$ , under stirring. The digested tissue was gently pressed through a strainer and centrifuged at 1000  $g$  for 10min. The cell pellet was incubated in lysis buffer (155mM  $\text{NH}_4\text{Cl}$ , 5.7mM  $\text{K}_2\text{HPO}_4$ , 0.1mM EDTA) for 10 min to remove erythrocytes and then centrifuged at 800  $g$  for 10 min. Cells were expanded in  $\alpha$ -modified Eagle's medium (Sigma-Aldrich) supplemented with 1% Antibiotic/Antimycotic (Gibco) and 10% Fetal Bovine Serum (FBS, Gibco).

**Real time monitoring of Fn adsorption by multi-parametric surface plasmon resonance (MP-SPR).** Fn adsorption was followed in real time with a multi-parametric instrument SPR Navi 200 (BioNavis, Finland), equipped with two lasers (670 and 785 nm) in both measurement channels. All measurements

were performed using a full angular scans. The protein adsorption was performed *in situ* by injecting Fn (10  $\mu\text{g}/\text{mL}$  in a serum free  $\alpha\text{-MEM}$ ) at a rate of 50  $\mu\text{L}/\text{min}$ . Upon signal stabilization, a washing step with a serum free  $\alpha\text{-MEM}$  was carried out and the liquid flow was replaced by air. The measurements in air were performed immediately after changing the media (detected by a pronounced shift in the resonance curves to lower angles) to guarantee the preservation of the protein organization. The spectra in  $\alpha\text{-MEM}$  and in air, both at 670 and 785 nm, were fitted using the Winspall software (version 3.02, Max Planck Institute for Polymer Research, Mainz, Germany). SPR angular scans of bare sensor surfaces were simulated first, and the parameters obtained in the fitting of the first layers (glass-chromium-gold) were used in further simulations with the films. The simultaneous determination of both thickness and refractive index (RI) was performed following previously described procedure.[16, 17]

**Characterization of the adsorbed Fn by Atomic force spectroscopy (AFM).** The substrates used in the MP-SPR experiments were removed from the SPR chamber and further analyzed with an atomic force microscope NanoWizard 3 (JPK Instruments, Germany). The measurements were performed in air-dry state in AC mode. Different areas of each substrates with dimensions of 5x5  $\mu\text{m}^2$  and 1x1  $\mu\text{m}^2$  were scanned in order to have representative data. The data were analyzed with the JPK data processing software.

**Real time characterization of protein adsorption by quartz crystal microbalance with dissipation (QCM-D).** The QCM-D experiments were performed with E4 instrument (Q-Sense, Sweden). All the assays were performed at 37  $^{\circ}\text{C}$  and thus, the used solutions were equilibrated at this temperature before being introduced into the measurement chamber. The QCM-D crystals with the SAMs were placed in the QCM-D flow chamber and a stable baseline was acquired by flowing a serum free  $\alpha\text{-MEM}$ . The Fn (10  $\mu\text{g}/\text{mL}$  in a serum free  $\alpha\text{-MEM}$ ) was then added at flow rate of 50  $\mu\text{L}/\text{min}$ . Upon stabilization of the signal, the flow was stopped for 30 min to allow the protein to adsorb. Finally, the sensors were rinsed with  $\alpha\text{-MEM}$  to remove loosely bound material. The resonance frequency shift,  $\Delta f$ , and the dissipative shift,  $\Delta D$ , were recorded at several harmonics ( $n = 3, 5, 7, 9, 11$  and 13). The Voigt model was applied to calculate the adsorbed protein mass, using two overtones (7th and 9th).

**In situ characterization of cell adhesion by quartz crystal microbalance with dissipation (QCM-D).** Immediately after the Fn deposition in the QCM-D (the step described above), ASCs ( $0.20 \times 10^6$  cells/mL) were introduced into the chamber at a flow rate of 150  $\mu\text{L}/\text{min}$ . Upon signal change, the flow was

stopped for 1h to allow cell attachment. Then, the sensors were rinsed with serum free  $\alpha$ -MEM at a rate of 300  $\mu$ L/min. The obtained data are presented as  $\Delta D/\Delta f$  (3<sup>rd</sup> overtone) plots.

**Characterization of cell spreading by live imaging.** The substrates used in these experiments were gold coated glasses modified with single component and mixed SAMs. ASCs (6000 cells/cm<sup>2</sup>) were seeded (serum free  $\alpha$ -MEM) on these substrates under standard conditions either in the absence of Fn or on substrates previously coated with Fn by incubation with protein solution in serum free  $\alpha$ -MEM (10  $\mu$ g/mL) at 37 °C for 30 min. Live monitoring of cell spreading was performed at 37°C in an inverted microscope (Zeiss Axio Observer) equipped with a temperature and CO<sub>2</sub> control device (5% CO<sub>2</sub>). Time-lapse images (20X) were captured every 1 min using Zen software. Cells were continuously observed for 5 h. Image stacks were analysed with image processing software Fiji (<http://fiji.sc/wiki/index.php/Fiji>). The typical cell behaviour for each substrate is shown by images taken at 5 min intervals and up to 45 min culture time as the most significant changes in the cell spreading were observed immediately after seeding.

**Cell characterization by immunocytochemistry.** Cytoskeleton organization and formation of focal adhesion was visualized for cells studied by QCM-D (1 h) and live imaging (1, and 3 hrs). The substrates with the cultured cells were removed from the respective equipment, washed twice with PBS, fixed with 10% neutral buffered formalin for 30 min at 4 °C, permeabilized with 0.1% Triton X-100 in PBS for 5 min, and blocked with 3% BSA in PBS for 30 min at room temperature. Cytoskeleton organization was visualized by phalloidin–TRITC conjugate (1:200 in PBS for 30 min, Sigma). Nuclei were counterstained with 4,6-diamidino-2-phenylindole (DAPI; 1:200 in PBS for 30 min). Formation of actin cap and normal focal adhesions was assessed using a primary antibody against paxillin (1:250 in 1% w/v BSA/PBS, VWR), followed by donkey anti-rabbit Alexafluor-488 (1:500 in 1% w/v BSA/PBS, Alfacene). Samples were washed with PBS, mounted with Vectashield (Vector) on glass slides and observed under an Imager Z1 fluorescence microscope (Zeiss). Photographs were taken with an Axio Cam MRm (Zeiss).

**Statistical Analysis.** The normality of the data was evaluated using Shapiro–Wilk test ( $p < 0.05$ ). When the data did not follow a normal distribution an initial Kruskal–Wallis test was executed followed by Mann–Whitney test. In all the cases, significant variations are marked with (\*) for  $p < 0.001$ .

### 8.3 RESULTS AND DISCUSSION

Fibronectin (Fn, S. Fig. 8-2) is a large size (440 kDa), ubiquitous ECM glycoprotein that can be found around all types of cells and throughout all stages of life. It has several domains (S. Fig. 8-2A) allowing simultaneous binding to cells and other ECM components, namely GAGs, other Fn molecules and other

ECM proteins.[1, 18, 19] While in solution it has a compact globular conformation with a diameter of 16-35 nm[20], around the cells Fn is organized in a network of fibers with a diameter of 2 nm and a length that can vary between 120-180 nm.[3, 18, 20] The assembly of this network is essential for cells and depends on the Fn dimerization via intramolecular disulfide bonds (S. Fig. 8-2B) and the multiple interactions of these dimers with integrins (e.g.  $\alpha 5 \beta 1$  binds to the RGD domain) and with other Fn molecules. It must be noticed that many of the Fn binding sites also have heparin (Hep) binding activity which indicates the involvement of this GAG in cooperative events influencing the interactions of Fn with other ligands. As an example, Hep binds reversibly to Fn type III (S. Fig. 8-2) inducing conformational change that is preserved even after the Hep unbinding.[21] The induced extended conformation reveals new binding sites for growth factors (e.g. VEGF) and thus, increases dramatically the affinity of Fn for these biomolecules.[21, 22] Noteworthy, this interaction is specific for Hep as other sulfated GAGs such as chondroitin sulfate or desulfated Hep do not alter the Fn conformation.[21]

Previous studies have demonstrated that Fn affinity for Hep is relatively low ( $K_D$  about 0.1-1  $\mu\text{M}$ , about 10-1000 folds weaker than the interaction with FGF-2) and based mainly on electrostatic interactions.[23-25] We have therefore created surfaces with an increasing charge density by mixing at different ratios alkanethiols with end groups representing the functionalities present in the GAGs molecules: -OH groups (polar groups, able to participate in H-bonding but with no charge) and  $-\text{SO}_3\text{H}$  groups (negative charge, able to participate in both H-bonding and electrostatic interactions). The self-assembly of these alkanethiols (S. Fig. 8-1, single component or mixtures) result in the formation of homogeneous SAMs with different charge (S. Table 8-1).[4, 5]

Next, we investigated *in situ* the interaction of Fn with these surfaces using QCM-D and MP-SPR. QCM-D is an acoustic method in which the material deposition and/or increasing of a film thickness affects the propagation of a wave through a sensor (quartz crystal disk) and causes changes of its resonance frequency ( $\Delta f$ ). Acoustic contrast is largely affected by coupled water and/or conformational changes. Change in the energy dissipation ( $\Delta D$ ) reflects this sensitivity and is measured by continuous switch on and off of the driving potential resulting in the damping of the oscillatory motion. On the other hand, SPR is an optical detection method whose contrast is determined by changes in the RI caused by the deposited film. The SPR signals are therefore proportional to the adsorbed mass and affected minimally by the hydration of the adsorbed entity. We complement these real time characterization techniques with AFM analyses. The space resolution of AFM is much higher in comparison with other microscopies (e.g. electron microscopy) as the force microscopy does not use lenses and thus, the diffraction and aberration are not limiting its spatial resolution. We therefore expected that the

combination of these three label-free techniques will give us a detailed information about the protein adsorption in terms of quantity, homogeneity and conformation.

Our results demonstrated that Fn adsorbs onto all surfaces (Fig. 8-1). Both real time techniques (QCM-D and SPR) showed a rapid initial adsorption that is slowing as the surface coverage increases (Figs. 8-1A, B). The QCM-D and SPR signals do not change upon washing of the adsorbed protein with a buffer indicating stable interactions of Fn with the underlying surface. The quantity of the adsorbed protein is different for the studied surfaces.

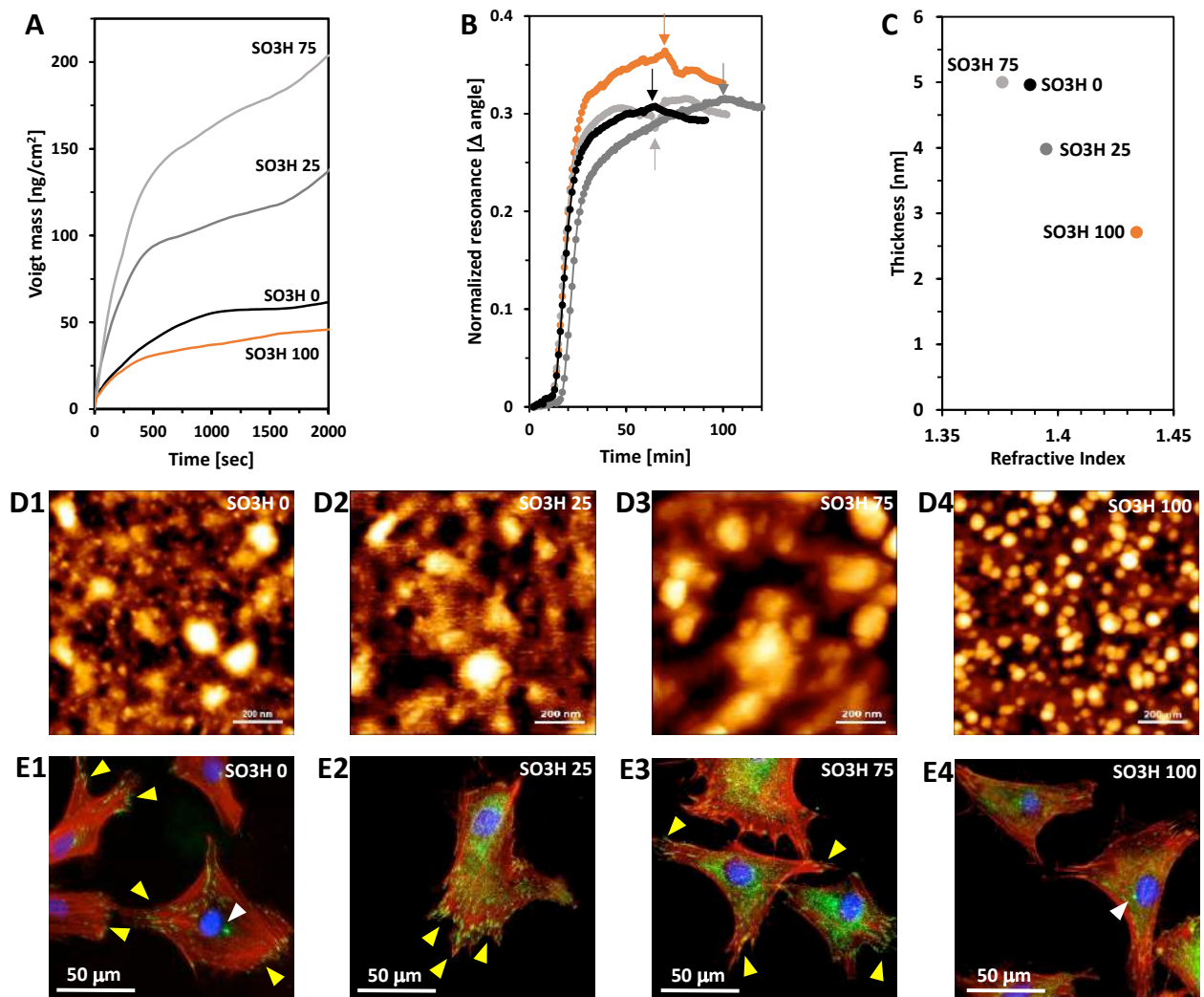


Figure 8-1. Adsorption profiles of Fn on different surfaces characterized by QCM-D (A), SPR (B, C) and AFM (D) and the respective cellular response (E). The sensorgrams (B) were recorded in  $\alpha$ -MEM at wavelength of 670 nm; the arrows indicate the washing step. At the end of the adsorption process the protein layer was characterized by two-color two-media MP-SPR (C) and AFM (D). The immunostaining of the adipose-derived stem cells (ASCs) was performed after recording their behaviour by QCM-D (1h on Fn coated substrates). Immunostaining of paxillin (green), actin (red) and nuclei (blue). White arrows indicate the centrosomes and yellow arrows show the focal adhesions. Images of the control samples (ASCs on QCM-D crystals without Fn) are provided in Fig S7.

The QCM-D data showed an increase of the adsorbed mass with the augmentation of the -SO<sub>3</sub>H concentration - a maximum was reached for the SO3H 75 surface and then a drop to a minimum for the

surface formed by self-assembly of  $\text{HS}(\text{CH}_2)_{11}\text{SO}_3\text{H}$  alone was measured (Fig. 8-1A). The results obtained for the single component systems are in good agreement with previous reports on the quantification of Fn adsorption on surfaces with defined chemistry using alternative characterization methodologies, namely protein radiolabelling[8], conjugation to fluorophores[26, 27] and Western blot characterization[9, 10]. All these studies refer to  $-\text{OH}$  functionalized surfaces as substrates with lower quantity of adsorbed Fn as compared with the hydrophobic  $-\text{CH}_3$ [8-10, 27] and the positively charged  $-\text{NH}_2$ [8, 12]. Moreover, our data are also in excellent agreement with study by Groth *et al*, who measured similar quantity of Fn adsorbed on  $-\text{OH}$  and  $-\text{SO}_3\text{H}$  functionalized surfaces with slight prevalence of protein on the  $-\text{OH}$  surface.[12]

The results obtained from them are striking alike to the reported herein, although the authors have used different methodology for quantification of the adsorbed protein, namely ELISA assays, and screened single component SAMs formed on silanised glass surfaces. Noteworthy, different behavior of  $-\text{SO}_3\text{H}$  groups as compared with other negatively charged groups (e.g.  $-\text{COOH}$ ) is reported in the same study: greater adsorption capacity for Fn and increased cell adhesion is demonstrated for the  $-\text{SO}_3\text{H}$  functionalities. In fact, we have also observed very similar tendency as the described above (Fig. 8-1A) when studying the FGF-2 binding affinity of these substrates (both mixed and single component SAMs).[4] We have demonstrated that the bias behavior of the  $\text{SO}_3\text{H}$  100 is not due to the very high content of  $-\text{SO}_3\text{H}$  groups but rather to the lack of  $-\text{OH}$  groups on these surfaces and their contribution to the adsorption via H-bonding.

As the deposited mass can also include water, we further analyze the Fn adsorption with MP-SPR and AFM. We have used the two-color SPR approach (wavelengths of 670 and 785 nm) combined with two media ( $\alpha$ -MEM and air) measurements to determine simultaneously the RI and the thickness of the deposited layer, i.e. we did not use any estimated or assumed values for the calculations (Fig. 8-1C).[16, 17] The water content and the protein conformation can differ for the Fn adsorbed on the studied substrates and these differences can affect the RI. Therefore, the use of estimated RI values commonly applied for thickness calculations can lead to inaccurate results as they do not reflect this change. Our results demonstrated that while all RI values are near to the used estimated RI for Fn (1.4[20]), substrate chemistry indeed affect the RI of the adsorbed layer (Fig. 8-1C). It is noteworthy mentioning that the only surface, which does not contain  $-\text{OH}$  groups, affect mostly the RI of the adsorbed Fn. This surface chemistry was also associated with the deposition of the thinnest Fn layer (2.7 nm). Previous study has demonstrated that nonspecific Fn adsorption on  $\text{TiO}_x$  surface results in formation of a layer with thickness of about 6 nm while the specific adsorption (biotinylated Fn adsorbed on



streptavidin monolayer) corresponds to a layer with thickness of 2 nm in which the Fn is in its linear conformation.[20] The obtained by us values are within these limits although they are different for each studied substrate (Fig. 8-2C). We therefore have speculated that conformational changes induced upon the protein adsorption can occur. Indeed, the QCM-D derivative plot of the adsorption profiles (S. Fig. 8-3) demonstrated that the process is complex for the surfaces containing both functional groups (SO<sub>3</sub>H 25 and SO<sub>3</sub>H 75). This stepwise process can be explained with an initial rapid absorption, followed by reorganization of the adsorbed protein on the surface that allows further protein molecules to adsorb on the resulted free area.[28] In fact, the adsorption profile of Fn for these two substrates does not reach a plateau (Fig. 8-1A and S. Fig. 8-3) demonstrating that the process of reorganization and additional adsorption is still ongoing. The SO<sub>3</sub>H 0 and SO<sub>3</sub>H 100 surfaces behave different – a simple adsorption profile was observed for these substrates (S. Fig. 8-3). The SPR data however demonstrated that the thickness of the Fn layer on these substrates is quite different. In fact, there is a great deal of research evidencing that substrates surface properties can influence not only the quantity of the adsorbed proteins but also their conformation.[8, 9, 27, 29, 30] The most studied surface property influencing Fn conformation is the wettability: hydrophobic surfaces induce material driven Fn fibrillogenesis while globular conformation is typical for the protein adsorbed on hydrophilic surfaces.[9, 10, 27, 30, 31] Our results are in good agreement with these previous reports. All surfaces studied by us are hydrophilic (S. Table 8-1) and the AFM analysis indeed revealed the expected formation of aggregates of different sizes on all –OH containing surfaces (Fig. 8-1 D1-3). We did not detect any material-induced Fn fibrillogenesis. However, very different organization of the Fn was observed on the SO<sub>3</sub>H 100 substrates (Fig. 8-1 D4) – the formed layer was homogeneous and composed by individual Fn molecules but not aggregates (size of about 1 nm x 30 nm has been previously reported for globular Fn[20]). This peculiar Fn organization is most probably a result of strong electrostatic interactions between the substrate and the protein, which overpower the supramolecular forces that drive the protein self-association. This result is in line with previously reported single-molecule AFM measurements showing yet globular but extended Fn conformation upon its adsorption in the presence of Hep (the biomolecule with the highest negative charge that exist in Nature).[21] This conformational change is related with the sulfate groups as the presence of either chondroitin sulfate (less sulfated than Hep) or the desulfated Hep derivative do not affect the Fn conformation.

Conformational changes can encrypt hidden binding domains[21, 32] and thus, in our next experiments we used ASCs to evaluate the effect of the substrate-protein interactions on the cell attachment process. It is well documented that upon adhesion cells reorganize the Fn into fibrillar

matrices by a complex multistep process involving interactions of the protein with activated integrins on the cell surface.[10, 18, 31, 33, 34] This process often involve inceptive removal of the pre-adsorbed Fn[26, 31, 35] and thus, it depends on the chemistry of the substrate and the respective adsorption force.[31] Altered protein conformation triggered by different surface chemistry also affect the integrin-Fn interactions and the following reorganization of the protein.[10, 36] Indeed, Garcia *et al* have demonstrated that Fn-coated SAMs are integrin specific: Fn on negatively charged surface (-COOH) supports both  $\alpha_v\beta_3$  and  $\alpha_5\beta_1$  binding while the Fn on -OH and -NH<sub>2</sub> surfaces selectively recruits  $\alpha_5\beta_1$  integrins.[8]

Herein, we used a combination of QCM-D, live imaging and immunocytochemistry to assess the cellular interactions with the SAMs and the effect of pre-adsorbed Fn on these interactions. The reason for using QCM-D with microscopy is that cells that look very similar under microscope can have quite different interfacial and mechanical properties and thus, their characterization requires combination of a microscopy with another method. On the other hand, QCM-D is sensitive only to changes that occur very near (nm) to the sensor surface because of the penetration depth of the QCM-D shear wave (the typical penetration depth of the shear acoustic waves in water is about 0.25  $\mu\text{m}$  at  $f = 5$  MHz[37]). Keeping in mind this peculiarity of the QCM-D technique, five processes that can influence the signal have been suggested: (i) the initial physical contact (cell seeding on the sensor surface) leading to the first QCM response; (ii) secretion of ECM components; (iii) cell spreading; (iv) modification of the adhesion properties at the interface, e.g. strength of adhesion and (v) changes in the cytoskeleton.[38] While the first two processes affect significantly the  $\Delta f$ , the last ones are reflected mainly in the magnitude of  $\Delta D$ . It must be noticed that some of these processes often occur simultaneously which makes the interpretation of the QCM-D data quite complex.

We present the QCM-D results as  $\Delta D/\Delta f$  plots (Fig. 8-2). This kind of presentation visualize readily the structural properties of the bilayers deposited on the sensor (e.g. adherent cells) and it is qualitatively independent of the number and spatial distribution of the deposits on the sensor as the shape of the lateral sensitivity variation for  $\Delta D$  and  $\Delta f$  are the same. The slopes in these plots represent the dynamics of the adhesion process and its different stages and thus, they are unique (but reproducible) for each type of cell and substrate and can be used to compare different systems.[39] Because of their specificity, these plots are often called cellular acoustic fingerprints.[37-39]

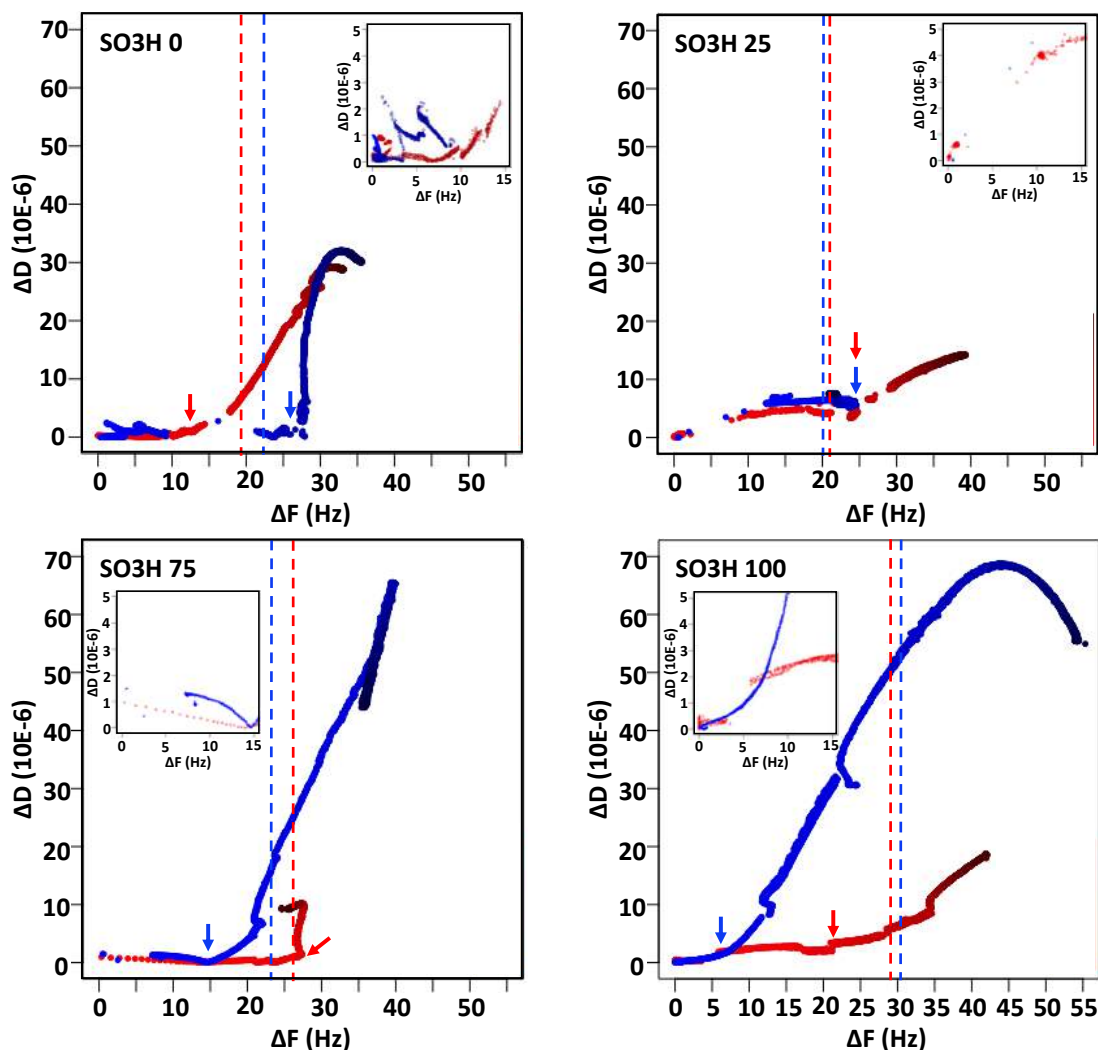
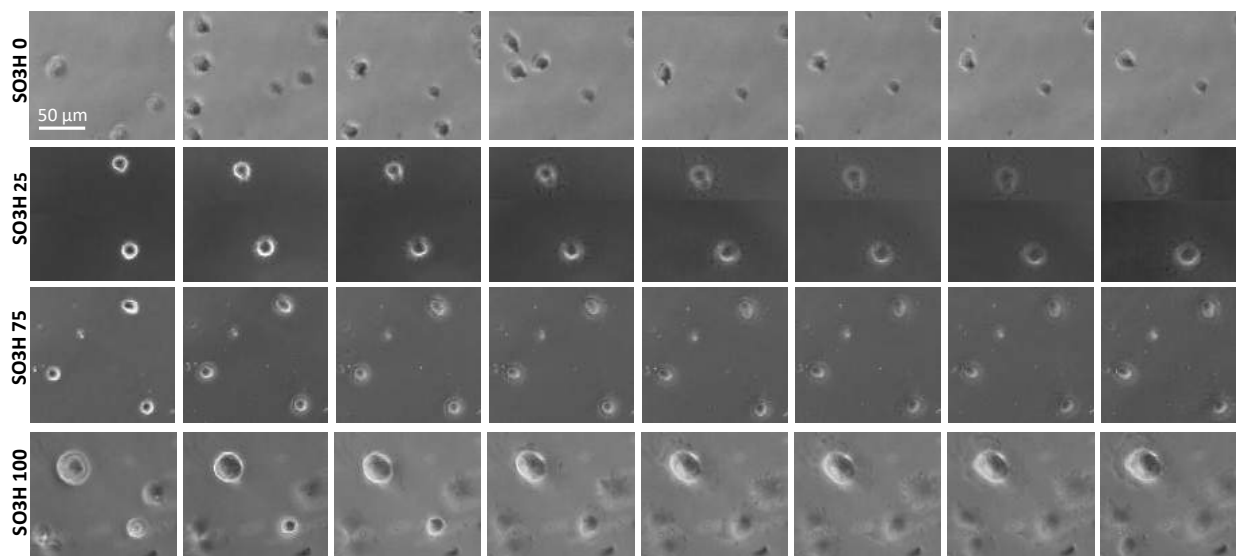


Figure 8-2. Representative  $\Delta D/\Delta f$  plots (3rd overtone) showing changes during adhesion of ASCs onto SAMs' surfaces with different concentration of -SO<sub>3</sub>H groups in the presence (blue points) and in the absence (red points) of Fn on the sensor surface. The broken lines show the points at which the cell flow was stopped. The time is indicated by a colour code: pale colour indicates the beginning of the process while darker nuances are associated with its end. Arrows indicate the end of the cell seeding process. The insets represent amplified data plots for the beginning of the process.

The comparison between the plots for different surfaces in the absence of pre-adsorbed Fn (Fig. 8-2, red lines) demonstrates the presence of at least two slopes with quite different shape, indicating different adhesion process/cellular behavior. The first slope is characterized by a fast (insets on Fig. 8-2: low density of points in  $\Delta D/\Delta f$  plots reveals fast kinetics) and significant increase of  $\Delta f$  with almost no change of  $\Delta D$  and it is associated with the initial cell seeding on the sensors (the end of this process is identified with arrows in Fig. 8-2). After this process, an increasing in the dissipation accompanied with mass deposition was observed for all surfaces. The absolute values of these changes in  $\Delta D$  and  $\Delta f$  are different for all the studied surfaces (S. Fig. 8-6). As mentioned above, the mass deposition at this stage is associated with secretion of proteins and other ECM components, while changes in the dissipation are related with either remodeling of the deposited ECM components or with the mechanical properties of

the seeded cells caused by their interactions with the substrates/sensors. The largest  $\Delta D$  was measured for the SO<sub>3</sub>H 0 surface and we associated it with relative weak cellular adhesion and spreading. When the surfaces have –SO<sub>3</sub>H groups, the absolute value of the  $\Delta D$  is 2-3 fold smaller, indicating that these groups induce different shear elasticity of the cytoskeleton most probably as a result of stronger adhesion. These results are in excellent agreement with the ASCs live imaging, which confirmed that in the absence of pre-adsorbed Fn, the presence of the –SO<sub>3</sub>H groups on the surface induces fast adhesion and spreading of ASCs and this is particularly evident in the case of SO<sub>3</sub>H 100 substrates (Fig. 8-3). The immunocytochemistry of the ASCs (S. Fig. 8-7) is also in line with QCM-D and live imaging outputs: we can observe spread cells on SO<sub>3</sub>H 100 substrates and round ones on the –OH functionalized substrates.

The pre-adsorbed Fn induces a tremendous difference in QCM-D signals (Fig. 8-2, blue lines and S. Fig. 8-6) especially for the -SO<sub>3</sub>H rich surfaces (SO<sub>3</sub>H 75 and SO<sub>3</sub>H 100). Similar large dissipation shifts have been previously observed for different surfaces and cells in the presence of serum or individual serum proteins.[39-41] However, there is no consensus in the literature about the magnitude of this change and the reasons behind it.[37] As mentioned above, cells attached to the sensor surface form acoustically thick layer (up to 15  $\mu$ m in the absence of pre-adsorbed Fn, Fig. 8-4B2).



**Figure 8-3.** Live imaging of adipose-derived stem cells adhering and spreading on the studied substrates without Fn adsorption. The first image was taken 5 min after the cell seeding and the following ones at intervals of 5 min up to 40 min.

In the case of pre-adsorbed protein this layer is even thicker (for QCM-D) with the cells placed above the Fn. We therefore suggest that the main reason behind the observed changes is the above mentioned reorganization of the pre-adsorbed Fn (that is nearest to the sensor surface and form a layer whose thickness is comparable with the penetration depth of the shear acoustic waves) by the attaching cells.

Previous studies have also suggested that the ECM layer between the cells and the sensor can play significant role in the QCM-D output signals.[37, 42] Particularly interesting and indicative are the results for the SO3H 0 substrate. In this case, we observed a large dissipation shift (Fig. 8-2), with no accompanying frequency shift. This signal indicates no production of ECM but only reorganization of pre-adsorbed Fn. Only after reorganizing this layer, cells start to secrete ECM components (changes in  $\Delta f$  are visible) and eventually spread (small change of  $\Delta D$ ). These results are in very good agreement with a recent work of Luo *et al*, who have demonstrated that adsorption force of Fn on  $-OH$  SAMs is much weaker than on hydrophobic ( $-CH_3$ ) and positively charged ( $-NH_2$ ) surfaces.[31] As a result, the protein is more flexible on  $-OH$  functionalized surfaces (SO3H 0) and its cell binding domains (Fig. 8-1) more accessible for interactions with integrins.[8, 31]

The results are different for SO3H 25 substrate: after the initial signal for cell seeding no further changes are detected neither for the deposited mass nor for the energy dissipation. Indeed, for this surface chemistry we have observed already reorganization of the Fn during the deposition (S. Fig. 8-3) and although some further reorganization can occur, the impact on the  $\Delta D$  is very small. In the case of the surfaces with higher content of  $-SO_3H$  groups we observe very large dissipation change concomitant with mass deposition. These signals demonstrate intensive ECM secretion and remodelling.

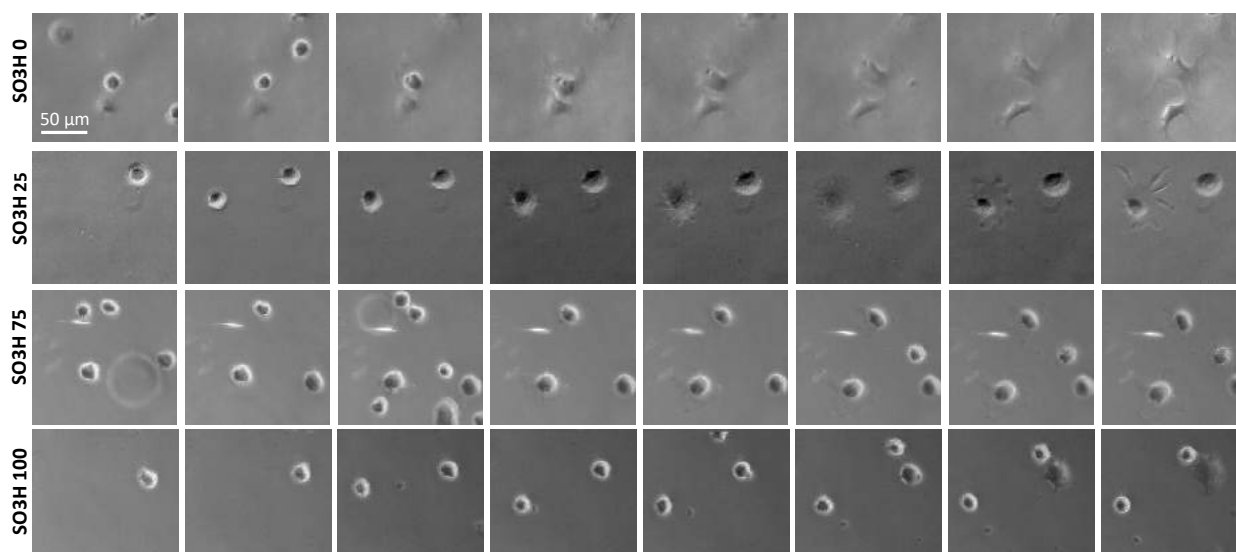


**Figure 8-4.** Live imaging of adipose-derived stem cells seeded on the studied substrates after Fn adsorption. The first image was taken 5 min after the cell seeding and the following ones at intervals of 5 min up to 40 min.

We therefore performed live imaging (Fig. 8-4) to complement the QCM-D data but also to obtain additional information beyond the cell surface properties. This further characterization reveals an opposite effect of the pre-adsorbed Fn on single component systems (SO3H 0 and SO3H 100); while it

promotes cellular adhesion and spreading on  $-OH$  functionalized surfaces, it inhibits these processes on  $-SO_3H$  functionalized ones (Fig. 8-4 first vs last row).

In fact, this behavior is in agreement with the QCM-D data (Fig. 8-2, beside the different absolute values the trend indicated by the red line of the  $SO_3H$  0 is similar to the blue line of the  $SO_3H$  100 and *vice versa*). In the absence of  $-SO_3H$  groups ( $SO_3H$  0), the cells recognize the pre-adsorbed Fn, form initial attachment points via their integrins, reorganize the protein layer that is “hold” on the surface only by weak H-bonding, and spread on the surface remodeled by them.

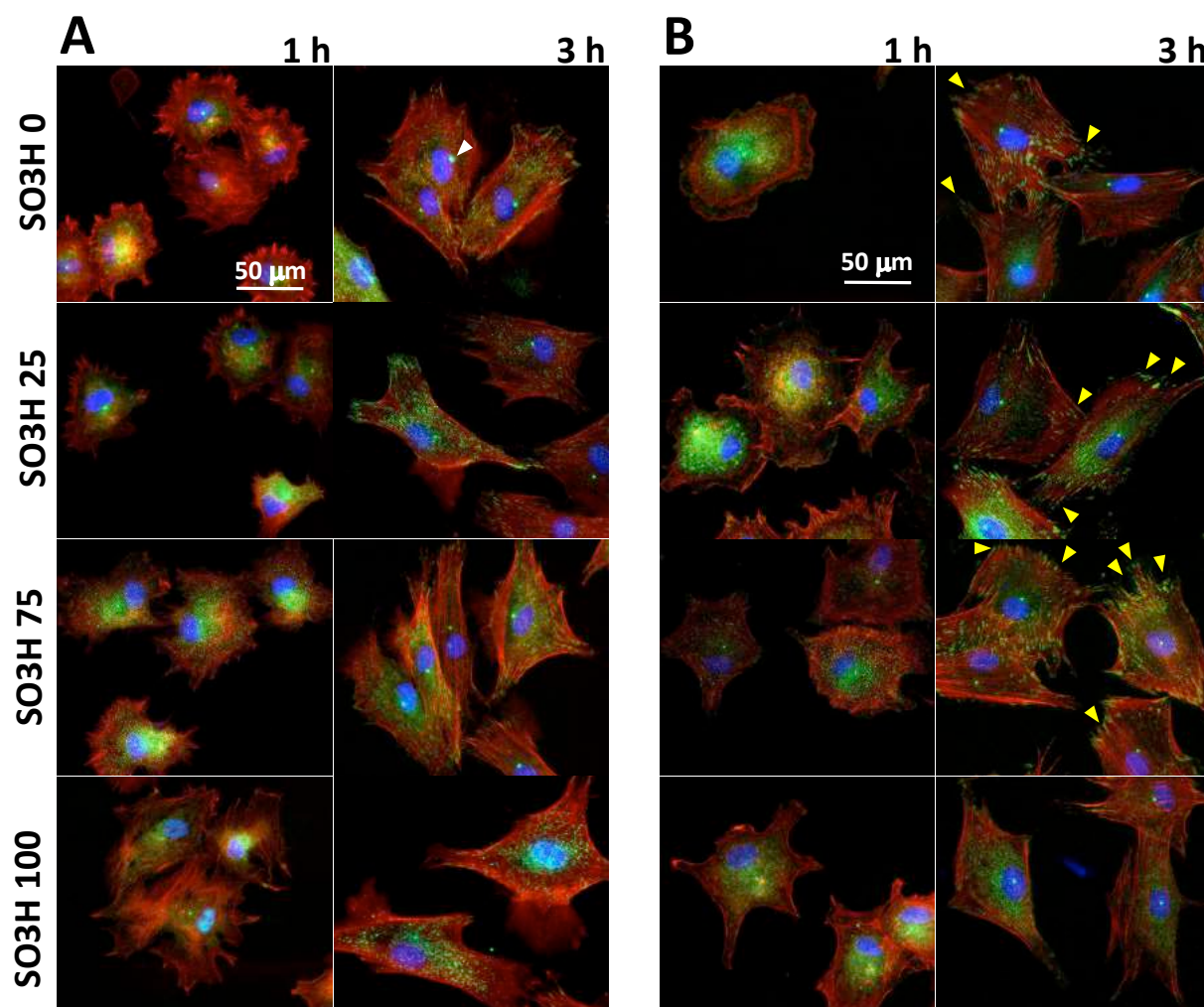


Figure 8-5. Representative fluorescence microscopy images of adipose-derived stem cells cultured on single and mixed SAMs at two different time points: 1 and 3 h without (A) and with (B) Fn. Immunostaining of paxillin (green), actin (red) and nuclei (blue). White arrow indicates centrosome and yellow arrows show the focal adhesions.

On the  $SO_3H$  100 surface, cells either cannot recognize the Fn or they recognize it but, because of the strong electrostatic interactions, cannot reorganize it in order to induce functional integrin binding. When mixed SAMs are used ( $SO_3H$  25 and  $SO_3H$  75) there is a balance between both trends.

These results were corroborated by immunocytochemistry (Figs. 8-1E, 5 and S. Fig. 8-7) and morphometric analysis (S. Fig. 8-8 and 8-9) of ASCs cultured during the QCM-D analysis (Figs 8-1E, S. Fig. 8-7 and 8-8) or at standard static culture conditions used for live imaging (no flow during the Fn adsorption and cell seeding) using gold coated slides as substrates and longer culture times (Figs. 8-5 and S. Fig. 8-9). The immunocytochemistry revealed another difference among the studied substrates: in the presence of Fn, ASCs cultured on –OH containing surfaces (SO<sub>3</sub>H 0, SO<sub>3</sub>H 25 and SO<sub>3</sub>H 75; Fig. 8-1 E1-3 vs S. Fig. 8-7 and Fig. 8-5A vs Fig. 8-5B) displayed organized actin stress fibers with prominent focal adhesion sites (FA). FAs are visible after 1h when the ASCs were cultured in the QCM-D instrument (Fig. 8-1 E1-3, yellow arrows) and after 3h at standard culture conditions (Fig. 8-5B, yellow arrows) suggesting that the flow accelerates and/or amplifies cell response to the surface chemistry. Noteworthy, we did not detect FAs at these time points for the ASCs cultured on SO<sub>3</sub>H 100 substrates in the presence of Fn. Altogether these data suggest different adhesion mechanism of ASCs in response to surface-induced organization/conformational changes of Fn.

#### 8.4 CONCLUSIONS

Our results demonstrate that QCM-D analysis provides unique information about the nanoscale interactions of cells with underlying surfaces. However, we suggest that in the presence of proteins and especially in the case of protein(s) pre-adsorbed on the substrate, the QCM-D data circumscribe mainly the reorganization of this protein layer, i.e. contribution of the cells' viscoelastic properties to the QCM signals is diminished because of the increased distance between the cells and the sensor.

We further demonstrate that tailored –SO<sub>3</sub>H concentration can be apply to finely tune environments around the cells by changing GAGs-protein interactions. Our data suggests that fully sulfonated surfaces alter the bioactivity of proteins as Fn, by binding them stronger. The delicate balance between different supramolecular interactions (e.g. the H-bonding and electrostatic interactions discussed above) that govern the bioactivity and the responsiveness of the closest cellular environment should be considered in the design of biomaterials that mimic this milieu.

#### 8.5 REFERENCES

1. Mouw, J.K., G.Q. Ou, and V.M. Weaver, Extracellular matrix assembly: a multiscale deconstruction. *Nature Reviews Molecular Cell Biology*, 2014. 15(12): p. 771-785.
2. Azevedo, H.S. and I. Pashkuleva, Biomimetic supramolecular designs for the controlled release of growth factors in bone regeneration. *Advanced Drug Delivery Reviews*, 2015. 94: p. 63-76.

3. Singh, P., C. Carraher, and J.E. Schwarzbauer, Assembly of Fibronectin Extracellular Matrix. *Annual Review of Cell and Developmental Biology*, 2010. 26: p. 397-419.
4. Amorim, S., et al., Interactions between Exogenous FGF-2 and Sulfonic Groups: in Situ Characterization and Impact on the Morphology of Human Adipose-Derived Stem Cells. *Langmuir*, 2013. 29(25): p. 7983-7992.
5. da Costa, D.S., et al., Sulfonic groups induce formation of filopodia in mesenchymal stem cells. *Journal of Materials Chemistry*, 2012. 22(15): p. 7172-7178.
6. Love, J.C., et al., Self-assembled monolayers of thiolates on metals as a form of nanotechnology. *Chemical Reviews*, 2005. 105(4): p. 1103-1169.
7. Lan, M.A., et al., Myoblast proliferation and differentiation on fibronectin-coated self assembled monolayers presenting different surface chemistries. *Biomaterials*, 2005. 26(22): p. 4523-4531.
8. Keselowsky, B.G., D.M. Collard, and A.J. Garcia, Surface chemistry modulates fibronectin conformation and directs integrin binding and specificity to control cell adhesion. *Journal of Biomedical Materials Research Part A*, 2003. 66A(2): p. 247-259.
9. Llopis-Hernandez, V., et al., Role of Surface Chemistry in Protein Remodeling at the Cell-Material Interface. *Plos One*, 2011. 6(5).
10. Rico, P., et al., Substrate-Induced Assembly of Fibronectin into Networks: Influence of Surface Chemistry and Effect on Osteoblast Adhesion. *Tissue Engineering Part A*, 2009. 15(11): p. 3271-3281.
11. Keselowsky, B.G., D.M. Collard, and A.J. Garcia, Integrin binding specificity regulates biomaterial surface chemistry effects on cell differentiation. *Proceedings of the National Academy of Sciences of the United States of America*, 2005. 102(17): p. 5953-5957.
12. Altankov, G., K. Richau, and T. Groth, The role of surface zeta potential and substratum chemistry for regulation of dermal fibroblasts interaction. *Materialwissenschaft Und Werkstofftechnik*, 2003. 34(12): p. 1120-1128.
13. Mrksich, M. and G.M. Whitesides, Using self-assembled monolayers to understand the interactions of man-made surfaces with proteins and cells. *Annual Review of Biophysics and Biomolecular Structure*, 1996. 25: p. 55-78.
14. Faucheux, N., et al., Self-assembled monolayers with different terminating groups as model substrates for cell adhesion studies. *Biomaterials*, 2004. 25(14): p. 2721-2730.
15. Gimble, J.M., A.J. Katz, and B.A. Bunnell, Adipose-derived stem cells for regenerative medicine. *Circ Res*, 2007. 100(9): p. 1249-1260.

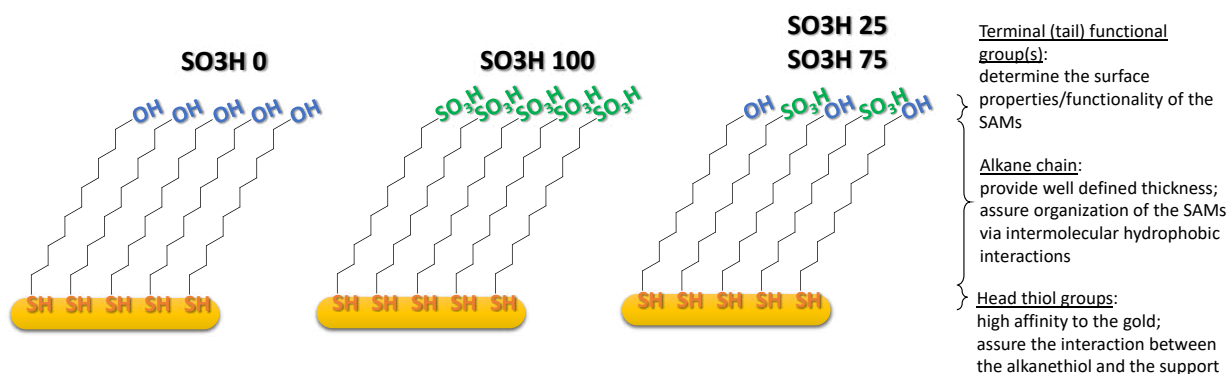


16. Liang, H., et al., Surface plasmon resonance instrument as a refractometer for liquids and ultrathin films. *Sensors and Actuators B: Chemical*, 2010. 149(1): p. 212-220.
17. Teixeira, R., R.L. Reis, and I. Pashkuleva, Influence of the sulfation degree of glycosaminoglycans on their multilayer assembly with poly-L-lysine. *Colloids Surf B Biointerfaces*, 2016. 145: p. 567-575.
18. Schwarzbauer, J.E. and D.W. DeSimone, Fibronectins, Their Fibrillogenesis, and In Vivo Functions. *Cold Spring Harbor Perspectives in Biology*, 2011. 3(7).
19. Bloom, L., K.C. Ingham, and R.O. Hynes, Fibronectin regulates assembly of actin filaments and focal contacts in cultured cells via the heparin-binding site in repeat III13. *Molecular Biology of the Cell*, 1999. 10(5): p. 1521-1536.
20. Lehnert, M., et al., Adsorption and Conformation Behavior of Biotinylated Fibronectin on Streptavidin-Modified TiO<sub>2</sub> Surfaces Studied by SPR and AFM. *Langmuir*, 2011. 27(12): p. 7743-7751.
21. Mitsi, M., et al., Heparin-mediated conformational changes in fibronectin expose vascular endothelial growth factor binding sites. *Biochemistry*, 2006. 45(34): p. 10319-10328.
22. Hubbard, B., et al., Heparin-dependent regulation of fibronectin matrix conformation. *Matrix Biology*, 2014. 34: p. 124-131.
23. Yamada, K.M., et al., Characterization of Fibronectin Interactions with Glycosaminoglycans and Identification of Active Proteolytic Fragments. *Journal of Biological Chemistry*, 1980. 255(13): p. 6055-6063.
24. Evington, J.R.N., M. Luscombe, and J.J. Holbrook, Interaction of Plasma Fibronectin with Heparin and Heparan-Sulfate. *Biochemical Society Transactions*, 1985. 13(1): p. 243-244.
25. Benecky, M.J., et al., Evidence That Binding to the Carboxyl-Terminal Heparin-Binding Domain (Hep-I) Dominates the Interaction between Plasma Fibronectin and Heparin. *Biochemistry*, 1988. 27(19): p. 7565-7571.
26. Altankov, G., F. Grinnell, and T. Groth, Studies on the biocompatibility of materials: Fibroblast reorganization of substratum-bound fibronectin on surfaces varying in wettability. *Journal of Biomedical Materials Research*, 1996. 30(3): p. 385-391.
27. Gugutkov, D., et al., Fibronectin activity on substrates with controlled -OH density. *Journal of Biomedical Materials Research Part A*, 2010. 92A(1): p. 322-331.
28. Roach, P., D. Farrar, and C.C. Perry, Interpretation of protein adsorption: Surface-induced conformational changes. *Journal of the American Chemical Society*, 2005. 127(22): p. 8168-8173.

29. Baugh, L. and V. Vogel, Structural changes of fibronectin adsorbed to model surfaces probed by fluorescence resonance energy transfer. *Journal of Biomedical Materials Research Part A*, 2004. 69A(3): p. 525-534.
30. Rico, P., et al., Material-Driven Fibronectin Assembly Promotes Maintenance of Mesenchymal Stem Cell Phenotypes. *Advanced Functional Materials*, 2016.
31. Lin, M., et al., Adsorption force of fibronectin on various surface chemistries and its vital role in osteoblast adhesion. *Biomacromolecules*, 2015. 16(3): p. 973-84.
32. Llopis-Hernandez, V., et al., Material-driven fibronectin assembly for high-efficiency presentation of growth factors. *Science advances*, 2016. 2(8): p. e1600188.
33. Baneyx, G. and V. Vogel, Self-assembly of fibronectin into fibrillar networks underneath dipalmitoyl phosphatidylcholine monolayers: Role of lipid matrix and tensile forces. *Proceedings of the National Academy of Sciences of the United States of America*, 1999. 96(22): p. 12518-12523.
34. Faucheux, N., et al., The dependence of fibrillar adhesions in human fibroblasts on substratum chemistry. *Biomaterials*, 2006. 27: p. 234-245.
35. Grinnell, F., Focal Adhesion Sites and the Removal of Substratum-Bound Fibronectin. *Journal of Cell Biology*, 1986. 103(6): p. 2697-2706.
36. Garcia, A.J., M.D. Vega, and D. Boettiger, Modulation of Cell Proliferation and Differentiation through Substrate-dependent Changes in Fibronectin Conformation. *Molecular Biology of the Cell*, 1999. 10: p. 785-798.
37. Tymchenko, N., et al., Reversible Changes in Cell Morphology due to Cytoskeletal Rearrangements Measured in Real-Time by QCM-D. *Biointerphases*, 2012. 7(1-4).
38. Fredriksson, C., et al., The piezoelectric quartz crystal mass and dissipation sensor: A means of studying cell adhesion. *Langmuir*, 1998. 14(2): p. 248-251.
39. Fredriksson, C., et al., In vitro real-time characterization of cell attachment and spreading. *Journal of Materials Science-Materials in Medicine*, 1998. 9(12): p. 785-788.
40. Lord, M.S., et al., Extracellular matrix remodelling during cell adhesion monitored by the quartz crystal microbalance. *Biomaterials*, 2008. 29(17): p. 2581-2587.
41. Nimeri, G., et al., Neutrophil interaction with protein-coated surfaces studied by an extended quartz crystal microbalance technique. *Colloids and Surfaces B-Biointerfaces*, 1998. 11(5): p. 255-264.
42. Nileback, E., et al., Acoustic monitoring of changes in well-defined hyaluronan layers exposed to chondrocytes. *Analyst*, 2014. 139(21): p. 5350-5353.

## SUPPLEMENTARY INFORMATION

- Formation and characterization of the self-assembled monolayers (SAMs)



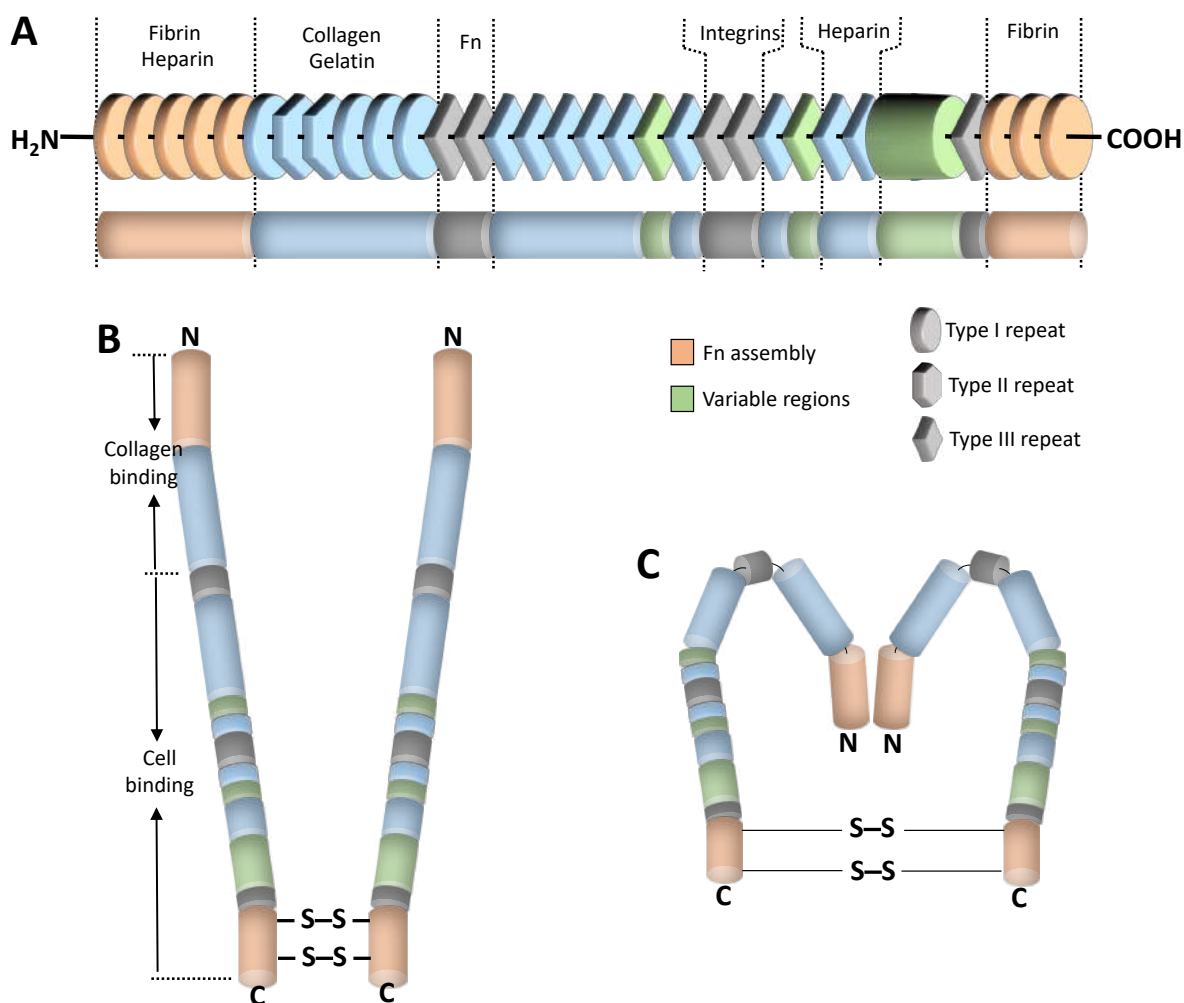
Supplementary Fig. 8-1. Schematic presentation of the used single component and mixed self-assembled monolayers (SAMs). The role of each component of the alkanethiols in the final assembly is highlighted.

Supplementary Table 8-1 Characteristics of the SAM coated surfaces used in this work

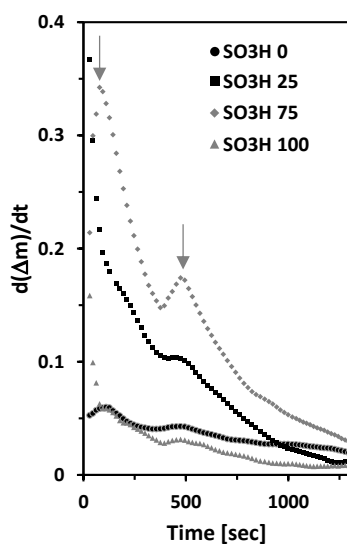
Sample	$\zeta$ potential at pH 7.4 [4]	Oxidized sulfur (XPS) (% of total sulfur content) [5]		Water contact angle (°) [4]
		Theoretical	Calculated	
SO3H 0	-64	0.0	0.0	21
SO3H 25	-75	20.0	20.6	18
SO3H 75	-81	42.9	29.9	32
SO3H 100	-89	50.0	52.6	41

Gold surface 81°.

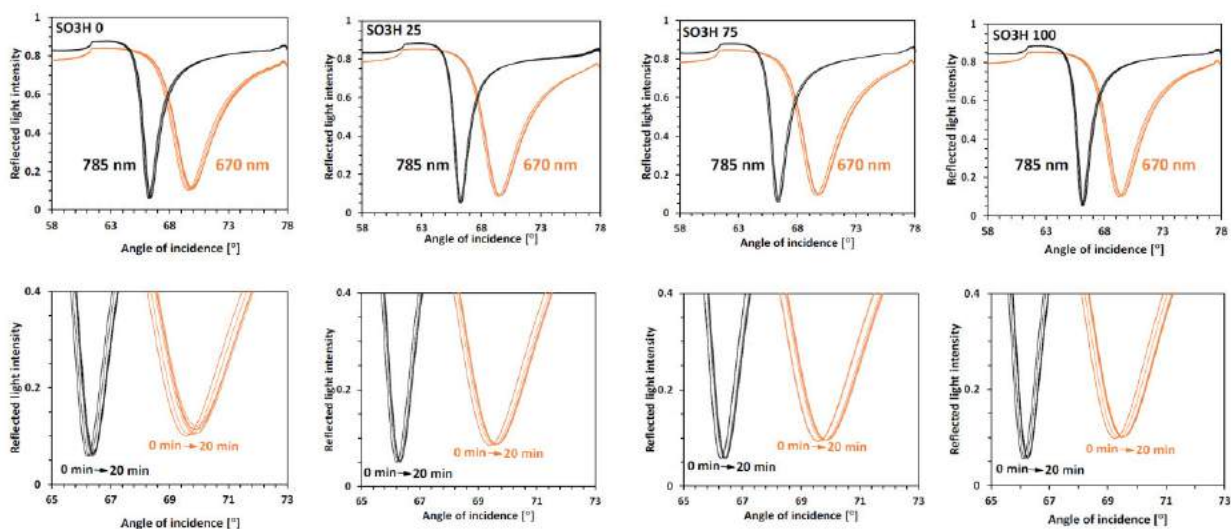
### ▪ Fibronectin (Fn) adsorption



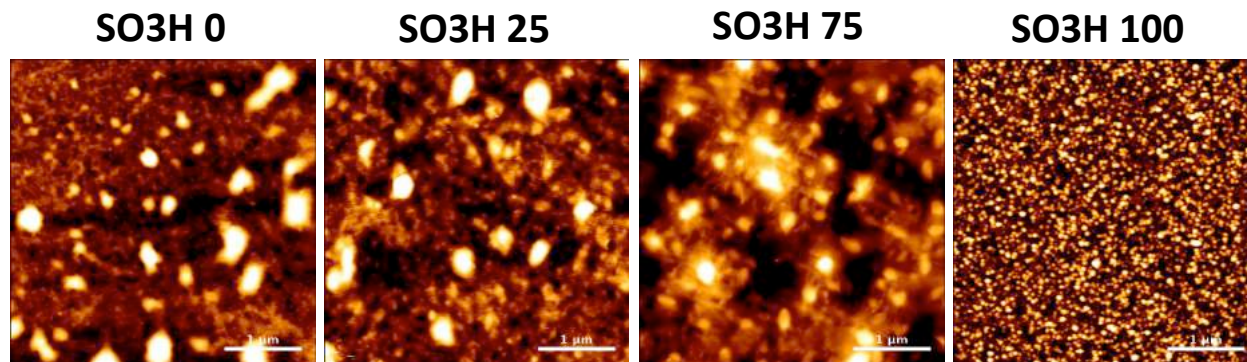
Supplementary Fig. 8-2. Schematic presentation of Fn structure and its domains to which ECM molecules and cell surface receptors bind (A). The Fn molecules form dimers via disulphide bonds (B) which are further deformed (C) to reveal binding sites for cell surface receptors. Adapted with permission from reference[1]. 2014, Nature Publishing Group.



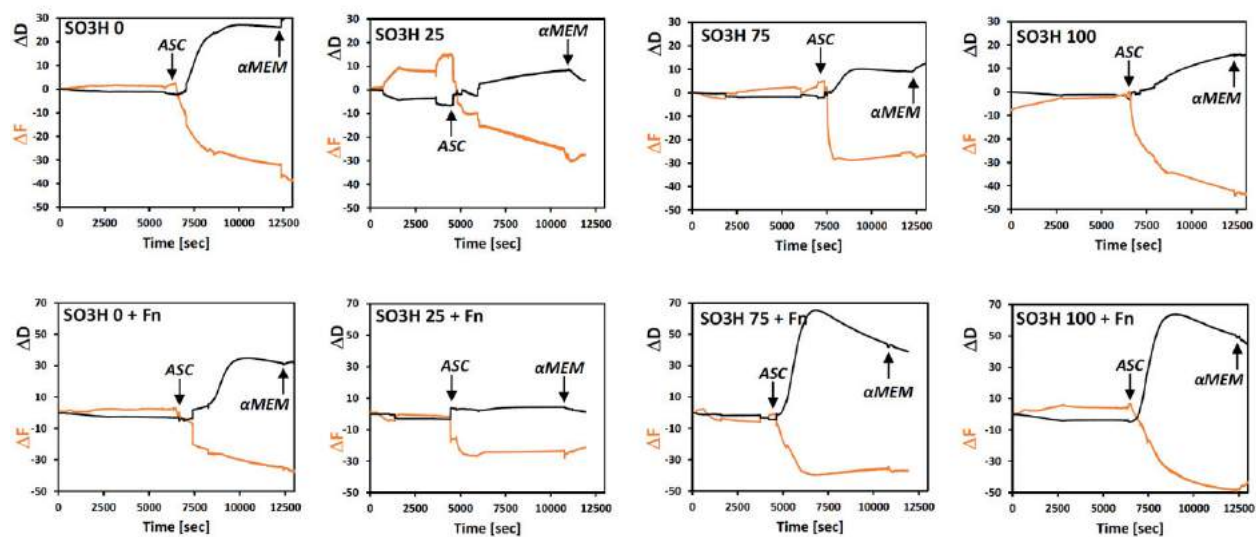
Supplementary Fig. 8-3 The QCM-D derivative plot with the initial adsorption profiles of Fn onto the studied substrates demonstrates simple, one step protein adsorption on surfaces made from a single component SAMs and complex, multistage adsorption process on surfaces containing both  $-\text{SO}_3\text{H}$  and  $-\text{OH}$  functional groups.



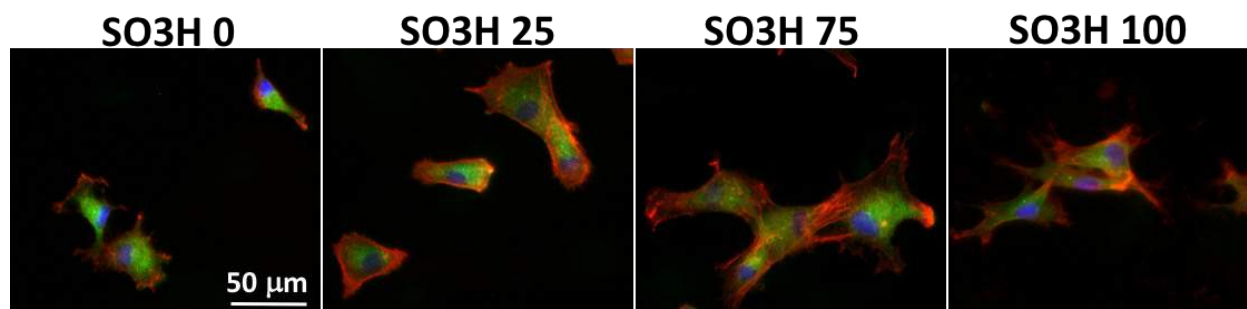
Supplementary Fig. 8-4 Reflectivity curves (SPR curves) of the fibronectin adsorption onto different substrates at two wavelengths (670 and 785 nm).



Supplementary Fig. 8-5. Representative AFM images of fibronectin adsorbed on different self-assembled monolayers.

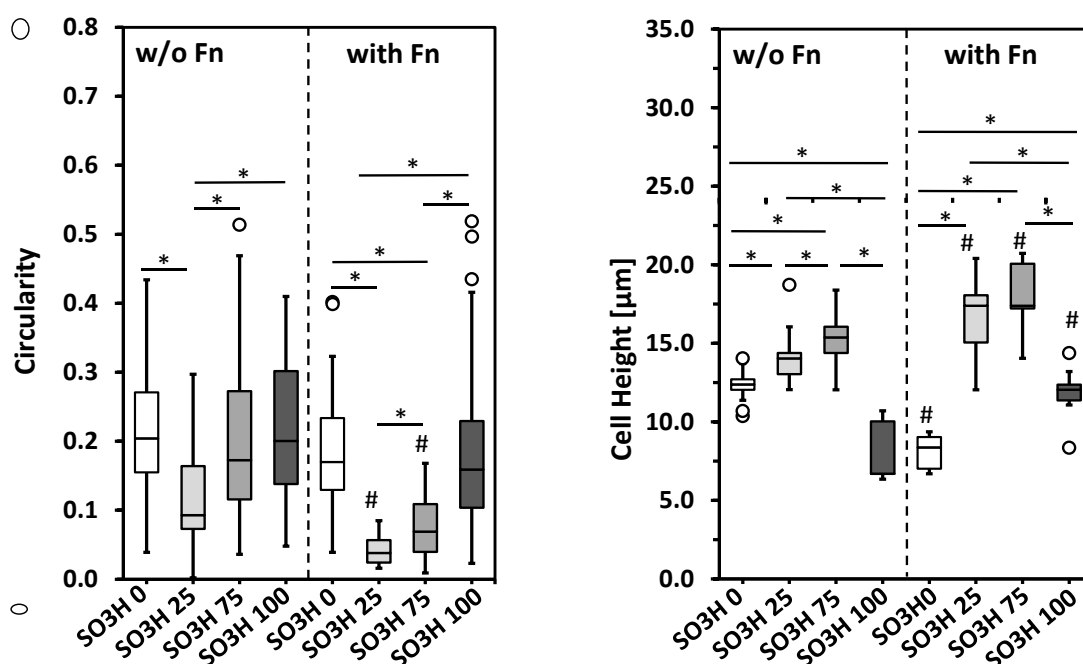


Supplementary Fig. 8-6. Raw data QCM-D data showing frequency and dissipation shifts measured during adipose-derived stem cells adhesion on different substrates without (up) and with (down) pre-adsorbed fibronectin.

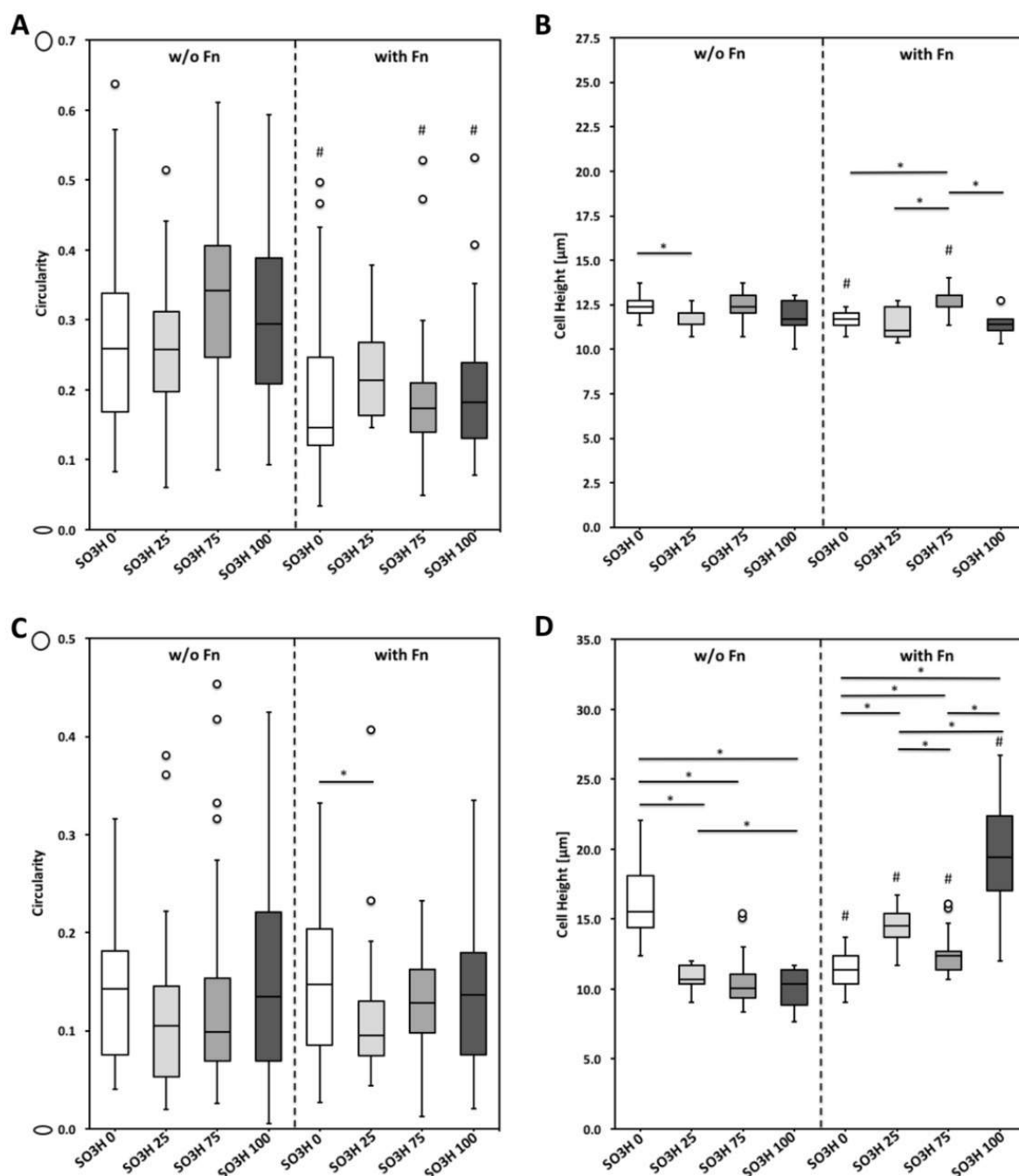


Supplementary Fig. 8-7. Immunostaining of adipose-derived stem cells (ASCs) after QCM-D characterization (1h in the QCM-D cell) in the absence of Fn. Spread cells with well pronounced actin fibers and numerous filopodia can be seen on  $-\text{SO}_3\text{H}$  rich surfaces (SO3H 75 and SO3H 100). No focal adhesion can be appreciated for any of the studied surfaces at these conditions. Paxillin (green), actin (red) and nuclei (blue).

**Cell morphometric analysis.** Cells characterized by immunocytochemistry were further subjected to morphometric analysis. The samples were observed under confocal laser scanning microscope (TCS SP8 Leica; objective x63). Z-scans were performed using phalloidin and DAPI stainings to determine the cell limits. Cell morphometric analysis was performed with image processing package Fiji.<sup>4</sup> At least 50 cells per condition were analyzed.



Supplementary Fig. 8-8. Morphometric analysis of ASCs on QCM-D crystals (1h) with different surface concentration of  $-\text{SO}_3\text{H}$  groups in the absence and presence of pre-adsorbed Fn. Significant differences ( $p \leq 0.001$ ) are marked with \* for different surface compositions and with # for the same surface compositions but different Fn content.



Supplementary Fig. 8-9 Morphometric analysis of ASCs cultured under standard conditions on single and mixed SAMs (in the presence and absence of Fn). Circularity (A,C) and cell height (B,D) are depicted for 1h (A, B) and 7h (C, D) of cell culture, respectively. Statistical analysis was executed using Kruskal–Wallis test followed by the Mann–Whitney test, where  $p < 0.001$  was deemed to be significant (\*). The symbol # represents statistically significant difference ( $p < 0.001$ ) between cells cultured on SAMs of equal surface chemistry but with and without the deposition of Fn.



**References**

1. Amorim, S.; Pires, R. A.; da Costa, D. S.; Reis, R. L.; Pashkuleva, I., Interactions between Exogenous FGF-2 and Sulfonic Groups: in Situ Characterization and Impact on the Morphology of Human Adipose-Derived Stem Cells. *Langmuir* 2013, 29 (25), 7983-7992.
2. da Costa, D. S.; Pires, R. A.; Frias, A. M.; Reis, R. L.; Pashkuleva, I., Sulfonic groups induce formation of filopodia in mesenchymal stem cells. *J Mater Chem* 2012, 22 (15), 7172-7178.
3. Mouw, J. K.; Ou, G. Q.; Weaver, V. M., Extracellular matrix assembly: a multiscale deconstruction. *Nat Rev Mol Cell Biol* 2014, 15 (12), 771-785.
4. <http://fiji.sc/wiki/index.php/Fiji>

## SECTION IV

## Chapter 9

### General conclusions and Final remarks

## CHAPTER 9

### GENERAL CONCLUSIONS AND FINAL REMARKS

The increased life expectancy, as well as the lifestyle of the population, which includes dietary habits and physical activity, are known factors that influence the onset and progression of a variety of diseases, such as cancer, neurodegenerative disorders, cardiovascular conditions, among many others. Epidemiological studies have shown that the intake of anti-oxidants, *e.g.* vitamin E, EGCG, among others (through the diet) is linked to healthier conditions, *e.g.* higher cognitive performance in the aged population. In addition, a large set of studies evaluating multiple potential therapeutic strategies have identified polyphenols as a class of bioactive molecules (present in a series of foods and drinks) that are able to generate health benefits. As an example, the polyphenol EGCG, is known to present anti-bacterial, anti-amyloidogenic and anti-tumour activity. Despite its mechanism of action not being completely understood, it is clear that, its chemical structure present key moieties, *e.g.* galloyl (Ga) units, that are fundamental players in their cytocompatibility and bioactivity. This has been proven, for example, by the higher anti-amyloidogenic bioactivity of EGCG in comparison with EGC [1] is due to the presence of the Ga units in the EGCG chemical structure, and their absence in EGC.

Based on this background knowledge, we started by extracting and purifying polyphenols from cork powder to evaluate their bioactive potential. We were able to collect a series of cork-based polyphenol-rich extracts and isolated two of the most prevalent ones, *i.e.* vescalagin and castalagin. We then evaluated their ability to act as anti-bacterial, anti-UV or anti-amyloidogenic agents, while trying to correlate bioactivity with their main structural features.

Therefore, in chapter 3, we investigated the potential of cork-based extracts/compounds as anti-bacterial agents against three Gram-positive bacteria, *i.e.* MRSE, SA and MRSA; as well as one Gram-negative bacterium, *i.e.* PA. All extracts/compounds, but especially vescalagin/castalagin, exhibited a higher capacity to alter the normal assembly of the peptidoglycans present in the bacterial cell wall (particularly in the Methicillin-resistant bacterial strains) leading to their disruption; it was also shown that vescalagin/castalagin were efficient inhibitors of biofilm formation; promoting an overall bacteria cell death. Despite the existence of different open questions concerning their mechanism of action, it was clearly demonstrated that vescalagin/castalagin are able to interfere with the PBP2a-mediated stabilization of the peptidoglycan layer at the bacterial cell wall of Methicillin-resistant bacteria (as the PBP2a protein takes a critical role in the crosslinking of the peptidoglycan mesh-like layer at the cell surface). In addition, they are also able to inhibit the formation of  $\beta$ -sheet supramolecular assemblies, that are crucial to support the biofilm formation and the bacterial cell wall functional integrity.

In chapter 4, a series of cork-based extracts (obtained by refluxing cork powder under water, *i.e.* CWE, or water:ethanol 50:50 mixture, *i.e.* CWEE) were evaluated for their ability to protect fibroblast-like cells (*i.e.* L929) from UV-mediated cellular damage. In this case the high anti-oxidant capacity of the compounds present in the extracts was a key-player in controlling the UV-mediated toxicity, as it was demonstrated its correlation with the capacity to decrease the concentration of UV-triggered ROS in the cellular milieu. Highest anti-UV activity was obtained by a purified cork fraction (fCWEE) that presented both the highest anti-oxidant activity and the highest concentration of vescalagin/castalagin, supporting the idea that the presence of these two polyphenols is critical to achieve the described outcome. Importantly, the CWE extract (with lower anti-oxidant activity than fCWEE, but with a significant amount of vescalagin/castalagin) showed an anti-UV capacity comparable to fCWEE. In general, cork extracts were able to: i) reduce the UV-mediated cell toxicity; ii) maintain healthy cellular morphology upon UV radiation; and iii) protect DNA from UV-mediated fragmentation. These data favor the hypothesis that vescalagin/castalagin are able to trigger other protective mechanisms, in addition to the ROS-based pathways.

After showing that vescalagin/castalagin were important bioactive components present in the cork-based extracts, we evaluated their ability to act in the context of neurodegenerative disorders, *i.e.* Alzheimer's disease (AD). Consequently, in chapter 5, we evaluated if vescalagin/castalagin (isolated and purified from cork powder) were able to reduce the cytotoxicity of A $\beta$  oligomeric structures and the deposition of A $\beta$  senile plaques, which are known hallmarks of AD. In this case, we tested both compounds in their ability to remodel the secondary structure of toxic A $\beta$  oligomers and to protect SH-SY5Y cells from A $\beta$ -mediated death. We showed that vescalagin is more prone than castalagin to interact with A $\beta$  and remodel its secondary structure from antiparallel  $\beta$ -sheets (characteristic of the cytotoxic oligomers) to parallel  $\beta$ -sheets (characteristic of the non-cytotoxic fibrils). This difference might be a consequence of the spatial organization of their OH group, at the C1 position of the glycosidic chain (previously reported to be determinant for the higher reactivity of vescalagin, as well as its increased polarity and lower lipophilicity). Thus, we found that vescalagin was able to inhibit the A $\beta$  supramolecular assembly through the production of off-pathway structures, as well as reducing the A $\beta$  cytotoxicity towards the SH-SY5Y neuroblastoma cell line.

The anti-amyloidogenic activity of vescalagin led us to evaluate if we could recapitulate its activity by presenting its main chemical moiety, *i.e.* Ga units, in the surface of a dendrimer. We then synthesized in chapter 6 three Ga-presenting dendrimers with two, six and nine Ga units in their surface and evaluated if they were able to modulate the cytotoxicity of oligomeric A $\beta$  species. We found that all the dendrimers interacted with A $\beta$  at their Glu, Ala and Val residues by H-bonding and were able to remodel the A $\beta$

supramolecular organization into non-cytotoxic aggregates in a Ga-mediated process, *i.e.* the terminal-ends groups of the dendrimers. In addition, the synthesized dendrimers were able to mimic the bioactivity of vescalagin. Importantly, the multivalent presentation of the Ga chemical motifs increases their capacity to remodel the A $\beta$  secondary structure. In particular, the 2G1-GaOH dendrimer (presenting six Ga units) displayed an adequate balance between the number of Ga units and hydrophilicity, maximizing the interaction with the Glu, Ala, and Val residues, reducing the presence of oligomeric A $\beta$  and lowering its cytotoxicity *in vitro*. These relevant *in vitro* results support the further evaluation of the efficacy of 2G1-GaOH against A $\beta$ -mediated cytotoxicity under an *in vivo* AD model.

In chapter 7, we evaluated the potential of glucosamine (GlcN) analogues for their capacity to complement the activity of vescalagin/castalagin/Ga-presenting dendrimers and recover cells from a number of A $\beta$ -mediated pathological features. We found that glucosamine-6-sulphate (GlcN6S) and glucosamine-6-phosphate (GlcN6P) were able to promote the recovery of AD-related dysfunctions, namely by reducing membrane dysfunction (and the homeostasis of Ca<sup>2+</sup> ions); normalizing the AChE enzymatic activity; re-establishing the basal levels of insulin signaling, through the activation of the IRS1 cascade; and reducing inflammation, by levelling the expression of ANXA1. Our results (obtained for GlcN6S and GlcN6P) are consistent with the important role of the negative charge of these monosaccharides in the interaction with A $\beta$  and in the reduction of its cytotoxicity.

Finally, in chapter 8, we studied the influence of the sulfation degree of GAGs in the presentation and bioactivity of fibronectin (Fn). We developed a self-assembling monolayer (SAM) system capable of presenting different sulfation degrees on a surface. The interaction of Fn with these surfaces was assessed, suggesting that fully sulfonated surfaces alter the bioactivity of Fn, by stronger binding and limiting its bioactive presentation to the surface, hampering its interaction with cells. Therefore, during the design of biomaterials, it should be considered a proper balance of non-covalent interactions between their surface and proteins (*e.g.* Fn) to allow the latter ones to be presented under a bioactive conformation to the cells.

Overall, the scientific achievements presented in this thesis pave the way to the development of vescalagin/castalagin-based strategies to promote anti-bacterial, anti-UV and anti-amyloidogenic bioactivities. From a chemical and biological perspective, our results contributed to a better understanding on the mechanism of action of the anti-bacterial and anti-amyloidogenic activities of these polyphenols (in both the bacteria cell wall and in the modulation of A $\beta$  cytotoxicity). We also demonstrated that it is possible to recapitulate the anti-amyloidogenic activity presented by vescalagin/castalagin using well defined synthetic dendrimers that mimic the presentation of their main chemical moiety, *i.e.* Ga units.

The combination of vesicalagin/castalagin/Ga-presenting dendrimers with GlcN6S or GlcN6P seems an interesting approach to tackle several AD hallmarks, as they presented complementary bioactivities. A possibility that should be explored in the future. In addition, we also hypothesize that the development of dendrimers presenting specific monosaccharide units (*e.g.* GlcN6S/GlcN6P) can generate multivalent nanosystems (*e.g.* dendrimers) able to efficiently remodel A $\beta$ , as well as reduce its cytotoxicity and the pathological hallmarks of AD and other neurodegenerative disorders.

## References

1. Bastianetto, S., et al., Neuroprotective effects of green and black teas and their catechin gallate esters against  $\beta$ -amyloid-induced toxicity. *European Journal of Neuroscience*, 2006. 23(1): p. 55-64.

